AECL EACL
AECL Research EACL Recherche

AECL-10714, COG-93-4

The Disposal of Canada's Nuclear Fuel Waste: The Vault Model for Postclosure Assessment

Le stockage permanent des déchets de combustible nucléaire du Canada : Le modèle d'installation souterraine pour l'évaluation de post-fermeture

L.H. Johnson, D.M. LeNeveu, D.W. Shoesmith D.W. Oscarson, M.N. Gray,
R.J. Lemire, N.C. Garisto

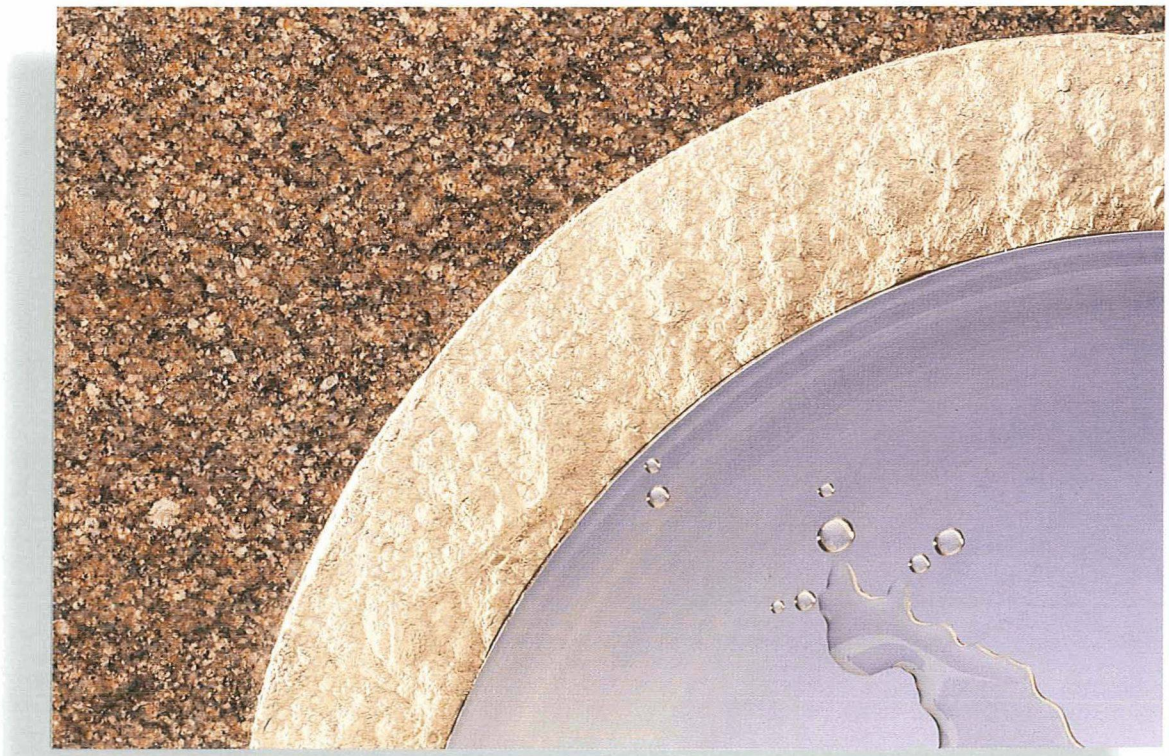

February 1994 février

AECL RESEARCH

THE DISPOSAL OF CANADA'S NUCLEAR FUEL WASTE: THE VAULT MODEL FOR POSTCLOSURE ASSESSMENT

by

L.H. Johnson, D.M. LeNeveu, D.W. Shoesmith,
D.W. Oscarson, M.N. Gray, R.J. Lemire,* N.C. Garisto**

* AECL Research
Chalk River Laboratories
Chalk River, ON K0J 1J0

** Beak Consultants Limited
14 Abacus Road
Brampton, ON L6T 5B7

The Canadian Nuclear Fuel Waste Management Program is funded jointly by AECL and Ontario Hydro under the auspices of the CANDU Owners Group.

Whiteshell Laboratories
Pinawa, Manitoba R0E 1L0
1994

AECL-10714
COG-93-4

LE STOCKAGE PERMANENT DES DÉCHETS DE COMBUSTIBLE NUCLÉAIRE DU CANADA : LE MODÈLE D'INSTALLATION SOUTERRAINE POUR L'ÉVALUATION DE POST-FERMETURE

par

L.H. Johnson, D.M. LeNeveu, D.W. Shoesmith
D.W. Oscarson, M.N. Gray, R.J. Lemire et N.C. Garisto

RÉSUMÉ

Le concept de stockage permanent des déchets de combustible nucléaire du Canada comporte la mise en place des déchets dans une installation creusée à une profondeur de 500 à 1 000 m dans la roche plutonique du Bouclier canadien. On isolerait les déchets solides de la biosphère par un système de barrières multiples composé de barrières ouvragées (artificielles), dont des conteneurs résistants à la corrosion et des matériaux de scellement d'étanchéité à base d'argile et de ciment, et de la barrière naturelle assurée par la formation géologique massive. On documente la possibilité de réalisation technique de ce concept et son impact sur l'environnement et la santé de l'être humain dans une Étude d'impact sur l'environnement (EIE) qu'on soumettra à des fins d'examen dans le cadre du Processus fédéral d'évaluation et d'examen en matière d'environnement. Le présent rapport est l'un d'une série de neuf documents de référence principaux d'EIE. On y décrit le modèle d'installation qui sert à calculer la libération, dépendante du temps, des contaminants radioactifs et non radioactifs du système de barrières ouvragées (installation) à la roche environnante (géosphère). Les calculs par modèle qui sont présentés concernent une installation de référence particulière qui renferme des grappes de combustible usé de réacteurs CANDU (CANada Deutérium Uranium) confinées dans des conteneurs de titane de nuance 2, lesquels seraient mis en place dans des trous forés du sol d'une excavation minée située à une profondeur de 500 m dans la roche plutonique. Les conteneurs seraient entourés d'un retardateur tassé composé d'un mélange de 50 % en poids de sable et 50 % en poids de bentonite. Les chambres de stockage permanent et les galeries seraient scellées de façon étanche au moyen d'une couche de mélange de remblai composé de 25 % d'argile de lac glaciaire et de 75 % de granit concassé et d'une couche sus-jacente de retardateur.

Le modèle d'installation est un programme de calcul des temps de rupture des conteneurs de titane, de la vitesse de libération des radionucléides des grappes de combustible usé aux eaux souterraines qui pénétreraient dans les conteneurs rendus défectueux et de la vitesse de migration des radionucléides du combustible à la roche environnante par le retardateur et le remblai saturés d'eaux souterraines. Ce modèle se sert des valeurs de paramètres distribuées ou probabilistes pour tenir compte de l'incertitude et de la variabilité. En décrivant le modèle, on met l'accent en particulier sur la compréhension mécaniste des processus conduisant à la libération et sur l'explication de la base de sélection des valeurs de paramètres dont se sert le modèle.

On examine la fiabilité du modèle d'installation quant à la vérification par des calculs indépendants, l'évaluation des résultats de recherche et des modèles fondamentaux, l'emploi d'hypothèses prudentes, les intercomparaisons de programmes de calcul et l'assurance de la qualité et l'échelle de temps proposée de 10 000 ans pour l'évaluation quantitative du risque.

Dans les cas où on a considéré qu'il ne convient pas d'inclure en particulier certains processus au modèle d'installation (par ex. la criticité nucléaire ou la production de gaz), on donne la justification de l'exclusion des processus ainsi que les résultats des analyses complémentaires.

Les renseignements concernant le modèle d'installation indiquent qu'il est prudent et qu'il convient à la description du comportement à long terme des barrières ouvragées d'une installation de stockage permanent des déchets de combustible nucléaire.

Le Programme canadien de gestion des déchets de combustible nucléaire est financé en commun par EACL et Ontario Hydro sous les auspices du Groupe des propriétaires de réacteurs CANDU.

EACL Recherche
Laboratoires de Whiteshell
Pinawa (Manitoba) R0E 1L0
1994

AECL-10714
COG-93-4

THE DISPOSAL OF CANADA'S NUCLEAR FUEL WASTE: THE VAULT MODEL FOR POSTCLOSURE ASSESSMENT

by

L.H. Johnson, D.M. LeNeveu, D.W. Shoesmith,
D.W. Oscarson, M.N. Gray, R.J. Lemire, N.C. Garisto

ABSTRACT

The concept for disposal of Canada's nuclear fuel waste involves emplacing the waste in a vault excavated at a depth of 500 to 1000 m in plutonic rock of the Canadian Shield. The solid waste would be isolated from the biosphere by a multibarrier system consisting of engineered barriers, including corrosion-resistant containers and clay- and cement-based sealing materials, and the natural barrier provided by the massive geological formation. The technical feasibility of this concept, and its impact on the environment and human health, is being documented in an Environmental Impact Statement (EIS) that will be submitted for review under the federal Environmental Assessment and Review Process. The present report is one of nine EIS primary references. The report describes the vault model, which is used to calculate the time-dependent release of radioactive and non-radioactive contaminants from the engineered barrier system (vault) into the surrounding rock (geosphere). The model calculations presented are for a specific reference vault design that comprises used CANDU (CANada Deuterium Uranium) fuel bundles in Grade-2 titanium containers, which would be emplaced in boreholes in the floor of a mined excavation located at a depth of 500 m in plutonic rock. The containers would be surrounded by a compacted buffer material that is a mixture of 50 wt.% sand and 50 wt.% bentonite. Disposal rooms and tunnels would be sealed with a layer of backfill mixture composed of 25% glacial lake clay and 75% crushed granite and an overlying layer of buffer material.

The vault model is a computer code that calculates the failure times of titanium containers, the rate of release of radionuclides from used-fuel bundles into the groundwater that would flow into the failed containers, and the rate of transport of radionuclides from the fuel through the groundwater-saturated buffer and backfill materials and into the surrounding rock. The vault model uses distributed or probabilistic parameter values to account for both uncertainty and variability. In describing the model, particular emphasis is placed on the mechanistic understanding of the processes leading to radionuclide release and on explaining the basis for selection of the parameter values used in the model.

The reliability of the vault model is discussed in terms of verification through independent calculations; the evaluation of research data and underlying models; the use of conservative assumptions, code intercomparisons and quality assurance; and the proposed 10 000-a time scale for quantitative risk assessment.

For those situations where it was considered inappropriate to specifically include certain processes in the vault model (e.g., nuclear criticality, or gas generation), the justification for excluding the process and the results of supplementary analyses are provided.

The information presented on the vault model indicates that it is a conservative model that is appropriate for describing the long-term performance of engineered barriers in a nuclear fuel waste disposal vault.

The Canadian Nuclear Fuel Waste Management Program is funded jointly by AECL and Ontario Hydro under the auspices of the CANDU Owners Group.

AECL Research
Whiteshell Laboratories
Pinawa, Manitoba R0E 1L0
1994

AECL-10714
COG-93-4

PREFACE

In 1992, 15% of the electricity generated in Canada was produced using CANDU nuclear reactors. A by-product of the nuclear power is used CANDU fuel, which consists of ceramic uranium dioxide pellets and metal structural components. Used fuel is highly radioactive. The used fuel from Canada's power reactors is currently stored in water-filled pools or dry storage concrete containers. Humans and other living organisms are protected by isolating the used fuel from the natural environment and by surrounding it with shielding material. Current storage practices have an excellent safety record.

At present, used CANDU fuel is not reprocessed. It could, however, be reprocessed to extract useful material for recycling, and the highly radioactive material that remained could be incorporated into a solid. The term "nuclear fuel waste," as used by AECL, refers to either

- the used fuel, if it is not reprocessed, or

- a solid incorporating the highly radioactive waste from reprocessing.

Current storage practices, while safe, require continuing institutional controls such as security measures, monitoring, and maintenance. Thus storage is an effective interim measure for protection of human health and the natural environment but not a permanent solution. A permanent solution is disposal, a method "in which there is no intention of retrieval and which, ideally, uses techniques and designs that do not rely for their success on long-term institutional control beyond a reasonable period of time" (AECB 1987).

In 1978, the governments of Canada and Ontario established the Nuclear Fuel Waste Management Program "... to assure the safe and permanent disposal" of nuclear fuel waste. AECL was made responsible for research and development on "... disposal in a deep underground repository in intrusive igneous rock" (Joint Statement 1978). Ontario Hydro was made responsible for studies on interim storage and transportation of used fuel and has contributed to the research and development on disposal. Over the years a number of other organizations have also contributed to the Program, including Energy, Mines and Resources Canada; Environment Canada; universities; and companies in the private sector.

The disposal concept is to place the waste in long-lived containers; emplace the containers, enveloped by sealing materials, in a disposal vault excavated at a nominal depth of 500 to 1000 m in intrusive igneous (plutonic) rock of the Canadian Shield; and (eventually) seal all excavated openings and exploration boreholes to form a passively safe system. Thus there would be multiple barriers to protect humans and the natural environment from contaminants in the waste: the container, the very low-solubility waste form, the vault seals, and the geosphere. The disposal technology includes options for the design of the engineered components, including the disposal container, disposal vault, and vault seals, so that it is adaptable to a wide range of regulatory standards, physical conditions, and

social requirements. Potentially suitable bodies of plutonic rock occur in a large number of locations across the Canadian Shield.

In developing and assessing this disposal concept, AECL has consulted broadly with members of Canadian society to help ensure that the concept and the way in which it would be implemented are technically sound and represent a generally acceptable disposal strategy. Many groups in Canada have had opportunities to comment on the disposal concept and on the waste management program. These include government departments and agencies, scientists, engineers, sociologists, ethicists, and other members of the public. The Technical Advisory Committee to AECL on the Nuclear Fuel Waste Management Program, whose members are nominated by Canadian scientific and engineering societies, has been a major source of technical advice.

In 1981, the governments of Canada and Ontario announced that "... no disposal site selection will be undertaken until after the concept has been accepted. This decision also means that the responsibility for disposal site selection and subsequent operation need not be allocated until after concept acceptance" (Joint Statement 1981).

The acceptability of the disposal concept is now being reviewed by a federal Environmental Assessment Panel, which is also responsible for examining a broad range of issues related to nuclear fuel waste management (Minister of the Environment, Canada 1989). After consulting the public, the Panel issued guidelines to identify the information that should be provided by AECL, the proponent of the disposal concept (Federal Environmental Assessment Review Panel 1992).

AECL is preparing an Environmental Impact Statement to provide information requested by the Panel and to present AECL's case for the acceptability of the disposal concept. A Summary will be issued separately. This report is one of nine primary references that summarize major aspects of the disposal concept and supplement the information in the Environmental Impact Statement. A guide to the contents of the Environmental Impact Statement, the Summary, and the primary references follows this Preface.

In accordance with the 1981 Joint Statement of the governments of Canada and Ontario, no site for disposal of nuclear fuel waste is proposed at this time. Thus in developing and assessing the disposal concept, AECL could not design a facility for a proposed site and assess the environmental effects to determine the suitability of the design and the site, as would normally be done for an Environmental Impact Statement. Instead, AECL and Ontario Hydro have specified illustrative "reference" disposal systems and assessed those.

A "reference" disposal system illustrates what a disposal system, including the geosphere and biosphere, might be like. Although it is hypothetical, it is based on information derived from extensive laboratory and field research. Many of the assumptions made are conservative, that is, they would tend to overestimate adverse effects. The technology specified is either available or judged to be readily achievable. A reference disposal system includes one possible choice among the options for such things as the waste form, the disposal container, the vault layout, the vault seals, and the system for transporting nuclear fuel waste to a disposal facility.

The components and designs chosen are not presented as ones that are being recommended but rather as ones that illustrate a technically feasible way of implementing the disposal concept.

After the Panel has received the requested information, it will hold public hearings. It will also consider the findings of the Scientific Review Group, which it established to provide a scientific evaluation of the disposal concept. According to the Panel's terms of reference "As a result of this review the Panel will make recommendations to assist the governments of Canada and Ontario in reaching decisions on the acceptability of the disposal concept and on the steps that must be taken to ensure the safe long-term management of nuclear fuel wastes in Canada" (Minister of the Environment, Canada 1989).

Acceptance of the disposal concept at this time would not imply approval of any particular site or facility. If the disposal concept is accepted and implemented, a disposal site would be sought, a disposal facility would be designed specifically for the site that was proposed, and the potential environmental effects of the facility at the proposed site would be assessed. Approvals would be sought in incremental stages, so concept implementation would entail a series of decisions to proceed. Decision-making would be shared by a variety of participants, including the public. In all such decisions, however, safety would be the paramount consideration.

The EIS, Summary, and Primary References

Environmental Impact Statement on the Concept for Disposal of Canada's Nuclear Fuel Waste (AECL 1994a)
Summary of the Environmental Impact Statement on the Concept for Disposal of Canada's Nuclear Fuel Waste (AECL 1994b)
The Disposal of Canada's Nuclear Fuel Waste: Public Involvement and Social Aspects (Greber et al. 1994)
The Disposal of Canada's Nuclear Fuel Waste: Site Screening and Site Evaluation Technology (Davison et al. 1994a)
The Disposal of Canada's Nuclear Fuel Waste: Engineered Barriers Alternatives (Johnson et al. 1994)
The Disposal of Canada's Nuclear Fuel Waste: Engineering for a Disposal Facility (Simmons and Baumgartner 1994)
The Disposal of Canada's Nuclear Fuel Waste: Preclosure Assessment of a Conceptual System (Grondin et al. 1994)
The Disposal of Canada's Nuclear Fuel Waste: Postclosure Assessment of a Reference System (Goodwin et al. 1994)
The Disposal of Canada's Nuclear Fuel Waste: The Vault Model for Postclosure Assessment (Johnson et al. this volume)
The Disposal of Canada's Nuclear Fuel Waste: The Geosphere Model for Postclosure Assessment (Davison et al. 1994b)
The Disposal of Canada's Nuclear Fuel Waste: The Biosphere Model, BIOTRAC, for Postclosure Assessment (Davis et al. 1993)

GUIDE TO THE CONTENTS OF THE ENVIRONMENTAL IMPACT STATEMENT, THE SUMMARY, AND THE PRIMARY REFERENCES

ENVIRONMENTAL IMPACT STATEMENT AND SUMMARY

Environmental Impact Statement on the Concept for Disposal of Canada's Nuclear Fuel Waste (AECL 1994a)

- provides an overview of AECL's case for the acceptability of the disposal concept

- provides information about the following topics:
  - the characteristics of nuclear fuel waste
  - storage and the rationale for disposal
  - major issues in nuclear fuel waste management
  - the disposal concept and implementation activities
  - alternatives to the disposal concept
  - methods and results of the environmental assessments
  - principles and potential measures for managing environmental effects
  - AECL's overall evaluation of the disposal concept

Summary of the Environmental Impact Statement on the Concept for Disposal of Canada's Nuclear Fuel Waste (AECL 1994b)

- summarizes the contents of the Environmental Impact Statement

PRIMARY REFERENCES

The Disposal of Canada's Nuclear Fuel Waste: Public Involvement and Social Aspects (Greber et al. 1994)

- describes the activities undertaken to provide information to the public about the Nuclear Fuel Waste Management Program and to obtain public input into the development of the disposal concept

- presents the issues raised by the public and how the issues have been addressed during the development of the disposal concept or how they could be addressed during the implementation of the disposal concept

- discusses social aspects of public perspectives on risk, ethical issues associated with nuclear fuel waste management, and principles for the development of a publicly acceptable site selection process

The Disposal of Canada's Nuclear Fuel Waste: Site Screening and Site Evaluation Technology (Davison et al. 1994a)

- discusses geoscience, environmental, and engineering factors that would need to be considered during siting

- describes the methodology for characterization, that is, for obtaining the data about regions, areas, and sites that would be needed for facility design, monitoring, and environmental assessment

The Disposal of Canada's Nuclear Fuel Waste: Engineered Barriers Alternatives (Johnson et al. 1994)

- describes the characteristics of nuclear fuel waste

- describes the materials that were evaluated for use in engineered barriers, such as containers and vault seals

- describes potential designs for containers and vault seals

- describes procedures and processes that could be used in the production of containers and the emplacement of vault-sealing materials

The Disposal of Canada's Nuclear Fuel Waste: Engineering for a Disposal Facility (Simmons and Baumgartner 1994)

- discusses alternative vault designs and general considerations for engineering a nuclear fuel waste disposal facility

- describes a disposal facility design that was used to assess the technical feasibility, costs, and potential effects of disposal (Different disposal facility designs are possible and might be favoured during concept implementation.)

- presents cost and labour estimates for implementing the design

The Disposal of Canada's Nuclear Fuel Waste: Preclosure Assessment of a Conceptual System (Grondin et al. 1994)

- describes a methodology for estimating effects on human health, the natural environment, and the socio-economic environment that could be associated with siting, constructing, operating (includes transporting used fuel), decommissioning, and closing a disposal facility

- describes an application of this assessment methodology to a reference disposal system (We use the term "reference" to designate the disposal systems, including the facility designs, specified for the assessment studies. Different disposal facility designs are possible and might be favoured during concept implementation.)

- discusses technical and social factors that would need to be considered during siting

- discusses possible measures and approaches for managing environmental effects

The Disposal of Canada's Nuclear Fuel Waste: Postclosure Assessment of a Reference System (Goodwin et al. 1994)

- describes a methodology for
  - estimating the long-term effects of a disposal facility on human health and the natural environment,
  - determining how sensitive the estimated effects are to variations in site characteristics, design parameters, and other factors, and
  - evaluating design constraints

- describes an application of this assessment methodology to a reference disposal system (We use the term "reference" to designate the disposal systems, including the facility designs, specified for the assessment studies. Different disposal facility designs are possible and might be favoured during concept implementation.)

The Disposal of Canada's Nuclear Fuel Waste: The Vault Model for Postclosure Assessment (this volume)

- describes the assumptions, data, and model used in the postclosure assessment to analyze processes within and near the buried containers of waste

- discusses the reliability of the data and model

The Disposal of Canada's Nuclear Fuel Waste: The Geosphere Model for Postclosure Assessment (Davison et al. 1994b)

- describes the assumptions, data, and models used in the postclosure assessment to analyze processes within the rock in which a disposal vault is excavated

- discusses the reliability of the data and model

The Disposal of Canada's Nuclear Fuel Waste: The Biosphere Model, BIOTRAC, for Postclosure Assessment (Davis et al. 1993)

- describes the assumptions, data, and model used in the postclosure assessment to analyze processes in the near-surface and surface environment

- discusses the reliability of the data and model

CONTENTS

continued...

CONTENTS (continued)

continued...

CONTENTS (continued)

continued...

CONTENTS (continued)

continued...

CONTENTS (continued)

continued...

CONTENTS (concluded)

LIST OF TABLES

continued...

LIST OF TABLES (continued)

continued...

LIST OF TABLES (concluded)

LIST OF FIGURES

continued...

LIST OF FIGURES (continued)

continued...

LIST OF FIGURES (continued)

continued...

LIST OF FIGURES (continued)

continued...

LIST OF FIGURES (continued)

continued...

LIST OF FIGURES (continued)

continued...

LIST OF FIGURES (continued)

continued...

LIST OF FIGURES (continued)

continued...

LIST OF FIGURES (continued)

continued...

LIST OF FIGURES (continued)

continued...

continued...

LIST OF FIGURES (continued)

continued...

LIST OF FIGURES (concluded)

EXECUTIVE SUMMARY

ES.1 INTRODUCTION

The Canadian Nuclear Fuel Waste Management Program (CNFWMP) was established jointly by the governments of Canada and Ontario in 1978 to develop a method to ensure the safe disposal of fuel waste from Canada's nuclear reactors (Joint Statement 1978). In the disposal concept under consideration, the waste would be immobilized in containers designed to have a minimum lifetime of 500 a; the containers, surrounded by clay-based buffer material, would be placed in a vault excavated at a nominal depth of 500 to 1000 m in plutonic rock of the Canadian Shield. The engineered and natural barriers of this disposal system would isolate the waste from the biosphere, with its humans and other biota, for many years. The long-term performance of such a system must be evaluated to ensure that the objectives of protection of human health and the environment are met.

In this document, we describe the vault model used to simulate the behaviour of the engineered barriers in the conceptual disposal vault in the postclosure phase, when the vault is full and has been decommissioned and sealed. The important processes included in the vault model were identified through a scenario analysis procedure, which involved identifying all possible factors and processes that might affect the isolation of the waste. The analysis procedure indicated that slow degradation of the containers and waste in groundwater, followed by diffusional transport of radionuclides through sealing materials into the surrounding rock, is by far the most probable scenario by which radionuclides might be released from the vault.

Mathematical models have been developed that describe these important processes. They are linked together to form the vault model, which is coupled to the geosphere and biosphere models through an executive code SYVAC (Systems Variability Analysis Code - Generation 3). The data for the models are probabilistic; i.e., for each parameter in the models, a range of values is defined rather than a single value. This allows uncertainty and variability to be taken into account. The output of the SYVAC calculations is a distribution of estimated dose rates to the most exposed group of individuals for various times in the future, which can be compared with quantitative risk criteria established by the Atomic Energy Control Board (AECB 1987). Because insufficient information is available to accurately model some of the significant processes, and because impacts must be assessed far into the future, the models incorporate conservatisms (i.e., they tend to overpredict consequences) and their output should not be considered accurate predictions. Assessment models were developed to describe performance for a period of 10^4 a, although the results are extrapolated to 10^5 a to illustrate trends. Beyond 10^4 a, reasoned arguments are presented outlining the expected performance of the engineered barriers.

ES.2 DESCRIPTION OF THE VAULT SYSTEM

A basic used-fuel disposal centre conceptual design, including both surface and underground facilities, has been described by Simmons and Baumgartner (1994). This design, referred to as the reference design, has been adopted, with some modifications, as the basis for the assessment case study. The case study has been carried out to illustrate the methodology used to assess the long-term performance of a nuclear fuel waste disposal system.

The reference disposal vault design, as modified for the case study, has an overall area of 3.16 km^2 and is assumed to be located at a depth of 500 m. In the design, emplacement rooms have boreholes drilled in the floor to accept titanium containers, each holding 72 used CANDU[1] fuel bundles. The containers are surrounded by a clay-sand mixture (the buffer), and all excavated areas are backfilled with low-permeability clay/crushed granite and clay/sand mixtures. Containers are spaced such that the decay heat leads to a maximum container skin temperature of 94°C. The total mass of fuel for disposal is assumed to be 161 730 Mg U in 118 680 containers, with an average fuel burnup of 685 $GJ \cdot kg^{-1}$ U.

ES.3 EVOLUTION OF NEAR-FIELD CONDITIONS AND MASS TRANSPORT THROUGH CLAY BARRIER MATERIALS

One of the most important functions of the clay-based buffer and backfill materials in the reference disposal system is to slow the rate of groundwater movement and, ultimately, the rate of radionuclide transport when the containers eventually fail. The reference buffer material, which surrounds the containers in the boreholes, is a 1:1 mixture of bentonite and silica sand compacted to a clay dry density of 1.22 $Mg \cdot m^{-3}$. The reference backfill consists of 25% glacial lake clay and 75% crushed granite aggregate. The reference buffer and backfill materials have hydraulic conductivities of $<10^{-11}$ and $<10^{-10}$ $m \cdot s^{-1}$ respectively; thus, diffusion would be the dominant contaminant transport process in the vault. To function as hydraulic barriers, the hydraulic properties of these materials would have to remain unaffected by transient effects caused by heat from the waste containers and eventual resaturation of the disposal vault environment with groundwater.

During the period immediately after container, buffer and backfill emplacement, the heat generated by the waste would cause moisture to move away from the containers; hence, some drying of the buffer would occur. During the same period, the water pressure at the buffer/rock and backfill/rock interfaces would increase, and saturation of the sealing materials would gradually occur. The time for resaturation might vary from several years

---

[1] CANada Deuterium Uranium, registered trademark of AECL.

to more than 1000 a, depending on the hydraulic conductivity of the surrounding rock. A final buffer swelling pressure of 1 to 2 MPa is expected once saturation is complete.

The temperature at the container/buffer interface is expected to reach a maximum of 94°C under saturated conditions. If resaturation was slow, the migration of moisture away from the container could result in a temperature maximum of ~105°C. Any cracking of the buffer as a result of shrinkage due to drying is expected to reseal as the buffer swells during resaturation. The backfill materials, which would ultimately reach a somewhat lower maximum temperature than the buffer, would also generate a swelling pressure (approximately 40 kPa) upon resaturation. This should eliminate the existence of voids and ensure that tight contact is maintained at the backfill/rock interface. The swelling and self-sealing properties of the buffer and backfill would ensure that, by the time containers failed, diffusion, rather than convection, would be the only significant mode of transport of radionuclides.

The potential effects of a number of processes on the long-term performance of the buffer and backfill materials as transport barriers have been studied. The gradual conversion of bentonite to illite, a non-swelling clay, has been the focus of laboratory and natural analogue studies. The results indicate that conversion would not occur to any appreciable extent at the relatively low temperatures expected in the disposal vault. As a result, the buffer material would retain its swelling properties.

The possibility of gas production in the vault, in particular H_2 and CH_4, has been examined. The rates of H_2 production from container corrosion and radiolysis are low enough, and the solubility of H_2 in groundwater is sufficiently high, that a gas phase is not expected to form in the vault for ~20 000 a. The rate of production of CH_4 by microbial degradation of inorganic matter in the clay is under study. The rate is expected to be inconsequential, because of the low organic carbon content of the buffer and backfill materials and the limited supply of nutrients for microbial growth.

The reference groundwater assumed for the case study, WR-500, has a composition based on the groundwater found in the Whiteshell Research Area (WRA) at a depth of 500 m. The composition of the groundwater, which has a total dissolved solids content of 11 250 $mg \cdot L^{-1}$, would be modified somewhat by contact with the buffer and backfill materials. The groundwater that ultimately contacted the container and used-fuel bundles would have a pH of ~8. The O_2 initially present in the vault would be consumed over a period of <300 a as a result of reaction with Fe^{2+} released from biotite, which is an important constituent of the crushed granite used in the reference backfill.

The low hydraulic conductivity of the buffer ensures that radionuclides would be transported predominantly by diffusion. The small pore size in the buffer would prevent movement of microbes or radionuclides present in colloidal form.

The diffusional transport of radionuclides in buffer and backfill materials in the vault model is determined largely by the apparent diffusion coefficient, which can be expressed as

$$D_a = \frac{D}{r}$$

where D is the total intrinsic diffusion coefficient, D_a is the apparent diffusion coefficient, and r is the capacity factor, representing storage (porosity) and sorption effects. Diffusion coefficients for the various radionuclides have been determined from the scientific literature and our own experimental studies, in conjunction with expert judgement. They vary over several orders of magnitude, depending on the chemical properties of the radionuclide.

ES.4 LIFETIME MODEL FOR GRADE-2 TITANIUM CONTAINERS

The reference container is a thin-shell (6.35 mm) packed-particulate design constructed from Grade-2 titanium. The container incorporates a basket that holds 72 fuel bundles with glass beads filling void spaces within the container. Analysis has shown that a minimum container wall thickness of 2 mm is required to prevent failure by buckling under an isotropic external loading of 10 MPa. The total load experienced by the container as a result of hydrostatic and buffer swelling pressures is expected to be <7 MPa. A wall thickness of 4.2 mm is therefore assumed to be available as a corrosion allowance, i.e., the wall thickness that can experience localized corrosion before the container is assumed to fail.

The containers would initially be exposed to oxidizing conditions, which might last up to 300 a, as a result of the O_2 entrapped in the pores of buffer and backfill materials and exposure to groundwater that was experiencing radiolytic decomposition from the γ-radiation emitted by the fuel.

Grade-2 titanium was selected because of its corrosion resistance and its simple α-phase structure, which is unlikely to experience destructive phase transformation either in the disposal vault or as a result of welding. Titanium metal is protected from corrosion by a passive TiO_2 film. The uniform corrosion rate of Grade-2 titanium is negligible, and it is considered to be immune to pitting, microbially induced corrosion and stress corrosion cracking under the conditions expected in a disposal vault. However, crevice corrosion has been observed on Grade-2 titanium under hot, saline oxidizing conditions. This process can be initiated when the O_2 is depleted in a creviced area (e.g., under a deposit on the metal or in a void region in a weld, should such a defect not be detected using non-destructive testing). The anodic dissolution of metal in the creviced area could then couple to the cathodic reduction of O_2 on the surrounding container surface. Although such a process is unlikely to occur, it is difficult to demonstrate that it would not. In the model used to predict container lifetimes in the case study, we have therefore conservatively assumed that crevice corrosion initiates on all containers. In laboratory experiments, artificially creviced samples were forced to crevice-corrode

over the temperature range of interest, and the measured corrosion rates, along with the temperature-time history of the vault, were used to predict the depth of penetration within the crevice as a function of time. Although the gradual consumption of O_2 in the vault is likely to lead to repassivation (i.e., cessation of crevice corrosion), the corrosion rates were assumed to be sustained until penetration of the container wall occurred. This represents a second important conservative assumption in the container lifetime model that tends to underpredict lifetimes.

The possibility that hydrogen-induced cracking (HIC) of titanium might occur cannot be ruled out absolutely. Two forms of HIC appear possible: general embrittlement, in the case of extensive hydride formation; or sustained load cracking, in the case of hydride formation at an advancing crack tip. In both cases, the larger the hydrogen content, the lower the stress required for cracking to be possible. Studies using the slow strain-rate technique on precracked compact tension specimens have shown that Grade-2 titanium is not susceptible to sustained load cracking and that hydrogen contents $\gtrsim 500\ \mu g \cdot g^{-1}$ are required for fast brittle failure to be a concern. Thus, the critical factor determining when the material becomes susceptible to HIC by fast brittle fracture is the rate of hydrogen pickup. The most likely mode of hydrogen pickup is as a result of proton reduction in an actively corroding crevice. In the model, we assume that this leads to sufficient hydrogen pickup to enable HIC, in conjunction with sustained tensile stresses, to eventually cause container failure. By analogy with the alloy Ti-6Al-4V, which is more susceptible to HIC than Grade-2 titanium and in which slow crack propagation has been observed at temperatures <20°C for hydrogen contents up to $255\ \mu g \cdot g^{-1}$, we expect HIC to be more likely at low temperatures, when the solubility of hydrides and the ability of the material to relieve stress by plastic deformation is lower. Consequently, in our model we assume that HIC occurs only when temperatures fall below 30°C.

The corrosion of welds in Grade-2 titanium has been studied in our laboratories. Welded or heat-treated specimens show no increase in the rate of crevice corrosion, nor is there any evidence to suggest that welded material is more susceptible to H_2 absorption or HIC.

Radiation can affect metals either by embrittlement resulting from neutron absorption, or by corrosion caused by the presence of water radiolysis products. Neutron emissions from used fuel are many orders of magnitude lower than levels that can induce embrittlement. At the expected initial γ-radiation dose rate at the container surface ($\sim 50\ Gy \cdot h^{-1}$), the crevice corrosion rate of titanium is comparable to or slightly less than the measured rate for unirradiated conditions.

The model for container lifetimes includes three potential failure modes: failures caused by undetected initial defects, failures caused by crevice corrosion, and failures caused by HIC.

For initial defects, we have assumed that between 1 in 10^3 and 1 in 10^4 containers might have defects that escape detection during inspection operations. Failure rates as a result of crevice corrosion have been described by coupling measured temperature-dependent crevice corrosion

rates with the temperature-time profiles calculated for various regions of the vault. Containers can be grouped into three categories ("hot", "cool" and "cold"), on the basis of this thermal analysis. The temperature-time profiles for each group are approximated by simple step functions and the crevice corrosion rates are applied to each to calculate failure times. When temperatures fall below 30°C, containers are assumed to fail rapidly by HIC.

The calculations with this model show that 0.23% of containers would fail by 1000 a, largely as a result of HIC and initial defects. The majority of containers (>97%) would fail by crevice corrosion between 1200 and 7000 a.

It is worth noting that if crevice corrosion did not initiate, or if repassivation occurred rapidly as a result of the consumption of O_2 by Fe^{2+} in the backfill, then lifetimes in excess of 10^4 a would be conservatively predicted (Johnson et al. 1994).

ES.5 THE MODEL FOR RADIONUCLIDE RELEASE FROM USED FUEL

CANDU fuel bundles consist of stacks of UO_2 pellets (a polycrystalline ceramic) contained in sealed zirconium alloy (Zircaloy) tubes held together by end plates. After being discharged from the reactor, the UO_2 pellets are ~98.8% UO_2, with the balance being fission products (0.8%) and activation products (0.4%). The Zircaloy sheath material contains small amounts of radionuclides as a result of neutron activation of stable zirconium and impurity elements. The quantities of radionuclides in used fuel have been calculated using reactor physics codes. The calculated inventories have been compared with measured values and good agreement has been observed for the important radionuclides. Many of the radionuclides in the fuel are soluble in UO_2 (i.e., the atoms occupy positions in the crystal lattice normally occupied by uranium atoms). Those that are not soluble may be present as interstitials or microscopic inclusions within the UO_2 grains, or may be released from the grains in small quantities. A fraction of the inventory of some fission products, such as ^{135}Cs, ^{129}I, ^{99}Tc and the noble gases, may accumulate at grain boundaries in the fuel or may be released to the fuel-sheath gap. Studies of the dissolution of used fuel in groundwater show that such fission products initially dissolve at a faster rate than the UO_2 grains dissolve. Eventually, as the inventory of segregated fission products is depleted by leaching, the dominant mode of release becomes dissolution of UO_2 grains, often referred to as matrix dissolution.

The rate of dissolution of the UO_2 matrix of used fuel is strongly dependent on the redox conditions, with the rate being highest under oxidizing (aerated) conditions. This observation is consistent with laboratory studies of the dissolution of pure UO_2 and with geochemical observations from uraninite ore bodies. These studies illustrate that, if surface oxidation is limited to the UO_2-U_4O_9 region (i.e., a low U(VI)/U(IV) ratio), the crystal structure remains intact and uranium solubility and dissolution rates are low. When the surface composition approaches U_3O_7, dissolution rates increase and dissolution becomes oxidative in nature.

The conditions in the disposal vault at the time of container failure are expected to be reducing, as a result of dissolution of minerals containing ferrous iron. These minerals are expected to establish a redox potential within the stability field of UO_2. At this stage, the only source of oxidant within the vault would be the radiolysis of water to produce molecular and radical species capable of oxidizing UO_2. Beyond the lifetime of the containers only α-radiolysis is likely to be significant. Experimental results on the effects of α-radiolysis suggest that the surface composition of the used fuel would not oxidize beyond U_4O_9/U_3O_7, where oxidative dissolution becomes significant. As a result, the dissolution of the matrix can be modelled using a solubility-limited model in which the uranium concentration gradient drives the dissolution process.

The model for radionuclide release from used fuel therefore consists of two separate components: an instant-release model, in which an instant-release fraction (IRF) combines gap and grain-boundary releases into a single term; and a matrix dissolution or congruent-release model, in which the remaining radionuclides are released at the same fractional rate as that in which the matrix dissolves.

The quantities of Cs, I and Xe present in the fuel-sheath gap have been measured for many fuel bundles, each with its own unique in-reactor power history. The results compare favourably with predicted releases of Xe based on the ELESIM fuel-performance code. This code and data on fuel-bundle power histories have been used to predict average gap releases of important fission products and the quantities of fission products accumulated at grain boundaries. Because information on release rates of radionuclides from grain boundaries is scarce, their release has been conservatively assumed to occur immediately upon exposure of the fuel to groundwater. Thus, gap and grain-boundary inventories are combined to form the IRF, which averages 8.1% for ^{135}Cs and ^{129}I, 6% for ^{99}Tc and 12% for ^{14}C.

The dissolution of the used-fuel matrix and the release of actinides and the remaining fission products are limited by the solubility of UO_2 (or U_4O_9) and the diffusional transport of uranium away from the fuel. The solubility of uranium is calculated using a thermodynamic model by sampling from a range of concentrations of groundwater species and E_h (oxidation potential) and pH values, with both temperature variability and uncertainty taken into account. Over 97% of the predicted solubility values are lower than 10^{-6} mol·L^{-1}.

The vault model allows for the possibility of precipitation of radionuclides and their subsequent redissolution as they move through the buffer. Some radionuclides that dissolve inside the container could precipitate as they migrate into a buffer region with a different chemical environment. One possible change in the chemical environment could result from radiolysis, which is assumed to produce conditions that are more oxidizing at the fuel surface (i.e., an E_h up to the U_4O_9/U_3O_7 boundary) than in the surrounding buffer and backfill, where the redox chemistry is dominated by Fe(II)/Fe(III) equilibria.

The model computes solubility limits for five elements: Pu, Tc, Th, Np and U. The remaining elements are conservatively assigned solubilities high enough to preclude precipitation.

To model precipitation and redissolution, the following sequence of steps is used for all elements except uranium:

- Solubility limits are first determined. For the five elements noted above, solubility limits must be computed at two electrochemical potentials, associated with the fuel surface and the buffer/backfill. The lower of the two computed limits is used because precipitation should occur at the region of lowest solubility.

- The rate of release of each radionuclide is calculated on the assumption that it is dissolving at its solubility limit. If this release rate is smaller than the release rate from the buffer calculated without imposing the nuclide-specific solubility limit, then precipitation of the contaminant within the buffer is indicated.

- If precipitation of a contaminant is indicated, its rate of release from the buffer would be reduced. The accumulation of the contaminant in the buffer is described using an ordinary differential equation that keeps track of the mass precipitated and the mass lost by subsequent redissolution, taking into account the effects of radioactive decay. Redissolution of the precipitates is described in a manner similar to that discussed above for congruent release from the used fuel, except that it uses the solubility limit of the contaminant within the buffer.

A special condition applies for uranium. It is assumed that uranium dissolves at its calculated solubility limit, using the electrochemical potential at the surface of the fuel. If precipitation in the buffer is indicated, then its accumulation and redissolution is simulated as in the preceding paragraph, with the added assumption that the solubility-controlled release rate of each uranium isotope is proportional to its fractional inventory.

The precipitation of uranium, however, would also enhance the dissolution rate of the used fuel, reducing the concentration of uranium in the water in the buffer. Consequently, the congruent release of all contaminants in the fuel matrix would be enhanced. This effect is simulated by assuming a zero-concentration boundary condition at the precipitate by using a buffer thickness equal to the distance from the container to the point at which precipitation in the buffer occurs, and by using the uranium concentration difference between the used-fuel surface and the precipitate for the source boundary condition. These modifications increase the rate of dissolution of the used-fuel matrix and subsequent release of all contaminants.

The chemical and structural similarities between used fuel and natural uraninite ores have prompted the study of uraninite ore deposits that can serve as analogues to the long-term performance of used fuel in a disposal vault. Of particular interest are the high-grade uranium ore deposit at Cigar Lake in northern Saskatchewan (age ~1.3×10^9 a) and the Oklo natural fission reactors in Gabon (age ~2×10^9 a). Studies of the Cigar Lake deposit indicate that uranium concentrations in groundwater within the ore

zone are $<10^{-6}$ mol·L^{-1}, consistent with uranium concentrations calculated for the vault model. Even in the case of the Oklo reactor, where temperatures of 400 to 600°C were reached during criticality, the bulk of the uraninite survived both the criticality and the subsequent period of exposure to groundwater without significant dissolution. These observations provide support to the argument that used fuel disposed of in a reducing environment would exhibit extremely limited dissolution.

ES.6 THE CONTAMINANT MASS TRANSPORT MODEL

The mass transport model for the vault calculates, for saturated conditions, the release of contaminants from the failed containers and their transport through the buffer and backfill materials and into the surrounding rock. The model incorporates diffusion, convection, retardation effects and radioactive decay and buildup.

The vault is divided into sectors, each of which is considered to have relatively uniform hydrogeological characteristics. Mathematical analysis, including three-dimensional finite-element calculations based on the actual borehole emplacement geometry, shows that the buffer and backfill can be represented as layers that cover the entire area of the vault, across which contaminant mass transport would occur. In the mass transport model, the buffer thickness is 25 cm, as specified in the reference disposal vault conceptual design. The backfill thickness (1.4 m) is such that it would have the same volume as the total volume of backfill in the vault. Calculations with a one-dimensional diffusion equation for such a layered system show that the breakthrough time for ^{129}I (a non-sorbing nuclide) into the geosphere is the same as for the three-dimensional transport model, confirming the validity of the layered representation of the vault.

Sensitivity analysis with the finite-element groundwater transport model MOTIF shows that contaminant transport up sealed service and waste shafts would be negligible; thus, they are not included in the geosphere network connected to the vault sectors. Similarly, other calculations with this model show that an excavation-damaged zone with a permeability one hundred times that of the surrounding rock has no deleterious effect on contaminant transport; thus, an excavation-damage zone is also not included.

The rate of release of contaminants from the vault to the geosphere is determined by the solution of one-dimensional convection-diffusion equations for radionuclides in a decay chain. The convection-diffusion equations are solved using a response-function approach. These represent solutions to the mass transport equations for finite layers (e.g., buffer and backfill) for a unit-impulse input, and are calculated using Laplace transform techniques. The source release rate of a radionuclide into a layer is convoluted with the response function to obtain the release rate from that layer. The source release rate is obtained by solving the convection-diffusion equations for appropriate source boundary conditions.

The source boundary conditions are determined by the model for the release of radionuclides from used fuel, and the exit boundary conditions assume that the release of radionuclides into the geosphere is proportional to their concentration at the backfill/rock interface. The proportionality factor is referred to as the mass transfer coefficient and represents resistance to contaminant transport across this interface and in the subsequent pathway through the rock. A large value of the mass transfer coefficient approaches a zero-concentration boundary condition at the vault-rock interface, whereas a small value corresponds to a semi-permeable condition. The interface resistance is conservatively assumed to be small, and the mass transport properties of the host rock are used to determine the value of the mass transfer coefficient.

Two mass transfer coefficients, one convective and the other diffusive, are calculated for both buffer and backfill mass transport. For the convective case, it is assumed that radionuclides diffusing from the buffer or backfill into the rock are carried away by water moving in the rock along the outer surface of the buffer or backfill. The convective mass transfer coefficient is determined from the steady-state concentration gradients that would eventually be established for this situation. The diffusive mass transfer coefficient is determined initially by the steady-state gradients that would occur in a three-layer (buffer, backfill and rock) system with no water movement. The larger of the diffusive and convective mass transfer coefficients is used to obtain the final value of the buffer and backfill mass transfer coefficients.

Two source boundary conditions are used: one representing instant release of radionuclides upon container failure, and the other representing solubility-controlled congruent release. For the latter, the convection-diffusion equation is solved for a constant-concentration source boundary condition and an exit boundary condition determined by a steady-state mass transfer coefficient.

The total source release is then convoluted with the container failure response function to account for the fact that containers fail at different times. The precipitation of radionuclides that may have exceeded their solubility (e.g., Pu, Th, Np and Tc) is then simulated. The rate of dissolution of the precipitate is calculated in the same manner as the matrix dissolution rate, except the solubility of the precipitate is used rather than the solubility of the matrix. The net release rate after precipitation is then convoluted with the buffer response function to give the release rate into the backfill. Finally, this rate is convoluted with the backfill response function to obtain the release from the backfill into the surrounding rock.

ES.7 THE MEDIAN-VALUE SIMULATION, VERIFICATION USING SIMPLE MODELS AND SENSITIVITY ANALYSIS

The results obtained with the vault model are illustrated through the presentation of results for a single simulation, where all parameters are given their median values. (A complete listing of all parameters in the vault model is presented in Appendix E.)

For the median-value simulation, in the period between 10 and 10^5 a after vault closure, the only radionuclide giving a dose rate above 10^{-10} Sv·a^{-1} is ^{129}I. The calculated peak dose rate of 4.3×10^{-7} Sv·a^{-1}, which occurs at 10^5 a, is one hundred times lower than the regulatory criterion of 5×10^{-5} Sv·a^{-1} established by the Atomic Energy Control Board (AECB) for periods up to 10^4 a. The sum of the dose rates for all radionuclides is also $\sim 4.3 \times 10^{-7}$ Sv·a^{-1} at 10^5 a. Other radionuclides of importance are ^{99}Tc and ^{14}C, although at several orders of magnitude lower dose rates than for ^{129}I. Some other radionuclides, such as ^{79}Se and ^{135}Cs, have higher release rates from the vault but their transport is greatly attenuated in the geosphere; thus, they do not contribute to dose in the total system simulation.

A number of comparisons have been made between the results from the median-value simulation and those obtained using simple mathematical expressions, to provide verification of the vault model. For example, the peak failure time for "hot" containers is estimated to be 1945 a using an approximate mathematical solution, whereas the median-value simulation gives a value of 1860 a. Good agreement was also obtained for all other cases where comparisons were made.

The results of the median-value simulation clearly illustrate the importance of the various barriers in attenuating dose. At 10^5 a, approximately 1% of the ^{129}I that was in the used-fuel bundles has been released from the vault; ~5% is in the backfill, and ~94% is still within the failed containers. The behaviour of ^{14}C is similar to that of ^{129}I, except that radioactive decay greatly decreases both the release from the vault and the dose. For ^{99}Tc, precipitation in the buffer as a result of reducing conditions virtually eliminates release from the vault. The very low solubility of uranium prevents any significant release from the vault and also ensures extremely small releases of any radionuclides contained in the used-fuel matrix.

Sensitivity analysis has been performed to identify the most important parameters in the vault model by varying the values of parameters within the full ranges of their probability distributions. Variation in the following parameters causes the largest change in releases from the vault to the geosphere up to 10^5 a:

- the initial inventories of ^{14}C and ^{129}I per kilogram of uranium,
- the anion correlation parameter (this correlates the diffusion coefficients and capacity factors of anions in the buffer),
- the instant-release fractions of ^{14}C and ^{129}I,
- the groundwater velocity scaling factor, and
- the tortuosity of the rock zone in which the vault is situated.

The ratio of the largest to the smallest releases of ^{129}I and ^{14}C to the geosphere when each of these parameters is varied separately throughout its entire range varies from 3 to 100.

Another approach to analyzing the relative importance of various aspects of the vault model is to examine how various assumptions made during the course of model development affect the calculated results.

Performance assessment models are typically developed from more complex models through simplifying assumptions. Expert scientific judgement plays an important role, and there must be a recognition that where simplifications are to be made, an appropriate degree of conservatism should be retained in the model. This may be accomplished through conservatism in the simplifying assumptions or in the values and value distributions specified for important parameters in the model.

Releases of ^{129}I, ^{14}C and ^{99}Tc from the engineered barriers lead to the highest predicted dose rates. This is a consequence of the assumed instant release of gap and grain-boundary material and the relatively high mobility of these radionuclides in the geosphere. Although the modelled gap release of ^{129}I and ^{137}Cs has been shown to be accurate, gap release of ^{14}C was poorly understood at the time the model was defined. Subsequent measurements have illustrated that the instant release of ^{14}C has likely been overestimated by a factor of approximately 100.

The used-fuel matrix dissolves extremely slowly in our model because we assume that the fuel surface, exposed to water experiencing α-radiolysis, does not oxidize beyond U_4O_9, and thus a solubility model can be used. This important assumption is the focus of research to develop an oxidative dissolution rate model that can be extrapolated to the range of redox conditions expected at the fuel surface. Our results tend to confirm that oxidation would indeed be limited to the range indicated. The fuel dissolution rate calculated using the rate derived for the corrosion potential at the U_4O_9/U_3O_7 boundary suggests that 1 to 2% of the fuel matrix could dissolve in 10^5 a. This is several orders of magnitude greater than the extent of dissolution calculated with the solubility model. Nonetheless, the impact on calculated radionuclide releases from the vault using the oxidative model would be very small, because instant releases of radionuclides such as ^{129}I, ^{135}Cs, ^{14}C and ^{99}Tc are already assumed to be 5 to 10%.

For titanium containers, the critical assumptions affecting lifetime are that crevice corrosion would initiate on all containers immediately upon emplacement and that it would propagate indefinitely. The more probable outcome - that repassivation would occur as residual oxygen in the disposal vault was consumed and the temperature decreased - is the focus of ongoing studies. These studies suggest that crevice corrosion would not be sustained long enough to lead to failure. If failure did not occur by crevice corrosion, hydrogen-induced cracking would likely be the eventual failure mode, since general corrosion of titanium is extremely slow. For this reason, hydrogen uptake rates in titanium are being measured to determine the time to reach a critical hydrogen concentration where failure might occur. It is likely that model predictions of container lifetimes would exceed 10^4 a, were it not for the highly conservative assumptions in the model. This would have a great impact on releases from the vault.

If a model can be shown to adequately represent the system it describes, it is said to have been validated. For the vault model, which performs simulations for periods up to 10^5 a, validation is clearly not possible. It is, nonetheless, possible to demonstrate that some components of the system performance are appropriately represented in the vault model. For example,

it has been shown that diffusion models of the type that are used for radionuclide transport in buffer and backfill can be used to predict transport in clays. It has also been confirmed that the in-reactor power history of a CANDU fuel bundle can be used to predict the gap release of certain fission products, demonstrating that the most important component of the source term in the vault model is accurately represented. Another type of validation that is possible involves comparison with relevant natural analogues. Comparisons of the behaviour of uraninite ore at Cigar Lake with the used-fuel dissolution model, and of ancient bentonites with buffer material, with respect to self-sealing capability, confirm that the models are appropriate representations of these aspects of long-term system performance.

A wide range of quality assurance measures has been taken to ensure that the vault model produces scientifically defensible and conservative results. These range from peer review of publications and the CNFWMP as a whole to an array of specific code-testing procedures. The testing procedures have repeatedly confirmed the accuracy of the vault model code.

The vault model has been examined to determine the time frame over which the results of simulations should be considered valid. In some respects, the model will tend to overpredict releases at long periods of time ($>10^5$ a) because of conservative assumptions in the model. For example, a redox gradient that enhances the dissolution rate of the used-fuel matrix is assumed to exist between the surface of the fuel and the surrounding buffer material as a result of α-radiolysis of water. At periods beyond $\sim 10^5$ a, the α-activity of used fuel would have declined to a level comparable to that of a rich uranium ore, such as that at Cigar Lake, and the redox gradient would no longer occur. As a result, the dissolution of used fuel beyond this time is likely to be estimated more accurately from natural analogue studies of such systems. Other processes, such as the potential generation of gases in the vault as a result of metal corrosion and changes in the groundwater flow field as a result of glaciation, may also add increasing uncertainty to the model calculations for such time frames.

ES.8 SUPPLEMENTARY ANALYSES

Several supplementary analyses have been performed to illustrate the safety of the disposal concept. Some of these have used the vault model to obtain the required results, whereas others have involved the development and application of other models.

The question of the applicability of vault model results to the siting of a disposal vault in other locations in the Canadian Shield has been examined. This was done by considering how a wider variation in groundwater chemistry (in particular, more saline groundwaters) might affect container lifetimes and used-fuel dissolution rates. Results suggest that Grade-2 titanium would not be recommended for highly saline groundwaters ($>15\ 000\ mg \cdot L^{-1}\ Ca^{2+}$), and that Grade-12 titanium would be a better choice. For ionic strengths

up to 3.4 $mol \cdot L^{-1}$, the solubility of uranium (and thus the dissolution rate of the used fuel) is not significantly different from that in WRA groundwater.

Three different mass transport models for calculating releases of ^{129}I from the vault to the geosphere have been compared. These are the mass transfer coefficient (MTC) model used in the vault model, a highly conservative zero-concentration boundary-condition model and a coupled solution model. The latter is based on continuity of flux and concentration conditions at the buffer/backfill and backfill/rock interfaces, and is likely to give the most realistic results over a broad range of mass transfer conditions. The coupled solution model has not been used in the vault model because of the large computer resources required and because a narrower spectrum of quality assurance tests have so far been applied to it. Comparison of results of the coupled solution model and the MTC model shows that, for the median-value simulation, the average dose from ^{129}I obtained with the MTC model may be underestimated by a factor of two at 10^5 a. The zero-concentration boundary-condition model greatly overestimates releases from the vault and is not recommended for this application.

A separate analysis has been performed to determine the releases from the approximately 1 in 5000 containers emplaced in the vault that might have a premature defect. This early release process is included in the vault model simulations, but the conditions within the failed container are assumed to be reducing. Although such an assumption is appropriate for failures occurring after 500 a, prior to this time the high γ-radiation field would likely cause oxidative dissolution and, therefore, more rapid release of radionuclides contained within the used-fuel matrix. Release and transport of seven radionuclides were simulated. The contribution from an increased rate of matrix dissolution was negligible. Under less reducing conditions the sorption of redox-sensitive species, such as ^{99}Tc, could decrease. This effect was also investigated for the release of ^{99}Tc from prematurely defected containers. The contribution to dose for this scenario was also negligible.

The potential for a sustained nuclear chain reaction (i.e., criticality) to occur in the reference disposal vault has been examined. Criticality cannot occur for intact CANDU used-fuel bundles for any configuration with light water as a moderator. The possibility that segregation and subsequent accumulation of plutonium could occur as a result of extensive dissolution of the fuel has also been examined. The analysis shows that the quantities of ^{239}Pu that could be released would be far less than the amount required to achieve criticality.

The database on the diffusion of radionuclides in buffer and backfill materials is now substantially larger than it was at the time the vault model data were originally defined. The effect of the new data on calculated doses has been determined with the vault model and the results indicate only small differences in estimated doses.

ES.9 SUMMARY AND CONCLUSIONS

Conceptual and mathematical models have been developed for evaluating the performance of engineered barriers in a reference disposal vault located in rock of the Canadian Shield. The models have been used to calculate releases from the vault for periods up to 10^5 a. When incorporated into the system model SYVAC, which also includes geosphere and biosphere models, calculations of radiation doses to the most exposed individual can be made. These calculations show that average doses are orders of magnitude below the regulatory limit established by the AECB for periods up to 10^4 a.

A methodology for performance assessment of engineered barriers has been developed, and the vault model and the results obtained with it give confidence that used fuel can be disposed of safely in a suitably designed and located vault in the Canadian Shield.

1. INTRODUCTION

1.1 THE DISPOSAL CONCEPT AND PERFORMANCE ASSESSMENT METHODOLOGY

The Canadian nuclear fuel waste disposal concept involves permanent burial at depths of 500 to 1000 m in plutonic rock of the Canadian Shield. The disposal system combines natural and engineered barriers to ensure long-term safety of humans and the environment. Figure 1-1 illustrates the main features of the concept. The nuclear fuel waste would be placed in corrosion-resistant containers, and a clay-based buffer material would be placed between the containers and the surrounding rock. Either the borehole emplacement configuration shown in Figure 1-1 or the in-room emplacement method (Johnson et al. 1994, Section 4.2) could be used. The remaining excavations would be backfilled and the shafts sealed. No further maintenance would be required.

Construction, operation and closure of such a facility is referred to as the preclosure phase, whereas the postclosure phase is concerned with the behaviour and performance of the facility after closure. Methodologies to assess the safety of the pre- and postclosure phases have been developed. For the postclosure safety assessment, the important processes and radionuclide transport pathways included in our assessment models were identified and selected through an extensive scenario analysis. By the term scenario, we mean a combination of factors (features, events and processes) that could affect the isolation of the waste in its disposal facility (Cranwell et al. 1987). Scenarios were constructed using a systematic procedure that involved searching for all possible factors; screening and eliminating factors on the basis of probability of occurrence, physical reasonableness, regulatory criteria, etc.; and combining the remaining factors into scenarios in all possible ways (Goodwin et al., in preparation). The focus in scenario analysis has been on radiation protection of humans.

The analysis identified one sequence of events as being, by far, the most likely to occur—slow degradation and failure of the waste containers followed by release of nuclides from the waste into the groundwater, diffusion through saturated buffer and backfill materials, convection and diffusion through faults and interconnected pores in the geosphere to surface water and soil, and, finally, environmental and human exposure through a multitude of pathways in the biosphere (Figure 1-2). This sequence of events has been analyzed using the probabilistic analysis code, SYVAC3, as part of the postclosure assessment. The scenario analysis approach and a complete list of the factors considered is given by Goodwin et al. (in preparation).

Because of the very long time frame of postclosure safety assessment, it is necessary to construct mathematical models that represent the key processes and assumptions used in determining the performance of the system. Separate mathematical models have been developed to simulate radionuclide movement through the vault, geosphere (Davison et al. 1994b) and biosphere (Davis et al. 1993). The various detailed models are probabilistic, i.e., for each parameter incorporated into the mathematical models, a range of

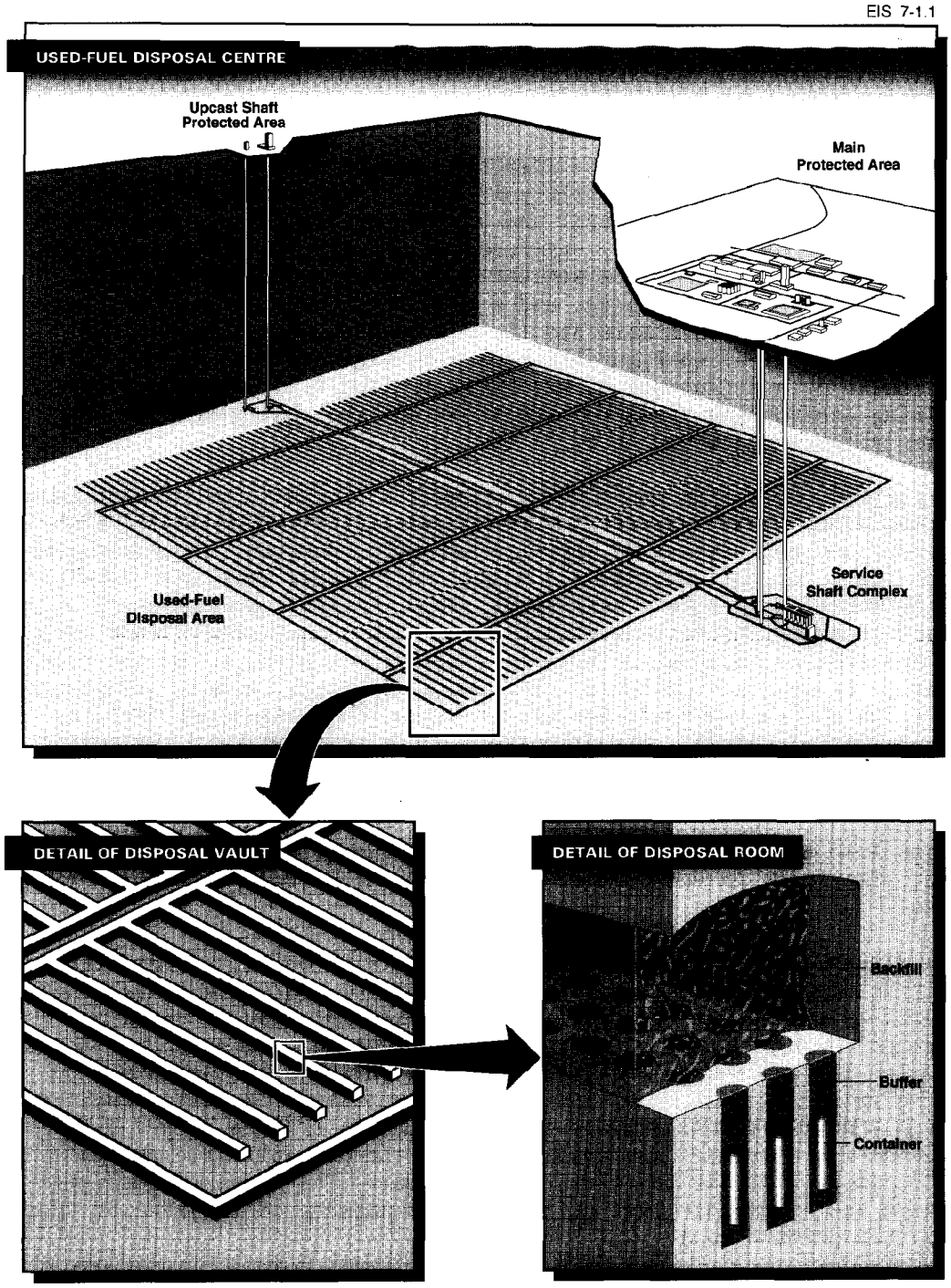

FIGURE 1-1: Schematic Representation of a Nuclear Fuel Waste Disposal Facility with Surface and Underground Structures. Enlarged insert shows a section through an emplacement room with containers emplaced in boreholes.

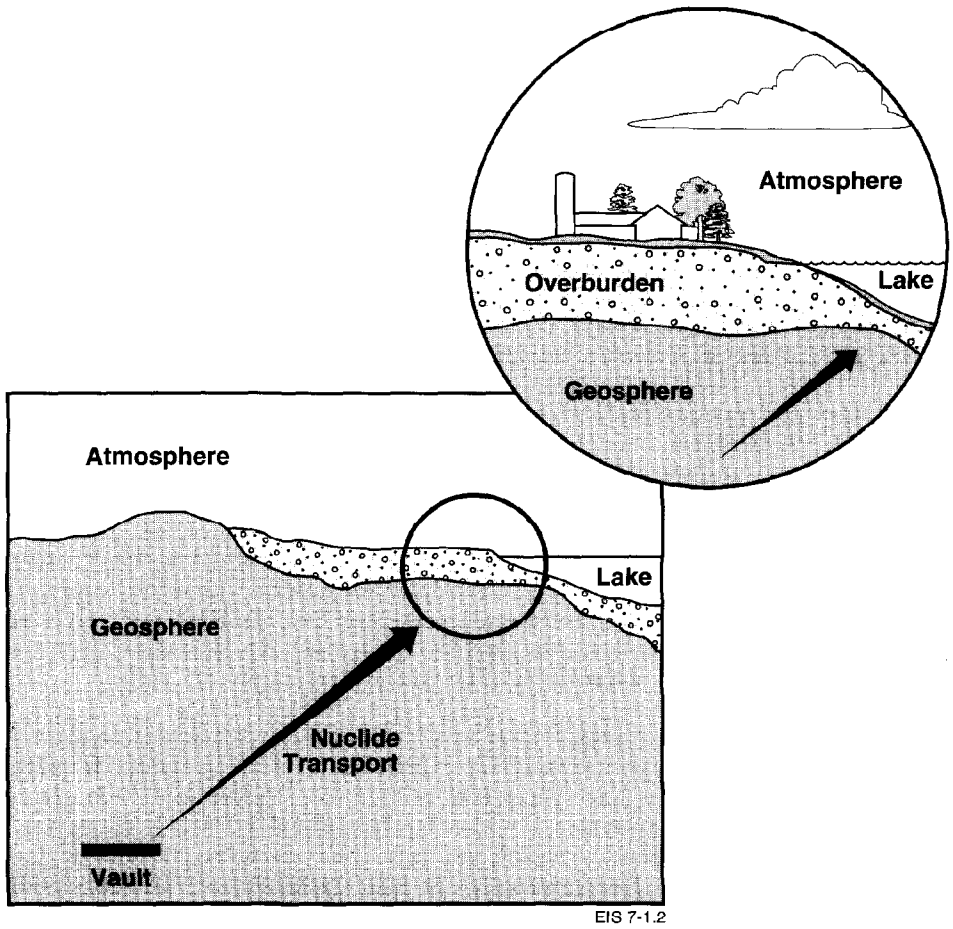

FIGURE 1-2: Schematic Representation of Groundwater Transport of Nuclides from the Vault to the Biosphere

values, rather than a single value, is defined through field and laboratory studies and expert judgement. These ranges permit uncertainty and variability in the various processes and parameters to be taken into account.

The models are integrated under the control of an executive code SYVAC3 (Systems Variability Analysis Code - Generation 3; Goodwin et al. (1994)), which repeatedly simulates the behaviour of the system as a whole by randomly sampling from each parameter distribution. The output is a distribution of nuclide concentrations in the environment, and of the radiological consequences to humans and other biota. These calculations, presented by Goodwin et al. (1994), provide a quantitative assessment of the performance of the system for comparison with criteria set by the regulatory agency (AECB 1987).

It is emphasized that the models used in the postclosure assessment case study have been developed to demonstrate that a methodology exists to carry out a performance assessment of a disposal system incorporating engineered and natural barriers. Although the models represent appropriate approximations of the behaviour of the various components of the system studied, the

assessment results depend on the specific characteristics assumed for the engineered and natural components of the system being modelled. The assumed system design and characteristics and the models representing them are referred to here as the postclosure assessment case study. Different results would be obtained for other cases, depending on the assumptions made regarding site characteristics (e.g., depth of the vault), vault design (e.g., maximum rock temperature, thickness of buffer material) and container and waste-form type (e.g., titanium or copper, used fuel or vitrified reprocessing wastes). These other options and their implications for system performance are discussed in detail by Johnson et al. (1994).

The models are, of necessity, simplified representations of the behaviour of the system components. In developing the models, care has been taken to ensure that where understanding is insufficient to accurately describe a process, the mathematical models (and their associated parameter values) tend to overestimate the consequences (i.e., the models incorporate conservatism). The reader is therefore cautioned against viewing the models and the long-term impacts calculated with SYVAC as actual predictions of what would occur. The distinction between conservative models and more realistic performance predictions is discussed in detail in the descriptions of the various models and is summarized in Section 7.3.2.

It is also emphasized that there are limitations in the application of these models over very long periods of time. The models were developed to describe vault performance for a period of 10^4 a. Used with caution, and combined with reasoned arguments regarding the long-term performance of the engineered barriers, the vault model can also be used to indicate trends for periods up to 10^5 a. The reasons for the limitations of the model are discussed in Section 7.5.

1.2 SCOPE AND OBJECTIVES OF THE VAULT MODEL REPORT

The vault model, based on a set of mathematical submodels, one for each of the engineered barriers, calculates a time-dependent flux of radionuclides into the geosphere. To develop these models it was necessary to make assumptions regarding a specific engineering design of the vault. The hypothetical vault is assumed to be located in the Whiteshell Research Area (WRA) (Figure 1-3) at a depth of 500 m. This location was assumed because detailed information was available on the properties of the rock as a result of the extensive characterization performed as part of the Underground Research Laboratory (URL) Program. The vault design is based largely on the Used-Fuel Disposal Centre conceptual design described in detail by Simmons and Baumgartner (1994). Some specific differences (e.g., the 1000-m depth for the latter study as opposed to the 500-m depth for the case study) are outlined in Chapter 2, which presents the details of the vault design assumed in the postclosure assessment case study.

Following the description of the vault system in Chapter 2, the performance of the clay-based buffer and backfill materials are described in Chapter 3. The behaviour of the buffer material before and after container failure is discussed, and a conceptual and mathematical model for diffusion of radionuclides through these materials is presented. The ranges of values of diffusion coefficients of radionuclides in the buffer and backfill materials are given, and the derivations of the model and data are discussed.

EIS 7-1.3

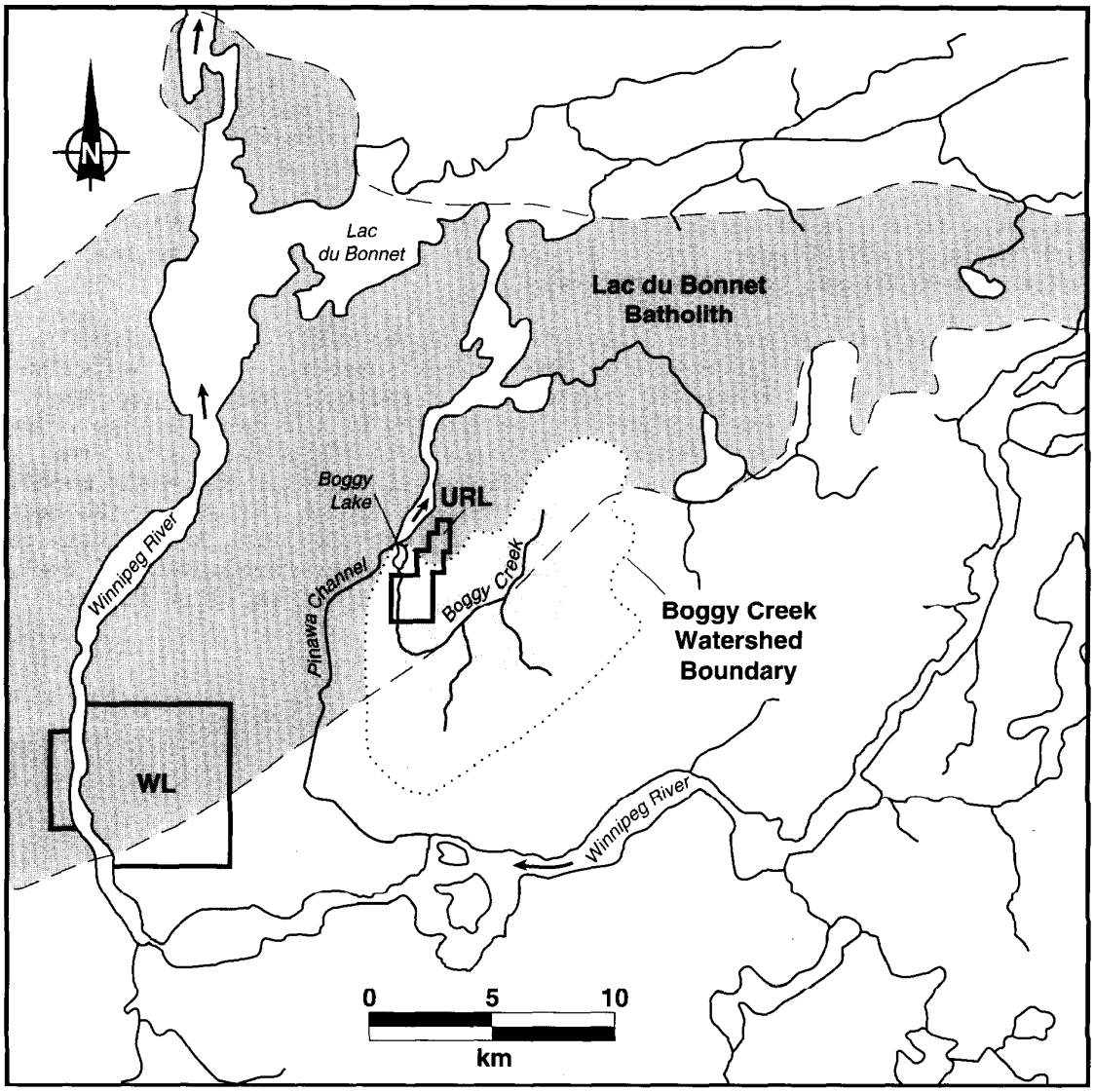

FIGURE 1-3: Map of the Whiteshell Research Area Showing the Location of the Underground Research Laboratory and the Whiteshell Laboratories

In Chapter 4, the conceptual and mathematical models used in the assessment of the lifetimes of titanium containers are presented. The corrosion properties of the material are discussed and the assumptions and data for the model are presented and justified. Finally, the calculated container lifetimes are presented.

Chapter 5 presents the model for the release of radionuclides from used fuel. The radionuclide release characteristics are described and the mathematical model and associated data are derived and presented.

The overall mathematical mass transport model for the vault is outlined in Chapter 6. The integration of the various engineered barrier models and the coupling of the vault model to the geosphere model are described in detail. Here we describe the justification for modelling radionuclide transport in the vault using a one-dimensional convection-diffusion equation to describe transport across a series of layers representing the buffer, backfill and rock (Figure 1-4).

Chapter 7 presents an example calculation with the vault model, using median values for all parameters in the various submodels. The simulation permits the reader to track the progression of radionuclides through the various barriers into the geosphere. The results of the calculations using median values for all parameters are compared with those calculated from simple mathematical expressions to provide verification of the vault model. The results of sensitivity analysis calculations, which illustrate the most important parameters in the models, are then presented. The sensitivity of the vault model results to key assumptions made in the development of the various submodels is discussed, as is the time frame of validity of the vault model.

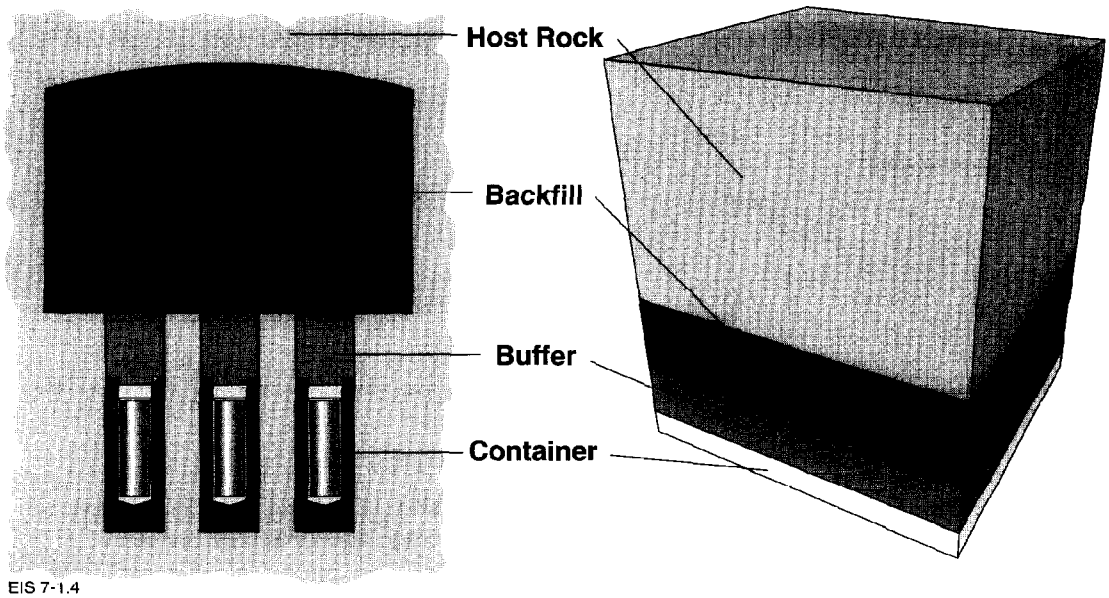

FIGURE 1-4: The Borehole Emplacement Method and the Layered Representation Used in the Vault Model Postclosure Assessment Case Study to Permit the Use of a One-Dimensional Convection-Diffusion Equation to Describe Radionuclide Transport. The model is described in detail in Chapter 6.

Chapter 8 presents supplementary analyses that are not explicitly incorporated into the vault model but are nonetheless required for a thorough evaluation of the performance of engineered barriers. This includes a detailed analysis of radionuclide release from prematurely defected containers, a criticality analysis, the use of alternative mass transport boundary conditions with the geosphere, and a discussion of the general applicability of the vault model results to the siting of a disposal vault at other locations and depths in the Canadian Shield.

2. DESCRIPTION OF THE VAULT SYSTEM

2.1 THE REFERENCE USED-FUEL DISPOSAL CENTRE CONCEPTUAL DESIGN

2.1.1 Introduction

The design of the vault system used in the postclosure assessment case study is based largely on the Used-Fuel Disposal Centre design presented by Simmons and Baumgartner (1994). The differences between the two designs and the reasons for them are outlined in Section 2.2. To explain these differences, it is necessary first to review some of the key design features of the Used-Fuel Disposal Centre reference vault.

2.1.2 The Vault Layout

The Used-Fuel Disposal Centre reference design assumes a disposal vault excavated at a depth of 1000 m in plutonic rock in the Canadian Shield. The overall plan dimensions of the reference vault are approximately 2 km x 2 km. The vault has a single-level room and pillar configuration with five vertical shafts for services and ventilation (Figure 2-1). The layout and dimensions are idealized, because fracture zones might be encountered during site characterization. The vault layout may be more complex to avoid these features. Boreholes are drilled into the floor of the disposal rooms to accept the waste containers (Figure 2-2). The vault layout and the spacing of the containers in the vault were determined from thermomechanical studies that were, in turn, based on the specification that the container skin and buffer temperature should not exceed 100°C. The vault is designed to accommodate 140 256 containers with a total of approximately 10.1 million bundles of used fuel.

The Container

The reference container is designed to hold 72 bundles of used CANDU[1] fuel and is constructed from American Society for Testing and Materials (ASTM) Grade-2 titanium (Figure 2-3). In 1984-85, when the reference Used-Fuel Disposal Centre specifications were developed, this represented the most appropriate material choice in light of our understanding of the corrosion performance, fabrication, structural properties and cost of a number of potential container materials. Alternative material choices are discussed in Chapter 3 of Johnson et al. (1994). A full-size prototype of the

---

[1] CANada Deuterium Uranium, registered trademark of AECL.

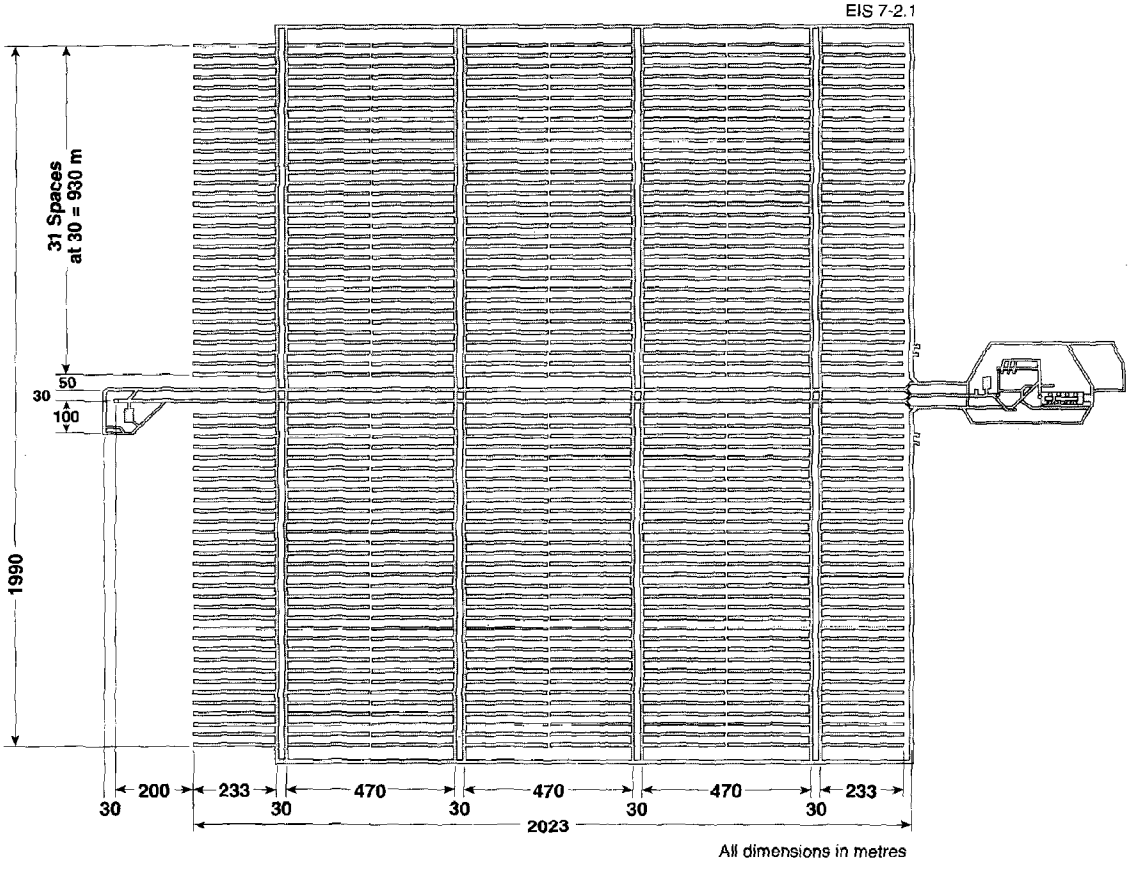

FIGURE 2-1: General Plan Layout of the Disposal Vault (Simmons and Baumgartner 1994)

reference container has been successfully tested to an external hydrostatic pressure of 10 MPa at temperatures up to 150°C. The container incorporates a carbon steel basket holding the 72 bundles in four arrays of 18 bundles. A particulate material (1-mm glass beads) compacted by vibration is used to fill the void spaces. The container top end-plate is pressed into place and diffusion-bonded to the container shell. Two inspections are performed after this operation: ultrasonic inspection of the final closure bond, and a helium leak test of the entire container (Johnson et al. 1994, Chapter 3).

2.1.3 Emplacement of Container and Sealing Materials

In the Used-Fuel Disposal Centre reference design, containers holding the used fuel are transported underground in shielded casks to the emplacement boreholes. Before the container is emplaced, buffer material is poured and compacted in the boreholes and a central hole is augered into the buffer to

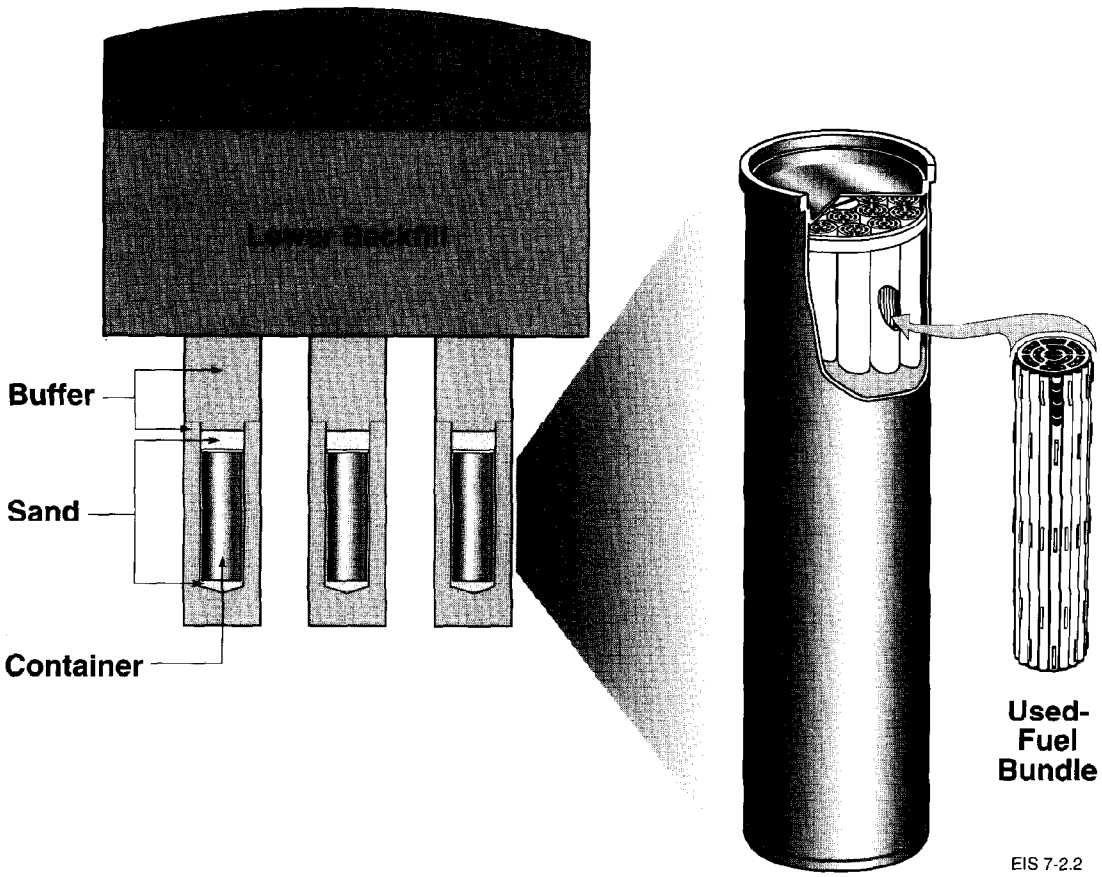

FIGURE 2-2: Cross Section of a Disposal Room

accept the container. The buffer material is a 1:1 mixture (by dry mass) of sodium bentonite and silica sand. This material was chosen because, when present in a compacted state, it has a high swelling capacity, low permeability to groundwater, and a high sorption capacity for many radionuclides.

After the container is lowered into the borehole, silica sand is used to fill the small annular gap between the container and buffer, and more buffer material is compacted into place above the container. The lower parts of the rooms and the access tunnels are filled with a mixture of 25% clay and 75% crushed granite. This material was selected on the basis of its availability and low permeability.

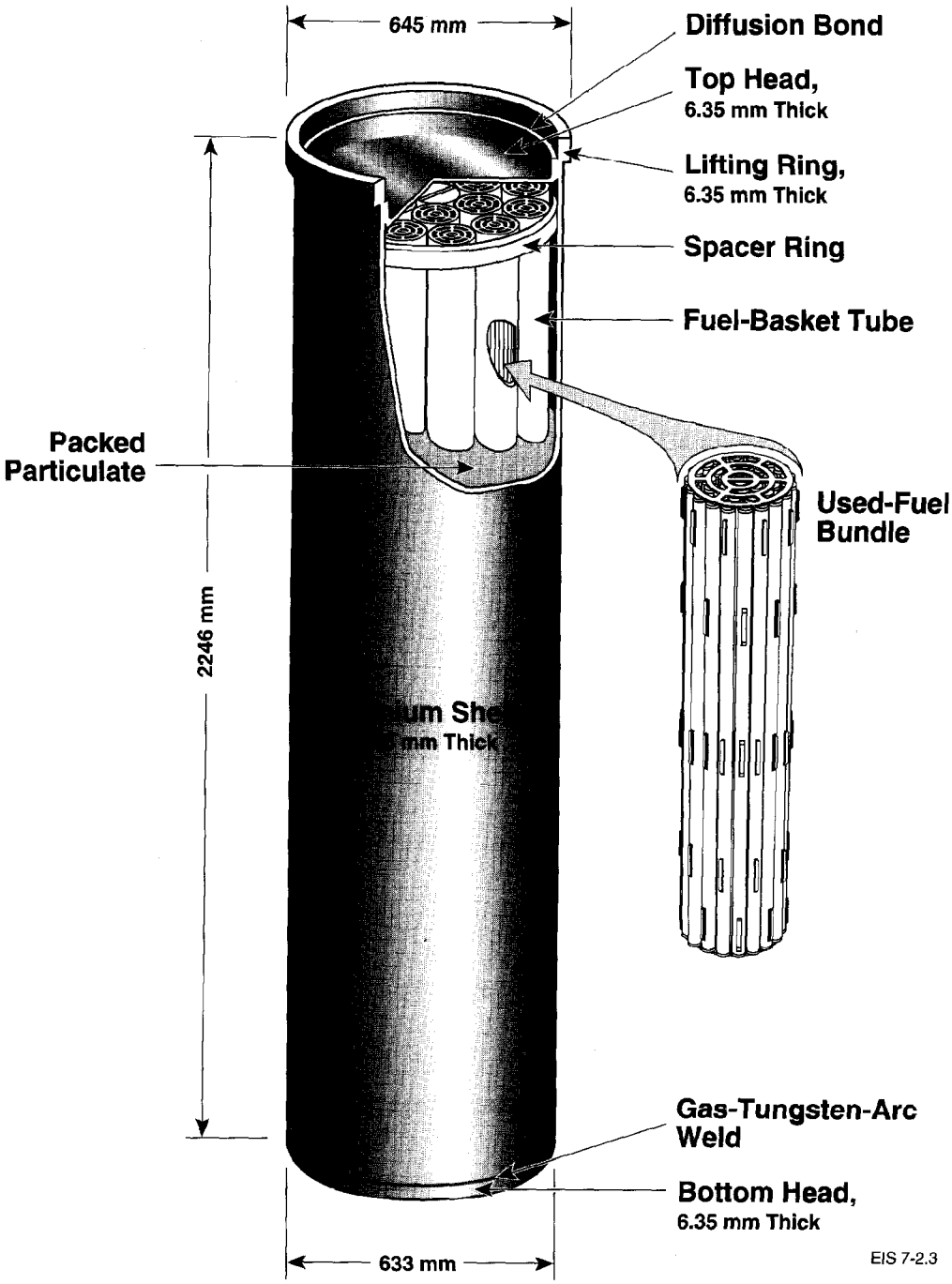

FIGURE 2-3: The Packed-Particulate, Supported-Shell Container for Used CANDU Fuel (Johnson et al. 1994). For the vault model analysis, the basket is assumed to be ceramic or a metal that produces little H_2 upon corrosion. The particulate material is assumed to contain a small percentage of magnetite to scavenge residual oxygen inside the container.

The upper parts of the disposal rooms and tunnels are filled with a 1:1 mixture of sand and bentonite. Backfill material is used to fill shafts, and composite shaft seals, comprising layers of highly compacted bentonite blocks adjacent to a high-performance concrete bulkhead, are placed at various locations in the shafts. Similar bulkheads are installed at the entrances to the disposal rooms as well as at strategic locations in the vault tunnels.

2.1.4 Used Fuel: The Source and Volume

The reference used fuel is assumed to be that from the Bruce Nuclear Generating Station, with an average burnup of 685 $GJ \cdot kg^{-1}$ U. The fuel is also assumed to have been stored at the reactor sites for ten years before emplacement in the vault.

The total mass of used-fuel bundles for disposal is approximately 240 000 Mg, equivalent to 191 133 Mg of elemental U initially present in the fuel. The latter units are more commonly used because radionuclide inventories in used fuel are calculated in units of moles per kilogram of uranium initially present in the fuel (see Appendix A). Projections for used-fuel arisings are discussed in the Environmental Impact Statement (AECL 1994a).

2.2 MODIFICATIONS TO THE USED-FUEL DISPOSAL VAULT DESIGN USED IN THE VAULT MODEL

A number of design changes were made to the used-fuel disposal vault for the postclosure assessment case study. Table 2-1 shows the values of important vault design parameters used in the case study, in comparison with the original values assumed in the Used-Fuel Disposal Centre design.

The depth of the vault is assumed to be 500 m in the case study, as opposed to 1000 m in the facility described by Simmons and Baumgartner (1994). This decision was taken because the quality and detail of hydrogeological data for the WRA at this depth were better than for 1000 m; thus, the uncertainties in the geosphere model predictions would be minimized. Moreover, we felt that the case study used to illustrate the methodology for assessing the safety of the concept should be based on the minimum burial depth proposed for the disposal concept, i.e., 500 m. The slightly lower ambient rock temperature at 500 m, compared with 1000 m, as a result of the geothermal gradient, means that the container skin temperatures are lower for the same container spacing.

The total area of the vault, and thus the total number of containers and mass of fuel for disposal, were reduced in the case study to the values given in Table 2-1. This was done to ensure that the vault could fit into the rock body without intruding into an assumed adjacent fracture zone. The revised vault layout is shown in Figure 2-4 and is discussed in detail in Chapter 6.

In addition to these changes in design parameters, some other design modifications have been assumed in order to ensure the validity of the models used to describe the performance of the engineered barrier system. As discussed in Chapter 3, if gas generation in a disposal vault results in

TABLE 2-1

DIFFERENCES BETWEEN THE USED-FUEL DISPOSAL CENTRE DESIGN AND THE DESIGN IN THE POSTCLOSURE ASSESSMENT CASE STUDY

Parameter	Value		Units
	Used-Fuel Disposal Vault (Simmons and Baumgartner 1994)	Postclosure Assessment Case Study	
Depth of vault	1 000	500	m
Total plan area of vault	4	3.16	km^2
Total mass of U in the vault	191 133	161 730	Mg
Number of containers in the vault	140 256	118 680	
Maximum container skin temperature	100	94	°C

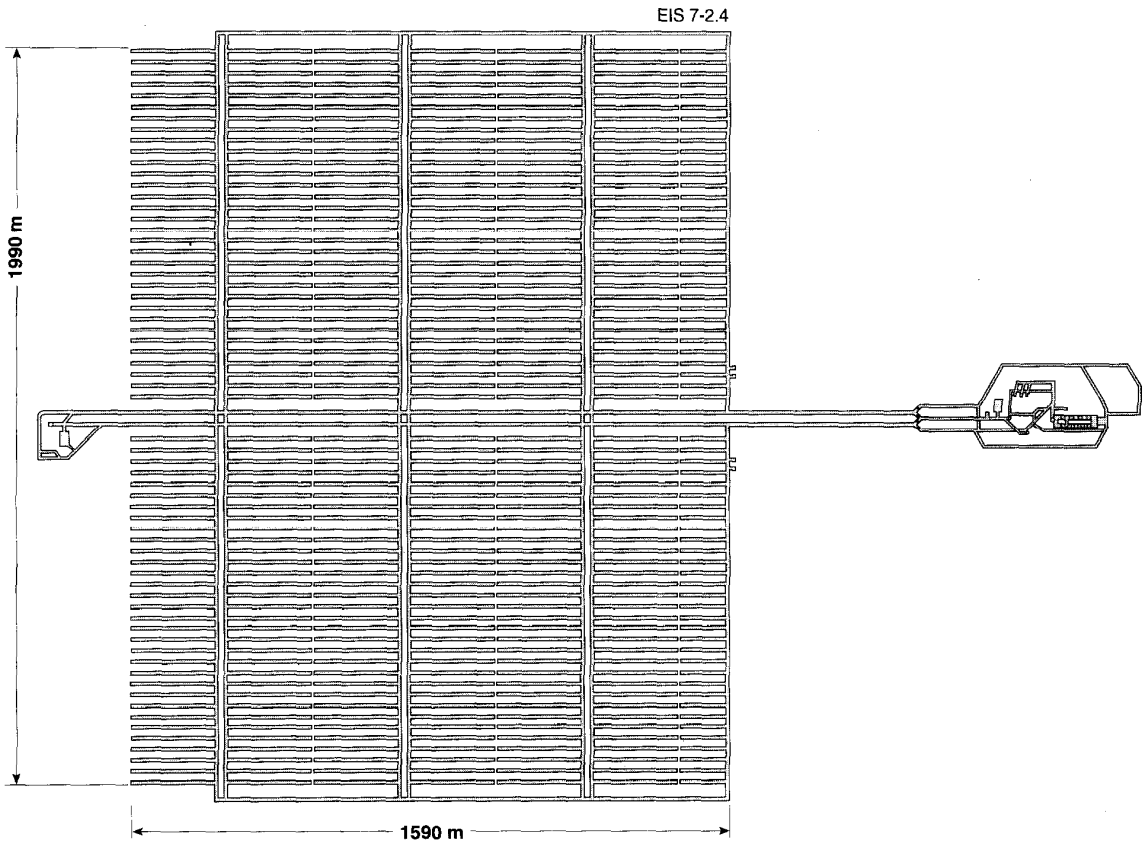

FIGURE 2-4: Layout of the Conceptual Disposal Vault Used in the Postclosure Assessment Case Study

the formation of a separate gas phase, the transport of radionuclides might not be accurately described by the aqueous diffusion and convection processes used in the geosphere and vault models. The use of materials that do not generate significant H_2 upon corrosion is therefore considered desirable. Corrosion of the carbon steel basket within the reference container was identified as a potential major source of H_2. For the vault model, therefore, it has been assumed that the basket is constructed from a ceramic or other material that does not produce significant quantities of gas upon contact with groundwater. In addition, to ensure that the effect of residual O_2 in the container on used-fuel corrosion after container failure need not be considered, a small quantity of particulate magnetite (an oxygen scavenger (Mattsson 1978)) is assumed to be added with the glass beads when the void space in the container is filled. Neither of these design modifications represents a significant technical or engineering impediment to the safe implementation of the disposal concept.

The groundwater composition in plutonic rock varies with depth and location in the Canadian Shield. The assumed composition of the groundwater at 500 m is that described by Gascoyne (1988) for a depth of 500 m in the WRA, where the hypothetical vault is located. The groundwater composition is discussed in detail in Chapters 3 and 5.

3. EVOLUTION OF NEAR-FIELD CONDITIONS AND MASS TRANSPORT THROUGH CLAY BARRIER MATERIALS

3.1 INTRODUCTION

In this chapter radionuclide diffusion through the porous clay media that would surround the waste containers and be used to backfill the excavations is discussed. The rationale for the selection of the numerical values for the diffusion properties of the buffer and backfill that are used for the analyses of the performance of the vault system is presented. Moreover, a discussion of (i) the processes occurring in the buffer and backfill materials during the period between emplacement of the waste containers and the attainment of water saturation of the clay-based seals, and (ii) various factors or processes that could potentially alter the mass transport properties of the buffer and backfill materials is given.

For radionuclides to be released from the vault, water must reach the waste and the waste must begin to dissolve. For this to occur, the buffer material must allow water through and, as a result of the corrosion processes described in Chapter 4, the container shell must be breached. Subsequently, the voids in the packed particulate inside the container must fill with water before radionuclides are released. Hence, to calculate the rates of migration of radionuclides through the vault, it is assumed for the vault model that the pores in the buffer and backfill materials are fully water-saturated.

Contaminants, such as dissolved radionuclides, can move through water-saturated, porous clay-barrier (buffer and backfill) materials under gradients in hydraulic potential, chemical concentration, temperature and

electrical potential (Mitchell 1976). For the purposes of the vault model it is assumed that the chemical concentration gradient is the only significant driving force in the buffer and backfill materials (i.e., Fickian diffusion is the only significant process by which radionuclides may be released from the vault). This assumption is based on the following knowledge.

The hydraulic conductivities of the water-saturated buffer and backfill are less than 10^{-10} $m \cdot s^{-1}$. Mitchell (1991) notes that advective contaminant flux (i.e., flow under a hydraulic gradient) can be ignored if hydraulic conductivities are less than 10^{-9} $m \cdot s^{-1}$. Moreover, there would be no significant electrical potential gradients acting across the clay barriers in the vault, and temperature gradients would be small and would tend to decrease with time. Values of temperature gradients have been calculated to be less than $2°C \cdot m^{-1}$ 1000 a after waste emplacement (Baumgartner et al., in preparation). Thus, to predict radionuclide migration in the buffer and backfill materials, values for Fickian diffusion coefficients in the clay-barrier materials for radionuclides released from the waste are required. These values, which depend on factors such as pore solution composition, temperature and the type and density of the clay, have been obtained either by direct measurement in laboratory experiments or from the scientific and engineering literature.

The reference buffer material is a 1:1 mixture (by dry mass) of Avonseal bentonite[2] and silica sand compacted to not less than 95% maximum modified Proctor dry density, with an effective clay dry density[3] (γ_c) of about 1.22 $Mg \cdot m^{-3}$ at a moisture content of 17 to 19% by dry mass (Gray and Cheung 1986). The reference backfill material consists of 25% Lake Agassiz[4] clay and 75% crushed and graded granite aggregate (mixed by dry mass) compacted to not less than 95% maximum modified Proctor dry density at a moisture content of 6 to 8% by dry mass (Yong et al. 1986). Compositions and selected properties of the reference buffer and backfill materials are presented in Table 4-4 of Johnson et al. (1994).

At the time of emplacement, the initial water contents used for moulding the buffer and backfill materials would be insufficient to saturate the voids in the materials. In the buffer, the degree of saturation[5] (S) would be between 75 and 85%; S in the backfill would range from 60 to 80%. The

---

[2] Bentonite is the name of natural smectite-rich clays; montmorillonite is the most common smectite mineral and it is the predominant component of bentonite. Bentonite generally contains other minor phases such as quartz, feldspar and carbonate.

[3] γ_c is the ratio of the dry mass of clay to the combined volume of clay and voids.

[4] Lake Agassiz clay is a glacial lake clay having properties that are typical of materials found in many similar deposits throughout the Canadian Shield.

[5] S is the volume of water/volume of voids per unit volume of material expressed as a percentage.

variations of S reflect the possible ranges in the initial water contents of the materials. Temperatures in the vault and hydraulic boundary conditions acting on the buffer and backfill would vary spatially and temporally. A number of different phenomena that could affect buffer and backfill performance are likely to result from these changes. Principally, moisture migration in the clay barrier materials would occur; this would cause volume changes in these materials. For example, the buffer and backfill materials would shrink as water was depleted and swell as water was added. The probable nature of these and other changes and their possible effects on the performance of the buffer and backfill are discussed in Sections 3.2, 3.3. and 3.4.

3.2 THE PRESATURATION PERIOD

Immediately after a waste container was placed in a buffer-lined borehole a number of coupled processes would begin that would lead ultimately to saturation of the buffer with water. The heat generated by the waste would begin to flow through the buffer and backfill, causing temperatures to rise; water would tend to diffuse down the temperature gradient and away from the container. Conversely, the potential of the water in the unsaturated buffer and backfill materials would be less than that of the water in the rock. Thus, the unsaturated clay barriers would tend to draw water from the rock. Around any one container, the opposing forces of the temperature and hydraulic gradients would cause the initial water content in the buffer to be redistributed; the total water content should tend to increase with time. The rate at which the latter occurred would depend on, amongst other factors, the hydraulic properties of the rock immediately adjacent to the clay barrier materials. Because of the natural spatial variations in the properties of the host rock, and the allowable variations in the specifications for the water content of the buffer and backfill materials, the moisture distributions in the buffer around containers, at any time prior to saturation, would likely vary across the vault.

The physical properties of clays vary with S. For example, decreasing S (drying) would cause the buffer and backfill to shrink and, likely, crack. In the case of the buffer, because of its high smectite content, increasing S would cause it to swell against the restraint of the adjoining materials (the rock, the container, drier buffer and backfill). Thus, the stresses in the buffer and backfill would vary with the spatial and temporal changes in boundary conditions and moisture content. The materials would deform as the stresses changed. Possible effects of these deformations on the performance of the saturated clay barriers are examined in the remainder of this chapter.

3.2.1 Boundary Conditions

Hydraulic conditions

The hydraulic conditions at the buffer/rock and backfill/rock boundaries are likely to strongly influence the duration of the presaturation period. Many factors could vary in space and time to influence these conditions. From observations made at AECL's URL and at the OECD/NEA (Organization for Economic Cooperation and Development/Nuclear Energy Agency) Stripa Mine in

Sweden (Gray 1993), it is possible to develop an understanding of and a scenario for the probable hydrogeological conditions with which the buffer and backfill would interact.

The natural stress field in the rock would be disturbed by excavation of the vault. These disturbances would be most extreme immediately adjacent to the excavation. Depending on a number of factors, such as rock type and strength, stress magnitude and direction, and excavation geometry and excavation technique, the excavation disturbance of the rock could range from complete crushing to virtually insignificant microcracking (Martin 1989). The excavation disturbance could create hydraulically active flow paths around the major tunnel and room excavations. This would become more probable if, as assumed by Simmons and Baumgartner (1994), drill and blast techniques were used to excavate the vault. In this circumstance, tests at the Stripa Mine (Pusch and Gray 1989) and at the URL have shown that excavation-disturbed zones (EDZ) with higher hydraulic conductivity than the undisturbed rock could be between 0.2 and 1 m thick. Assuming that water flows in the fractured rocks at Stripa could be described by the application of Darcy's law, researchers calculated the hydraulic conductivity of the undisturbed rock to be lower than 10^{-11} $m \cdot s^{-1}$, compared with values up to 10^{-7} $m \cdot s^{-1}$ for the disturbed zone. Tests carried out in the floor of a room excavated using drill and blast methods at the 240 Level of the URL showed that the damaged zone was about 0.3 m thick. Using this thickness, and assuming that Darcy's law applies, we estimated the equivalent hydraulic conductivity of the blast-damaged zone to be between 4×10^{-6} and 2×10^{-7} $m \cdot s^{-1}$ (Martin et al. 1992). The test conditions affected the measured hydraulic conductivity values. Doubling the length of the path for water flow through the blast-damaged zone caused the tenfold decrease shown in the measured values. At both the URL and Stripa, outside the blast-damaged zone, a stress-disturbed zone with hydraulic conductivities similar to those of the undisturbed host rock exists. There is evidence from the Stripa program that the hydraulic conductivity of this disturbed zone may be anisotropic. Hydraulic conductivity parallel with the axis of the excavations can be higher than that at right angles to the axis. Because the stress state in the rock would be site-specific, and the choice of excavation technique might also influence the degree of excavation damage, actual values of hydraulic conductivity for the EDZ in the reference disposal vault are unknown, but are expected to fall between 10^{-11} and 10^{-7} $m \cdot s^{-1}$.

In the reference vault, the boreholes in which the buffer and containers are placed are drilled in the floors of the rooms. They pass through the EDZ created by room excavation and, in turn, create their own pattern of disturbance in the stress field. In the reference vault configuration, emplacement boreholes 1.24 m in diameter are drilled in rows three abreast at 2.1-m centres across the width of an emplacement room. Thus, the minimum thickness of the rock web between the boreholes is 0.86 m. With this geometry and under the average natural stress conditions in the granitic rocks of the Canadian Shield, it has been shown (Tsai 1993) that, at greater than a 1-m depth into the deposition boreholes, the rock walls would be stable during excavation, buffer compaction and waste deposition. There might be some instability in the rock walls in the uppermost metre of

the boreholes. In relation to the long-term stability of the rock web in a vault, the effects of heating the rock, and the support provided to the rock by the clay sealing materials, remain uncertain; it is possible that fracturing greater than that caused by borehole excavation might occur. It is likely that such fracturing would increase the hydraulically active porosity of the rock adjacent to the buffer. Some possible effects of these increases in porosity on water flow in the rock web have been examined by Chan and Stanchell (1990). Assuming that the more highly conductive disturbed zone is not connected to other hydraulically active features in the host rock, calculations show that water particle velocities could be decreased by increased fracturing in the rock web. Conversely, if connections were made to water-bearing features in the rock, then flow velocities in the rock could also increase.

Relationships between the EDZ and radionuclide transfer from a disposal vault to the geosphere are examined by Davison et al. (1994b) and in Section 6.2.3 of this report. Here, for the purposes of discussing the period during which the buffer and backfill would not be water-saturated, it is observed that in a vault it would be possible for water to gain access to the buffer within two extreme bounding conditions. Where rock stresses were high, the rock web fractured and the porosity connected to ample water supplies in the geosphere, water could be supplied in sufficient quantity to meet the suction demand of the buffer. This upper bound condition is to be contrasted with the lower bound, for which the borehole wall would remain intact and water flow into the buffer would be controlled by the low hydraulic conductivity of the rock. Both bounding conditions were studied during the Buffer Mass Test of the OECD/NEA Stripa Project (Gray 1993). The lower bound case is being examined by AECL in the URL Buffer/Container Experiment now in progress. Pertinent results from this in situ work are given in Section 3.2.2 of this document.

The EDZ should not influence the final hydraulic pressure (which varies principally with the height of the water table) of the groundwater in contact with the buffer. After the vault was closed and sealed, the hydraulic pressure at the buffer/rock interface in the room at a depth of 500 m would rise with the restoring groundwater table and eventually reach a pressure of 5 MPa. At this pressure the boiling point of water is approximately 260°C.

Before vault closure, hydraulic pressures at the buffer/rock and buffer/backfill interfaces would be strongly influenced by the EDZ. The hydraulic pressure at the surface of open excavations is the same as that of the atmosphere in the excavation. Data from the URL (Kozak and Davison 1992) and Stripa (Pusch et al. 1985a) show that with increasing radial distance away from the excavation, hydraulic pressures in granitic rock can increase to values corresponding to those expected from knowledge of the regional groundwater pressures within about one opening diameter. Water pressure at the surface of the excavation would begin to rise as rooms and tunnels were backfilled. The magnitude of the rise would depend on the degree of connectivity of the EDZ with open excavations and the fracture characteristics of the rock. Results from the Stripa Buffer Mass Test show that, despite groundwater pressures of up to 1.5 MPa only 10 m away from the face of the excavation, the hydraulic pressure at the excavation face had risen

to only 45 kPa two and a half years after complete backfilling. Groundwater drained through the EDZ to the nearest open excavation. In this context, it is noted that excavating a vault and completely filling it with waste would take approximately 60 a. While the deposition rooms would be backfilled soon after the waste was deposited, the access ways would remain open for a longer period of time for a variety of purposes, including monitoring the vault. From the Stripa test results it may be inferred that the hydraulic pressures in the groundwater in the EDZ, which would interconnect with the open excavations during this period, would remain low. In regions of the vault where the EDZ was not naturally connected to open excavations, or where grouting had been used to minimize flow, water pressures could rise to reflect the values in the intact rock even before the vault was closed and sealed.

Temperature

The temperature in a vault would depend on the rate of heat output from the waste, the geometric arrangement of the containers, the initial temperature of the rock, the heat-transfer properties of the buffer and backfill materials and the host rock, the location of sealing material in the vault, and time. For the reference vault configuration, thermal calculations, based on a simple heat conduction model, indicate that temperatures in a vault at a depth of 1000 m would be less than 100°C and that the maximum temperature would be reached approximately 30 a after vault closure (the corresponding maximum temperature at 500 m would be 94°C (Table 2-1)) (Mathers 1985). This analysis uses a rock thermal conductivity of 3.0 $W \cdot m^{-1} \cdot °C^{-1}$ and a thermal conductivity of 1.5 $W \cdot m^{-1} \cdot °C^{-1}$ for both the buffer and backfill. The approximate temperature profile across a half-section of an emplacement room and its variation with time are shown in Figure 3-1.

The analyses indicate that the temperature of the surface of the containers located centrally in the room would rise to approximately 100°C. The data also show that temperature gradients across the buffer material would decrease with time and be higher before the container surface temperature reached maximum. Specifically, the calculated maximum temperature gradient decreases from approximately $30°C \cdot m^{-1}$ 1 a after waste deposition to about $7°C \cdot m^{-1}$ 100 a after vault closure. The gradient drops to less than $2°C \cdot m^{-1}$ after 1000 a. If the buffer undergoes significant drying, with a decrease in thermal conductivity to 0.7 $W \cdot m^{-1} \cdot °C^{-1}$, analyses (Baumgartner et al., in preparation) show that the temperature at the container surface could increase by as much as 5°C because of the increased thermal resistance of the clay.

The maximum surface temperature of the containers and the induced temperature gradients in the buffer and backfill would vary with time and location in the vault. Variations would arise from local differences in the heat-transfer properties of the rock, variations in the heat output of the containers, and the moisture content distribution in the buffer and backfill. For the latter case, Radhakrishna (1982) has shown that the thermal conductivity of unsaturated buffer and backfill materials increases with increasing moisture content. Because of uncertainties in the system it is not possible to deterministically predict precise variations in temperature.

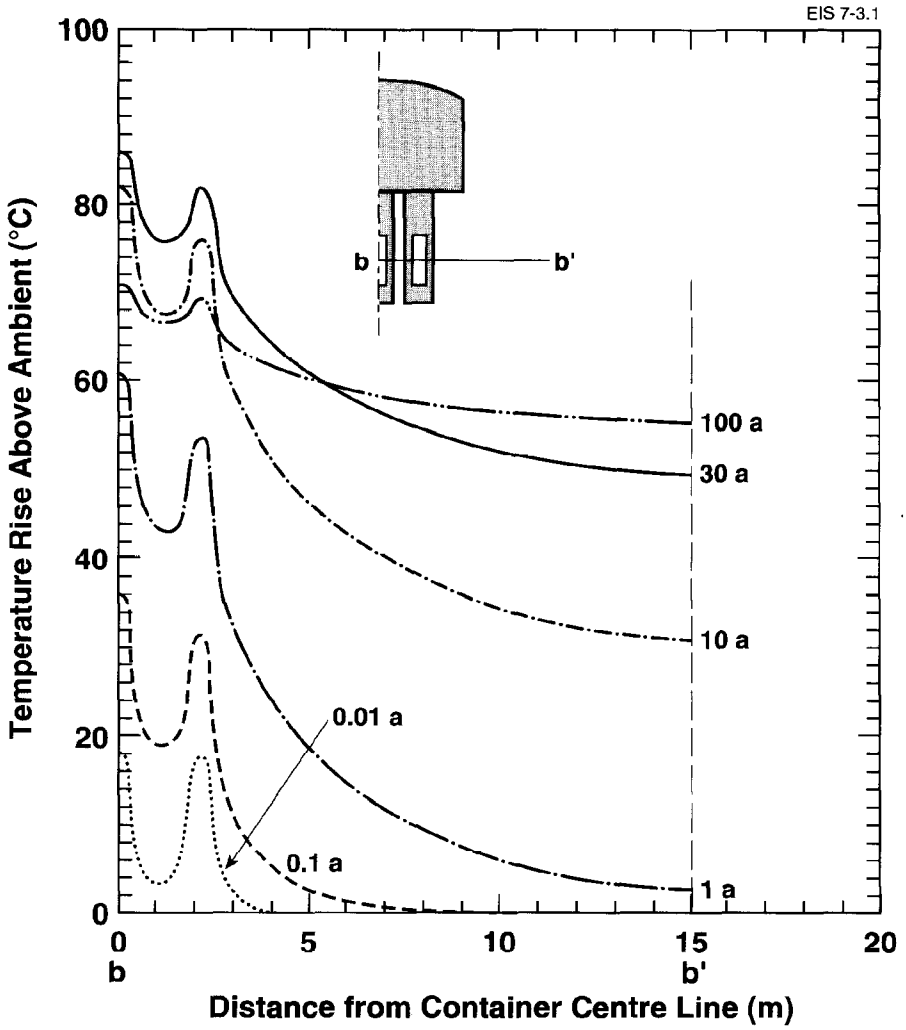

FIGURE 3-1: Temperature Profiles Along the Line b-b' in the Borehole Vertical Plane at Selected Times after Waste Emplacement (after Mathers 1985). Ambient temperature at 500 m is about 11°C and at 1000 m 17°C.

However, calculations have been completed that allow for a judgement to be made of the possible magnitude of the range in maximum container surface temperature. A more realistic model for heat transfer in the buffer material has been developed (Radhakrishna et al. 1989). Based on the Philip and DeVries (1957) formulation for coupled movement of heat and moisture in porous media, the model has been coded for computer-based numerical applications. The code is termed TRUCHAM. Advancing from the simple thermal conductivity model, TRUCHAM accommodates with some success the spatial and temporal changes that occur in the thermal conductivity of the buffer arising from predictions of moisture migration.

The model has been applied to the URL Buffer/Container Experiment, which is a physical, full-size model of a unit cell of the vault comprising a single emplacement borehole containing the reference buffer and a simulated heat-emitting waste container. Lower bound water-supply conditions prevail at the buffer/rock boundary. For this configuration, calculations show that a power output of between 1000 and 1300 W is required to elevate the maximum surface temperature of the container to 100°C. This is equivalent to a temperature rise of 83°C at the container surface. The range in power output is related to the increasing thermal conductivity of the clay with increasing water content. In the URL experiment a power output of 1200 W increased the temperature of the container surface by 76°C. An analysis of the data indicates that temperature changes at the container surface can be predicted with an accuracy of, at worst, ±10%. This is consistent with the findings of the International Stripa Project (Gray 1993). The average power output of a container holding 72 bundles of 10-a-old used fuel is approximately 300 W, which, for a single isolated emplacement borehole such as that in the URL experiment, would raise the container surface temperature by a maximum of only 30°C. In a vault, the temperatures and temperature gradients would be controlled largely by the interaction between the heat flow fields from different containers. This would tend to decrease local temperature variations of the containers arising from variations in fuel burnup. Although fuel bundle burnup (and associated decay heat) varies considerably, ranging from ~360 to ~1100 $GJ \cdot kg^{-1}$ U (Wasywich 1993), it is unlikely that the average heat output from a container would vary significantly from the value calculated for 72 fuel bundles with an average burnup of 685 $GJ \cdot kg^{-1}$ U. The standard deviation of fuel bundle burnup is approximately 90 $GJ \cdot kg^{-1}$ U (see Wasywich 1993, Figure 20). If one assumes a linear relationship between heat generation rate and burnup, this corresponds to a standard deviation in heat output of 13%. However, for a container with 72 fuel bundles with randomly selected burnups, according to the central limit theorem, the standard deviation is only $13/\sqrt{72} = 1.5\%$. Such a small variability would result in maximum container temperatures in the vault varying by less than ±5°C.

Pore-water chemistry

Fresh potable water would be used to mix the buffer and backfill materials. Thus, the average pore-solution composition in the buffer and backfill would be determined by the residual salts present in these materials and their solubility in the mixing water. During the presaturation period, the concentration of the dissolved solutes in the buffer pore water could be altered by the movement of water. Water movement would involve both the redistribution of the mixing water and the ingress of the groundwater from the rock to the clay. Thus, the concentration of solutes in the pore water would be determined by the initial solute concentrations in the mixing water, the dissolved solutes in the granite groundwater and the interactions between the solutes and the clay (see also Section 3.4.1). Precise predictions of the variations of solute concentrations in the pore water in unsaturated clay barrier materials with time cannot be made. However, after the buffer and backfill materials became saturated, the pore-solution composition would gradually approach equilibration with, but never equal, that of the groundwater (Lemire and Garisto 1989, Wanner 1987, Oscarson and Dixon 1989a).

During presaturation, the spatial variations in solute concentrations in the pore water in the buffer and backfill would generate osmotic potential gradients that could cause water movement in these materials. Experiments have shown that moisture-transfer processes in unsaturated clays are largely controlled by the temperature and hydraulic gradients (Yong et al. 1990). The osmotic potential effects in unsaturated clay-barrier materials are included in the hydraulic potentials (suctions) in the clay pore water that control the hydraulic gradients.

3.2.2 Moisture-Content Transient

Using the appropriate hydraulic boundary conditions at the buffer/rock and backfill/rock interface, the container heat output established in Section 3.2.1 and the appropriate material parameters, it should be possible to describe the moisture-content transients that would occur in the buffer and backfill from the unsaturated flow equations in porous media (Yong and Warkentin 1975). Knowledge of the thermohydraulic diffusivities of unsaturated buffer and backfill materials is required. These values are not well defined and this partly accounts for the imprecision of the TRUCHAM model predictions for temperature change described in the preceding section.

Research to define the thermohydraulic diffusivities for buffer material under appropriate thermal and hydraulic boundary conditions is in progress (Yong et al. 1992). To bound the problem and to evaluate the important parameters, a series of laboratory-scale model tests has been conducted (Selvadurai 1990; Radhakrishna et al. 1990; Yong et al. 1990, 1992). The results of these experiments confirm that moisture would be redistributed in the buffer. Some understanding of possible processes occurring in a vault can be obtained from the results of the Buffer Mass Test (BMT) at the Stripa facility (Pusch et al. 1985a).

The BMT was specifically designed to determine the moisture transients and their effects on the mechanical and thermal performance of highly compacted bentonite (HCB). The HCB was a Na-bentonite compacted to a dry density in excess of 1.70 $Mg \cdot m^{-3}$ with an initial S of approximately 50%. Like the Canadian reference buffer material (RBM), the HCB has a hydraulic conductivity of $<10^{-11}$ $m \cdot s^{-1}$, but has a greater swelling potential than the RBM because of its higher density. Cylindrical assemblies consisting of a heater, simulating a disposal container, surrounded by blocks of HCB were placed in six, 760-mm-diameter, 3-m-deep holes drilled in the floor of a room in the Stripa mine. The tops of the assemblies were confined either by a sand-bentonite backfill (heater holes 1 and 2) or by large steel and concrete caps (holes 3 to 6). Water was allowed ingress to the buffer under the natural hydraulic conditions at the borehole wall and under temperature gradients generated with constant heater power output. For the main test all the heaters were powered at 600 W. Special tests were later carried out in individual holes with the power set at 1200 or 1800 W.

The hydraulic boundary conditions reflected the natural variability of the rock mass: each of the heater holes had different water inflow characteristics. Some of the holes intersected discrete water-bearing fractures. The hydraulic boundary conditions along the walls of the backfilled

sections of the room also varied locally. In terms of the hydraulic boundary conditions described in Section 3.2.1, holes 3, 4 and 6 could be considered to represent the lower bound (dry) boundary conditions. Holes 1, 2 and 5 could be considered to represent the upper bound (wet) condition, although most of the inflow to the holes was through discrete fractures that the boreholes intersected. Tests were run for periods ranging from 0.9 to 3.3 a.

For the HCB, under both wet and dry boundary conditions at the buffer/rock interface, pore water in the HCB was initially driven away from the heater (under the influence of the temperature gradient) and collected at cooler locations in the buffer. Thus, in both dry and wet conditions, an envelope of saturated or nearly saturated buffer surrounded a drier inner core of buffer. The drier material shrunk and cracked, and the wetter outer envelope swelled and sealed against the rock. In the dry holes, this situation persisted throughout the test periods. For the wet holes, water was subsequently drawn into the buffer, at a rate determined by the suction properties of the buffer, until saturation was reached, in periods of about 1 a after the buffer/heater systems had been installed and the heaters turned on. Before the buffer/heater systems were installed, it was noted that groundwater flow into the boreholes was not evenly distributed along the borehole walls; it occurred primarily through fractures in the rock that the borehole intersected. In spite of this, measurements of temperature and total swelling pressures exerted by the HCB on the borehole walls during the progress of the tests and post-test moisture sampling, and measurements of buffer moisture in dry holes 3, 4 and 6, showed that the saturated outer envelopes in the HCB were evenly spaced in the annuli of buffer between the heater and the rock. The water distribution patterns did not reflect the fracture features in the borehole walls. It was observed that during the progress of the tests, under the swelling pressures generated by the HCB, the bentonite had extruded to limited and predictable distances into the open fissures in the rock. Evidently, this buffer/rock interaction had led to alteration of the hydraulic boundary conditions acting at the buffer/rock interface.

Yong et al. (1992) have shown that, in unsaturated RBM under opposing heat and hydraulic gradients, temperatures rise to accommodate the heat transfer. Changes in water content occur more slowly than the temperature changes. This behaviour was observed in the HCB in the Buffer Mass Test, in which temperature distributions around the heaters became stable within weeks of power being supplied to the heaters, whereas moisture contents in the dry holes were changing several years after the heaters were powered. Similar phenomena are being observed in the URL Buffer/Container Experiment (Kjartanson et al. 1991). Although definitive statements on the results of this experiment cannot be made until the test is completed, two observations are noteworthy. First, with a heater power output of 1200 W, temperature distributions in the RBM around the heater became stable within weeks of powering the heater. Second, almost two years after the heater was turned on, moisture continues to be redistributed in the RBM around the heater. The RBM in the URL Buffer/Container Experiment appears to be responding similarly to the HCB in the dry holes in the Stripa BMT (Gray et al. 1993). However, there appear to be some dissimilarities in behaviour

resulting from the presence of a sand layer between the heater and the RBM and, possibly, the presence of high water-vapour pressures in this sand.

At Stripa, the backfills used to fill the rooms above BMT heater holes 1 and 2 were sand-bentonite mixtures with clay contents between 10 and 20% by dry mass. The moisture content measurements made in the backfills confirm that, while a non-uniform inflow distribution was visible along the floor, walls and back of the test room, wetting of the backfill was, spatially, a relatively uniform process, controlled more by the water uptake properties of the backfill than the non-uniformity of the flow conditions at the boundaries. As observed for the HCB material, envelopes of saturated backfill material near the rock/backfill boundary surrounded central unsaturated zones. Temperatures and temperature gradients in the backfill were much lower than those in the buffer and, thus, did not significantly influence moisture redistribution and inflow (Pusch et al. 1985a).

The moisture and heat transfer properties of the RBM, the HCB and the sand-bentonite backfill materials tested at Stripa are similar. The physical, mechanical and hydraulic properties of the RBM lie between those of the HCB and the backfill used in the Stripa experiments. The moisture transients observed in the BMT are expected to occur in the RBM and the backfill materials proposed in the Canadian reference vault design. This expectation is further supported by the results of laboratory-scale model tests (Selvadurai 1990, Radhakrishna et al. 1990).

Available information, both in terms of site-specific boundary conditions and material properties, does not allow for the precise prediction of the time needed to saturate either the buffer or the backfill with water. However, it is clear that the time would vary with the hydraulic conditions at the borehole wall, which are likely to differ significantly between boreholes, both locally and within sectors of the vault. The buffer in dry boreholes may take hundreds or, possibly, thousands of years to saturate. Andrews et al. (1986) carried out sensitivity analysis of the resaturation of backfilled tunnels in granite. The results showed that the resaturation time can range from greater than 1000 a to less than 100 a when the hydraulic conductivity of the granite is changed from 10^{-12} to 10^{-9} $m \cdot s^{-1}$. This study, however, did not consider the role of gas generation/entrapment and thermal effects, which could increase the time. In wet boreholes, as shown by the BMT, saturation could occur in 2 or 3 a.

Further complexities arise when the sand layer between the RBM and the container is considered. Immediately after emplacement, the voids in this layer would be dry and filled with air, which, like the air in the backfill in the BMT, could pressurize and resist water inflow. The potential benefit of a water-saturated buffer separated from the container by a dry sand layer can be envisaged as there would be, in effect, no diffusive pathway. More data and theoretical knowledge are needed to confirm this possibility. Thus, the likely effects of delaying container corrosion processes are not considered in the vault model. In the vault, radionuclide release would occur only after the buffer was saturated. Because of uncertainties in the borehole rock wall conditions, the presaturation period could range from two to thousands of years. Hence, this presaturation period has not been considered in the vault model.

3.2.3 Summary

Before a vault is closed and sealed, the EDZ would strongly influence the hydraulic pressure at the buffer/rock and backfill/rock interfaces. Conditions would vary spatially in the vault, although, after waste was emplaced, there would be a tendency for the hydraulic pressure at any one location to increase with time. The rock, with a hydraulic conductivity ranging from 10^{-12} to 10^{-7} $m \cdot s^{-1}$, would likely be saturated with water. The condition for a specific waste-emplacement borehole or emplacement room cannot be predicted with precision. During the buffer and backfill presaturation period, the rock may or may not allow sufficient free flow in the groundwater to saturate the buffer or backfill by suction. After a vault was closed and sealed, hydraulic pressures would rise with the restoring groundwater conditions. At a depth of 500 m, the ultimate hydraulic pressure would be approximately 5 MPa.

The maximum container-surface temperature is expected to be <100°C. Initially, temperature gradients across the buffer material would be high (30°C·m^{-1} after one year, for example), but they would decrease as temperatures in the vault rose. When the maximum container-surface temperature is reached, approximately 30 a after vault closure, temperature gradients are expected to be in the range from 4 to 8°C·m^{-1}. Subsequently, as the vault temperatures decreased, temperature gradients across the buffer would decrease to values of less than 2°C·m^{-1} 1000 a after vault closure.

The solute concentrations in the pore water in the buffer and backfill would vary with time and location in the vault. Osmotic potential differences generated in the materials would not significantly influence moisture migration during the presaturation period.

In general, the buffer would first dry next to the container and become wet towards the periphery of the borehole. Water would then diffuse into the buffer under the total water-potential gradients existing between the water in the rock (higher potential) and the buffer (lower potential). This process would eventually lead to saturation of the buffer with water. The saturation process could take from a few years to millennia to complete. Because of the uncertainty in the duration of the presaturation period, this time is not taken into account in the vault model. The consequences of the air pocket entrained in the sand layer next to the container are not predictable for the presaturation period, and the probable delaying effects on container failure and dissolution of the radionuclides are, duly, not taken into account in the vault model. Work on modelling the hydraulic interaction between the buffer, sand, rock and backfill is in progress, as are studies to address the issue of gas transfer through buffer material.

3.3 FACTORS AFFECTING BUFFER AND BACKFILL PERFORMANCE

The mass transport processes (i.e., transport arising from hydraulic conductivity and diffusion) in the saturated buffer and backfill materials are of critical importance. They depend on the connected porosity of the material, which is related to clay density. Hydraulic conductivity decreases with an increase in the clay density (see Johnson et al. 1994, Figure 4-4). Other factors, such as pore-water salinity and temperature,

also affect the hydraulic conductivity (Yong and Warkentin 1975). The mechanisms through which these and other factors also influence the chemical diffusion coefficient for radionuclides, and the extent to which the effects are accounted for in the vault model, are discussed in Section 3.5. In the following section, we examine several processes or factors that could potentially alter the mass transport properties of the buffer and backfill materials.

3.3.1 The Smectite-Illite Transformation

The elemental and mineralogical compositions of the Avonseal bentonite are given by Oscarson and Dixon (1989a) and Quigley (1984). The swelling properties of the RBM are derived from the smectite present in the bentonite. The question of whether or not transformation of smectite into clays with a lower swelling capability could influence the self-sealing properties of the RBM and its mass transport properties therefore needs to be addressed. The most frequently observed metasomatic alteration of smectite clays is the incorporation of illite layers as the smectite is progressively transformed to illite through a series of intermediate steps represented by mixed-layer illite/smectite clay. The progressive increase of non-expanding illite layers in consolidated illite/smectite clays with increasing burial depth and temperature is observed in sedimentary basins of all ages throughout the world (see, for example, Weaver 1979).

The smectite-to-illite conversion involves three fundamental steps: (1) the creation of a high layer charge by the replacement of Si^{4+} with a cation of lower valence, such as Al^{3+} or Mg^{2+}; (2) the influx of K^{+} to saturate the cation-exchange sites of the now highly charged smectite intermediate (K^{+} is important in this reaction because of its size and relatively low hydration energy); and (3) irreversible collapse of the high-charge smectite to the non-expanding illite.

The reaction is a function of several variables, including temperature, time, pore-solution composition, and composition of smectite. The elevated temperatures in a disposal vault and the time scales over which the buffer must function necessitate consideration of this reaction.

The first step depends strongly on the temperature. At temperatures less than 100°C, the rate at which the high-charge smectite is formed is so slow that the rate of conversion is thought to be negligible (Anderson 1983).

The availability of K^{+} and the concentrations of other cations in the reacting solution are also critical factors in the conversion reaction (Roberson and Lahann 1981). Cations such as Ca^{2+}, Mg^{2+} and Na^{+} compete with K^{+} for positions on the exchange sites of the clay and consequently slow the reaction rate of smectite to illite. Given the relatively low $K^{+}/(Ca^{2+} + Mg^{2+} + Na^{+})$ ratio in deep groundwaters in the Canadian Shield (Gascoyne 1988), the conversion reaction will be extremely slow even at relatively high temperatures. This is confirmed by field evidence. Altaner et al. (1984) studied a bentonite bed from the Marias River Formation in the Montana disturbed belt that lies between rock strata containing K-bearing minerals. The deposit is 50 to 76 Ma old, and has experienced temperatures of 100 to 200°C for sustained periods of time. They reported

an increase of K^+ and of the proportion of illite layers in the illite/smectite interlayer material from the centre of the bed towards both edges, from about 50% to 70%. The illite/smectite material at the edges of the bed were found to be 3 to 4 Ma older than the illite/smectite in the centre. Potassium for the illite formation was considered to have been derived from a breakdown of K-bearing minerals in the surrounding shale and the subsequent diffusion into the bentonite. The younger age of the material in the centre of the bed was attributed to the very slow diffusion of K^+ through the bentonite. A similar phenomenon has been reported by Brusewitz (1986) for a bentonite of Ordovician age in the Kinnekulle region of Sweden.

Thus, the smectite-to-illite conversion, even when the temperature rises to levels sufficient to create the high-layer-charge smectite, and K^+ is readily available, is very slow.

The consensus is that the smectite-to-illite conversion at temperatures <100°C and with a relatively low K^+ concentration in the pore solution is an extremely slow process (Anderson 1983, 1984; Peacor et al. 1986; *Johnston and Miller* 1985; *Coons* 1987; Pusch and Karnland 1990). Illitization rates for highly compacted bentonite in a disposal vault have been estimated by Pusch (1992). For bentonite layer thicknesses of 250 mm or more, his model predicts the conversion time to be tens of thousands to millions of years at temperatures below 100°C (Gray 1993).

In the unlikely event that conversion of smectite to an illite/smectite mixed-layer clay occurred, the converted material should still function effectively as a buffer material. Mixed-layer clays have some capacity to swell, have an acceptably low hydraulic conductivity and high sorption capacities, and a total porosity about the same as that of the unaltered clay. Moreover, the diffusivity of compacted illite/smectite mixed-layer clay is about the same as that of bentonite at a comparable density (Oscarson, in press).

The available evidence indicates that Ca^{2+}-saturated smectites are inherently more stable, vis-à-vis illitization, than are Na^+-saturated smectites (Roberson and Lahann 1981). Even though Avonlea bentonite is predominantly saturated with Na^+ initially (Quigley 1984), the clay would gradually become saturated with Ca^{2+} as groundwater with a relatively high level of Ca^{2+}, such as that present in the Canadian Shield (Gascoyne 1988), came into contact with the barrier materials (Oscarson and Dixon 1989a; Oscarson and Heimann 1988). This process would further limit the transformation rate in a disposal vault.

3.3.2 Swelling and Self-Sealing Properties and the Effects of Steam

In the reference design, the buffer is confined by the rock and the backfill. In addition to swelling to fill any cracks (the swelling process is described by Johnson et al. (1994) Section 4.6.1), the saturated material would also exert pressures (P_s) on confining media. The magnitude of these pressures would depend principally on clay density, γ_c, temperature, moisture content and the ionic concentration in the groundwater (Dixon et al. 1985, Yong and Warkentin 1975). The saturated buffer at a density of

~1.2 $Mg \cdot m^{-3}$ could exert a pressure of between 1 and 2 MPa on the rock, container and backfill. This pressure is additive to the hydraulic pressure (Dixon et al. 1986). At $\gamma_c > 1.7$ $Mg \cdot m^{-3}$, maximum pressures of approximately 10 MPa were measured in the HCB tested in the wet boreholes of the BMT at Stripa (Pusch 1978, 1988). These pressures were measured in the later stages of the tests as the material approached saturation at elevated temperatures.

Dixon et al. (1985) have shown that oven-drying of the RBM causes gross volumetric shrinkage of between 2 and 4%. This is accompanied by cracking. Given access to water, the oven-dried clay swelled, and hydraulic conductivities of $<10^{-11}$ $m \cdot s^{-1}$ were measured in the resaturated RBM. In other studies, samples of dry compacted buffer were intentionally cut with a band saw, resulting in a slot 2 to 3 mm thick across the entire sample. Upon access to free water, the slotted buffer quickly swelled to close the slot, and within a few days the hydraulic conductivity of the slotted samples was the same as that of an unslotted buffer at the same density. This is supported by the work of Oscarson et al. (1990) on unprocessed bentonite (bentonite that had not been crushed, ground and dried by the suppliers). Initially the clay as collected from the field was highly fractured; however, as in the case with fractured or slotted processed buffer, upon access to water, the unprocessed clay swelled and exhibited a very low permeability (see also Section 3.3.6).

At temperatures above 100°C, steam might be generated in the buffer material during the presaturation period, depending on a number of factors, such as the pressure acting on the system. Couture (1985) reported that in as little as a few days the presence of steam causes an irreversible reduction in the specific sediment volume of bentonite.[6] Oscarson and Dixon (1989b) confirmed Couture's results, and showed that in an uncompacted state, even at temperatures as low as 110°C for a few weeks, in a closed system such as that contained within the saturated buffer envelope during the presaturation period, there is a significant reduction in the specific sediment volume of the clay. The mechanisms through which steam decreases the swelling capacity of loose clay remain obscure, but it may involve the precipitation of Si and/or Al oxides on the edges of the clay particles, thereby altering the edge charge, which, in turn, affects the aggregation of the clay particles.

Experiments on the effects of steam on dense bentonite clays ($\gamma_c > 1.2$ $Mg \cdot m^{-3}$) indicate that when the clay is heated to temperatures as high as 125°C in a closed system and then directly tested at the same temperature, there is little effect on swelling pressure generated by the dense clay (Oscarson and Dixon 1990). Moreover, the hydraulic conductivity increased only slightly relative to an untreated bentonite at the same density. Given that the temperature in a disposal vault would be <100°C (Section 3.2.1), the results indicate that the effects of steam would not be significant to overall vault performance and can be ignored in the vault model.

---

[6] The specific sediment volume is a measure of the swelling capacity of a clay.

3.3.3 Expansion and Extrusion

Compacted bentonite and bentonite-sand mixtures are being increasingly used as barriers for the isolation of hazardous wastes. They are used as liners on the inverts of liquid-waste ponds and have been employed to cap solid-waste disposal sites. In both uses seal failures have been reported (Schulz et al. 1989), which may raise concerns for the long-term performance of the buffer and other seals containing the swelling bentonite.

Failures of caps occur primarily because of repeated cycles of wetting and drying and freezing and thawing of the clay. Cracks thus generated in the cap allow infiltration of rain or meltwater to the waste, which can be leached away. The buffer in a disposal vault would not be repeatedly exposed to these cyclic conditions, and this form of failure is not considered possible.

Liners fail as a result of loss of clay density. Clay density is decreased as the clay swells. Moreover, a clay-density decrease can be localized as the clay migrates under its own swelling potential within the liner or into neighbouring materials with higher porosity. Thus, hydraulic conductivity increases or becomes heterogeneous.

In a disposal vault, the following mechanisms of clay-density decrease can be postulated.

1. The buffer could expand into the backfill—the rock mass acting as a virtually rigid restraint to the swelling buffer.

2. The buffer could penetrate into fractures that intersect the emplacement boreholes.

3. The clay in the buffer could move into the sand layer next to the container.

The first two of these hypotheses were tested as part of the BMT at Stripa. Measurements showed that under the fully developed swelling pressure of 10 MPa the HCB from heater holes 1 and 2 expanded into the backfill by between 5 and 7 cm. These values were predicted using a relatively simple punching shear model and assuming appropriate strength and stiffness parameters for the backfill (Pusch et al. 1985a). This model has been applied to the RBM as well. In this case, swelling pressures are much less than those developed by the HCB—maximum values of approximately 2 MPa are predicted—and the backfill is stiffer and has higher internal friction (Chan and Radhakrishna 1986) than the sand-bentonite backfill tested in the BMT. Moreover the frictional resistance between the RBM and the borehole wall is expected to be greater than that between the HCB and the borehole wall. Under these circumstances the predicted displacement at the buffer/backfill interface is less than 3 cm. If one assumes that this displacement is uniformly distributed throughout the buffer, the average γ_c of the buffer would decrease by only 0.01 $Mg \cdot m^{-3}$. This decrease would not significantly alter either the swelling or the mass transport properties of the buffer. Because of the internal friction properties of the RBM ($\phi' \sim 14°$, Saadat et al. 1989), the density of the annular layer of buffer radially

separating the container from the rock is unlikely to be affected by movement at the buffer/backfill interface.

Laboratory tests and theoretical studies (Pusch 1978) have shown that HCB will penetrate joints and fractures in the rock. The rate and depth of penetration are influenced by the fracture aperture of the rock, the swelling pressure and the frictional resistance between the bentonite and the rock. For compacted HCB, the fracture aperture of the rock must exceed approximately 0.1 mm. Data from the BMT tends to confirm the laboratory and theoretical studies. The HCB penetrated natural fractures with apertures of approximately 0.5 mm to a distance of 5 to 10 mm. The swelling pressures of the RBM are less than those of the HCB, and the sand in the RBM should result in higher frictional resistance between the RBM and granite than between the HCB and granite. Extrusion of the RBM into fractures intersected by the borehole would be minimal and insignificant to the mass transport and other physical properties of the buffer. In this context it was noted that, with respect to the possible decrease in density, the sand-bentonite backfill tested in the BMT did not significantly penetrate the fractures intersected by the test room.

In view of the above, extrusion of the bentonite from the buffer into the very small pores of the sand layer next to the container would be virtually impossible. Indeed, sand layers are often used in engineering construction to prevent clay particles from pumping into granular materials. If movement of clay particles occurs, it happens only under the pumping action of repeated cyclic loading, which would not be experienced by the buffer in the reference vault design.

3.3.4 Hydrogen Generation and Transport

The production of gases by processes occurring in a disposal vault and the effects of potential gas-phase formation are important considerations in postclosure performance assessment. If the gas production rate exceeded the rate at which dissolved gas could diffuse away, and a separate gas phase formed in the near field, the movement of groundwater and dissolved contaminants might be affected. Possible consequences of the formation of a gas phase include (i) potential gas-phase migration of ^{14}C released from the fuel as CO_2 or CH_4; (ii) high gas pressures that could affect the integrity of shaft seals or bulkheads; and (iii) expulsion of groundwater in the near or far field because of gas buildup. The latter might have both positive and negative impacts, such as enhancement of transport of contaminated groundwater and prevention of water access to the containers. Gas buildup in the vicinity of the container is not expected to affect the integrity of the buffer. Pusch et al. (1985b) have shown that gas will channel through the largest pores without affecting the surrounding saturated mass of buffer.

Several possible sources of gas production exist in the reference disposal vault. Gamma radiolysis (prior to container failure) and α-radiolysis (after container failure) are potential sources of H_2. Hydrogen is also produced by the corrosion of metals, such as steels, Zircaloy and titanium. Microbial processes, such as degradation of organic matter in the buffer and backfill, are capable of producing gases such as CH_4 and CO_2. Whether

or not the production of these gases via the various mechanisms would be significant would depend on a number of factors. These include (i) the volume of pore space available in the container, sand layer, buffer and backfill; (ii) the initial water content of the buffer and backfill; (iii) the production rates and solubilities of the various gases under the temperature and pressure conditions in the vault; and (iv) the maximum rate of diffusive transport of the dissolved gases into the surrounding rock. Each of these is discussed in detail to determine the probable time to achieve saturation of gases in the near field. The relevant data and calculations are summarized in Appendix B.

The total pore volume available for buildup of gases produced includes the combined pore volumes in the container, sand layer, buffer materials and backfill material. The estimated total volume is ~9000 L per container. The pore volume contained within the surrounding EDZ and overlying rock mass is ignored in the calculations, because of the very low porosity in the rock. A layer of rock 150 m thick overlying the vault is required to give about the same pore volume as provided by the buffer and backfill.

Before considering the rate of production of various gases, it is instructive to examine the fate of entrapped air in the conceptual disposal vault (see Section 3.4.2). The oxygen is likely to be consumed relatively rapidly as a result of oxidation of minerals containing Fe(II) (see Section 3.4.2). The estimated N_2 concentration in the pore water is ~9 x 10^{-3} mol·L^{-1}, less than the solubility of N_2 at 5 MPa; thus, no N_2 gas bubble is expected to form in the vault, except during the period prior to restoration of full hydraulic pressure.

A preliminary examination of the production rates of H_2 as a result of corrosion of carbon steel suggests that the groundwater would rapidly become saturated with H_2 if carbon steel were used to construct the basket that retains the fuel bundles within the container. Scoping calculations based on the data of Simpson and Schenk (1989) suggest production rates of 3 to 30 mol·a^{-1} of H_2 resulting from general corrosion of the steel basket once the container is breached. At such a rate, H_2 solubility would be exceeded in the near field within decades. As a result, the use of a ceramic material or a metal with a very low uniform corrosion rate (a stainless steel, for example) would be a more appropriate choice. For the same reason, rock bolts used for ground support should be fabricated from stainless steel.

The uniform corrosion of Zircaloy sheath and titanium would produce H_2 at much lower rates than would the corrosion of carbon steel. Using the data of Mattsson and Olefjord (1984) for the general corrosion rate of titanium in bentonite pore water, and assuming the same rate for Zircaloy, gives estimated H_2 production rates per container of 1.8 x 10^{-3} mol·a^{-1} for titanium and 1.6 x 10^{-2} mol·a^{-1} for Zircaloy. Some of this H_2 may be taken up as hydrides of titanium and zirconium during the corrosion process, but this effect is neglected in the calculations.

The production rate of H_2 as a result of γ-radiolysis is expected to be quite small (see Section 3.4.2). A rate of 8 x 10^{-3} mol·a^{-1} has been estimated by Christensen and Bjergbakke (1982) for a γ-field of 9.7 Gy·h^{-1},

similar to the field (52 $Gy \cdot h^{-1}$) expected at the surface of the reference container. This production rate would decrease by a factor of 10^4 within 500 a; thus, the contribution from γ-radiolysis is ignored in subsequent calculations.

Alpha-radiolysis could make a significant contribution to H_2 production for an extended period of time because of the long half-lives of some of the important alpha emitters. The possible production rates for light-water reactor fuel have been calculated by Christensen and Bjergbakke (1982), and Garisto (1992) has performed similar calculations for CANDU fuel. The calculations illustrate that the production rates are critically dependent on the potential for the Fe^{2+}/Fe^{3+} system to act as a recombiner, i.e., to regenerate water via recombination reactions. Without such a system, the production rate could be as high as 0.48 $mol \cdot a^{-1}$. However, if a finite quantity of Fe^{2+} is available and is consumed, resulting in Fe^{2+}/Fe^{3+} acting as a recombiner (Christensen and Bjergbakke 1982), the production rate would drop to 9×10^{-3} $mol \cdot a^{-1}$. This is considered to be the most probable scenario, since the buffer material contains very little Fe^{2+} and would retard the diffusion of Fe^{2+} towards the container, leaving only the initial quantity of Fe_3O_4 redox additive within the container (see Section 2.2) to provide Fe^{2+} to interact with radiolysis products.

Having established the probable H_2 production rates as a result of corrosion and radiolysis, it is necessary to examine the potential rate of diffusion of dissolved H_2 into the surrounding rock. The transport time through the buffer and backfill materials would be relatively short (approximately 100 a to diffuse across the buffer for a diffusion coefficient of 10^{-3} $m^2 \cdot a^{-1}$). Because the porosity of the surrounding rock is much smaller than that of buffer and backfill, and the rock is a more massive barrier, the steady state is expected to be dominated by transport through the rock. Thus, the steady-state transport across a planar rock barrier of 500 m as determined in Appendix B provides a reasonable estimate of the H_2 transport rate. At steady state, the rate is calculated to be $\sim 10^{-6}$ $mol \cdot a^{-1}$. This is orders of magnitude below the total production rate of ~ 0.025 $mol \cdot a^{-1}$ resulting from corrosion and radiolysis. It is evident, therefore, that saturation would ultimately occur. At the estimated production rates, saturation would be reached in approximately 18 000 a. However, at the estimated gas-production rate, the H_2 partial pressure would reach only 10 MPa in approximately 40 000 a. The gas phase at this time would occupy only 1% of the total pore space in the buffer and backfill; thus, the effects are unlikely to be significant in the time frame of assessment calculations.

Besides the production of H_2 from corrosion and radiolysis, the only other potential source of gas in the reference disposal vault is the decomposition of organic matter, which might result in the production of CH_4 and/or CO_2. Studies are in progress to estimate the production rates of these gases. Production rates are expected to be low because of the small quantity of organic matter present in the vault and the limited availability of nutrients for microbial growth.

3.3.5 Effect of Cement on Clay Barrier Properties

Cement is used in the reference disposal concept for grouting, and/or as seals and bulkheads. The primary concern in the interaction of cements with clay-based barriers is the creation of a high pH environment, since clay minerals are relatively unstable at high pH. As components of the cement dissolved, an alkaline plume would move, by diffusion, from the cement/clay interface through the clay. This has important implications for the type and extent of hydrothermal reactions that the clay would undergo. The likely result of a high pH environment would be the formation of framework silicates, such as zeolites (Johnston and Miller 1984). In some respects this may he beneficial: zeolites, for example, are effective in sorbing some species, such as Cs^+.

It is likely that cement would be in contact with some of the backfill material at the room/backfill interface (Johnson et al. 1994, Figure 4-17). Because of the thickness of the backfill material, only a fraction of the material adjacent to the cement would be affected. The amount would depend on factors such as the mass of cement used in a particular location, the buffering or neutralizing capacity of the backfill, and the pH and temperature at which adverse mineral transformations occurred. The temperature at a backfill/cement interface would be relatively low because it would be a considerable distance from the waste containers. S Consequently, phase transformations that are known to occur in high-temperature, high pH environments would not occur in the disposal vault.

The pH of water in direct contact with cement might initially be greater than 13, as a result of the dissolution of sodium and potassium hydroxides from the cement. Later, when these hydroxides had been removed, the pH would be expected to decrease to around 10 to 11 and would be controlled by the dissolution of calcium compounds from the cement (Atkinson et al. 1986). The release of $Ca(OH)_2$ would continue at its solubility limit for long periods; it has been estimated that groundwater in contact with concrete can maintain a pH >10 for more than 10^6 a (Atkinson et al. 1986). The use of cement-based materials containing silica fume could substantially decrease the amount of free $Ca(OH)_2$ present, and such materials would likely be used in a disposal vault to ensure that the impact of cements on the vault environment was minimal (Coons 1987).

Anderson et al. (1982) reported that, after 70 a of contact between bentonite and concrete, mineralogical changes had occurred in the bentonite to a depth of only approximately 50 μm from the clay/concrete interface. The predominant mineralogical change observed in the bentonite was the formation of analcime. Pusch (1982) has also investigated the interaction between compacted bentonite and cement. Zeolites were not identified with certainty in his study. On the basis of various assumptions, however, it was estimated that at a temperature of 10 to 20°C, a layer of clay no more than 1 cm thick would be converted to zeolite over a period of 500 to 1000 a.

There would be no cement-based materials in the vicinity of emplacement boreholes (concrete room bulkheads would be ~12 m away); thus, the buffer material would be unaffected by the presence of cement-based materials in the vault.

3.3.6 Natural Analogues

An examination of the properties of bentonite as it occurs in the field can provide valuable information on the potential long-term performance of a bentonite-based barrier material in a disposal vault. Oscarson et al. (1990) studied the swelling and hydraulic properties of samples of intact, unprocessed clay (clay that was not crushed, ground or dried by the suppliers) from the Avonlea bentonite deposit in south-central Saskatchewan, Canada; the processed bentonite from this deposit is being considered for the clay component of the RBM. The field dry density of the clay ranges from 1.1 to 1.3 $Mg \cdot m^{-3}$—similar to the γ_c value of the clay component of the RBM. This clay deposit is 75 to 85 Ma old. The clay still maintains a significant swelling capacity (>250 kPa) and low hydraulic conductivity ($<10^{-11}$ $m \cdot s^{-1}$). Moreover, the clay exhibits a remarkable ability to self-seal. Initially, the clay as collected from the field was highly fractured, and in some cases the flow rate of water through the samples was as high as 10^{-5} $m^3 \cdot s^{-1}$; this flow rate, however, rapidly decreased to 10^{-10} $m^3 \cdot s^{-1}$ as the clay absorbed water and swelled.

Pusch et al. (1987a) and Pusch and Karnland (1990) examined a number of smectite-containing clays ranging in age from tens to hundreds of millions of years, and from a wide range of environments. The unprocessed clays generally exhibited low permeabilities and high swelling capacities. The authors also estimated that when the smectite content of clays is greater than 15 to 25%, clays have self-sealing capabilities.

Historical evidence also indicates that clay-based barriers can be effective for thousands of years in limiting the movement of water and air in an underground environment (Lee, C.F. et al. 1986).

Studies such as these provide support to the contention that clay minerals can function effectively as barrier materials for tens of thousands of years under a wide range of conditions.

3.3.7 Summary

In the conceptual disposal system, the buffer would swell as it became wet. This swelling would be sufficient to close cracks generated by shrinkage as a result of drying during the presaturation period. The swelling capacity would be influenced by clay density, temperature and the ionic concentration in the groundwater. For the expected vault conditions the swelling properties of the buffer would be expressed as a swelling pressure acting on the rock, the container and the backfill. For the RBM the pressure is expected to be between 1 and 2 MPa. The hydraulic conductivity of the saturated buffer should not be significantly influenced by steam and would remain less than approximately 10^{-11} $m \cdot s^{-1}$. The swelling and, thus, self-sealing capacities of the buffer would depend on the properties of the smectite clay minerals in the bentonite. These minerals are sufficiently stable under vault conditions to ensure the effective performance of the buffer for tens of thousands of years. Moreover, the buffer would be sufficiently well restrained by the rock and the backfill to ensure that significant density changes would not occur and the buffer's self-sealing properties would be maintained.

3.4 CHEMICAL CONDITIONS AND THE EFFECTS OF RADIATION

The chemical conditions in a disposal vault would determine the corrosion rates of the containers, the dissolution rates of the used fuel and the solubilities of the various radionuclides. The expected groundwater composition at the depth of the conceptual vault, and the composition changes resulting from interaction of the groundwater with buffer and backfill materials, are discussed in Section 3.4. Also described are the evolution of the redox chemistry, the effects of radiolysis of water on redox conditions, and the potential role of microbial activity, colloids and organic matter in engineered barrier performance.

3.4.1 Groundwater Composition

The reference groundwater assumed in the case study is designated WRA-500 and its composition is given in Table 3-1a (Gascoyne 1988). This composition is the average of 12 samples taken from depths of ~350 m to ~800 m in the Whiteshell Research Area. It is accepted as the reference composition at 500 m, the depth of the waste disposal vault for the case study. Also shown in Table 3-1a are (i) the groundwater composition at 1000 m in the WRA (WRA-1000), and (ii) the compositions of synthetic granitic groundwaters designated as WN-1 and SCSSS (standard Canadian Shield saline solution) (Abry et al. 1982), which have been used in many of the experiments performed in the Canadian Nuclear Fuel Waste Management Program (CNFWMP).

The groundwater in the pores of the buffer and in contact with the waste container and, ultimately, the used nuclear fuel, would be conditioned by contact with the buffer and backfill materials. This solution might be quite different from the reference groundwater, WRA-500. The impact of the clay buffer on the composition of the groundwater has been considered by Oscarson and Dixon (1989a), Lemire and Garisto (1989) and Wanner (1987). The characteristics of the "conditioned" or "contact" water would depend strongly on the ion exchange capacity of the buffer, the minor components of the buffer material, and how much water had passed through the buffer. The concentration ranges calculated for use in the vault model for the major or important species in the contact water are given in Table 3-1b; the assumption of loguniform distributions in this table is for convenience only and implies nothing about natural variation.

3.4.2 Redox Conditions

Groundwaters deep in granitic rock are expected to have relatively low redox potentials because of the absence of dissolved O_2 and the presence of reduced Fe, S and Mn species in the groundwaters and minerals. Studies indicate typical redox potentials of -100 to -300 mV_{SHE} at pH 7 to 9 (Wikberg 1986, 1988; Nordstrom 1986). Studies of the redox chemistry of groundwaters in the WRA at depths of 500 m indicate somewhat less reducing potentials (0 to -100 mV_{SHE} at pH 7 to 9), although the waters are clearly O_2-free (Gascoyne 1992).

TABLE 3-1a

COMPOSITIONS OF GROUNDWATERS FROM THE WHITESHELL RESEARCH AREA (WRA-500 AND WRA-1000) AND SYNTHETIC GROUNDWATERS (WN-1 AND SCSSS)

	$mg \cdot L^{-1}$			
	WRA-500	WRA-1000	WN-1	SCSSS
Na	2 300	7 000	1 910	5 050
K	10	20	14	50
Mg	30	25	61	200
Ca	1 800	5 000	2 130	15 000
Sr	20	50	24	20
Fe	1	1	0.56	-
Si	5	3	0	15
HCO_3	50	20	68	10
Cl	6 000	19 000	6 460	34 260
SO_4	1 000	1 300	1 040	790
NO_3	0	-	33	50
F	2	5	0	-
Br	30	60	-	-
PO_4	<0.5	-	-	-
U	0.02	-	-	-
I	0.02	-	-	-
Al	<0.05	-	-	-
B	1.2	-	-	-
TDS*	11 247		11 740	55 400
pH	7.8	8.0	7 ± 0.5	7 ± 0.5
Eh	-30 mV			

*total dissolved solids

TABLE 3-1b

DISTRIBUTION OF CONTACT-WATER PARAMETERS USED IN THE VAULT MODEL

Parameter	Units	Distribution	Minimum	Maximum	Mode
$[CaCl_2]$	$mol \cdot kg^{-1}$	loguniform	$10^{-3.5}$	$10^{-1.0}$	-
[NaCl]	$mol \cdot kg^{-1}$	loguniform	$10^{-2.3}$	$10^{-0.5}$	-
$[Na_2SO_4]$	$mol \cdot kg^{-1}$	loguniform	$10^{-2.2}$	$10^{-1.0}$	-
[tot. inorg. C]	$mol \cdot kg^{-1}$	loguniform	$10^{-3.6}$	$10^{-1.7}$	-
[tot. F]	$mol \cdot kg^{-1}$	loguniform	$10^{-6.0}$	$10^{-2.8}$	-
[tot. inorg. P]	$mol \cdot kg^{-1}$	loguniform	$10^{-8.0}$	$10^{-5.2}$	-
pH		triangular	5.0	10.0	8.0
E_z* (pH = 0)	V	uniform	0.000	0.516	-

* see Section 5.3

It is clear that significant uncertainties exist regarding the interpretation of redox potentials in natural systems. These arise from operational difficulties associated with remote measurements made in boreholes, from the probability that mixed potentials arising from more than one redox couple are being measured, and from lack of redox equilibrium at the low ambient temperatures of the groundwaters. As a result, the values quoted should be used with considerable caution and do not, in themselves, provide sufficient basis for selecting potentials for solubility and speciation calculations. Nonetheless, when used in conjunction with other observations (e.g., the presence of dissolved S^{2-} or Fe^{2+} or the absence of dissolved O_2), they demonstrate that deep groundwaters in granite are O_2-free and that the ingress of O_2 into the vault from the surrounding rock after sealing would be negligible. As a result, the redox conditions in a disposal vault would be determined largely by the interaction of the various vault components with the groundwater.

Immediately after closure of the conceptual vault, the most significant factors that would affect redox chemistry include:

- entrapped O_2 present in the pores of the buffer and backfill materials at the time of emplacement;
- Fe(II)-bearing minerals in crushed granitic rock, which would be used as a component of the backfill material; and
- Fe(II) minerals, organic matter and microbes in the clays used for both buffer and backfill materials.

Based on the porosity and the degree of saturation (60-80 vol.%) of the backfill, the total O_2 content (gaseous plus dissolved) of the backfill immediately after emplacement is expected to be about 0.2 $mol \cdot m^{-3}$. The surface area of the crushed granite would be approximately 0.15 $m^2 \cdot g^{-1}$, based on an estimate of the particle size distribution (Yong et al. 1986). The principal Fe(II)-containing minerals in granite are magnetite (0.9 wt.%) and biotite (2.2 wt.%) (Tammemagi et al. 1980). The biotite may contain 15 to 20 wt.% FeO (Kamineni et al. 1984). Alteration of these minerals would release substantial quantities of Fe^{2+} to the pore solution, which could then react with dissolved O_2. Since the half-life of Fe^{2+} at pH 7 in air-saturated water is less than an hour (Davison and Seed 1983), the rate-limiting step in the reduction of O_2 in the backfill is the dissolution rate of the minerals.

The dissolution rate of biotite is relatively rapid, and is reported to range from $10^{-16.9}$ to $10^{-15.5}$ $mol \cdot cm^{-2} \cdot s^{-1}$ (Velbel 1985, Nesbitt and Young 1984). Using the lowest reported rate and the surface area of biotite in the crushed granite in 1 m^3 of the backfill (620 m^2 for a backfill that is 75% crushed granite), we calculate an Fe^{2+} release rate of 2.5×10^{-3} $mol \cdot a^{-1}$ in 1 m^3 of backfill. Since the Fe^{2+} is oxidized by the reaction

$$4Fe^{2+} + O_2 + 2H_2O \rightarrow 4Fe^{3+} + 4OH^-$$

the O_2 present in the pores of the backfill material could be consumed in

$$(4 \times 0.2 \text{ mol})/(2.5 \times 10^{-3} \text{ mol}\cdot\text{a}^{-1}) = 320 \text{ a at } 25°C \quad .$$

If one assumes an activation energy of 59 $kJ\cdot mol^{-1}$ for biotite dissolution and an Arrhenius temperature dependence (Lasaga 1981), the consumption of O_2 from the dissolution of biotite at 80°C (the average vault temperature 30 a after waste emplacement) could occur in approximately eight years.

There are other Fe(II) minerals present in granite (e.g., magnetite) that would also contribute to establishing reducing conditions in the disposal vault. In addition, the Lake Agassiz clay—the reference backfill clay—contains 0.73 wt.% Fe(II) (Oscarson and Dixon 1989a), which would contribute significantly to the redox buffering capacity of the backfill material. The oxidation of organic carbon, which constitutes ~0.3 wt.% of the reference backfill material (Oscarson, in press), may also serve to reduce the redox potential. In consuming the O_2 present in the vault, less than 1% of the Fe(II) in the backfill would be consumed; thus, the redox buffering capacity of the system would remain substantial.

Biotite weathers to secondary phases that include Fe-oxyhydroxides, vermiculite and kaolinite (Law et al. 1991). A typical reaction is

$$KFe_3AlSi_3O_{10}(OH)_2 + H^+ + 8H_2O + 3/4O_2 = K^+ + 2H_4SiO_4 + 3Fe(OH)_3 + 1/2Al_2Si_2O_5(OH)_4$$

The logarithm of the mass action equation is

$$\log(K_T) = 33.73 = \log[K^+] + 2\log[H_4SiO_4] + pH - 3/4\log[O_2]$$

Substituting the representative concentrations of various groundwater species for WRA-500 groundwater (Table 3-1a) yields $[O_2] = 10^{-44}$ Pa and $[H_2] = 10^{-29}$ Pa. This is equivalent to an E_h of +40 mV_{SHE} (see Figure 3-2), in reasonable agreement with the value of -30 mV_{SHE} reported by Gascoyne (1988). If it is assumed that biotite weathers to goethite (FeO(OH)), a redox potential of -200 mV_{SHE} is calculated. Both of these equilibria are illustrated in Figure 3-2. The existence of FeO(OH) in weathering profiles, rather than $Fe(OH)_3$, suggests that the lower E_h values are more probable. The magnetite-goethite equilibrium results in very similar redox potentials and is used in model calculations of uranium solubility, as discussed in Section 5.5.3.2.

Oxygen would also be entrapped in the pore space of the buffer material and the sand layer adjacent to the container. Very little Fe^{2+} is present in the buffer material (~0.1%) (Oscarson and Dixon 1989a); thus, the water initially contacting the container is likely to be oxygenated. The O_2 would gradually be depleted by reaction with Fe^{2+} diffusing towards the containers from the surrounding rock and backfill and by diffusion of O_2 out of the buffer into the rock and backfill. Oxygen would also be consumed by corrosion of the container material.

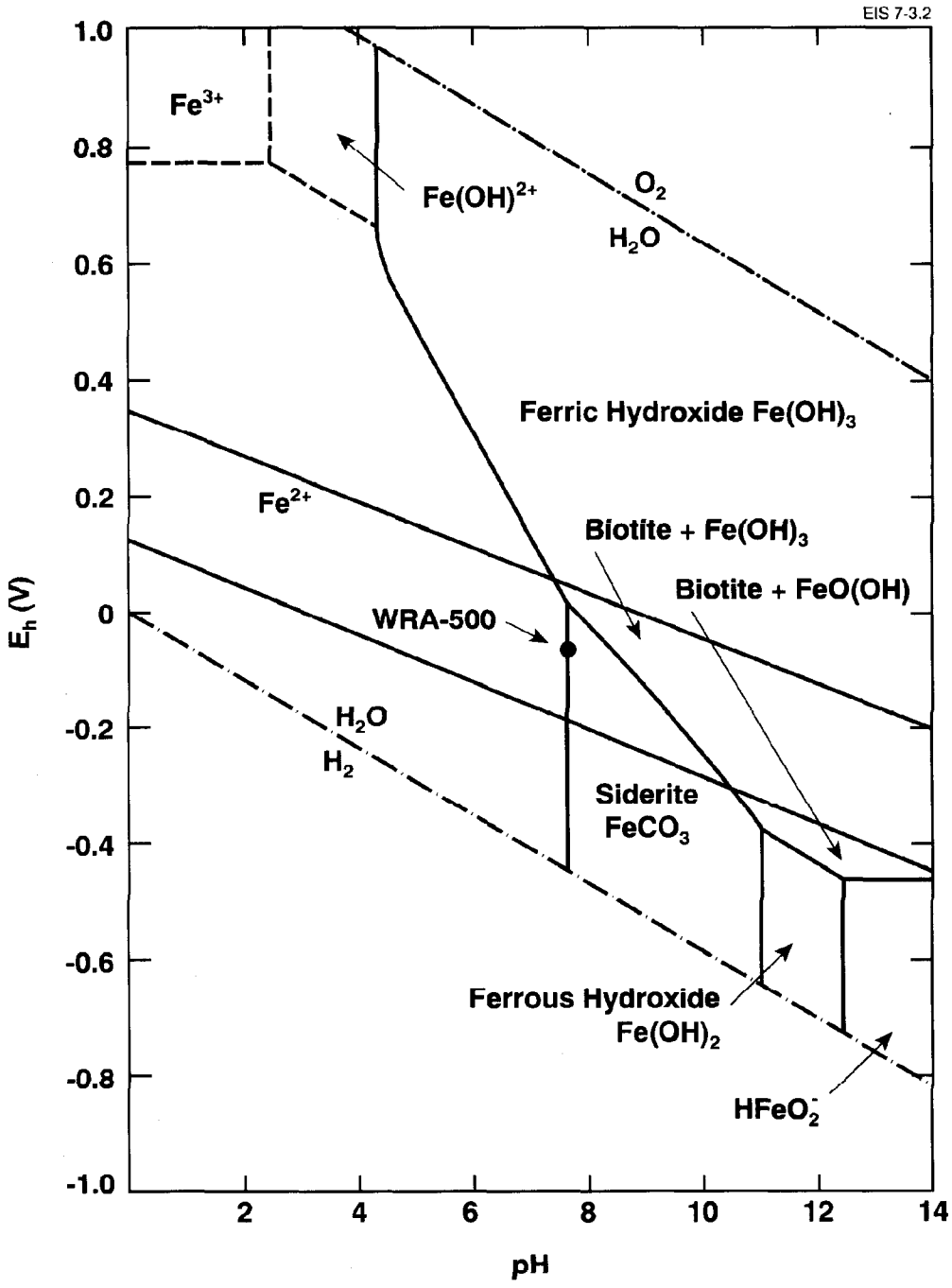

FIGURE 3-2: Stability for Biotite/$Fe(OH)_3$ and Biotite/FeO(OH) Equilibria for the WRA-500 Groundwater (see Table 3-1a). ● - measured E_h (Gascoyne 1988).

The other factor that may influence the redox condition in the buffer material is the γ-radiation emitted by the used-fuel container. Shielding calculations for the reference container design for the ten-year-cooled fuel indicate that the initial γ-field at the surface of the container in contact with the buffer would be ~52 $Gy \cdot h^{-1}$ (Simmons and Baumgartner 1994). The γ-field at the buffer/rock interface would be about 20 times lower than at the container surface. The γ-field would decrease by more than three orders of magnitude over the first 500 a.

Gamma radiolysis of the pore water in a dense saturated bentonite-sand mixture produces equal amounts of oxidizing and reducing species, which may react with each other and with solute species in the pore water. The primary species formed during radiolysis of pure (deionized distilled) water are e^-_{aq}, $H^\cdot$, $OH^\cdot$, and $HO_2^\cdot$ radicals, H_3O^+ ions and H_2, O_2 and H_2O_2 molecular species. At dose rates of ~100 $Gy \cdot h^{-1}$ in pure water, steady-state concentrations of radicals in solution are of the order of 10^{-8} $mol \cdot L^{-1}$ (Spinks and Woods 1964), with steady-state concentrations being proportional to dose rate (Christensen and Bjergbakke 1984). The primary yield of radical and ionic species is greater than the yield of molecular species. These yields are strongly influenced by solution pH, dose rate, and reactions with molecular, ionic and colloidal impurities in solution. Radiolysis can also alter the E_h of the solution. Changes in E_h would depend on the rate of H_2 production (by radiolysis or by container corrosion), the relative rates of diffusion of molecular species (particularly H_2) out of the buffer region, and reactions of radicals, H_2O_2, and O_2 with solution species such as Fe^{2+}/Fe^{3+}, NO_3^-, CO_3^{2-}, or Cl^-. In general, since the concentrations of solution species in the buffer pore water capable of reacting with radical species would be about 10^{-6} $mol \cdot L^{-1}$ or greater (Table 3-1a), they could compete effectively with radical/radical recombination reactions. Thus, in typical pore waters, steady-state concentrations of radical species are likely to be lower than 10^{-8} $mol \cdot L^{-1}$.

Some constituents of the buffer (iron minerals, calcite, organics) may participate in reactions with radical or molecular species formed in the pore water by radiolysis. However, the smectite component (~80% in Avonlea bentonite (Quigley 1984)) is expected to be unaffected by radiolysis, since it consists largely of fully oxidized constituents (Si^{4+}, Na^+, Ca^{2+}, Al^{3+}) that are not reduced by reactions with radiolytically generated free radical or molecular species.

Experiments involving γ-irradiation of a deaerated groundwater/bentonite system for 70 to 100 d showed that dose rates of 100 $Gy \cdot h^{-1}$ had little effect on solution pH; however, the solution E_h (as determined by a Pt electrode) tended to decrease (Wisbey 1986). Similarly, Tait et al. (1986) showed that O_2 was consumed in irradiated (4 $Gy \cdot h^{-1}$) suspensions of bentonite in aerated groundwater in contact with granite coupons for 485 d at 100°C, but was not consumed in unirradiated control samples. These results suggest that O_2 consumption in Fe^{2+}/Fe^{3+} systems is accelerated by γ-irradiation. Under aerated conditions, the bentonite/water solution pH remained about the same as for unirradiated solutions (Wisbey 1986). The bentonite is clearly able to buffer the small quantities of acid generated from radiolysis of N_2 present in the groundwater under aerated conditions.

3.4.3 Microorganisms, Organic Material and Colloids

Microorganisms would be present in a nuclear fuel waste disposal vault, although their capacity to reproduce would be limited by the nutrient availability (Stroes-Gascoyne 1989). Microbial processes that could affect mass transport through the buffer material include alteration of radionuclide mobility due to changes in pH and E_h, complexation of radionuclides by organic materials, and adsorption of radionuclides on mobile microorganisms.

Because of their relatively large size, both microorganisms and organically complexed radionuclides are expected to be relatively immobile in the compacted buffer and backfill materials where there is a complex capillary structure and the average pore size is very small (Eriksen and Jacobsson 1982, De Regge et al. 1988, Neretnieks and Skagius 1978). For example, Pusch et al. (1987b) have estimated that the average pore size in bentonite compacted to a density of 1.3 $Mg \cdot m^{-3}$ is 0.1 to 0.5 μm.

Laboratory studies designed to assess the effects of microorganisms on the transport of selected radionuclides through columns of backfill materials (Lake Agassiz clay and crushed granite) have been conducted (Goyette 1987); natural populations of microorganisms from saline surface sediments were used in the tests. No significant increase in the rate of transport of radionuclides in these materials was observed as a result of microbial activity. The microbial activity in the columns stabilized at 10^5 to 10^6 organisms$\cdot cm^{-3}$; this is similar to levels found in natural environments (Pedersen et al. 1991).

The potential effect of organic matter in clay sealing materials on the performance of a nuclear fuel waste disposal vault has been examined by Oscarson et al. (1986). They concluded that the small amount of organic material (<1.2 wt.%) present in the clay sealing materials would not adversely affect the engineering performance and mass transport properties of the barrier materials. More recent studies (Oscarson, in press) have confirmed that the organic matter content of buffer and backfill materials would be very low. The Avonlea bentonite contains 0.31 wt.% organic carbon (i.e., 0.15 wt.% for the 50:50 sand/bentonite mixture), and the backfill clay contains 1.2 wt.% organic carbon (i.e., 0.3 wt.% for the 25:75 clay/granite mixture). The potential production of CH_4 as a result of microbial degradation of this organic matter is under study. Because of the relatively low concentration of organic matter and the elevated temperatures in the disposal vault, CH_4 production rates are expected to be very low (see Section 3.3.4).

With respect to the transport of colloidal particles, because of size similarities, diffusion measurements of large molecules in dense bentonite are relevant. Lignosulfonates (molecular weight (MW) = 5600 to 30 000 $g \cdot mol^{-1}$), disodium 2,4,5,7-tetrabromofluorescein (MW = 646 $g \cdot mol^{-1}$), and sodium anthraquinone-2-sulfonate (MW = 354 $g \cdot mol^{-1}$) have been examined, and the diffusion coefficients are $<10^{-15}$ $m^2 \cdot s^{-1}$ (Eriksen and Jacobsson 1982)—at least three orders of magnitude lower than the diffusion coefficients of Cs^+ and Sr^{2+} in this clay. The transport of colloidal particles that might be produced upon radionuclide release from used fuel is, therefore, expected to be extremely slow. As a result, the transport of

radionuclides in colloidal form through the buffer material is not included in the vault model.

It is concluded that microorganisms, organic materials and colloids present in a disposal vault would not adversely affect the mass transport properties of the buffer and backfill materials.

3.4.4 Radiation and Smectite Stability

In the conceptual system, radiation fields experienced by the buffer would be limited to γ-radiation until the containers failed and the waste form dissolved, releasing α- and β-emitters to groundwater. The available data indicate that γ-radiation has little or no effect on the crystal structure of clay minerals (Oscarson and Cheung 1983, Pusch et al. 1992). Furthermore, γ-irradiation (^{60}Co) up to 9.5×10^7 Gy has no significant effect on the water permeability of dense bentonite (Bradley et al. 1983), nor does γ-radiation significantly affect the sorption properties of clays (Bonne and Heremans 1982).

Beta-emitters, like γ-emitters, are mainly short-lived fission products that would decay to very low levels within 300 a, well within the projected lifetime of the containers. Therefore, structural damage to the buffer material from β-radiation would be negligible.

On the other hand, considerable damage to clay mineral structures can be caused by α-particles (Haire and Beall 1979). Because of the very limited range of α-particles, however, clay minerals would be subjected to α-particle damage only in the event of significant transport of Pu or Am into the buffer and their subsequent decay. Significant transport of these species is highly unlikely because of their very low solubilities and low diffusion coefficients in the buffer (see Section 5.5.3.1 and Table 5-1).

As noted in Section 3.4.2, radiation may also have a significant effect on the pH and E_h in the pore solution of the buffer material because of radiolysis of the groundwater. Changes in the oxidation state of the structural components of clay, for example, Fe, can affect the stability of the clay mineral. However, neither Fe nor other redox-sensitive elements (Mn and Cr, for example) are important structural components of the reference clays (Oscarson and Dixon 1989a). Hence, changes in E_h should not have a significant effect on the stability of the clay.

The pH should have no adverse effect on the clay if it remains in the range from 6 to 9; deep groundwaters in granitic rock in the Canadian Shield are generally within this pH range (Frape et al. 1984, Gascoyne 1988, Table 3-1a). At lower pH values kaolinite or dickite may form. The formation of Al-hydroxy interlayers in the original smectite is also a possibility at lower pH values (Johnston and Miller 1984). At higher pH values, framework-type silicates, such as zeolites, are likely to form.

Because of the shielding effect of the buffer material, no other materials in the vault would experience significant radiation fields. For example, the radiation field at the buffer/borehole interface would be ~1 $Gy \cdot h^{-1}$ upon emplacement of a container of the reference fuel.

3.4.5 Summary

The groundwater in the pores of the buffer and that in contact with the waste containers would be conditioned by its contact with the buffer and backfill materials. This contact solution might be different from the reference groundwater, and its composition would depend on the ion-exchange capacity of the buffer, the minor components of the buffer, and how much groundwater had passed through the buffer. The concentration ranges of the important species in this contact solution have been presented.

In the conceptual system, when the containers fail, the environment of the near field is expected to be reducing. Thus, diffusion of radionuclides in buffer and backfill materials is considered to take place under reducing conditions. Iron(II) minerals in the granite and the backfill materials would be largely responsible for controlling the redox potential in the disposal vault.

Microorganisms would be present in a nuclear fuel waste disposal vault. Microbial processes that could affect mass transport through buffer material include complexation of radionuclides by organic materials and adsorption of radionuclides on motile microorganisms. Because of their relatively large size, however, both microorganisms and organically complexed radionuclides would be comparatively immobile in the compacted buffer and backfill materials where the average pore size is very small. The same argument applies to the transport of colloidal particles through buffer and backfill materials.

The buffer and backfill would contain a small amount of organic matter (<0.3 wt.%). It is concluded, however, that the amount would be too small to adversely affect the engineering performance or the mass transport properties of the barrier materials.

For the buffer, structural changes in the smectite minerals are unlikely to result from γ- and β-emissions from the used fuel. Alpha particles could affect the mineral structure, but, because of the very low solubilities of species that emit α-radiation, such effects are improbable. Changes in the pH and E_h of pore solution arising from the effects of radiation are not likely to influence the structure of smectite minerals.

3.5 MASS TRANSPORT THROUGH SATURATED BARRIERS

3.5.1 Hydraulic Conductivity and Convective Flux

Water flow through porous media is generally described by Darcy's law:

$$v = k \nabla h \qquad (3.1)$$

where v is the velocity of flow, k is the hydraulic conductivity and ∇h is the hydraulic gradient. For saturated porous media, h is normally taken as the sum of the hydraulic pressure and elevation potentials in the water, ψ_p and ψ_z respectively. In bentonite, the Darcian flow rate arising from electrochemical effects can be incorporated by considering the osmotic potential, ψ_π, in the pore fluids as in Equation (3.2):

$$v = k \nabla(\psi_p + \psi_z + \psi_\pi) \quad . \tag{3.2}$$

The osmotic potential in the pore solution of the buffer would always be less than that in the adjacent groundwater (Yong and Warkentin 1975). At the same elevation, the difference in ψ_p across the buffer must exceed the difference in ψ_π between the groundwater and the buffer before water flow across the buffer could occur.

In compacted clay, a threshold hydraulic gradient is found to exist for Darcian flow to occur. Yong et al. (1986) indicate that this gradient for the buffer is much greater than 10.

The k values shown for the buffer in Figure 4-4 of Johnson et al. (1994) were determined under very high pressure gradients ($\nabla\psi_p > 3000$). Pusch et al. (1985a) suggest that under these gradients flow occurs principally through channels in the material arising from microscopic inhomogeneities in its fabric. These inhomogeneities likely exist at lower pressure gradients, and the full prevention of water flow under very small gradients may not occur. However, the effective k value would be very much less than those shown in Figure 4-4 of Johnson et al. (1994). This is likely to be the case in the vault where $\nabla\psi_p$ in the rock is <0.1 (Chan 1988, Davison et al. 1994b). These very low k values virtually ensure that radionuclide migration through the buffer could occur only by diffusion after restoration of the water table.

3.5.2 Diffusion in Clay Barriers

Diffusion of an inert solute in porous media can be described by the pore diffusivity, D_p:

$$D_p = D_o \tau \tag{3.3}$$

where D_o is the diffusivity of the solute in bulk water and τ is the pore geometry factor (here τ includes both the tortuosity of the diffusion path and the pore constrictivity that accounts for the size and shape of the pores). At a buffer density of 1.3 $Mg \cdot m^{-3}$, $\tau \simeq 0.1$ (Oscarson et al. 1992).

In the absence of advection, Fick's first law for one-dimensional diffusion adapted to porous media is

$$J = -D_p \epsilon (\partial C/\partial x) \tag{3.4}$$

where J is the diffusive flux, ϵ is the porosity, C the concentration of the diffusant, and x the distance. $D_p\epsilon$ is the total intrinsic diffusion coefficient, D, a proportionality constant relating the flux to the concentration gradient of the diffusant.

In clay-water systems the diffusant is often sorbed on the clay; this affects diffusion in the transient state. Fick's second law, applied to sorption governed by a linear sorption isotherm for porous media, is given as

$$\partial C/\partial t = (D_p/R)\, \partial^2 C/\partial x^2 \tag{3.5}$$

where R is the retardation factor given as

$$R = 1 + K_d \gamma_d / \epsilon \tag{3.6}$$

where γ_d is the dry bulk density of the clay and K_d is the solid/liquid distribution coefficient defined as

$$K_d = q/C \tag{3.7}$$

where q is the amount of a species associated with the solid phase and C is the concentration of that species in solution at equilibrium. A linear sorption isotherm, as assumed in Equation (3.7), is considered to be a reasonable assumption for many contaminants, particularly when present at low concentrations (Gillham and Cherry 1982, Meier et al. 1987), as would be the case for radionuclides in the pore solution of the buffer and backfill.

D_p/R in Equation (3.5) is termed the apparent diffusivity, D_a. Note that if a diffusant is poorly sorbed on the clay, K_d is approximately zero and $D_a \simeq D_p$.

In summary, from the above,

$$D = D_o \tau \epsilon \tag{3.8}$$

$$D_a = D_o \tau \epsilon / (\epsilon + K_d \gamma_d) \tag{3.9}$$

and

$$D/D_a = \epsilon + K_d \gamma_d \quad . \tag{3.10}$$

The quantity $\epsilon + K_d \gamma_d$ is termed the capacity factor, r. It is a measure of the capacity of the solution and clay per unit volume of clay to hold more of the diffusant as its concentration in the solution phase increases.

In practice, D and D_a are obtained from experiments under steady-state and transient conditions respectively.

Ideally, values for both D and r are required for all radionuclides present in used fuel for the ranges of parameters expected in the buffer and backfill (such as density, temperature, and pore-solution composition). This is not possible within a reasonable time frame because of the large number of species involved and the long time periods required to measure diffusion coefficients in some cases. The values chosen for D and r are based to a large extent on the expert opinion and the arguments espoused by Cheung and co-workers (Cheung 1989, 1990; Cheung and Gray 1989), as well as on the data obtained in our laboratories and that in the literature. The K_d values used to calculate r (Equation (3.10)) were obtained largely from published compilations (Allard et al. 1982, Oscarson et al. 1984). The discussion that follows summarizes the basis on which the D and r values used in the vault model were selected.

3.5.3 Rationale for Buffer and Backfill Diffusion Data

Surface diffusion has been proposed as a potentially important transport mechanism for certain cationic radionuclides through dense clay-based media (Cheung 1990, Cook 1988). This process involves the migration of adsorbed solutes along the surface of clay particles under a concentration gradient. If surface diffusion were an important mechanism, D values would be greater because of the addition of a term that is proportional to the surface diffusion coefficient and the K_d (Cheung 1990, Cook 1988). Capacity factors would remain unchanged because r values do not depend on surface diffusion. Because both D and r depend on K_d, they would be positively correlated and the values of these parameters would increase and decrease in concert. The assumption of surface diffusion also means there would be at least two distinct diffusion pathways in the clay, one associated with the water bound to the clay surface (surface diffusion) and another in the bulk water. It is also assumed that surface diffusion would be more pronounced in the buffer than in the backfill, because of the greater specific surface area of the buffer material.

To make the analysis tractable, the radionuclides were grouped into five categories on the basis of their probable chemistry in clay/water systems and, hence, the nature of their interaction with clay: ion-exchanged species, chemisorbed species, non-sorbed anions, neutral species and technetium. Technetium is anomalous because of the large uncertainty associated with its diffusion under reducing conditions. The characteristics of the probability distributions for the D and r values for radionuclides in each of the five categories were chosen on the basis of the assumptions outlined below.

Ion-exchanged species are attracted to the clay surface and, hence, migrate by surface diffusion, which occurs predominantly in the surface water in compacted bentonite. This means that D values would be relatively high. Ion exchange involves an electrostatic or ionic interaction between a cation and the negatively charged clay surface. For example, the alkali and alkaline earth metals and many of the transition metals, such as Ni and Cr, are sorbed on clays predominantly via an ion exchange mechanism (Bohn et al. 1985).

Chemisorbed species (e.g., Pu and Np) are assumed to be primarily in the surface water but are thought to be so strongly sorbed on the clay as to be immobile. Chemisorption, also called specific sorption, involves the formation of a chemical bond between the sorbate and the clay surface. It is a relatively strong interaction, and K_d values for chemisorbed species can be much greater than those involving ion exchange. Most of the actinides and lanthanides are sorbed onto clay largely by chemisorption (Allard et al. 1982). Therefore, r values are large, but since surface diffusion is assumed not to occur, D values are relatively small.

Non-sorbed anions are assumed to move predominantly in the bulk water and to be excluded from the surface water (i.e., the layers of water molecules adjacent to the surface of the clay) because of electrical repulsion by the negatively charged surface. Since most of the water in the dense buffer material is thought to be surface water (Cheung 1990, Cheung and Gray

1989), D values for non-sorbed anions would be relatively small. Inasmuch as many anions, such as I^-, Br^-, HCO_3^- and $HSeO_3^-/SeO_4^{2-}$ are poorly sorbed on clay (Bohn et al. 1985), r for these species would also be relatively small.

Neutral species, such as the noble gases, are assumed to migrate in both the surface and bulk water, but are either not sorbed or very weakly sorbed. Therefore, r and D would be neither excessively small nor large.

Technetium is in a separate category because of the large uncertainty associated with its diffusion and sorption behaviour under reducing conditions. The distributions chosen for Tc were based largely on the available experimental data (Sawatsky and Oscarson 1991, Ito and Kanno 1988) and expert judgement.

All radionuclides would experience similar chemical conditions when they are released to the buffer and backfill; thus, the parameter values describing their mass transport should be correlated. For instance, when the sampled D for one radionuclide is large, other radionuclides in the same category should have similar values. Also, from Equation (3.10), D values for different radionuclides are related through the values of the porosity and density. For this reason, D values are correlated to capacity factors. For simplicity, all correlation coefficients were given a value of 1.0. As a result, all diffusion coefficients and capacity factors for radionuclides in the same category are varied in concert, using the dummy correlation parameters in Tables 3-2 to 3-5.

The values for the distributions for D and r for buffer and backfill are given in Tables 3-2 to 3-5. In these tables the symbol 'α' refers to the linear correlation coefficient. The characteristics of the probability distribution function and the correlation coefficients were chosen on the basis of expert judgement. The distributions for D and r values reflect experimental uncertainties and the expected effects of variability in T, γ_d and salinity in the vault.

3.5.4 Recent Developments

Recent experimental data suggest that surface diffusion is perhaps not as important as was once thought (Berry and Bond 1990, Cho et al. 1993), and a model based on Equations (3.8) and (3.9) is probably adequate to predict the diffusion of most radionuclides in dense saturated clay (Gillham et al. 1984; Robin et al. 1987; Sharma and Oscarson 1989; Oscarson, in press). This means that the D values used for ion-exchanged species in the buffer are conservative. In any event, these species do not make a significant contribution to the dose (see Chapter 7).

To examine the effect that different D and r values would have on the output of the SYVAC submodel, other values of D and r for the most important radionuclides, ^{129}I, ^{99}Tc and ^{14}C, were substituted for those in Tables 3-2 to 3-5 in a separate sensitivity analysis study. The new values were obtained from recent experimental measurements. The effect of changing the distribution and the correlation parameters was also examined. The results of the sensitivity analysis are discussed in Chapter 8.

TABLE 3-2

DIFFUSION DATA FOR BUFFER

Category	Species	Characteristics of Correlated Lognormal Distribution					
		Geometric Mean D ($m^2 \cdot a^{-1}$)	Geometric Standard Deviation	Lower Bound D ($m^2 \cdot a^{-1}$)	Upper Bound D ($m^2 \cdot a^{-1}$)	Correlated to*	α^+
	Cs, Rb, K	7.3×10^{-3}	1.6	1.8×10^{-3}	3.0×10^{-2}	DFBCAT	1.0
Ion-Exchanged Species	Sr, Ca, Be, Cd, Cr, Zn, Ni, Pd, Ra	2.5×10^{-3}	1.4	9.0×10^{-4}	7.2×10^{-3}	DFBCAT	1.0
	Pb, Bi, Po, Sn, Sb	5.2×10^{-3}	1.8	9.0×10^{-4}	3.0×10^{-2}	DFBCAT	1.0
Chemi-sorbed Species	Lanthanides and Actinides Zr, Nb, Mo Hf, Ac, Si	1.1×10^{-5}	3.2	3.6×10^{-7}	3.6×10^{-4}	DFBACT	1.0
Tc	Tc	1.1×10^{-5}	3.2	3.6×10^{-7}	3.6×10^{-4}	DFBACT	1.0
Non-Sorbed Anion	I, Br, C, Se	1.8×10^{-5}	2.7	9.0×10^{-7}	3.6×10^{-4}	DFBANI	1.0

Category	Species	Characteristics of Normal Distribution					
		Mean D ($m^2 \cdot a^{-1}$)	Standard Deviation ($m^2 \cdot a^{-1}$)	Lower Bound D ($m \cdot a^{-1}$)	Upper Bound D ($m^2 \cdot a^{-1}$)	Correlated to*	α
Non-Sorbed Neutral Species	H, Kr, Rn, Ar	2.4×10^{-3}	1.0×10^{-4}	2.1×10^{-3}	2.7×10^{-3}	DFBTRA	1.0

* Dummy correlation parameters used to correlate D_i values in the same group and to correlate D and r values

\+ α is the correlation coefficient

TABLE 3-3

CAPACITY FACTORS FOR BUFFER

Category	Species	Characteristics of Normal Distribution					
		Mean r	Standard Deviation	Lower Bound r	Upper Bound r	Correlated to*	α^+
Ion-Exchanged Species	Cs, Rb, K	18	5.2	2.0	33	DFBCAT	1.0
	Sr, Ca, Be, Cd, Cr, Zn, Ni, Pd, Ra	4.5	1.2	1.0	8.0	DFBCAT	1.0
	Pb, Bi, Po, Sn, Sb	17	5.3	1.0	33	DFBCAT	1.0
Non-Sorbed Neutral Species	H, Kr, Rn, Ar	0.40	0.017	0.35	0.45	DFBTRA	1.0

Category	Species	Characteristics of Correlated Lognormal Distribution					
		Geometric Mean r	Geometric Standard Deviation	Lower Bound r	Upper Bound r	Correlated to*	α
Chemisorbed Species	Lanthanides and Actinides Zr, Nb, Mo Hf, Ac, Si	53	6.8	0.17	17000	DFBACT	1.0
Tc	Tc	53	6.8	4.2×10^{-3}	17000	DFBACT	1.0
Non-Sorbed Anion	I, Br, C, Se	6.3×10^{-3}	4.0	1.0×10^{-4}	0.40	DFBANI	1.0

* Dummy correlation parameters used to correlate D_i values in the same group and to correlate D and r values.

\+ α is the correlation coefficient

TABLE 3-4

DIFFUSION DATA FOR BACKFILL

Category	Species	Characteristics of Normal Distribution					
		Mean D ($m^2 \cdot a^{-1}$)	Standard Deviation ($m^2 \cdot a^{-1}$)	Lower Bound D ($m^2 \cdot a^{-1}$)	Upper Bound D ($m^2 \cdot a^{-1}$)	Correlated to*	α^+
	Cs, Rb, K	8.1×10^{-3}	6.0×10^{-4}	6.0×10^{-3}	9.9×10^{-3}	DFKCAT	1.0
Ion-Exchanged Species	Sr, Ca, Be, Cd, Cr, Zn, Ni, Pd, Ra	4.0×10^{-3}	1.8×10^{-4}	3.4×10^{-3}	4.5×10^{-3}	DFKCAT	1.0
	Pb, Bi, Po, Sn, Sb	6.7×10^{-3}	1.1×10^{-3}	3.4×10^{-3}	9.9×10^{-3}	DFKCAT	1.0
Chemi-sorbed Species	Lanthanides and Actinides Zr, Nb, Mo Hf, Ac, Si	2.3×10^{-3}	1.5×10^{-4}	1.8×10^{-3}	2.7×10^{-3}	DFKACT	1.0
Tc	Tc	2.3×10^{-3}	1.5×10^{-4}	1.8×10^{-3}	2.7×10^{-3}	DFKACT	1.0
Non-Sorbed Anion	I, Br, C, Se	2.3×10^{-3}	1.5×10^{-4}	1.8×10^{-3}	2.7×10^{-3}	DFKANI	1.0
Non-Sorbed Neutral Species	H, Kr, Rn, Ar	2.3×10^{-2}	1.5×10^{-3}	1.8×10^{-2}	2.7×10^{-2}	DFKTRA	1.0

* Dummy correlation parameters used to correlate D_i values in the same group and to correlate D and r values

\+ α is the correlation coefficient

TABLE 3-5

CAPACITY FACTORS FOR BACKFILL

Category	Species	Characteristics of Normal Distribution					
		Mean r	Standard Deviation	Lower Bound r	Upper Bound r	Correlated to*	α^+
Ion-Exchanged Species	Cs, Rb, K	6.0	0.67	4.0	8.0	DFKCAT	1.0
	Sr, Ca, Be, Cd, Cr, Zn, Ni, Pd, Ra	1.4	0.20	0.80	2.0	DFKCAT	1.0
	Pb, Bi, Po, Sn Sb	4.4	1.2	0.80	8.0	DFKCAT	1.0
Non-Sorbed Anions	I, Br, C, Se	0.25	0.017	0.20	0.30	DFKANI	1.0
Non-Sorbed Neutral Species	H, Kr, Rn, Ar	0.25	0.017	0.20	0.30	DFKTRA	1.0

Category	Species	Characteristics of Correlated Lognormal Distribution					
		Geometric Mean r	Geometric Standard Deviation	Lower Bound r	Upper Bound r	Correlated to*	α
Chemisorbed Species	Lanthanides and Actinides Zr, Nb, Mo Hf, Ac, Si	2.0×10^3	2.2	2.0×10^2	2.0×10^4	DFKACT	1.0
Tc	Tc	2.0×10^3	2.2	31	2.0×10^4	DFKACT	1.0

* Dummy correlation parameters used to correlate D_i values in the same group and to correlate D and r values

\+ α is the correlation coefficient

3.5.5 Summary

The hydraulic conductivity of the reference buffer material is $<10^{-11}$ m·s^{-1}. A critical hydraulic gradient likely exists below which the hydraulic conductivity tends towards zero. These buffer properties ensure that diffusion is the only significant mechanism through which radionuclides released from a breached container could migrate through the water-saturated buffer.

Total intrinsic diffusion coefficients, D, and capacity factors, r, are required for all radionuclides present in nuclear fuel waste. Ranges of D and r values and their distribution characteristics were obtained from experimental data and expert judgement. Radionuclides were grouped into five categories on the basis of their behaviour in clay/water systems. Insufficient data are available to describe the probability distribution for each range; normal or lognormal distributions were specified on the basis of expert opinion and the limited available data.

4. LIFETIME MODEL FOR GRADE-2 TITANIUM CONTAINERS FOR NUCLEAR FUEL WASTE

4.1 INTRODUCTION

To ensure isolation of the used fuel during the period when the fission product activity in the conceptual disposal system is high, the waste containers must survive for 300 to 1000 a. Providing no failures occurred as a result of mechanical effects, the main factor limiting their survival is expected to be corrosion in the groundwater to which they would be exposed. Two general classifications of container materials have been studied internationally: corrosion-allowance and corrosion-resistant materials. Corrosion-allowance materials possess a measurable general corrosion rate, but are not expected to be susceptible to localized corrosion processes. By contrast, corrosion-resistant materials are expected to have very low general corrosion rates, because of the presence of protective surface oxide films. However, breakdown of this film could render them susceptible to localized corrosion processes, such as pitting, crevice corrosion or stress-corrosion cracking (SCC). A more extensive discussion of the various corrosion-allowance and corrosion-resistant materials considered as candidate container materials is available elsewhere (Johnson et al. 1994).

The corrosion-resistant material titanium has been chosen as the reference container material for the engineering and performance assessment case studies in the CNFWMP. Specifically, the corrosion performance of ASTM Grade-2 titanium and, to a lesser extent, that of ASTM Grade-12 titanium has been evaluated. In this chapter, the corrosion performance of these materials is compared, and the model developed to predict the lifetimes of containers constructed from Grade-2 titanium is described. The mechanistic understanding and the assumptions upon which this model is based are explained, and predictions of container lifetimes are presented.

4.2 CONTAINER DESIGN

A number of container designs have been evaluated and are discussed in detail elsewhere (Crosthwaite, in preparation; Johnson et al. 1994). The thin-shell, packed-particulate design was chosen for the reference container (see Figure 2-3). In this design, a 6.35 ± 0.15-mm-thick titanium shell is internally supported by industrial glass beads. These beads have a distribution of diameters between 0.7 and 1.2 mm; they are compacted by vibration into the residual spaces after the fully loaded used-fuel basket is inserted into the container.

The container will fail mechanically only if a region of the shell is not supported by glass beads. When unsupported in this manner, the container wall will deform plastically. If the maximum strain due to plastic deformation exceeds 5.3% the container will fail. Such large strains can result from instabilities leading to buckling or local stretching (Teper 1992). To prevent failure by buckling, a minimum overall thickness of 2 mm is required, assuming a uniform loading of 10 MPa hydrostatic pressure is acting on the container (Teper 1988). Since the total pressure expected to act on the container at a vault depth of 500 m (the reference vault depth used in this case study) is ~6.5 MPa (5 MPa hydrostatic pressure plus ~1.5 MPa from the swelling pressure of the buffer), this mechanical allowance can be considered sufficient.

Mechanical failure of the shell could also occur at regions of localized corrosion under certain conditions. If the largest dimension of a localized corrosion patch that had thinned the shell to a thickness of less than 2 mm exceeded 33.5 mm, and the area behind the patch was unsupported because of a void in the particulate, the maximum strain of 5.3% could be exceeded (Teper 1992, Johnson et al. 1994). If it could be guaranteed that the largest dimension of a locally corroded patch would never reach 33.5 mm, then a residual wall thickness of less than 2 mm might be acceptable. Since such a guarantee cannot be given, we accept 2 mm of the total wall thickness as unavailable for corrosion allowance. This wall thickness is the minimum required to guarantee structural integrity, independent of the size of any corroded area.

The remainder of the container wall thickness is available as a corrosion allowance. This allowance is taken to be 4.2 mm, the lower limit of available wall thickness of as-received plate material ordered from manufacturers to specification ASTM B265. This specification tabulates the permissible variations in thickness of commercially supplied titanium.

The rationale for selecting 4.2 mm as the accepted corrosion allowance for titanium containers is described in detail elsewhere (Crosthwaite 1992a, 1992b; Johnson et al. 1994).

4.3 MATERIAL COMPOSITION AND MECHANICAL PROPERTIES

The ASTM specified compositions of a number of grades of titanium are given in Table 4-1. Grades 1 to 4 are α-phase alloys with a hexagonal close-packed (hcp) crystalline structure. These grades are generally single-phase alloys, although small amounts of iron-stabilized β-phase, with a

TABLE 4-1

ASTM NOMINAL MAXIMUM COMPOSITIONS (WEIGHT %) FOR VARIOUS GRADES OF TITANIUM

Grade	N	C	H	Fe	O	Mo	Ni	Pd
1	0.03	0.10	0.015	0.20	0.18			
2	0.03	0.10	0.015	0.30	0.25			
3	0.05	0.10	0.015	0.30	0.35			
4	0.03	0.10	0.015	0.50	0.40			
7	0.03	0.10	0.015	0.30	0.25			0.2
11	0.03	0.10	0.015	0.20	0.18			0.2
12	0.03	0.10	0.015	0.30	0.25	0.3	0.8	

body-centred cubic structure (bcc), and FeTi intermetallics may be present. Grades 7 and 11 (containing small amounts of Pd) are also α-phase alloys, possessing the same mechanical properties as Grades 2 and 1 respectively. The addition of small amounts of Pd serves to increase their corrosion resistance over that of Grades 1 and 2.

Alloying with molybdenum and nickel (Grade 12 in Table 4-1) increases the strength of titanium, through solid-solution strengthening and the creation of a two-phase structure. Thus, Grade 12 is an α-alloy containing small amounts of nickel-stabilized β-phase and Ti_2Ni intermetallics. This alloy was designed to reduce the susceptibility of titanium to crevice corrosion. More extensive discussions of the mechanical properties of titanium alloys and the principles behind the alloying of titanium have been published elsewhere (Nuttall and Urbanic 1981, Schutz 1986, Schutz and Thomas 1987).

A number of advantages are gained by choosing the compositionally and microstructurally simple Grade-2 titanium as the reference container material. It is a thermodynamically stable material that will not undergo destructive phase transitions under disposal vault conditions, and it is not expected to form complex unstable structures as a consequence of mechanical treatments, such as cold working or welding.

4.4 EXPOSURE ENVIRONMENT

4.4.1 Groundwater Composition

The reference groundwater composition to which the container in the conceptual model is exposed is designated WRA-500 and is given in Table 3-1a (Gascoyne 1988). Also shown in this table are compositions for the synthetic granitic groundwaters WN-1 and SCSSS, which have also been used in the corrosion evaluation of titanium.

Before coming into contact with the container, the groundwater would be conditioned by passage through the buffer and/or backfill materials. The

impact of a clay buffer on the composition of groundwater has been considered by Oscarson and Dixon (1989a), Wanner (1987), and Lemire and Garisto (1989). The major ionic components in the conditioned water would depend primarily on the mineral content of the clay. Depending on the groundwater flow conditions within the vault, the thermodynamic estimates of Lemire and Garisto (1989) show that a transitory increase in sulphate and fluoride levels to ~10^{-1} mol·L^{-1} and ~10^{-3} mol·L^{-1} respectively is possible. The expected composition range of this "contact" water is given in Table 3-1b.

4.4.2 Redox Conditions

The presence and concentration of oxidants in the disposal vault would be major factors in determining the corrosion performance of waste containers. The conditions within the vault would be determined initially by the air and other oxidants trapped within the buffer/backfill medium. For longer exposure periods, conditions would be controlled by the amount of oxidant transported into the vault by the groundwater and by the products of water radiolysis resulting from the impact of γ-radiation from the used fuel on the water in the surrounding environment. For vaults in deep rock of the Canadian Shield, the original quantity of trapped oxidant would be consumed, at least partially, by reaction with oxidizable minerals within the surrounding rock and buffer/backfill. Significant subsequent transport of oxygen into the vault is not expected, since the oxygen content of groundwater at these depths is negligible. The evolution of redox conditions with time has been discussed in more detail in Section 3.4.2. The time for conditions to become anoxic has been conservatively estimated to be <320 a.

4.4.3 Buffer/Backfill Materials

In the conceptual disposal system, buffer and backfill materials are assumed to become saturated with groundwater when the disposal vault is sealed. As discussed in Section 3.2.2, the time required for groundwater to saturate the buffer may range from several years to ~1000 a. In the container lifetime model, the corrosion processes that would occur under saturated conditions are assumed to initiate immediately upon closure of the vault. Corrosion of titanium under unsaturated vault conditions is expected to be negligible (Shoesmith et al., in preparation (a)) and has not been included in the container lifetime model.

The properties and performance of the reference buffer and backfill materials surrounding the container have been described in Chapter 3. These materials are expected to exert a number of major influences on the corrosion of containers:

1. They would impede the transport of oxygen (required to drive the corrosion process) to the container surface.

2. Minerals in the backfill would consume oxygen, thereby driving the redox conditions anoxic.

3. They would buffer the pH of the water contacting the container between 7 and 9, a range generally benign from the corrosion point of view.

4. The heat-transfer properties of the buffer and backfill materials would be important factors in controlling the temperature of the containers and, hence, their corrosion rate.

4.4.4 Radiation Levels

According to Glass (1981) there are two ways in which radiation can affect container corrosion:

1. Particle irradiation (e.g., by neutrons or α-particles) could cause radiation damage to the metal and/or the protective oxide film.

2. Radiolysis of groundwater could produce oxidizing species, such as OH, H_2O_2, O_2, Cl^-, ClO^- and Cl_2^-, which could directly cause corrosion.

The maximum neutron flux expected outside the container is $\sim 10^2$ neutrons$\cdot$cm$^{-2}\cdot$s^{-1} (Wilkin 1992), which is many orders of magnitude ($>10^9$) below the levels capable of inducing mechanical damage in the metal (Stobbs and Swallow 1962) and, hence, is insignificant. However, γ-radiation is capable of yielding a significant dose outside the body of the thin-walled container.

For a container filled with reference used fuel (see Section 2.1.4), the initial gamma dose rate at the external surface of the container would be ~ 50 Gy$\cdot$h^{-1} (5×10^3 rad$\cdot$h^{-1}). This represents the maximum radiation dose rate available to affect container corrosion. It is the dose rate to the medium surrounding the container and is calculated from the radioactive decay characteristics of the fuel as attenuated by the packed particulate (glass beads) and the container wall thickness (Tait et al. 1989). The dose rate would decrease with time as the γ-emitting radionuclides decayed, and the decay characteristics of the rapidly decaying fission products would define the time interval over which irradiation could affect container corrosion.

4.5 TEMPERATURE

The surface temperature of the containers would influence the corrosion rate. This temperature would be determined by the heat generated as a result of radioactive decay within the fuel, and its rate of dissipation to the surrounding buffer/backfill/rock environment. Consequently, the temperature would vary depending on the age of the fuel at emplacement, the relative positions of the containers, the overall geometry of the vault, and the thermal conductivities of the surrounding buffer, backfill and rock. The procedures used to calculate container surface temperature and temperature gradients within the buffer and backfill (for the reference used fuel defined in Section 2.1.4) are described in Section 3.2.1. The calculations assume that buffer and backfill materials are saturated with

groundwater. If the buffer experienced significant drying, temperatures could increase by as much as 5°C (Section 3.2.1); however, the corrosion rate would be negligible under such conditions (Shoesmith et al., in preparation (a)).

The schematic presented in Figure 4-1 shows the arrangement of the conceptual vault; it is a simplified version of Figure 2-4. The unshaded areas represent disposal rooms filled with containers, and the shaded areas represent access tunnels free of containers. The vault is divided into 12 sectors, as shown by the dashed lines in the figure (see Section 6.2.1). These sectors are chosen to facilitate the coupling of the output from the vault model to that describing the flux of radionuclides through the geosphere. For such a coupling to be achieved, it is essential to predict the container failure times within each individual sector. Each sector represents a portion of the vault in which the characteristics important to the modelling of radionuclide transport are relatively uniform (Section 6.2).

Each container within the vault would possess a distinct temperature-versus-time profile. However, the general shape of these profiles would be similar; an early period of high temperature, lasting between 100 and 200 a, followed by a much longer period of slow cooling lasting tens of thousands of years. The hot containers would be located in the centre of the vault, with cooler containers located at the edges, and cold containers at the corners. Figure 4-2 shows three examples of temperature-time profiles taken from different areas within the vault. Heat production leading to the early period of high temperature can be attributed to the relatively rapid decay of γ-emitting fission products in the used fuel. The subsequent long period of slow cooling can be attributed to the heat generation during the much slower decay of α-emitting actinides.

4.6 CORROSION PROPERTIES OF TITANIUM ALLOYS

In this section the corrosion properties of titanium alloys are reviewed with the purpose of demonstrating that, with the alloys chosen for study, only a limited number of corrosion processes are possible and capable of leading to failure of the container. The corrosion processes most likely to cause failure are crevice corrosion, hydrogen-induced cracking and, to a lesser degree, general corrosion, and these processes are discussed in detail. The major emphasis has been placed on discussing and comparing the properties of Grades-2 and -12 titanium, the two materials studied in most detail in the CNFWMP.

4.6.1 General Properties

Titanium metal is unstable in air and water, but is inevitably rendered passive by the presence of a protective oxide film that forms rapidly when a fresh metal surface is exposed to air or moisture. This stable, protective oxide film gives titanium its excellent corrosion resistance, and is the primary reason for its selection as a candidate container material. Because the nature of the film remains essentially unaltered by traces of metallic impurities (e.g., Fe in Grade-2 titanium) or minor alloy constituents (e.g., Ni and Mo in Grade 12), all the grades listed in Table 4-1 exhibit excellent resistance to general corrosion.

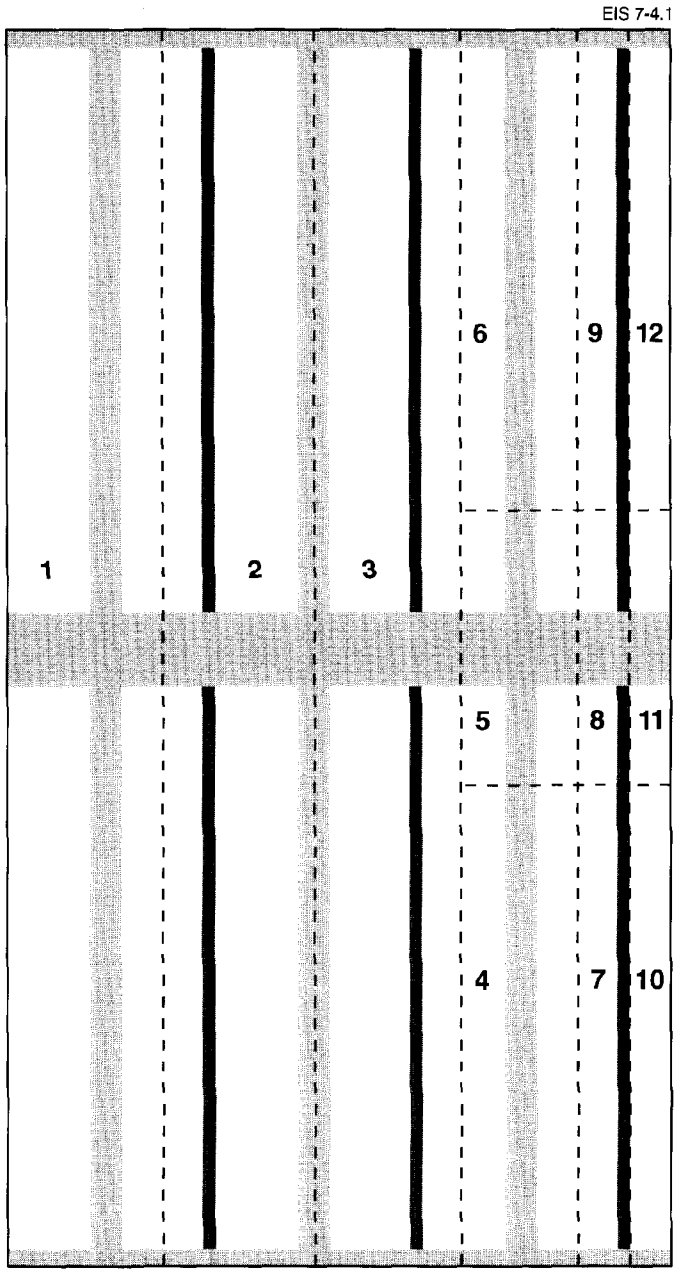

FIGURE 4-1: Schematic Showing the Arrangement of the Vault. The unshaded areas represent emplacement rooms filled with containers, the light shaded areas represent access tunnels free of containers, and the dark shaded areas represent rock between emplacement rooms. The dashed lines outline the individual sectors (numbered) within the vault, defined to facilitate the coupling of the container failure model to the geosphere transport model.

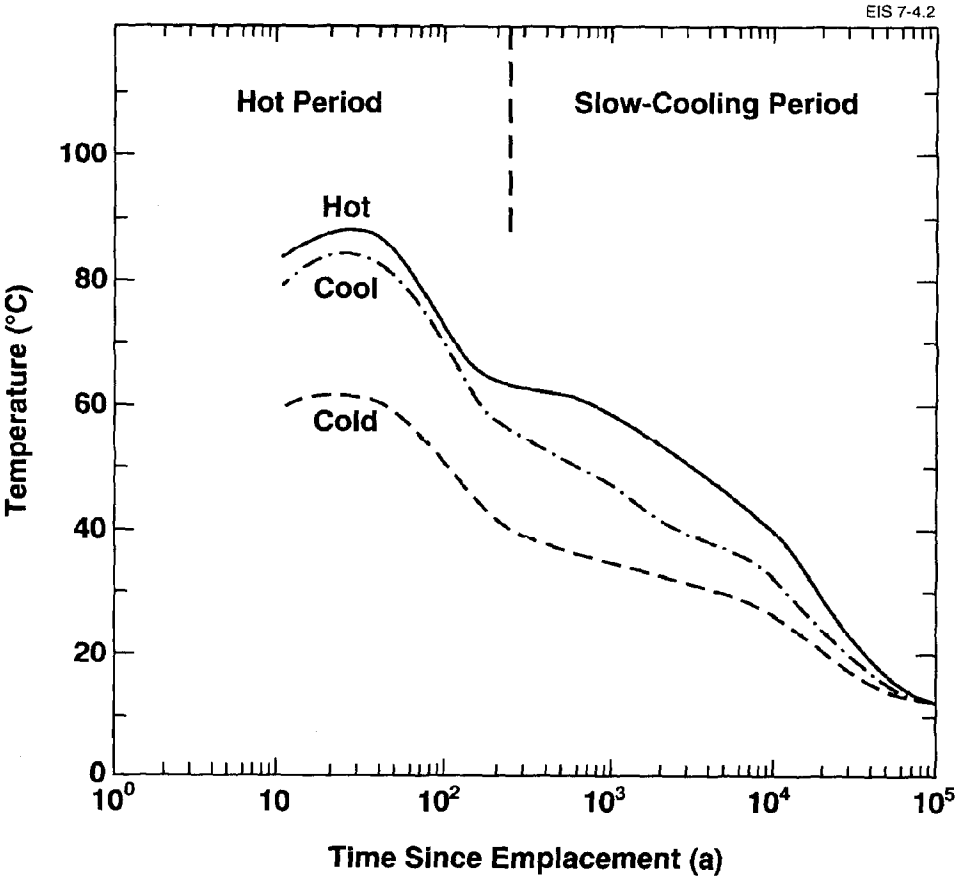

FIGURE 4-2: Representative Temperature-Time Profiles for Containers Designated Hot, Cool and Cold

Like most passive metals and alloys, titanium alloys are susceptible to some localized corrosion processes. However, when discussing such susceptibilities it is necessary to distinguish between two classes of alloy:

- alloys commonly used in industrial applications in which corrosion resistance is a primary requirement. These alloys are single α-phase (hexagonally close-packed crystal structure) or near α-phase alloys containing relatively small amounts of β-phase (body-centred cubic crystal structure) in an α-matrix. This class encompasses all the materials listed in Table 4-1, including the two alloys Grades 2 and 12.

- alloys developed for applications in which strength is a primary requirement. Increased strength is achieved by solid-solution alloying and the stabilization of an α-β phase structure.

The materials in the first class are expected to exhibit relatively few modes of degradation in comparison with those of the second class. Thus, while materials in class two can be susceptible to SCC in aqueous chloride solutions, those in class one are considered immune to SCC except in a few environments (e.g., anhydrous methanol/halide solutions, red fuming HNO_3 (Schutz and Thomas 1987)) impossible under waste vault conditions. As discussed below, a similar difference in susceptibility to hydrogen-induced cracking exists between the two classes.

Pitting potentials for titanium alloys around room temperature are invariably very large, i.e., of the order of +5 to 10 V_{SHE} in chloride solutions. Even at temperatures in the range from 175 to 250°C pitting potentials are >1.0 V_{SHE} (Schutz and Thomas 1987), and results recorded in 0.5 $mol \cdot L^{-1}$ NaCl at 150°C yield values >2.0 V_{SHE} (Shoesmith et al., in preparation (b)), compared with corrosion potentials close to 0 V_{SHE}. For maximum vault temperatures around 100°C, pitting potentials between 5 and 7 V_{SHE} are expected. Since these potentials are many volts more positive than the most positive corrosion potentials measured under vault conditions ($\leq$0.5 V_{SHE}), the possibility of container failure by pitting can be ruled out.

Of the commonly used engineering metals and alloys, titanium and its alloys are the only ones for which microbially induced corrosion (MIC) has not been reported (Schutz 1991, Pope et al. 1989, Little et al. 1991). For this reason (among others) it is the commonly recommended material for many seawater and biomedical applications. There appear to be a number of major reasons for this immunity:

1. The passive film on titanium is extremely inert. The thermodynamic calculations summarized in the potential-pH diagram of Figure 4-3 show that, for 25°C, very acidic conditions are required for the film to become unstable. Such acidities would be extremely difficult to achieve by microbial activity.

2. Temperatures >70°C are required for the initiation of localized corrosion processes such as crevice corrosion (Schutz 1991). Since MIC is not generally supported at these temperatures, it is unlikely to cause initiation.

3. Because of its electronic structure, titanium cannot act as a biological catalyst (Wackett et al. 1989). In the cationic form many metals can act as biological catalysts, generally in the form of metalloenzymes. The existence of the transition metals in a variety of oxidation states is a key property in their redox activity in biological reactions. This redox activity, and the ability of the metal to coordinate directly with organic ligands containing electron donor groups, can be attributed to the presence on the metal cation of a partially filled set of d electron orbitals. Although its electronic configuration places titanium at the front of the first transition series, it exists in aqueous solution and in passive films almost exclusively in the +4 oxidation state. As a result, its ions have no available d electrons plus a closed-shell configuration,

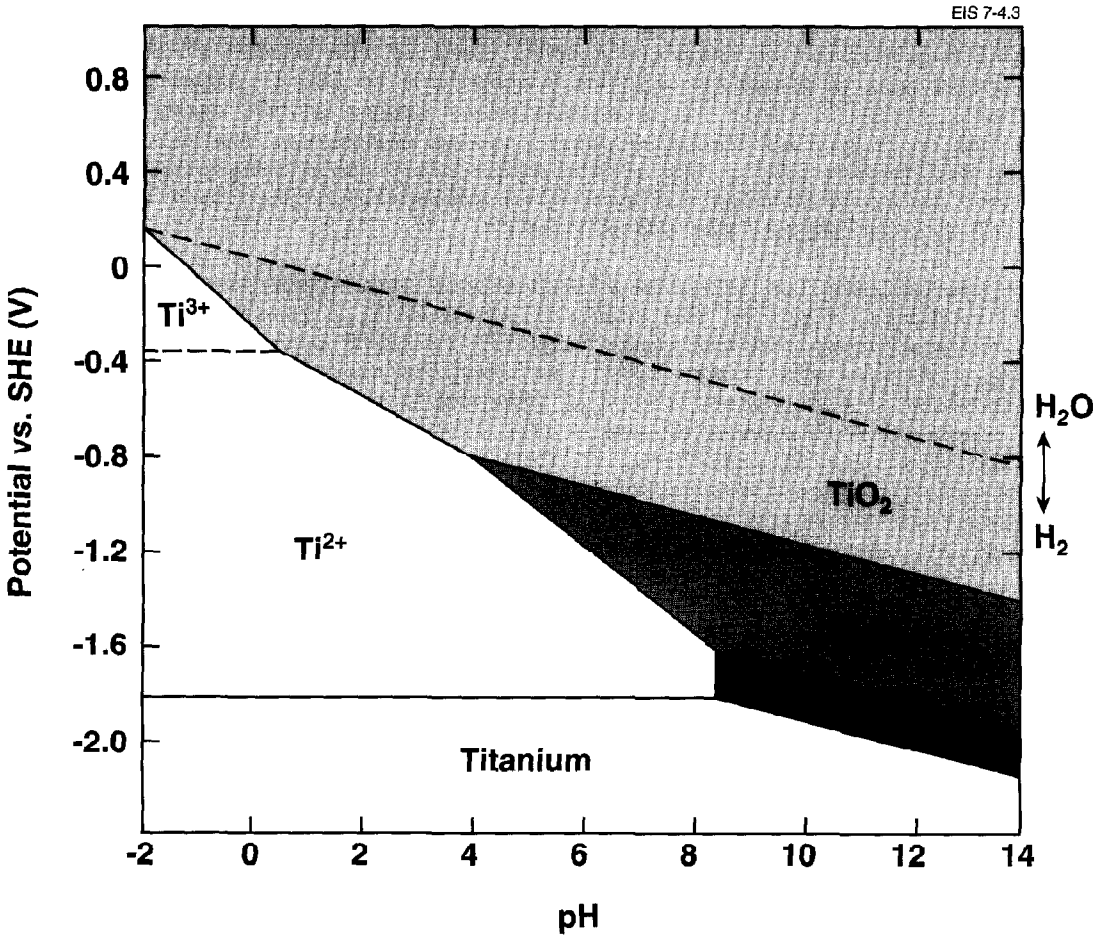

FIGURE 4-3: Partial Potential-pH Diagram for the Titanium/H_2O System (Pourbaix 1966)

which precludes the formation of titanium-containing enzymes or cofactors, thus making titanium unavailable for biologically supported redox chemistry (Wackett et al. 1989).

However, titanium is not biotoxic and permits the growth of biofilms, which are known to act as crevice formers on some materials (Schutz 1991, Mansfeld and Little 1991). Hence, the possibility that microbial activity may lead to the initiation of crevice corrosion is not discounted, despite the fact that no case of localized corrosion has ever been reported under such a biofilm formed on titanium.

The two localized corrosion processes most likely to lead to failure of a titanium container are crevice corrosion and hydrogen-induced cracking (HIC). As will become obvious in the discussion presented below, these two

processes are inextricably linked. Consequently, the remaining discussion of corrosion properties deals with these two processes and general corrosion, since they would have the biggest effect, either individually or synergistically, on the lifetime of containers. Since the container is likely to be welded and would be exposed to a radiation field, a discussion of weld corrosion and the effects of radiation on various corrosion processes is also included.

4.6.2 General Corrosion

Titanium and its alloys are very resistant to general corrosion in water, natural waters, and steam to temperatures in excess of 300°C. Slight weight gains are observed as a result of the thickening of the passive film, particularly at higher temperatures. The typical contaminants expected in natural waters, such as iron, sulphide, sulphate and carbonate, do not affect this resistance (Schutz and Thomas 1987).

Of more relevance to our requirements is the resistance to corrosion in saline environments, since such environments are anticipated in a Canadian waste vault. Titanium alloys exhibit negligible corrosion in seawater to temperatures as high as 260°C (Schutz 1986, Schutz and Thomas 1987), and unalloyed titanium has been used for over 20 a in seawater applications, such as power generation, desalination and oil refining. Compilations of general corrosion rates for Grades-2 and -12 titanium list the rate as nil (Schutz and Thomas 1987).

This high resistance to general corrosion in saline solutions has been confirmed for Grades-2, -7 and -12 titanium by the studies of Braithwaite and Molecke (1980) and Molecke et al. (1982) in concentrated brines at temperatures up to 250°C. Also, on the basis of weight-change measurements, no measurable general corrosion was observed on either Grade 2 or 12 after exposure to SCSSS, buffer slurries in SCSSS, or compacted bentonite saturated with SCSSS at temperatures between 100°C and 150°C for exposure periods up to 5 a in the presence of irradiation (4.5 ± 0.5 Gy·h^{-1}) (Ikeda and Clarke 1986, Shoesmith et al., in preparation (b)).

The most detailed investigation of general corrosion has been performed by Mattsson and Olefjord (1984, 1990) and Mattsson et al. (1990), who studied the rate of oxide thickening on Grade-2 and Grade-7 titanium in groundwater-saturated bentonite at 95°C for exposure periods up to 6 a. Oxide thickening according to a logarithmic growth law, and the absence of any detectable dissolved titanium over the six years, confirmed that a steady-state film thickness controlled by the finite dissolution rate of TiO_2 was not obtained. Corrosion involved oxide film formation by the transport of titanium and oxygen ions through the thickening film under the influence of the large electrical field across the oxide. This growth law was found to apply irrespective of the oxygen content, the salinity of the groundwater, and the absence/presence of bentonite.

If corrosion according to this growth law were to continue indefinitely, container failure by general corrosion would be impossible. However, at longer exposure times (5 to 6 a) Mattsson and Olefjord (1990) and Mattsson

et al. (1990) found, from transmission electron microscopy studies, that the originally amorphous passive film started to crystallize to yield the thermodynamically stable rutile. This leads to the formation of grain boundaries, which could provide rapid transport pathways for the ions involved in film growth. As a consequence, oxide film thicknesses after 5 to 6 a were somewhat greater than predicted by the logarithmic growth law. If one assumes that linear growth kinetics apply if such crystallization continues (i.e., the corrosion rate remains constant indefinitely), the data of Mattsson and Olefjord still lead to predicted container lifetimes in excess of 10^6 a.

Negligible corrosion was observed on titanium coupons exposed for up to 47 months in various simulated disposal vault environments at 100°C and with a 5.4 $Gy \cdot h^{-1}$ γ-radiation field (Ryan et al. 1994). The weight changes observed on these coupons were small and a statistical analysis of the results suggests that the errors in the measurements were larger than the values themselves. The derived corrosion rates were in the range from 0.01 to 0.06 $\mu m \cdot a^{-1}$, which still leads to a predicted container lifetime (based on uniform corrosion) of $\sim 10^6$ a even in a radiation field.

Clearly, container failure by general corrosion does not appear to be possible over the required container lifetime (500 a). However, since the redox conditions within the vault are expected to become reducing, the corrosion of titanium would eventually be sustained by reaction with water:

$$Ti + 2H_2O \rightarrow TiO_2 + 2H_2 \quad . \qquad (4.1)$$

According to Schutz (1991) the oxide film on titanium remains intact under fully deoxygenated conditions down to a pH of 2 at 100°C. However, Reaction (4.1) introduces the possibility that hydrogen absorption by the metal may occur, leading to the possibility of container failure by hydrogen degradation mechanisms. Hydrogen absorption by the metal arising from transport through the passive film should be extremely slow, if not negligible, in the absence of an applied cathodic potential (Schutz and Thomas 1987), and cannot proceed faster than the rate of Reaction (4.1).

The possibility of failure due to hydrogen absorption during general corrosion is addressed in Section 4.6.4.3

4.6.3 Crevice Corrosion

Despite the excellent resistance of titanium alloys to general corrosion, their use in hot saline environments is sometimes limited by their tendency to crevice-corrode.

For many reasons, crevice corrosion is an unlikely event on a waste container, since no natural crevices exist. However, under the hot, saline, and initially oxidizing conditions in a disposal vault, it is impossible to rule out the formation of occluded cells. In an occluded cell, active corrosion at a localized deaerated acidic site is maintained by the reduction of oxidants on passive, non-corroding adjacent surfaces. Corrosion within such a cell would propagate in a manner analogous to that in a well-defined crevice.

4.6.3.1 Possible Crevice Sites on the Surface of a Container

There appear to be five potential crevice sites on the surface of a container packed in compacted bentonite in a waste vault:

- under a section of compacted buffer,
- under a hydrothermally formed deposit,
- under an embedded iron particle,
- in the closure weld between the lid and the main body of the container, and
- under a biofilm.

(i) Under a section of compacted buffer

Establishing a crevice under a section of compacted buffer appears highly unlikely and has never been observed in immersion tests in solutions up to ~1.0 $mol \cdot L^{-1}$ in salinity (SCSSS, Table 3-1a) and temperatures as high as 150°C (Shoesmith et al., in preparation (b)). Chemically, the buffer would maintain the pH of the pore water in the range from 7 to 9 (Lemire and Garisto 1989), making it difficult to establish the acidic conditions required to initiate and propagate crevice corrosion. Also, the buffer's ability to control both redox conditions and the transport of oxidants to the container surface would prevent extensive propagation. Finally, the ionic conductivity of the buffer is likely to be too low to enable a significant area of the container to act as a supporting cathode to sustain metal dissolution within the creviced area. Despite these favourable factors, crevice corrosion cannot be completely ruled out at such sites.

(ii) Under a hydrothermally formed deposit

Crevice corrosion underneath surface deposits has been observed (Schutz 1988). For corrosion to be significant, the deposit must be capable of supporting the highly acidic anoxic conditions required. Hence, crevice corrosion is unlikely under alkaline salt deposits, such as carbonates, or under scales containing significant amounts of oxidized compounds, such as iron(III) oxides; it has not been observed in immersion tests under saline conditions for temperatures up to 150°C (Shoesmith et al., in preparation (b)). In the presence of compacted clay at temperatures $\leq$100°C, the formation of such deposits is highly unlikely.

(iii) Under an embedded iron particle

This process is termed smeared-iron surface pitting and can occur when iron, carbon steel, or low-alloy steel is gouged, scratched or embedded into a titanium surface breaching the titanium oxide film. Corrosion of the iron can cause local acidic conditions (Liening 1983). Because of the pH and redox buffering properties of the bentonite, it is unlikely that, if this form of corrosion occurred, it could be sustained for long enough to cause more than a minor penetration into the container wall. It could be avoided by careful handling of the container.

(iv) In the closure weld

Although difficulties in producing a good closure weld are not anticipated (Maak and Moles 1986; Johnson et al. 1994, Chapter 3), this area represents a possible site for the initiation of a crevice. The presence of a void, crack, or residual notch cannot be ruled out. The majority of such defective welds would be detected in the final weld inspection, and the containers would be rejected. The small number that avoided detection would be included in the initial failure fraction (1 in 10^3 to 1 in 10^4) accounted for in the container failure model. Those welds that were not defective are not expected to be any more susceptible to crevice corrosion than the main body of the container (see Section 4.6.5 below).

(v) Under a biofilm

The initiation of crevice corrosion under biofilms has never been observed for titanium (see Section 4.6.1). However, since titanium is not biotoxic such a process is not ruled out.

4.6.3.2 Mechanism of Crevice Corrosion for Grades-2 and -12 Titanium

Many general discussions of the crevice corrosion process are available (Oldfield and Sutton 1978a,b, 1980; Kruger and Rhyne 1982; Oldfield 1987; Sharland and Tasker 1988; Sharland et al. 1989), and Schutz (1988) has discussed the parameters that influence the crevice corrosion of titanium alloys. An extensive experimental program, described in detail elsewhere (Shoesmith et al., in preparation (b)), has been conducted in the CNFWMP to determine the susceptibility to, and mechanism of, crevice corrosion of Grade-2 and Grade-12 titanium. With a view to eventually optimizing the properties of the chosen material, the impacts of varying both the material composition and the microstructure of Grade-2 titanium have been studied. The advantages of alloying additions were determined by studying Grade 12, an alloy designed to have superior resistance to crevice corrosion.

The essential details of the mechanism of crevice corrosion of titanium are reviewed here to establish the basis for the failure model described below. Our understanding of this mechanism is based on an extensive series of electrochemical experiments under a wide variety of conditions. In these experiments, the parameters most likely to influence crevice corrosion have been systematically studied. These include the nature of the crevice, in particular its geometry; solution composition, in particular the concentrations of oxidant and chloride, and the pH; and composition and microstructure of the alloy. Only a brief review is given here; a more extensive discussion of experimental results is available elsewhere (Shoesmith et al., in preparation (b)).

The initiation of crevice corrosion occurs when oxygen is depleted within the creviced area. Oxygen is consumed in attempting to repair the passive oxide film broken down by the action of chloride within the crevice. For deep, tight crevices, the transport of oxygen into the crevice from the aerated bulk of solution is too slow to maintain the repair process. When this oxygen depletion is complete, an occluded cell is established; i.e., the chemical environment inside the crevice is different from the bulk

environment outside the crevice. An active (bare metal) titanium anode is generated within the crevice, supported by the cathodic reduction of oxygen, supplied from the surrounding environment, on the passive titanium surface outside the crevice.

As with other localized corrosion processes, the initiation of crevice corrosion is unpredictable and often irreproducible under normal corrosion test conditions (Schutz 1988). To avoid this problem, artificially creviced specimens, with a severe crevice geometry established using a polytetrafluoroethylene (PTFE) crevice former, were used to force initiation to occur (Ikeda et al. 1989, 1990a,b). In these experiments, initiation may also have been assisted by the release of fluoride ions from the PTFE spacers used to form the artificial crevices. The inescapable consequence of this approach is that, in the failure model to be described below, it is necessary to assume that crevice corrosion initiates on all containers. This represents a very conservative assumption, but avoids the need to predict the occurrence of a stochastic event, initiation, not well understood by the corrosion science community.

Often, the creviced electrodes were coupled to large titanium cathodes. Such an arrangement simulates the coupling of a creviced area on the container surface with a much larger uncreviced area that acts as a cathode. By inserting a zero-resistance ammeter between the creviced electrode and the titanium cathode, the progress of the crevice propagation reaction was followed by measuring both the crevice potential and the current flowing between the crevice and the coupled cathode without disturbing the natural corrosion conditions.

The overall chemical processes involved in the subsequent propagation of the crevice corrosion of Grade-2 titanium are shown schematically in Figure 4-4. Hydrolysis of dissolved metal cations within the crevice leads to the formation of a tight deposit of hydrated titanium oxide and the production of protons. This deposit causes the formation of smaller, individual crevice sites underneath the original crevice former; i.e., once the process is propagating the original crevice former becomes somewhat redundant.

The production of protons drives the pH down within the crevice, and values of pH $\leq$ 1 can be sustained within tight crevices since equilibration with the environment outside the crevice is impeded by slow transport processes (Yao et al. 1991). Under these acidic conditions crevice corrosion is sustained by two cathodic processes (Figure 4-4):

- oxygen reduction outside the crevice, and

- proton reduction within the crevice.

Since proton reduction is a short-circuited corrosion reaction that occurs entirely within the crevice, it does not yield a current measurable by the zero-resistance ammeter. The extent of corrosion due to this reaction can only be assessed by weight-change measurements once the experiment is complete. The current flowing through the ammeter is a measure of the rate of crevice propagation supported by the external reduction of oxygen.

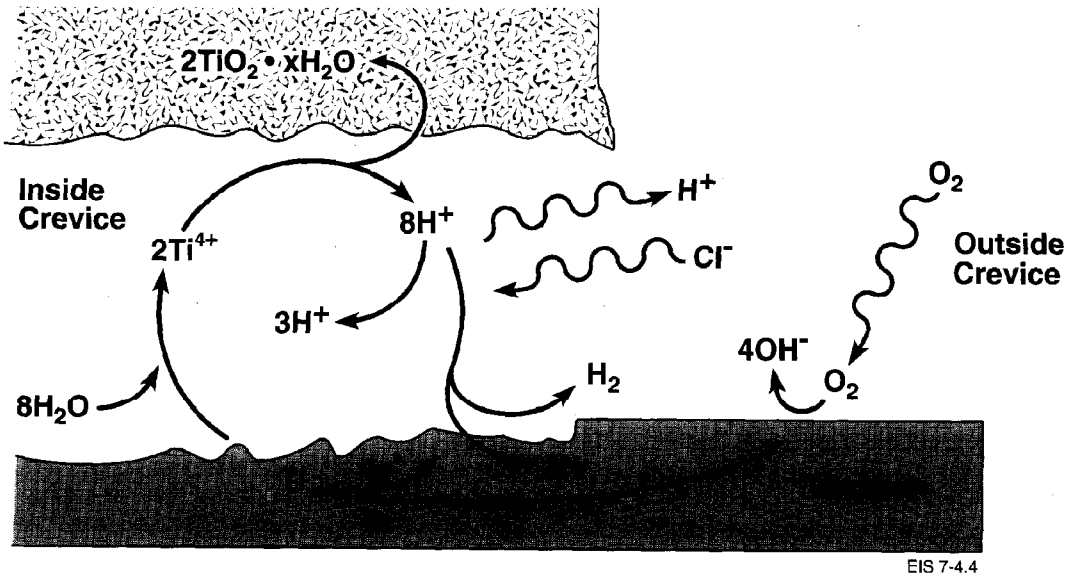

FIGURE 4-4: Schematic Showing the Basic Electrochemical, Chemical and Transport Steps Involved in the Crevice Corrosion of Titanium

Since proton reduction can only occur if a low pH is established inside the crevice by oxygen reduction outside the crevice, the external cathodic reaction is essential for crevice corrosion to propagate. Hence, in electrochemical experiments, the value and duration of the coupled current provide an indication of the progress of crevice corrosion.

The general forms of the crevice current, crevice potential, and the potential of an uncreviced electrode included in the same experiment are shown in Figure 4-5a (Ikeda et al., in press). An illustrative set of experimental curves is shown in Figure 4-5b for Grade-2 titanium contained in a sealed vessel (Ikeda et al. 1991). After a short induction period (generally only a few hours), initiation occurs, and the crevice current rises as the crevice potential falls. This is the activation period and the increasing current is caused by the onset of active crevice corrosion on an increasingly large surface area of metal. Beyond the peak the current falls as the limited amount of oxygen in the sealed pressure vessel is consumed. Eventually, when the oxygen in the pressure vessel is totally consumed, the current falls to zero and the crevice becomes starved. When this occurs, the crevice inevitably repassivates, and the crevice potential changes to a value close to that of the uncreviced electrode (Figures 4-5a and 4-5b). The decrease in potential of the planar electrode does not represent an activation process, merely a response of this passive electrode to the drop in oxygen concentration in the pressure vessel.

For Grade-12 titanium, crevice corrosion initiates but widespread activation of the artificially creviced area is suppressed. This is indicated by much lower crevice currents and much less negative crevice potentials than achieved with Grade-2 titanium. Also, crevice repassivation occurs before the oxygen is totally consumed. These differences between the two grades can be appreciated by comparing Figures 4-5b and 4-5c.

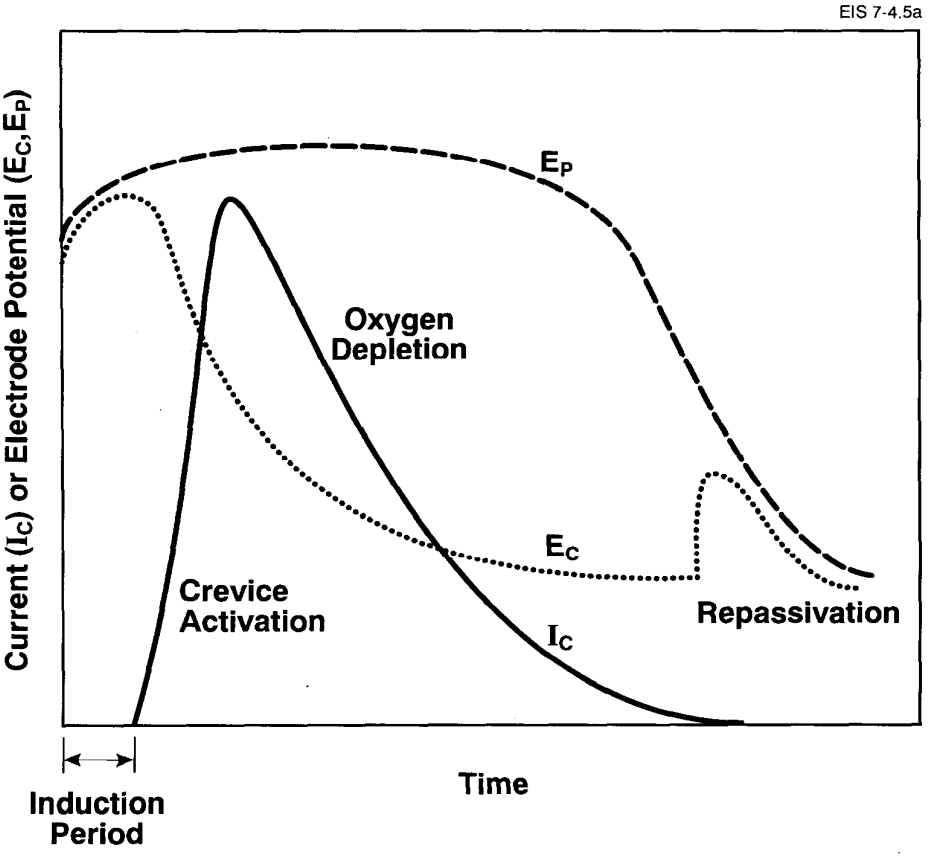

FIGURE 4-5a: Schematic Showing the General Form of Crevice Current (I_C) and Crevice Potential (E_C) Recorded on Artificially Creviced Titanium Electrodes Coupled Through a Zero-Resistance Ammeter to a Large Titanium Counter Electrode. The potential (E_P) of an uncreviced planar electrode in the same experiment is also illustrated.

With Grade-2 titanium, a predominantly α-phase material containing very minor amounts of iron-stabilized β-phase, crevice corrosion propagates at a rate determined jointly by the area undergoing crevice corrosion and the concentration of oxidant outside the crevice. Propagation continues until the oxygen in the system is exhausted, at which time the crevice repassivates by reaction with water. Subsequent additions of oxygen fail to cause a reinitiation. The chemistry and electrochemistry of this situation have been discussed in detail (Ikeda et al. 1989, 1990a,b; Ikeda and McKay 1985; McKay and Mitton 1985; McKay 1984a,b). From results such as these one can conclude that (i) for α-phase titanium containing very little iron, crevice propagation can only be supported if sufficient oxygen is available; and (ii) a crevice, having once repassivated because of lack of oxygen, will not reinitiate.

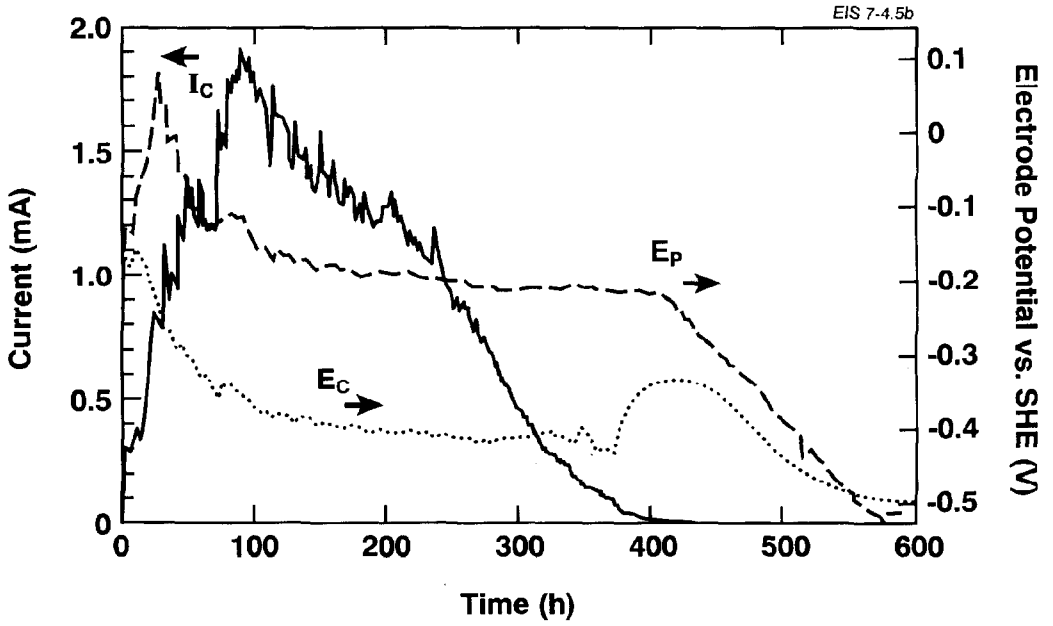

FIGURE 4-5b: The Crevice Current (I_c), Crevice Potential (E_c), and Planar Potential (E_p) Recorded on Grade-2 Titanium at 125°C in 0.27 mol·L^{-1} NaCl

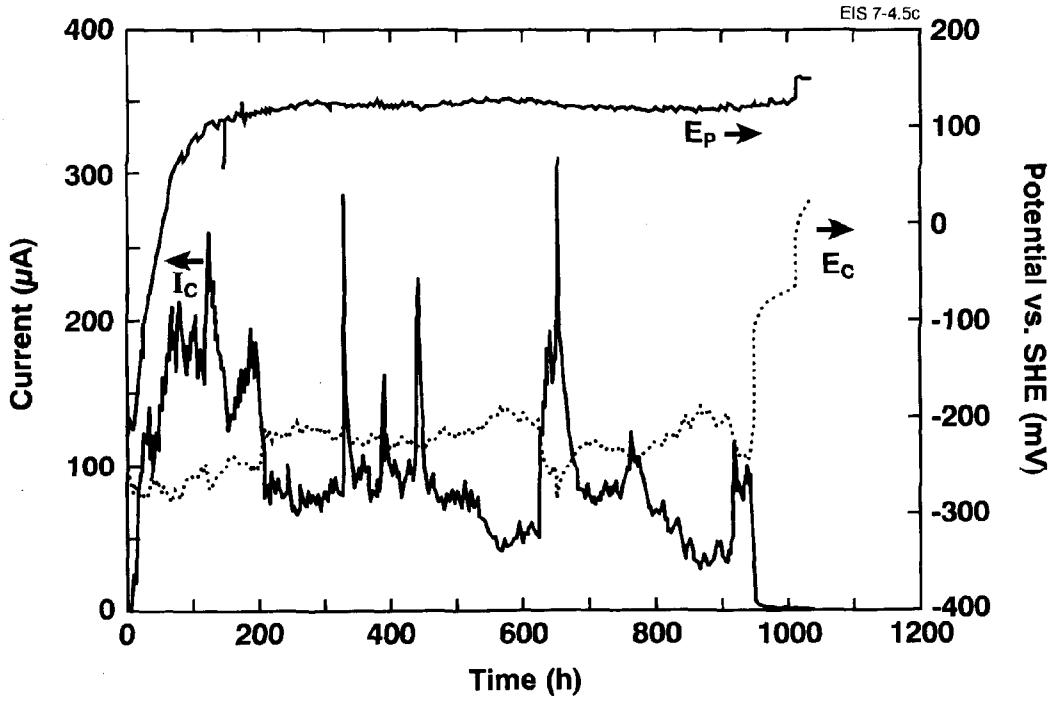

FIGURE 4-5c: Crevice Current (I_c), Crevice Potential (E_c), and Planar Potential (E_p) for Grade-12 Titanium for the Conditions Noted in Figure 4-5b

The other parameter that exerts a major influence on crevice corrosion is temperature. Both the ability to initiate crevice corrosion and the propagation rate increase with temperature. According to Schutz (Schutz and Thomas 1987, Schutz 1988), initiation does not occur at temperatures below ~70°C, although other authors have initiated crevices under extremely saline conditions at temperatures as low as ~40°C (Kobayashi et al. 1980). Once a crevice is initiated, Ikeda et al. (1990b) have shown that crevice propagation can be sustained, at least temporarily, at temperatures down to ~30°C, provided sufficient oxygen is available.

As discussed in Sections 4.4 and 4.5, both the amount of available oxygen in the conceptual vault and the surface temperature of the containers would decrease with time. Consequently, the rate of propagation of a crevice on a container surface would decrease with time after emplacement, and eventually the crevice would repassivate when all the available oxidant was consumed. The specific time at which repassivation occurred would be determined primarily by a combination of temperature and oxidant concentration, although, as discussed below and in more detail elsewhere (Shoesmith et al., in preparation (b)), certain groundwater constituents might accelerate the process.

Since the temperatures of the containers in the conceptual model vary with time from a maximum of ~90°C down to ~12°C after 10^5 a (Figure 4-2), it is necessary to know the crevice propagation rate as a function of temperature over this range. This temperature dependence was obtained from electrochemical experiments. Crevice corrosion was initiated at ~105°C, and the current was allowed to achieve an approximately constant value, i.e., a condition of steady propagation at an approximately constant creviced area. The temperature was then decreased in steps and the crevice current measured as a function of temperature. By keeping the time at each temperature relatively short, major depletion of oxygen over the course of the experiment was avoided. In this manner the crevice propagation rate was measured as a function of temperature for a constant creviced area and an approximately constant and high oxygen concentration. This procedure circumvented the difficulties involved in initiating crevices of reproducible area at a series of temperatures, especially those below 80°C. The crevice currents, measured in this manner, fitted an Arrhenius relationship over the temperature range from 30 to 150°C (Shoesmith et al. 1989, Ikeda et al. 1990b). An activation energy of ~55 $kJ \cdot mol^{-1}$ suggests that a single chemical reaction step within the overall crevice corrosion process is rate-controlling. A linear dependence of crevice current on the square root of oxygen concentration was observed, which suggests that the rate of crevice propagation is controlled by the rate of oxidant reduction on surfaces external to the crevice (Shoesmith et al., in preparation (b)).

The susceptibility of Grade-2 titanium to crevice corrosion is related to its impurity content and microstructure. When the iron content is increased (to >0.1 wt.%), or when this higher iron-content material is heat-treated (860°C), the susceptibility to crevice corrosion decreases significantly (Ikeda et al. 1990c). This improvement appears to be related to the stabilization of the β-phase (with iron, or by heat treatment), which catalyzes the proton reduction within the crevice and drives the crevice potential to more positive values, i.e., forces the crevice to

repassivate. It should be noted that this ability to force repassivation of the Grade-2 material containing >0.1 wt.% iron is not maintained at higher salinities ($[Cl^-] > 0.5$ mol·L^{-1}) (Bailey et al., in preparation).

The ability to repassivate is greatly enhanced in the Grade-12 alloy, in which significant quantities of β-phase and the intermetallic, Ti_2Ni, are deliberately stabilized by the alloying addition of 0.8 wt.% nickel (Table 4-1). The presence of 0.3 wt.% molybdenum may also assist the repassivation process. The crevice corrosion of Grade-12 titanium has been studied as a means of limiting the extent of crevice propagation. So far, these studies are incomplete and the available results are discussed elsewhere (Bailey et al., in preparation; Ikeda et al. 1990b; Schutz and Hall 1984). The crevice propagation rates are much lower for Grade-12 than for Grade-2 titanium, and repassivation occurs at temperatures $\lesssim$70°C even in the presence of substantial oxygen concentrations. The crevice corrosion behaviour of Grade-12 appears to be determined as much by the chemical and microstructural properties of the alloy as by the properties of the environment.

The extent and rate of crevice propagation on Grade-2 titanium is not particularly dependent on chloride concentration over the range anticipated in a vault in the crystalline rock of the Canadian Shield at the 500-m depth (Bailey et al., in preparation). For Grade-12 titanium, concentrations in the range from 1.0 to 2.0 mol·L^{-1}, which are close to those in SCSSS (~0.97 mol·L^{-1}) but greater than those in the reference groundwater WRA-500 (~0.17 mol·L^{-1}, Table 3-1a), are the most aggressive. Other groundwater constituents that could influence the rate and extent of crevice corrosion include Mg^{2+}, Ca^{2+} and the anions HCO_3^-/CO_3^{2-}, SO_4^{2-} and F^-. The last two anions could be concentrated in the groundwater as a result of contact with the buffer/backfill (Section 4.4.1). Experiments performed in natural groundwaters close in composition to those listed in Table 3-1a invariably yield crevice propagation rates lower than those recorded in solutions containing the equivalent chloride concentration. Similarly, in experiments containing buffer slurries, the crevice propagation is suppressed (Shoesmith et al., in preparation (b)).

Experiments designed to investigate the specific effects of changes in concentration of specific ions show different effects for different species, some of which are not yet fully understood. The anions SO_4^{2-} and HCO_3^-/CO_3^{2-} suppress crevice propagation rates. Both appear capable of preventing the decrease in pH within the crevice, which is vital to sustain rapid propagation: sulphate possibly by complexing Ti^{4+} ions, thereby preventing hydrolysis (Figure 4-4); and HCO_3^-/CO_3^{2-} possibly by neutralizing the acidity produced by hydrolysis of dissolved titanium (Figure 4-4). Fluoride ions are unlikely to affect crevice propagation, despite their well-known ability to induce initiation (Schutz 1988). Since initiation is assumed to be inevitable in the failure model, the importance of fluoride becomes marginal. Both Mg^{2+} and Ca^{2+} have been shown to increase the depths of penetration in both Grades-2 and -12 titanium (Westerman 1990, Shoesmith et al., in preparation (b)), but not at the concentrations present in the groundwaters listed in Table 3-1a. Although a complete understanding of the effects of groundwater constituents remains to be revealed, the results of experiments performed in natural groundwaters or

in NaCl solutions of similar chloride content are clearly representative of the expected behaviour under disposal conditions. In NaCl solutions these results are inevitably conservative.

A special form of crevice corrosion, possible with the Grade-2 alloy, is smeared-iron corrosion. This can occur when iron, carbon steel or low-alloy steel is gouged, scratched, smeared or embedded into the titanium surface, thereby breaching the passive film. The embedded iron can lead to the development of local acidic conditions if occluded by titanium metal smears or laps. Grade-12 titanium is much more resistant to this form of corrosion. Smeared-iron corrosion can be avoided by careful handling, and by the use of container-handling equipment constructed from materials other than those mentioned. Nevertheless, such problems are difficult to eliminate totally and examples have been seen, albeit infrequently and to a minor extent, in immersion tests (Schutz and Thomas 1987, Schutz 1988).

Although electrochemical experiments establish the mechanistic basis for a container failure model, they do not provide crevice corrosion rates that can be used directly to predict container penetration rates. Such rates have been obtained for Grade-2 titanium (low iron content) from immersion tests. In immersion tests it proved impossible to initiate corrosion on the metal/metal or metal/clay buffer crevices anticipated under waste vault conditions. However, initiation was achieved with metal/PTFE-creviced specimens similar to those used in electrochemical experiments. It is possible that fluoride ions leached from the PTFE aided the initiation process.

The propagation rates (tabulated in Table 4-2) were measured on metal/polysulfone-creviced specimens exposed to initially aerated 5.9 wt.% NaCl solution at 100°C for a period of 3 months in the presence of a γ-radiation field of 4.2 ± 0.2 Gy·h^{-1}. In these immersion tests, the amount of available oxidant was fixed by the one atmosphere of air present at the beginning of the experiment. The total weight changes observed indicated that not all the oxygen in the pressure vessel was consumed. Crevice-potential measurements suggested that repassivation of the crevices occurred after three to four weeks of the total three-month exposure period (Ikeda and Clarke 1986), despite the residual presence of substantial quantities of oxygen. Repassivation was attributed to the production of oxidants within the crevice by water radiolysis (Shoesmith et al., in preparation (b)).

The rates in Table 4-2 were calculated from the total weight change divided by the length of the exposure period and, hence, represent corrosion rates averaged over the total creviced area and the total exposure period of three months. Consequently, they underestimate the actual rate over the first three to four weeks when the crevices were active, but overestimate the rates over the remaining nine to ten weeks when the crevices had repassivated. From the results of electrochemical experiments relating weight changes to the total amount of oxygen consumed (Ikeda et al. 1991), it is possible to estimate the amount of oxygen consumed to produce the weight changes observed in these three-month immersion tests. From this

TABLE 4-2

CREVICE CORROSION DATA FOR GRADE-2 TITANIUM RECORDED USING ARTIFICIALLY CREVICED COUPONS AT 100 ± 5°C IN IRRADIATED 5.9 wt.% NaCl (dose rate = 4.2 ± 0.2 $Gy.h^{-1}$) (Ikeda et al. 1990a)

Exposure Period (h)	Crevice Corrosion Rate ($\mu m.a^{-1}$)
2304	5.7
2304	6.7
2304	11.0
2304	6.6
2304	16.0
2304	17.0
	10 ± 5*

* Average value with the standard deviation as the error

comparison it can be calculated that the rates in Table 4-2 represent the range of crevice propagation rates expected if the crevices had remained active over the full exposure period in the presence of a constant oxygen concentration in the solution of ~0.02 to 0.03 $\mu g.g^{-1}$. The use of these crevice corrosion rates in the model to be described below means that container lifetimes are calculated on the assumption that this oxygen concentration exists over the lifetime of the container. However, once the initial charge of oxygen present in the vault is consumed (in <320 a, Section 3.4.2) the concentration of available oxygen would be <0.005 $\mu g.g^{-1}$, the detection limit for oxygen concentrations in deep groundwaters of the Canadian Shield (Gascoyne 1992). At oxygen concentrations this low, crevice repassivation would occur (Shoesmith et al. 1992). Because the model ignores the onset of repassivation and assumes that crevices propagate indefinitely, it significantly underestimates the container lifetimes.

The use of the corrosion rates in Table 4-2 implies that the penetration front within a creviced area is planar. However, results obtained by using a combination of metallographic and image analysis techniques have shown that corrosion propagates at individual sites within crevices, making penetration uneven (Clarke et al. 1989, Quinn et al. 1993). For Grade-2 titanium, penetration proceeds in the form of localized areas ahead of a general corrosion front. Examples of corrosion penetration profiles for both materials are shown in Figure 4-6. For Grade-12 titanium, the general corrosion front is very shallow, often non-existent, and penetration is confined to local sites. Consequently, the corrosion allowance would be breached by such localized penetrations earlier than would be predicted by a model based on average penetration rates from weight-change measurements. This situation is illustrated schematically in Figure 4-7a.

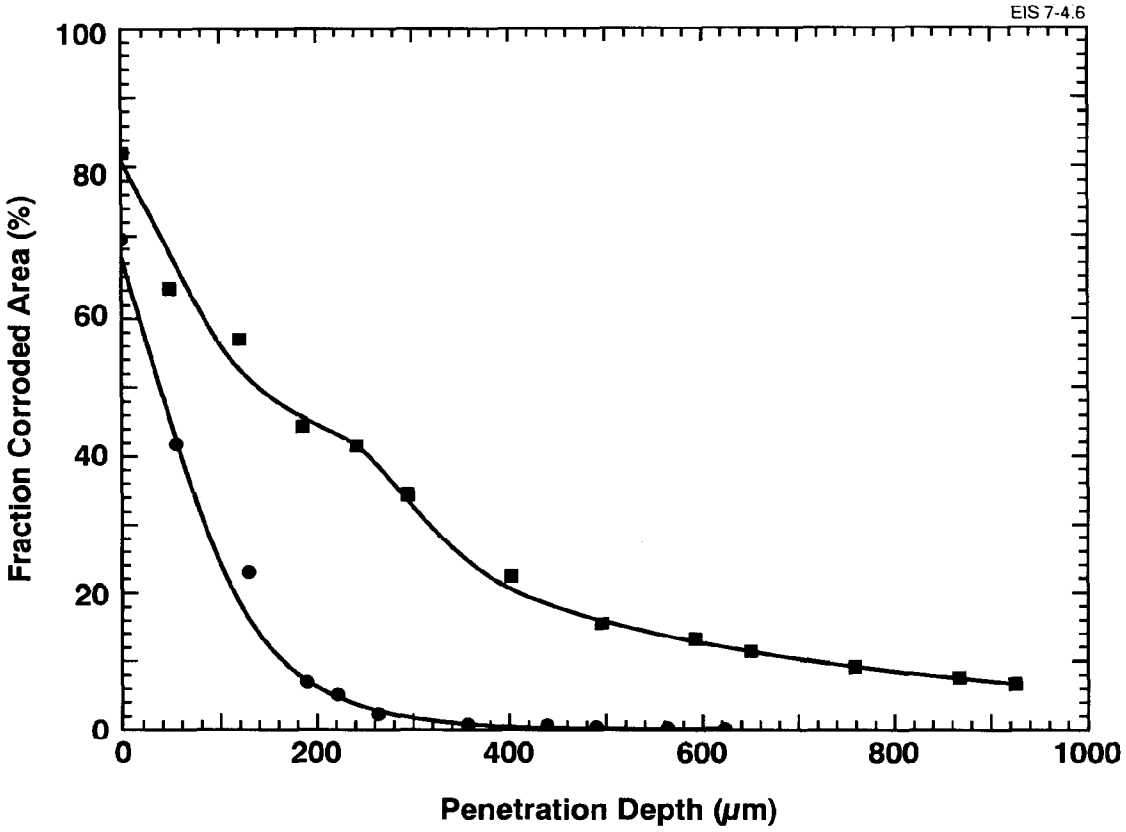

FIGURE 4-6: Corrosion Penetration Profiles (Fraction of Artificially Creviced Area Corroded as a Function of the Depth of Corrosion Penetration) for Creviced Specimens of Grade-2 (– ■ –) and Grade-12 Titanium (– ● –) Exposed to 0.27 mol·L^{-1} NaCl Solutions at 125°C. The "apparent" residual fraction of corroded area at the point of maximum penetration depth on the Grade-2 material is an artefact produced by the progression of crevice corrosion around corners on the edge of the specimens (Quinn et al. 1993).

Even under the most aggressive combination of chloride concentration and temperature, and after extensive propagation to total depletion of oxygen in pressure vessels initially containing substantial amounts of oxygen, penetration within a crevice on Grade-2 titanium does not exceed 1 mm, and the deepest localized penetrations are invariably less than 0.6 mm ahead of the general corrosion front (Shoesmith et al., in preparation (b)). Also, the localized penetrations are small; their maximum dimension across the surface (generally <5 mm) is well below the 33.5 mm beyond which the mechanical integrity of the container cannot be guaranteed (Section 4.2). Consequently, they should not lead to mechanical failure of the container even if the penetration depth exceeds the corrosion allowance.

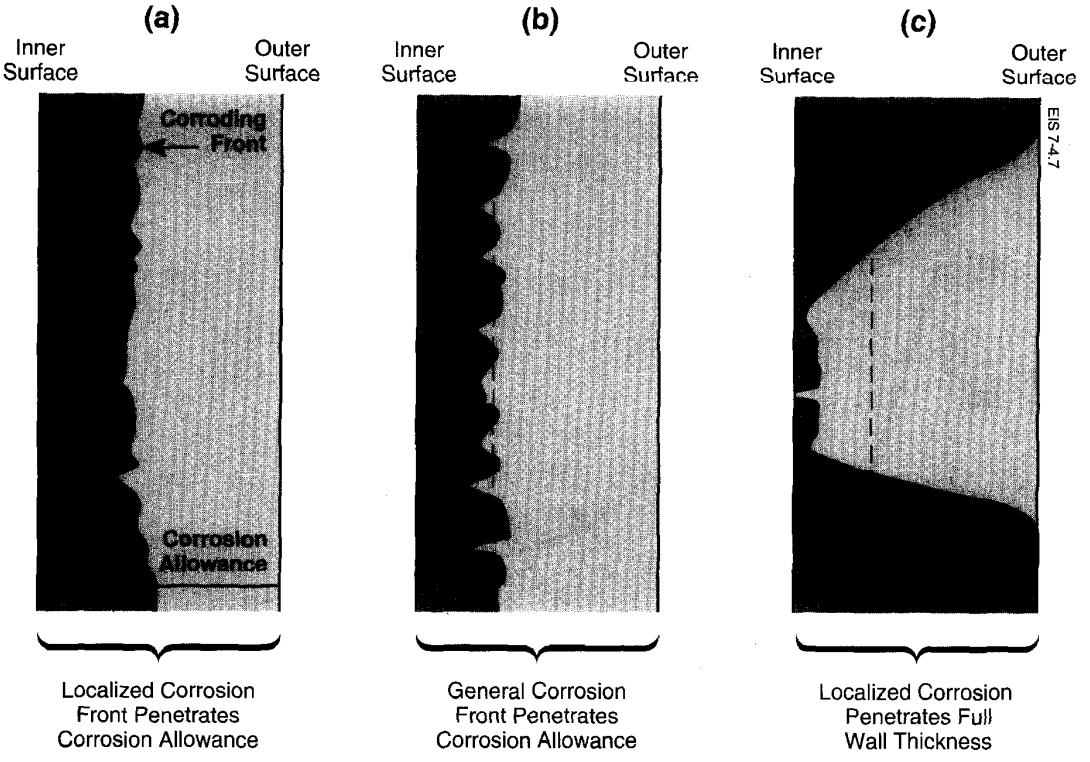

FIGURE 4-7: Schematic Showing the Progress of a Localized Corrosion Front Ahead of a General Corrosion Front for Various Definitions of Container Failure

The size of the general corrosion front, however, would be much larger, and could exceed the size of a corrosion patch beyond which mechanical failure could occur. Hence, the time at which the depth of the general corrosion front exceeds the corrosion allowance represents the minimum time beyond which the mechanical integrity of the container cannot be guaranteed. When this situation arises, the deepest localized penetrations should be $\lesssim$0.6 mm ahead of this general front, and will not have penetrated the remaining wall thickness of 2 mm (Section 4.2). This situation is depicted schematically in Figure 4-7b, and represents the most reasonable definition of container failure.

A less conservative definition of failure, applicable when crevice corrosion is limited to small areas of the surface (less than 33.5 mm in its largest dimension (Section 4.2)), would be when the deepest localized penetration exceeds the full wall thickness, as shown in Figure 4-7c.

4.6.3.3 Summary of the Container Corrosion Mechanism Under Vault Conditions

Figure 4-8a summarizes schematically the expected changes in vault parameters that are likely to affect the corrosion of waste containers. Apart from early perturbations due to the leaching of salts from the clay-based buffer/backfill materials, the groundwater composition, particularly the salinity, is expected to remain constant throughout the lifetime of the containers. The transitory high levels of fluoride and sulphate may help crevice initiation (fluoride), but should suppress the propagation rate (sulphate). At the high temperatures and oxygen concentrations initially present in the conceptual vault, it is judicious, but definitely conservative, to assume that crevice corrosion would initiate rapidly on all containers. The rate of crevice propagation is expected to be controlled by the kinetics of oxygen reduction on passive areas of the container surface surrounding the actively crevice-corroding area.

With time, the rate of crevice propagation would decrease as the temperature and the oxygen concentration decreased. The rate of temperature decrease with time can be fairly accurately calculated (Section 3.2.1 and Figure 4-2), but the period required for the consumption of oxygen (by reaction with minerals containing Fe^{2+}) is not well established (Section 3.4.2). A decrease in both of these vault parameters would lead eventually to the starvation of the propagation reaction and to repassivation of the crevice as shown schematically in Figure 4-8b. The period over which crevice propagation is sustainable is not yet established. It would be influenced not only by temperature and oxygen concentration but also by the composition and microstructure of the chosen material. Thus, crevice propagation would proceed faster and for a longer time on Grade-2 than on Grade-12 titanium. For Grade-2 titanium the concentration of the impurity iron and its distribution within the material could influence the time at which repassivation occurred. It is possible that, as propagation rates decreased and repassivation became probable, the rate would become controlled by transport processes, either of species within the crevice (e.g., protons) or of oxygen to passive surfaces outside the crevice.

Although it has been demonstrated that repassivation should eventually occur, even on the most susceptible Grade-2 material, the factors controlling the onset of this event are not clearly understood. A judicious choice of material, such as Grade 12 or a palladium-containing alloy, would limit propagation and guarantee eventual repassivation.

Once repassivation occurred, general corrosion would continue on passive surfaces under anoxic conditions (Figure 4-8b). This would involve the reaction of titanium with water (Reaction (4.1)), leading to an increase in the thickness of the oxide film. If this film grew parabolically, the corrosion rate would rapidly become negligibly small. A less conservative possibility (Section 4.6.2) is that the film would recrystallize to the thermodynamically stable form (rutile), and the introduction of ionic transport pathways down grain boundaries would lead to a corrosion rate that was, at worst, linear with time. Whatever the form of the general corrosion kinetics, the corrosion rate would be extremely low.

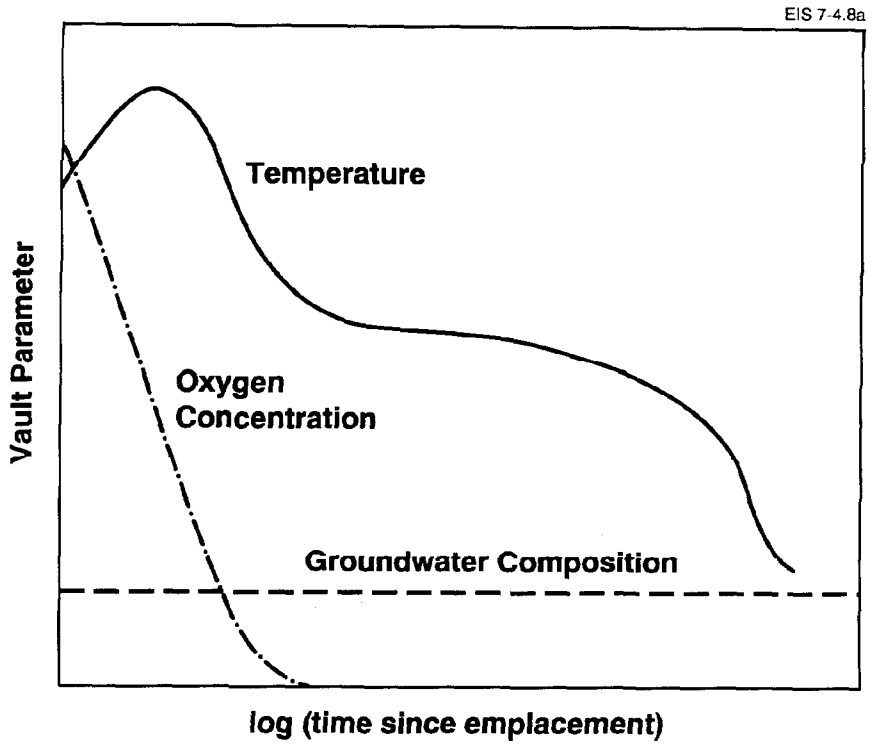

FIGURE 4-8a: Expected Changes in Those Vault Parameters That Would Affect the Corrosion of Containers

4.6.4 Environment-Induced Cracking

Environment-induced cracking is the brittle fracture of a stressed metal as a consequence of its exposure to corrosive conditions. Failure by this mechanism requires the presence of both stress and the appropriate environment. The process is frequently classified into two broad categories: stress corrosion cracking (SCC) and hydrogen-induced cracking (HIC). Opinion on such a categorization is divided, and HIC is sometimes considered a special form of SCC. Failure via SCC occurs when the anodic corrosion reaction is concentrated at the crack tip, which, in conjunction with the applied stress, causes the crack to lengthen. Failure by HIC is generally caused by hydrogen produced by the cathodic reaction. The entry of this hydrogen into the metal can cause the formation of a brittle phase within the metal and/or the introduction of strain because of lattice expansion to accommodate hydrogen in solid solution. Also, for materials like titanium, HIC could potentially occur without environmental assistance, because of hydrides already present in the commercially supplied material.

All the grades of titanium listed in Table 4-1 are considered immune to SCC over a wide range of environments (Section 4.6.1). They are considered

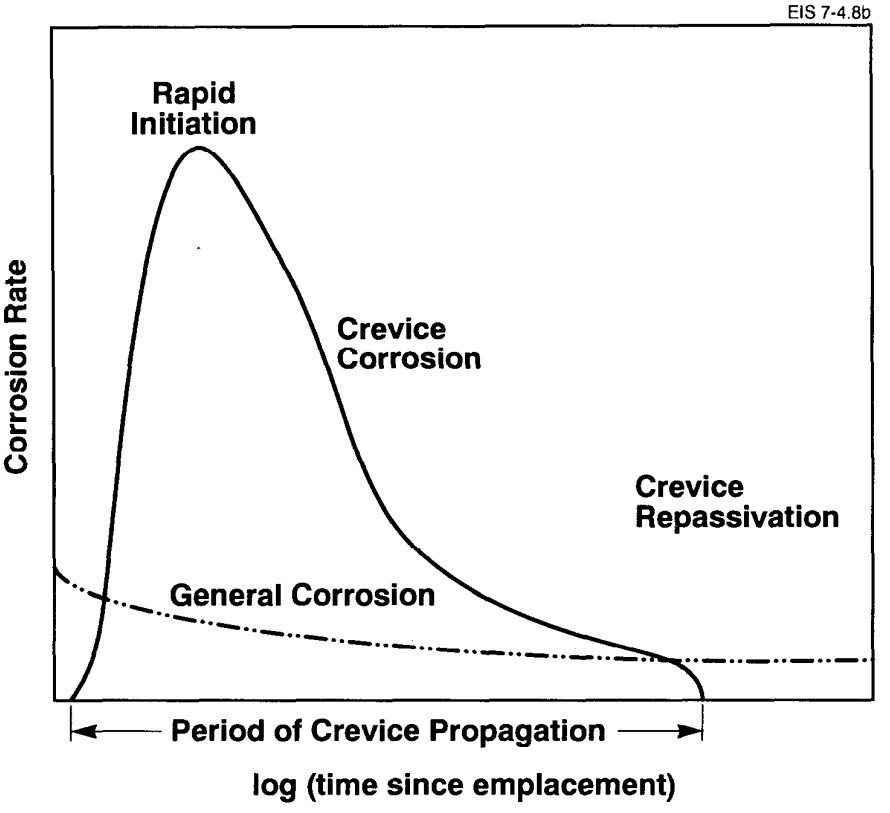

FIGURE 4-8b: Anticipated Evolution in Corrosion Behaviour of Containers as a Consequence of the Changes in Vault Parameters

immune to chloride-induced or enhanced cracking regardless of stress level, metallurgical condition, temperature or pH, except in a few specific environments that would not occur in a waste vault (Schutz and Thomas 1987). Although SCC need not be considered, the possibility of HIC resulting from the presence of hydrogen cannot be ignored.

4.6.4.1 Hydrogen-Induced Cracking

Titanium and its alloys have long been known to be embrittled by hydrogen (Williams 1962), either present in the fabricated material or absorbed from the environment, and the subject has been investigated extensively over nearly thirty years. The deleterious effects of hydrogen are normally recognized in material specifications, and the level of hydrogen is kept low during melting and fabrication processes. The ASTM standard for hydrogen in titanium stipulates a maximum concentration of 150 $\mu g \cdot g^{-1}$ (Donachie 1982). Where particularly low levels are essential, the material may be subjected to a vacuum annealing treatment by which hydrogen contents

<50 $\mu g \cdot g^{-1}$ are readily achievable (compared with a solubility of ~20 $\mu g \cdot g^{-1}$ (Paton et al. 1971)).

Despite these precautions, two forms of HIC merit consideration in the context of waste containers: slow crack growth (SCG), generally in the form of delayed hydride cracking (sometimes referred to as sustained load cracking (SLC)), where hydride formation at the tip of an advancing crack is the important requirement; and fast crack growth (FCG) in the form of general embrittlement, where extensive hydride formation is observed in the metal, and brittle failure can occur without a pre-existing crack or stress raiser. For both forms of HIC it would normally be expected that the stress required for crack propagation leading to failure would be lower at higher hydrogen concentrations.

In the as-received state at 25°C, both Grade-2 and Grade-12 titanium contain more than the maximum solubility level for hydride in α-titanium calculated from the temperature relationship proposed by Paton et al. (1971), i.e., around 20 $\mu g \cdot g^{-1}$ hydrogen. Consequently, the possibility of hydrogen-induced failure by SLC is of most immediate concern, since sufficient hydrogen is already present for such a process to be possible. General embrittlement is expected to require much higher hydrogen contents, and failure by this process would only be anticipated after substantial hydrogen absorption during crevice corrosion (Section 4.6.3.1 and Figure 4-4). However, while crevice propagation continued, the rate of metal loss would exceed the rate of hydrogen adsorption, and crevice corrosion would remain the most probable failure process.

It is generally observed that SLC is confined to those titanium alloys having both an α/β structure and high strength. The SLC observed in titanium alloys (Chesnutt and Paton 1980, Pardee and Paton 1980, Sommer and Eylon 1983) has been variously attributed to either a creep mechanism (Williams 1974, 1975; Hack and Leverant 1982) or a strain-induced precipitation of hydride (Pardee and Paton 1980), the latter being a process well characterized in zirconium alloys (Simpson and Ells 1974). The cracking process is quite rapid (Pardee and Paton 1980, Boyer and Spurr 1978), with crack growth rates $\geq 10^{-5}$ $mm \cdot s^{-1}$, and the continuity of the β-phase appears to have a significant influence upon the crack velocity (Nelson et al. 1972). More detailed discussions of SLC in titanium alloys is given elsewhere (Hardie 1990, Clarke et al. 1992).

Since Grade 2 is a single-phase α-alloy and Grade 12 is a near α-alloy containing only small amounts of β-phase (see Section 4.3), and both have relatively low yield strengths compared with the α/β alloys, neither is expected to be susceptible to SLC. However, in view of isolated reports of its occurrence in α-alloys under temperature cycling conditions (Paton 1984), it has proven necessary to investigate the susceptibilities of both materials to the slow crack growth associated with SLC as well as to the fast crack growth associated with hydride cracking (fast brittle failure).

In these tests, compact tension specimens, precracked in fatigue, were charged with hydrogen to known concentrations and strained to failure using the slow strain rate technique. Failure of the specimen is inevitable in these tests, and all that is required is a deduction of whether it is

promoted entirely by overload or whether there is a contribution from HIC. From a visual examination of the fracture surface, the slow and fast crack growth regions can be determined. The dimensions of these two regions were used to determine the stress intensity factors required to initiate both SCG and FCG, associated with embrittlement. The experimental procedure, and a detailed discussion of the results, have been given elsewhere (Clarke et al. 1992). Since a comprehensive understanding of HIC in Grades-2 and -12 titanium is unavailable, these experiments are continuing. Also, the values of stress intensity factors determined in these slow strain rate tests are being checked in a series of static load tests.

These results indicate that neither Grade-2 nor Grade-12 titanium suffers from HIC at the hydrogen levels normally encountered in the as-received condition. The fractures appeared to be extremely ductile, and the crack had to be continually pushed through the specimen by increasing strain. Under such circumstances retention of container integrity becomes merely a question of prudent engineering, and it becomes essential to determine whether circumstances change such that HIC becomes possible during emplacement in the vault.

Extensive investigations of both SCG and FCG as a function of hydrogen content have revealed certain similarities as well as significant differences between the two materials (Clarke et al. 1992). Essentially, both materials appear to suffer some form of SCG at hydrogen contents up to ~500 $\mu g \cdot g^{-1}$, but require high critical stress intensity factors for this process in the range of 60 $MPa \cdot m^{1/2}$ to promote growth. These critical stress intensity factors are almost independent of hydrogen content up to 500 $\mu g \cdot g^{-1}$. For Grade 12, values of the critical stress intensity factor for SCG measured under static load conditions are only slightly lower, confirming the validity of the slow strain rate tests. Examples of the variations in critical stress intensity factors for SCG with hydrogen content are given in Figures 4-9a and 4-9b for Grades 2 and 12 respectively. The mechanism of the SCG process remains to be elucidated, but appears to be different in the two materials (Shoesmith et al. 1992). Above a hydrogen content of ~500 $\mu g \cdot g^{-1}$ in the Grade-12 material and ~700 $\mu g \cdot g^{-1}$ in the Grade-2 material, SCG is no longer observed; only FCG, requiring a progressively lower stress intensity factor as the hydrogen content is increased above this critical hydrogen level, is observed (Figures 4-9a and 4-9b).

The critical hydrogen level for FCG varies with material and microstructure. In cases where the orientation is particularly unfavourable for crack propagation through hydride precipitates, the hydrogen content of the material appears to have little effect on the high critical stress intensity factors required for either SCG or FCG. This is the case when the crack is attempting to propagate in a direction perpendicular to the rolling plane when the dispersed β-phase in the material is flattened into almost continuous plates parallel to this plane (Clarke et al. 1992). Both grades may also exhibit FCG subsequent to SCG over a certain range of hydrogen concentrations (Figures 4-9a and 4-9b), but present evidence suggests significant differences between the two materials in this regard. Grade 2 appears to be so susceptible to ductile rupture under high stresses at low hydrogen concentrations that no FCG can develop at levels below

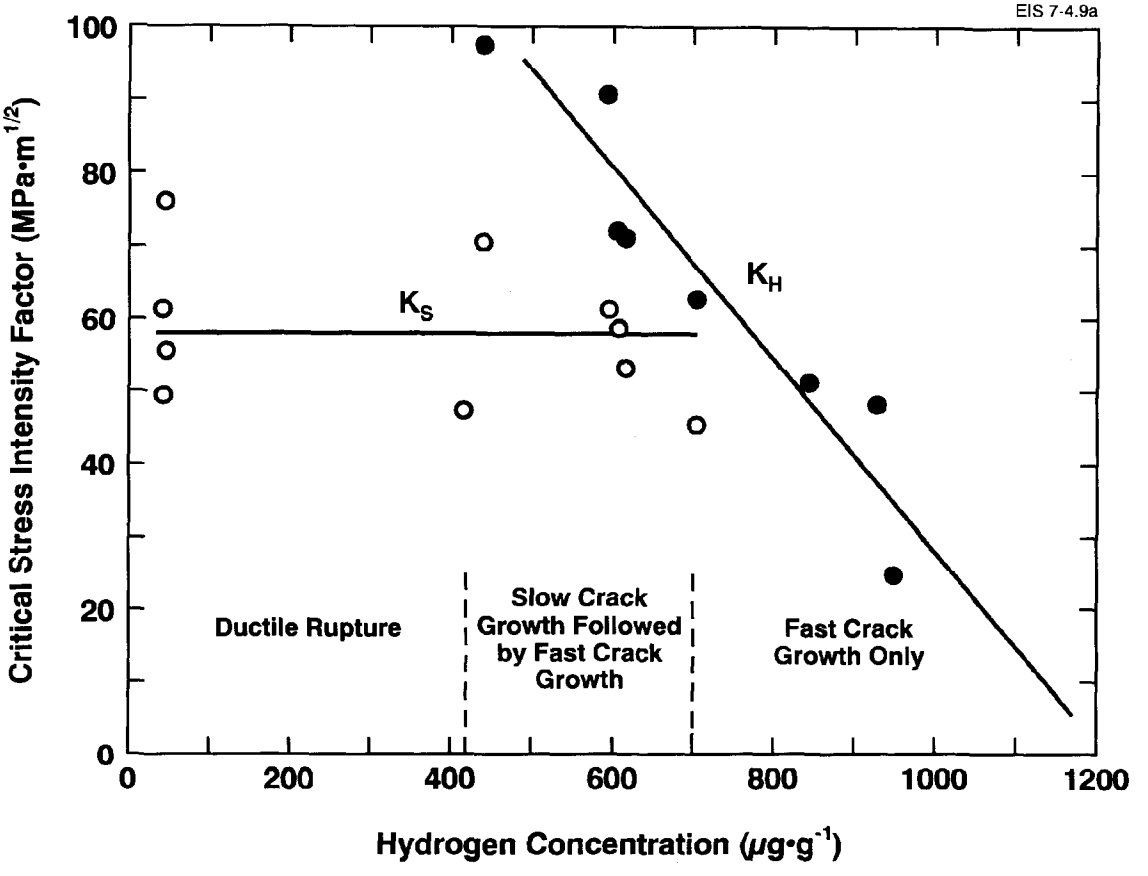

FIGURE 4-9a: Variation of the Critical Stress Intensity Factors with Hydrogen Content for Grade-2 Titanium (Transverse-Longitudinal (T-L) Orientation): o - Slow Crack Growth (K_S); • - Fast Fracture (K_H)

~500 $\mu g \cdot g^{-1}$ (Figure 4-9a). By contrast, except at hydrogen concentrations below ~50 $\mu g \cdot g^{-1}$, Grade 12 exhibits FCG over the whole range of hydrogen concentrations, but SCG is a necessary precursor at concentrations up to ~500 $\mu g \cdot g^{-1}$ (Figure 4-9b). The actual critical hydrogen limit depends upon the detailed microstructure and texture of the fabricated material (Clarke et al. 1992).

These measurements of critical stress intensity factors as a function of hydrogen concentration delineate three areas of behaviour associated with FCG, SCG or no failure, as illustrated in Figure 4-10. Such a diagram can be used to specify a limiting critical stress intensity factor at low hydrogen concentrations and a limiting hydrogen level, $[H]_c$, for a particular critical stress intensity factor.

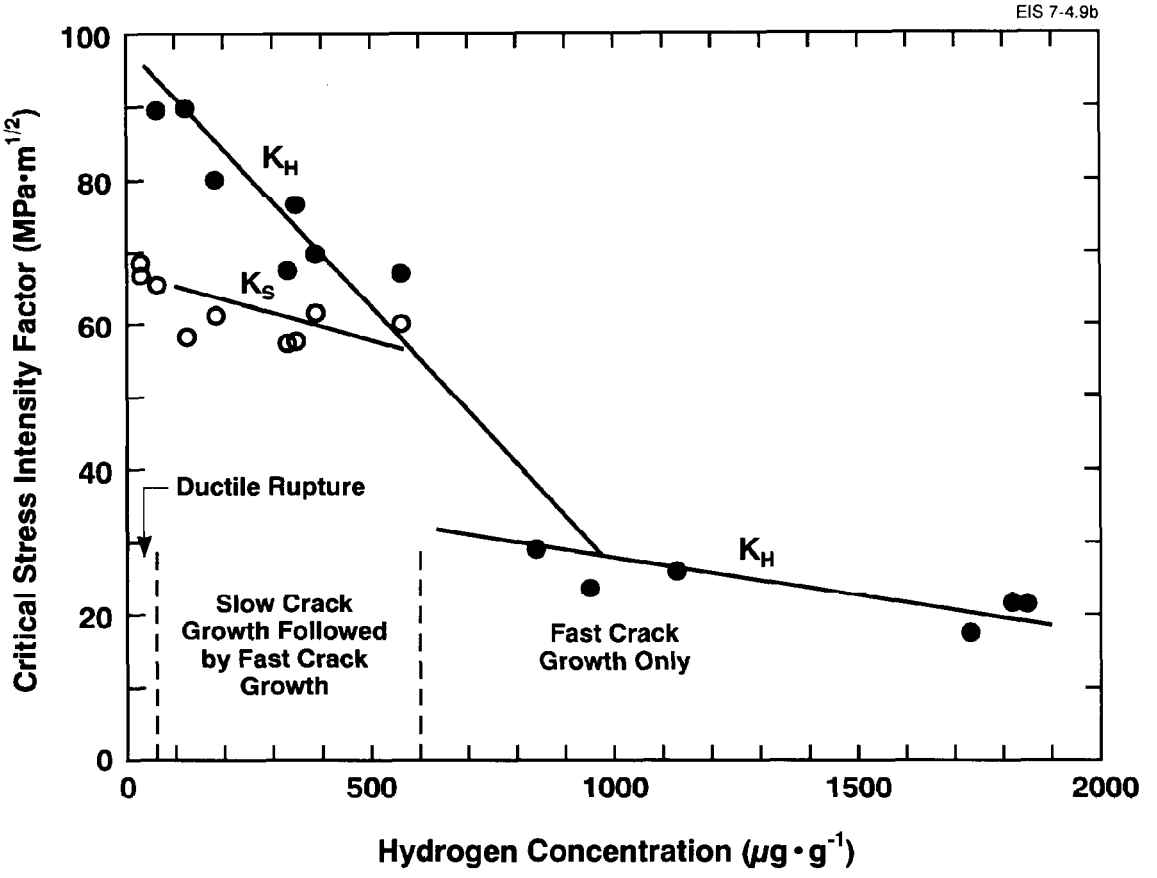

FIGURE 4-9b: Variation of the Critical Stress Intensity Factors with Hydrogen Content for Grade-12 Titanium (T-L Orientation): o - Slow Crack Growth (K_S); • - Fast Fracture (K_H)

So far, the cracking behaviour of Grades-2 and -12 titanium has been studied only at room temperature. Consequently, no reliable prediction can be made of the influence of temperature on the hydrogen-induced failure process. Present understanding is based on the limited amount of published work on SLC in α/β alloys (Boyer and Spurr 1978; Moody and Gerberich 1980, 1982; Lederich et al. 1982). Boyer and Spurr (1978) observed some crack growth at room temperatures (~20°C) in almost every specimen of Ti-6Al-4V tested with hydrogen levels up to 255 $\mu g \cdot g^{-1}$, but the extent was minor and crack stabilization occurred within 10 d. The amount of crack growth at temperatures below ~20°C increased with decreasing temperature to a maximum (around -20°C to -40°C), and then decreased at higher temperatures. The implication of their results was that extremely high stress intensities, probably leading to ductile overload, were necessary to produce even minor crack growth at temperatures above room temperature. Other workers have also observed a maximum in the crack growth rate/temperature relationship, either at room temperature (Moody and Gerberich 1980) or between 58°C and

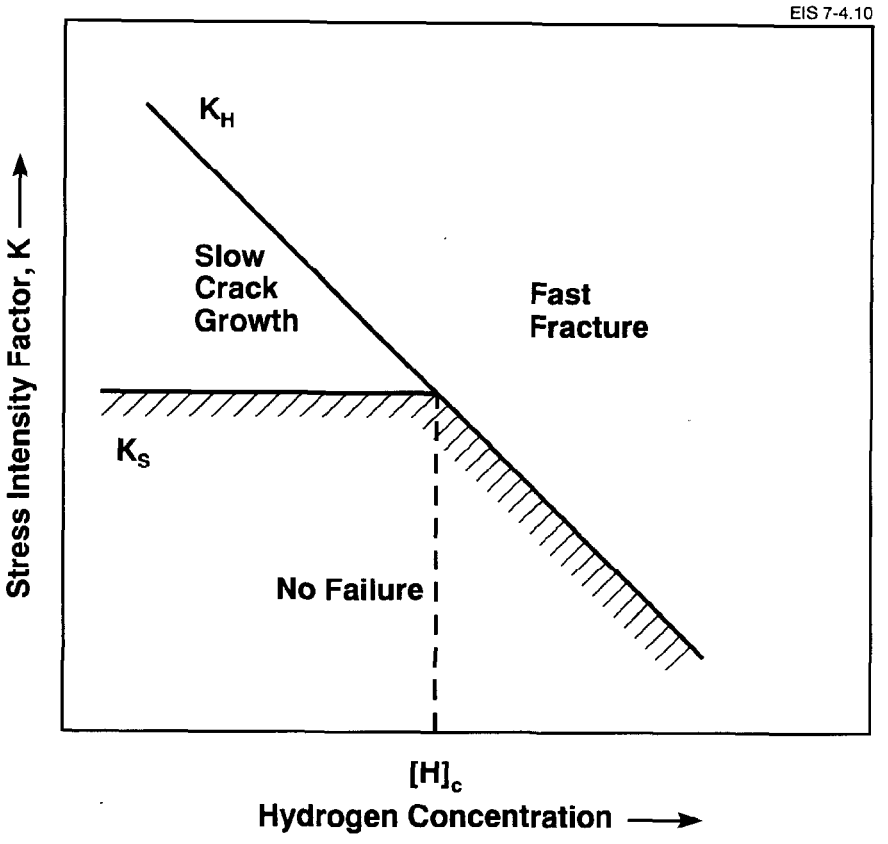

FIGURE 4-10: Schematic Representation of the Combinations of Critical Stress Intensity Factor and Hydrogen Concentration Leading to Fast Fracture, Slow Crack Growth or No Failure in Titanium. K_S represents the stress intensity factor for initiation of slow crack growth and K_H the stress intensity factor leading to fast fracture. $[H]_c$ is the critical hydrogen concentration for hydrogen-induced failure.

90°C (Lederich et al. 1982). The higher temperatures related to materials with unusual microstructures containing continuous β-phase, which will not be present in Grade-2 and Grade-12 titanium. Such a maximum has also been generated theoretically by Pardee and Paton (1980) on the premise that strain-induced precipitation of hydride is responsible for SLC, and that this process depends upon diffusion of hydrogen to the plastic zone ahead of any crack. The maximum is attributed to limitations on the crack growth rate resulting from the low diffusion rate of hydrogen at low temperatures and from hydride solubility, which limits the volume fraction of hydrides formed at higher temperatures.

Whether or not failure of Grades-2 and -12 titanium can occur by strain-induced hydride precipitation remains to be demonstrated. Evidence

currently available favours failure by a creep mechanism, not by SLC (Clarke et al. 1992).

4.6.4.2 Implications for Modelling Hydrogen-Induced Failure

Modelling HIC becomes a matter of establishing the combination of stress and hydrogen concentration that leads to failure, whether this occurs by plastic rupture, hydrogen-induced SCG or general embrittlement (FCG). The limiting hydrogen level for container failure would depend upon the stress distribution in the container; thus a dependable analysis of this and its variation with time become a requirement for a predictive model.

At present, the stress distribution in the container subsequent to closure by welding, and its variation throughout the lifetime of the container, are not known. Consequently, for the time being, it is necessary to assume that stresses will not relax with time after emplacement in the vault. However, the need for a high critical stress intensity factor, and the independence of this factor from hydrogen concentration up to ~500 $\mu g \cdot g^{-1}$ makes SCG an extremely unlikely process in either Grade-2 or Grade-12 titanium. Thus, critical stress intensity factors in the region of 60 $MPa \cdot m^{1/2}$ are necessary to promote SCG at hydrogen levels below ~500 $\mu g \cdot g^{-1}$ (Figures 4-9a and 4-9b). Even with stresses of magnitude corresponding to a stress of 400 MPa (approaching the yield stress of Grade-12 titanium), a critical crack length of 14 mm (more than twice the wall thickness of the container) would be required for failure to occur (Shoesmith et al. 1992). A reduction of the stress intensity factor to 20 $MPa \cdot m^{1/2}$, a value critical only for high hydrogen contents (Figures 4-9a and 4-9b), would reduce the critical defect size to only ~2 mm, well within the detection limits of pre-emplacement inspection procedures.

If the data of Boyer and Spurr (1978) for Ti-6Al-4V are accepted as applicable to both Grade-2 and Grade-12 titanium, a conservative assumption especially in the case of Grade 2, then cracking should not be possible before considerable cooling of the containers occurred. According to the results for Ti-6Al-4V, 20°C appears to be an upper temperature limit above which failure only by ductile overload appears possible.

For FCG, the hydrogen content must exceed the critical hydrogen level ($[H]_c$ in Figure 4-10). It is possible that higher hydrogen levels could be tolerated if stresses within the container relaxed with time.

4.6.4.3 Hydrogen Absorption by Grades-2 and -12 Titanium

Crack growth rates, even for slow processes such as SLC, are expected to be fast compared with the expected lifetime of the containers (10^{-2} $mm \cdot s^{-1}$ to 10^{-5} $mm \cdot s^{-1}$, Moody and Gerberich (1980), Boyer and Spurr (1978)), and once the critical combination of stress and hydrogen concentration for failure is achieved, it is judicious to assume that failure would be rapid. Consequently, the major requirement if HIC is to be modelled is a measure of the rate of hydrogen absorption.

There are three processes that could lead to the absorption of hydrogen into the metal:

- proton reduction within active crevices,
- general corrosion under anoxic conditions when oxidation of titanium metal is sustained by the reduction of water (Reaction (4.1)), and
- the production of hydrogen atoms and molecules by the radiolysis of water.

The third process is discussed later in Section 4.6.6.

(i) Hydrogen pickup during crevice corrosion

Hydrogen pickup by Grade-2 titanium during crevice corrosion is well documented (Schutz and Thomas 1987, Clarke et al. 1989). When crevice corrosion rates are high, hydrides precipitate close to the actively corroding surface, and the advance of the crevice-corroded front continually removes them (Clarke et al. 1989). However, since the temperature of most containers would remain high for a considerable time (Figure 4-2), the bulk of the container wall would act, at least partially, as a diffusion sink during the period when crevice corrosion was propagating most rapidly. The rate and total amount of hydrogen absorption would be determined by the rate of crevice propagation, the area of the container surface actively undergoing crevice corrosion, and the period for which propagation occurred prior to repassivation. Obviously, a material such as Grade-12 titanium, on which crevice propagation is slow and limited because of repassivation (Section 4.6.3.2), would not absorb hydrogen as rapidly, or for as long, as Grade-2 titanium.

Since crevice corrosion on either grade is an improbable event, it is unlikely that a large number of crevices would initiate on each container, and the area of actively corroding surface would be limited. This, coupled with the ability of the container to act, at least partially, as a diffusion sink, should make the rate of attainment of the critical hydrogen concentration for hydrogen-induced failure ($[H]_c$, Figure 4-10) a slow process. At present, the rates of hydrogen pickup under crevice corrosion conditions are unknown, although experiments to measure such rates are in progress.

(ii) Hydrogen absorption during general corrosion under anoxic conditions

Once all oxygen within the conceptual vault was consumed and crevices had repassivated, hydrogen absorption could continue to occur as a consequence of general corrosion according to Reaction (4.1). Under these conditions absorption by the metal would require transport through the passive film (TiO_2) and would be extremely slow. Exposure tests conducted by Shoesmith et al. (in preparation(b)) in a variety of possible vault environments showed no hydrogen absorption by Grade-2 titanium under passive conditions. Similarly, Mattsson (1979) observed no measurable absorption by Grade 2 exposed to seawater for 300 d at 130°C. Indeed, hydrogen absorption by passive Grade-2 titanium is generally observed only when the metal is galvanically coupled to less noble metals and alloys, e.g., carbon steel (Schutz and Thomas 1987, Shimogori et al. 1977), or when either a cathodic

current or negative potential is impressed on the metal (Phillips et al. 1972, Murai et al. 1977, Covington 1979, Foroulis 1980, Riskin et al. 1984, Lee, J.I. et al. 1986). On the basis of very long experiments (up to 180 d), Murai et al. (1977) established that a potential of -0.6 to -0.7 V_{SCE} at 30°C represented a threshold above which measurable hydrogen absorption did not occur.

Under anoxic conditions, the corrosion potential for passive titanium will reside at a value at which water reduction is possible on the passive film, and hence must be at, or more negative than, the thermodynamic stability line for water. At such potentials, titanium hydrides are thermodynamically stable with respect to the metal (Beck 1973). Consequently, the passive film can be considered only as a transport barrier to the formation of hydrides. According to Dyer and Leach (1978) and others (Torresi et al. 1987a,b; Ohtsuka et al. 1987), hydrogen deposition into TiO_2 films occurs in parallel with the redox transformation

$$TiO_2 + H^+ + e \rightarrow TiOOH \qquad (4.2)$$

in the film. This conversion commences around -0.6 V_{SCE}, approximately the same potential claimed as a threshold for hydrogen absorption by Murai et al. (1977). The chemistry of this situation is depicted schematically in Figure 4-11. In reality, the situation is more complex, and the state of hydrogen within the passive film is not completely understood (Weber et al. 1982). A more complete discussion is presented elsewhere (Shoesmith et al., in preparation(b)).

Since the rate of corrosion determines the rate of formation of hydrogen (Reaction 4.1), the rate of hydrogen absorption at the corrosion potential cannot proceed any faster than the corrosion rate. An estimate of the maximum rate of hydrogen absorption by Grade-2 titanium has been made by Shoesmith et al. (in preparation(b)) on the basis of the corrosion rate data of Mattsson and Olefjord (1990) and Mattsson et al. (1990) for corrosion in clay. If one assumes that the rate of corrosion is linear with time at the maximum rate (Section 4.6.2), and that all the hydrogen produced is absorbed by the metal (an extremely conservative assumption), then ~2 x 10^4 a would be required before the hydrogen concentration exceeded the critical value of 500 $\mu g \cdot g^{-1}$ required for hydrogen-induced failure. If one chose a lower, perhaps more realistic, corrosion rate from the results of Mattsson and co-workers, greater than 4 x 10^5 a would be required.

Whether Grade-12 titanium would exhibit similar slow rates of hydrogen absorption under passive conditions is not clear. Exposure tests by Shoesmith et al. (in preparation(b)) under similar conditions to those used with Grade 2 showed no measurable hydrogen absorption. By contrast, Westerman (1990) and Kim and Oriani (1987a,b) observed small but measurable absorption by Grade 12 exposed to very saline Na/Ca/Mg brines, characteristic of those anticipated in a salt repository (e.g., WIPP).[7] Clarke et al. (1986) found that Grade 12 failed by a brittle fracture process in slow strain rate tests conducted in 3.5% NaCl, but only at T $\geq$ 120°C and with

---

[7] Waste Isolation Pilot Plant, New Mexico

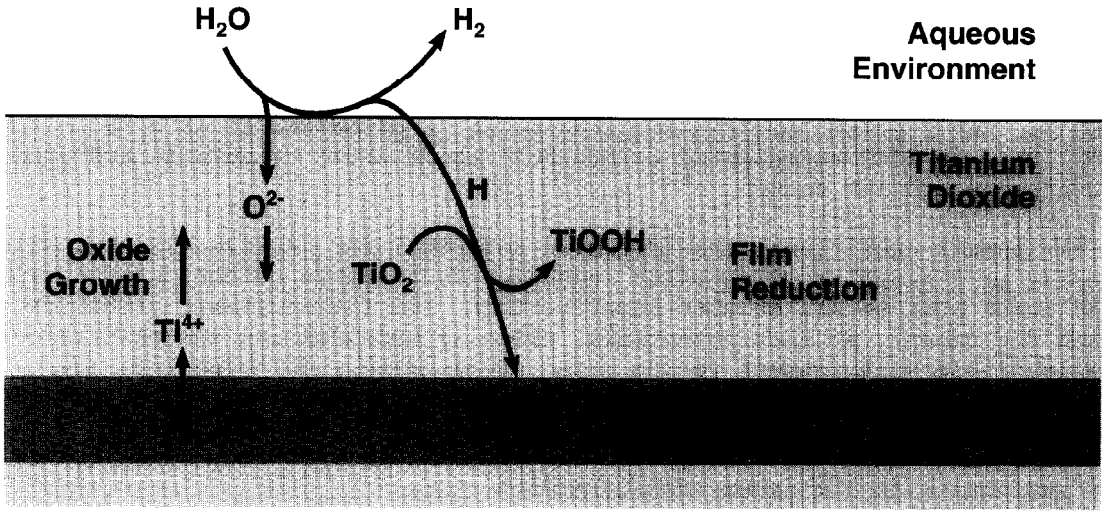

FIGURE 4-11: Schematic Showing the Chemistry of Hydrogen Absorption on Passive (Oxide-Covered) Titanium Under Anoxic Conditions

very negative applied potentials. These observations are consistent with those of other authors (Sorensen and Ruppen 1985, Sorensen 1990).

Although these conditions are far more aggressive, in terms of salinity, temperature, and/or applied negative potential, than can be achieved under Canadian disposal vault conditions, they raise questions concerning the ability of passive films on Grade-12 titanium to resist hydrogen absorption by the underlying metal. With Grade 12 it is possible that the oxide film is incomplete over the Ti_2Ni particles known to exist locally in this material. Since these particles are likely to sustain faster rates of water reduction than the α-titanium grains (Glass 1983), they may act as sites for hydrogen entry. This is consistent with the observations of Schutz and Covington (1981), who showed that the thermally grown oxide on Grade 12 did not provide as effective a barrier to hydrogen entry as that on Grade 2.

4.6.4.4 The Coupling of Crevice/General Corrosion and Hydrogen Absorption Under Vault Conditions

Figure 4-12 summarizes schematically the relationship between the container corrosion rate by either crevice corrosion or general corrosion (from Figure 4-8b) and the extent of hydrogen absorption. The largest fraction of this hydrogen would be absorbed during crevice corrosion; the amount would be determined by the rate and length of time for which crevice corrosion actively propagated. Once crevices repassivated, both general corrosion and the rate of hydrogen absorption would be extremely slow.

If crevice corrosion was rapid, or if it propagated extensively for a considerable period of time, then container failure would be by this process or by HIC. Early failure by SCG appears extremely unlikely

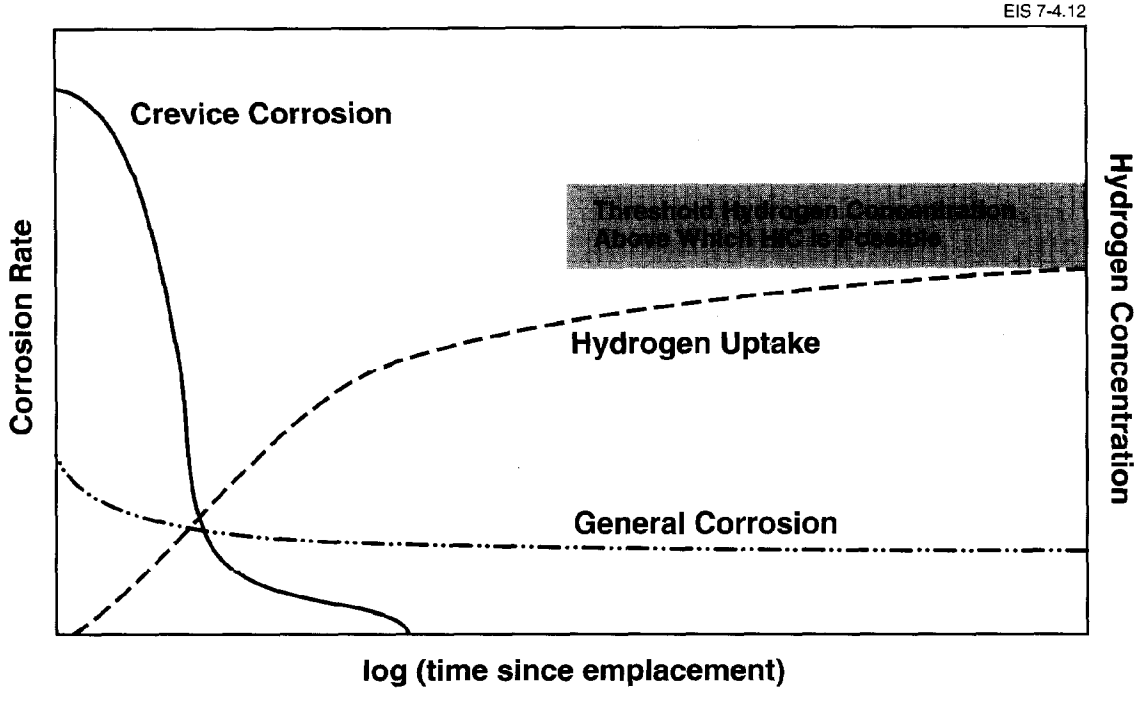

FIGURE 4-12: The Relationship Between Container Corrosion Rate, by Either Crevice or General Corrosion, and the Extent of Hydrogen Pickup as a Consequence of Corrosion

(Section 4.6.4.1), and failure by FCG would only occur at long times, since $[H]_c$, the critical hydrogen concentration for FCG, is large (~500 μg/g).

Consequently, it is the rate and extent of crevice propagation that would have the greatest impact on container failure times, and the best way to achieve long lifetimes is to limit the extent of crevice propagation. As discussed in Section 4.6.3.2, the extent of crevice propagation would be limited for Grade-2 titanium as temperatures decreased and oxygen was consumed with time. For Grade-12 titanium the period of crevice propagation would be shortened considerably by this material's ability to repassivate in the presence of considerable concentrations of oxygen. If repassivation occurred rapidly, then hydrogen absorption would be limited and container lifetimes would be extended.

At present, the vault conditions for which crevice repassivation would occur are unclear, mainly because the rate of evolution of redox conditions from oxic to anoxic is not known with certainty. Also, for the Grade-2 material it has not been proven that a decrease in temperature alone would lead to repassivation (Section 4.6.3.2). Consequently, it has been assumed in the model that crevice corrosion can propagate indefinitely, which is equivalent to assuming that sufficient oxygen would always be present to sustain crevice propagation. This is a very conservative assumption, and guarantees that most containers are predicted to fail by crevice corrosion.

If crevice corrosion is assumed to propagate indefinitely, then substantial amounts of hydrogen would be absorbed, and those containers that did not fail by crevice corrosion would eventually fail by HIC. Since a knowledge of the evolution of stresses in the container is unavailable, it is assumed they would always be large enough to yield stress intensity factors sufficient to cause HIC (either SCG or FCG) (Figure 4-10). Also, it is assumed that sufficient hydrogen would be absorbed by the time containers cool to ≤30°C to make failure by HIC inevitable. A temperature of 30°C is 10°C above the threshold temperature determined by Boyer and Spurr (1978) for HIC in Ti-6Al-4V. Above this temperature of 20°C, failure appears possible only by ductile overload, a process avoidable by prudent engineering of the container.

4.6.5 Corrosion of Welds

In many engineered structures, the welds can often be sites where corrosion is enhanced. This is particularly true of complex, multiphase alloys, which can undergo significant metallurgical changes when subjected to the heat treatments associated with the weld itself and the surrounding heat-affected zones. Since Grades-2 and -12 titanium contain so little alloy and second phase, metallurgical changes during welding are not expected to be significant. This is borne out by our many long-term exposure tests (1 a to 5 a) on welded coupons, which showed neither an increase in general corrosion rate nor an increased susceptibility to the initiation of crevice corrosion (Shoesmith et al., in preparation (b)).

These results reflect the corrosion behaviour of welds under passive conditions when general corrosion rates are very low (see Section 4.6.2). Since crevice corrosion is expected to be the predominant corrosion process in a disposal vault, tests under the active acidic conditions anticipated in propagating crevices are more relevant. Tests on weldments, and specimens heat-treated to simulate the effects of welding, in hot (boiling) acidic solutions show only minor increases in corrosion rate compared with the base material (Molecke et al. 1982, Fukuzuka et al. 1980, Covington and Schutz 1981). Tests, using the galvanic coupling technique described in Section 4.6.3.2 at temperatures (150°C) and salinities (0.27 $mol \cdot L^{-1}$) greater than those anticipated in a waste vault, have shown no increase in the rate of crevice propagation on either welded specimens or specimens heat-treated to simulate the effects of welding (Ikeda et al. 1990c). In fact, if the iron content is high enough (>0.1 wt.%), heat treatment leads to a decrease in the propagation rate. Also, attempts to initiate crevice corrosion on welded specimens of the Grade-2 material (0.13 wt.% iron), under conditions where the base material did not crevice-corrode, were unsuccessful.

For welding to affect HIC, the weldment or heat-affected zone would have to act as a site for preferential hydrogen absorption or be more susceptible to HIC. Although data are scarce, there is no evidence to suggest that it does (Fukuzuka et al. 1980). Under crevice corrosion conditions the rate of hydrogen absorption is tied to the rate of crevice propagation (Section 4.6.3.2). Since the latter appears to be unaffected by welding, a significant change in the rate of hydrogen absorption is unlikely.

From the above discussion it is clear that very little effect of welding on either crevice corrosion or HIC is expected. If anything, the minor metallurgical changes caused by the increased temperatures experienced during welding are likely to decrease the materials' susceptibility to crevice corrosion. This is especially true for Grade-2 material containing sufficient iron to lead to the formation of minor amounts of β-phase on heat treating.

4.6.6 Effect of Radiation

The only effect of radiation likely to be of importance in determining container durability is the radiolysis of groundwater (Section 4.4.4). There appear to be two possible ways in which radiolysis products can adversely affect the corrosion performance of titanium:

- oxidizing species (e.g., OH, H_2O_2, O_2, Cl^-, ClO^-, Cl_2^-) could increase the rates of general and crevice corrosion; and
- reducing species (e.g., H, H_2) could increase the rates of hydrogen absorption, leading eventually to radiation-induced hydriding.

In general, materials that are protected by adherent passive films, such as the titanium alloys, should not be affected significantly by the products of water radiolysis (Glass 1981). The passive film would prevent acceleration of the corrosion reaction and act as a barrier to hydrogen absorption. Also, acid generation due to the radiolysis of N_2 under oxic conditions has been shown to be insignificant (Section 3.4.2).

(a) General Corrosion

A very minor, generally negligible, impact of irradiation on the general corrosion rate of both Grades-2 and -12 titanium has been observed in most exposure environments (Braithwaite and Molecke 1980, Molecke et al. 1982, Kim and Oriani 1987a, Ikeda et al. 1990b). The one exception appears to be a combination of high dose rates (10^5 Gy·h^{-1}) and high temperature (>200°C), when some increase in the general corrosion rate of Grade 2 was observed (Braithwaite and Molecke 1980, Molecke et al. 1982).

(b) Radiation-Induced Hydriding

Since the rates of general corrosion are not significantly affected by radiation, we would not expect a significant increase in the absorption of hydrogen produced by corrosion. This is borne out by the results of Ikeda et al. (1990b), Westerman et al. (1982), Molecke et al. (1982) and Kim and Oriani (1987a,b). The possibility of direct absorption of hydrogen produced by water radiolysis appears to be remote, and only for Grade 12 at high dose rates (10^4 Gy·h^{-1}) and high temperatures (250°C) is there any evidence for such a process (Westerman et al. 1982).

Unfortunately, the data on hydrogen absorption by both grades of titanium are sparse and somewhat contradictory, and in the absence of detailed studies it is difficult to draw any firm conclusions, except, perhaps, that

the rate of hydrogen absorption increases substantially for dose rates greater than ~10^3 Gy·h^{-1}. At the low dose rates (~50 Gy·h^{-1}; Section 4.4.4), salinities and temperatures anticipated in a Canadian disposal vault, it is unlikely that the impact of radiation would lead to significant hydrogen absorption. This conclusion is supported by exposure tests over periods up to 5 a (Shoesmith et al., in preparation (b)).

(c) Crevice Corrosion

There appear to be two possible effects of radiation on crevice corrosion, one detrimental, one beneficial:

- The production of oxidizing species outside the crevice could increase the oxidant concentration, leading to an increase in the rate of crevice propagation.

- The production of oxidizing species inside the crevice could inhibit crevice corrosion by forming oxides on the internal crevice surfaces, thereby preventing the maintenance of the occluded cell necessary for crevice propagation.

The experimental results of Ikeda and Clarke (1986) and Ikeda et al. (1990a,b) with Grade-2 titanium suggest the second effect is dominant. Although information is sparse, in situations where corrosion was actively propagating, the presence of radiation (at dose rates ≥4 Gy·h^{-1}) appeared to decrease the propagation rate or induce repassivation of the crevice before all the oxidant was consumed. This behaviour is in contrast with observations in the absence of radiation when repassivation was not observed until all the oxygen was consumed (Figure 4-5b).

4.7 CONTAINER LIFETIME MODEL

Three potential modes of failure are considered in the model: (1) failures caused by undetected initial defects; (2) failures resulting from crevice corrosion at different temperatures; and (3) failures caused by HIC.

4.7.1 Failures Caused by Initial Defects

There is a low probability that some containers placed in a vault would have critical defects (Nuttall 1983). These defects would be either detectable faults missed by the inspection procedure, or undetectably small faults located so as to lead to premature container failure. Failure would occur when the full wall thickness was penetrated. Subsequently, irrespective of the size of the penetration, the container is assumed to offer no further protection against the ingress of water and subsequent leaching of the fuel. A variety of defects, depending on their type (crack, void, inclusion, etc.), position (weld, sidewall), and size,[8] can be expected.

---

[8] The inspection procedure is expected to be capable of detecting defects in diffusion bonds as small as 0.127 mm in width (Maak and Moles 1986).

Some of these defects would lead to rapid failure, whereas others would require some time to grow before perforation occurred.

The probability of critical defects being present has been estimated from a statistical analysis of failures of other mass-produced products, such as pressure vessels and CANDU reactor pressure tubes. On the basis of these analyses, Doubt (1984, 1985) has estimated that between 1 in 10^4 and 1 in 10^3 containers would contain defects capable of causing early failures.

At present, there is little information upon which to base a prediction of failure times for such defects. However, containers with the largest critical defects would be expected to fail almost immediately, whereas those with smaller defects should require some time before failure. It has been assumed that these failures follow a simple ramped distribution with the largest number of defected containers failing at t = 0 and all failures being complete after a short period of time.

To take into account the small number of containers in some vault sectors, the actual number failing prematurely in a given sector was determined by sampling from the binomial distribution for N trials, each with a probability, p, of failure, where N is the number of containers in each sector and p is sampled from a lognormal distribution. The lognormal distribution for p was chosen to have a geometric mean of 2.0×10^{-4} failures per year and a geometric standard deviation of 1.5. The distribution was truncated at a lower value of 10^{-4} failures per year and an upper value of 10^{-3} failures per year to reflect the information compiled by Doubt (1984, 1985).

4.7.2 Failures Resulting from Crevice Corrosion

Unless the period of crevice propagation (Figure 4-12) can be limited as described in Section 4.6.4.4, crevice corrosion remains the most probable failure mechanism, especially for Grade-2 titanium, the reference container material for the case study. Unfortunately, the detailed crevice corrosion models published by Oldfield and Sutton (1978a,b, 1980) and by Sharland and Tasker (1988) and Sharland et al. (1989) are difficult to apply to titanium under waste vault conditions for two reasons:

- they require that the crevice geometry be specified, an impossible task under vault conditions where geometries could be irregular and would vary from crevice to crevice; and

- they require a good quantitative understanding of the high-temperature hydrolysis and complexation of dissolved titanium species, information not currently available.

In the model presented here, it is assumed that crevice corrosion initiates on all containers as soon as the vault is closed. The rate of crevice propagation is controlled by the rate of oxygen reduction on passive surfaces surrounding the creviced area (Figure 4-4), a reaction that exhibits an Arrhenius relationship with temperature over the whole range of vault temperatures (Section 4.6.3.2). It is also assumed that, despite the evolution of redox conditions and temperature within the vault, repassivation does not occur (Figure 4-5a) and crevice corrosion propagates

indefinitely. This assumption guarantees that the predicted failure is either by crevice corrosion or by HIC as a consequence of hydrogen absorption during crevice corrosion.

Failure by crevice propagation is assumed to occur when the depth of the general corrosion front within a creviced area exceeds the corrosion allowance of 4.2 mm (Figure 4-7b). When this occurs it is assumed that the area of the container surface subjected to crevice corrosion is unsupported by packed particulate and large enough that the breaching of the container wall occurs mechanically. Once this failure has occurred, the container provides no further protection against ingress of water and subsequent leaching of the fuel.

The crevice propagation rates listed in Table 4-2 are used in the model. Calculated on the basis of weight-change measurements, they are consistent with the definition of failure described above (Section 4.6.3.2 and Figure 4-7 (b)). Their use can be considered conservative for a number of reasons:

1. They were measured on commercially available Grade-2 titanium containing ~0.02 wt.% iron as an impurity. This is the material most susceptible to rapid crevice corrosion.

2. They were measured in solutions containing ~1.5 $mol \cdot L^{-1}$ NaCl, a concentration well in excess of the concentration expected in the reference disposal vault (Table 3-1a) and at which the crevice propagation rate would be at a maximum.

3. They represent the propagation rate expected for an oxygen concentration in solution of ~0.02 to 0.03 $\mu g \cdot g^{-1}$ (Section 4.6.3.2), which is assumed not to diminish over the lifetimes of the containers; i.e., the expected repassivation of crevices after the initial oxidizing period, conservatively estimated to be no more than 300 a (Section 3.4.2), is assumed not to occur.

Since the expected change in temperature over the lifetime of the vault is fairly accurately known, and because the rate of crevice corrosion is a strong function of temperature, the effect of temperature on crevice propagation rates has been accounted for in the model. Each container would possess a distinct temperature-time profile, making it difficult to determine the effect of temperature on crevice corrosion for every container in the vault. To simplify the analysis of temperature effects, the containers have been assigned to one of three categories according to the general characteristics of their cooling behaviour. To facilitate calculations of crevice corrosion rates and, hence, container failure times, the temperature data for each category has been averaged and the real temperature-time profiles approximated by simple step functions.

For containers whose initial temperature remains high for a substantial time, the real profiles are approximated by a two-level step function (Figure 4-13a). Approximately 63% of containers, designated hot, are included in this category and are located primarily in the centre of the

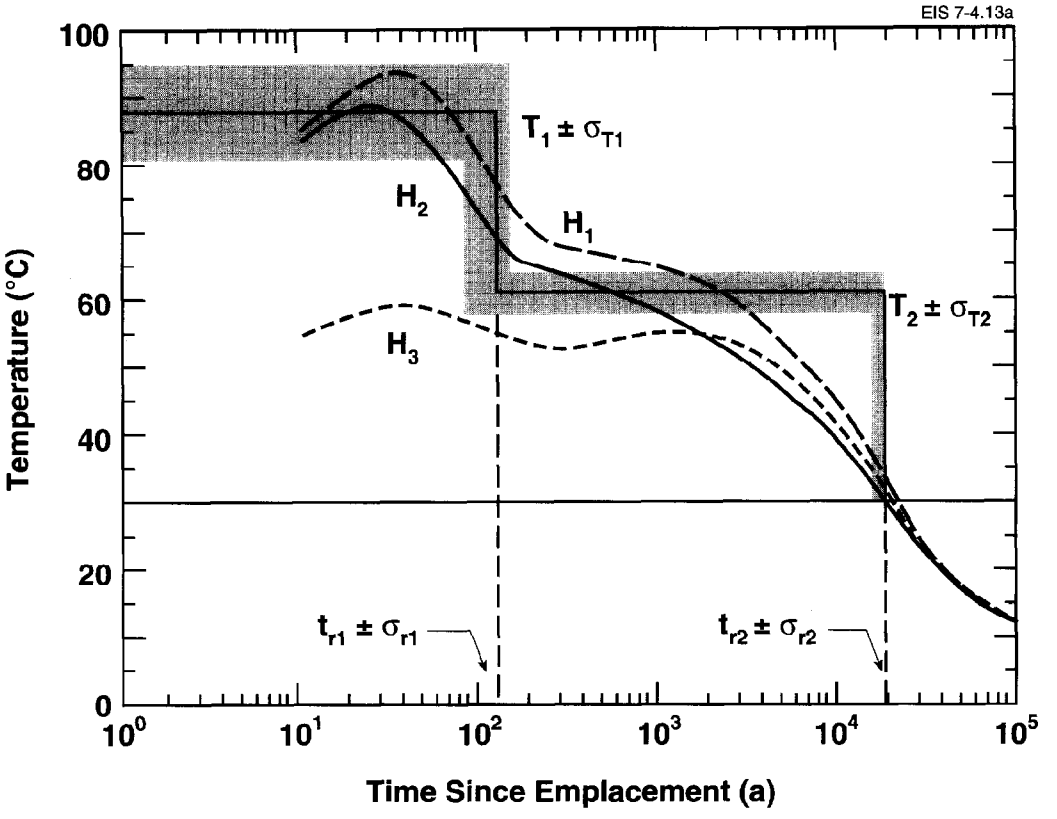

FIGURE 4-13a: Step Function Used to Approximate the Temperature Profiles for Hot Containers. The horizontal solid lines and associated shaded areas indicate the mean temperature (T) and the standard deviations ($T \pm \sigma$). The vertical solid lines and associated shaded areas indicate the mean transition times (t_r) and the standard deviations ($t_r \pm \sigma$) (see Table 4-3). Three real profiles representing the range of profiles averaged within the hot category are shown. The location of the corresponding containers is shown in Figure 4-14.

vault (see Figure 4-14). For the remaining containers, the real profiles are represented by two single-step functions (Figures 4-13b and 4-13c). Containers designated cool are located around the periphery of the vault and those designated as cold are located on the extreme edges (Figure 4-14). Approximately 34% of the containers are classified as cool, with the remaining 3.3% designated cold. The fraction of containers in each of the 12 vault sectors (Figure 4-1) is given in Table 4-3. These fractions are taken as constants (for a particular vault geometry) in the container failure function (Section 4.7.5.4). A number of real profiles are shown for each category in Figure 4-13a-c, and the locations of the corresponding containers within the vault are indicated in Figure 4-14.

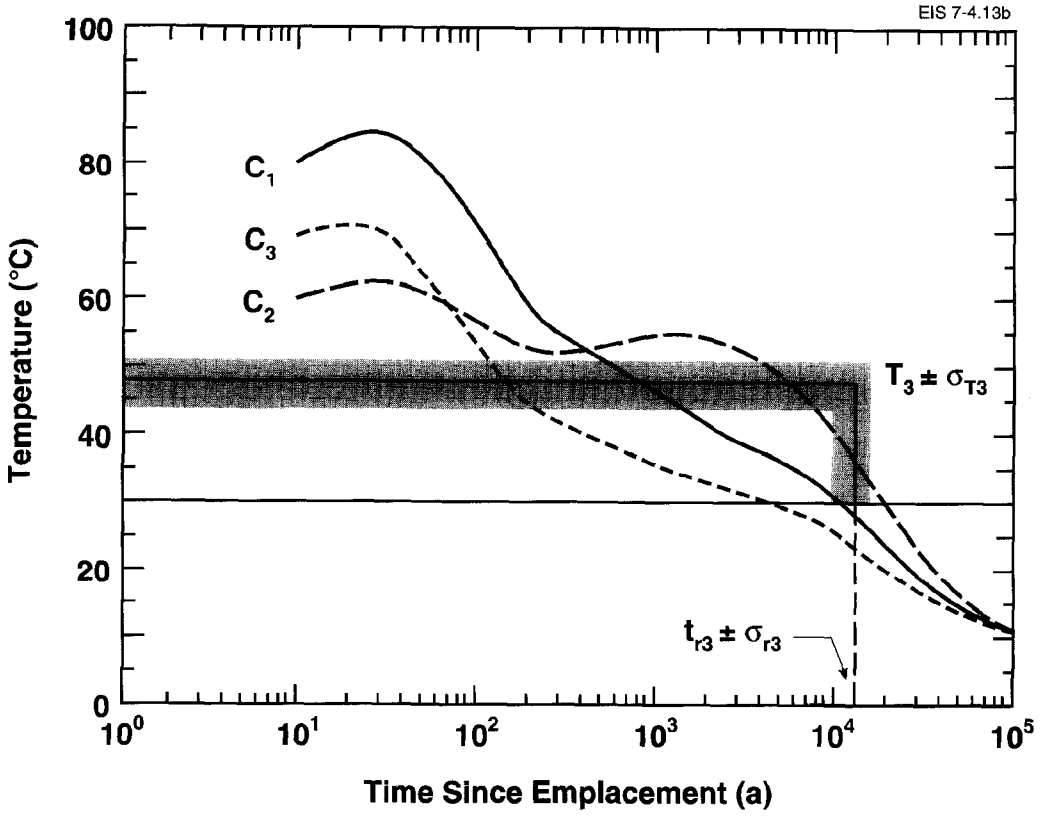

FIGURE 4-13b: Step Function Used to Approximate the Temperature Profiles for Cool Containers. The horizontal solid line and associated shaded areas indicate the mean temperature (T) and the standard deviation ($T \pm \sigma$). The vertical solid line and associated shaded area indicates the mean transition time (t_r) and the standard deviation ($t_r \pm \sigma$) (see Table 4-3). Three real profiles representing the range of profiles averaged within the cool category are shown. The location of the corresponding containers is shown in Figure 4-14.

The temperature values and transition times that describe the step functions are listed in Table 4-4. The second transition time for hot containers and the transition times for cool and cold containers are the times at which HIC, rather than crevice corrosion, is assumed to become the predominant failure process. These times are the average times at which the containers in that category cool to 30°C. The reasons for selecting this temperature were given in Section 4.6.4.4 and are discussed further in Section 4.7.3. The procedure for assigning containers to these categories and the averaging procedure by which the values in Table 4-4 were obtained are described in more detail in Appendix C. Since cold containers cool rapidly, the average temperature to define the step function in Figure 4-13c is calculated at 100 a, as opposed to at 500 a for cool and hot containers.

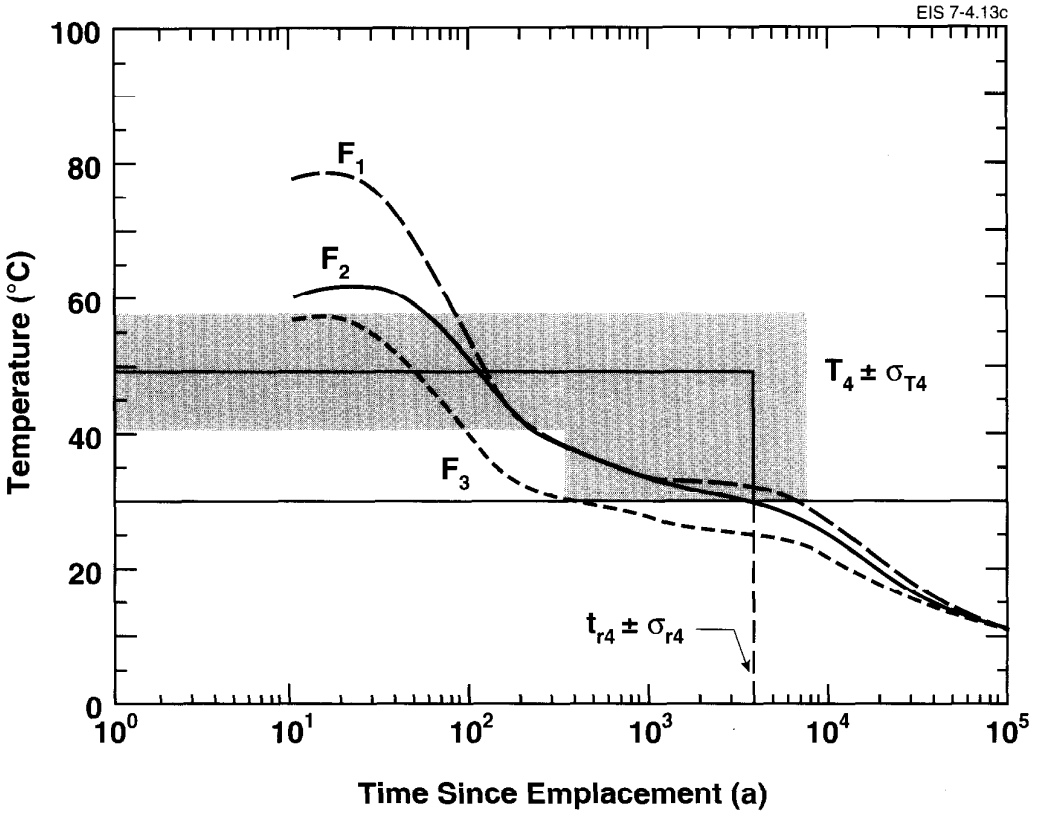

FIGURE 4-13c: Step Function Used to Approximate the Temperature Profiles for Cold Containers. The horizontal solid line and associated shaded area indicate the mean temperature (T) and the standard deviation ($T \pm \sigma$). The vertical solid line and associated shaded area indicate the mean transition time (t_r) and the standard deviation ($t_r \pm \sigma$) (see Table 4-3). Three real profiles representing the range of profiles averaged within the cold category are shown. The location of the corresponding containers is shown in Figure 4-14.

As a consequence of this averaging at shorter times, the cold containers have a higher average temperature than the cool containers (Table 4-4).

The crevice corrosion rate as a function of temperature was estimated from the measured value at 100°C (Table 4-2) multiplied by the fraction $(I_c)_T/(I_c)_{100°C}$ (Table 4-5). This fraction is the ratio of the steady-state crevice current, measured on a metal/PTFE specimen at temperature T, to the same current measured at 100°C on the same specimen in the same experiment. The measured rate at 100°C, calculated by averaging the weight change over a three-month exposure period, is equivalent to measuring the propagation rate at an O_2 concentration of ~0.02 $\mu g \cdot g^{-1}$ that remains constant over the lifetime of the container (Section 4.6.3.2). Implicit in the use of this ratio to calculate rates as a function of temperature is

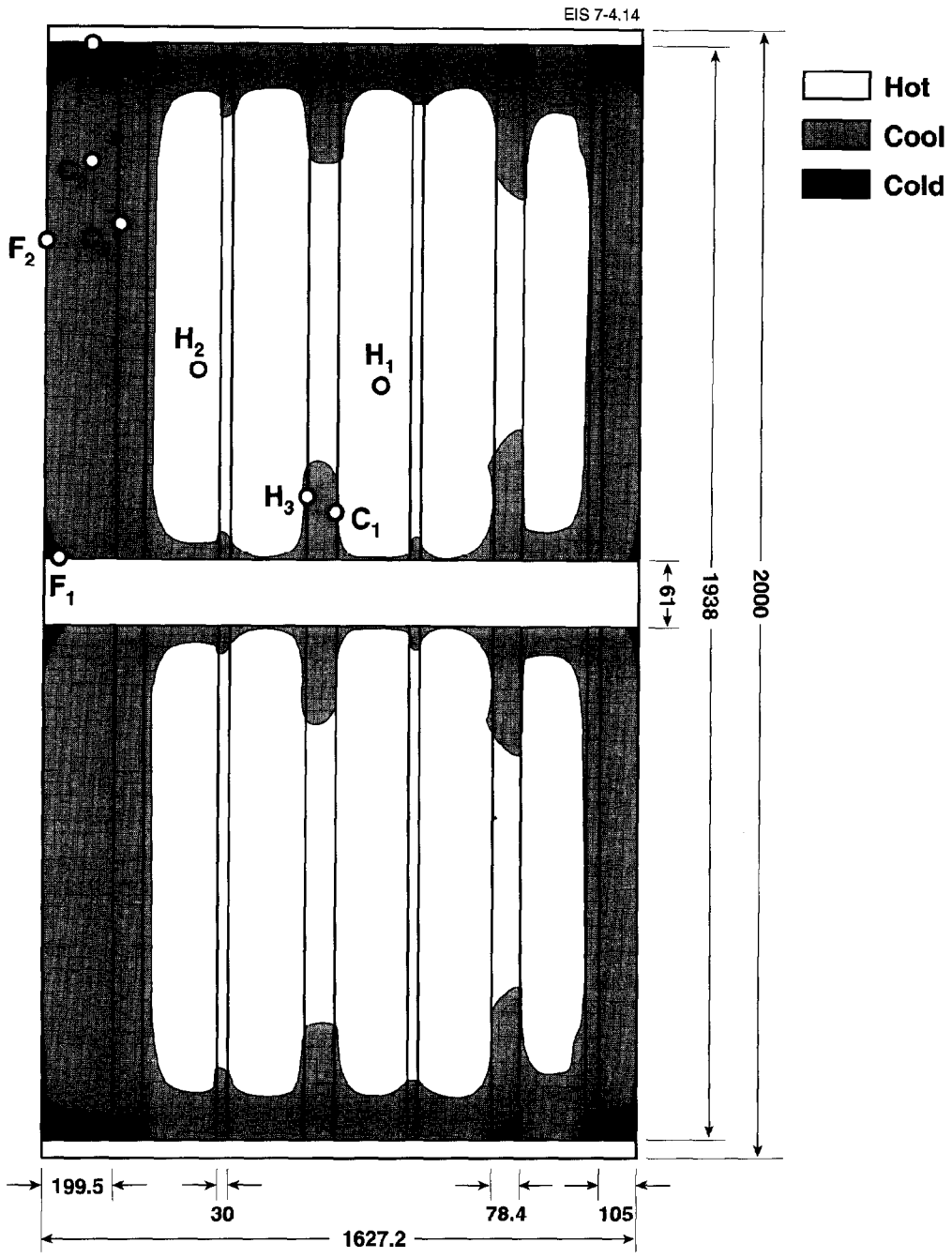

FIGURE 4-14: Distribution of Each Category of Container (Hot, Cool and Cold) Throughout the Vault. The labelled dots show the location of the containers for which the real profiles are shown in Figures 4-13a-c. Dimensions are in metres. The lack of symmetry in the distribution of cold and cool containers between the left and right sides of the vault is due to the asymmetry of the vault layout.

TABLE 4-3

FRACTION OF HOT, COOL, AND COLD CONTAINERS IN EACH SECTOR IN THE DISPOSAL VAULT

Sector Number	Fraction	Distribution Type
	COOL Containers	
AFRACA(01)	0.68811	Constant
AFRACA(02)	0.13531	Constant
AFRACA(03)	0.12185	Constant
AFRACA(04)	0.16422	Constant
AFRACA(05)	0.29852	Constant
AFRACA(06)	0.16422	Constant
AFRACA(07)	0.30361	Constant
AFRACA(08)	0.56608	Constant
AFRACA(09)	0.30361	Constant
AFRACA(10)	0.88683	Constant
AFRACA(11)	0.86686	Constant
AFRACA(12)	0.88683	Constant
	COLD Containers	
AFRACE(01)	0.09866	Constant
AFRACE(02)	0.00000	Constant
AFRACE(03)	0.00000	Constant
AFRACE(04)	0.00352	Constant
AFRACE(05)	0.00000	Constant
AFRACE(06)	0.00352	Constant
AFRACE(07)	0.01054	Constant
AFRACE(08)	0.00000	Constant
AFRACE(09)	0.01054	Constant
AFRACE(10)	0.11317	Constant
AFRACE(11)	0.13314	Constant
AFRACE(12)	0.11317	Constant
	HOT Containers	
AFRACR(01)	0.21323	Constant
AFRACR(02)	0.86469	Constant
AFRACR(03)	0.87815	Constant
AFRACR(04)	0.83226	Constant
AFRACR(05)	0.70148	Constant
AFRACR(06)	0.83226	Constant
AFRACR(07)	0.68585	Constant
AFRACR(08)	0.43392	Constant
AFRACR(09)	0.68585	Constant
AFRACR(10)	0.00000	Constant
AFRACR(11)	0.00000	Constant
AFRACR(12)	0.00000	Constant

TABLE 4-4

AVERAGE TEMPERATURES AND TRANSITION TIMES

Container Designation	Temperature (°C)	σ (°C)	Transition Time (a)	σ (a)
Hot	88.1	7.42	105.5	30.3
	61.1	3.18	18 410	1810
Cool	47.7	3.94	12 638	3060
Cold	49.1	3.91	4 000	2510

TABLE 4-5

EXTRAPOLATED CREVICE CORROSION RATES AS A FUNCTION OF TEMPERATURE

T (°C)	$(I_c)_T/(I_c)_{100\,°C}$	Rate ($\mu m \cdot a^{-1}$)
95.52	0.856	8.56
88.10	0.649	6.49
80.68	0.486	4.86
64.28	0.245	2.45
61.10	0.213	2.13
57.92	0.185	1.85
53.01	0.147	1.47
51.64	0.138	1.38
49.10	0.122	1.22
47.70	0.114	1.14
45.19	0.101	1.01
43.76	0.094	0.94

the assumption that the mechanism of crevice corrosion does not change with O_2 concentration.

Analyzing the corrosion rates as a function of temperature in this manner makes it easy to determine the rate for a single temperature. However, in the model it is necessary to distribute the crevice corrosion rates according to the normal distributions of temperatures used to define the profiles in Figures 4-13a-c. However, the rate is related to temperature non-linearly by an Arrhenius relationship. Hence, the conversion of a normal distribution of temperatures using this relationship produces skewed rather than a normal distribution of rates. This conversion has been done approximately by taking the $\pm 1\sigma$ values of the temperature values in

Table 4-4 and calculating the corresponding rates and then determining a linearized mean-rate value. Because of the non-linear dependence of rate on temperature these mean rates correspond to slightly higher temperatures than those of Table 4-4, making this procedure conservative. These temperatures (linearized mean temperatures) and the corresponding corrosion rates are given on the right-hand side of Table 4-6. The step functions in Figure 4-13a-c are constructed using the linearized mean temperatures.

TABLE 4-6

LINEARIZED TEMPERATURES AND CORRESPONDING CREVICE CORROSION RATES

Container Designation	Mean Temp. (°C)	Standard Deviation (°C)	Rate ($\mu m \cdot a^{-1}$)	Linear Temp. (°C)	Standard Deviation ($\mu m \cdot a^{-1}$)	Mean Rate ($\mu m \cdot a^{-1}$)
Hot	88.1	7.42	6.49	89.0	1.85	6.71
	61.1	3.18	2.13	61.2	0.30	2.14
Cool	47.7	3.94	1.14	48.1	0.22	1.16
Cold	49.1	3.91	1.22	49.4	0.23	1.24
	Values from Table 4-5			Values after linearization		

4.7.3 Failures Caused by Hydrogen-Induced Cracking

In the model, containers that have not already failed by crevice corrosion fail by HIC once their surface temperature falls to ≤30°C. This condition assumes that the cracking behaviour of Grade-2 titanium parallels that of the more susceptible α/β alloys, and that the correct combination of stress and hydrogen content is present when this temperature is achieved. It is also assumed that cracking, once initiated, is unpredictably rapid. Consequently, once the right conditions of stress, hydrogen concentration and temperature exist, HIC is effectively instantaneous.

According to the step functions of Figures 4-13a-c,

- residual hot containers start to fail by HIC at $t = t_{r2}$,
- residual cool containers start to fail by HIC at $t = t_{r3}$, and
- residual cold containers start to fail by HIC at $t = t_{r4}$,

where t_{r2}, t_{r3} and t_{r4} are the respective times at which the step functions achieve a temperature of 30°C.

Obviously, it is unrealistic to view crevice corrosion as "switching off" and HIC as "switching on" at times t_{r2}, t_{r3} and t_{r4}. In reality, a gradual switch from one failure mechanism to the second would occur. Such a gradual switch can be considered accounted for in the averaging of the transition times t_{r2} to t_{r4}. At these times the crevice corrosion rates would be seriously overestimated by using the step functions of Figures 4-13a-c for the hot and cool containers. Consequently, it is assumed that the decrease in crevice corrosion rate due to the cooling of the containers makes it reasonable to assume that failure by HIC would replace failure by crevice corrosion somewhere in the vicinity of these transition times. For hot and cool containers, failure of individual containers by HIC is assumed to occur rapidly for $T \leq 30°C$, with these failures spread out over $t_r + \sigma$ (for t_{r2} and t_{r3}). This time period represents the distribution of times over which these containers cool to 30°C.

For cold containers it is assumed that failures by HIC would occur over a wide range of times representative of the actual distribution of times to cool to 30°C, i.e., $t_{r4} \pm \sigma$.

4.7.4 Summary of Assumptions in the Model

1. A small number of containers contain undetected defects leading to early failure.

2. Crevice corrosion initiates instantaneously on all containers.

3. The reference container material is a low-iron-content Grade-2 titanium, the material most susceptible to crevice corrosion.

4. There is always sufficient oxygen available for crevice corrosion to propagate indefinitely without repassivation.

5. The rate of crevice propagation decreases as the temperature of the containers decreases.

6. Failure by crevice corrosion occurs when the depth of the general corrosion front within the creviced area exceeds the corrosion allowance.

7. Containers that do not fail by crevice corrosion fail by HIC once their temperature falls to ≤30°C.

8. The required combination of stress intensity and hydrogen content for HIC to occur is present when $T \leq 30°C$.

9. Once HIC starts, failure is instantaneous.

10. Once failure has occurred, the container provides no further protection against ingress of water and subsequent leaching of the fuel.

4.7.5 Mathematical Specification of the Model

4.7.5.1 Initial Defects

Failures caused by the presence of undetected defects are not considered to be temperature- and, hence, sector-dependent. Consequently, the number of containers failing prematurely in a given sector of the vault would be proportional to the total number of containers in that sector.

This early failure rate, $f_I^c(t)$, is given by

$$f_I^c(t) = \frac{2I^F}{t^F}\left[1 - \frac{t}{t^F}\right] \qquad (4.3)$$

$$\text{for } 0 \leq t \leq t^F \quad . \qquad (4.4)$$

In Equation (4.3), I^F is the fraction of containers that fail, and t^F is the period over which the failures occur, and

$$f_I^c(t) = 0 \qquad (4.5)$$

$$\text{for} \qquad t < 0 \text{ and } t \geq t^F \qquad (4.6)$$

i.e., no failures occur until the vault is closed ($t = 0$), and all failures are complete after a period ($t = t^F$) of 50 a.

4.7.5.2 Crevice Corrosion

The failure rate resulting from crevice corrosion must be computed for each of the three groups of containers within the vault, i.e., hot, cold and cool. As discussed in Section 4.7.2, the containers are assumed to crevice corrode at a rate determined by the temperature profile of the container. These temperatures, and hence the rates, have been approximated by the step functions of Figures 4-13a-c. Within each step of these three functions, the crevice corrosion rate is constant for a given container, but normally distributed from container to container, according to the distribution in container temperatures. This distribution accounts for the real variations in container temperatures with position within the vault.

Our experimental crevice corrosion rate, measured at 100°C, is normally distributed about a mean value of 10 $\mu m \cdot a^{-1}$ with a standard deviation of ± 5 $\mu m \cdot a^{-1}$. In the calculation of container lifetimes presented in this chapter, the mean value is used. In the case study (Goodwin et al. 1994), a value of rate at 100°C is sampled from the normal distribution of rates around, and including, this mean value (μ) truncated at an upper limit of $\mu + 3\sigma$ (25 $\mu m \cdot a^{-1}$ at 100°C (Table 4-2)) and a lower limit of 0.01 $\mu m \cdot a^{-1}$. The truncation at the upper limit avoids the inclusion of unrealistically high rates. The truncation at lower rates avoids the sampling of negative rates. The value of 0.01 $\mu m \cdot a^{-1}$ is the upper limit of expected general corrosion rates at 100°C (Ikeda and Clarke 1986).

Using this mean value of experimental crevice corrosion rate, we can then calculate the distribution of rates according to the distribution of container temperatures as defined by the step functions of Figures 4-13a-c. The container failure rate within each sector of the vault can then be computed knowing the fraction of hot, cool and cold containers in each sector. In this chapter, predictions are given for the whole vault, not sector by sector.

Hot containers are subject to a temperature profile approximated by the two-step function in Figure 4-13a. The total number of hot containers that fail by crevice corrosion (expressed as a fraction) is given by the sum of the number that fail in each temperature regime (T_1 and T_2). For the first temperature interval of duration t_{r1}, the crevice corrosion rate, r_1^N, is characterized by a mean value, μ_{r1}, and a standard deviation, σ_{r1}, determined by the standard deviation in the mean temperature. The container failure rate, $f_N^C(t)$, expressed as the fraction failing per unit time is given by

$$f_N^C(t) = \frac{w^x(1 - I^F)}{(2\pi)^{1/2}\sigma_{r1}P_1 t^2} \exp\left[-\left[\frac{w^x - \mu_{r1}t}{2^{1/2}\sigma_{r1}t}\right]^2\right] \qquad (4.7)$$

where w^x is the container corrosion allowance, and P_1 is a normalization factor to account for the truncation of the distribution function for $r_1^N \leq 0$. This factor is required since negative crevice corrosion rates are physically meaningless. The term $(1 - I^F)$ takes account of the premature failures due to pre-existing defects, and is the fraction of containers remaining after these early failures are complete.

For crevice corrosion in temperature interval T_2 (Figure 4-13a), two distributions must be considered. The containers have a distribution in thicknesses, p(w), resulting from corrosion whilst at T_1, as well as a distribution of corrosion rates (r_2^N) at temperature T_2, p(t,w), where

$$w = w^x - r_1^N t_{r1} \quad . \qquad (4.8)$$

The corrosion rate has a normal distribution of values about a mean value, μ_{r2}, with a standard deviation, σ_{r2}, determined by the standard deviation in T_2. The container failure rate during the second temperature period, $f_P^C(t)$, is obtained by combining these two distributions and integrating over the total range of container thicknesses (i.e., from w = 0 to $w = w^x$),

$$f_P^C(t) = \int_0^{w^x} p(t,w)p(w)\, dw \quad . \qquad (4.9)$$

This rate must be multiplied by the normalization factor $(1 - I^F)(P_1P_3)^{-1}$ to eliminate negative corrosion rates and to account for previous failures caused by defects and crevice corrosion in the first temperature interval, T_1. The term P_3 is the area under the normally distributed second container failure rate from t = 0 to $t = \infty$. At the end of temperature

interval T_2 (i.e., at $t = t_{r2}$), it is assumed that crevice corrosion stops completely and HIC begins (see Section 4.7.3).

Containers designated cool and cold would be subject to temperature profiles approximated by single-step functions (Figures 4-13b and 4-13c). Hence, the container failure rates due to crevice corrosion in these regions (at T_3, T_4) are determined by an identical procedure to that employed for containers at temperature T_1.

4.7.5.3 Hydrogen-Induced Cracking

Containers that do not fail by crevice corrosion are assumed to fail by HIC once the vault cools to ≤30°C; i.e., for times greater than t_{r2}, t_{r3} and t_{r4} for hot, cool and cold containers respectively (Figures 4-13a-c). These failure rates ($f_H^C(t)$) are assumed to have a triangular distribution. The width of the distribution varies depending in which region of the vault the containers are located. For hot and cool containers, the distribution is assumed to be narrow since significant hydrogen absorption is assumed to occur during the crevice corrosion periods.

The initial HIC failure rate (i.e., at $t = t_{r2}$, t_{r3}, t_{r4}) is equated to the failure rate resulting from crevice corrosion at the transition times. The peak of the triangular distribution is arbitrarily chosen so that there are equal areas on either side of the peak. The total area under this distribution (A^T) must be chosen so that the total area under all distributions is equal to one. This last condition guarantees that all containers that do not fail prematurely because of defects or subsequently by crevice corrosion, fail from HIC. Hence, for hot containers

$$1 = A^I + A^N + A^P + A^T \tag{4.10}$$

or

$$A^T = 1 - \left[I_F + \int_0^{t_{r1}} f_N^C(t)\, dt + \int_{t_{r1}}^{t_{r2}} f_P^C(t)\, dt \right] = \int_{t_{r2}}^{\infty} f_H^C(t)\, dt \tag{4.11}$$

where A^I is the area under the distribution of initial failures and A^N and A^P are the areas under the distributions of failures by crevice corrosion in the first and second temperature regions respectively. A similar expression can be derived for cool containers.

For cold containers, the average time for the temperature to pass through 30°C is chosen as the apex of the triangular distribution. The starting point for the distribution is chosen as the time when the fastest-cooling container cools to 30°C, i.e., as the time for the first failure by HIC. The final time is chosen to maintain the symmetry of the triangular distribution. Prior to achieving a temperature of 30°C (defined by the real temperature profile), cold containers crevice-corrode at a rate determined by the temperature T_4 (Figure 4-13c).

4.7.5.4 Failures from All Causes

The total container failure rate, $f_k^C(t)$, for sector k of the vault is the sum of the failure rates resulting from initial defects, crevice corrosion, and HIC.

For hot containers in sector k of the vault (see Section 6.2.1),

$$f_k^C(t) = A_k^R\left[f_I^C(t) + f_N^C(t) + f_P^C(t - t_{r1}) + f_H^C(t - t_{r2})\right] \quad . \qquad (4.12)$$

For cool containers in sector k of the vault,

$$f_k^C(t) = A_k^A\left[f_I^C(t) + f_N^C(t) + f_H^C(t - t_{r3})\right] \quad . \qquad (4.13)$$

For cold containers in sector k of the vault,

$$f_k^C(t) = A_k^E\left[f_I^C(t) + f_N^C(t) + f_H^C(t - t_{r4})\right] \quad . \qquad (4.14)$$

In the above equations A_k^R, A_k^A and A_k^E are the fractions of hot, cool and cold containers in sector k of the vault respectively (Table 4-3), and

$$A_k^R + A_k^A + A_k^E = 1 \quad . \qquad (4.15)$$

The arguments $(t - t_{ri})$, where i = 1,. . .,4 are used because the failure rate distributions are specified for time beginning at t = 0.

The container failure rate for region k of the vault is the sum of Equations (4.12) to (4.14). The total failure rate for the whole vault is the sum of the rates, weighted by the fractional sector area, for all sectors (k = 1 to 12) of the vault.

4.7.6 Prediction of Container Lifetimes

4.7.6.1 Reference Case

Table 4-7 summarizes the parameters, the reference values used to predict container failure rates and times, and the forms of the parameter distributions used in SYVAC. Figure 4-15 shows the total container failure rate and the failure rates for the individual container groupings, hot, cool and cold. Figures 4-16a-b show the corresponding cumulative fractions failed as a function of time and log(time) in the vault. These rates and fractions are for the total vault and do not discriminate between failures in the various vault sectors. The full SYVAC analysis computes the failure rate per vault sector, a procedure necessary in order to couple radionuclide release rates to the geosphere transport model.

The predictions of Figures 4-15 and 4-16a-b show that, apart from the few early failures resulting from initial defects (~0.05% of the total, visible in the logarithmic plot, Figure 4-16b), only 1.1% of the cold containers (0.037% of the total number of containers) fail during the first 500 a. By 1000 a, 1.8% of the cold containers (0.06% of the total) fail. None of the

TABLE 4-7

PARAMETER VALUES USED IN THE CASE STUDY FOR THE PREDICTION OF FAILURE TIMES FOR GRADE-2 TITANIUM CONTAINERS

	Parameter	Symbol and Units	Value	Distribution Type	Upper Bound	Lower Bound
(a)	Fraction of containers that fail prematurely because of defects	I_F	5×10^{-4} * ±1.5**	lognormal	1×10^{-3}	1×10^{-4}
(b)	Time period during which containers fail prematurely because of defects	t_F (a)	50	constant	-	-
(c)	Mean corrosion rate (r_1^N) of containers designated hot during the first temperature period, T_1	μ_{r1} ($\mu m \cdot a^{-1}$)	6.71 ±3.36*	normal	12.3	0.01
(d)	Standard deviation of the corrosion rate during the first temperature period, T_1	σ_{r1} ($\mu m \cdot a^{-1}$)	1.85	constant	-	-
(e)	The average time when the temperature for containers designated hot drops below 72°C	t_{r1} (a)	105.5	constant	-	-
(f)	Mean corrosion rate (r_2^N) of containers designated hot during the second temperature period, T_2	μ_{r2} ($\mu m \cdot a^{-1}$)	2.14 ±1.07*	normal	3.05	0.01

continued...

TABLE 4-7 (continued)

	Parameter	Symbol and Units	Value	Distribution Type	Upper Bound	Lower Bound
(g)	Standard deviation of the corrosion rate during the second temperature period, T_2	σ_{r2} ($\mu m \cdot a^{-1}$)	0.30	constant	-	-
(h)	The average time when the temperature for containers designated hot drops below 30°C	t_{r2} (a)	18 410	constant	-	-
(i)	The length of time containers designated as hot take to fail by hydrogen-induced cracking	$t_2 - t_{r2}$ (a)	2 860	constant	-	-
(j)	Fraction of the total number of containers designated as hot	A^R	0.626**	-	-	-
(k)	Mean corrosion rate (r_3^N) of containers designated cool during the temperature period T_3	μ_{r3} ($\mu m \cdot a^{-1}$)	1.16 ±0.58*	normal	1.82	0.01
(l)	Standard deviation of the corrosion rate during the temperature period T_3	σ_{r3} ($\mu m \cdot a^{-1}$)	0.22	constant	-	-
(m)	The average time when the temperature for containers designated cool drops below 30°C	t_{r3} (a)	12 638	constant	-	-
(n)	The length of time containers designated as cool take to fail by hydrogen-induced cracking	$t_3 - t_{r3}$ (a)	2 940	constant	-	-

continued...

TABLE 4-7 (concluded)

	Parameter	Symbol and Units	Value	Distribution Type	Upper Bound	Lower Bound
(o)	Fraction of total number of containers designated as cool	A^A	0.341**	-	-	-
(p)	Mean corrosion rate (r_4^N) of containers designated cold during the temperature period T_4	μ_{r4} ($\mu m \cdot a^{-1}$)	1.24 ±0.62*	normal	1.93	0.01
(q)	Standard deviation of the corrosion rate during the temperature period T_4	σ_{r4} ($\mu m \cdot a^{-1}$)	0.23	constant	-	-
(r)	The earliest time when the temperature for containers designated cold drops below 30°C	t_{r4} (a)	300	constant	-	-
(s)	The length of time containers designated as cold take to fail by hydrogen-induced cracking	$t_4 - t_{r4}$ (a)	7 400	constant	-	-
(t)	Fraction of total number of containers designated as cold	A^E	0.033**	-	-	-

* The value used in the case study is 2×10^{-4}, the geometric mean of the bounding values

** Geometric Standard Deviation

* This value is the mean (μ) plus or minus the standard deviation (σ) of a series of measured values. In the case study a value is sampled from the range $\mu + 3\sigma$ (e.g., 16.8 $\mu m \cdot a^{-1}$) and a lower limit of 0.01 $\mu m \cdot a^{-1}$ (uniform corrosion rate).

** This number is the fraction of all the containers within the vault. For the case study this fraction is defined for each of the sectors within the vault. See Table 4-3.

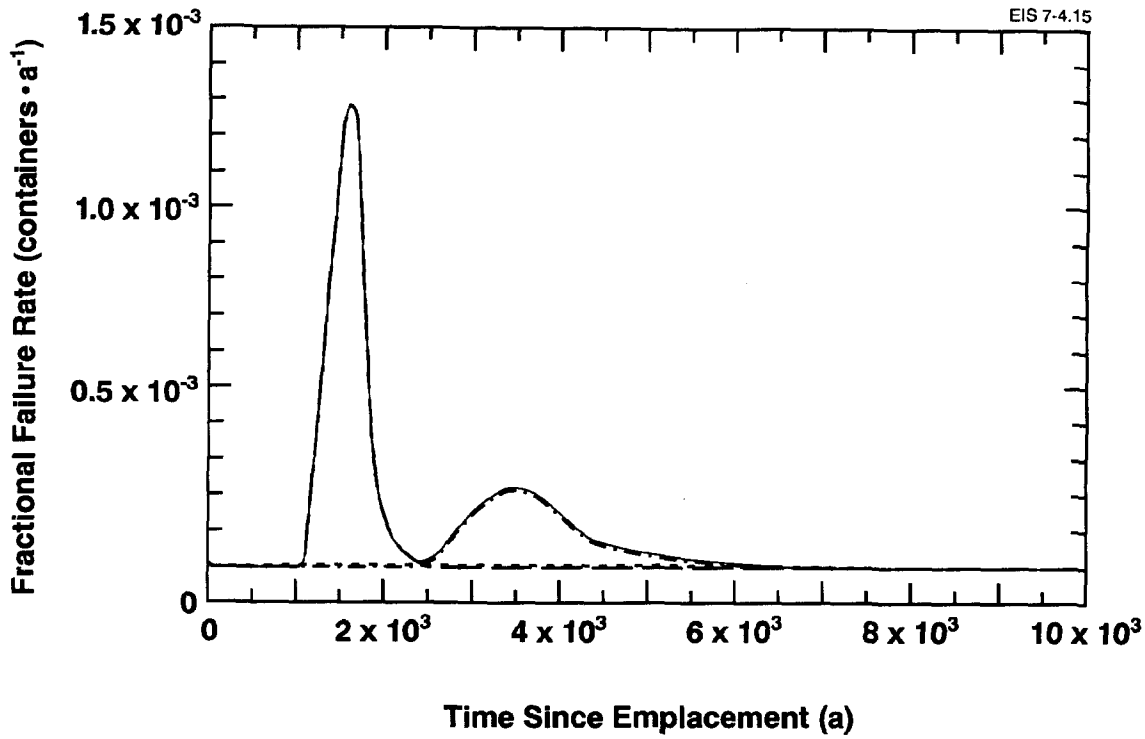

FIGURE 4-15: Model Predictions of Container Failure Rates for Hot, Cool, Cold and Total Containers for the Parameter Values in Table 4-6; — — Hot, - · - · Cool; ----- Cold; ——— Total

cool containers fail, and only 0.002% of the hot containers fail by crevice corrosion. The total percentage of containers predicted to fail during the 1000-a period is ~0.1%.

4.7.6.2 Failure of Cold Containers

The first containers predicted to fail are the cold containers, located in the farthest corners of the vault (Figure 4-14). These failures appear as an extremely shallow triangular peak in the plot of failure rate in Figure 4-15, and as a very shallow slope on the leading edge of the plot of cumulative fraction failed versus time in Figure 4-16b plotted on logarithmic scales. Failures start at 300 a, the time when the first container cools to 30°C, and are complete after 7700 a. Since the crevice corrosion rate is very low at T_4 (= 49.4°C; rate = 1.24 $\mu m \cdot a^{-1}$, Table 4-6), the 3.3% of containers designated as cold all fail by HIC.

The assumption that failure by HIC would not occur until the temperature falls to ≤30°C is based on the observation that cracking is inevitably a low-temperature phenomenon (Section 4.6.4.1). However, the hydrogen absorption required before HIC can occur would be very slow, if it occurred at all, at the temperatures experienced by cold containers. Hence, it does

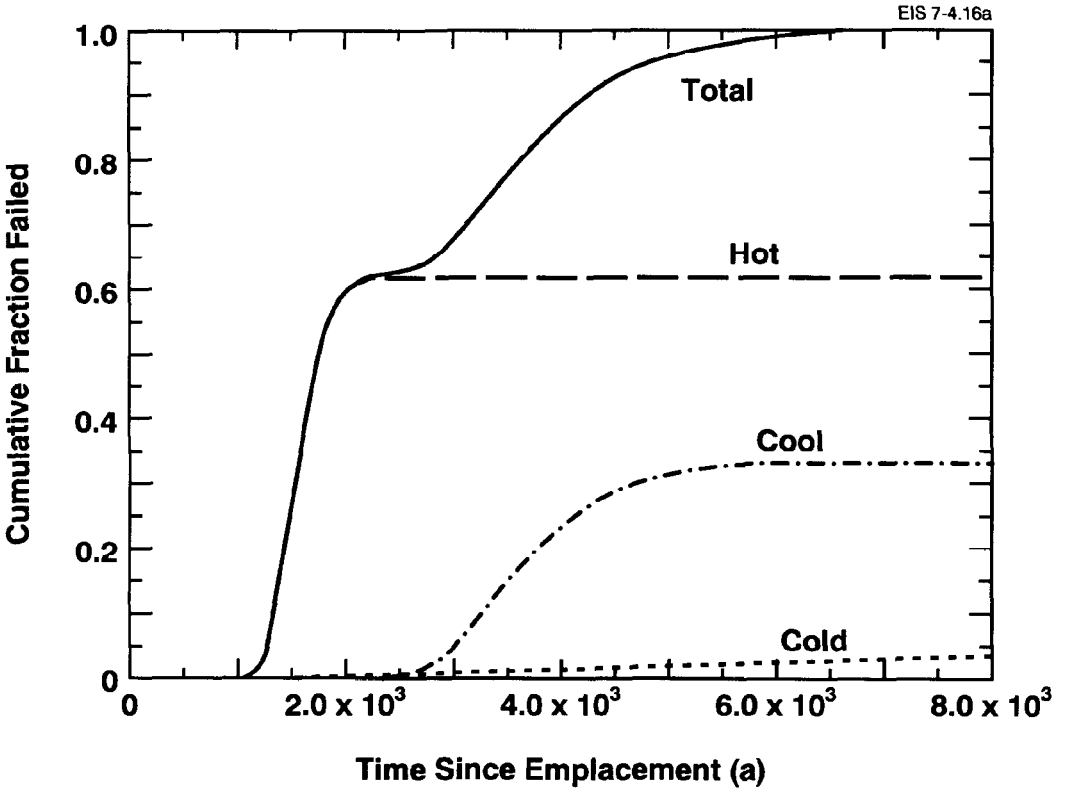

FIGURE 4-16a: Model Predictions of the Fraction of Hot, Cool, Cold and Total Containers Failed for the Parameter Values in Table 4-6

not make sense that the coldest containers crack earliest. Their predicted early failure is a direct consequence of the conservative assumption that HIC occurs as soon as the temperature falls to 30°C. A more realistic prediction of failure by HIC cannot be made until a more complete understanding of the effects of a combination of stress and hydrogen content, and a knowledge of the hydrogen absorption rate as a function of temperature, are available.

Since the predicted surface temperature of most of these cold containers never exceeds 70°C, the initiation of crevice corrosion is highly unlikely. Consequently, they should survive for very long times before finally failing either by general corrosion or by HIC as a consequence of hydrogen absorbed during general corrosion (Figure 4-12).

4.7.6.3 Failure of Hot and Cool Containers

For the majority of containers (the 62.6% designated hot and the 34.1% designated cool), predicted failure is by crevice corrosion, commencing

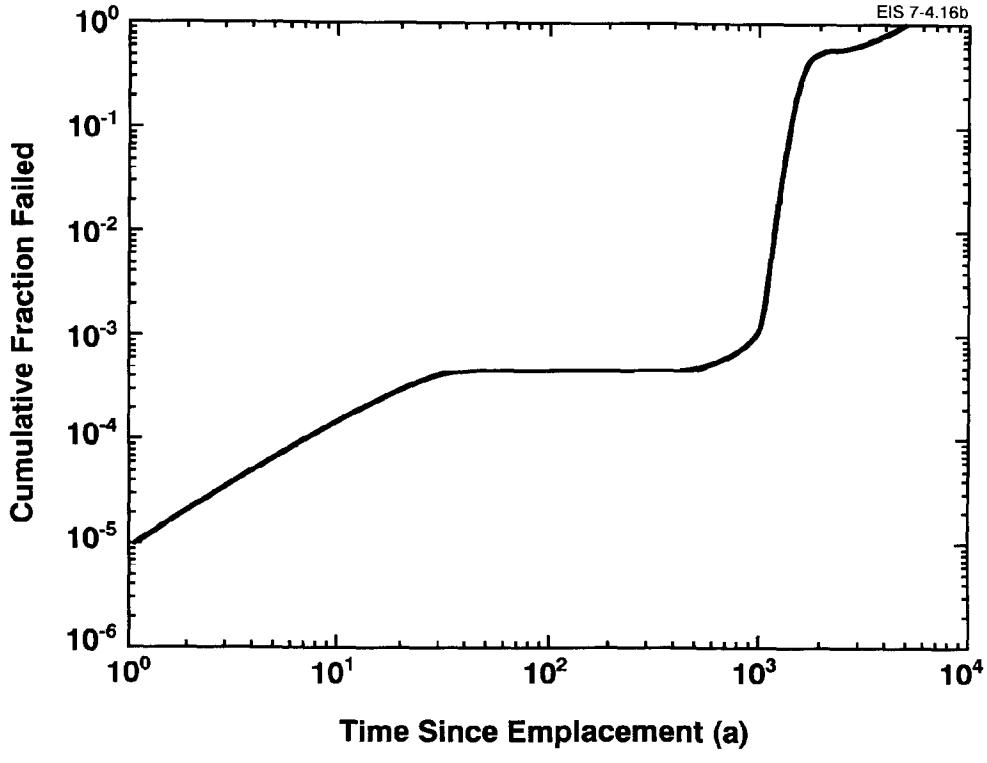

FIGURE 4-16b: Model Predictions of the Fraction of Hot, Cool, Cold and Total Containers Failed Plotted on a Logarithmic Scale to Show the Fraction of Containers Failed Due to Undetected Defects

around 1200 a. The distributions of failure rates for hot and cool containers are distinct (Figure 4-15), and skewed to longer times. From Figure 4-15 it is clear that the majority of hot containers are predicted to fail between 1200 and 2500 a, and the majority of cool containers between 2500 and 6000 a, leading to the two distinct plateaus in the plot of the cumulative fraction failed in Figures 4-16a-b. No hot or cool containers survive long enough to cool to 30°C, where they would fail by HIC.

By using a single-step function to represent the temperature profile for the cool containers, the early high-temperature period lasting approximately 100 a (Figure 4-13b), when crevice corrosion would be proceeding at a much faster rate, is ignored. By estimating the extra crevice penetration that would occur at a temperature of 80°C over the first 100 a, it can be shown that the cumulative fraction failed curve for the cool containers shifts to shorter times by ~500 a. Such a shift would not affect the total fraction of containers failed between 1000 a and 2000 a; i.e., ignoring the early faster crevice corrosion period for cool containers does not threaten the ability of Grade-2 titanium to meet the minimum containment period of 500 a.

The distinct distributions for the failure of hot and cool containers are caused by the separation of containers into the two distinct categories, hot and cool, and to the temperature-averaging procedure used to calculate the step functions in Figures 4-13a-c. More realistically, the distribution of failures for hotter containers would be skewed to longer times and that for cooler containers to shorter times, leading to a blurring of the distinct distribution in Figure 4-15.

4.8 SUMMARY

A model predicting the failure of Grade-2 titanium waste containers has been developed. Two major corrosion failure modes are included in the model: failure by crevice corrosion and failure by HIC. A small number of containers are assumed to be defective and fail within 50 a of emplacement.

A simple, experimentally justified model is proposed for crevice corrosion. Crevice corrosion is assumed to initiate on all containers upon emplacement, and the rate of propagation, the process eventually leading to failure, is dependent on temperature and the concentration of oxygen. The latter is assumed to be sufficient to maintain crevice corrosion until failure. The temperature dependence of the propagation rates is determined from an analysis of experimental rates and the temperature-time profiles of the containers.

At the hydrogen contents realistically achievable under waste vault conditions, HIC is assumed to be a low-temperature phenomenon that leads to failure only at temperatures below 30°C.

On the basis of these assumptions, predictions of container failure times have been made for reference vault conditions. According to these predictions ~96.7% of all containers fail by crevice corrosion, but only a small number (0.1%) fail before 1000 a. The remaining 3.3% fail by HIC. These latter containers are situated around the outer edges of the vault where cooling is more rapid. Of this small number of failures by HIC, ~1.8% (0.037% of the total number of containers) fail before 1000 a, with the earliest failure occurring after 300 a. All the containers in the vault fail by ~6000 a.

5. MODEL FOR RADIONUCLIDE RELEASE FROM USED FUEL

5.1 INTRODUCTION

We expect that, following failure of the containers by the processes outlined in Chapter 4, water would gradually fill the void space within the container (see Figure 2-3) and contact the used-fuel bundles. The composition of this contact water would have been determined by its interactions with materials in the vault, as discussed in Chapter 3. Further interaction of the groundwater with the internal constituents of the container (i.e., the Zircaloy sheaths on the fuel bundles, the glass beads and the basket material) is expected to have little impact on the groundwater composition.

Radionuclides are present both in the Zircaloy sheath, mainly because of their production by neutron activation while the bundles are in the reactor, and within the fuel pellets, where they are produced by fission of U and Pu and by neutron capture. Radionuclide release would occur initially, therefore, as a result of corrosion of the Zircaloy sheath. Upon failure of the sheath, the groundwater would contact the fuel, initiating release of fission products and actinides. Here we present a model for the release of radionuclides from used fuel and Zircaloy. The model is based on extensive experimental studies of used fuel and UO_2 dissolution, and on thermodynamic modelling of the solubility of uranium and of various radionuclides under the conditions expected in the disposal vault.

In this chapter, we summarize and justify the key assumptions of the radionuclide release model. The reader is also referred to Chapter 2 of Johnson et al. (1994), which discusses the characteristics of used fuel. The radionuclides considered in the model are based on a screening study by Goodwin and Mehta (in preparation). The radionuclide inventories for the reference used fuel, based on calculations with the ORIGEN-S code, are given in Appendix A. A more detailed list of inventories, as well as thermal and radiation emissions from used fuel are given by Tait et al. (1989).

The radionuclide release model presented here provides boundary conditions for the solution of the mass transport equations describing the migration of radionuclides away from the used fuel into the buffer (see Chapter 6). The solution to these equations provides the source term, i.e., the total radionuclide flux (resulting from all the release mechanisms) into the buffer as a function of time (Garisto and Garisto 1988a, Garisto and LeNeveu 1991). Detailed specifications for the computer code used to calculate the source term are given by LeNeveu (in preparation) in terms of data flow diagrams (Yourdon 1989).

5.2 THE EXPERIMENTAL BASIS FOR AND CONCEPTUAL OVERVIEW OF THE DISSOLUTION MODEL

Used CANDU fuel is a polycrystalline ceramic with an average grain size of 10 μm. For the reference burnup of 685 GJ/kg U, the fuel is 98.8% UO_2; the remainder consists of other actinides (0.4%) and fission products (0.8%) (Johnson et al. 1994). Approximately 0.5% of the total fuel mass is made up of elements that are insoluble in UO_2. These include metallic fission products such as Tc, Mo and Ru, which typically form microscopic inclusions at grain boundaries in the fuel. Other fission products that are insoluble in UO_2 include Cs, I and the noble gases, which reside partially in bubbles at grain boundaries. A small fraction of the inventory of these elements, which are volatile or semivolatile under in-reactor conditions, are released from the fuel matrix and reside in the fuel-to-sheath gap region or within cracks in the fuel (Johnson and Shoesmith 1988). The amount present in such locations is commonly referred to as the gap inventory.

The relatively small quantity (~1% of the fuel mass) of radionuclides either substituted in the lattice (e.g., Pu, Am and the lanthanides) or present as interstitials has an insignificant effect on the thermodynamic properties of the UO_2 crystal structure. As a result, such properties as

the solubility of used fuel can be considered essentially identical to that of pure UO_2. This represents an important assumption that simplifies calculation of the solubility of the used-fuel matrix.

Much of the early literature on the dissolution kinetics of UO_2 (e.g., Grandstaff 1976, Eary and Cathles 1983, Hiskey 1979) deals with the details of dissolution under conditions that are substantially more oxidizing than would occur under the conditions of deep burial in granitic rock. Although the results of these studies provide valuable insight into the factors governing dissolution of UO_2, their applicability to the development of a used-fuel dissolution model for a disposal vault in granite is limited.

More recent studies of used fuel and UO_2 dissolution have focused on the following key areas:

- the heterogeneity and variability of used fuel, in particular the quantities of fission products released from the UO_2 grains during in-reactor irradiation;
- the factors governing dissolution of unirradiated UO_2, particularly under weakly oxidizing and reducing conditions, since most fission products and all the actinides are incorporated into the UO_2 grains;
- the effects of radiation, in particular the α-radiolysis of water, on the dissolution behaviour of UO_2 and used fuel; and
- the degree of dissolution and migration of U from natural uraninite ore bodies, since this particular uranium ore is chemically similar to used fuel.

Studies in all these areas, combined with experimental investigations of used-fuel dissolution, have permitted evaluation of different approaches to modelling used-fuel dissolution. Here, we summarize the key observations from some of these studies and illustrate how they offer both direct and indirect support for the dissolution model presented in Section 5.5. More comprehensive reviews of used-fuel characteristics and UO_2 dissolution are available (Johnson and Shoesmith 1988, Sunder and Shoesmith 1991). Natural analogue studies of uraninite ore are discussed in Section 5.6.

The dissolution of used light-water reactor (LWR) and CANDU fuel has been studied over the temperature range from 25 to 200°C in a wide variety of groundwaters. Typical experiments involve static leaching of fuel fragments, or short sections of fuel elements with the sheath attached, in groundwater. These studies have clearly illustrated that used fuel is a complex and highly variable material. This factor, as well as differences in experimental conditions, makes direct comparison of the data obtained difficult. Nonetheless, several observations are consistently made in these experiments:

1. Rapid release of a fraction of the inventory of certain fission products occurs from the gap.

2. Release rates of fission products decrease throughout the duration of the tests.

3. Concentrations of some elements (e.g., Pu, Am) typically appear to reach saturation values at very low concentrations; i.e., the concentrations of these elements are limited by their own solubilities rather than by the rates at which they are released from the fuel.

4. For elements that do not have low solubilities, there is a tendency toward congruent dissolution (i.e., the proportion of the inventory of a radionuclide released per unit time is the same as the proportion of the U dissolved) after long periods of time, indicating that the dissolution of the used-fuel matrix[9] eventually controls release of contained fission products and actinides. It should be noted, however, that congruency is observed only under conditions where the concentrations of radionuclides in solution are less than their saturation concentrations.

The short-term release of some fission products from the fuel-sheath gap of CANDU fuel has been the subject of detailed study (Stroes-Gascoyne et al. 1987). More difficult to quantify have been the quantities of specific fission products segregated to grain boundaries during fuel irradiation and the kinetics of their release (Johnson et al. 1988, Gray and Strachan 1991, Stroes-Gascoyne et al. 1993). These studies suggest that the leaching of fission products from grain boundaries may make a small contribution to short-term release and that the majority of the inventory at grain boundaries would only be released upon extensive dissolution of the fuel. Figure 5-1 illustrates some of the typical characteristics of radionuclide release from used CANDU fuel. The rapid release of Cs is attributed to the leaching of the gap inventory. Cesium leach rates remain higher than the rate of UO_2 matrix dissolution for several years. This is likely a result of slight preferential leaching from grain boundaries, which are more rapidly corroded than the UO_2 grains. Radionuclides such as ^{90}Sr, which are largely dissolved in the UO_2 grains (Kleykamp 1979), are eventually released at a rate comparable to the U dissolution rate, implying that release is controlled by the rate of dissolution of the UO_2 grains.

The lower dissolution rates of Pu in Figure 5-1 are typical of the behaviour of actinides that are less soluble than U (e.g., Am and Cm). In such cases, a low-solubility hydrous oxide phase probably controls the solubility (Rai 1984, Rai et al. 1987). The same behaviour is observed for U in cases where solutions are infrequently replenished. The time period required to reach saturation depends on a number of experimental variables, including solid surface area to solution volume ratio, temperature and flow (or solution replenishment) rate. The U phases controlling solubility have been identified in some cases (Stroes-Gascoyne et al. 1986, Wilson and Shaw

---

[9] The term matrix is commonly used to signify the UO_2 grains in which the actinides and the majority of the fission product inventory are contained.

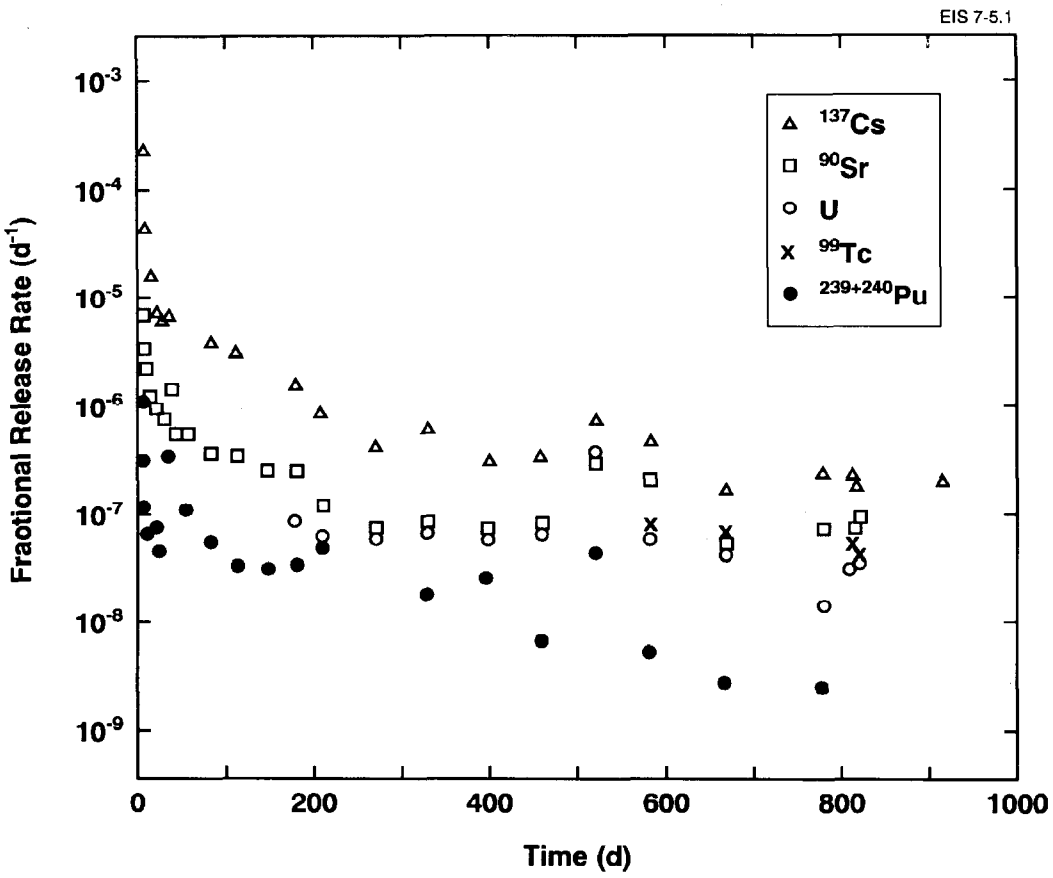

FIGURE 5-1: Fractional Release Rates of Radionuclides Measured in a Replenished Leach Test in Air-Saturated KBS (Swedish) Groundwater (Johnson 1982)

1987). Table 5-1 summarizes results from a number of studies where saturation of radionuclides was observed.

For Tc, apparent saturation is not observed unless conditions are reducing; under such conditions concentrations of $<10^{-7}$ mol·L^{-1} have been observed (Stroes-Gascoyne et al. 1992), probably indicating that the solubility is controlled by a reduced oxide of Tc (e.g., TcO_2). The data illustrate that redox conditions play an important role in controlling the saturation values and the overall extent of dissolution of the fuel matrix. For Pu and Am, saturation concentrations are very low under all redox conditions.

In the case of U, higher concentrations are observed under oxidizing than reducing conditions. In addition, fission product releases resulting from UO_2 matrix dissolution are also greater under oxidizing conditions.

The observations from used-fuel dissolution studies are consistent with our understanding of the effects of redox conditions on the dissolution of unirradiated UO_2 (Sunder and Shoesmith 1991). The redox chemistry of UO_2

TABLE 5-1

APPARENT SATURATION CONCENTRATIONS OF SELECTED RADIONUCLIDES IN USED-FUEL DISSOLUTION STUDIES

Radionuclide	Concentrations ($mol \cdot L^{-1}$)	Experimental Conditions	Reference
U	7×10^{-7}	100°C, O_2-free WN-1* synthetic groundwater, 484 d	Stroes-Gascoyne et al. (1989)
	7×10^{-8}	100°C, O_2-free SCSSS, 484 d	Stroes-Gascoyne et al. (1989)
	4.2×10^{-8}	200°C, basalt groundwater + basalt, 166 d	Rawson et al. (1988)
	2.5×10^{-6}	150°C, air-saturated WN-1 groundwater, 10 d	Stroes-Gascoyne et al. (1986)
	$<3 \times 10^{-7}$	150°C, H_2-saturated WN-1 groundwater, 30 d	Stroes-Gascoyne et al. (1986)
	6×10^{-9} to 1×10^{-7}	25°C, H_2-saturated synthetic granite groundwater	Werme and Forsyth (1988)
	4×10^{-6}	25°C, air-saturated granite groundwater	Werme and Forsyth (1988)
Pu	$\sim 1 \times 10^{-9}$	100°C, O_2-free WN-1 and SCSSS, 484 d (unfiltered solution)	Stroes-Gascoyne et al. (1989)
	8.4×10^{-10}	25°C, air-saturated granite groundwater, 200 d	Werme and Forsyth (1988)
	4×10^{-11}	25°C, air-saturated tuff groundwater (filtered solution)	Wilson (1988)
	3×10^{-11}	200°C, basalt groundwater + basalt, 166 d (filtered solution)	Rawson et al. (1988)
Am	2×10^{-12}	200°C, basalt groundwater + basalt, 166 d (filtered solution)	Rawson et al. (1988)
	3×10^{-13}	25°C, air-saturated tuff groundwater (filtered solution)	Wilson (1988)
Tc	2×10^{-8} to 2×10^{-9}	100°C, O_2-free WN-1 and SCSSS, 484 d	Stroes-Gascoyne et al. (1989)

* WN-1 and SCSSS are synthetic groundwaters representing typical, saline groundwaters in the Canadian Shield. WN-1 is similar in composition to WRA-500 (Table 3-1a).

dissolution is summarized in Figure 5-2, which illustrates that dissolution becomes significant when the surface composition of the UO_2 is oxidized to values approaching $UO_{2.33}$ ($\equiv U_3O_7$). This composition is the end of the fluorite crystal structure range; greater oxidation leads to major restructuring of the crystal lattice and accelerates dissolution. In the case where surface oxidation is limited to the UO_2-U_4O_9 region, the surface oxide remains intact (U_4O_9 is formed by diffusion of oxygen into the UO_2 matrix (Aronson et al. 1957) and is crystallographically similar to UO_2 (Johnson and Shoesmith 1988)). Under such redox conditions, the rate of oxidative dissolution (i.e., dissolution of U(VI) species) is extremely low, and it is more appropriate to consider that dissolution occurs without oxidation of U(IV) to U(VI). As a result, a model for dissolution of the UO_2 matrix based on its solubility is considered appropriate if the redox conditions can be shown to remain in the UO_2-U_4O_9 region (Garisto and Garisto 1985, Shoesmith and Sunder 1991). The presence of Fe(II) minerals in the disposal vault is expected to produce such a redox condition (see Section 3.4.2).

The question of whether or not γ- and α-radiolysis of water, which produce radical and molecular oxidants, can affect the redox condition of the groundwater that would eventually contact the fuel has been carefully examined.

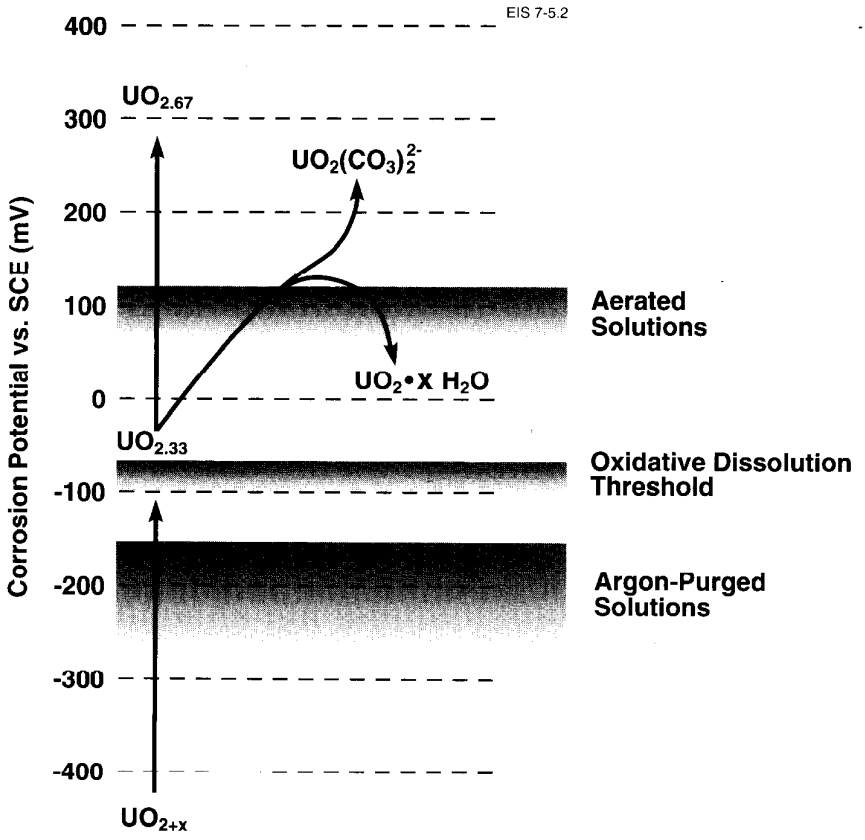

FIGURE 5-2: Redox Chemistry of UO_2 Dissolution (Shoesmith and Sunder 1992)

The conditions under which dissolution would be either oxidative or non-oxidative has been outlined on the basis of electrochemical and corrosion studies on unirradiated UO_2, including the effects of radiolysis (Shoesmith and Sunder 1991). By comparing electrochemically predicted rates for oxidative dissolution of UO_2 with rates expected for non-oxidative dissolution (established by comparison with rates for similar oxides, e.g., NiO), it is possible to place limits on the duration of oxidative dissolution under vault conditions. Using this procedure we predict that oxidative dissolution of CANDU fuel as a result of γ-radiolysis would be unsustainable beyond ~200 a, as a result of the rapid decrease in the γ-radiation field. This is a short period in comparison with the anticipated lifetimes of Grade-2 titanium waste containers (~1200 a to 6000 a, Section 4.7.6); thus, the effects of γ-radiation can be ignored in the dissolution model.

For α-radiolysis, the period for which oxidative dissolution could be sustained has been determined from experiments involving exposure of UO_2 electrodes to solutions experiencing radiolysis at various α-dose rates. These dose rates can be equated to fuel decay time. Using the same electrochemical model discussed above (Shoesmith and Sunder 1991), but more recent data (Sunder and Shoesmith 1992), we calculated dissolution rates of UO_2 as a function of α-dose rate. The results (Figure 5-3) illustrate that oxidative dissolution would be unimportant beyond a period of approximately 600 a. As a result, a UO_2 solubility model is considered appropriate for modelling the dissolution of the used-fuel matrix at times longer than 600 a.

The experimental results obtained for dissolution of unirradiated UO_2 in the presence of α-radiolysis (Bailey et al. 1985, Shoesmith and Sunder 1991) represent conditions under which radiolysis products are concentrated at the UO_2 surface and do not take into account many of the factors likely to counter the oxidizing effects of α-radiolysis under disposal conditions. For example, radical scavengers such as dissolved H_2, produced by container corrosion and α-radiolysis, suppress α-radiolytic surface oxidation of unirradiated UO_2 fuel at 100°C (Sunder et al. 1990). When used-fuel dissolution experiments are performed at a temperature of 100°C in the presence of reducing agents, such as H_2 or ferrous minerals, U and Tc concentrations saturate at low levels indicative of reducing conditions, and the surface of the used fuel shows very limited oxidation (Tait et al. 1991). This suggests that the absence of oxidants in the disposal vault at the time of container failure, the presence of Fe^{2+} from the dissolution of ferrous minerals, and the presence of other reducing agents, such as sulphide and H_2, would effectively counter the oxidative effects of α-radiolysis (see Section 3.4.2). The limited degree of surface oxidation of used fuel and UO_2 observed in experimental studies and the lack of oxidation of ore at Oklo (see Section 5.6) suggest that the extensive oxidation postulated by Neretnieks (1982) would not occur in a disposal vault.

The preceding discussion of the dissolution of UO_2 and used fuel under conditions approximating those in a disposal vault suggests that a radionuclide release model for used fuel should represent the following processes:

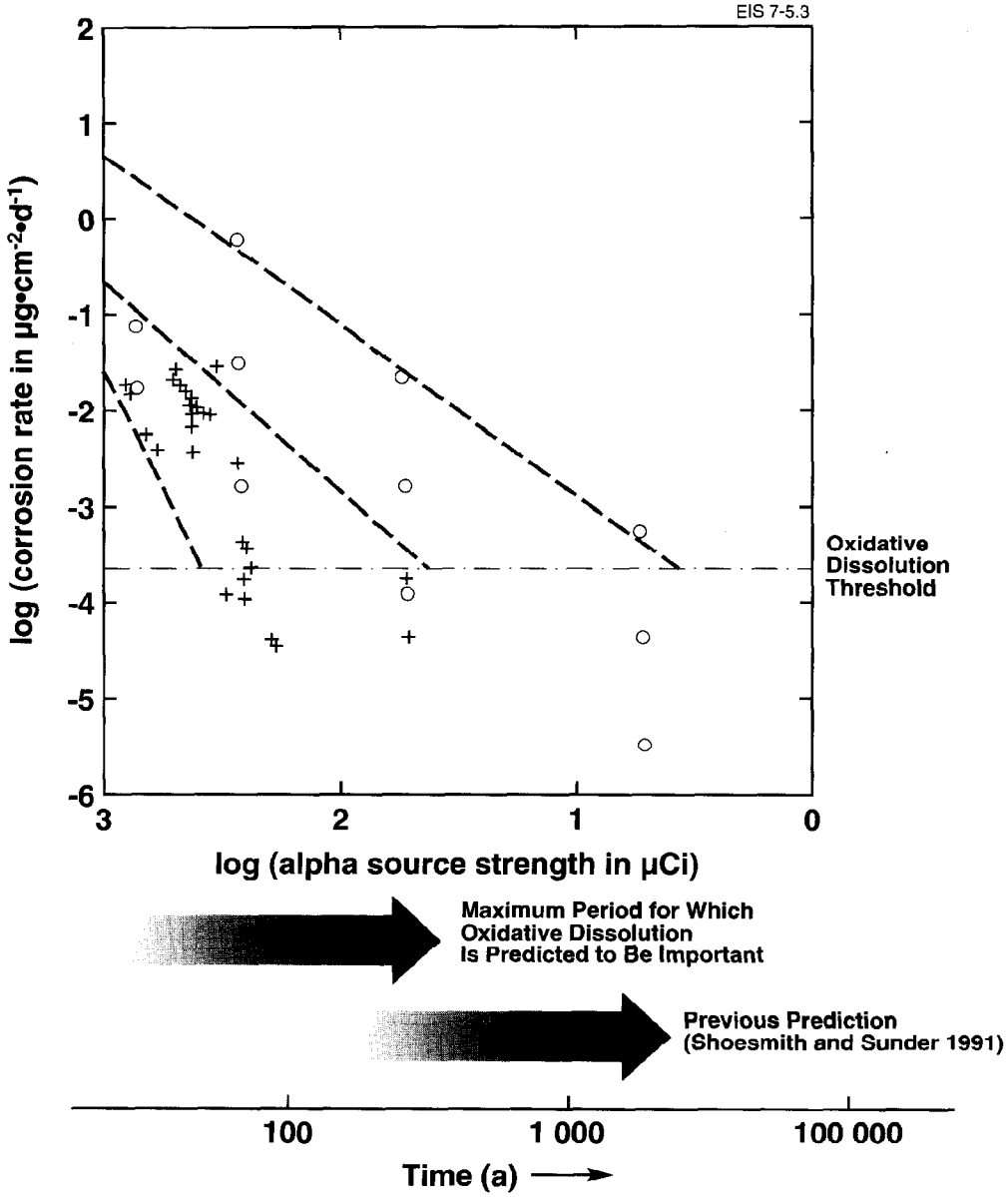

FIGURE 5-3: Dissolution Rates Predicted for Used Fuel as a Function of the Logarithm of Alpha Source Strength. The time axis shows the time at which such activity levels are achieved on the surface of CANDU fuel with a burnup of 685 GJ·kg^{-1} U, (1 Ci = 37 GBq): + new data (Sunder and Shoesmith 1992); o preliminary data previously published in Shoesmith and Sunder (1991). The diagonal dashed lines serve only to encompass the data and define the period for which oxidative dissolution is predicted to be important.

- rapid release of a fraction of the inventory of certain fission products from the fuel-sheath gap, along with the possibility of preferential release of fission products from grain boundaries;

- congruent dissolution of the UO_2 matrix (grains), which would result in release of contained fission products and actinides; and

- precipitation of certain radionuclides when their elemental concentrations exceed solubilities.

Several crucial assumptions have been made in the development of this model. The most important of these are outlined below:

1. Correlations between fission gas release to the gap during in-reactor irradiation and the leaching of Cs and I from fuel elements provide an appropriate basis for developing an average rapid release (i.e., gap) source term for all used-fuel bundles for a variety of fission products (see Section 5.5.1).

2. The fraction of the inventory of fission products such as I and Tc that is present at grain boundaries is rapidly released upon exposure to groundwater along with the fission products present in the gap (see Section 5.5.1). This is a conservative assumption, made because of the uncertainty regarding the quantities of various fission products at grain boundaries and because of the limited data available on their preferential release. Recent data (Stroes-Gascoyne et al. 1993) have confirmed the highly conservative nature of this assumption.

3. The thermodynamic properties of the used-fuel matrix are identical to those of pure UO_2.

4. The fuel matrix is thermodynamically stable in the vault environment. In this context, "stable" means that it would not be oxidized beyond U_4O_9, the composition beyond which oxidative dissolution may become significant. In such an equilibrium condition, uranium concentrations in solution can be calculated using chemical equilibrium models. The dissolution rate of the fuel is then controlled by the transport rate of uranium away from the fuel surface.

5. The maximum redox potential expected at the fuel surface (consistent with the U_4O_9/U_3O_7 boundary (see Section 5.3)), which may result from α-radiolysis, is greater than the assumed potential in the buffer/backfill material, which is established by Fe(II)/Fe(III) equilibria. The redox potential in the buffer/backfill and the implications for the fuel dissolution rate are discussed in Section 5.5.3.2.

The conceptual model, with the various calculation steps, data requirements and outputs, is shown in Figure 5-4. Sections 5.3, 5.4 and 5.5 describe the various components of the model.

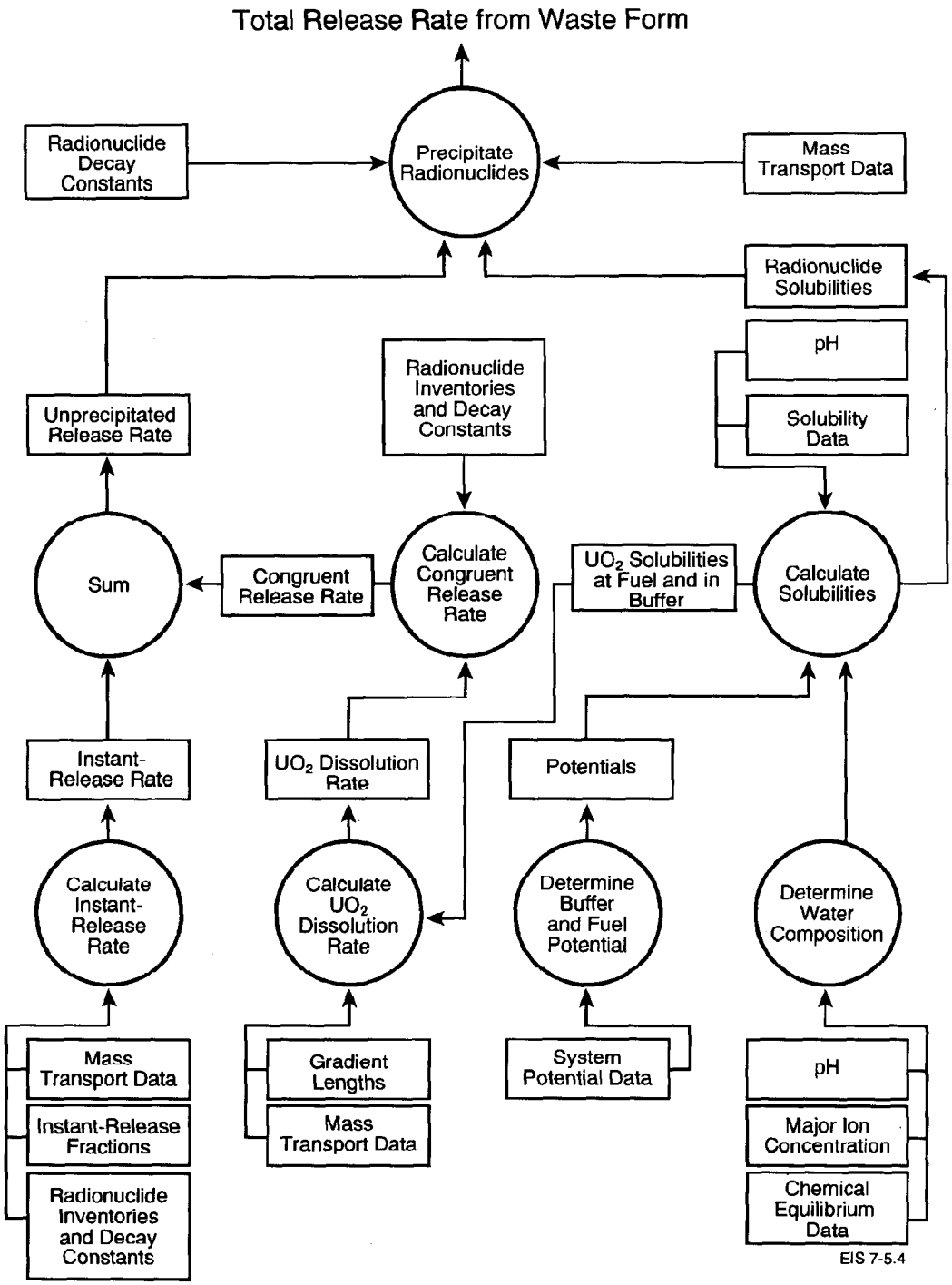

FIGURE 5-4: Conceptual Representation of Procedure for Calculating Radionuclide Release from Used Fuel

5.3 DEFINITION OF THE CHEMICAL ENVIRONMENT

The composition of the aqueous solution in contact with the fuel and Zircaloy sheath is important in determining the concentrations of U in solution and, hence, the rate of release of other radionuclides from the fuel matrix. The solubilities of other elements, such as Pu, Np, Tc and Th, would also be affected by the solution composition. Dissolved salts can influence the solid solubilities by complexation, and the nature and concentrations of ions affect the apparent equilibrium constants of dissolution and complexation reactions.

The reference groundwater for a depth of 500 m in the WRA is given in Table 3-1a; it is primarily a solution of sodium chloride, calcium chloride and sodium sulphate. As discussed in Section 3.4.1, the water contacting the used fuel (referred to as contact water) would be conditioned by the buffer and backfill. The resulting range of compositions is shown in Table 3-1b. The wide range of concentrations for the various constituents is based on analysis of groundwaters in the WRA (Gascoyne 1988), experiments with the reference buffer material (Oscarson and Dixon 1989a) and calculations on the dissolution of minerals in the buffer (Lemire and Garisto 1989, Appendix B). Loguniform distributions for the initial concentrations of the contact water species (Table 3-1b) were used. However, the calculated distributions of the solubilities of U, Np, Pu, Th and Tc (cf. Sections 5.5.2.2 and 5.5.3.1) are not strongly dependent on the shape of the distributions of concentrations for the contact-water species (e.g., use of uniform rather than loguniform distributions) (Lemire and Garisto 1992). As shown by Lemire and Garisto (1989), even the assumption of salinities markedly higher than those of the contact water has only a limited effect on the solubilities, actually shifting the distribution for solubility of U solids to lower solution concentrations. Solubility calculations for higher salinities are discussed in more detail in Section 8.2.

Complexation effects on solubilities are addressed by including aqueous complexes of carbonate, chloride, phosphate, fluoride and sulphate in the solubility calculations (Lemire and Garisto 1989). The apparent equilibrium constants are assumed to be constant within specified ranges of ionic strength.

The values of the equilibrium constants for complexing species are required at the temperature of the vault. Detailed thermal analyses of the vault have shown (Tsai 1993; Baumgartner et al., in preparation) that the maximum temperature within a used-fuel container would be only a few degrees higher than the container surface temperature after 100 a (see Figure 3-1). The temperature distribution used to evaluate the equilibrium constants is based on the peak in the temperature-versus-time profile for a container in the centre of the vault over the period from 200 to 1000 a (see Figure 4-2). The higher temperatures occurring prior to 200 a are not used in the solubility calculations because an insignificant number of containers are expected to fail during this period. A separate analysis of releases from prematurely defected containers is presented in Chapter 8. The thermal calculations were performed using the analytical methods developed by Mathers (1985), taking variability and uncertainty into account. Five hundred simulations were done with this thermal model for 300, 700 and

1000 a after disposal, with input parameters sampled to reflect the uncertainty and variability. Figure 5-5 shows the results of these simulations in the form of container surface temperature histograms at the position in the vault where the temperature is highest. The resulting temperatures are normally distributed with a mean μ = 337.5 K and a standard deviation σ = 3.1 K. Temperature cutoffs were imposed at T_{max} = 423.0 K and T_{min} = 284.0 K, beyond which the thermodynamic estimates are not valid. During the period from 1000 to 10^5 a, the temperature in the vault will range from a maximum of ~340 to 285 K. Further information on temperature distributions within the vault and their impact on container corrosion rates are discussed in Chapter 4.

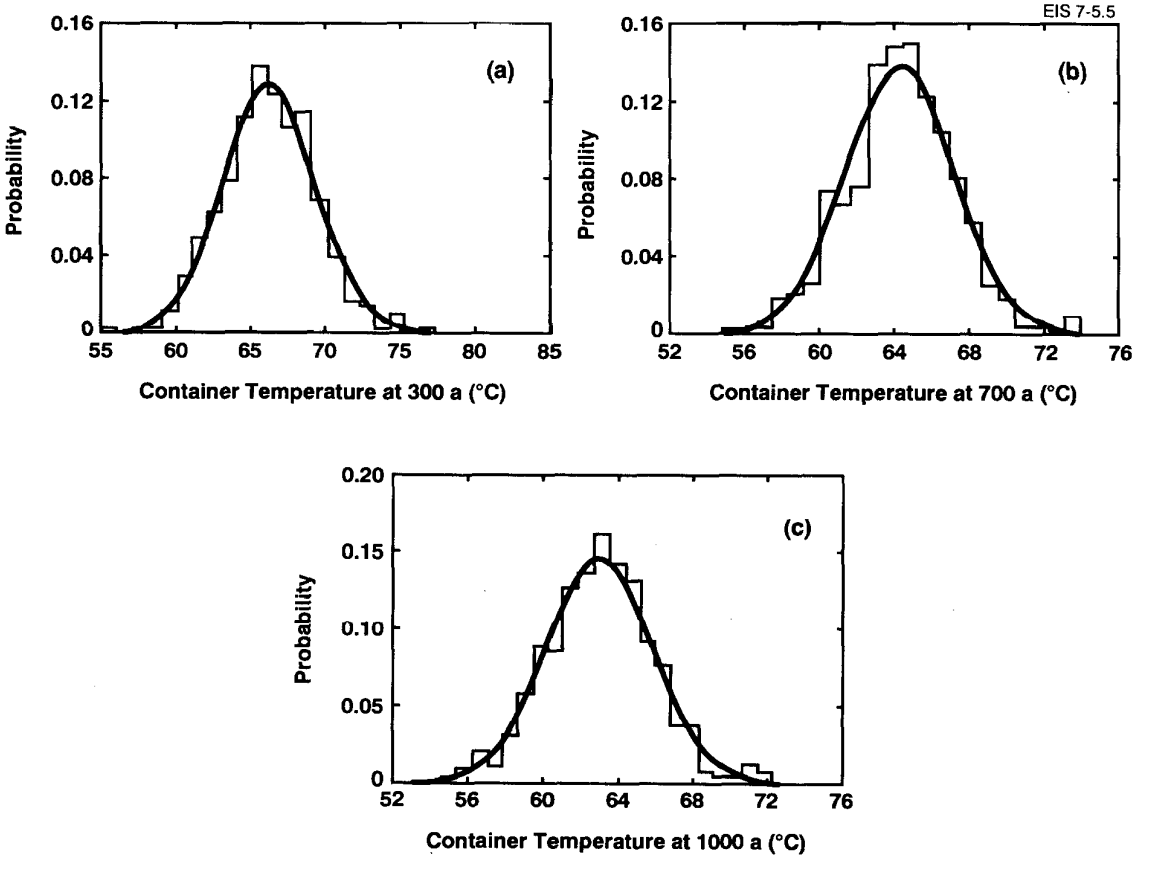

FIGURE 5-5: Container Surface Temperature Histograms for a Container in the Centre of the Vault for Times of (a) 300, (b) 700 and (c) 1000 a After Disposal. The broad temperature range reflects the uncertainty and variability in input parameters for the thermal model.

The equilibrium constants governing the contact-water compositions are calculated from equations of the following type:

$$\log K_{iT} = (298.15/T)(\log K_{i298} + m_i(T - 298.15)) \qquad (5.1)$$

where

$$284\ K < T < 423\ K$$

where K_{iT} is the equilibrium constant at temperature T, and m_i is a fitting parameter describing the slope of the Gibbs energy of reaction-versus-temperature curve. The values of $\log K_{i298}$ and m_i are sampled from distributions based on the uncertainties in these values within the ionic strength range consistent with the composition given in Table 3-1b. This equation assumes that neither the heat capacity of reaction nor the temperature range of interest is very large (Lemire and Garisto 1989), which is reasonable given the relatively small temperature range in the disposal vault and the reactions that determine UO_2 solubility.

Equilibrium constants, which relate to the most important complexing species (Lemire and Garisto 1989), are calculated for the following:

- the solubility product of $CaSO_4$,
- the solubility product of $CaCO_3$,
- the solubility product of CaF_2,
- the solubility product of $Ca_5(PO_4)_3OH$ (hydroxyapatite),
- the ion product of H_2O,
- the first and second protonation constants of the carbonate ion, and
- the second protonation constant of the phosphate ion.

The redox conditions for the groundwater in contact with the fuel and Zircaloy sheath are assumed to be within the UO_2 and U_4O_9 stability fields (see Figure 5-6). This assumption is based on the conclusion that various reducing agents, such as S^{2-} and Mn^{2+} and, in particular, Fe^{2+}, arising from mineral dissolution (see Sections 3.4.2 and 5.5.3.2), would react with any oxygen or oxidants initially present in the vault and would maintain reducing conditions. Microorganisms present would also contribute to producing a reducing environment, as oxygen is the preferred electron donor for cell growth (Stroes-Gascoyne 1989). In this context, it is noted that microorganisms of the type that are used in solution mining of uranium (Brierley 1982) and that thrive in an acidic, oxidizing environment are not expected to thrive in the neutral to alkaline pH, reducing environment of the disposal vault. Thus, microbial oxidation of used fuel would not be expected to occur. The U_4O_9/U_3O_7 potential line in Figure 5-6 defines the maximum redox potential (0.516 V at pH = 0) expected at the used-fuel surface. The minimum redox potential expected is that associated with the H_2/H_2O boundary (0.0 V at pH = 0).

The Nernstian slope, S_E, for the temperature T at the container surface is used to calculate the oxidation potential (E_h) in the contact water from the sampled potential (E_s) for pH = 0, and the sampled pH according to

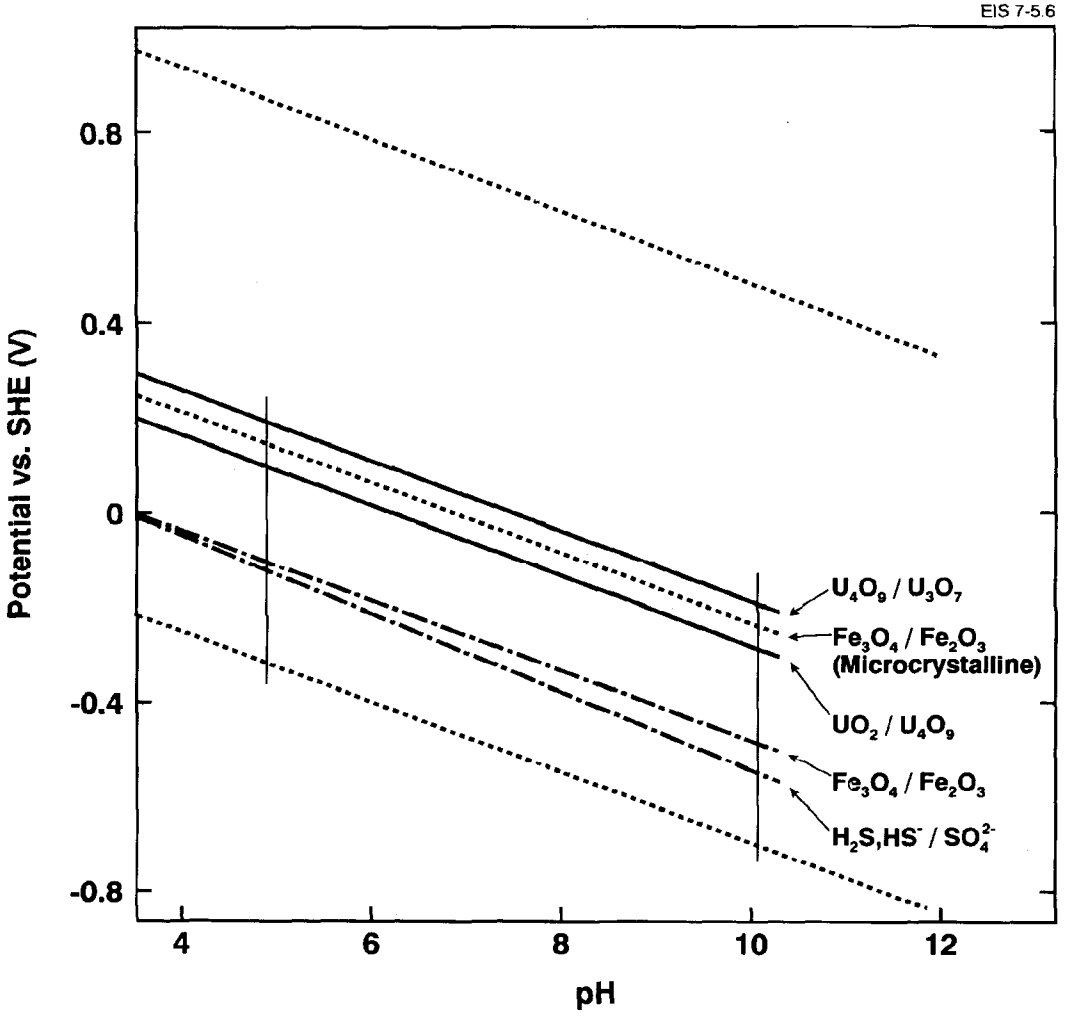

FIGURE 5-6: E_h-pH Diagram Showing UO_2-U_4O_9 Stability Field and Region of Buffering by Fe(II)/Fe(III) Redox Couples in WN-1M Groundwater at 100°C. WN-1M groundwater is similar in composition to WRA-500 (Table 3-1a) (Gascoyne 1988). The upper and lower dotted lines represent the O_2/H_2O and H_2O/H_2 boundaries respectively.

$$E_h = E_z + S_E \text{ pH} \quad . \tag{5.2}$$

Next, the ionic strength of the solution is calculated on the basis of the sampled contact-water composition. Because sodium sulphate and calcium chloride concentrations are sampled from rather wide distributions, the selected solution may be supersaturated with respect to calcium sulphate. If so, the quantity of calcium sulphate that will precipitate is calculated, and the solution concentrations of Ca^{2+} ions and SO_4^{2-} ions are reduced appropriately. The ionic strength is then recalculated.

The contact-water composition is then checked for supersaturation with respect to hydroxyapatite ($Ca_5(PO_4)_3OH$), fluorite (CaF_2) and calcite ($CaCO_3$). If the composition is such that the solution would be supersaturated with respect to these solids, the respective solution concentrations of inorganic phosphorus, fluoride and inorganic carbon are reduced to the saturation values. Any charge imbalance (from shifted equilibria at a fixed pH) is corrected by addition of Na^+ or Cl^-, and the ionic strength is again recalculated.

The contact-water composition for a given simulation is then used to calculate the solubilities of the various radionuclides.

5.4 THE CORROSION PERFORMANCE OF ZIRCALOY AND RADIONUCLIDE RELEASE FROM THE ZIRCALOY SHEATH

Zircaloy-4 is a highly corrosion-resistant material, in many respects similar to titanium in its corrosion performance. As a result, it is likely that the irradiated Zircaloy sheath would provide an additional barrier to radionuclide release from the fuel after failure of the container. Although it has been argued that the Zircaloy sheath is sufficiently resistant to uniform corrosion to provide containment for thousands of years after disposal (Rothman 1984), some uncertainties remain regarding possible failure as a result of crevice corrosion, hydrogen-induced cracking and stress corrosion cracking. In addition, no studies of Zircaloy corrosion rates or mechanisms under projected Canadian disposal conditions have been published. In the absence of sufficient data for predicting the lifetime of the sheath, we have conservatively assumed failure by a localized corrosion process immediately upon breach of the container; i.e., all the fuel-element sheaths for the 72 bundles in each container fail simultaneously with the container, permitting immediate access of contact water to the used fuel. In the vault model, this is physically represented by the instantaneous removal of all the fuel sheaths when the container fails; thus, no credit is included for the ability of the failed sheaths to retard radionuclide release from the fuel.

Irrespective of the time of failure of the sheath, its corrosion would lead to the gradual release of activation products contained in the sheath material itself. The concentrations of activation products in Zircaloy sheath, as calculated by the ORIGEN-S code, are shown in Table A-1 of Appendix A. The passive oxide film on the sheath is typically coherent and tightly bound to the underlying Zircaloy. As the corrosion front moved through the metal, converting it to ZrO_2, the activation products are expected to be incorporated into the growing oxide film. The release of radionuclides into the groundwater would subsequently occur as the oxide film dissolved. Although detailed studies of this corrosion mechanism have not been performed under the conditions expected in a disposal vault, comparable studies of uniform corrosion of titanium have been performed. Mattsson and Olefjord (1984, 1990) and Mattsson et al. (1990) have studied the corrosion of Ti in water-saturated bentonite over periods of up to six years using surface analysis methods. These studies showed that the oxide film remained tightly bound to the underlying metal and that corrosion rates were extremely low (~0.002 $\mu m \cdot a^{-1}$). If one assumes similar results for Zircaloy, this suggests that no separation of the oxide from the metal

would occur that could lead to preferential release of entrained activation products from the sheath. We therefore assume that, although local failure of the fuel sheath may occur relatively rapidly, this type of failure would not lead to significant release of activation products present in the sheath material itself. The release of contained activation products would thus be determined by the dissolution rate of the ZrO_2. This rate would be controlled by the solubility of ZrO_2 in the contact water and by the rate of diffusion of dissolved zirconium species through the pore water in the buffer material and into the surrounding rock. The model for radionuclide release from the sheath is essentially the same as that for the congruent release of radionuclides from the used-fuel matrix. The mathematical source-term model is described in Section 5.5.2.3.

The solubility of zirconium oxide in the groundwater is required to calculate the release of activation products from the fuel sheath. The aqueous chemistry of Zr is similar to some other metals with a predominant (IV) oxidation state, such as Ti and Th. There are very few thermodynamic data available for Zr solution species near room temperature (Wagman et al. 1982), and essentially none for higher temperatures. Zirconium hydrolyzes more readily than Th, but less readily than Ti(IV) (Baes and Mesmer 1976). Zirconium complexes with fluoride are known and are apparently somewhat stronger than those of Th (Bond and Hefter 1980). As in the case of Th, phosphate and sulphate complexes are known, although the Zr species are apparently more hydrolyzed (Cotton and Wilkinson 1972, Sillen and Martell 1964).

To a first approximation, the solubility of zirconium dioxide is expected to be similar to that of thorium dioxide (Baes and Mesmer 1976). Distributions for the solubility of precipitated thorium dioxide in groundwater are given by Lemire and Garisto (1989). The logarithm of the molar solubility at 298 K ($\log_{10}[Th]_{298} = (-8.75 \pm 2.53)$ if the distribution of $[Th]_T$ is assumed to be lognormal) is greater and the distribution is broader than at 373 K ($\log_{10}[Th]_{373} = (-10.74 \pm 1.40)$).

The solubility of Zr in the vault at all temperatures, based on the solubility of zirconium oxide, has been selected to be the same as the mean value for thorium oxide at 298 K, with the same standard deviation [$\log_{10}[Zr]_{298} = (-8.75 \pm 2.53)$, GM (Geometric Mean) = 1.8×10^{-9} mol·kg^{-1}, GSD (Geometric Standard Deviation) = 3.4×10^2] - i.e., it was selected to be the same as the higher Th solubility with the higher standard deviation. The possibility that complexation may enhance zirconium oxide solubility to a greater degree than thorium oxide solubility is largely taken into account by this selection of a large standard deviation. Furthermore, the zirconium dioxide solubilities are essentially values for precipitated ZrO_2, as they are derived from values for precipitated ThO_2. However, it is probable that ZrO_2 on the Zircaloy surface is a more ordered (and, hence, less soluble) oxide.

Used CANDU fuel bundles typically have small quantities of crud (oxide deposits incorporating activation products) adhering to external sheath surfaces (Wasywich 1993, Johnson et al. 1994). Characterization of this crud indicates that the radionuclide inventories are extremely small

relative to the quantities in the fuel and sheath. Consequently, they have been ignored in the vault model analysis.

5.5 THE RADIONUCLIDE RELEASE MODEL FOR USED FUEL

5.5.1 The Instant-Release Model

5.5.1.1 The Conceptual Instant-Release Model

The assessment of used nuclear fuel disposal requires information on the gap and grain-boundary inventories of radionuclides in used fuel (Garisto et al. 1990). The distribution of various radionuclides within a fuel element is illustrated conceptually in Figure 5-7 (see also Section 2.2.5 of Johnson et al. (1994)). These inventories, along with data on the aqueous chemistry of the radionuclides, determine the instant-release fractions, i.e., the fractions of the total inventory of given radionuclides in the used-fuel bundles that are available for fast release when the used fuel comes into contact with groundwater.

The instantly released radionuclides from all 72 bundles in a container are assumed to dissolve in the contact water and diffuse into the waste container immediately upon container flooding, and to reach uniform, inventory-limited concentrations in the groundwater inside the container (LeNeveu and Johnson 1986, Apted et al. 1987). The total radionuclide flux into the buffer is the instant-release source term. For ^{99}Tc, the solubility inside the container is also taken into account in determining the upper bound on its concentration inside the containers (Lemire and Garisto 1989). The mathematical procedure for taking solubility into account is based on a compartmental model (Garisto and LeNeveu 1989) and is described in detail in Section 5.5.1.3.

In the model, we treat both gap and grain-boundary radionuclide inventories as instant-release fractions (IRFs). This conservatism has been adopted because of the limited information available on inventories of fission products at grain boundaries and their kinetics of release. Although gap inventories for CANDU fuel have been well characterized for a number of radionuclides, experimental data on the chemical nature and quantities of fission products at grain boundaries are more limited (Johnson and Shoesmith 1988, Gray and Strachan 1991). Recent data indicate that grain-boundary inventories of ^{137}Cs in CANDU fuel are comparable to values calculated with the ELESIM code, but that dissolution of the fuel under aggressive conditions (i.e., acid solutions) is required for release from grain boundaries to occur (Stroes-Gascoyne et al. 1993). This emphasizes the high degree of conservatism adopted in the vault model in assuming that both gap and grain-boundary inventories contribute to the IRF.

Radionuclides that would have significant IRFs include ^{129}I, ^{135}Cs, ^{99}Tc, ^{79}Se, ^{126}Sn, ^{3}H, ^{14}C, ^{137}Cs, ^{90}Sr, ^{39}Ar, ^{42}Ar, ^{85}Kr, ^{81}Kr and ^{40}K (Garisto et al. 1990; Oversby 1987; Apted et al. 1989b; Goodwin and Mehta, in preparation). We have estimated IRFs for these radionuclides taking uncertainty and variability in the data into account. We then use these IRFs to derive the corresponding instant-release source terms.

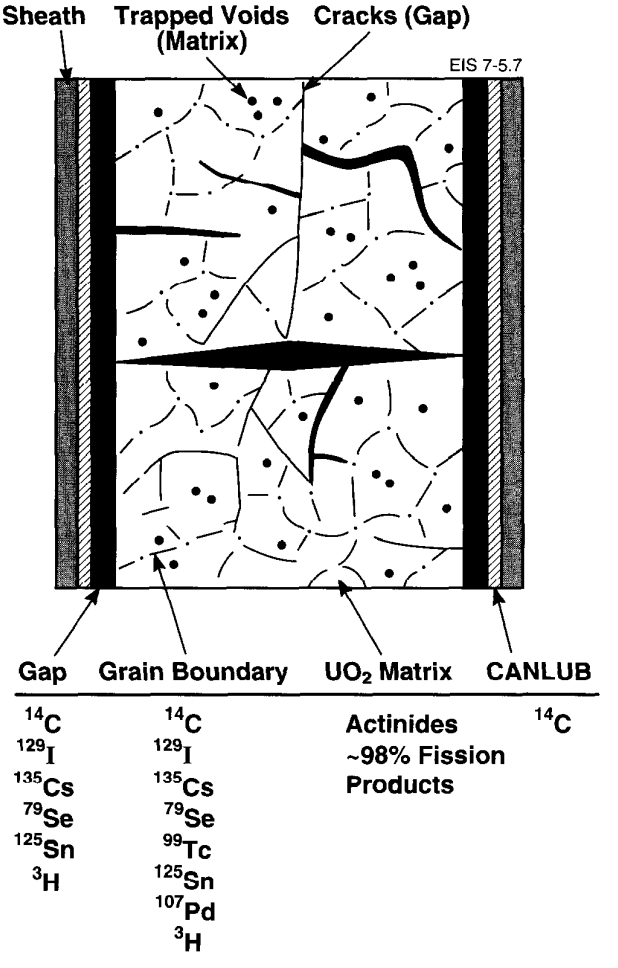

FIGURE 5-7: Conceptual Distribution of Some Fission and Activation Products Within a Used-Fuel Element

5.5.1.2 Instant-Release Fractions

Because the experimental data on gap and grain-boundary inventories is limited to a few radionuclides, we rely on a combination of experimental data, theoretical calculations and chemical analogues to derive the IRFs for the fourteen radionuclides listed in Section 5.5.1.1.

The IRFs for ^{129}I and ^{135}Cs

The I and Cs gap inventories have been derived using experimental results (Johnson et al. 1983, Stroes-Gascoyne et al. 1987, Stroes-Gascoyne and Sellinger 1986) and fuel-performance calculations with the ELESIM code (Notley 1979). The details of the derivation are given by Garisto et al. (1990). The resulting gap inventories depend on the fuel power history.

To derive the I and Cs grain-boundary inventories, we assume that the known relationship between the Xe grain-boundary inventory and its gap inventory (Garisto et al. 1990) applies also to these elements. This assumption is based on the similarity in the migration mechanisms of Xe, ^{137}Cs and ^{129}I in used fuel (Manzel et al. 1984) and has, to a limited degree, been verified for CANDU fuel for ^{137}Cs (Stroes-Gascoyne et al. 1993).[10] The resulting standard deviation for a typical value of the IRF of 10% is 8.0%, i.e., IRF = 0.10 ± 0.08.

It is interesting to note that recent X-ray photoelectron spectroscopy studies of fission-product oxides at grain boundaries (Hocking et al. 1990 and unpublished data for CANDU fuel with 950 GJ/kg U burnup and a peak linear power of 50 kW/m) have shown that the inventory of Cs at grain boundaries is approximately 5f% where f is the UO_2 grain-boundary roughness factor, assuming cesium oxide monolayer coverage. Electron fractographs of used fuel (Hastings 1982) indicate that the roughness factor (estimated by visual inspection) is approximately 2, corresponding to a grain-boundary inventory of approximately 10%, in agreement with the inventory estimated for the present model.

The IRF of a given radionuclide cannot be specified as a single value because of both uncertainty in the derivation of the inventory data and variability in these data. The major source of variability is the variation in irradiation history of the used fuel. Figure 5-8 presents the distribution of gap and grain-boundary inventories of Cs and I in used CANDU fuel bundles with typical irradiation histories (Garisto et al. 1990). The irradiation histories used to derive Figure 5-8 are similar to those presented in Johnson and Joling (1984) and are not repeated here. The fuel irradiation histories used to derive the IRFs were for Bruce power reactor fuel, which generally operates at higher power ratings than Pickering fuel; thus, the derived values are expected to overestimate the average IRFs for CANDU fuel.

For each bundle, the sum of the gap and grain-boundary inventories represents the IRF for I and Cs. When we consider all fuel bundles discharged from the core of a CANDU reactor (taking into account the fuel bundle shifting sequences and the relative burnup and power distributions for fuel elements within each fuel bundle), the weighted average value calculated by the method of Johnson and Joling (1984) for the IRF of Cs and I per bundle is 8.1% (with 2.1% for gap and 6.0% for grain-boundary inventory), and the standard deviation arising from variability (of fuel irradiation history) is 3.2%.

We assume that for one fuel bundle the total range of the IRF arising from both uncertainty and variability can be represented by one standard deviation with the value $(8.0^2 + 3.2^2)^{1/2} = 8.6\%$. For a large quantity of fuel, however, the standard deviation is much smaller. For example, the standard

---

[10] The release of ^{135}Cs ($t_{1/2}$ = 2.3 x 10^6 a) has not been studied. The release characteristics of ^{135}Cs are assumed to be the same as those of ^{137}Cs.

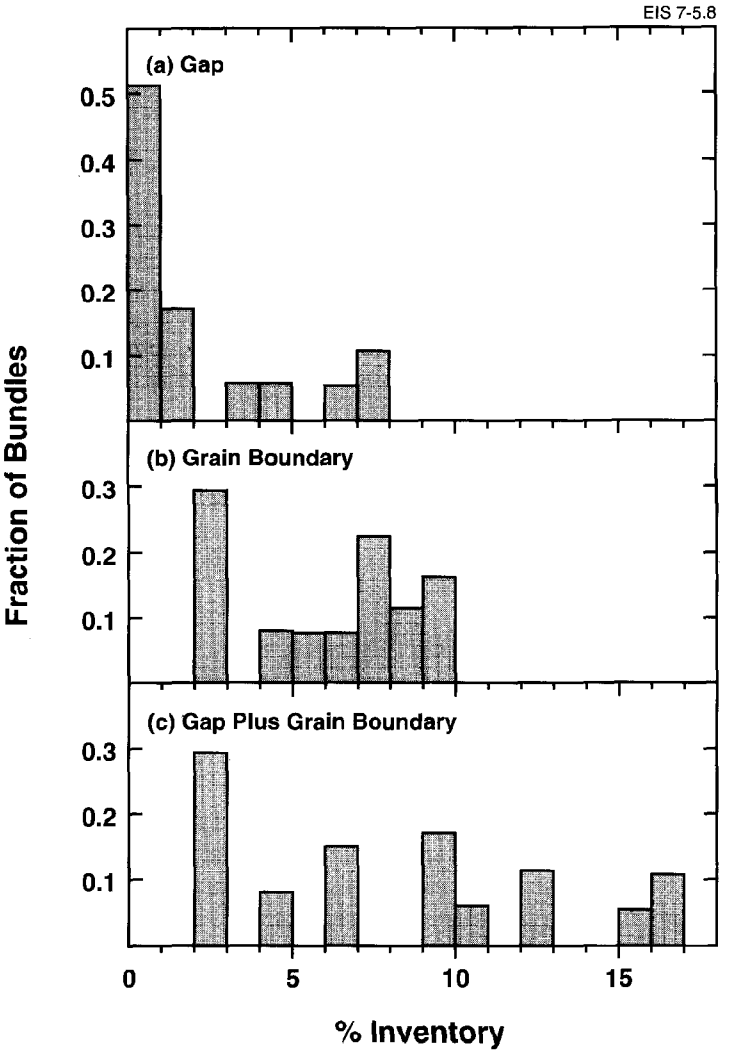

FIGURE 5-8: Distribution of (a) Gap, (b) Grain-Boundary and (c) Gap Plus Grain-Boundary Inventories of Cesium and Iodine in Used-Fuel Bundles (Garisto et al. 1990)

deviation associated with having 72 bundles in a container, assuming a random distribution of irradiation histories, is $8.6/72^{0.5} \simeq 1.0\%$. This standard deviation (σ) is small in comparison with the standard deviation of the IRF per bundle and is used for the IRF distribution.

To avoid the inclusion of unreasonable values, upper and lower cutoff values for the IRF were estimated by considering the maximum and minimum operational power ratings for CANDU fuel bundles. Figure 5-8 shows that the maximum combined gap and grain-boundary inventory of Cs and I for a fuel bundle is approximately 17%; thus, the minimum inventory retained within UO_2 grains exceeds 80%. However, maximum fuel bundle power ratings

can, in principle, be somewhat in excess of values used to calculate the data in Figure 5-8. The design bundle overpower envelope represents the highest power values experienced during normal operation for CANDU fuel bundles (Gacesa et al. 1983). The maximum outer element[11] fission gas inventory in the gap calculated with the ELESIM code using this envelope is 20%, corresponding to a maximum average gap inventory for the fuel bundle of ~15%. The corresponding average inventory of fission gas at grain boundaries is approximately 10%, giving a maximum combined inventory of fission gas in the gap and grain boundaries, for such a high-power-rating fuel bundle, of ~25%, a value that we have selected as the upper limit for the IRF for Cs and I. This figure is clearly conservative since normal reactor operating conditions could not lead to all fuel bundles having such high power ratings.

A value of 1.2% for the lower cutoff, representing gap release only, was suggested by Johnson and Joling (1984), based on the Bruce reactors operating at 92% of full power. A value lower than this would imply reactors being operated for extended periods at powers significantly lower than the design ratings, which is clearly improbable.

In summary, the IRFs for ^{135}Cs and ^{129}I are sampled from truncated normal distributions with a mean of 8.1%, a standard deviation of 1.0%, a lower bound of 1.2% and an upper bound of 25%.

The IRFs for ^{79}Se and ^{126}Sn

The IRFs for ^{79}Se and ^{126}Sn are assumed to be the same as those of ^{129}I and ^{135}Cs, i.e., a truncated normal distribution with μ = 8.1% and σ = 1.0%, on the basis of their similar properties in the fuel under reactor operating conditions. There is currently no direct experimental data on the instant release of these radionuclides from CANDU fuel. However, we expect the IRFs for Se and Sn to be very conservative, because measured total inventories of these radionuclides in LWR fuel are generally almost one order of magnitude lower than the corresponding total inventories calculated with ORIGEN-2 (Blahnik et al. 1988).

The IRF for ^{99}Tc

Technetium is not volatile under reactor operating conditions and is unlikely to be present in the gap. Thermodynamic data suggest that Tc is present in used CANDU fuel in metallic form (Paquette et al. 1980). Indeed, Hastings et al. (1976) have identified Tc in metallic inclusions also containing Mo, Ru, Rh and Pd on the grain boundaries of used CANDU fuel. In LWR fuel, Tc has also been found in metallic alloy inclusions (Jeffery 1967, Kleykamp 1979). Studies of the diffusion of fission products in UO_2 indicate that the diffusion rate of Tc to grain boundaries during reactor irradiation is somewhat smaller than for Cs, I and Xe (Prussin et al. 1988).

---

[11] Refers to the outer ring fuel elements in a bundle, which operate at higher power rating than elements closer to the centre of the bundle.

Experimental results on the leaching of ^{99}Tc from used CANDU fuel indicate that 0.13% of the total ^{99}Tc inventory is released in short-term leaching tests (Garisto et al. 1990), whereas up to 4.5% ± 0.8% is leached from fuel that has been oxidized to U_3O_8 (such oxidation separates individual fuel grains, thus exposing the grain boundaries) (Stroes-Gascoyne and Sellinger 1986). More limited oxidation to U_3O_7, which exposed the grain boundaries but avoided the structural changes to the UO_2 lattice associated with oxidation to U_3O_8, yielded maximum ^{99}Tc releases to groundwater from grain boundaries of ~1.5% in leaching experiments of 300-d duration. These results and the observation that diffusion of Tc in UO_2 during in-reactor irradiation is slower than for Cs, I and Xe, suggest that the ^{99}Tc grain-boundary inventory is no greater than that of Cs and I. We therefore adopt the same value for the grain-boundary inventory.

We also assume that all the grain-boundary inventory of ^{99}Tc is available for instant release. Thus, the mean IRF is 6.0% and the standard deviation per container is approximately 1.0%.

For a variety of reasons already discussed, the IRF for Tc overestimates the probable ^{99}Tc releases from used fuel.

The IRF for ^{14}C

Carbon-14 is produced in reactors by neutron capture reactions involving nitrogen, oxygen and carbon. The principal reactions are $^{14}N(n,p)^{14}C$, $^{17}O(n,\alpha)^{14}C$ and $^{13}C(n,\gamma)^{14}C$, with the first reaction being by far the most important source because of the high capture cross section. Nitrogen and carbon are present as impurities in fuel, and ^{17}O is a low-abundance, naturally occurring isotope, inevitably present in UO_2 fuel.

Under the high temperatures and highly reducing conditions prevailing in used fuel during in-reactor irradiation, and in the presence of CANLUB,[12] which contributes to the inventory of carbon (stable and radioactive), the ^{14}C is unlikely to experience any oxidation and will be present in elemental (and non-volatile) form. Nonetheless, for the purposes of calculating transport of ^{14}C from the container and into the buffer, the dissolved ^{14}C is assumed to be present as CO_3^{2-}.

At the time the assessment data for ^{14}C were defined, there were limited data on instant release of ^{14}C from LWR fuel, and essentially no data on ^{14}C release from CANDU fuel. The experimental data indicated that the fractional release of ^{14}C from used fuel may range from approximately 1 to 25% (Wilson and Shaw 1987; Van Konynenburg et al. 1985, 1987; Neal et al. 1988; Wilson 1988). Because of the scarcity of the data, we conservatively assumed a range of IRF values of 1 to 25%. A uniform distribution was adopted because the data provide no firm basis for quantitatively ascribing different probabilities to given IRF values within the estimated range (Oversby 1987), or for estimating standard deviations. The large range selected also allows for the uncertainties in estimating releases of this

---

[12] CANLUB is a commercial graphite suspension applied to the internal sheath surface to prevent fuel element failures from power ramps.

nuclide from the oxide film on the sheath. In this regard, Van Konynenburg et al. (1987) have reported rapid release of a fraction (<1%) of the ^{14}C inventory of the sheath in air oxidation and water corrosion studies.

Recent data on ^{14}C release from used CANDU fuel (Stroes-Gascoyne et al. 1992) indicate that very low releases (≪1%) occur at 25°C; thus, the selected range is considered very conservative. The impact of these findings on the assessment results is discussed in more detail in Section 7.3.

The IRF for ^{3}H

Tritium is a ternary fission product with a very low yield (Tait et al. 1989). The diffusion coefficient of ^{3}H in UO_2 is relatively high; however, pickup of ^{3}H by the sheath tends to reduce the gap inventory. No measurements of ^{3}H release from CANDU fuel have been reported, although some data are available for LWR fuel. Goode and Cox (1970) reported that puncture tests indicated that the gap inventory of ^{3}H is only 10^{-5} of the total ^{3}H inventory. Ohuchi and Sakurai (1988) reported that 10% of the ^{3}H inventory is retained in the UO_2 and approximately 60% is present as hydride in the Zircaloy sheath; the remaining 30% was assumed (by difference) to be present in the gap. These apparently contradictory results led to the selection of an IRF of 30 to 40% for ^{3}H. Subsequent communication with Ohuchi (Kempe 1992) indicated that the Ohuchi and Sakurai (1988) paper contained a misprint, and that they actually found that the gap release of ^{3}H was <1%. The IRF of 30 to 40% is therefore extremely conservative.

The IRF for ^{90}Sr

Experiments on the leaching of intentionally defected used-fuel elements and fuel fragments suggest that ^{90}Sr is released preferentially from the fuel in short-term leaching experiments (Stroes-Gascoyne et al. 1989, Forsyth and Werme 1985, Werme and Forsyth 1988). The measured inventory fraction released into solution ranges from 0.001 to 0.3% for used CANDU fuel under various redox and fuel burnup conditions (Garisto et al. 1990). The measured released fractions of Sr are approximately three orders of magnitude higher than the measured release fractions of U (Stroes-Gascoyne et al. 1989). There are two mechanisms that may contribute to this short-term incongruent release of Sr from fuel:

1. Strontium may be preferentially leached from segregated inclusions located at grain boundaries, where it has been detected as a minor constituent (Jeffery 1967). As Sr itself is relatively immobile at fuel irradiation temperatures, and is expected to be mainly dissolved in the fuel matrix (Kleykamp 1979), it is possible that the Sr species in the grain boundaries originate from radioactive Br, Kr and Rb precursors, which are more mobile in the UO_2 lattice (Garisto et al. 1990).

2. Strontium may actually be released from the fuel congruently, and the apparent incongruency may be a result of low concentrations of U in solution caused by the precipitation of uranium-

containing solids following fuel dissolution (Garisto and Garisto 1986).

The first mechanism would appear to be the most probable. On the basis of experimentally measured values, the IRF of ^{90}Sr is assumed to be a uniform distribution from 0.001 to 0.3%.

Miscellaneous IRFs

Screening calculations identified approximately 30 fission products that could contribute significantly to a radiation dose and/or chemical toxicity impact as a result of the disposal of used fuel (Goodwin and Mehta, in preparation). Among these, several radionuclides could have a non-zero IRF. Additional radionuclides that are considered in estimating the instant-release source term are listed in Table 5-2. Because of the lack of data, their IRFs have been estimated using chemical analogy arguments that assume that the elements in question, which are either noble gases, halogens or alkali metals, behave like Xe, ^{135}Cs and ^{129}I. Their IRFs are, therefore, assumed to be normally distributed with μ = 8.1%, σ = 1%, a lower bound at 1.2% and an upper bound at 25%.

Summary of the Instant-Release Fractions

The parameter distribution functions for the IRF values derived here are summarized in Table 5-3. These IRFs enable the assimilation of currently available data on the short-term release of radionuclides from used fuel into source-term models for the assessment of used-fuel disposal.

5.5.1.3 The Instant-Release Source Term

The flux of instantly released radionuclides at the container-buffer interface, $G_i^I(t)$ is given by Equation (5.3) (Garisto and LeNeveu 1991). The instant-release fraction (f_i^I) is one of the variables determining $G_i^I(t)$, for a radionuclide i. In the framework of the mass transport model discussed in Chapter 6, this flux is given by

$$G_i^I(t) = \left[-D_i^B \frac{\partial C_i}{\partial x} \bigg|_{x=0} \right] I_i(t) f_i^I \qquad (5.3)$$

where x = 0 represents the container-buffer interface and $C_i(x,t)$ is a solution to the diffusion equation

$$\frac{\partial C_i}{\partial t} = \frac{D_i^B}{r_i^B} \frac{\partial^2 C_i}{\partial x^2} - \lambda_i C_i \qquad (5.4)$$

with the source boundary condition

$$p^c V^A \frac{\partial C_i}{\partial t} = I^o \delta(t) - \lambda_i p^c V^A C_i + D_i^B \frac{\partial C_i}{\partial x} \qquad \text{at } x = 0 \ . \qquad (5.5)$$

TABLE 5-2

ADDITIONAL RADIONUCLIDES OR ELEMENTS HAVING SIGNIFICANT INSTANT-RELEASE FRACTIONS

Radionuclide	Source
^{39}Ar	AP* from fuel impurities
^{42}Ar	AP* from fuel impurities
Br	Chemically toxic fission product
^{85}Kr	Fission product
^{40}K	AP* from fuel impurities
^{81}Kr	Fission product
^{87}Rb	Fission product

* AP = Activation Product

TABLE 5-3

PARAMETER DISTRIBUTION FUNCTIONS FOR INSTANT-RELEASE FRACTIONS

Radionuclide	Distribution	μ (%)	σ (%)	Cutoffs (%)
^{135}Cs	normal	8.1	1.0	1.2-25
^{129}I	normal	8.1	1.0	1.2-25
^{79}Se	normal	8.1	1.0	1.2-25
^{126}Sn	normal	8.1	1.0	1.2-25
^{99}Tc	normal	6.0	1.0	1.2-25
^{14}C	uniform	-	-	1-25
^{3}H	uniform	-	-	30-40
^{90}Sr	uniform	-	-	0.001-0.3
^{39}Ar	normal	8.1	1.0	1.2-25
^{42}Ar	normal	8.1	1.0	1.2-25
Br	normal	8.1	1.0	1.2-25
^{40}K	normal	8.1	1.0	1.2-25
^{85}Kr	normal	8.1	1.0	1.2-25
^{81}Kr	normal	8.1	1.0	1.2-25

We have used the following notations:

I^o	is a unit inventory,
$I_i(t)$	is the total inventory of radionuclide i in the vault at the time of container failure,[13]
C_i	is the pore-water concentration of radionuclide i inside the container,[14]
D_i^B	is the total intrinsic diffusion coefficient in the buffer for radionuclide i,
r_i^B	is the capacity factor of radionuclide i in the buffer,
V^A	is the volume-to-surface-area ratio of the container plus sand layer,
$\delta(t)$	is the Dirac delta function,
λ_i	is the decay constant of radionuclide i,
x	is the distance (normally) from the container surface into the buffer, and
p^c	is the capacity factor of the container.[15]

The first term on the right-hand side of Equation (5.5) represents the instantaneous release of radionuclide i, upon container and fuel sheath failure, into the void volume in the container (plus the sand layer around the container). The second term takes into account radioactive decay and the third term is the diffusional loss of the radionuclide into the buffer material.

For the purposes of defining the instant release, the buffer is considered to be semi-infinite. This is a simplifying assumption considered reasonable because groundwater transport in the surrounding backfill and rock is estimated to have only a small effect on the instant-release source term.

A discussion of the mass transport parameters D_i^B and r_i^B appears in Chapters 3 and 6.

The solution for G_i^I was obtained using Laplace transform techniques. The transformed solution was inverted analytically and the solution is given by Garisto and LeNeveu (1989).

Note that the instant-release source term was derived assuming that radionuclide transport in the buffer occurred exclusively by diffusion, because, as discussed in Section 3.5.1, it is assumed that convective flow in the buffer is negligible.

---

[13] Later in the calculation the contribution from all containers is taken into account through a convolution process (see Equation (5.19)).

[14] The concentration in the buffer pore water and the container (and sand layer) is assumed to be equal at the interface between the two.

[15] p^c is radionuclide-independent because there is assumed to be no sorption on the sand layer or the container and its contents.

Figure 5-9 shows an example of G_i^I as a function of time for ^{129}I release from used fuel for the median-value simulation compared with release of ^{129}I from congruent dissolution (see Chapter 7), calculated using IRF = 8.1%. The instant-release flux drops sharply at short times and continues to decrease gradually at long times because diffusion causes depletion of the ^{129}I inventory in the pore water in the container. It is important to note that, in this case, the instant-release source term is much higher than the corresponding ^{129}I congruent-release source term (calculated for a UO_2 solubility of 1.5×10^{-10} mol·L^{-1}) (Lemire and Garisto 1989), which represents the long-term release of ^{129}I trapped in the UO_2 grains as a result of the dissolution of the fuel matrix itself.

5.5.2 The Model for UO_2 Matrix Dissolution

5.5.2.1 The Conceptual Model

In the conceptual model, radionuclides would be released from the used-fuel matrix as it dissolved. This slow process would control the release of the major portion (~95%) of the radionuclides trapped in the used fuel. This congruent release concept is supported by long-term leaching experiments (see Section 5.2). The dissolution rate of the used fuel would be limited by the solubility of UO_2 (or U_4O_9, as discussed in Section 5.2) if the groundwater flow was slow enough for saturation to occur and if the chemical conditions in the vault were consistent with UO_2/U_4O_9 being the thermodynamically stable uranium solid. This type of model is frequently referred to as a solubility-limited dissolution model.

This type of model might not be valid if UO_2 (or U_4O_9) was not the thermodynamically stable uranium solid in the vault environment, as would be the case, for example, if oxidation of the fuel surface beyond U_4O_9 occurred. In addition, in saline groundwaters with high calcium ion concentrations, calcium/uranium solids such as calcium uranates are predicted to be more stable than UO_2 under certain groundwater conditions (Paquette and Lemire 1981, Lemire 1988). The formation of such compounds would appear to be kinetically inhibited in mildly reducing environments, however, and their occurrence is limited to oxidizing environments (Kimberley 1978, Finch and Ewing 1989).

The validity of the assumption that the used-fuel matrix can be considered thermodynamically equivalent to UO_2 is discussed below. Used fuel comprises approximately 99% UO_2 and 1% other actinides and fission products present in solid solution (actinides and lanthanides) or as interstitials and inclusions (fission products insoluble in UO_2). The effect of the elements present in solid solution on the Gibbs energy of formation of the resultant oxide is extremely small. For example, a 1% solid solution of other actinides in UO_2 would reduce the solubility by approximately 1%. The presence of insoluble interstitials and the effects of radiation damage in used fuel are not expected to affect its crystallinity. Early studies of radiation effects on UO_2 showed that used fuel retains the fluorite (uraninite) structure, modified by a slight lattice expansion and minor lattice strain (Lustman 1961). More recent data have confirmed that used and unirradiated CANDU fuels are almost indistinguishable by X-ray diffraction (Wasywich et al. 1993).

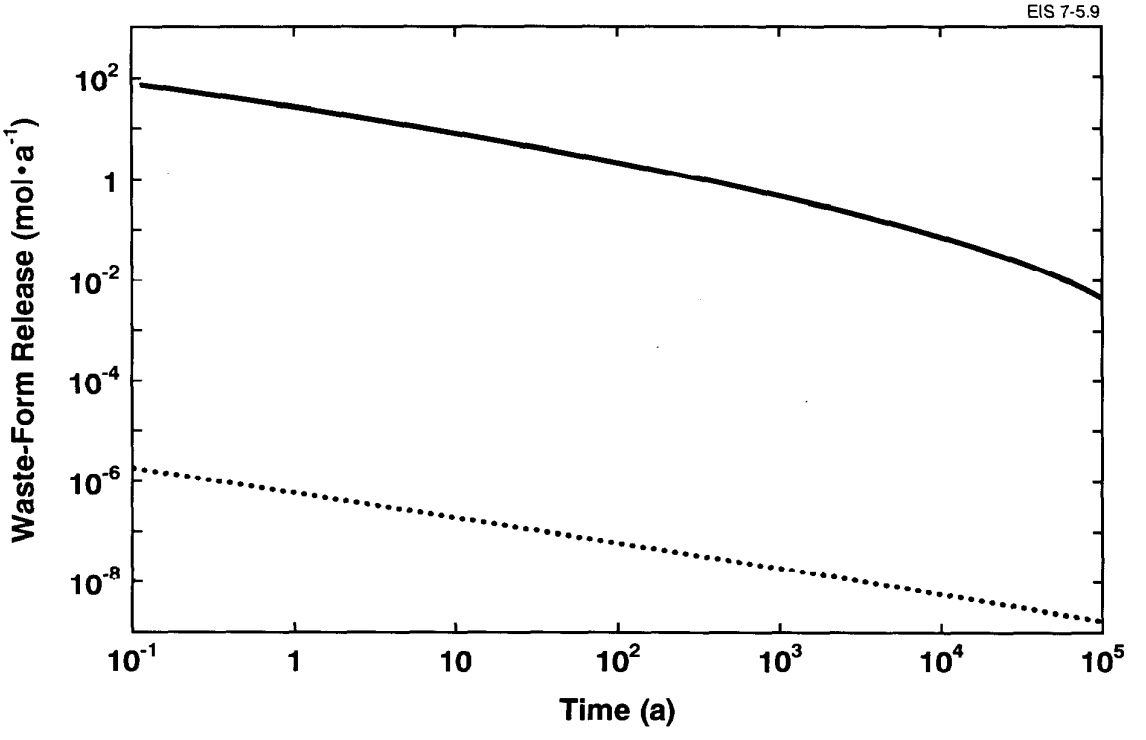

FIGURE 5-9: An Example of the Instant-Release (solid line) and the Congruent-Release (dotted line) Source Terms for ^{129}I Release from Used Fuel as a Function of Time

In the following sections, the predicted solubility of the uranium oxide matrix in the contact water is calculated, as are the solubilities of possible precipitating solids of Np, Pu, Th and Tc.

5.5.2.2 The Uranium Solubility Function

Calculation of U Concentration

The calculation of the total uranium solubility is discussed in detail by Lemire and Garisto (1989), and is summarized below.

If solution species with no more than one complexing anion contribute significantly to the solubility, then the dissolution of uranium dioxide in aqueous solution can be described by reactions of the type

$$rUO_2 + pH_2O + ne^- + qY^m = U_rO_{(2r+p)}H_vY_q^{(mq-2p-n+v)} + (2p - v)H^+ \qquad (5.6)$$

where $U_rO_{(2r+p)}H_vY_q^{(mq-2p-n+v)}$ is a solution species and Y^m is a complexing ligand. (Equation (5.6) is equivalent to Equation (5) in Lemire and Garisto (1989).)

The value of the logarithm of the equilibrium constant, K_{i298}, for Reaction (5.6) at 25°C, for the appropriate ionic strength range of the contact water (Section 5.3), is sampled from a distribution reflecting the uncertainties in log K_{i298}. The value of the equilibrium constant at the temperature of the vault is then calculated using the equation

$$\log K_{iT} = (298.15/T) \log K_{i298} + m_i(T - 298.15) \qquad (5.7)$$

and sampled values of m_i, as discussed previously for the constants for the contact-water equilibria (see Section 5.3). In this case i refers to a uranium solution species. The concentration of each solution species is calculated and expressed in terms of the equilibrium constant of Reaction (5.6), K_{iT}, the pH, the E_h and the concentration of the ligand Y^m.

For used fuel, the uranium solids for which the solubility-limited dissolution model is applied are UO_2 and U_4O_9. The size of each solid stability field varies with temperature. Above 25°C, the sampled redox potentials can extend slightly into the region of stability of U_3O_7 (see Section 5.5.3.2, Equation (5.28)). However, if we assume for simplicity that U_4O_9 (or UO_2) is the stable solid in such cases, we will overestimate the solubility of the used-fuel matrix. More importantly, for the temperature range expected in the vault, the selected potentials are always less than the potential along the U_3O_7/U_3O_8 boundary (beyond which the solubility-limited dissolution model is not necessarily valid) (Lemire and Garisto 1989).

The number of solution species that are important in determining the solubility of U, and the stoichiometry of such species, were identified from calculations using a large chemical thermodynamic database (Lemire and Garisto 1989). The ligands that were used include OH^-, F^-, HPO_4^{2-}, Cl^-, SO_4^{2-} and CO_3^{2-}. Allowance has also been made in the solubility model for two additional (as yet unspecified) trace-level ligands (for which concentrations must be sampled from distributions) that could be used to include organic complexes. Scoping calculations of the effects of organic ligands on U solubility indicate that ignoring organic complexation will have a small impact on U solubilities. These calculations are presented in Appendix D. All the aqueous species that, for any values of the pH, oxidation potential and anion concentrations within the ranges described in Table 3-1b, accounted for more than 1% of the total equilibrium concentration of U in solution were retained for the solubility calculations. Species contributing less than 1% to the total U solubility were ignored.

If the stable uranium oxide solid for the contact water is U_4O_9 rather than UO_2, the concentration of each solution species is lower than its concentration in contact with UO_2 by a factor U_F:

$$\log U_F = (E_Z - E_{UB})/(2S_E) \qquad (5.8)$$

where E_{UB} is the potential (versus the standard hydrogen electrode (SHE)) along the UO_2/U_4O_9 stability line at the temperature and ionic strength of the contact water, E_Z is the sampled potential for pH = 0, and S_E is the Nernstian slope at the temperature of interest. The values of E_{UB} at the ionic strength and temperature of the contact water are calculated from

$$E_{UB} = E_{U298} + E_{UM}(T - 298.15) \quad (5.9)$$

where E_{U298} is the value of the potential at 25°C and E_{UM} is a parameter reflecting the temperature dependence of the potential.

The total solubility for uranium from the used fuel is obtained by summing the solubility contributions of the various uranium solution species. Figure 5-10 shows the distribution of calculated uranium solubilities for 40 000 compositions of contact waters sampled from ranges in Table 3-1b at 100°C. More than 85% of the cases resulted in total uranium solubilities below 10^{-8} mol·L^{-1} at 100°C, and fewer than 3% exceeded 10^{-6} mol·L^{-1}. The high-solubility cases were traced to sampled compositions in which U_4O_9 was dissolved oxidatively to form uranium(VI) complexes (Lemire and Garisto 1989). The calculated solubilities shown in Figure 5-10 are consistent with used-fuel dissolution studies in which, under mildly reducing conditions, the measured uranium concentrations are generally below 10^{-7} mol·L^{-1} and, under oxidizing conditions, are reported to range from 10^{-7} to 10^{-4} mol·L^{-1} (see Table 5-1 and Stroes-Gascoyne 1992).

Assumptions Specific to the Solubility Model

Aside from the assumption that the composition of the contact water is such that UO_2 or U_4O_9 is the stable uranium solid in contact with the solution, which is inherent to using the solubility model for used fuel, there are several assumptions specific to the model as it has been incorporated in

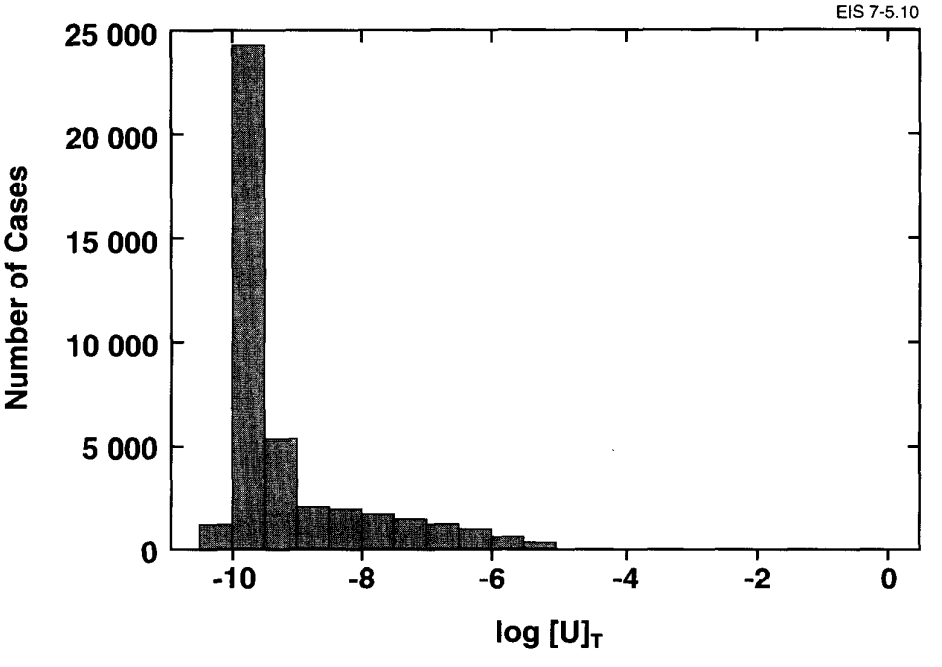

FIGURE 5-10: Distribution of the Solubility of Uranium (mol·kg^{-1}) in Contact Waters (based on 40 000 sampled contact waters) at 100°C (Lemire and Garisto 1989)

the vault model of SYVAC. These are of two types—assumptions that are part of the model as programmed, and assumptions made in the data selection.

The model does not include formation constants for HF°, $H_3PO_4^{\circ}$, PO_4^{3-}, HSO_4^- and $CaOH^+$, which only contribute to solubility under acid or strongly alkaline conditions. Therefore, the model is not valid if the pH is outside the range of 5 to 10. The probability distribution used to sample pH was triangular with a lower bound of 5, an upper bound of 10 and a mode of 8. Also, although provision is made in the model for two additional (possibly organic) complexing ligands, these ligands are restricted to species that do not undergo significant protonation or deprotonation in the selected pH range. Because of the simplified method used to estimate equilibrium constants at temperatures above 25°C (Equation (5.7)), the uncertainties in calculated solubilities increase as the temperature increases. However, because temperatures in the vault would not exceed 100°C, the increased uncertainty at the highest temperatures at which the model is applicable (i.e., 125-150°C) has no impact on the results.

The species used in the model have been selected for their importance at temperatures no greater than 125°C, and for ligand concentrations no larger than the maximum values in the contact-water distributions. Beyond these limits, other species might be required, as would revised temperature parameters. Reselection of the "important species" and their temperature parameters could be done easily; changes to the model would not be required. Different input data could be used to expand the range of ionic strength of the contact waters; indeed, many of the necessary values for one such solution have already been documented (Lemire 1988). However, extensive new experimental work would be required to estimate the constants needed to do calculations for very saline groundwaters, such as SCSB (standard Canadian Shield brine, ionic strength (I) $\simeq$7.7 $mol \cdot L^{-1}$), and the results would be specific to the particular groundwater (Lemire 1988). A discussion of the effect of such saline groundwaters on the solubilities of radionuclides is included in Chapter 8.

5.5.2.3 The Mathematical Source Term for the Long-Term Solubility-Controlled Congruent Release

The release rate, $F_i(t)$, into the buffer of a radionuclide, i, released by a solubility-controlled, congruent dissolution of the used-fuel matrix[16] is given by Garisto and LeNeveu (1989):

$$F_i(t) = \frac{I_i(t)}{I^{\circ}} F^U(t) \qquad (5.10)$$

---

[16] It should be noted that the approach is identical for calculating the release of radionuclides from the Zircaloy sheath; in this case, zirconium oxide is assumed to be the matrix material.

where $I_i(t)$ is the molar inventory of the radionuclide, i, in the used-fuel matrix in the vault,
I^o is the molar inventory of the used-fuel matrix in the vault at time t = 0, and
$F^U(t)$ is the dissolution rate of the used-fuel matrix; i.e.,

$$F^U(t) = \left[-D^B \left. \frac{\partial C}{\partial x} \right|_{x=0} + v^B C(0,t) \right] A^F \qquad (5.11)$$

where A^F is the vault surface area (see Table 2.1) and C(x,t) is the solution to the diffusion-convection equation,

$$\frac{\partial C}{\partial t} - \frac{D^B}{r^B} \frac{\partial^2 C}{\partial x^2} + \frac{v^B}{r^B} \frac{\partial C}{\partial x} + \lambda C = 0 \qquad (5.12)$$

with a constant-concentration boundary condition at x = 0,

$$C(0,t) = C^s \qquad (5.13)$$

and a mass transfer coefficient boundary condition at the exit from the buffer (see Chapter 6).

We have used the following notations:

C(x,t) is the concentration of uranium in the buffer pore water,
λ is the decay constant of ^{238}U in the used-fuel matrix,
C^s is the solubility of uranium in the pore water,
D^B is the total intrinsic diffusion coefficient for uranium in the buffer,
v^B is the Darcy velocity in the buffer (assumed to be 0, as discussed in Chapter 3),
r^B is the capacity factor of uranium in the buffer, and
x is the distance (normally) from the container surface into the buffer.

A discussion of the mass transport parameters (i.e., D^B, v^B and r^B) is given in Chapters 3 and 6.

The initial conditions are

$$C(x,0) = 0 \qquad 0 \le x \le a^B \qquad (5.14)$$

where a^B is the thickness of the buffer and t = 0 is the time at which the first container fails.

The solution for $F^U(t)$ is given by Garisto and LeNeveu (1991). The solution was obtained using Laplace transform techniques and the transformed solution was inverted analytically (LeNeveu 1987).

5.5.3 Precipitation Models

The vault model accounts for the precipitation of radionuclide solids in the vault. Two aspects of radionuclide precipitation are explicitly considered:

1. The vault model takes into account individual radionuclide solubilities. Specifically, if the calculated concentrations of given isotopes (other than U) at x = 0 (i.e., inside the containers) exceed their solubility limits, the vault model simulates their precipitation. The subsequent dissolution of the precipitate results in a smaller release rate into the buffer than if precipitation had not occurred. The data and the conceptual model for this effect are described in Section 5.5.3.1

2. The vault model simulates the potential precipitation of U-containing solids in the buffer at a distance from the dissolving used-fuel matrix determined by the redox gradient (see Section 5.5.3.2). Such precipitation limits the release of U from the buffer, but could lead to an enhancement of fission product release from the vault (see Section 5.5.3.2).

5.5.3.1 Individual Radionuclide Solubilities

The vault model simulates precipitation of radionuclides inside the containers following release from the fuel, if the individual concentration of a given isotope of the radionuclide exceeds the calculated solubility (Garisto and LeNeveu 1991). The calculation of the limiting concentrations of Np, Pu, Th and Tc in the groundwater is discussed in detail by Lemire and Garisto (1989), and the procedure is summarized below. For all other radionuclides, many of which are expected to have high solubilities, the maximum solubilities are set at 2 $mol \cdot L^{-1}$ to ensure that precipitation does not occur.

In the used fuel, the actinides Th, Np and Pu are in solid solution occupying U crystallographic sites in the UO_2 grains. Therefore, they are released congruently from the fuel in direct proportion to their concentrations as the UO_2 dissolves. The transport of these elements and some of the fission products released from the fuel may be restricted by precipitation. Thus, for example, if the dissolution rate of the UO_2 is fast enough that the Pu concentration near the fuel exceeds the solubility limit of a solid Pu compound under the expected vault conditions, then the Pu in solution could precipitate and the rate of release of Pu from the vault to the geosphere would decrease. In the vault model, precipitation of U, Pu, Np, Th and Tc is considered (see Section 5.5.3.2 for a discussion of the redox potential in the buffer). For a given simulation, the same sampled values for contact-water parameters are used for all solubility calculations.

Frequently, the amorphous form of a solid is precipitated first rather than the crystalline form; i.e., the solution becomes supersaturated with respect to the crystalline solid. Therefore, for our solubility model we

assume that precipitation of Np, Th and Pu occurs only if the concentrations of these elements exceed the solubility limit for the amorphous form of the corresponding oxides: $Np(OH)_4(s) \equiv$ hydrated $NpO_2(am)$, $ThO_2(ppt)$ and $Pu(OH)_4(s) \equiv$ hydrated $PuO_2(am)$. This assumption is conservative in that the calculated actinide releases to the geosphere would be lower if precipitation of the crystalline oxides were to occur.

As described in Section 5.5.2.2 for U, the total solubilities of Np, Pu, Th and Tc dioxides (or hydrated amorphous dioxides) are obtained by summing the solubility contributions of the species. The number of solution species that are important in determining the solubility of each element, and the stoichiometry of such species, were identified from calculations using a large chemical thermodynamic database (Lemire and Garisto 1989). All the aqueous species that, for any value of the pH, oxidation potential and anion concentrations within the ranges described in Table 3-1b, accounted for more than 5% of the total solubility of Np, Pu, Th and Tc were retained for the solubility calculations (as opposed to the 1% cutoff for U species). However, in many cases the selected sets of species (i.e., those that accounted for >5% of the total solubility) reproduce the solubilities calculated using the full databases to better than 1%. For example, in the case of Tc, the use of only the selected species reproduces the solubility calculated using the full thermodynamic database to better than 0.5% under all conditions. For Pu the solubility is reproduced to within 1% under all conditions and to better than 0.5% for pH $\geq$ 6.0. For Th, the maximum deviation is less than 1% for all conditions. For Np the selected species reproduce the solubility to better than 2% under all conditions and better than 0.5% for pH values <8.5. Distributions of solubilities of Tc, Pu, Th and Np are shown in Figures 5-11 to 5-14.

Because of the scarcity of reliable activity coefficient data for species of these elements, no effects other than complexation are taken into account in the calculation of the solubilities. Nevertheless, provision has been made in the vault model, as incorporated in SYVAC CC3, to allow ionic strength effects to be introduced in the same manner as described above for U (see Section 5.5.2.2).

In the vault model a portion of the Tc inventory is assumed to be released immediately into the contact water at the time a container fails (Section 5.5.1.2); the rest of the inventory is released congruently as the used-fuel matrix dissolves. Both TcO_2 and metallic technetium (Tc(cr)) have wide ranges of stability within the potential-pH range of the contact waters, and the solubility of each solid, in its range of stability, can vary by many orders of magnitude. Therefore, both solids have been considered as possible precipitated phases of Tc in the vault.

If the stable Tc solid for the contact water is metallic Tc (Tc(cr)) rather than TcO_2, the concentration of each solution species is lower than the concentration over TcO_2 by a factor $(T_F)^r$ (r is the stoichiometric number of Tc atoms in the Tc solution species).

$$\log T_F = 4(E_{TB} - E_z)/S_E \qquad (5.15)$$

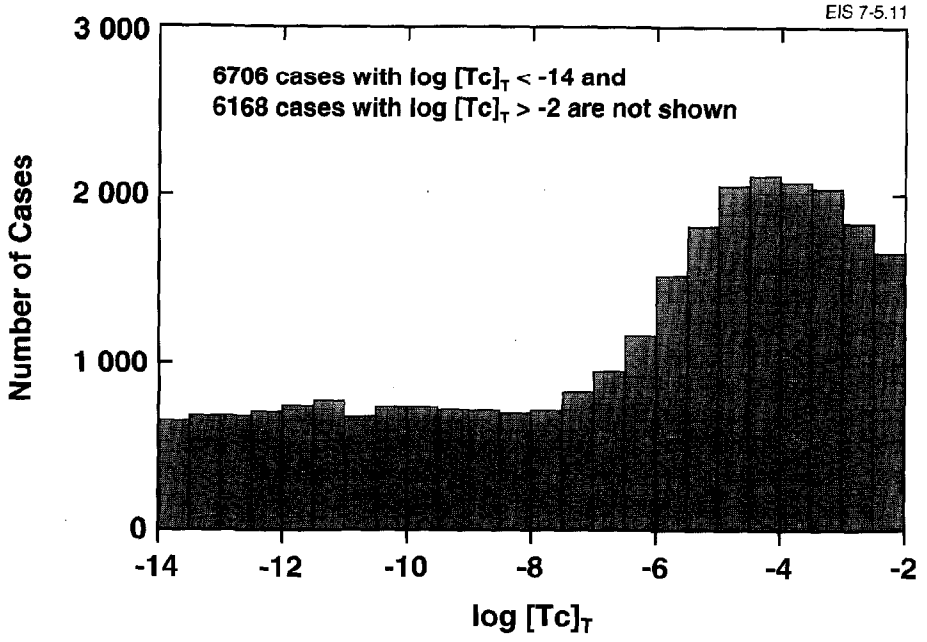

FIGURE 5-11: Distribution of the Solubility of Tc ($mol.kg^{-1}$) in Contact Waters (based on 40 000 sampled contact waters) at 100°C (Lemire and Garisto 1989)

where E_{TB} is the potential (versus the SHE) along the Tc/TcO_2 stability line, i.e., the potential for the reaction

$$TcO_2 + 4H^+ + 4e^- = Tc(cr) + 2H_2O \qquad (5.16)$$

at the temperature and ionic strength of the contact water, S_E is the Nernstian slope and E_z is the sampled redox potential for pH = 0.

The broad range of Tc solubilities calculated for 6000 simulations with the vault model is shown in Figure 5-15.

The values of E_{TB} at the temperature of the contact water are calculated from

$$E_{TB} = E_{T298} + E_{TM}(T - 298.15) \qquad (5.17)$$

where E_{T298} is the value of the potential at 298 K (25°C), and E_{TM} is a parameter reflecting the temperature dependence of the potential.

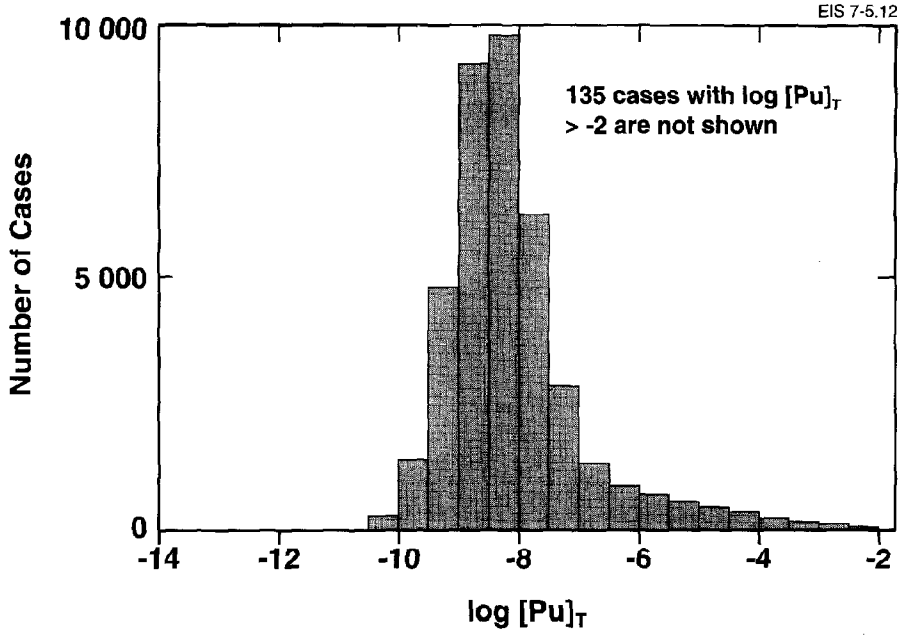

FIGURE 5-12: Distribution of the Solubility of Pu ($mol \cdot kg^{-1}$) in Contact Waters (based on 40 000 sampled contact waters) at 100°C (Lemire and Garisto 1989)

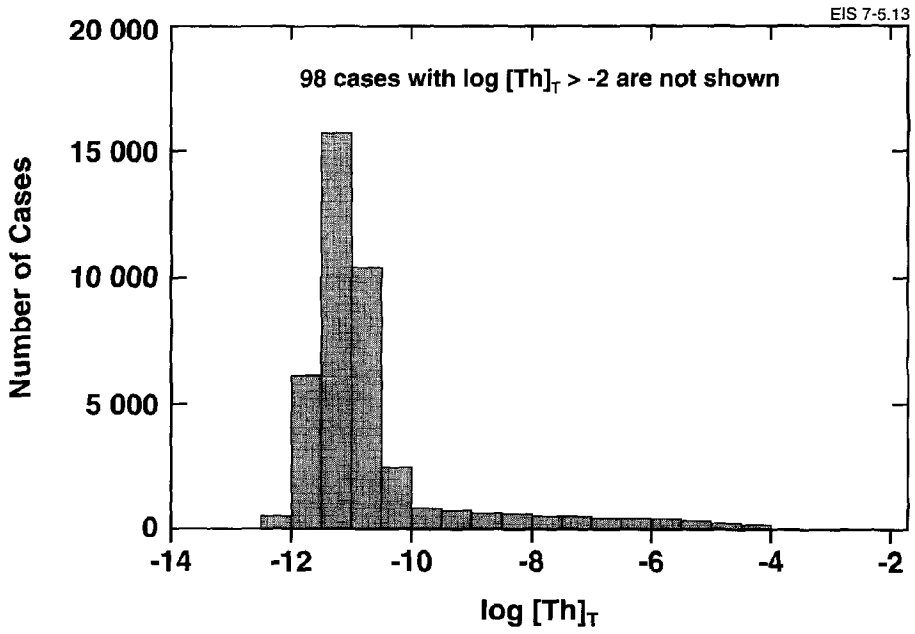

FIGURE 5-13: Distribution of the Solubility of Th ($mol \cdot kg^{-1}$) in Contact Waters (based on 40 000 sampled contact waters) at 100°C (Lemire and Garisto 1989)

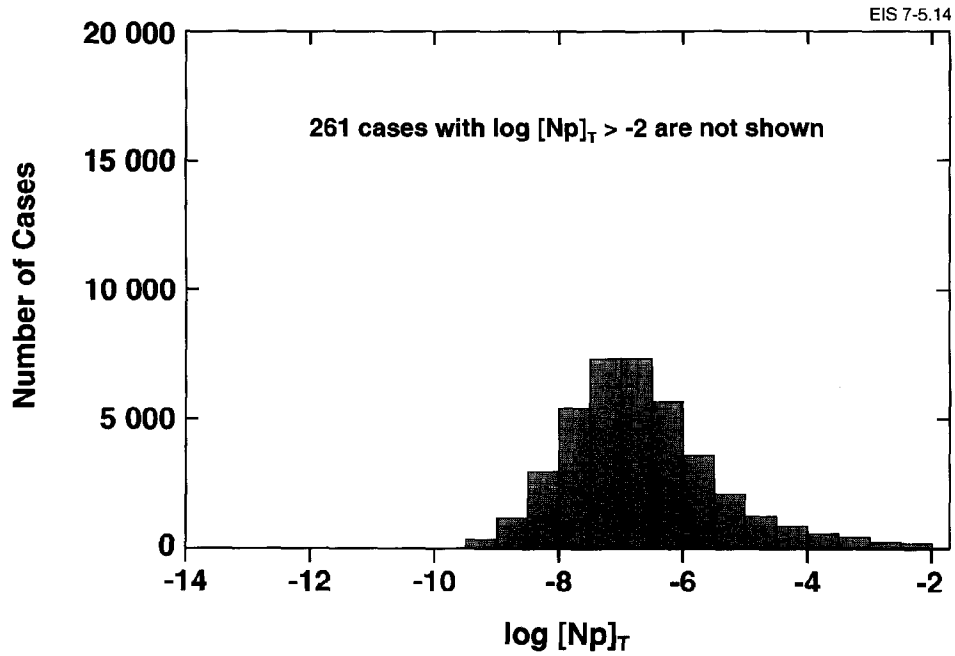

FIGURE 5-14: Distribution of the Solubility of Np ($mol \cdot kg^{-1}$) in Contact Waters (based on 40 000 sampled contact waters) at 100°C (Lemire and Garisto 1989)

The selected species and the values or distributions of all of the parameters used in the solubility calculations are described in Lemire and Garisto (1989).

Precipitation is simulated in the vault model using the compartmental model (Andres, in preparation) from the SYVAC executive program (Goodwin et al. 1987). The compartment used for precipitation is a mathematical construct at x = 0 (i.e., inside the container) in which precipitation is simulated; i.e., we deal with precipitation by allowing it to occur inside the container rather than simulating it elsewhere in the vault. Recent calculations (Garisto and Garisto, in press) have shown that precipitation of radionuclides away from the dissolving fuel (rather than at x = 0) further decreases the release from the vault to the geosphere. Therefore, the compartmental model (applied at x = 0) is conservative.

To determine whether precipitation of radionuclide i occurs, the instant release, $G_i^I(t)$, and congruent release, $F_i(t)$, from the entire used-fuel inventory in the vault are summed to obtain $F_i^W(t)$:

$$F_i^W(t) = G_i^I(t) + F_i(t) \quad . \tag{5.18}$$

$F_i^W(t)$ is then convoluted with the container failure rate to obtain the container failure modified release rate from the used fuel, $F_i^T(t)$:

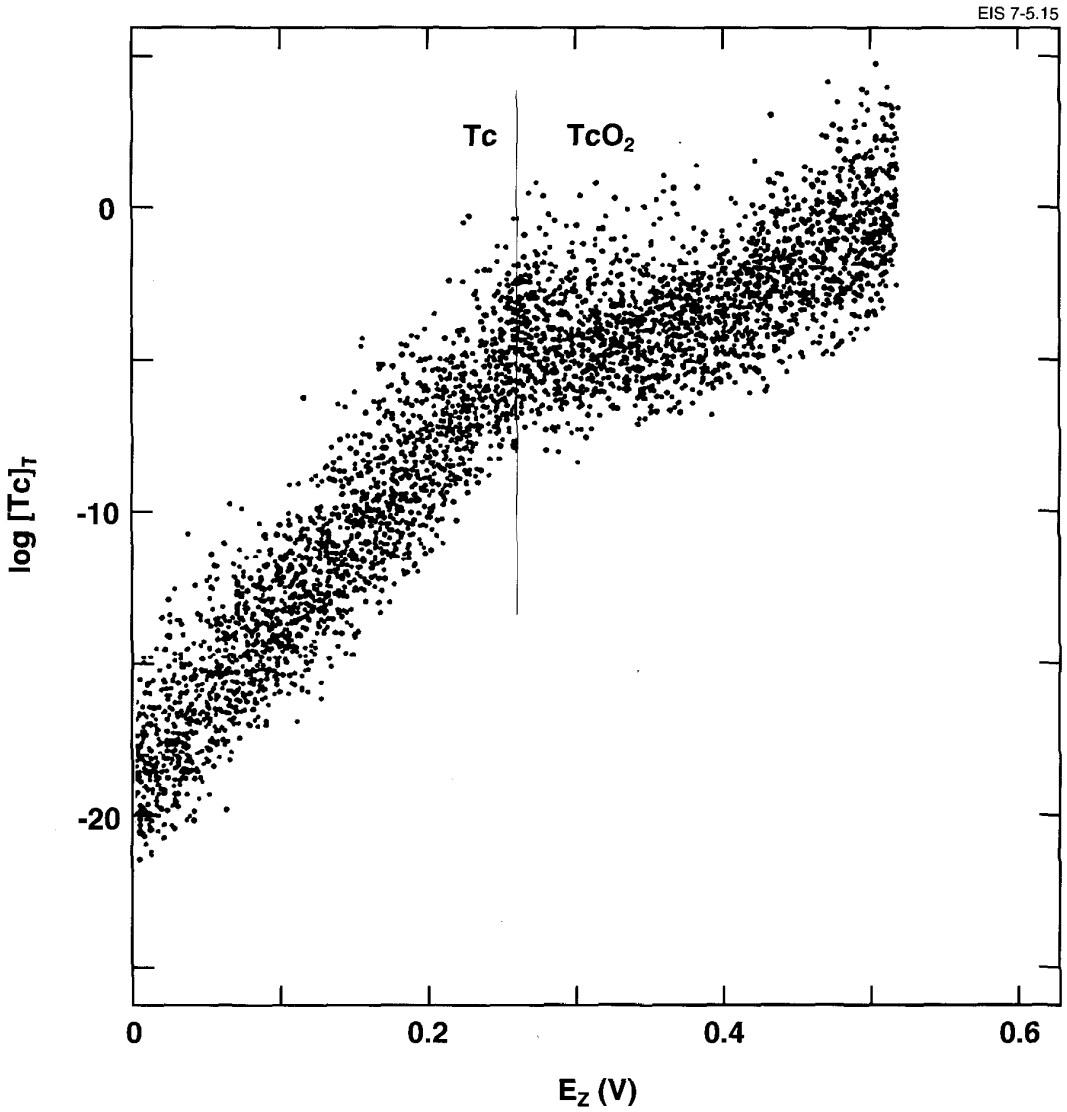

FIGURE 5-15: Solubility of Tc (mol·kg^{-1}) in the Vault as a Function of E_z (potential at pH = 0 versus the SHE) for 6000 Simulations Using the Vault Model

$$F_i^T(t) = \sum_{j=1}^{i} \int_0^t F_j^W(t-t') f_{ij}^c(t')\, dt' \qquad (5.19)$$

where the summation is over all the precursors, j, of radionuclide i.

$$f^c_{ij}(t) = f^c(t) \sum_{k=j}^{i} \exp(-\lambda_k t) x^j_{ik} \qquad (5.20)$$

where $f^c(t)$ is the container failure rate and x^j_{ik} are the Bateman coefficients used to determine the change in the initial inventory of radionuclide i due to radionuclide transformations up to the time of failure. Equation (5.20) is required because as each new container fails, the initial inventory in that container has changed somewhat as a result of radioactive transformation.

Next, the container failure modified release rate, $F^T_i(t)$, is compared with the container failure modified release rate as determined by radionuclide solubility, $F^P_i(t)$,

$$F^P_i(t) = \frac{I_i}{I^\circ} \int_0^t F^S_i(t') f^c(t-t')\, dt' \quad \text{for uranium isotopes} \qquad (5.21)$$

$$F^P_i(t) = \int_0^t F^S_i(t') f^c(t-t')\, dt' \quad \text{for all other isotopes} \qquad (5.22)$$

where $F^S_i(t)$ is given by the solution to Equations (5.10) to (5.14) with the solubility of the radionuclide, i, used instead of the solubility of the UO_2. For the determination of $F^P_i(t)$, the contributions from precursors as determined by the Bateman coefficients are not required because $F^S_i(t)$ does not depend on radionuclide inventory.

Note that in considering elemental solubilities we ignore the contributions to the concentration from other isotopes of the same radionuclide arising from other decay chains, except for uranium isotopes. This is a conservative assumption.

If $F^T_i(t)$ exceeds $F^P_i(t)$, then a precipitate will form. When there is a precipitate the release to the buffer, $F^A_i(t)$, is given by $F^P_i(t)$ rather than $F^T_i(t)$. The amount of the precipitate accumulated is given by the difference of $F^T_i(t)$ and $F^P_i(t)$, the decay constant, λ_i, and the contribution to the precipitate from the ingrowth of a precipitated parent, $P_{i-1}(t)$. If $F^T_i(t)$ falls below $F^P_i(t)$ some time after the precipitate forms, the release to the buffer is still determined by $F^P_i(t)$ until all the precipitate redissolves. The mathematical statement of these conditions is given by Equations (5.23) to (5.27) below. These equations make up a compartment model that represents precipitation of radionuclides in the containers.

If $F^T_i(t)$ exceeds $F^P_i(t)$, or any amount of precipitate, $A_i(t)$, where $A_i(t)$ is calculated according to Equation (5.26) below, has accumulated, then the release to the buffer, $F^A_i(t)$, is given by $F^P_i(t)$. That is, if

$$A_i(t) > 0 \text{ or } F^T_i(t) > F^P_i(t) \text{ then } F^A_i(t) = F^P_i(t) \qquad (5.23)$$

otherwise $F_i^A(t) = F_i^T(t) + P_{i-1}(t)$ (5.24)

where $P_{i-1}(t)$, the contribution to $F_i^A(t)$ from the decay of a precipitated parent is given by

$$P_{i-1}(t) = \lambda_{i-1} A_{i-1}(t) \tag{5.25}$$

and
$$A_i(t) = \int_0^t F_i^T(t-t') R_i^P(t')\, dt' - \int_0^t F_i^P(t-t') R_i^P(t')\, dt' + \int_0^t P_{i-1}(t-t') R_i^P(t')\, dt' \tag{5.26}$$

where
$$R_i^P(t) = e^{-\lambda_i t} \quad . \tag{5.27}$$

In Equation (5.26), the first term represents the time integration of the total radionuclide release into the containers, including decay; the second represents the time-integrated solubility-limited output from the containers into the buffer, including decay; and the third represents the time-integrated contribution to the amount accumulated within the containers from the decay of the parent.

The solution to this system of equations, provided by the compartment model in the SYVAC executive program, uses time series routines with an adaptive time-stepping package for evaluation of the convolution integrals. The accuracy of the solutions can be controlled through an input variable in the input file. Typically, the input variable is set so that the estimated error in the time-integrated value of the quantities $F_i^T(t)$, $F_i^P(t)$ and $A_i(t)$ will be less than 0.5%.

5.5.3.2 The Effect of Mass Transport-Precipitation Coupling on the Long-Term Release of Radionuclides from Used Fuel

In the solubility-limited dissolution model, the rate of fuel dissolution is controlled by mass transport of dissolved uranium species into the buffer. Thus, if the transport of dissolved uranium is slow, the finite solubility of uranium limits the rate of fuel dissolution.

Inhomogeneities, such as temperature, concentration of groundwater components (e.g., calcium ions), or redox-potential gradients (determined by radiolysis and redox species), might cause the solubility of UO_2 to vary from location to location in the vault. Such solubility differences could lead to gradients in U concentration and, hence, diffusion of U down the concentration gradient as a result of precipitation of U-containing solids at some distance from the dissolving fuel. This precipitation, if it persisted for long times, would lead to enhanced transport of uranium from one location to another (Garisto 1986). Redox-potential gradients, for example, are important in uranium ore deposition (Langmuir 1978). Precipitation of solids that contain uranium, in the buffer, would increase the concentration gradient when the solubility of the precipitate is much smaller than the solubility of UO_2 and, hence, increase the dissolution

rate of the used-fuel matrix (Garisto 1986, Garisto and Garisto 1986). This would also result in an increase in the release rate of radionuclides in the fuel matrix (Paquette and Lemire 1981, Garisto and LeNeveu 1989).

The enhancement of the dissolution rate of used fuel as a result of the mass transport-precipitation coupling effect (i.e., the enhancement factor) has been investigated in detail using analytical (Garisto and Garisto 1988a) and numerical (Garisto and Garisto 1986, 1988b) mass transport models. Quantitative estimates of the dissolution enhancement factor were derived for fuel dissolution under probable disposal vault conditions (Garisto and Garisto 1986, Garisto and LeNeveu 1989) (see Figure 5-16).

Upper bounds on the release enhancement factor were determined (Garisto and Garisto 1988a), and explicit expressions for the asymptotic ($t \rightarrow \infty$) behaviour of the fuel dissolution rate were derived (Garisto and Garisto 1988b).

The results indicate that the enhancement factor is small ($\simeq 1$) at times less than 100 a for precipitation distances $\gtrsim 3$ cm from the dissolving interface, and that it increases with time (see Figure 5-16). For finite system geometries (such as the used fuel/buffer system), the enhancement factor approaches a constant value as $t \rightarrow \infty$. Thus, precipitation of U-containing solids in the buffer limits the release of U and coprecipitating elements into the geosphere, but may enhance significantly the dissolution rate of the used fuel, thereby increasing the release rate of radionuclides that dissolve congruently with the used fuel and do not themselves precipitate.

Finally, the calculations of Garisto and Garisto (1986) show that the enhancement factor depends strongly on the magnitude of the concentration gradient near the used fuel/buffer interface (see also Apted et al. 1989b). Since the solubility of used fuel is largely controlled by redox conditions, it is important to ensure that the effects of a redox potential gradient are included in the dissolution model through incorporation of mass transport-precipitation coupling effects.

The sequence of events being analyzed using SYVAC simulations includes such mass transport-precipitation coupling. In the vault model, it is assumed that there would be a redox gradient in the buffer, with the system potential, E^z, being more oxidizing (larger) at the used-fuel surface (because of α-radiolysis) than in the buffer. For the buffer/backfill material, it is assumed that iron-bearing silicates and magnetite would react with any dissolved oxygen present in the vault when it is sealed, resulting in a low redox potential, possibly close to the magnetite-hematite buffer potential ($E^\circ \simeq +200$ mV_{SHE} at 70°C). The formation of persistent, metastable ferric oxides/hydroxides would be likely, however, and could result in significantly more oxidizing potentials, up to a few hundred millivolts more positive than the crystalline magnetite/hematite buffer. Hereafter, the various ferric oxide and hydroxide phases are collectively referred to as Fe(III) oxide.

The magnetite/Fe(III) oxide redox potential can be related to the solubility of the Fe(III) oxide phase. At 25°C, the redox potential increases by 177 mV for every order of magnitude by which the oxide solubility product

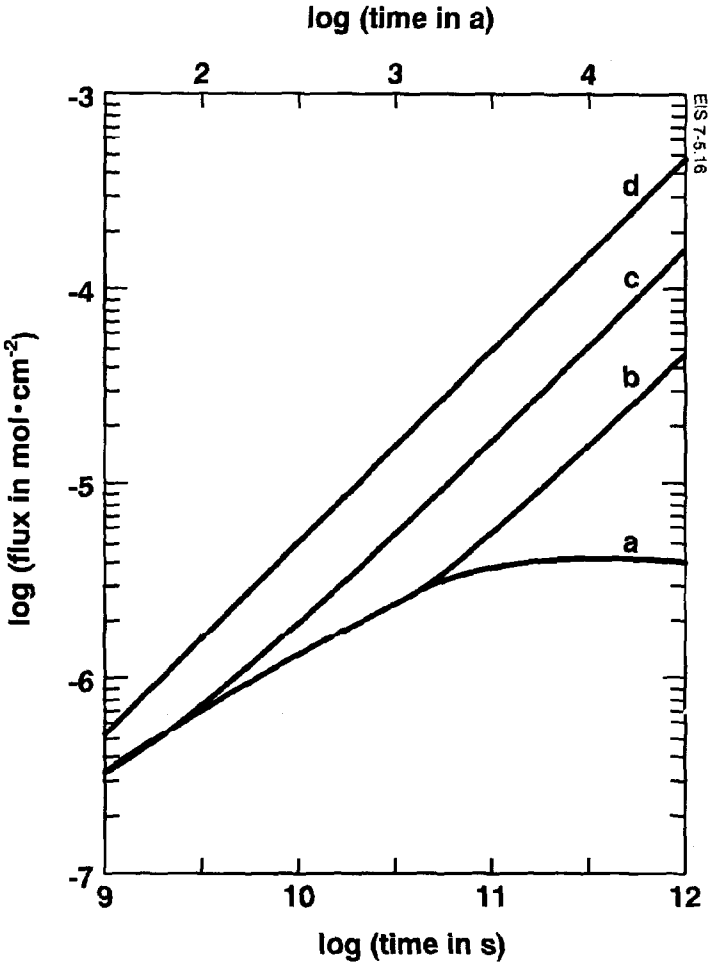

FIGURE 5-16: Cumulative Release Flux, F, as a Function of Time (Garisto and Garisto 1986): (a) No Uranium Precipitation in the Buffer; (b), (c) and (d), Uranium Precipitates at 20, 5 and 1 cm Respectively from the Fuel Buffer Interface

exceeds that of coarsely crystalline hematite. Both the particle size and crystallographic form of the Fe(III) oxide are important factors in determining the oxide solubility and, hence, the redox potential of the magnetite/Fe(III) oxide assemblage (Langmuir 1969, 1971). Solubilities of Fe(III) oxide phases span about five orders of magnitude at 25°C, or about 3.5 orders of magnitude if the most ephemeral amorphous solids are ignored (Langmuir 1969, Lindsay 1988).

The relative ease of crystal ripening and interconversion of Fe(III) oxide and hydroxide phases is strongly dependent on solution chemistry (Blesa and Matijevic 1989, Cornell et al. 1989). It is likely, however, that only

goethite or hematite would persist at vault temperatures. Coarse-grained goethite and hematite have almost identical stability and solubility in water at 70°C, goethite becoming marginally more stable than hematite at lower temperatures (Langmuir 1971). Particle size effects are therefore likely to predominate in determining the magnetite/Fe(III) oxide redox potential.

Making some allowance for aging of the Fe(III) oxide under vault conditions, we estimate a likely range of 1.5 orders of magnitude in solubility at 25°C. This corresponds to a minimum effective cubic particle size of 25 nm for goethite, or <10 nm for hematite (Langmuir 1971). This solubility range is equivalent to a range of 265 mV in magnetite/Fe(III) oxide potential at 25°C, with the theoretical crystalline-phase potential defined as the lower limit. Since the particle size effect is predominantly enthalpic, a similar range of potentials at 70°C is expected; thus, the sum of the magnetite-hematite potential (200 mV) and this 265-mV range has been rounded to a value of 470 mV for the maximum potential that has been incorporated in the model.

Two solubilities of the uranium, C^N and C^P, determined by two different system potentials, are calculated by the method described in Section 5.5.2.2, the first at the used-fuel surface and the second at a distance, a^u, in the buffer.

The redox potential at the used-fuel surface, E_I^z, is sampled from a uniform distribution between 0 and 516 mV (see Section 5.3). The potential in the buffer, E^P, is calculated from the following equation:

$$E^P = E_M^z + R^B(\min(E_I^z, E_X^P) - E_M^z) \qquad (5.28)$$

where E_M^z is the minimum system potential ($E_M^z = 0$),

E_X^P is the maximum buffer potential, and

R^B is the random factor sampled from a beta distribution characterized by an upper limit and two shape parameters. These are given in Table 5-4 and are chosen such that E^P will be a uniform distribution between E_M^z and E_X^P.

The conditions for precipitation of uranium oxides to occur have been investigated by Garisto and Garisto (1988b). If the solubility of uranium in the buffer is less than the steady-state concentration obtained without precipitation, then precipitation is considered to occur.

If precipitation occurs, the dissolution rate of the fuel is determined from Equations (5.10) to (5.14) with $C^S = C^N - C^P$ and using a distance over which the concentration gradient occurs (gradient length) equal to a^u instead of the buffer thickness a^B ($a^u \leq a^B$). As a^u becomes smaller, the concentration gradients increase and the dissolution rate increases in an unbounded fashion. The lower limit on a^u is found by taking the minimum of a^B and $(D_u^B/\alpha^u + a^I)$ where D_u^B is the total intrinsic diffusion coefficient for uranium species, α^u is the dissolution rate constant for UO_2, and a^I is

the initial value of the gradient length in the buffer (i.e. $0 \leq a^I \leq 0.25$ m).

The values of the parameters used in calculations of mass transport-precipitation coupling in the model are summarized in Table 5-4.

The limiting value for the gradient length, D_u^B/α^u, as a^I tends to zero was obtained from Equation (20) of Garisto and Garisto (1988b). The value of α^U was derived from a study by Stroes-Gascoyne et al. (1986). In Garisto and Garisto's formulation, a kinetic constraint was included to limit the dissolution rate as the gradient length approached zero (without which the dissolution rate would become infinite). We determined an equivalent minimum gradient length given by D^B/α^u that, when used with the dissolution rate Equations (5.11) to (5.14), will give the same minimum dissolution rate given by the kinetic constraint in the study by Garisto and Garisto (1988a). This will result in a small overestimate in the radionuclide release rate for congruently released radionuclides in the vault model.

When precipitation occurs, the release of ^{238}U into the geosphere is determined from the dissolution rate of the precipitate (i.e., Equation (5.13) with $C^s = C^p$). Note that for U, the contribution of different U isotopes from different decay chains to the concentration has been taken into account in the vault model.

5.6 NATURAL ANALOGUES

In the conceptual disposal vault, radionuclides contained in the used-fuel matrix would be released by congruent dissolution, with the solubility of

TABLE 5-4

PARAMETER DISTRIBUTION FUNCTIONS FOR

MASS TRANSPORT-PRECIPITATION COUPLING OF URANIUM

Parameter Name	Symbol	Distribution	Lower Limit	Upper Limit	Shape Parameter 1	Shape Parameter 2
System Potential	E_I^Z	uniform	0.0 V	0.516 V	-	-
Maximum Buffer Potential	E_X^P	constant	0.47 V	0.47 V	-	-
Random Factor	R^B	beta	0.0	1.0	5.0	0.5
Dissolution Rate Constant	α^U	uniform	3.15 m/a	6.30 m/a	-	-
Initial Gradient Length	a^I	uniform	0.0 m	0.25 m	-	-

UO_2 (or U_4O_9) controlling the dissolution rate. Since the dominant solid uranium phase found in many natural uranium ore deposits is also UO_2, these mineralizations have been studied as analogues for fuel-matrix dissolution (Cramer 1994). The study of UO_2 stability during the geological evolution of a mineralization can provide quantitative information on the dissolution of used fuel in a disposal vault.

5.6.1 The Cigar Lake Deposit

The high-grade uranium deposit found near Cigar Lake in northern Saskatchewan has been studied since 1984 by AECL in co-operation with COGEMA Resources Inc. and the Cigar Lake Mining Corporation. Subsequently, AECL and the Swedish Nuclear Fuel and Waste Management Company (SKB) jointly funded a three-year research program from 1989 to 1992, and since 1991 AECL and the U.S. Department of Energy (USDOE) have been collaborating in a five-year research program. The main uranium mineral in the Cigar Lake deposit is UO_2 (uraninite), with a chemical composition very similar to that of the used-fuel matrix of CANDU UO_2 fuel. The estimated inventory of U in the Cigar Lake deposit is comparable to that of the disposal vault for the case study. Geochronological, mineralogical and chemical data for the Cigar Lake ore indicate that UO_2 has survived with minimal dissolution during 1.3×10^9 a of contact with groundwater. This has contributed to the lack of any direct evidence, on the present-day ground surface, of the rich uranium ore body at a depth of 430 m.

Detailed study of the groundwater composition in the deposit at Cigar Lake indicates that dissolved U concentrations are consistently low, even when the groundwater is in contact with the ore. The average grade of the deposit is 7.9 wt.% U; high-grade zones range up to 55 wt.% U. Dissolved U concentrations in groundwater from the ore zone are below 10^{-6} mol·L^{-1} and average 10^{-9} mol·L^{-1} in waters from outside the ore zone (Cramer 1986; Cramer et al. 1987; Cramer and Nesbitt, in preparation). These concentrations, in waters with pH values between about 6 and 8, and E_h values between about -250 and +250 mV (Figure 5-17), are consistent with the low solubility of uranium calculated in the vault model (Figure 5-10).

The very low dissolved uranium concentrations in Cigar Lake groundwaters indicate reducing conditions corresponding to the observed mineralogy. The uranium oxide in the ore zone is associated with sulphides and reduced organic phases. Analysis of high-resolution X-ray photoelectron spectroscopy (XPS) spectra show that the oxidation state of uranium on the surface of these minerals is equal to, or lower than, that of U_3O_7 (Sunder et al. 1988, 1992). X-ray diffraction (XRD) data confirm the presence of an oxidized phase, most likely α-U_3O_7, in addition to UO_2. Scanning electron microscopy (SEM) images show that the surface of the UO_2 crystals consists of a layer of crystals <1 μm in size, which have been tentatively identified as U_4O_9-U_3O_7 mixtures. Although the hydraulic conductivity of the ore zone is low, and much of the uranium mineralization occurs inside a clay matrix, the ore zone is, and most likely has always been, saturated with groundwater that has reacted with the uranium minerals producing surface layers of higher oxidation products. Thus, even though, locally, uraninite crystals may not be in contact with water, the bulk of the mineralization is water-saturated. Calculations based on the presence of U_3O_7 in contact

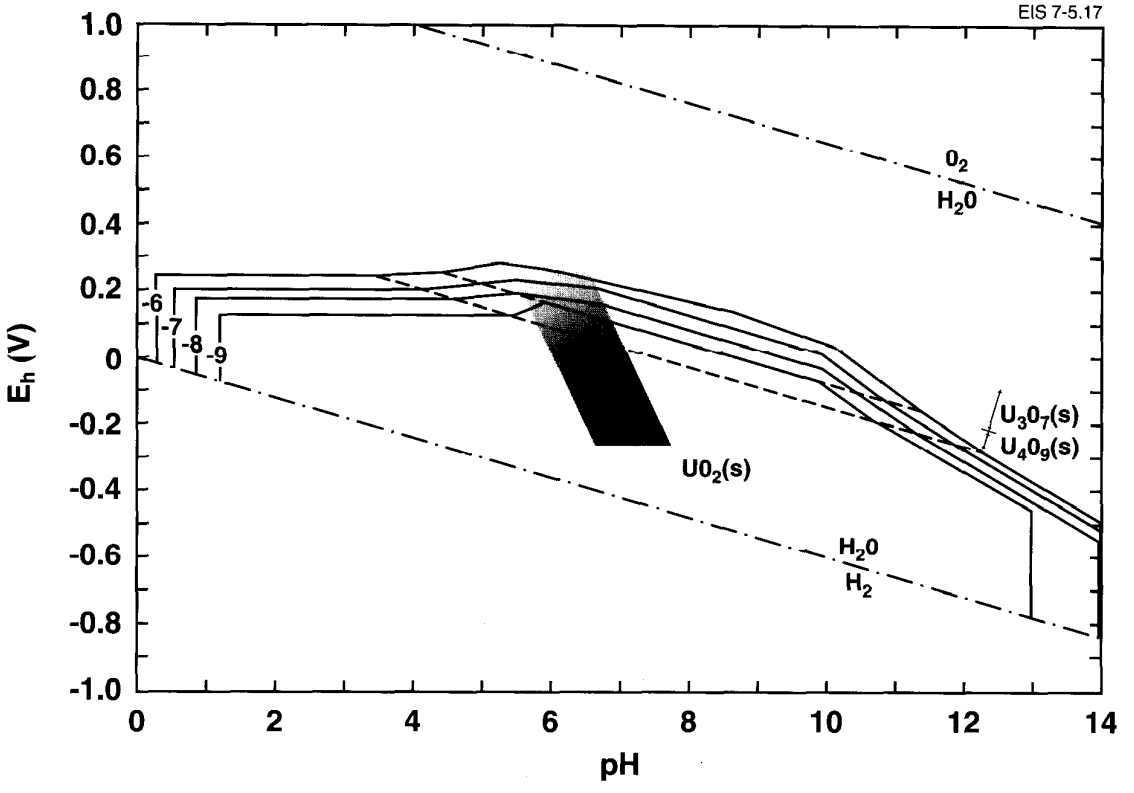

FIGURE 5-17: Isosolubility Diagram for Uranium Oxides in Cigar Lake Groundwaters at T = 25°C and 0.1 MPa. The shaded area on the E_h-pH diagram includes the data points for groundwaters from the ore zone. The contours -6 to -9 represent total dissolved uranium from 10^{-6} to 10^{-9} mol.L^{-1} U.

with groundwater, containing uranium concentrations in the range from 10^{-7} to 10^{-9} mol.L^{-1}, indicate an upper limit for the oxygen fugacity of about 10^{-40} Pa. Measured E_h values in groundwater from the ore zone range between about -250 and +100 mV_{SHE}, which are consistent with such a low oxygen fugacity (Cramer and Nesbitt, in preparation). This information supports observations from experimental work on the oxidation and dissolution of UO_2 fuel (Shoesmith et al. 1984), which shows that the dissolution rate of the UO_2 does not become significant until it is oxidized beyond the $UO_{2.33}$ (U_3O_7) stage. A contributing factor to the overall reducing nature of the groundwaters in the deposit is microbial activity, such as the presence and activity of sulphate-reducing bacteria in the ore zone (Cramer and Smellie 1993).

Further evidence for the integrity of primary uraninite crystals is obtained from the determination of the abundances of radioisotopes from the natural fission in the high-grade mineralization. This natural fission has occurred since the formation of the primary mineralization and continues

today, producing extremely small quantities of fission and activation products. Data obtained for ^{239}Pu and ^{129}I concentrations in uranium ore samples from Cigar Lake indicate that the ore contains relatively high abundance ratios for both isotopes (~1.9×10^{-12} $^{239}Pu/U$ and ~2.1×10^{-12} $^{129}I/U$ (Fabryka-Martin and Curtis 1993)). If one assumes that the uranium ore has been water-saturated during at least the last few million years, these data support the congruent dissolution model for UO_2 suggesting limited isotope dissolution from a used-fuel matrix.

5.6.2 The Oklo Natural Reactors

The high-grade uranium deposit, located at Oklo, Gabon, Africa, was formed 2.05 Ga ago in a sandstone host rock. The uranium mineralization, presently exposed in a large open-pit mine, consists of high-grade lenses (25-60 wt.% U) of uraninite within the low-grade sandstone, in which uranium occurs both as uraninite and as pitchblende. Shortly after deposition of the high-grade lenses, the ^{235}U-rich (>3%) ore went critical and sustained spontaneous chain reactions for a period of several hundred thousand years. The natural reactors operated at a depth of several kilometres below surface at pressures of around 100 MPa, reaching temperatures between 400 and 600°C, and produced alteration halos in the surrounding sandstone host rock. The chain reactions also produced fission and activation products, while consuming about 10^7 g of ^{235}U. The fossil remnants of these reactor lenses or zones have survived through two billion years of erosion, uplift and exposure to near-surface conditions in a relatively open system of sandstone host rock. During this two-billion-year history, the ore zones and their host rocks remained water-saturated, allowing water-rock reactions and mass transport processes to take place.

Although uraninite in the reactor zones survived for two billion years, there is evidence that small portions of the uraninite were dissolved and removed from these zones (Curtis 1985). Evidence for the disappearance of uraninite from the reactor zones comes from detailed analysis of the various isotopic signatures remaining from the fission and activation products, in particular neodymium (Curtis et al. 1989). The dissolution of uraninite is thought to have occurred because of the extreme conditions in the reactor zones during criticality, including locally oxidizing conditions produced by radiolysis. However, of the nuclear reaction products, more than 80% of the U, Th, Pu, Nd, Zr, Pd and Te have been retained within the rocks where they were formed. Although the processes of retention and loss are complicated, uraninite, surviving for two billion years in a relatively open system, appears to have played an important role in this retention as the host for these elements. Curtis et al. (1989) suggest that the retention or loss of certain non-volatile elements may be related to the formation, within the uraninite host matrix, of separate phases for these elements under the extreme conditions of criticality. While not detected in the Oklo uraninites, such phases are found in used UO_2 reactor fuel. At Oklo, the stability of each phase, under the conditions prevailing during the last two billion years, would thus have determined the extent of retention within the uraninite host.

Uraninite from the reactor zones shows poor retention for nuclear reaction products that were volatile during criticality, such as Cs, Cd and I

(Curtis 1985, Curtis et al. 1989). It is likely, therefore, that the loss of these elements occurred during criticality, when the physical conditions imposed on the uraninite host were most severe. These conditions are more severe than those expected for used fuel in contact with groundwater, and hence conditions in a disposal vault may not affect these elements to the same extent as observed at Oklo. In addition, the poor retention of lead in uraninite in the reactor zones may result from the loss of a gaseous element from the uraninite crystals. Radon, the intermediate gaseous daughter in the uranium decay series, may readily escape from the UO_2 matrix and be flushed away where the uraninite occurs in an open system. The relative absence of lead in the Oklo uraninite may thus indicate that, subsequent to the period of criticality, at least parts of the reactor zones remained in a relatively open system, allowing groundwater access and flushing of radon gas.

5.6.3 Conclusions

The following points summarize observations on natural uraninite as an analogue to UO_2 fuel, with respect to the long-term stability and integrity of disposed fuel waste:

- Natural uraninite, under suitable low-temperature conditions, shows long-term stability that is consistent with predictions based on thermodynamic data, solubility and limited water access.

- Natural uraninite under extreme conditions, such as those of sustained criticality observed at Oklo, undergoes limited dissolution and degradation. However, the bulk of the uraninite in the reactor zone survived criticality plus two billion years of subsequent erosion and uplift in a relatively open system.

- Natural uraninite in the Oklo reactor zones exhibits poor retention of gaseous elements and of those that are volatile under the extreme conditions of criticality.

- Natural uraninite, under suitable low-temperature conditions, shows good retention capability for certain nuclear reaction products, occurring either in solid solution or as separate phases within the UO_2 matrix, such as Th, Pu and Te.

5.7 SUMMARY

The conceptual and mathematical framework of the radionuclide release model for used fuel has been described. The model includes instantaneous release of a fraction of the inventory of some fission products and the slow dissolution of the used-fuel matrix.

The instant-release model for radionuclides, such as ^{129}I, ^{135}Cs, ^{99}Tc and ^{14}C, is based on experimental measurements and estimates of the inventories in the fuel/sheath gap and at grain boundaries. The release from grain boundaries is conservatively assumed to be instantaneous.

The dissolution of the used-fuel matrix is based on a solubility model, with the assumption that the UO_2/U_4O_9 stability field describes the matrix solubility. Radionuclides are then released in proportion to their concentrations in the matrix and the fraction of the matrix dissolved. The assumption that the used-fuel matrix remains within the UO_2/U_4O_9 stability field is based on experimental studies of UO_2 dissolution in the presence of the products of α-radiolysis of water and the recognition that minerals in the disposal vault would create reducing conditions. The possibility that mass transport-precipitation coupling would accelerate dissolution is incorporated in the model.

The concentrations of Tc, Th, Pu, Np and U in the groundwater are limited by their solubilities under the assumed groundwater conditions in the disposal vault. The amorphous oxides are conservatively assumed to be stable under these conditions.

The release of radionuclides contained within the Zircaloy sheath (i.e., activation products) is assumed to be controlled by the solubility of ZrO_2 in the same fashion as the model for the used-fuel matrix. The Zircaloy sheath is assumed to provide no protection; i.e., groundwater contacts the fuel immediately upon failure of the containers.

The modal instant-release fractions for the model are 8.1% and 6% for ^{129}I and ^{99}Tc respectively, and a range of 1 to 25% for ^{14}C.

Geological evidence illustrates that ores of uraninite located in reducing environments (e.g., Cigar Lake and Oklo) exhibit extremely limited dissolution over time frames exceeding 10^9 a.

6. THE RADIONUCLIDE MASS TRANSPORT MODEL

6.1 INTRODUCTION

This chapter describes the conceptual and mathematical framework of the radionuclide mass transport model (MT model) used in the vault model. The MT model represents the release of radionuclides from used fuel upon container failure and their subsequent mass transport through the clay-based sealing materials surrounding the waste containers and into the geosphere. In the MT model, it is assumed that the buffer and backfill are water-saturated. The behaviour of the conceptual vault under unsaturated conditions is discussed semi-quantitatively in Chapter 3.

The MT model described is for the case study (see Goodwin et al. 1994). The layout of the vault for the case study is described in Chapter 2, and the mass transport properties of the buffer and backfill materials are specified in Chapter 3. The geometrical design parameters for the vault and the mass transport data for radionuclides in the buffer and backfill provide input for the MT model. The MT model uses these data, along with the source terms (see Chapter 5) and information on the hydrogeochemical conditions in the rock adjacent to the vault, to calculate the release rates of radionuclides from the vault as a function of time. These release

rates give an indication of the performance of the engineered barriers and are also used as input rates into the geosphere model (Davison et al. 1994b), which calculates the transport of radionuclides through the rock surrounding the vault and into the biosphere.

The processes in the vault model can be classified as

- container failure,
- radionuclide release from used fuel,
- precipitation,
- mass transport in buffer and backfill,
- sorption in buffer, backfill and rock, and
- mass transfer from buffer to backfill and backfill to rock.

Container failure is implemented through a container failure function that gives the fractional rate of container failure as a function of time. The detailed failure mechanisms, such as fabrication defects, crevice corrosion, and hydrogen-induced cracking, are used to define the characteristics of the failure function.

There are assumed to be two types of release of radionuclides from used fuel, congruent and instant. Congruent release refers to the slow dissolution of the used fuel matrix and the entrained radionuclides. This dissolution is assumed to be controlled by the solubility of UO_2/U_4O_9. For radionuclides entrained in the Zircaloy fuel sheath, congruent dissolution is assumed to be the sole radionuclide release mechanism.

Instant release refers to the release of radionuclides that have migrated during irradiation in the reactor to the fuel-sheath gap and the grain boundaries of the fuel. These radionuclides would dissolve in the water that is assumed to fill the interior of the waste containers immediately upon container failure, and reach uniform, inventory-limited concentrations in the water inside the container and in the sand layer surrounding the container. From this initial distribution their diffusion into the surrounding buffer material is calculated.

For both congruent and instant release, mass transport of radionuclides following container failure is modelled as if the container is instantly removed upon failure; i.e., it provides no hindrance to mass transport.

There is a possibility that the release of a given radionuclide from used fuel would result in the solubility of the radionuclide being exceeded in the water contacting the used fuel. Should this occur, the amount in excess of the solubility is assumed to precipitate. The accumulation and dissolution of precipitates is modelled by considering the interior of the container and the sand layer around the container as a well-mixed compartment.

Mass transport in the buffer and backfill is determined from solutions to the convection-dispersion equation for a decay chain. Convection is assumed to have a minor contribution to mass transport in the backfill and to have no contribution in the buffer (see Chapter 3).

Sorption is modelled using the linear sorption isotherm in which the amount sorbed in the solid portion of the medium is proportional to the concentration in the pore water. With this assumption, sorption can be incorporated into the convection-dispersion equation through the use of the radionuclide-dependent capacity factor. The capacity factor can be defined as the ratio of the total concentration in the solid plus solution (bulk concentration) to the concentration in the solution only.

The convection-dispersion equation for this application has been simplified to consider only one spatial variable (one-dimension) instead of three. This has been achieved by modelling the system as a series of plane layers in which concentrations vary in the direction perpendicular to the layers but are uniform in the other two spatial directions.

The actual disposal room and borehole geometry is quite complex and the simplified one-dimensional approximation will not capture the details of mass transport at the local scale around the rooms and boreholes. However, viewed from some distance above, the vault appears like a plane source. Consequently, the concentration profiles at some distance into the rock should develop as if they had originated from a plane source, provided container failure is not too widely distributed in time and space.

A three-dimensional solution using the detailed geometry around a representative borehole and disposal room segment has been developed using the finite-element code MOTIF (Chan and Scheier 1987). The results from this analysis are discussed in more detail in Section 6.2.2 and tend to confirm the supposition that representing the vault as a layered plane source is adequate in terms of predicting radionuclide release to the geosphere.

Spatial heterogeneity across the vault has been incorporated by dividing the vault into twelve sectors. Mass transport properties are constant within a sector but are allowed to vary from sector to sector. The buffer and backfill are assumed to have constant properties throughout the vault. The heterogeneity occurs in the container failure rates and the mass transport properties of the surrounding rock. More sectors are clustered in the region closest to a major fracture zone because the distance to that fracture zone is expected to have a strong effect on mass transfer from the vault. Containers near the centre of the vault would be hotter than those near the edge; thus sectors with a higher proportion of containers near the edges of the vault have longer container lifetimes on average.

One might speculate that it would be preferable to use the MOTIF finite-element code directly in the vault model to obtain a more detailed representation of the geometry; however, there are several practical considerations that prevent this:

- In an application where repeated random simulations are done, it is difficult to quantify the errors involved in the finite-element method.

- It is not possible to capture the detailed borehole geometry for each and every container in the vault: the finite-element mesh size would be so large as to exceed the computer capacity for use in probabilistic assessments. However, the computational

capacity of computers is increasing rapidly, and this may be only a temporary restriction.

- The MOTIF finite-element code has not been developed to include the effects of radionuclide precipitation, distributed container failure, or a confined inventory-limited source pertinent to instant release.

- The MOTIF finite-element code has not been developed to handle mass transport of decay chains.

Furthermore, if the far-field behaviour in the rock can be adequately predicted or at least bounded by the use of one-dimensional geometrical approximations, a more detailed geometrical representation might not be necessary or even desirable. Estimates of the errors involved with the one-dimensional approximation are given in Section 6.2.2. Since source release rates drive the mass transport process, it can be argued that it is more important to accurately determine or bound these release rates than capture the details of the geometry.

Analytical solutions have been developed to the convection-dispersion equation for use in the vault model that entail some further simplifications and assumptions in addition to the aforementioned one-dimensional approximation. Analytical solutions have the advantage of being accurate and efficient and they lend themselves more easily to quality assurance.

The analytical solutions to the convection-dispersion equation require the specification of both source and exit boundary conditions. For convenience and flexibility, an artifice has been used which specifies the source boundary condition as a unit of mass initially injected across the source boundary into the medium. The solution to the convection-dispersion equation for this condition is called a response function (Heinrich and Andres 1985). The solution for any time-varying source boundary release can be determined by approximating the release as a series of pulses, each of different size. The envelope of these pulses can be made to approximate any time-varying source release. The final solution is obtained by summing the effect of each pulse in a process called a convolution. Numerical routines that perform the convolution to within a specified target error have been used for this process (Andres, in preparation).

Release rates of radionuclides from the used fuel constitute the source boundary conditions. The constraints of radionuclide precipitation and container failure are applied to the two types of radionuclide release, congruent dissolution and instant release, for use in the convolution procedure.

The exit boundary condition required for the solution is characterized by a mass transfer coefficient, which is a measure of the mass transfer resistance of the remaining pathways in the system. For the buffer, the remaining pathways are through the backfill and the rock. For the backfill the remaining pathway is through the rock. A high value of the mass transfer coefficient corresponds to rapid mass transfer in the remaining pathways,

such as could be caused by high groundwater flow rates in the rock. It is assumed that the rock region around the vault interfaces with a fracture zone, or with a region of higher permeability rock at some distance from the vault where the mass transfer rates are sufficiently high to maintain "swept away" conditions. Swept away conditions refer to mass transfer removal rates at the exit from a medium that are sufficiently large as to maximize the release rates through the medium.

As an additional analysis tool, a second set of coupled response functions has been developed for a two-layer system. The second layer is assumed to be semi-infinite, and continuity of both flux and concentration are applied at the interface between the layers. These coupled solutions are more complex than the solutions with mass transfer coefficients but have more complete interfacial boundary conditions. The coupled solutions have been solved by Laplace transform methods utilizing numerical inversions of the transforms. The coupled solutions have been used for comparative purposes.

Verification of the MT model was carried out in a series of scoping calculations using comparisons with analytical limits and other near-field assessment codes. These analyses have been documented elsewhere (Garisto and LeNeveu 1989, 1990; Apted et al. 1989a; Engel et al. 1989; Chan and Advani 1991). Chapter 7 contains an analysis of the calculations carried out with the MT model, including a comparison of the results with analytical approximations. These analyses show that the algorithm in the MT model performs as expected and that the results of the calculations are consistent with our understanding of the model.

6.2 THE MODEL GEOMETRY

6.2.1 Overview

In the vault model, the conceptual vault is divided into a number of sectors (Figure 6-1). A sector is a portion of the vault in which the characteristics important to the modelling of radionuclide transport are relatively uniform. These characteristics include properties of the rock adjoining each vault sector, since rock properties influence mass transfer rates. Similarly, the geosphere in the geosphere model (Davison et al. 1994b) is divided into a number of segments. A segment is a part of a flow pathway in the geosphere that is assigned uniform hydrogeological properties, including groundwater flow velocities, groundwater chemistry and mineralogy. A group of segments joined together form a flowpath that leads from the vault to a discharge point in the biosphere. To define vault sectors, we use information on the geosphere segments that adjoin the vault. This ensures that the hydrogeochemical properties of the rock that determine mass transfer rates from each vault sector are approximately uniform.

The sector and segment concept is important because the plan area of the conceptual vault is several square kilometres (see Table 2-1). Over this scale, plutonic rock is expected to exhibit significant variations in its hydrogeological properties and, consequently, significant differences in

the rate at which radionuclides would be transported into and through it. Use of the vault sectors and geosphere segments allows us to realistically represent these differences in analyzing mass transport.

The actual vault geometry is obviously three-dimensional. However, two- and three-dimensional models are very complex and are not suitable at present for a direct application in probabilistic assessments. For example, a three-dimensional calculation of the water movement using a simplified representation of the vault, in which the backfill is assumed to have the configuration of large thin slabs rather than discrete rooms, and buffer and containers are ignored, has been done with the MOTIF code (Chan and Scheier 1987). This model has approximately 16 000 nodes in the finite-element mesh and requires one day of execution time to complete one simulation on an FPS M64-140 computer.

The vault model uses mass transport equations in one spatial dimension that calculate transport perpendicular to various plane layers to achieve efficiency in computer resources. Therefore, the conceptual vault design is converted into a series of layers, or slabs, in each sector for use in the model (see Figure 6-2, and also Figure 1-4). Mass transport is then calculated across these layers and into the surrounding rock.

6.2.2 The Justification of One-Dimensional Model Geometry

The suitability of representing the vault as a large thin slab is based in part on the consideration of interaction between the many containers.

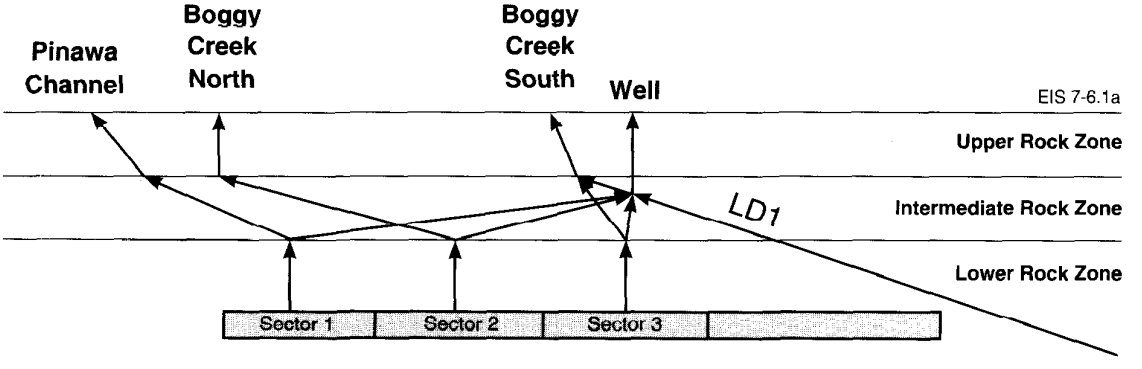

(a)

continued...

FIGURE 6-1: A Schematic Diagram of the Vault Sectors and Geosphere Segments: (a) Side View, (b) Three-Dimensional View (c) Overhead View of the Vault for the Case Study Illustrating the 12 Sectors

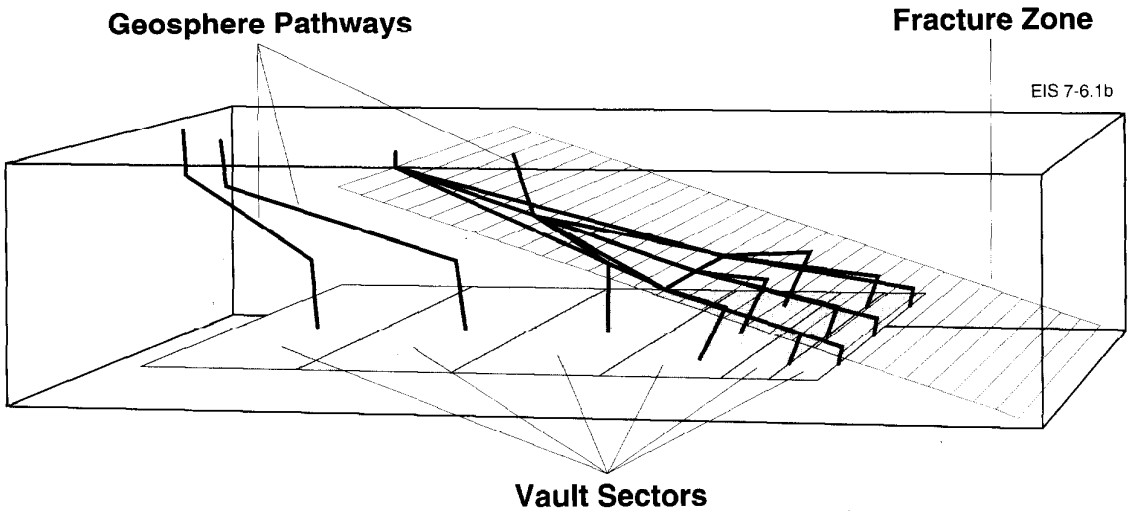

(b)

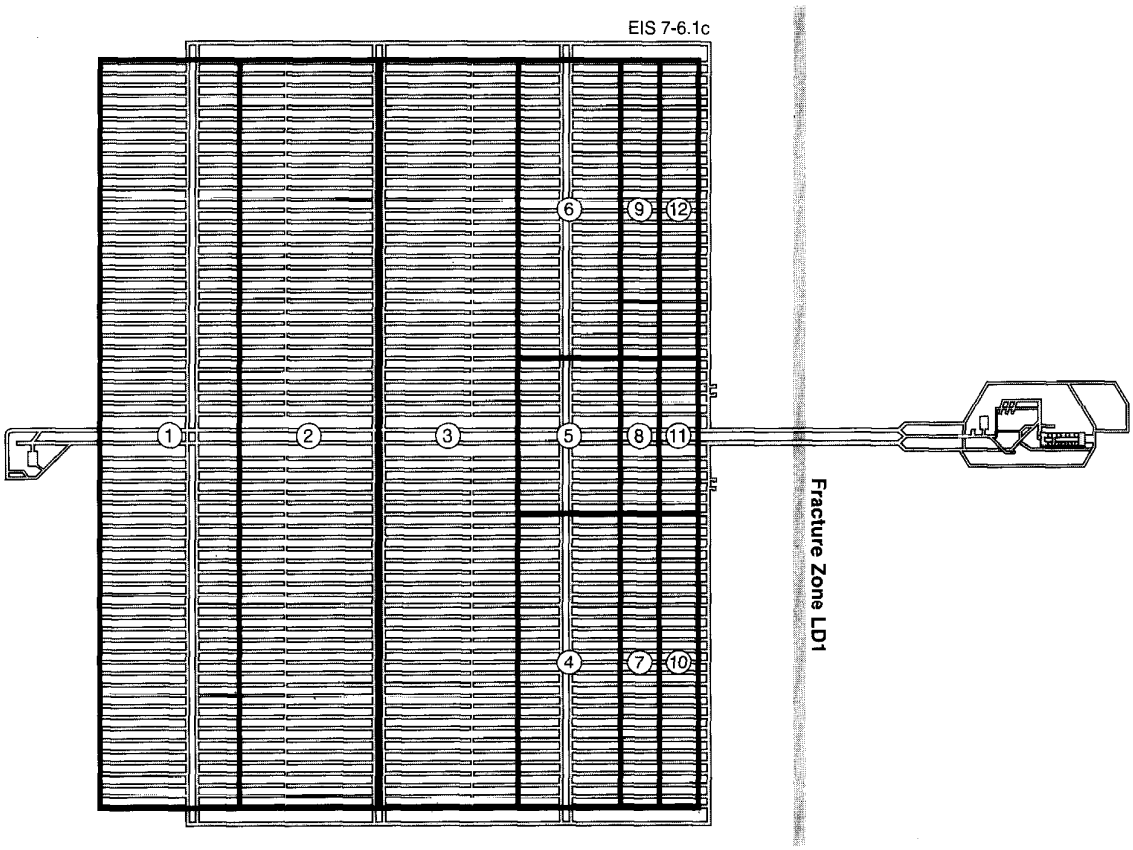

(c)

FIGURE 6-1: (concluded)

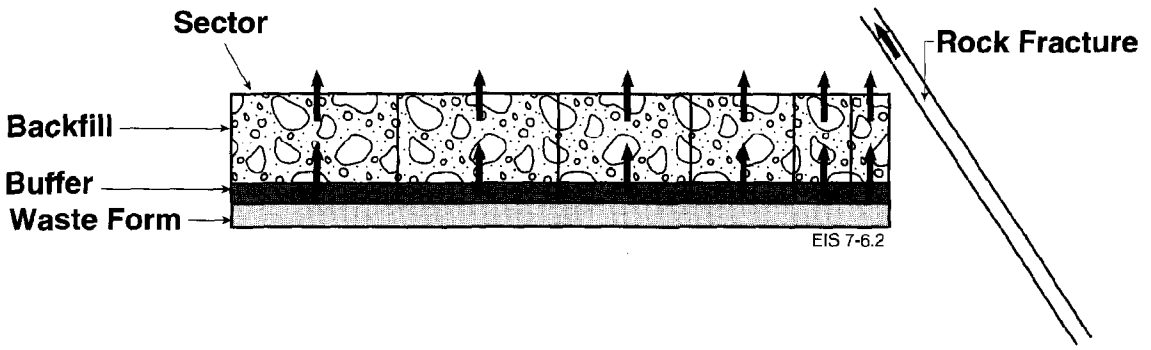

FIGURE 6-2: A Schematic Diagram of the Vault Model Geometry for the Case Study Showing Two-Layer, One-Dimensional Sectors

Viewed from above (see Figure 2-1), the vault resembles a large plate with many sources, namely the containers, distributed within the plate. For a failure of a single container, a released contaminant would begin to spread out in all directions into the rock after penetrating the buffer. Once all containers had failed, the concentration between containers would eventually become uniform and mass transport would proceed mainly in the direction perpendicular to the plane of the vault (Ahn et al. 1986).

In the early stages of container failure, before the releases from many containers begin to interact, the use of layers and one spatial variable to characterize mass transport might not be appropriate. To quantify this approximation, the release of a radionuclide per unit waste-form area from a plane waste form is contrasted to the release per unit waste-form area from a spherical waste form imbedded in a medium infinite in all directions. The total flux of the radionuclide, $M_s(t)$, per unit waste-form area from a spherical waste form of radius a, into an infinite medium integrated up to a time, t, is given by

$$M_s(t) = \frac{(C_b D_a t)}{a} + \frac{2C_b (D_a t)^{1/2}}{(\pi)^{1/2}} \qquad (6.1)$$

obtained from the limit of Equation (B.18) in Garisto and Garisto (1988b) as α approaches infinity.

The total flux of the radionuclide, $M_p(t)$, per unit waste-form surface area from a planar source into a semi-infinite medium integrated up to time t, is given (Garisto and Garisto 1988b) by

$$M_p(t) = \frac{2C_b (D_a t)^{1/2}}{(\pi)^{1/2}} \quad . \qquad (6.2)$$

The ratio, M_s/M_p is given by

$$M_s/M_p = 1 + \frac{(D_a t\pi)^{1/2}}{2a} \qquad (6.3)$$

where a is the radius of the spherical waste form, D_a is the apparent diffusion coefficient of the radionuclide in the medium (see Section 3.5.2) and C_b is the bulk concentration of the radionuclide in the medium at the surface of the sphere and plane, assumed to be constant for all time, $t > 0$. The bulk concentration is obtained from the product of the pore-water concentration and the capacity factor of the radionuclide in the medium.

The radius of a sphere having a surface area equal to the waste container is 1.28 m. The apparent diffusion coefficient of ^{129}I for the median value simulation (see Chapter 7) is 2.8×10^{-3} $m^2 \cdot a^{-1}$. Using these values, the ratio M_s/M_p would be less than 4, for times less than 6.6×10^3 a. By 6.6×10^3 a most containers would have failed (see Figure 7-6), and it would no longer be appropriate to treat the waste form as a sphere representing a single failed container in an infinite medium. For times $>6.6 \times 10^3$ a, representing the waste form as a larger plane source rather than a sphere should give a more accurate representation of the release because of the interaction between containers. At progressively earlier times, the discrepancy between plane geometry and spherical geometry becomes progressively smaller. From these considerations, the use of a one-dimensional transport model representing a series of plane layers should be a good approximation (the ratio $M_s/M_p < 4$) over the entire time scale.

The effect of the changing properties of the medium as the contaminant passes through the barriers of the buffer, backfill and rock has been examined by comparing the results of two one-dimensional solutions differing in their treatment of the boundary conditions describing the interfaces between the different barriers. These two solutions are called the mass transfer solution and the coupled solution. The mass transfer solution, implemented in the vault model, characterizes these interfaces by the use of mass transfer coefficients. The coupled solution uses continuity of concentration and flux to characterize these interfaces. The second solution has a more realistic interface boundary condition, but it uses an additional assumption, namely that the second of the two interfacing media is semi-infinite. A comparison between the results of these solutions for ^{129}I is given in Section 8.3.

Mass transport by diffusion for the actual three-dimensional configuration of the borehole disposal geometry has been modelled using the finite-element hydrogeological code MOTIF (Chan et al. 1987, Garisto and LeNeveu 1991). Because of the symmetry of the emplacement geometry, only one and a half boreholes were modelled across the width of the disposal room. A horizontal fracture zone that would remove contaminant immediately upon arrival was assumed to be 25 m above the containers. The modelling assumptions and geometry are discussed in more detail in Garisto and LeNeveu (1991). Figure 6-3 shows the concentration profiles at 2.71×10^3 a for a

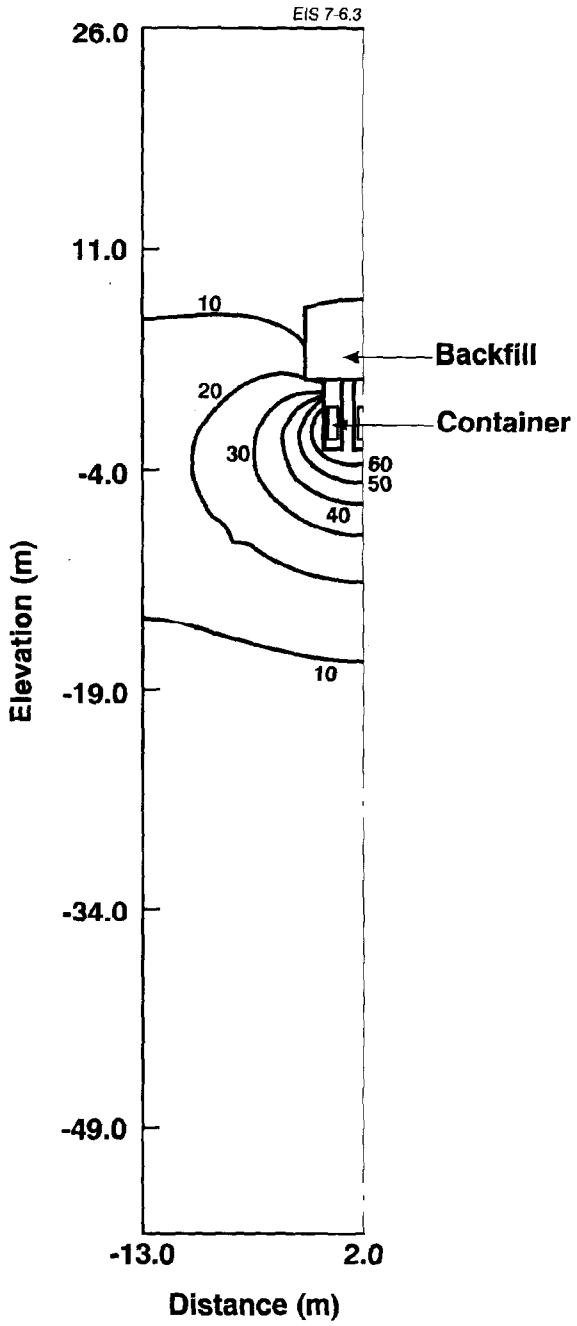

FIGURE 6-3: Concentration Profiles at 2.71 x 10^3 a for a Vertical Section Through the Waste Containers. Profiles are for a non-sorbing contaminant maintained at a constant concentration of 100 (arbitrary units) over the surface of the container.

non-sorbing contaminant released from containers over which the surface concentration of the contaminant was maintained constant at an arbitrary value of 100 units. The profiles are for a vertical section through the centre of the waste containers. The contaminant diffuses upward toward the fracture zone to a greater degree in the rock than in the backfill. In effect the backfill slows the migration toward the fracture zone. The backfill takes much longer to fill with contaminant than the corresponding volume of rock because the backfill contains a much larger amount of water per unit volume than does the rock. Specifically, the porosity of the backfill in the finite-element simulation is 0.30 while that of the rock is 4.0×10^{-3}.

In the finite-element simulation described above, some of the contaminant diffuses through the buffer to the rock and then into the backfill, while the rest enters the backfill directly from the buffer. In the one-dimensional transport model used in the vault model, the buffer is treated as a slab that interfaces directly with a slab of backfill. No pathway exists from buffer through the rock to the backfill in the one-dimensional model. However, provision is made in the one-dimensional model to exclude the backfill from the transport pathway through the use of a switch called BACKSWT. If BACKSWT is positive, the backfill is in the transport path; if it is negative, the backfill is excluded. In the case study, BACKSWT is always positive. Negative values would be used when there is a strong downward convective field in the rock preventing contaminants from entering the backfill from the rock. Such a convective field could also draw contaminant out of the buffer that lies above the container, preventing diffusion of contaminants upwards through the buffer directly into the backfill.

To implement the one-dimensional solutions, the thicknesses of the buffer and backfill slabs must be specified. The thickness of the buffer was taken as the difference between the inner and outer radii of the buffer in the borehole (0.25 m). In the one-dimensional solution, the slab representing the backfill extends over the entire plan area of the vault, whereas in the actual three-dimensional layout, the backfill is confined to separated rooms excavated from the rock. The thickness of the slab representing the backfill (1.4 m) was specified such that the slab would have the same volume as the total volume of backfill in the conceptual vault.

With the slab thicknesses specified as described, the same breakthrough time for ^{129}I to the fracture zone was obtained for the two one-dimensional solutions as the three-dimensional finite-element solution. This indicates that the lack of a direct pathway from buffer to rock in the one-dimensional solution is not an important omission. The mass transfer solution also requires a specific value for the mass transfer coefficient to obtain this correspondence in breakthrough times. The details of the determination of the value for the mass transfer coefficient are given in Sections 6.8.2, 6.8.3 and 6.8.4.

A third one-dimensional solution that simulates two finite layers was also developed for analysis purposes. It is also a coupled solution but differs from the previously discussed coupled solution in that the second layer of a two-layer system is finite, with a zero-concentration exit boundary

condition, rather than semi-infinite (Garisto et al. 1992). A zero-concentration boundary condition is used to obtain a "swept away" condition, which maximizes the removal rate of material away from the exit boundary. This third one-dimensional solution has not been implemented into the vault model.

Simulations with the one-dimensional solutions indicate that complex interactions can occur between radionuclides in a multimember decay chain with respect to the geometry of the different engineered and geological media in and around the vault. For instance, the coupled solutions predict that a daughter radionuclide, which accumulates because of preferential sorption of the parent in the rock, could move in response to its concentration gradient from the rock into the buffer and backfill. The mass transfer coefficient solution allows for migration in the sequence buffer to backfill to rock, or buffer to rock, and not the reverse. The coupled solutions provide a better description of such complex interactions. However, significant differences occur between the predictions of the two coupled solution models, depending on the boundary conditions (Garisto et al. 1992), indicating that uncertainties remain pertaining to the assumptions used. The dose to man from the radionuclides in multimember chains is negligible because of sorption, which severely limits the mobility of these radionuclides (see Chapter 7). Because of the dominance of sorption effects, the discrepancies in model predictions for the complex interactions between chain members is not an important factor in the assessment for time periods $<10^5$ a.

We conclude that the one-dimensional solution with mass transfer coefficients implemented in the case study provides an adequate representation of release rates of the radionuclides contributing most to dose (e.g., ^{129}I). The coupled solution model that has been developed further enhances our analysis capabilities and provides a method of verification of the mass transfer coefficient solution.

6.2.3 Vault Sectors for Interface with the Geosphere Model

The hydrogeological finite-element code MOTIF (Chan et al. 1987) has been used to perform three-dimensional simulations of groundwater flow in the rock surrounding the engineered barriers in the conceptual vault. This model treats the fracture zones, the regions of moderately fractured rock and the sparsely fractured rock regions as equivalent porous media and includes the backfilled disposal panels, tunnels, shafts and the excavation-damaged zones. It predicts the spatial and temporal distributions of piezometric head and groundwater velocity in the rock. From this velocity distribution, a numerical particle-tracking technique is used to derive the convective travel paths and travel times of water-coincident tracer particles from the vault, through the geosphere, to the biosphere (Chan et al. 1986).

The particle paths determined from the detailed MOTIF model are then used to construct the geometry of the SYVAC geosphere model, which consists of a network of one-dimensional segments (see Figure 6-1). For each segment, the geosphere model solves the convection-dispersion-retardation equations

for a radionuclide decay chain using response function and Laplace transform techniques (Heinrich and Andres 1985). The rate of input of radionuclides into each geosphere segment is equal to the release rate of radionuclides from each corresponding vault sector.

Each vault sector and geosphere segment represent a layer through which mass transport can be characterized in the direction perpendicular to the plane of the layer. The thickness of each geosphere layer (segment) is determined by the distance between a source node and the closest approach of the fracture zone overlying the vault (LD1). The source nodes are located within the interface plane between each vault sector and geosphere segment. The source nodes for the geosphere network in the reference case study are shown schematically in Figure 6-1 in relation to the vault structure. The one-dimensional vault mass transport calculations are applied to each sector, with the output for each sector weighted by the fractional sector area.

Ventilation, service and waste shafts from the surface to the plane of the conceptual vault have been simulated in the three-dimensional finite-element model of groundwater flow through the rock (Chan and Stanchell 1990) (cf. Figures 6-4 and 1-1.) In the case study the service and waste shafts are located under the topographical high within the WRA (Davison et al. 1994b); consequently, at the level of the vault, groundwater movement through the rock in the vicinity of these shafts is predominantly downward and away from the shafts. This water movement would essentially prevent any contaminant released from the vault from reaching these shafts. Sensitivity studies (Chan and Stanchell 1990) have indicated that the shafts have no appreciable effect on transport of contaminants in the geosphere unless they, together with the backfilled rooms, are left open or are filled with highly permeable materials, such as crushed rock. In the reference concept, however, they would be filled with clay/granite backfill, with concrete and bentonite shaft seals at various locations (Johnson et al. 1994). For this reason, the service and waste shafts are not included in the geosphere network connecting to the vault sectors.

In the case study, the ventilation shafts on the other side of the vault are located under a local height of land. Groundwater movement in the rock near the top of the shafts is downward, preventing any contaminant transport to the surface by convection. Particle tracking simulations (Chan and Stanchell 1990) indicate that particles released from vault sectors nearest the ventilation shafts take longer than one million years to reach the surface by convection. This means that, at vault depth, contaminant transport from this region of rock around the vault would be dominated by diffusion. The shafts occupy such an insignificant portion of the volume of rock in the diffusion pathway (~0.003% of the volume of rock overlying the vault) that they could not influence mass transport in this region. Hence, the ventilation shafts are not included in the geosphere network connecting to the vault sectors.

Sensitivity studies have been conducted to determine the effect on groundwater movement of an excavation-damaged zone around the vault. In these studies, a 3-m-thick excavation-damaged zone around the entire vault was assigned permeability values up to 100 times the value of the sparsely

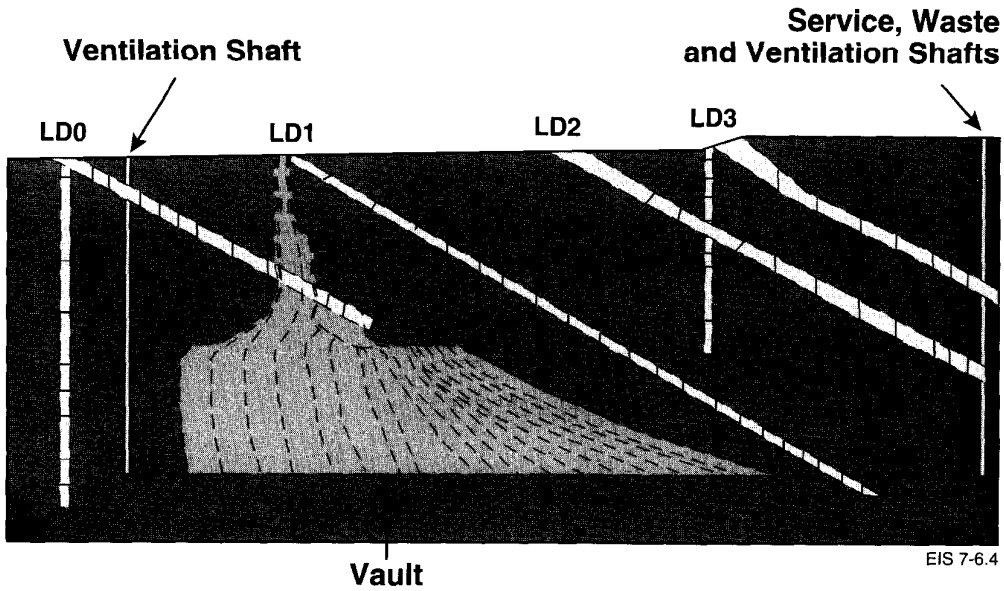

FIGURE 6-4: Typical Convective Flow Paths for Particles Released from the Vault. The features labelled LD0, LD1, LD2 and LD3 are fracture zones. The fracture zone LD1 has been artificially extended to intercept the plane of the vault.

fractured rock in the region around the vault. The studies showed that the excavation-damaged zone had no deleterious effect on convective contaminant transport from the vault. For this reason, an excavation-damaged zone is not included in the geosphere network connecting to the vault sectors (Chan and Stanchell 1990).

In the geosphere network, transport parameters pertaining to a single vault and geosphere segment are assigned single values. Segment and sector boundaries and parameter values are specified to reflect spatial variation in transport properties. Most sectors are clustered near the closest approach of the assumed fracture zone to the vault because an important mass transport property, namely the distance from the vault to the fracture zone, varies most rapidly in this region. Each sector is allocated a fraction of the waste containers in proportion to its plan area. The sectors also have different internal properties, such as container failure rate and mass transfer coefficients (described below), depending on the location of the sector within the vault.

The vault model calculations are done separately for each sector. Inter-sector coupling and vault edge effects are ignored. This is an essential feature of the one-dimensional approximation used in the vault model. A large part of the data used in the vault model calculations is sector-dependent; however, to simplify the notation, we do not use a sector-dependent subscript in the present chapter.

6.2.4 The Parameters Defining the Model Geometry

Tables 6-1 and 6-2 summarize the values of the parameters defining the model geometry.

6.3. SYNOPSIS OF THE MATHEMATICAL METHODS

The rate of release of contaminants from the conceptual vault is determined by the solution of one-dimensional convection-diffusion equations for

TABLE 6-1

SECTOR GEOMETRIES

Sector No.	Fractional Sector Area	Length of Adjoining Geosphere Segment (m)
1	2.16×10^{-1}	1.77×10^{2}
2	2.16×10^{-1}	1.78×10^{2}
3	2.04×10^{-1}	1.77×10^{2}
4	6.44×10^{-2}	1.53×10^{2}
5	3.85×10^{-2}	1.53×10^{2}
6	6.45×10^{-2}	1.53×10^{2}
7	2.49×10^{-2}	8.20×10^{1}
8	1.48×10^{-2}	8.20×10^{1}
9	2.49×10^{-2}	8.20×10^{1}
10	2.49×10^{-2}	4.65×10^{1}
11	1.48×10^{-2}	4.65×10^{1}
12	2.49×10^{-2}	4.65×10^{1}

TABLE 6-2

GEOMETRICAL PARAMETERS

Parameter	Value
Buffer thickness	0.25 m
Backfill thickness	1.40 m
Vault area per container	26.6 m^2
Vault geometric area	3.16×10^{6} m^2

radionuclides in a decay chain of arbitrary length. In the equations, we have not included the effects of coupled processes (except for mass transport/precipitation coupling (see Chapter 5)), microbial processes, and colloidal and gas transport. The justifications for omitting these processes and their effect on the performance of the engineered barriers are discussed in Chapter 3.

The initial concentration of the radionuclides in the vault is taken as zero; the source boundary conditions are determined by models for the release of radionuclides from used fuel (see Chapter 5), and the exit boundary condition assumes that the release of radionuclides is proportional to their concentration at the vault/host rock interface. The proportionality factor, referred to as the mass transfer coefficient (Bird et al. 1960), represents resistance to radionuclide transport across the vault/rock interface (see Section 6.8). Thus, a large mass transfer coefficient approaches a zero-concentration boundary condition at the vault-rock interface, whereas a small mass transfer coefficient corresponds to a semi-impermeable condition at the interface (LeNeveu and Garisto 1988).

Mass transfer coefficients are determined by two means: one by assuming diffusion is the only method of mass transport, and the other by assuming convection is the dominate method of mass transport. The larger of these two coefficients is used, since this implies larger rates of mass transfer.

One of the difficulties in using mass transfer coefficients is that the value of the coefficients would change as concentration gradients change at the boundary interface. Mass transfer coefficients are usually determined for steady-state conditions that apply at long times when concentration gradients in the system are no longer changing. At shorter times, when radionuclides would be just beginning to migrate, concentration gradients and mass transfer coefficients would be larger. In this application, the mass transfer coefficients determined for steady-state conditions have been augmented (increased in value). This augmented but constant value is applied to both short and longer time frames. Details on the augmentation procedure are given in Section 6.8.4

Four advantages of using mass transfer coefficients are as follows:

- the mass transport properties of the remaining media are collapsed into a single parameter;
- the solutions to the convection-dispersion equation for one medium are separated from the other media in the system, making it possible to apply the same solution in succession to the various media;
- a wide range of conditions, ranging from "swept away" conditions at the exit from a medium to totally insulating conditions where no mass transfer occurs out of the medium, can be modelled; and

- two-dimensional effects in the remaining media, such as convection parallel to a boundary surface and dispersion perpendicular to that surface, can be incorporated into the value of the mass transfer coefficient.

One disadvantage of the mass transfer coefficient approach is that, while continuity of flux can be maintained at the interface between adjoining media by using the exit flux from the first medium as the source flux for the second, continuity of concentration cannot be maintained. Continuity of concentration means that the concentration of a radionuclide in the pore water of the first medium is equal to the concentration of pore water in the second medium at the boundary interface. This condition would be expected to apply, provided the chemical activity of the radionuclide is equal in the two media and there is no boundary resistance to mass transfer across the interface.

As an alternative, a second set of coupled response functions have been developed for a two-layer system. The second layer is assumed to be semi-infinite, and continuity of both flux and concentration are applied at the interface between the layers. These coupled solutions are more complex than the solutions with mass transfer coefficients. The coupled solutions have been solved by Laplace transform methods utilizing numerical inversions of the transforms. Although the coupled solutions have more complete interfacial boundary conditions than those of the mass transfer coefficients, they have some disadvantages, as outlined below:

- The second medium is semi-infinite, which might be a poor approximation for relatively thin media such as the backfill.

- Both media are represented by one-dimensional models; hence two-dimensional boundary effects, such as flow parallel to the boundary interface, cannot be determined. (This effect can be incorporated to some degree into a mass transfer coefficient.)

- The implementation for long decay chains is more intensive in the use of computer resources than the implementation with mass transfer coefficients.

- The numerical algorithm currently used for the inversion does not have an error estimate, and hence the accuracy of the solution is unquantified.

For these reasons the coupled solutions have been used for comparative purposes only (see Section 8.3).

The MT model calculations are performed in each sector using the properties of the host rock adjacent to each sector. The mass transport properties of the host rock affect the mass transport processes in the vault through the mass transfer coefficient (Bird et al. 1960, LeNeveu 1986, LeNeveu and Garisto 1988).

As explained in Chapter 3, we have adopted a bulk-medium approach in the MT model to account for porous medium effects (Eriksen and Jacobsson 1984,

Skagius and Neretnieks 1985, Lever 1986). In this approach, the total quantity of a species stored in a unit volume of porous medium is given by the product of its pore-water concentration and the capacity factor of the medium (Lever 1986). Capacity factors are equal to the ratio of the total intrinsic diffusion coefficients and the apparent diffusion coefficient (Equation (3.10)), and thus include storage and sorption effects (storage refers to radionuclides dissolved in the buffer pore water in the absence of sorption). In this approach, effective steady-state diffusion coefficients, also called total intrinsic diffusion coefficients, are used to model diffusion in the buffer and backfill. This model is sufficiently general to encompass diffusion via several pathways, which might occur in compacted clays (Torstenfelt and Allard 1986, Cheung 1989).

Inherent in this approach is the assumption that all sorption processes are linear with concentration and that equilibrium is maintained between sorbed and mobile species. An approximate, equivalent linear sorption model could be derived for use in the vault model (Walker and LeNeveu 1987) should experimental data indicate that sorption processes are non-linear. However, even this equivalent model does not fully account for saturation of available sorption sites. Such saturation is not expected because radionuclide concentrations in groundwater are expected to be low under disposal conditions. Discussions of the validity of the bulk-medium approach and the associated data for the expected vault conditions are given by Cook (1988) and Cheung (1989) respectively (see Chapter 3).

The MT model is applicable to mass transport in homogeneous, porous media. A separate, numerical mass transport model was developed for studying diffusion and convection of radionuclides in cracked, porous media (Garisto and Garisto 1990a, 1990b). In addition, analytical expressions were derived for the enhancement of the flux due to potential cracks in the buffer (Garisto and Garisto 1989). These expressions can be incorporated into the MT model to estimate the effects of potential buffer cracks on the performance of the vault. However, there is strong experimental evidence that if cracks did develop in the buffer, they would heal in a short period of time (see Chapter 3). Moreover, a preliminary analysis using the detailed models indicates that buffer cracking has no significant effect on the mass transport of dissolved uranium.

A response-function approach is used in the vault model for the solution of the convection-diffusion equations (LeNeveu 1987). The response functions, i.e., the solutions to the mass transport equations in a finite layer (e.g., buffer, backfill) for a unit impulse input are discussed in Section 6.7. The response functions are calculated using Laplace transform methods, and analytical methods are used to invert the Laplace transform solutions (LeNeveu 1987).

The release rate of a radionuclide into a layer, referred to as the source release rate, is convoluted with the response function to obtain the rate of release from that layer (see Figure 6-5). The source release rate is obtained by solving the convection-diffusion equation for appropriate source boundary conditions.

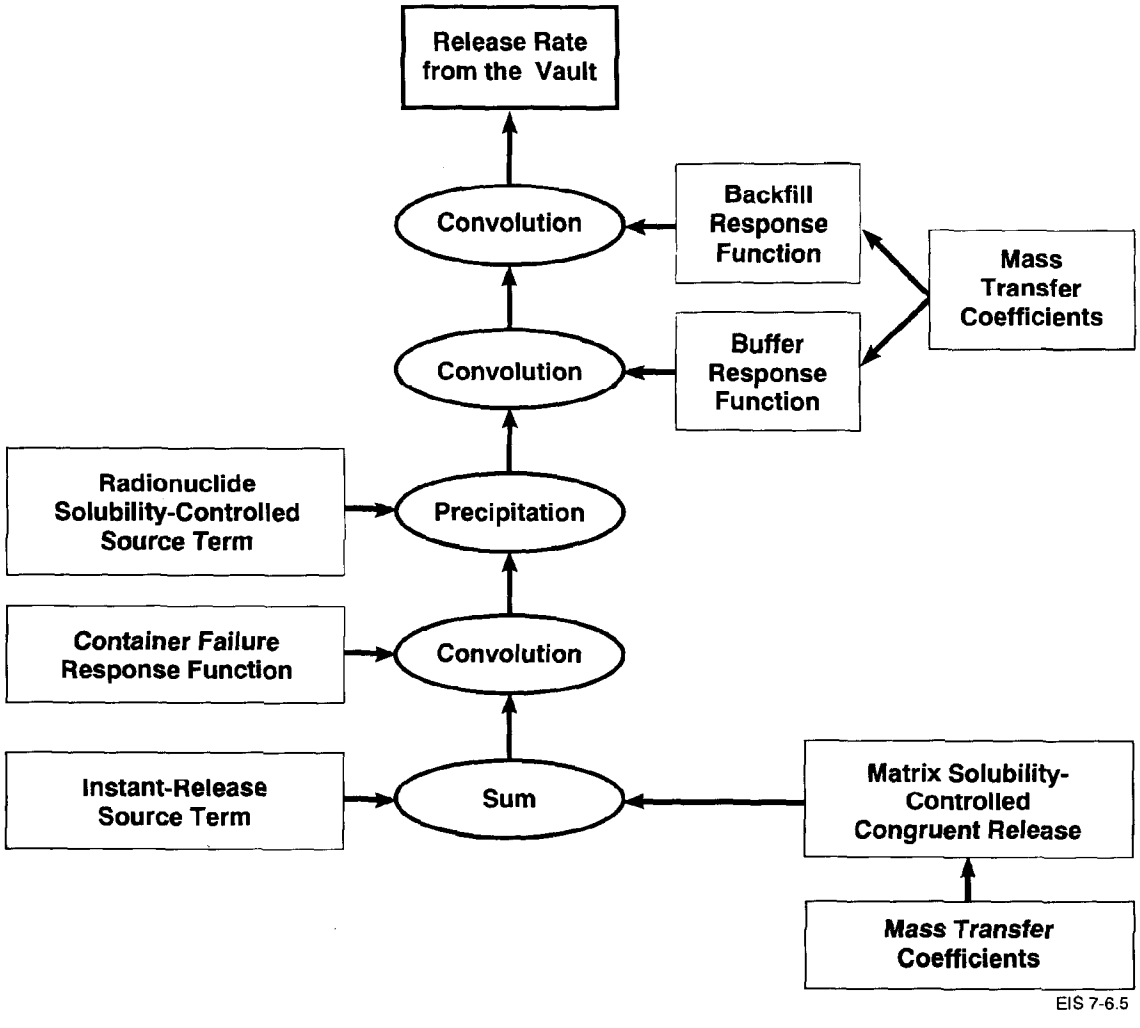

FIGURE 6-5: The Overall Procedure in the Vault Model

Two source boundary conditions are used: one representing instant release of radionuclides upon container failure, and another representing long-term, solubility-controlled, congruent release (see Chapter 5). Evaluation of the flux at the source using these solutions gives the source term into the buffer.

The source boundary condition for congruent release of a radionuclide is given by the dissolution rate of the used-fuel matrix multiplied by the time-varying ratio of the inventory of the radionuclide in the matrix to the inventory of the matrix. The dissolution rate of the matrix is determined from a solution of the convection-diffusion equation with a constant-concentration (the solubility of the matrix in the waste container (Lemire and Garisto 1989)) source boundary condition and an exit boundary condition determined by a steady-state mass transfer coefficient. Studies have shown that the steady-state mass transfer coefficient is a reasonable boundary condition to apply here (Garisto and LeNeveu 1991).

During the transient that occurs before steady state, the exit boundary condition has no appreciable effect and the solution is the same as for a semi-infinite medium. Therefore, in this transient regime, the solution should be accurate. Once steady state is achieved, the solution should also be accurate because the mass transfer coefficient for waste-form release is evaluated for steady-state conditions. The transient dissolution rates are larger than those for steady state. During the transition between transient and steady state, the solution could give somewhat low values because the use of mass transfer coefficients can lead to an underprediction of the duration of the transient release. This inaccuracy is expected to be small in comparison with the range of dissolution rates calculated from the uncertainty in solubilities. For most simulations the inaccuracy should not occur until after 10^4 a, as illustrated by Figure 7-15 (in Chapter 7). It is only in those cases where uranium-containing solids precipitate within the buffer that steady state should be reached before 10^4 a. This inaccuracy does not apply to cases where uranium precipitates because the dissolution of the UO_2 matrix is controlled by the location of the precipitate in the buffer and is not influenced by the rock and backfill media properties (Garisto and Garisto 1986). Furthermore, it is only in the cases where uranium precipitates that congruent release can approach the levels of instant release. Thus the aforementioned small underestimate of congruent release rate as steady state is approached should have no effect on simulation results.

A compartmental model (Andres, in preparation) from the SYVAC executive (Goodwin et al. 1987) is used to shut off the radionuclide release from the used-fuel matrix when all of the used fuel is dissolved. However, complete dissolution of the used fuel is not expected to occur within the time frame of the assessment. The compartmental model is a general-purpose routine that gives the solution to a set of first-order linear differential equations describing the dependent input and output from a given compartment as a result of a linear process, such as radioactive decay and buildup. It has several applications in the vault model (see also Section 5.5.3.1).

For the source boundary condition for instant release, it is assumed that, at the time of container failure, the instant-release inventory is uniformly diluted throughout the available pore volume in the container, which is assumed to be saturated with water. It is also assumed that the inventory is subsequently depleted by mass transport into the buffer. These assumptions are used to form the source boundary condition for the evaluation of the instant source release. It is further assumed that the buffer layer is semi-infinite. This approximation best describes the release of the initial portion of the instant-release inventory into the buffer, before the occurrence of significant breakthrough into the backfill. A finite layer model with a steady-state mass transfer coefficient for the exit boundary condition is not used for instant release because there is no steady state in this case.

The derivation of the source terms for instant release and for solubility-controlled congruent release is discussed in Section 6.5 and is given in detail by Garisto and LeNeveu (1991). The instant-release rate and the congruent-release rate are summed to give the total source release of a radionuclide into the buffer.

The source release is then convoluted with the container failure response function (LeNeveu, in preparation) to account for the fact that not all containers fail at the same time, which dissipates the release rate into the buffer. (The container failure rate is different from the container failure response functions because the latter accounts for changes in radionuclide inventory due to decay before failure, while the former does not.) The result of this convolution gives the net release rate into the buffer for the entire vault, taking into account the effect of precipitation. It is assumed that the buffer is fully saturated with water at the time of container failure. It is also assumed, conservatively, that the container fails over the entire surface and does not restrict release to the buffer. The convolution is done only in time and not in space. Thus, the containers are treated as a smeared source whose input rate to the buffer gradually increases with time because of container failure. In other words, the time for the release from one container to spread and interact with another container is ignored. This is a reasonable approach because, at distances away from the containers that are large compared with the separation distance between the containers, the release from a series of discrete sources is expected to be indistinguishable from that of a single smeared source (Ahn et al. 1986). The change in the amount of a radionuclide in the container before failure as a result of nuclear transformation is also accounted for in this step.

After calculation of the total source release, and convolution with the container failure response function, precipitation is simulated in the container (see Figure 6-5) by using the compartment model. For this calculation, individual radionuclide solubility-limited dissolution rates must be provided. The solubility-limited dissolution rate is given by the same method as the matrix dissolution rate, with the radionuclide solubility replacing the solubility of the matrix. The solubility-limited dissolution rate is then convoluted with the container failure rate to account for the gradual failure of containers. Should the matrix-controlled congruent-dissolution rate, as modified by container failure, exceed the radionuclide solubility-limited dissolution rate, the compartment model is used to determine the amount of the accumulated precipitate and to set the net release rate equal to the solubility-limited dissolution rate. For simplicity, isotopes of the same element are treated separately (except for uranium isotopes, which are treated more rigorously; see Section 5.5.3.1). In reality, isotopes of the same element would be expected to coprecipitate. Since coprecipitation would lead to a lower effective solubility of an isotope, it is conservative to disregard this effect. In the absence of any information, it is further assumed that the area of constant concentration for the precipitate is the same as the area used for the matrix. The release from the compartment model for precipitation is the net release rate into the buffer.

The net release rate into the buffer is convoluted with the buffer response function to give the release rate from the buffer (see Section 6.7). All contributions from precursors are summed during this process. Finally, the release rate from the buffer is convoluted with the backfill response functions to obtain the release rate from the backfill into the surrounding rock.

6.4 THE CONVECTION-DIFFUSION EQUATIONS

The governing equations used to describe mass transport in the vault are the set of one-dimensional convection-diffusion equations for a decay chain of arbitrary length:

$$\frac{\partial C_1}{\partial t} - \frac{D_i}{r_1}\frac{\partial^2 C_1}{\partial x^2} + \frac{v}{r_1}\frac{\partial C_1}{\partial x} + \lambda_1 C_1 = 0$$

$$\frac{\partial C_2}{\partial t} - \frac{D_i}{r_2}\frac{\partial^2 C_2}{\partial x^2} + \frac{v}{r_2}\frac{\partial C_2}{\partial x} + \lambda_2 C_2 - \frac{\lambda_1 r_1}{r_2} C_1 = 0$$

$$\vdots$$

$$\frac{\partial C_i}{\partial t} - \frac{D_i}{r_i}\frac{\partial^2 C_i}{\partial x^2} + \frac{v}{r_i}\frac{\partial C_i}{\partial x} + \lambda_i C_i - \frac{\lambda_{i-1} r_{i-1}}{r_i} C_{i-1} = 0 \qquad (6.4)$$

and the initial conditions are assumed to be

$$C_j(x,o) = 0 \ , \ 0 \le x \le a \text{ for all radionuclides, } 1 \le j \le i \qquad (6.5)$$

where $C_j(x,t)$ is the concentration of a radionuclide in the pore water of the medium (buffer or backfill) as a function of space and time, $1 \le j \le i$,
v is the Darcy velocity in the medium;
D_i is the total intrinsic diffusion coefficient (Lever 1986) in the medium for the last radionuclide i in the chain;
r_j is the capacity factor (Eriksen and Jacobsson 1984) of the medium for radionuclide j; and
λ_j is the decay constant of radionuclide j, $1 \le j \le i$.

The terms involving λ_{i-1} represent the buildup of radionuclide i from its parent, and the terms involving λ_i represent the decay of radionuclide i.

We have assumed that all the radionuclides in a decay chain have the same D_i value, i.e., that of the radionuclide under consideration. This simplifies the analytical solution of the equations (see Section 6.7), which would otherwise be extremely complicated. By using D_i and r_i, explicit use of a porosity variable in the equations is avoided. D_i includes the porosity as an implicit variable (i.e., $D_i = f(\epsilon)$), and D_i/r_i is sometimes called the apparent diffusion coefficient, D_{ai}. The advantage in using these variables lies in the fact that D_i and D_{ai} can be obtained from direct experimental measurements of diffusion under steady-state and transient conditions respectively (see Section 3.5).

The values of the parameters in Equations (6.4) and (6.5) are as follows: the values of λ_i are defined in Appendix A; the parameter distribution functions for D_i and r_i are defined in Section 3.5. In addition, Table 6-3

TABLE 6-3

MEDIAN-VALUE TOTAL INTRINSIC DIFFUSION COEFFICIENTS AND MEDIAN-VALUE CAPACITY FACTORS IN THE VAULT FOR SELECTED RADIONUCLIDES

MEDIUM-VALUE TOTAL INTRINSIC DIFFUSION COEFFICIENTS		
Element	Buffer ($m^2 \cdot a^{-1}$)	Backfill ($m^2 \cdot a^{-1}$)
C	1.80×10^{-5}	2.25×10^{-3}
Cs	7.31×10^{-3}	8.10×10^{-3}
I	1.80×10^{-5}	2.25×10^{-3}
Ni	2.55×10^{-3}	3.96×10^{-3}
Pd	2.55×10^{-3}	3.96×10^{-3}
Se	1.80×10^{-5}	2.25×10^{-3}
Tc	1.14×10^{-5}	2.25×10^{-3}
U	1.14×10^{-5}	2.25×10^{-3}

MEDIAN-VALUE CAPACITY FACTORS			
Element	Buffer	Backfill	Rock
C	6.33×10^{-3}	2.50×10^{-1}	3.00×10^{-3}
Cs	1.75×10^{1}	6.00	7.06
I	6.33×10^{-3}	2.5×10^{-1}	3.00×10^{-3}
Ni	4.50	1.40	0.36
Pd	4.50	1.40	7.50×10^{-2}
Se	6.33×10^{-3}	2.5×10^{-1}	0.34
Tc	5.28×10^{1}	2.00×10^{3}	7.80×10^{-3}
U	5.28×10^{1}	2.00×10^{3}	7.14×10^{-2}

summarizes the median values of the parameter distribution functions of D_i and r_i for selected radionuclides.

The Darcy velocity, v, is taken to be zero in the buffer. In the backfill it is calculated in each simulation by the geosphere model (see Davison et al. 1994b). The calculated values of v in the backfill in the various vault sectors for the median-value simulation (i.e., for the simulation where all parameters are fixed at their median values) are given in Table 6-4.

6.5 THE SOURCE TERMS

The release model provides boundary conditions for the solution of mass transport equations simulating the migration of contaminants away from the used fuel/buffer interface. The mathematical formulation of these boundary conditions is given in Chapter 5. The solution of the mass transport equations provides the source term, i.e., the radionuclide flux (from all

TABLE 6-4

DARCY VELOCITIES IN BACKFILL
FROM THE MEDIAN-VALUE SIMULATION

Vault Sector Number	Backfill Darcy Velocity ($m \cdot a^{-1}$)
1	6.5×10^{-7}
2	8.8×10^{-7}
3	7.8×10^{-7}
4	2.1×10^{-7}
5	2.2×10^{-7}
6	8.9×10^{-7}
7	5.9×10^{-7}
8	5.3×10^{-7}
9	6.6×10^{-8}
10	1.3×10^{-7}
11	6.6×10^{-8}
12	9.4×10^{-7}

the release mechanisms) at the container/buffer interface as a function of time. The mathematical expressions for the source terms are given in detail by Garisto and LeNeveu (1991) and are not repeated here. The solutions take the form of sums of infinite series. The summations were truncated such that the relative error in the sums would be <0.1%.

6.6 THE PRECIPITATION MODELS

Both the precipitation of individual radionuclides (leading to a solubility-limited release of radionuclides into the geosphere) and the mass transport/precipitation coupling resulting from the precipitation of uranium-containing solids (leading to an enhanced release of certain fission products into the geosphere) (Garisto and Garisto 1986) are discussed in Chapter 5.

6.7 RESPONSE FUNCTIONS FOR THE MASS TRANSPORT EQUATIONS

The response-function approach is used to solve the equations for mass transport through a finite layer. In this approach the source boundary condition is a unit impulse input. The mass transport of any arbitrary time-varying source can be solved by convolution with the response function. This allows considerable flexibility in the definition of the source term. Also, the solution to the convection-diffusion equation is often simpler for an impulse input than for a more complex boundary condition.

As discussed in Section 6.3, a mass transfer coefficient has been used to specify the exit boundary condition in the MT model. Thus the boundary conditions for the response functions are as follows:

At $x = 0$,

$$-D_i^B \frac{\partial C_j}{\partial x}\bigg|_{x=0} + v^B C_j = I_j^u \delta(t) \qquad 1 \le j \le i \tag{6.6}$$

where I_j^u is a unit amount of radionuclide j, and δ is the Dirac delta function, and v^B is the Darcy velocity in the buffer.

At $x = a^B$,

$$-D_i^B \frac{\partial C_j}{\partial x}\bigg|_{x=a^B} + v^B C_j = K_i^B C_j \qquad 1 \le j \le i \tag{6.7}$$

where K_i^B is the mass transfer coefficient for radionuclide i and a^B is the thickness of the medium. In Equations (6.6) to (6.9), the superscript B refers to the buffer. Note that we assume that all the radionuclides in a decay chain have the same mass transfer coefficient, K_i^B, where i denotes the last member of a radionuclide chain. This assumption simplifies the analytical solution, which is otherwise extremely complicated. However, this assumption is not always valid because the mass transfer coefficient could depend on all the members of the radionuclide chain, not just the last member. The consequence of this is discussed in Chapter 8 where the mass transfer coefficient solution is compared with the coupled solution, which does not use this assumption. The assumption that all radionuclides in a decay chain have the same mass transfer coefficient is valid under conditions of high convective flow in the rock, where the mass transfer boundary condition can be replaced by a zero-concentration boundary condition.

The initial conditions for calculating the response functions are

$$C_j(x,0) = 0 \qquad 1 \le j \le i, \qquad 0 \le x \le a^B \ . \tag{6.8}$$

The release rate, $R_{ij}^B(t)$, of radionuclide i per unit impulse input of radionuclide j from a medium is given by

$$R_{ij}^B(t) = K_i^B C_{ij}(a^B,t) \tag{6.9}$$

where $C_{ij}(a^B,t)$ is the contribution to the concentration of radionuclide i from the unit impulse input of radionuclide j, $1 \le j \le i$.

The same response functions are used for the backfill, with the superscript B replaced by F. The response function solution is given by LeNeveu

(1987). The solution is obtained using Laplace transform methods. The Laplace-transformed solutions are then inverted analytically (producing infinite series) using two complementary methods, one that converges quickly for small values of time and one that converges quickly for large values of time. The solution methods are essentially the same as those outlined by Carslaw and Jaeger (1959). The solutions take the form of summations of infinite series. The series have been truncated so that the relative error is <0.1%.

A numerical routine from the SYVAC executive program (Goodwin et al. 1987) is then used to convolute the analytical response functions with given time-dependent sources to solve for radionuclide transport in a finite region, for a given value of the mass transfer coefficient (see Section 6.8). Thus, for the given source terms, $S_j(t)$, the release rate, $F_i^Y(x,t)$, of radionuclide i from the system defined by Equation (6.4) is given by convoluting the response function with each precursor source term and summing over all the precursors, including the last radionuclide, i,

$$F_i^Y(x,t) = \sum_{j=1}^{i} \int_0^t S_j(t')R_{ij}(x,t-t')\,dt' \; . \qquad (6.10)$$

The fractional error in the numerical convolution is estimated to be 1×10^{-3} for a single-simulation case (e.g., the median run) and 3×10^{-2} for a multiple-simulation case (see Goodwin et al. 1994). The fractional error for the response function and the source term is estimated to be 1×10^{-3} (i.e., 0.1%).

6.8 THE VAULT-GEOSPHERE COUPLING

6.8.1 The Mass Transfer Coefficient Approach

Four mass transfer coefficients are calculated by the MT model:

- the radionuclide mass transfer coefficient, K_i^B, for use in the response functions for the buffer;
- the radionuclide mass transfer coefficient, K_i^F, for use in the response functions for the backfill;
- the source mass transfer coefficient, K^S, for use in the calculation of the matrix release rate, $F^U(t)$; and
- the precipitation mass transfer coefficient, $K_i^P(t)$, for use in the calculation of the solubility-limited release from the used fuel.

These mass transfer coefficients are derived from a steady-state diffusive mass transfer coefficient, K_n^D, calculated on the assumption that mass transport in the rock is dominated by diffusion, and a steady-state convective mass transfer coefficient, K_n^C, calculated on the assumption that mass transport in the rock is dominated by convection. The determination and

use of the mass transfer coefficient follows methods similar to those of the SKB in Swedish assessment studies (Nilsson et al. 1991, Andersson et al. 1982) of mass transfer theory (Bird et al. 1960), and to methods used in heat transfer (Carslaw and Jaeger 1959). The subscript n refers to the number of layers in the system, where n = 1 refers to the buffer, n = 2 the buffer and backfill and n = 3 the buffer, backfill and rock. The subscript i, referring to the radionuclide for which the calculations are done, is omitted in the remainder of this chapter for clarity.

For a constant-concentration source boundary condition, radionuclide decay has the effect of increasing concentration gradients along the transport path (Garisto and LeNeveu 1989). Thus, K^S and K^P, determined for steady-state conditions, are functions of the radionuclide decay constant. The values of K^S and K^P will be greater for larger decay constants. However, K^S and K^P for an instant-release source boundary condition would not be affected by decay because the radionuclide concentration is not continuously replenished to create a constant source concentration. K^B and K^F are calculated using the asymptotic form of the mass transfer coefficient equations for a zero decay constant.

During the transient, the concentration gradients across the buffer/backfill interface and the backfill/rock interface would generally be expected to be larger than during steady state. From detailed studies of mass transport by diffusion only, a method has been devised for increasing the value of the steady-state mass transfer coefficient to account for this effect in calculating the response functions (Garisto and LeNeveu 1991). Both K^B and K^F are augmented (increased) to account for the transient conditions.

Other methods (referred to as coupled-solution methods) for solving the mass transport equations directly, without using the mass transfer coefficient approach, have been developed recently (Garisto et al. 1992). A comparison of the vault model results using the various solution methods indicates that the mass transfer coefficient provides a suitable approximation for one-member decay chains. Under certain conditions, however, it is a poor approximation for calculating the mass transport of radionuclides in a decay chain. This is of little consequence in the case study because the mass transport of radionuclides in decay chains is so restricted by low solubilities and by high sorption that there is insignificant release of such radionuclides from the vault. This is discussed in more detail in Section 8.3. The vault model code has been extended to include an option that allows the use of coupled solutions that do not involve mass transfer coefficients (Garisto et al. 1992).

Note, however, that the computation time required to implement the coupled solution method is much longer than for the mass transfer coefficient method: for example, the median SYVAC simulation for the 4n + 2 decay chain requires 14.4 h CPU time on the VAX 6400 with the coupled solution method, compared with 36.9 min with the mass transfer coefficient method.

6.8.2 The Mass Transfer Coefficient for Convective Mass Transport in the Rock and Backfill

The convective mass transfer coefficient, K^c, applies to a situation where mass transfer from the buffer to the rock is controlled by water movement in the rock. In particular, K^c is determined by assuming that mass transport in the rock is determined by convection in the direction parallel to the boundary between the buffer and rock and by dispersion in the direction perpendicular to the boundary. The mass transport model for this situation is two-dimensional. The mass transfer coefficient, K^c, is determined by the flux crossing the boundary averaged over a finite length, w, of the boundary divided by the concentration at the boundary, C_B. The geometry is illustrated in Figure 6-6 where

- D^R is the transverse dispersion coefficient in the rock, obtained from Equation (6.32),
- v^R is the Darcy velocity in the rock,
- w is the length of the mass transfer zone,
- C_B is the concentration along the boundary (assumed constant), between the buffer and the rock, and
- x, z are the spatial coordinates.

The governing equation is

$$\frac{D^R}{r^R}\frac{\partial^2 C}{\partial x^2} - \frac{v^R}{r^R}\frac{\partial C}{\partial z} - \lambda C = 0 \qquad (6.11)$$

where r^R is the capacity factor in the rock and λ is the radionuclide decay constant.

The boundary conditions are

$$C(x,0) = 0, \qquad 0 \le x < \infty \qquad (6.12)$$

$$C(0,z) = C_B, \qquad 0 < z < \infty \qquad (6.13)$$

$$C(x,z) \text{ remains finite as } x \to \infty \text{ and } z \to \infty, \qquad 0 \le z < \infty \ . \qquad (6.14)$$

The mass transfer coefficient is given by

$$K^c = \frac{1}{w}\int_0^w \frac{D^R}{C_B}\frac{\partial C}{\partial x}\bigg|_{x=0} dz \ . \qquad (6.15)$$

The solution derived by Laplace transform methods for K^c is

$$K^c = \left(\frac{D^R}{r^R\lambda}\right)^{1/2}\frac{v^R}{w}\,\mathrm{erf}\left(\frac{r^R\lambda w}{v^R}\right)^{1/2} \ . \qquad (6.16)$$

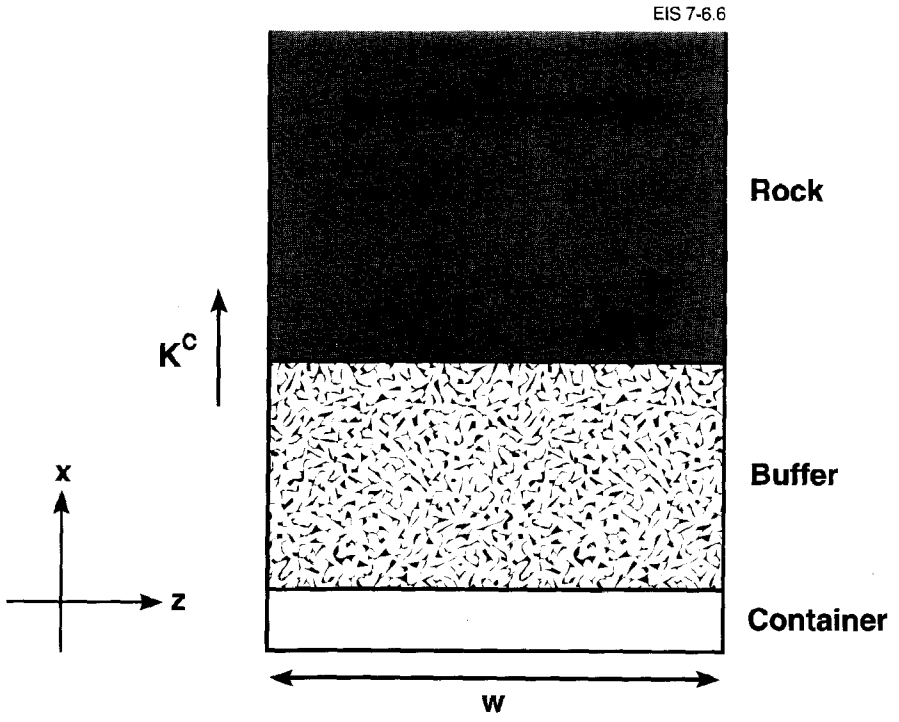

FIGURE 6-6: The Geometry for Deriving a Convective Mass Transfer Coefficient

As $\lambda \rightarrow 0$, the expression for K^C approaches the usual form for a convective mass transfer coefficient (Bird et al. 1960),

$$K^C = \left(\frac{4D^R v^R}{\pi w}\right)^{1/2} . \qquad (6.17)$$

Detailed calculations have shown that solutions reach an asymptote for values of $K^C > 50\ D/a^B$, where D is the total intrinsic diffusion coefficient (or dispersion coefficient) in the first medium (buffer) and a^B is the thickness of the medium. This corresponds to a C = 0 or "swept away" exit boundary condition.

It should be noted from Equation (6.17) that K^C depends on w, the length of the interface between rock and buffer as determined by the direction of groundwater flow in the rock (also called mass transfer length). Hydrogeological studies indicate that the groundwater flow in the rock is generally vertical in the vicinity of the vault (Chan and Scheier 1987); thus the height of the emplacement borehole would correspond to the length of interface between buffer and rock. However, radionuclides might not be distributed along the entire length of this interface. The height of the container from whence the radionuclides originate is smaller than the

height of the borehole. Thus if there were no vertical diffusion as the radionuclides diffuse horizontally across the buffer, the length of the interface between the buffer and the rock that would become contaminated with radionuclides would equal the height of the container. A smaller value of this length (w) would result in a larger value of the mass transfer coefficient and a larger release rate from the vault to the geosphere (a conservative approximation). For these reasons w was taken to be the height of the container.

Equations (6.11) and (6.17) are also used to calculate a convective mass transfer coefficient for the backfill. In this case, the mass transfer length, w, is taken to be the vertical height of the backfilled room.

There is considerable uncertainty as to the value for the transverse dispersion coefficient for this application. Values for dispersion coefficients are usually based on large-scale field tests. The application of these values for calculation of mass transfer coefficients may be inappropriate for vault conditions where mass transport in the buffer and backfill is over much smaller distances than in field tests (Neuman 1987). The appropriate value of the dispersion coefficient for the determination of mass transfer coefficients would likely be smaller than the value derived from field tests. However, larger values of the dispersion coefficient would give larger values of the mass transfer coefficient, which in turn would give larger release rates from the vault to the geosphere; thus the dispersion coefficient derived from large-scale field tests was used. To further ensure that conservative values were obtained for the convective mass transfer coefficient, the value used for the longitudinal dispersion coefficient for the rock is larger than the transverse dispersion coefficient (see Equation (6.32)).

6.8.3 The Mass Transfer Coefficient for Diffusive Mass Transport in the Rock and Backfill

The diffusive mass transfer coefficient, K_n^D, applies to a situation where mass transport in the buffer, backfill and rock is controlled by diffusion. In particular, K_n^D is determined for a three-layer system: buffer, backfill and rock under steady-state conditions where there is no groundwater movement (see Figure 6-7). (The subscript n denotes the layers.) The rock layer is the region between the vault and the nearest fracture zone with sufficient groundwater movement that any contaminant appearing in the fracture zone will be "swept away." This is equivalent to the assumption of a zero-concentration condition at the exit from the rock layer. Continuity of flux and concentration at the interface with the other layers is assumed, and the water in the system is assumed to be stagnant. Two mass transfer coefficients, K_1^D and K_2^D, are defined for the exit from the first and second layers (buffer and backfill respectively). The mass transfer coefficients are the ratios of the steady-state flux to the concentration at the exit from a layer:

$$K_n^D = - \frac{D_n}{C_n} \frac{\partial C_n}{\partial x} \qquad \text{at } x = a_n \qquad\qquad n = 1, 2 \qquad\qquad (6.18)$$

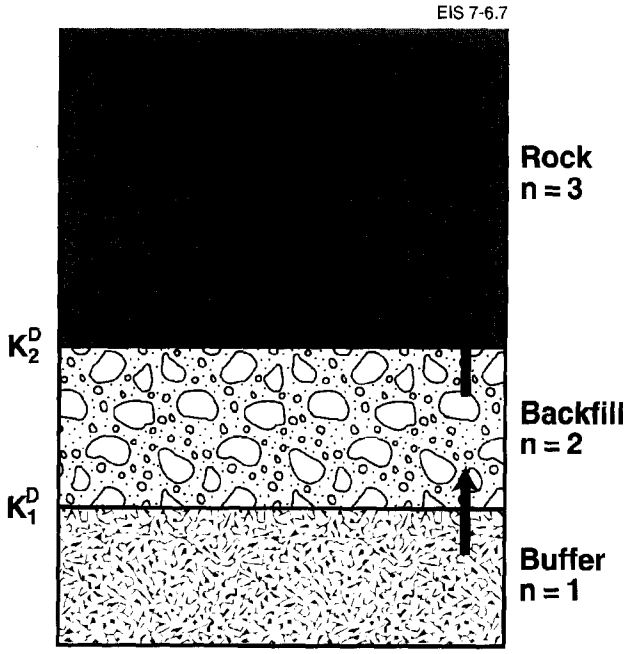

FIGURE 6-7: The Geometry for Deriving a Diffusive Mass Transfer Coefficient

where D_n is the total intrinsic diffusion coefficient in layer n,
C_n is the concentration in layer n, and
a_n is the thickness of layer n.

The governing equation is

$$\frac{D_n}{r_n}\frac{\partial^2 C_n}{\partial x^2} - \lambda C_n = 0 \qquad n = 1, 2, 3 \qquad (6.19)$$

where r_n is the capacity factor in layer n, and
λ is the radionuclide decay constant.

The boundary conditions are as follows:

$$C = C_o \text{ (constant)} \qquad \text{at } x = 0 \qquad (6.20)$$

$$C_n = C_{n+1} \qquad \text{at } x = a_n \qquad n = 1, 2 \qquad (6.21)$$

$$D_n \frac{\partial C_n}{\partial x} = D_{n+1} \frac{\partial C_{n+1}}{\partial x} \qquad \text{at } x = a_n \qquad n = 1, 2 \qquad (6.22)$$

$$C_3 = 0 \qquad \text{at } x = a_3 \tag{6.23}$$

i.e., $$K_3^D = \infty \quad . \tag{6.24}$$

The solution for K_n^D is

$$K_n^D = \frac{(D_{n+1}b_{n+1})^2 \sinh(b_{n+1}) + D_{n+1}b_{n+1}a_{n+1}K_{n+1}^D \cosh(b_{n+1})}{D_{n+1}b_{n+1}a_{n+1} \cosh(b_{n+1}) + (a_{n+1})^2 K_{n+1}^D \sinh(b_{n+1})} \tag{6.25}$$

In the limit as $K_3^D \to \infty$ (corresponding to a zero-concentration boundary condition at the exit from layer 3), the expression for K_2^D becomes

$$K_2^D = \frac{D_3 b_3 \cosh(b_3)}{a_3 \sinh(b_3)} \tag{6.26}$$

where

$$b_n = \left[\frac{r_n \lambda}{D_n}\right]^{1/2} a_n \quad . \tag{6.27}$$

In the limit as $\lambda \to 0$, the expression for K_n^D reduces to the same form as for the equation for addition of resistances in electrical circuits,

$$\frac{1}{K_n^D} = \frac{1}{K_{n+1}^D} + \frac{a_{n+1}}{D_{n+1}} \quad . \tag{6.28}$$

The above equations for K_n^D can be applied to a system with any number of layers.

6.8.4 The Augmentation Factor for the Diffusive Mass Transfer Coefficient

The convective and diffusive mass transfer coefficients expressed above are determined for steady-state conditions that apply at long times when concentration gradients in the system are no longer changing. At shorter times when radionuclides would be just beginning to migrate, concentration gradients and mass transfer coefficients would be larger. This section describes how the value of the diffusive mass transfer coefficient has been augmented to account for this effect. The convective mass transfer coefficient has not been augmented because steady-state conditions should be established quickly near the boundaries where groundwater flow rates are large.

The augmentation factor for the diffusive mass transfer coefficient was determined by comparing solutions obtained using mass transfer coefficients with those obtained using continuity of flux and concentration at the boundary for a two-layer (e.g., buffer or backfill and rock) system.

The coupled equations are

$$\frac{\partial C_n}{\partial t} = \frac{D_n}{r_n}\frac{\partial^2 C_n}{\partial x^2} - \lambda C_n \qquad n = 1, 2 \tag{6.29}$$

with the boundary conditions given in Equations (6.20) to (6.23) and the following two boundary conditions at $x = 0$:

$$-D_1 \frac{\partial C_1}{\partial x}\bigg|_{x=0} = I^U \delta(t) \tag{6.30}$$

or

$$C_1(x,t) = C_0 \qquad \text{at } x = 0 \tag{6.31}$$

and initial condition $C_n(x,0) = 0$.

Boundary condition (6.30) was applied to analyze instant release and boundary condition (6.31) was applied to analyze congruent release. These equations were solved numerically using Laplace transform techniques and Talbot's inversion algorithm (Talbot 1979). A wide range of parameter values was used for D_n, r_n and λ, covering the range of values expected in the vault.

We found that it was necessary to augment the value of the mass transfer coefficient by an increasing amount ($\exp(y_n)$) as the ratio between the breakthrough time to steady state in the remaining medium (i.e., the rock) to the duration of the response to unit impulse in the first medium (i.e., the buffer or backfill) increased. The breakthrough time in the rock was used rather than the breakthrough time for the backfill because the dose consequence estimate is determined by the former rather than the latter. The expressions for y_n and its values are given by Garisto and LeNeveu (1991). However, the value of the augmented mass transfer coefficient was often found to exceed 50 D_n/a (the asymptotic value corresponding to a zero-concentration exit boundary condition). In these cases, the vault model mass transport calculations are carried out using K^B or $K^F = 50\ D_n/a$. In the vault model, n, the subscript denoting layer number, equals one for the buffer and two for the backfill. A lower limit of $v^B/2$ or $v^F/2$ is also applied to the value of K^B or K^F respectively to simplify the mathematics (LeNeveu 1987), where v^B and v^F are the Darcy velocities in the buffer and backfill respectively. This allows us to extend the range of applicability of the MT code to cases with substantial groundwater flow in the buffer or backfill.

6.8.5 The Parameters Defining the Mass Transfer Coefficients

The parameters required for calculating the mass transfer coefficients include the dispersion coefficient in the rock, the Darcy velocities in the backfill and rock, the mass transfer lengths in the buffer and backfill, the segment length adjacent to the relevant vault sector, the diffusion

coefficients in the buffer and backfill and the nuclide capacity factors. The dispersion coefficient is given by (see Davison et al. 1994b)

$$D^R = D_0 \epsilon^R / (\tau^R)^2 + \alpha^R v^R \qquad (6.32)$$

where values for D_0, ϵ^R, τ^R, v^R and α^R are given in Tables 6-5 and 6-6. The remaining parameters are given in Tables 6-3 and 6-4 (see also Chapter 3 and Davison et al. 1994b).

6.9 THE RELATIONSHIP BETWEEN THE VAULT MASS TRANSPORT MODEL AND DETAILED MODELS

The major detailed models supporting the MT model in the vault model are as follows:

1. A hydrogeological model, MOTIF (Chan and Scheier 1987), is used to derive the vault model sector geometry and data required to calculate the mass transfer coefficients.

2. Geochemical and reaction path models (e.g., CHEMP, Garisto and Garisto 1984) are used to evaluate groundwater/buffer interactions and to calculate radionuclide solubilities for the source terms and the precipitation models (Lemire and Garisto 1989).

TABLE 6-5

PARAMETERS REQUIRED TO CALCULATE THE CONVECTIVE MASS TRANSFER COEFFICIENT

Parameter	Definition	Value	
	mass transfer length for the buffer	2.25 m	(i.e., height of container)
	mass transfer length for the backfill	5.0 m	(i.e., height of disposal room)
D_0	free water diffusion coefficient	4.70×10^{-2} $m^2 \cdot a^{-1}$	(median value)
ϵ^R	rock porosity	3.0×10^{-3}	(median value)
τ^R	rock tortuosity	4.1	(median value)
α^R	dispersion length	10.5 m	(median value)
v^R	rock Darcy velocity	see Table 6-6	

TABLE 6-6

GEOSPHERE MEDIAN-VALUE PARAMETERS

FOR INPUT INTO VAULT

Vault Sector No.	Median Darcy Velocity in the Rock ($m \cdot a^{-1}$)
1	1.8×10^{-7}
2	2.4×10^{-7}
3	2.1×10^{-7}
4	5.8×10^{-8}
5	5.8×10^{-8}
6	1.1×10^{-7}
7	1.6×10^{-7}
8	2.4×10^{-7}
9	1.8×10^{-8}
10	3.6×10^{-8}
11	1.8×10^{-8}
12	2.5×10^{-7}

3. Fuel performance models (e.g., ELESIM (Notley 1979)) are used to derive the instant-release fractions for the instant-release source term (Garisto et al. 1990).

4. Diffusion-reaction models can be used to derive equivalent sorption models for use in the vault model (e.g., Garisto and Garisto 1990c).

5. Coupled diffusion-precipitation models are used to derive the enhancement factors for estimating the effect of precipitation of uranium-containing solids on the release flux (e.g., Garisto 1986, Garisto and Garisto 1988a).

6. Fractured-media transport models (e.g., CBC (Garisto and Garisto 1989)) can be used to estimate the effect of buffer cracks on the performance of the vault.

7. A thermal model (HOTROK (Mathers 1985)) is used to calculate the spatial and temporal temperature distribution in the vault for the mass transport data and the container failure model.

6.10 SUMMARY

The overall computational procedure in the vault model is described in qualitative terms in Section 6.3. Using the mathematical formalism outlined in Sections 6.4 to 6.8, we can now summarize the overall procedure in qualitative terms.

For each simulation for each vault sector, the MT model calculates two mass transfer coefficients for the buffer and two mass transfer coefficients for the backfill:

1. On the assumption that mass transport in the surrounding rock is dominated by diffusion, it calculates K_1^D for the buffer from a three-layer calculation (buffer/backfill/rock), and K_2^D for the backfill from a two-layer calculation (backfill/rock).

2. On the assumption that mass transport in the surrounding rock is dominated by convection, it calculates K^C for the buffer from a two-layer calculation (buffer/rock) and K^C for the backfill from a two-layer calculation (backfill/rock).

The MT model then chooses the larger of the two mass transfer coefficients for the buffer and backfill respectively.

The instant-release source term, $G_i^I(t)$, and the congruent-release source term, $F_i(t)$, are then calculated and summed. The net source term is then convoluted with the container failure function, and precipitation is taken into account.

The resultant release rate into the buffer is then convoluted with the buffer response function, $R_{ij}^B(t)$, and with the backfill response function, $R_{ij}^F(t)$, using the mass transfer coefficients to produce the release rate from the vault into the rock for each radionuclide and in each sector.

7. THE MEDIAN-VALUE SIMULATION, VERIFICATION USING SIMPLE MODELS AND SENSITIVITY ANALYSIS

7.1 INTRODUCTION

In the median-value simulation, all the parameters having frequency distributions are given their median values. The results of the median-value simulation are discussed here in detail. This simulation is provided as an example to explain the workings of the vault model. Results from the median-value simulation have been compared with simpler bounding calculations or calculations on specific features of the model. These bounding calculations do not replace the more complex calculations used for the assessment analysis. They are used to verify the more complex assessment models over a restricted range of parameter values where a comparison is appropriate.

A complete listing of all parameters in the vault model is presented in Appendix E (Table E-1). Each parameter is identified by a code name used in SYVAC3-CC3 and the parameter is defined. The median value and probability density function are given, along with a reference to the section of this report where the justification for the attributes is presented.

After the behaviour of the median-value simulation is explained, the results of sensitivity analyses are presented. The most important

parameters in the vault model are identified by a fractional factorial analysis (Goodwin et al. 1994). This approach limits the discussion of sensitivity analysis to an examination of how the assessment results obtained are influenced by variation within the parameter distributions explicitly defined in the vault model. Following this, a discussion is presented of the sensitivity of the assessment results to the key assumptions made in developing the various models describing engineered barrier performance that are used in the vault model. This is a more qualitative analysis, which serves to highlight the extent of conservatism in some of these models and to emphasize which key assumptions result in elements of the model being realistic, i.e., having little inherent conservatism.

Finally, we discuss the time frame of validity of the vault model. As can be seen from simulation results presented in Section 7.2, calculations are generally restricted to periods $<10^5$ a. The reasons for this restriction are discussed and reasoned arguments are presented for the performance of the used fuel and clay-based barriers over longer time frames.

7.2 THE MEDIAN-VALUE SIMULATION AND VERIFICATION USING SIMPLE MODELS

All significant contaminants were included in the median-value simulation, and contaminant release rates from the vault into the rock are calculated. Release rates from the vault are defined as the total amount of contaminant entering the rock from the entire vault per unit time. For the median-value simulation incorporating the geosphere and biosphere models in the period up to ten thousand years after closure, none of the estimated dose rates exceed a value of 10^{-10} Sv·a^{-1}, a factor of about five hundred thousand lower than the dose rate implied by the Atomic Energy Control Board (AECB) risk limit (AECB 1987). The overall assessment results are presented in detail by Goodwin et al. (1994).

Ninety-nine radionuclides and chemically toxic elements are represented in the simulation. These include one decay chain with two members, three chains with three members each, and one chain with four members. Chains are shortened, and some radionuclides are assumed to be in secular equilibrium, where appropriate, to simplify the calculations (Goodwin and Mehta, in preparation).

Within the period of 10^5 a, the only radionuclide in the simulation with a dose rate above 10^{-10} Sv·a^{-1} is ^{129}I, which gives a maximum dose rate of 4.3×10^{-7} Sv·a^{-1}, occurring at 10^5 a. The second highest dose rate is from ^{14}C, which gives a maximum dose rate of 3.8×10^{-11} Sv·a^{-1} at 56 000 a. Figure 7-1 shows the dose rate as a function of time for the two major contributors, ^{129}I and ^{14}C, as well as for ^{99}Tc. These dose rates do not exceed the AECB R-104 derived dose limit of 5×10^{-5} Sv·a^{-1} (AECB 1987), nor does the sum of the dose rate estimates for all the released radionuclides.

The release rates of ^{129}I and ^{14}C from the vault to the geosphere up to 10^5 a are presented here in detail, since they are the major contributors to dose. Other contaminants are also discussed if their behaviour provides insight into vault performance.

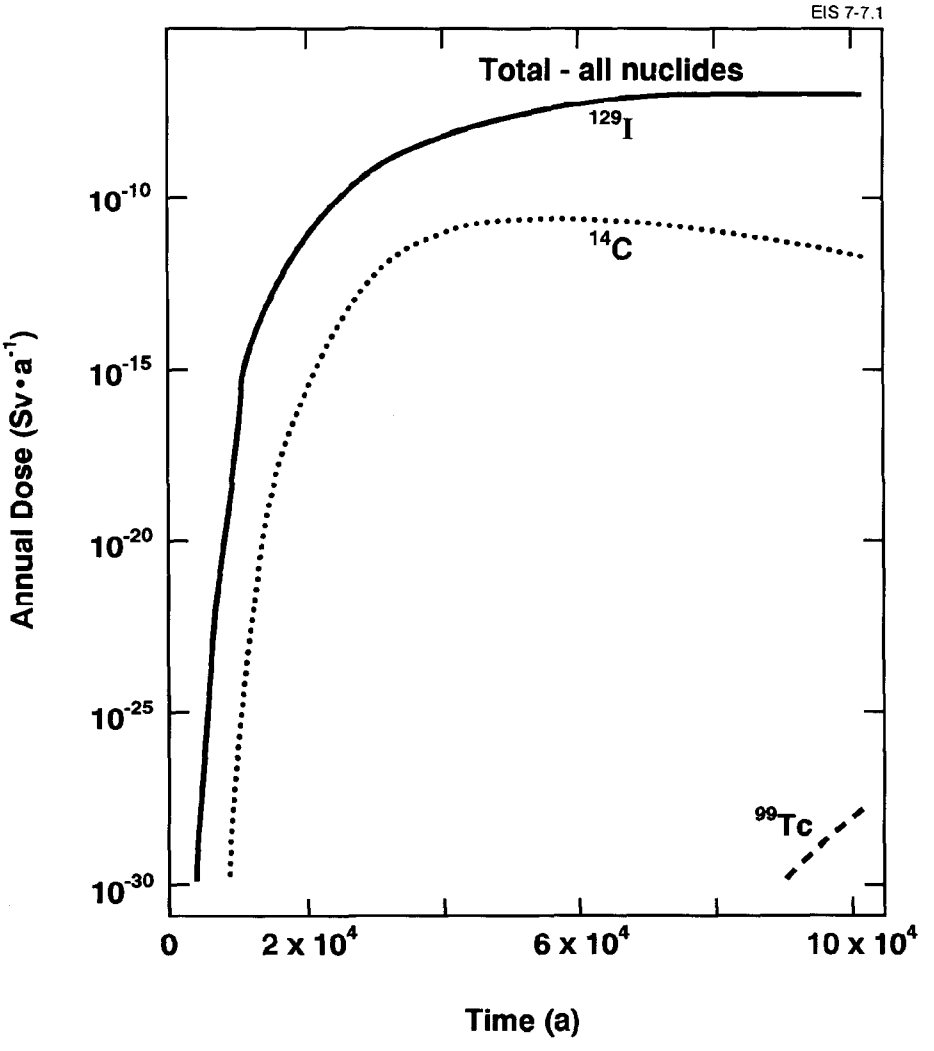

FIGURE 7-1: Dose Rates as a Function of Time for ^{129}I, ^{14}C and ^{99}Tc for the Median-Value Simulation. The dose rate curves for ^{129}I and all nuclides are superimposed.

We also compare the results of calculations of container lifetimes and release rates of radionuclides from the used fuel, buffer and backfill materials, using simple models, with the results obtained with the vault model to verify that the model calculations are correct.

7.2.1 The Progression of the ^{129}I Release from the Vault to the Biosphere

The layout of the postclosure assessment reference vault, the location of the potential pathways for contaminant migration in the geosphere, and discharge locations in the biosphere are described in detail by Goodwin et al. (1994).

The median-value simulation of the total amount of ^{129}I released from the vault to the geosphere up to 10^5 a is illustrated in Figure 7-2. The height of the blocks represents the amount released from each sector per unit area, and the volume represents the total amount released. The differences in the total amounts released are largely a result of the differences in the groundwater velocities in the geosphere segments adjacent to the vault sectors. For instance, the magnitude of the groundwater velocity in sector 12 is larger than in sectors 4 to 11. Consequently, the total amount of ^{129}I released per unit area up to 10^5 a is larger in sector 12 than in sectors 4 to 11. Overall, however, the differences are small and the release per unit sector area across the entire vault varies by only a factor of approximately three.

The total amount of ^{129}I that diffuses completely through the lower rock and enters the fracture zone LD1 up to 10^5 a is illustrated in Figure 7-3. The lower rock is the region of intact rock between the vault and the closest major fracture zone (Figure 6-1). The vault sector numbers adjoining each rock segment are given. The release into the fracture zone from segments having the longest path length from the vault to the fracture zone is attenuated during mass transport through the rock barrier to relatively insignificant levels. Consequently, of the 519 mol of ^{129}I that enter the rock in 10^5 a, only 0.32 mol diffuse through the rock and enter the fracture zone in the same period. The rest is retained in the rock. The lower rock segments interfacing with sectors 10, 11 and 12 have the shortest path length from the vault to the fracture zone and, consequently, the largest releases. The differences in the releases between segments 10, 11 and 12 are attributable to different groundwater velocities in the rock segments.

There is both convergence and divergence in the remaining pathways to the discharge locations (see Figure 6-1). A portion of the ^{129}I release originating near the fracture zone discharges to Boggy Creek South, with the remainder discharging to a well that intersects fracture zone LD1. In the median-value simulation, the releases of ^{129}I to the well provide the major contribution to the calculated dose rates. Thus the portion of the release of ^{129}I discharging to the well determines the maximum dose rate in the median-value simulation. Figure 7-4 shows the amount of ^{129}I released from the lower rock segments, identified by sector of origin, that eventually discharges to the well (0.08 mol in 10^5 a). It is clear that the release originating in sector 11 contributes the most to the final ^{129}I dose rate. This occurs because of the location of the well in the fracture zone in relation to the vault sectors. Sector 11 is expected to make the largest contribution to dose for other radionuclides as well. For this reason the analysis of the release from the vault for the median-value simulation is focused on sector 11.

7.2.2 Releases from the Vault

Figure 7-5 shows the simulation release rates from sector 11 into a segment in the lower rock zone as a function of time for eleven selected radionuclides. As mentioned earlier, the major contributor to dose is ^{129}I, followed by ^{14}C. Both ^{79}Se and ^{135}Cs have higher release rates than ^{129}I and ^{14}C, but because they are much more strongly retarded in the geosphere than ^{129}I and ^{14}C they do not significantly contribute to the dose up to 10^5 a.

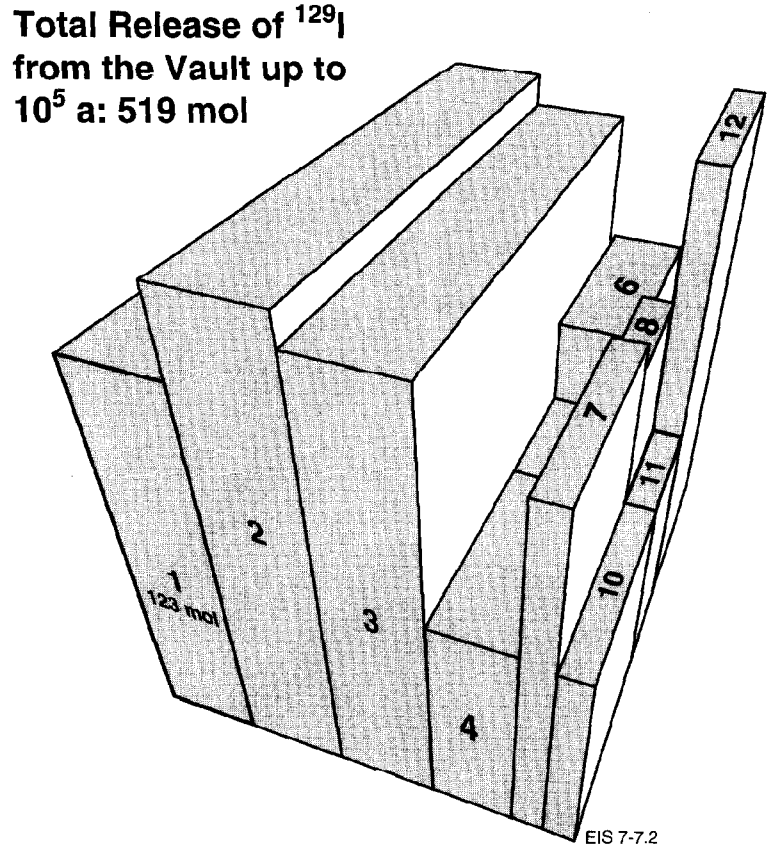

FIGURE 7-2: Amount of ^{129}I Released from the Vault up to 10^5 a. The height of the blocks represents the amount of ^{129}I released per unit sector area up to 10^5 a. The area of the blocks represents the sector area and the position of the blocks reflects the vault sector layout. The volume of the blocks represents the total amount of ^{129}I released from each sector up to 10^5 a. The data are obtained from the median-value simulation. The total release from Sector 1 is shown to give perspective.

The other radionuclides shown in Figure 7-5 have lower release rates than ^{129}I and ^{14}C and are also substantially retarded in the geosphere. In our presentation of the vault release analysis, in addition to ^{129}I and ^{14}C releases we discuss analyses of ^{99}Tc, as an example of a radionuclide that precipitates in the buffer in the median-value simulation, and the members of the ^{238}U (4n + 2) series as an example of how a decay chain behaves.

Analysis of the results from the median-value simulation show that the UO_2 matrix solubility is very low, and the uranium released does not precipitate in the buffer (see Chapter 5). Technetium encounters conditions in the buffer that cause it to precipitate.

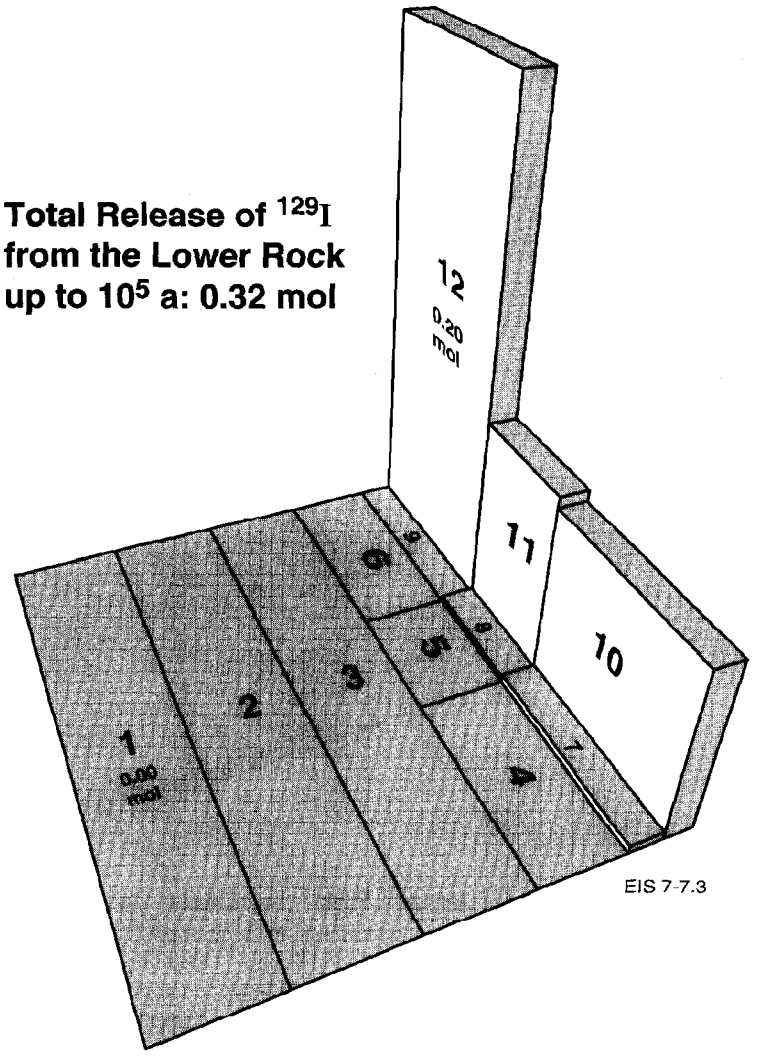

FIGURE 7-3: Amount of ^{129}I Released from the Lower Rock to the Fracture Zone up to 10^5 a. Each block corresponds to a line segment used to represent the flowpath from the vault through the lower rock to the fracture zone. The blocks are labelled with the number of the vault sector adjoining each line segment. The height of the blocks represents the amount of ^{129}I released from each segment per unit area up to 10^5 a. The area of each block represents the area of the vault sector adjoining each geosphere segment. The volume of each block represents the total amount of ^{129}I released from each segment up to 10^5 a. The position of the blocks reflects the vault sector layout. The data are obtained from the median-value simulation.

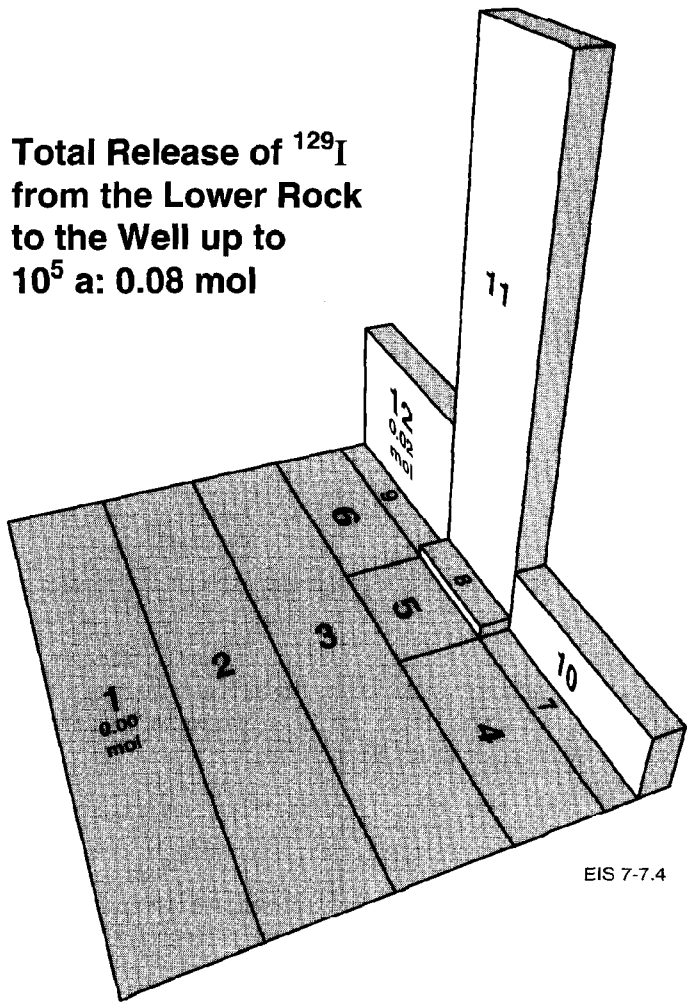

FIGURE 7-4: Amount of ^{129}I Released from the Lower Rock up to 10^5 a That Discharges to the Well. Each block corresponds to a line segment used to represent the flowpath from the vault through the lower rock to the fracture zone. The blocks are labelled with the number of the vault sector adjoining each line segment. The height of the blocks represents the amount of ^{129}I released from each segment per unit area up to 10^5 a that eventually discharges to the well. The area of each block represents the area of the vault sector adjoining each geosphere segment. The volume of each block represents the total amount of ^{129}I released from each segment up to 10^5 a that eventually discharges to the well. The position of the blocks reflects the vault sector layout. The data are obtained from the median-value simulation.

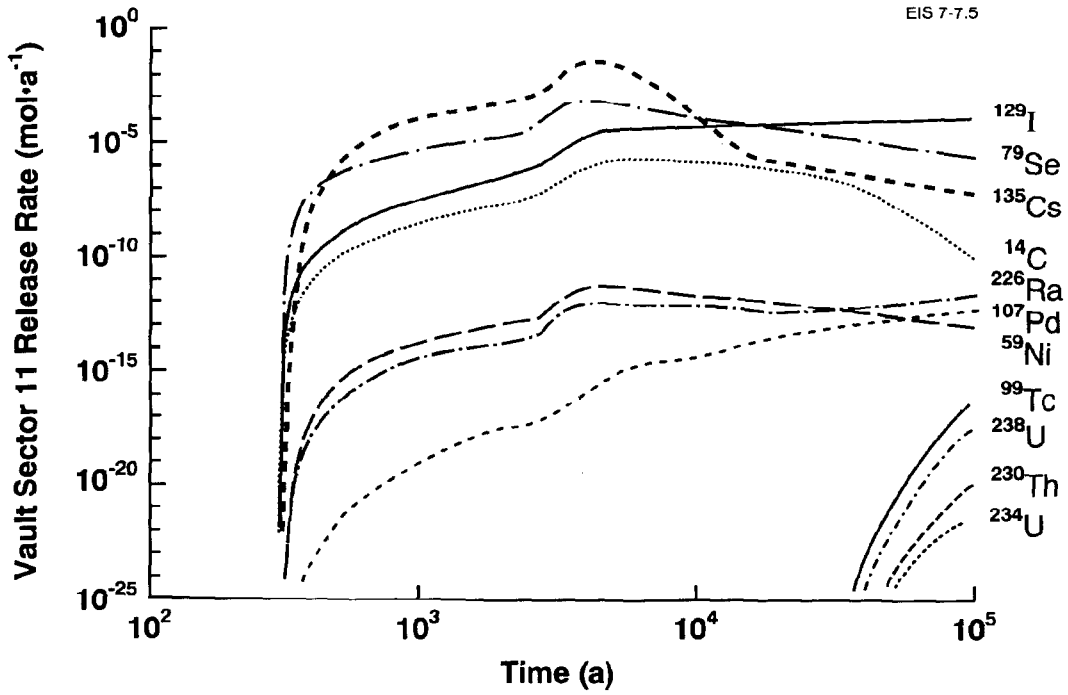

FIGURE 7-5: Release Rates of the Most Important Radionuclides from Sector 11 of the Vault into a Segment in the Lower Rock Zone for the Median-Value Simulation

7.2.2.1 Container Failure

The container failure rate for the median-value simulation is illustrated in Figures 7-6 and 7-7, which show the fractional rate of failure and the accumulated fraction of containers failed as a function of time, for representative sectors.

These plots show that almost all of the containers fail between 10^3 and 10^4 a after vault closure. In sectors 1, 6 and 11, 90.1, 99.8 and 86.7%, respectively, of the containers fail from crevice corrosion. The remainder fail from HIC. One container in ten thousand fail early (before fifty years) from fabrication defects in the median-value simulation. Based on this frequency, in sectors 1 to 6, from one to five containers fail early, depending on the total number of containers in the sectors. Each of the remaining sectors have fewer containers and no early failures. The rate of early container failure is too small to be visible on the graphs. The impact of such early failures is discussed in Chapter 8.

All the containers fail by 10^4 a after closure. Thus, the entire inventory of radionuclides available for instant release is discharged to the container interiors by that time.

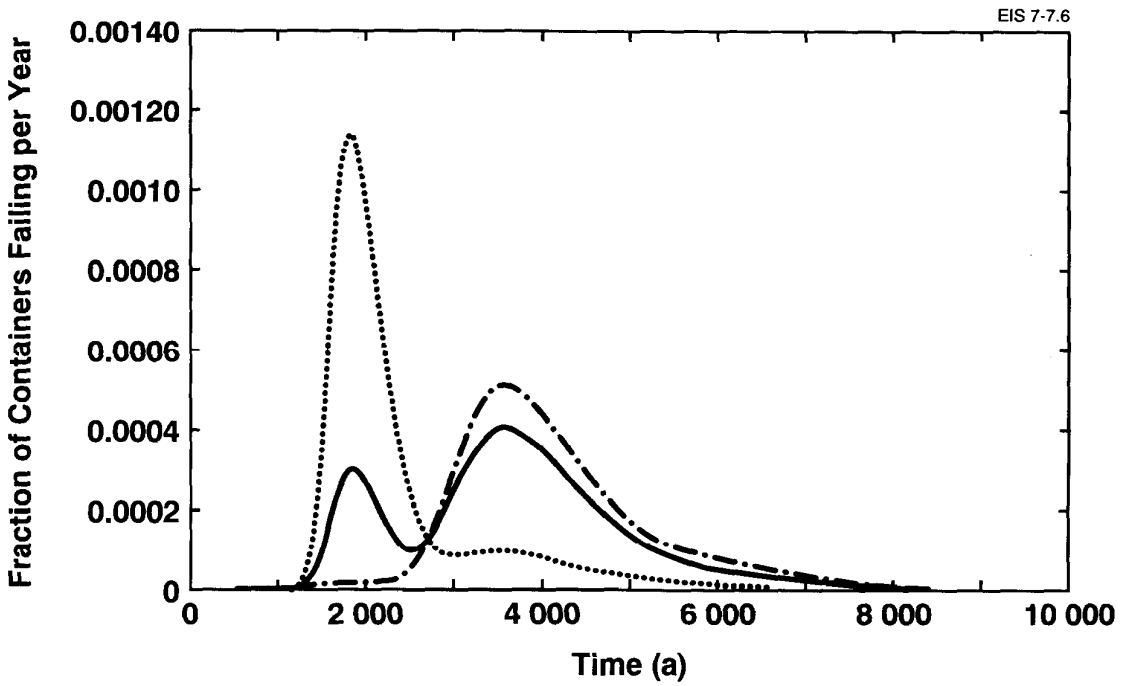

FIGURE 7-6: Fractional Rate of Container Failure for the Median-Value Simulation. The fractional rate of failure of the titanium containers is shown as a function of time for sectors 1 (—), 6 (-·-·) and 11 (····). The data are obtained from the median-value simulation.

The time of failure from crevice corrosion is calculated by dividing each sector into regions in which containers are designated as hot, cool or cold. The fraction of containers in each sector designated as hot, cool and cold are denoted as A^R, A^A and A^E respectively (see Section 4.7.6). The temperature as a function of time for hot containers is approximated by a two-step function where the temperature is assumed to be constant up to a time t_1^R, whereupon it falls instantly to a second constant temperature up to a time t_2^R. A distribution of crevice corrosion rates is associated with each temperature. The times at which the rate of container failure would be largest for hot, cool, and cold containers has been estimated by using the mean crevice corrosion rates μ_{r1}, μ_{r2}, μ^A and μ^E for these categories of containers, as defined in Table 7-1, rather than a distribution of corrosion rates. The failure times estimated using such an approach should compare favourably with the peak failure times calculated in the median-value simulation.

The failure time based on crevice corrosion for a hot container, t_p^R, can be estimated from the mean corrosion rates by the following equations:

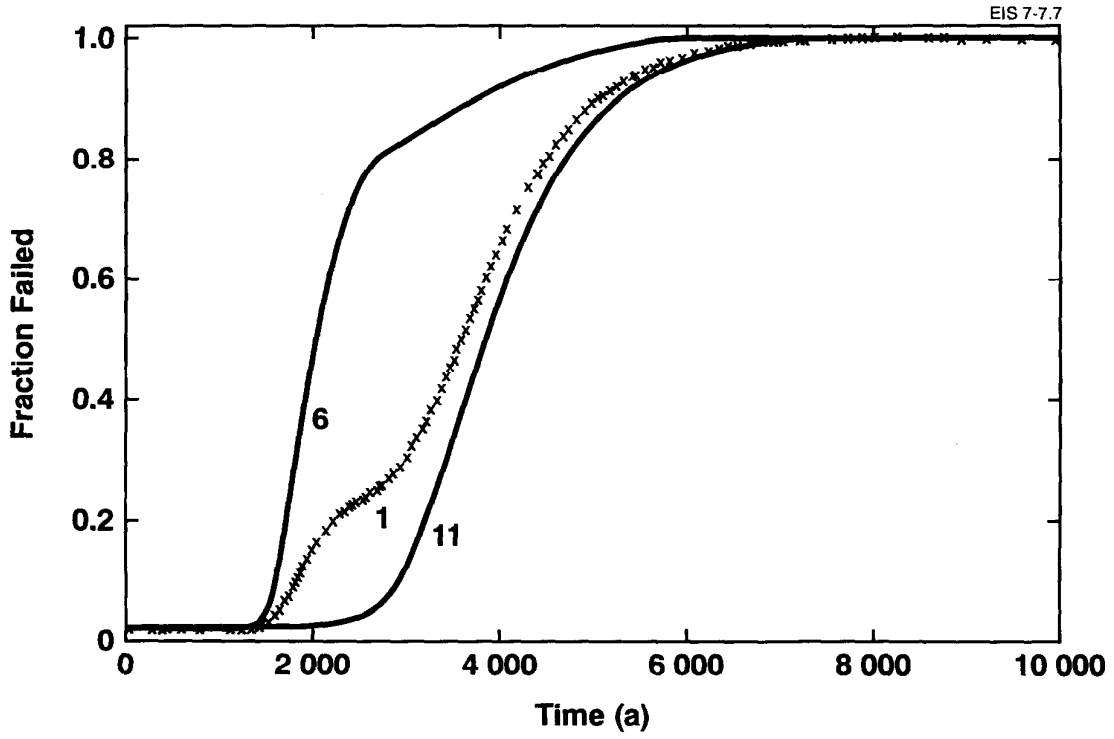

FIGURE 7-7: Accumulated Fraction of Containers Failing for the Median-Value Simulation. The accumulated fraction of the titanium containers failing is shown as a function of time for sectors 1, 6 and 11. The data are obtained from the median-value simulation.

$$t_p^R = \frac{w^X}{\mu_{r1}} \qquad \text{provided} \quad t_p^R \leq t_1^R \tag{7.1}$$

$$t_p^R = t_1^R + \frac{w^X - \mu_{r1} t_1^R}{\mu_{r2}} \qquad \text{provided } w^X/\mu_{r1} \leq t_p^R \leq t_2^R \tag{7.2}$$

where w^X is the effective container thickness (i.e., the container wall thickness that could corrode before the remaining container shell is assumed to fail by mechanical overload (Section 4.2)).

The crevice corrosion rates for cool and cold containers are approximated as constants up to times t_1^A and t_1^E respectively, whereupon the rates are assumed to drop to zero. The mean corrosion rates are μ^A and μ^E respectively. The corrosion times for cool and cold containers, t_p^A and t_p^E, can be estimated from Equations (7.3) and (7.4):

$$t_p^A = \frac{w^X}{\mu^A} \qquad \text{provided} \quad t_p^A \leq t_1^A \tag{7.3}$$

$$t_p^E = \frac{w^X}{\mu^E} \quad \text{provided} \quad t_p^E \leq t_I^E \quad . \tag{7.4}$$

For times greater than t_I^A and t_I^E the containers do not fail by corrosion, but are assumed to fail by HIC, and the failure times can be estimated by

$$t_p^A = t_I^A + t_H^A/2 \quad \text{provided} \quad t_p^A > w^X/\mu^A \tag{7.5}$$

$$t_p^E = t_I^E + t_H^E/2 \quad \text{provided} \quad t_p^E > w^X/\mu^E \tag{7.6}$$

where t_H^A and t_H^E are the times taken to fail by HIC for cool and cold containers after crevice corrosion has ceased.

The container failure data for sectors 1, 6 and 11 of the vault from the median-value simulation are given in Table 7-1.

The estimated failure times for hot, cool and cold containers determined from Equations (7.1) through (7.6) are given in Table 7-2. These failure times are sector-independent, because the crevice corrosion rates are also sector-independent. The fractions of containers designated as hot, cool and cold vary from sector to sector.

The times at which the maximum failure rate occurs as determined in the median-value simulation shown in Figure 7-6 are 3.62×10^3 a and 1.86×10^3 a. These times are in good agreement with failure times estimated by Equations (7.1) to (7.6) for cool and hot containers respectively. The relative areas under the peaks in Figure 7-6 correspond to the fractions of containers designated hot and cool.

The containers designated as cold fail entirely by HIC, which conforms with the fact that the time at which the cold temperature period ceases occurs before the estimated failure time for cold containers (t_p^E). The failures due to HIC for containers designated as cold begin at 300 a and continue to 7700 a. These comparisons of the container failure model results from the median-value simulation with values calculated with Equation (7.1) through (7.6) confirm that the model has been correctly implemented in the vault model.

7.2.2.2 Congruent and Instant Release of Radionuclides from the Used Fuel into the Buffer

In this section we compare results for the release of radionuclides from the used fuel into the buffer for the median-value simulation with results obtained using simple equations. In the median-value simulation, the dissolution of the UO_2 matrix in the vault is so slow that only a minute fraction, 6.2×10^{-9}, of the UO_2 in the vault is dissolved in 10^5 a. During this period, the dissolution rate of UO_2 monotonically decreases, but never reaches a steady-state value. The relatively high capacity factor for uranium in the buffer and a relatively small mass transfer rate of uranium into the geosphere delays the onset of steady state (i.e., the

TABLE 7-1

MEDIAN-VALUE CONTAINER FAILURE PARAMETERS

Symbol	Parameter Description	Median Value	SI Unit
A_1^R	Fraction of containers hot (sector 1)	2.13×10^{-1}	-
A_1^A	Fraction of containers cool (sector 1)	6.88×10^{-1}	-
A_1^E	Fraction of containers cold (sector 1)	9.87×10^{-2}	-
A_6^R	Fraction of containers hot (sector 6)	8.32×10^{-1}	-
A_6^A	Fraction of containers cool (sector 6)	1.64×10^{-1}	-
A_6^E	Fraction of containers cold (sector 6)	3.52×10^{-3}	-
A_{11}^R	Fraction of containers hot (sector 11)	0	-
A_{11}^A	Fraction of containers cool (sector 11)	8.67×10^{-1}	-
A_{11}^E	Fraction of containers cold (sector 11)	1.33×10^{-1}	-
μ_{r1}	Mean corrosion rate for 1st hot temperature period	6.60×10^{-6}	$m \cdot a^{-1}$
μ_{r2}	Mean corrosion rate for 2nd hot temperature period	1.90×10^{-6}	$m \cdot a^{-1}$
μ^A	Mean corrosion rate for cool temperature period	1.08×10^{-6}	$m \cdot a^{-1}$
μ^E	Mean corrosion rate for cold temperature period	1.15×10^{-6}	$m \cdot a^{-1}$
t_1^R	Time at which 1st hot temperature period ceases	1.06×10^{2}	a
t_2^R	Time at which 2nd hot temperature period ceases	1.84×10^{4}	a
t_1^A	Time at which cool temperature period ceases	1.26×10^{4}	a
t_1^E	Time at which cold temperature period ceases	3.00×10^{2}	a
t_H^A	Duration of HIC for cool containers	2.94×10^{3}	a
t_H^E	Duration of HIC for cold containers	7.40×10^{3}	a
w^X	Effective container thickness	4.20×10^{-3}	m

Note: The corrosion rate for cold containers is somewhat higher than for cool containers because the former is averaged over a shorter time, as illustrated in Figures 4-13b and 4-13c.

time at which the entire buffer is saturated with uranium). The fraction of the uranium inventory in the fuel released into the buffer can be verified by comparing it with the fraction, f_u, released into a semi-infinite buffer. This can be expressed as (LeNeveu 1986)

$$f_u = \frac{2(D_u r_u t)^{1/2} C_u A}{I_u (\pi)^{1/2}} \qquad (7.7)$$

TABLE 7-2

ESTIMATED FAILURE TIMES FOR HOT, COOL AND COLD CONTAINERS

Symbol	Temperature Designation	Estimated Failure Time (a)
t_p^R	Hot	1945
t_p^A	Cool	3873
t_p^E	Cold	4000

where D_u is the total intrinsic diffusion coefficient of uranium in the buffer (1.14×10^{-5} $m^2 \cdot a^{-1}$), r_u is the capacity factor of the buffer for uranium (52.8), C_u is the solubility of UO_2 (1.6×10^{-7} $mol \cdot m^{-3}$), A is the plan area of the vault (3.16×10^6 m^2), t is the simulation time (10^5 a) and I_u is the total amount of uranium in the vault (7.18×10^8 mol). The parameter values given are from the median-value simulation. The value of f_u from Equation (7.7) is 6.4×10^{-9}, which is in good agreement with the fraction determined from the median-value simulation (6.2×10^{-9}).

Similarly, the dissolution rate of Zircaloy is extremely low; thus only a minute fraction of the radionuclides contained in the fuel sheath is released by congruent dissolution in 10^5 a.

Since congruent dissolution of the fuel is so slow, instant release of the radionuclides in the gap and grain boundaries is expected to dominate. Iodine-129, ^{14}C and ^{99}Tc have different fractional instant releases, amounting to 8.1, 13.0 and 6.0% respectively of the inventories in the vault. That is, these fractions of the container inventories are instantaneously released to the interior of each container when it fails.

Next we develop equations for the estimated congruent and instant release of radionuclides from used fuel into the buffer, at this stage neglecting the effects of container failure. We compare results obtained with these equations to those from the median-value simulation, where the convolution that takes container failure into account (Equation 5.19) has not yet been performed.

At short times, instant- and congruent-release rates from the used fuel into the buffer can be approximated by the equation for release by diffusion from a constant-concentration source into a semi-infinite medium (the buffer) (LeNeveu 1986). For congruent release the initial release rate in moles per year of radionuclide i, $F_i^s(t)$, from the entire vault, can be approximated by

$$F_i^S(t) = \frac{I_i(t)(D_u r_u)^{1/2} C_u A(1 - f_i^I)}{I_u(\pi t)^{1/2}} \qquad (7.8)$$

where I_i is the molar inventory of radionuclide i in the vault, f_i^I is the instant-release fraction of radionuclide i, t is time and D_u, I_u, r^u, C_u and A are defined as in Equation (7.7) (LeNeveu 1986).

For instant release, the initial release rate in moles per year from the used fuel into the buffer for the entire vault, $G_i^S(t)$, can be approximated by

$$G_i^S(t) = \frac{(D_i^B r_i^B)^{1/2} C_i A^C N^C}{(\pi t)^{1/2}} \qquad (7.9)$$

where C_i is the initial concentration ($mol \cdot m^{-3}$) in a container, A^C is the area (m^2) of the container (LeNeveu 1986), N^C is the total number of containers in the vault, D_i^B is the total intrinsic diffusion coefficient of radionuclide i in the buffer ($m^2 \cdot a^{-1}$), and r_i^B is the capacity factor of radionuclide i in the buffer (dimensionless).

For instant release into the buffer, the initial concentration in the container, C_i, will be $I_i f_i^I/(Vp^C N^C)$, where I_i is the initial amount of radionuclide i in the vault, V is the volume of the container and p^C is the capacity factor of the container. Thus $G_i^S(t)$ can be expressed as

$$G_i^S(t) = \frac{(D_i^B r_i^B)^{1/2} I_i f_i^I}{(\pi t)^{1/2} V^A p^C} \qquad (7.10)$$

where V^A is the ratio of volume to surface area of the container (Garisto and LeNeveu 1989).

The median-value simulation results for instant- and congruent-release rates from the used fuel into the buffer for ^{129}I, ^{14}C and ^{99}Tc are shown in Figures 7-8, 7-9 and 7-10. The release rates from the used fuel into the buffer are for Sector 11 and are shown as if there were no containers present. For the purposes of these comparisons, normalized release rates were used. This means that the fractional sector area of Sector 11 was set to 1. Thus release rates are for the entire vault; however, data from sector 11 are used for the sector-dependent parameters describing mass transfer into the geosphere, because sector 11 has the highest release rate per unit area. All release rates exhibit the initial slope of 1/2 on a logarithm release rate versus logarithm time scale, characteristic of a $t^{1/2}$ behaviour. The values of the release rates from the median-value simulation have been compared with the values predicted by Equations (7.8) and (7.9) at the time of one year after vault closure. This early time is used because, as time increases, the predictions from the simplified Equations (7.8), (7.9) and (7.10) will progressively depart from those of the more complex equations used for the assessment. The parameter values for the median-value simulation for Equations (7.7) to (7.10) are given in Table 7-3.

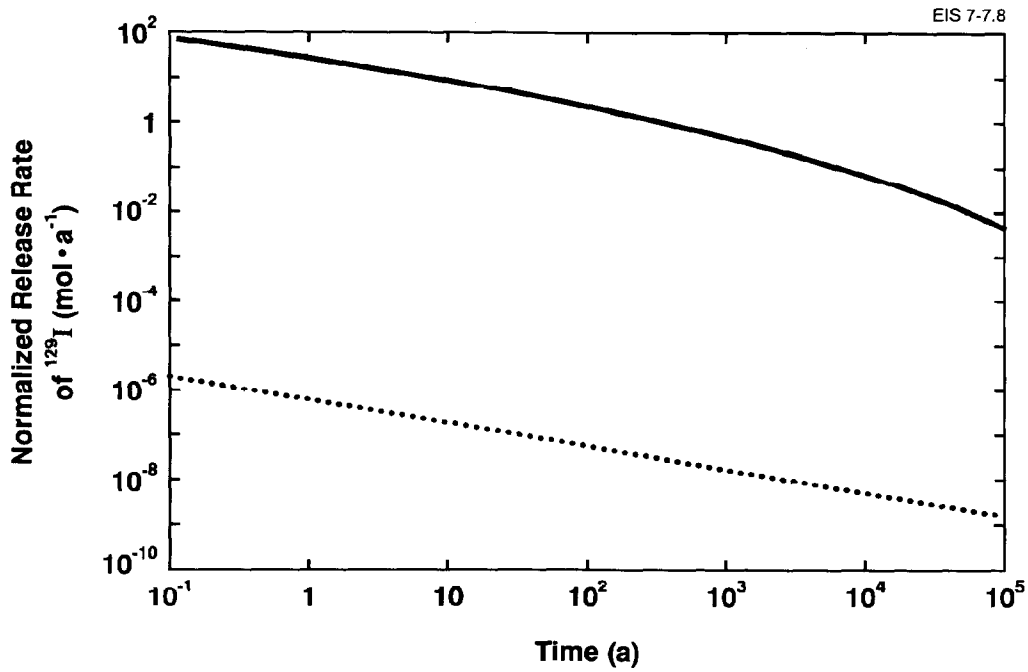

FIGURE 7-8: Instant (——) and Congruent (···) Release Rates of ^{129}I from the Used Fuel into the Buffer for the Entire Vault. The data are obtained from the median-value simulation where the sector-dependent mass transfer data from sector 11 are used, because this sector has the highest release rate per unit area. The releases are calculated as if there were no containers present.

The results of the comparison are given in Table 7-4. The release rates estimated using Equations (7.8) to (7.10) and release rates from the median-value simulation agree, except for the instant release of ^{99}Tc: the ^{99}Tc release rate from the median-value simulation is lower than the estimated rate. Technetium-99 has a much higher capacity factor in the buffer than ^{14}C or ^{129}I. This means that ^{99}Tc is drawn from the void space inside the container into the buffer at a higher rate than ^{14}C or ^{129}I, and the concentration in the container is depleted more rapidly. This causes the release rate for ^{99}Tc to depart more rapidly from a constant-concentration source condition, which is assumed in Equation (7.9), than do the rates for ^{14}C or ^{129}I. This effect can be verified by comparing the instant-release rate of ^{99}Tc from the median-value simulation with the estimated rate at an earlier time, such as 1.0×10^{-4} a. At this time the median-value ^{99}Tc release rate is 7.7×10^{5} mol·a^{-1} and the estimated value is 7.5×10^{5} mol·a^{-1}, which is in good agreement.

Carbon-14 and ^{129}I have identical mass transport parameter values (see Table 7-3 and Section 3.5.3). They differ only in their initial amounts in the fuel, instant-release fractions and half-lives. Consequently, the release rates from the used fuel into the buffer are very similar except at

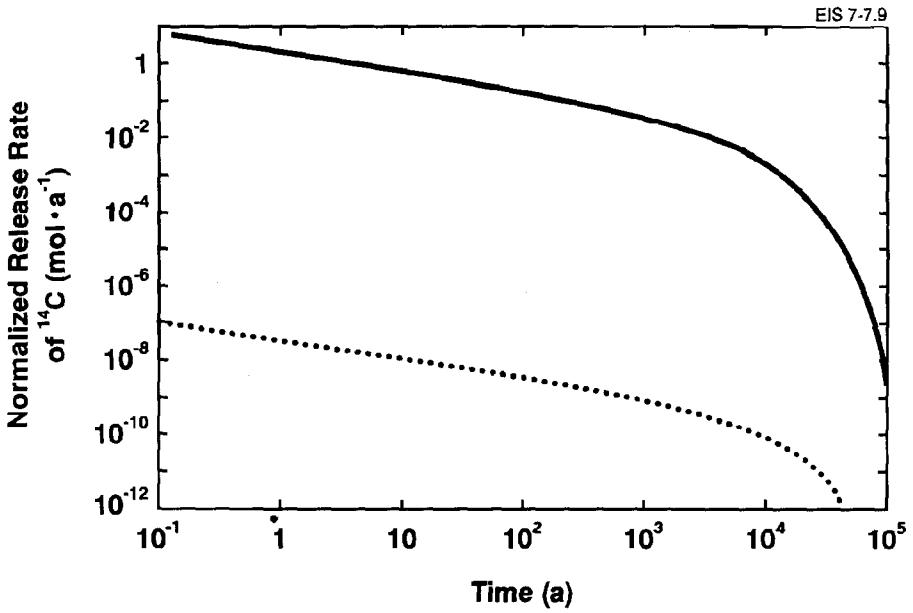

FIGURE 7-9: Instant (——) and Congruent (···) Release Rates of ^{14}C from the Used Fuel into the Buffer for the Entire Vault. The data are obtained from the median-value simulation where the sector-dependent mass transfer data from sector 11 are used, because this sector has the highest release rate per unit area. The releases are calculated as if there were no containers present.

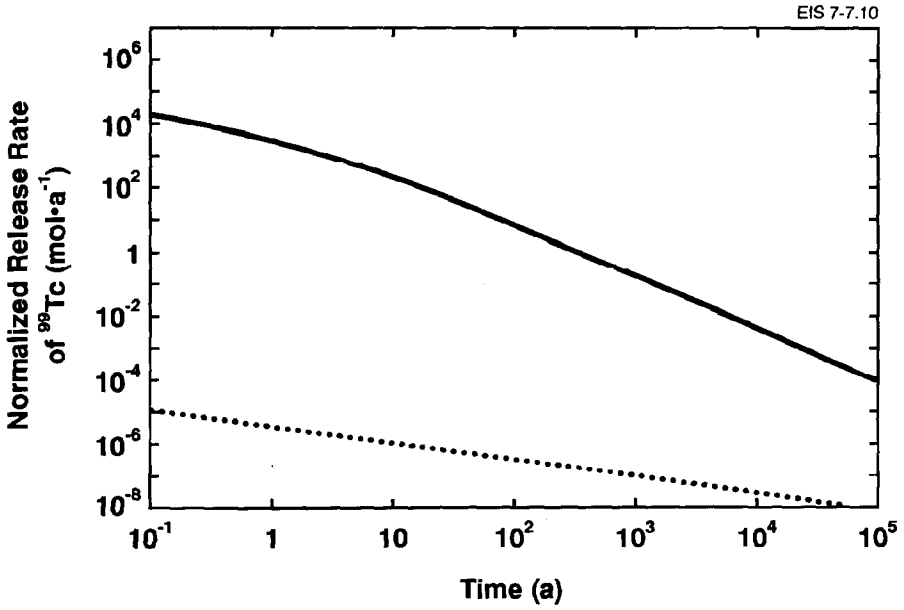

FIGURE 7-10: Instant (——) and Congruent (···) Release Rates of ^{99}Tc from the Used Fuel into the Buffer for the Entire Vault. The data are obtained from the median-value simulation where the sector-dependent mass transfer data from sector 11 are used, because this sector has the highest release rate per unit area. The releases are calculated as if there were no containers present.

TABLE 7-3

PARAMETER VALUES FOR EQUATIONS (7.7) TO (7.10)

Radionuclide-Specific Parameters				
Radionuclide	Total Intrinsic Buffer Diffusion Coefficient, D_i^B ($m^2 \cdot a^{-1}$)	Buffer Capacity Factor, r_i^B	Radionuclide Amount, I_i (mol)	Instant-Release Fraction, f_i^I
^{129}I	1.80×10^{-5}	6.33×10^{-3}	6.02×10^{4}	8.10×10^{-2}
^{14}C	1.80×10^{-5}	6.33×10^{-3}	3.19×10^{3}	1.30×10^{-1}
^{99}Tc	1.14×10^{-5}	5.28×10^{1}	3.59×10^{5}	6.00×10^{-2}
^{238}U	1.14×10^{-5}	5.28×10^{1}	7.18×10^{8}	0

Non-Radionuclide-Specific Parameters			
Symbol	Parameter Description	Parameter Value	Units
A	plan area of the vault	3.16×10^{6}	m^2
C	solubility of UO_2	1.60×10^{-7}	$mol \cdot m^{-3}$
V^A	container volume to surface area ratio	1.60×10^{-1}	m
p^C	capacity factor of container	2.487×10^{-1}	

TABLE 7-4

RELEASE RATES FROM USED FUEL INTO THE BUFFER FOR THE MEDIAN-VALUE SIMULATION COMPARED WITH ESTIMATED VALUES AT A TIME OF ONE YEAR

Radionuclide	Median-Value Congruent Release Rate ($mol \cdot a^{-1}$)	Estimated Congruent Release Rate ($mol \cdot a^{-1}$)	Median-Value Instant-Release Rate ($mol \cdot a^{-1}$)	Estimated Instant-Release Rate ($mol \cdot a^{-1}$)
^{129}I	5.6×10^{-7}	5.60×10^{-7}	2.3×10^{1}	2.33×10^{1}
^{14}C	2.8×10^{-8}	2.81×10^{-8}	1.9	1.98
^{99}Tc	3.4×10^{-6}	3.42×10^{-6}	2.7×10^{3}	7.50×10^{3}

long times. The release rates for ^{14}C begin to drop much more rapidly after 10^4 a than they do for ^{129}I because of the shorter half-life of ^{14}C (5.73×10^3 a compared with 1.57×10^7 a).

7.2.2.3 Radionuclide Transport Through the Buffer and Backfill

After the used fuel and containers, the next barriers to mass transport in the conceptual vault are the buffer and the backfill. The median-value simulation release rates of ^{129}I, ^{14}C and ^{99}Tc from the containers, precipitate (where it occurs), buffer and backfill are shown in Figures 7-11, 7-12 and 7-13. Also shown in these figures, for comparison, are the release rates of these radionuclides from the used fuel into the buffer. The model calculates that precipitation of most radionuclides, except ^{99}Tc, would be a very rare event. Precipitation is discussed in more detail in Chapter 5. The time period of the releases of ^{129}I and ^{99}Tc have been extended beyond the assumed period of validity of the models (10^5 a) for the purposes of illustrating the entire release curve.

The Darcy velocity in the buffer is assumed to be zero, and in the backfill it is so small ($<10^{-6}$ m·a^{-1}), as determined by calculations with the geosphere model, that diffusion is the dominant mass transport mechanism in both barriers. Because the backfill is thicker than the buffer, there is a longer time for transport of the contaminants from the backfill to the rock than from the buffer to the backfill.

The highest instant-release rate from the buffer to the backfill of radionuclide i, R_i^B, in sector 11, normalized to the entire vault, ignoring radioactive decay and assuming that all the instant inventory is discharged into the buffer immediately upon container failure, can be approximated by

$$R_i^B = \min\left[f_m^c, \frac{K_i^B}{r_i^B a^B}\right] I_i f_i^I \qquad (7.11)$$

where K_i^B is the buffer mass transfer coefficient for sector 11 for radionuclide i, which depends on the properties of backfill and rock; f_m^c is the maximum container failure rate for sector 11 (5.07×10^{-4} a^{-1}); and a^B is the thickness of the buffer (Garisto and LeNeveu 1989). This is based on the principle that the mass transfer coefficient is analogous to an equivalent flow rate of water past the buffer (Neretnieks 1978). Material will be removed from the buffer according to the product of the flow rate, the average concentration of radionuclide i within the buffer, and the surface area of the buffer. The average concentration within the buffer can be determined from the initial inventory, I_i, the capacity factor of the buffer, r_i^B, the thickness of the buffer, a^B, the instant-release fraction, f_i^I, and the surface area of the buffer. The surface area of the buffer cancels when the product is evaluated; thus, it does not appear in Equation (7.11). The maximum release rate calculated using Equation (7.11) will remain constant at this value for long periods of time in the absence of decay, provided K_i^B is sufficiently small that swept away conditions are not encountered, i.e., $K_i^B \ll 50\ D_i^B/a^B$. The highest instant-release rate calculated with this equation will be greater than that calculated with the

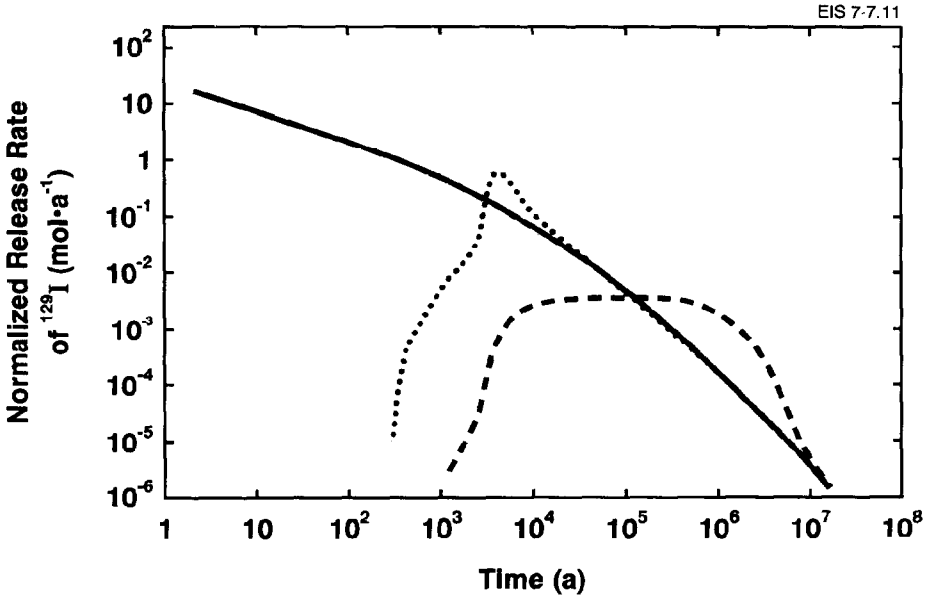

FIGURE 7-11: Release Rates of ^{129}I from the Used Fuel (——), Containers (···), Buffer (···) and Backfill (– – –) for the Entire Vault. Note that the curves for releases from containers and buffer are identical. The data are obtained from the median-value simulation, where the sector-dependent mass transfer data and container failure rates for sector 11 are used, because this sector has the highest release rate per unit area.

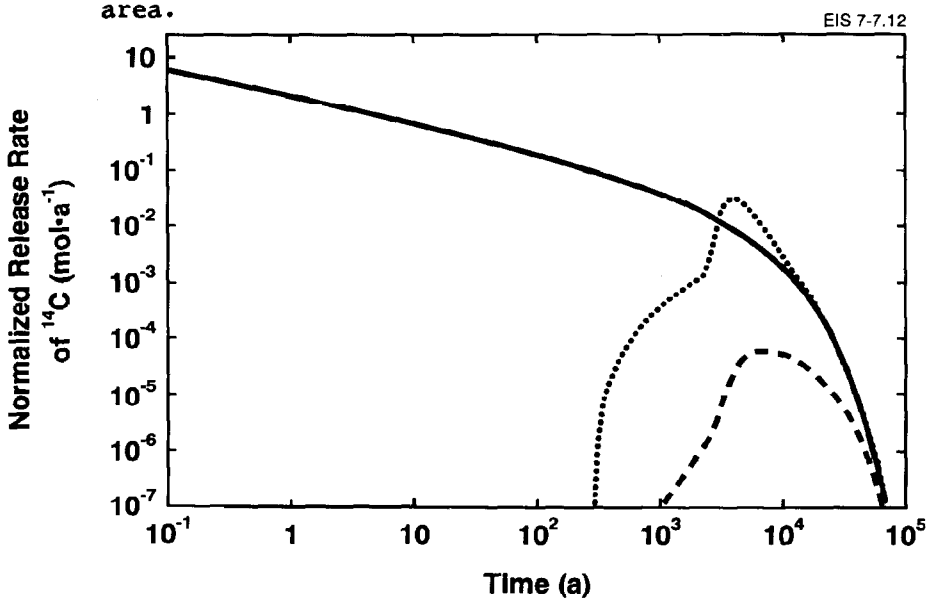

FIGURE 7-12: Release Rates of ^{14}C from the Used Fuel (——), Containers (···), Buffer (···) and Backfill (– – –) for the Entire Vault. Note that the curves for releases from containers and buffer are identical. The data are obtained from the median-value simulation, where the sector-dependent mass transfer data and container failure rates for sector 11 are used, because this sector has the highest release rate per unit area.

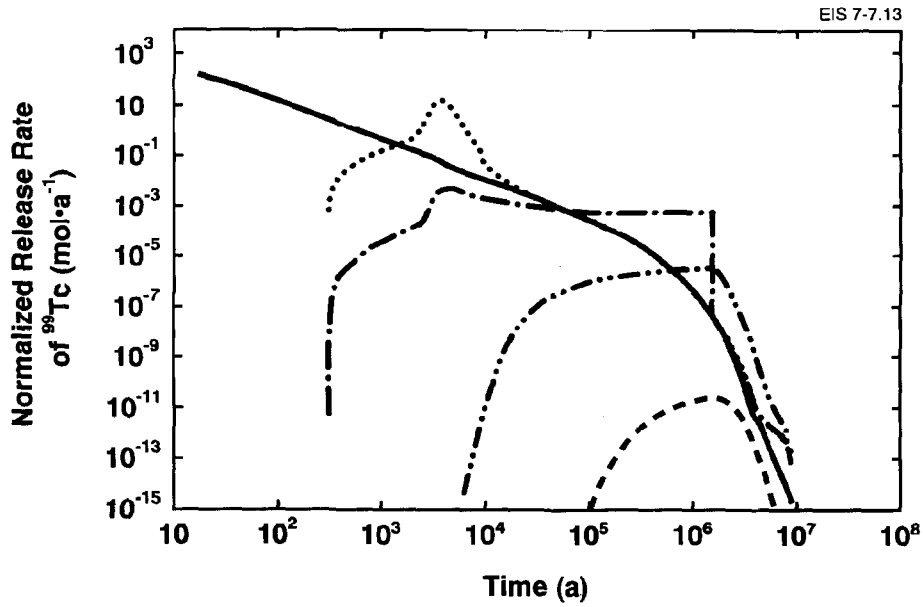

FIGURE 7-13: Release Rates of ^{99}Tc from the Used Fuel (——), Containers (···), Precipitate (-·-·-), Buffer (-··-··) and Backfill (- - -) for the Entire Vault. The data are obtained from the median-value simulation, where the sector-dependent mass transfer data and container failure rates for sector 11 are used, because this sector has the highest release rate per unit area.

vault model, which takes into account diffusion from the container infilling material into the buffer.

The delay time in the buffer, t_i^B, can be estimated (Neretnieks 1977) from

$$t_i^B = \frac{r_i^B a^{B^2}}{D_i^B} \quad . \tag{7.12}$$

This equation is derived by approximating the barrier as an infinitely thick layer and is not influenced by the effect of adjoining media. It gives the time required for approximately half of the initial amount released as a pulse at the start of the medium, to move by diffusion to a distance a^B into the medium. For the system of buffer and backfill it provides only a rough estimate of delay times in the buffer.

The mass transfer coefficients, estimated delay times, estimated peak release rates in sector 11 and peak release rates from the median-value simulation, for the buffer, normalized to the entire vault, are given in Table 7-5. The thickness of the buffer is 0.25 m.

Equation (7.12) can also be applied to the backfill (effective thickness = 1.4 m) (Section 6.2.2), with superscript F replacing superscript B. The results for backfill are shown in Table 7-6.

TABLE 7-5

ESTIMATED BUFFER DELAY TIMES AND PEAK RELEASE RATES FROM THE BUFFER IN SECTOR 11

Nuclide	Mass Transfer Coefficient, K_i^B, for Sector 11 ($m \cdot a^{-1}$)	Estimated Delay Time (a)	Estimated Peak Release Rate ($mol \cdot a^{-1}$)	Median-Value Peak Release Rate ($mol \cdot a^{-1}$)
^{129}I	3.60×10^{-3}	2.2×10^{1}	1.2	5.9×10^{-1}
^{14}C	3.60×10^{-3}	2.2×10^{1}	1.0×10^{-1}	3.1×10^{-2}
^{99}Tc	2.92×10^{-7}	2.9×10^{5}	4.8×10^{-4}	3.2×10^{-6}

TABLE 7-6

ESTIMATED BACKFILL DELAY TIMES AND PEAK RELEASE RATES FROM THE BACKFILL IN SECTOR 11

Nuclide	Capacity Factor, r_i^F	Intrinsic Diffusion Coefficient, D_i^F ($m^2 \cdot a^{-1}$)	Mass Transfer Coefficient, K_i^F Sector 11 ($m \cdot a^{-1}$)	Estimated Delay Time (a)	Estimated Peak Release Rate ($mol \cdot a^{-1}$)	Median-Value Peak Release Rate ($mol \cdot a^{-1}$)
^{129}I	2.5×10^{-1}	2.25×10^{-3}	3.51×10^{-7}	2.2×10^{2}	4.9×10^{-3}	3.9×10^{-3}
^{14}C	2.5×10^{-1}	2.25×10^{-3}	3.51×10^{-7}	2.2×10^{2}	4.2×10^{-4}	6.3×10^{-5}
^{99}Tc	2.0×10^{3}	2.25×10^{-3}	2.02×10^{-7}	1.7×10^{6}	1.5×10^{-6}	3.1×10^{-11}

The peak release rates from the buffer for the median-value simulation are smaller than the estimated rates for several reasons. For ^{129}I, much of the instantly released inventory is still in the pore space in failed containers at the time of the peak release from the buffer. However, for the estimated release, it was assumed that all of this instantly released inventory is discharged to the buffer at the time of container failure. Consequently, by the time the ^{129}I release has progressed through the backfill, much more of the instantly released inventory has left the container, and the peak release rate estimated from Equation (7.11) agrees more closely with the rate calculated for the median-value simulation.

For ^{14}C, the peak release rate in the backfill for the median-value simulation is much smaller than the estimated rate because radioactive decay is ignored in calculating the estimated peak release rate.

Technetium-99 precipitates in the buffer in the median-value simulation. This reduces the release rates. There is no simple equation for estimating the peak release rates in the buffer and backfill following precipitation; however, the event of precipitation can be verified. If precipitation occurs, the release rate would be lower than in the absence of precipitate. The ratio of the release rates at early times in the presence and the absence of precipitation for the entire vault, r_i^I, based on a constant-concentration source diffusing into a semi-infinite medium, is

$$r_i^I = \frac{C_i A V^A p^C}{I_i f_i^I} \qquad (7.13)$$

where C_i is the solubility of contaminant i in the buffer and V^A is the ratio of the volume to surface area of the container. This equation is derived from Equations (7.10) and (7.8). Equation (7.8) has been modified to apply to radionuclide solubility limits. For ^{99}Tc, which has a low solubility, this ratio is much less than one, which indicates that ^{99}Tc should precipitate in the buffer.

In the median-value simulation, at early times, the release rate of ^{99}Tc without precipitation is much larger than with precipitation, but at later times the rates reverse. This means the precipitate first forms, then redissolves. At 1.5×10^6 a all of the precipitate has redissolved and the release rate falls abruptly to the rate in the absence of precipitation.

At times greater than 1×10^6 a, the decay of ^{99}Tc also becomes a factor in causing the release rates to drop. Because of precipitation and decay, the peak release rates from the median-value simulation for ^{99}Tc are much smaller than the rates estimated using Equation (7.11). The equations describing precipitation are given in Chapter 5.

The delay times for the contaminant release to break through a barrier for the median-value simulation can be inferred from the initial rise in the curves in Figures 7-11, 7-12 and 7-13. The delay times for ^{129}I and ^{14}C in the backfill are underpredicted by Equation (7.12), whereas the delay times for ^{99}Tc in the buffer and backfill are overpredicted. However, the estimate provides a reasonably accurate means of ranking the delay times of radionuclides in the buffer and backfill.

7.2.2.4 The Distribution of Radionuclides in the Vault at 10^5 a

The median-value simulation of the distribution of ^{129}I, ^{14}C and ^{99}Tc in the vault at 10^5 a is summarized in Table 7-7 and in Figure 7-14. Table 7-7 also includes the amounts of radionuclides in the system (vault, geosphere and biosphere) after decay at 10^5 a and the amount released to the geosphere at 10^5 a.

TABLE 7-7

DISTRIBUTION OF RADIONUCLIDES IN THE VAULT AT 10^5 a

FOR THE MEDIAN-VALUE SIMULATION

Radio-nuclide	Initial Inventory (mol)	Amount in System* at 10^5 a (mol)	Amount in Containers at 10^5 a (mol)	Amount in Buffer at 10^5 a (mol)	Amount in Backfill at 10^5 a (mol)	Amount Released to the Geosphere up to 10^5 a (mol)
^{129}I	5.61×10^4	5.59×10^4	5.22×10^4	$<5.0 \times 10^1$	3.11×10^3	5.19×10^2
^{14}C	2.98×10^3	1.66×10^{-2}	1.47×10^{-2}	$<1.5 \times 10^{-5}$	1.62×10^{-3}	1.85
^{99}Tc	3.35×10^5	2.42×10^5	2.27×10^5	1.46×10^4	1.22×10^{-1}	1.72×10^{-10}
^{238}U	6.70×10^8	6.70×10^8	6.70×10^8	4.17	8.30×10^{-3}	1.22×10^{-11}
^{234}U	3.30×10^4	3.39×10^4	3.39×10^4	2.12×10^{-4}	4.09×10^{-7}	2.00×10^{-15}
^{230}Th	8.93×10^{-1}	6.27×10^3	6.27×10^3	4.80×10^{-5}	9.76×10^{-6}	1.13×10^{-14}
^{226}Ra	4.25×10^{-5}	1.28×10^2	1.28×10^2	9.81×10^{-7}	2.96×10^{-8}	3.43×10^{-6}

* Amount in system is the amount in the vault, geosphere and biosphere after decay at 10^5 a

The time-integrated quantity of ^{129}I release from the vault to the geosphere up to 10^5 a is 5.2×10^2 mol, or 0.93% of the initial ^{129}I inventory. In this time, only 2.5×10^2 mol of the initial 5.6×10^4 mol of ^{129}I is lost to decay. The total amount of ^{129}I in the fuel and void space in the containers at 10^5 a is 5.2×10^4 mol or 94% of the total amount remaining in the system after decay. Virtually all of the inventory available for congruent release (i.e., within the fuel matrix) at 10^5 a is still in the used fuel. Of the inventory available for instant release, 20% is in the containers, 69% is in the backfill, <0.1% is in the buffer and 11% is in the geosphere and biosphere at 10^5 a.

The difference in the distribution of ^{14}C and ^{129}I in the vault at 10^5 a is primarily a result of decay of ^{14}C. The time-integrated release of ^{14}C from the vault to the geosphere up to 10^5 a is 1.85 mol. Most of the initial inventory decays away during transit in the geosphere during the first 10^5 a. Of the amount of instant inventory that has not decayed at this time, given by the product of the instant-release fraction and the amount of ^{14}C in the system at 10^5 a, 14% is still in the containers, 75% is in the backfill and the remaining 11% is in the geosphere and biosphere (Table 7-7). At 10^5 a, the amount of ^{14}C in the used fuel and the void space in the containers, 1.47×10^{-2} mol, is virtually all (98%) congruent inventory (i.e., still contained in the UO_2 and Zircaloy matrices).

The instant inventory of ^{99}Tc is released more quickly from the container void into the buffer than ^{14}C or ^{129}I, so that at 10^5 a very little of the instant inventory remains in the failed containers.

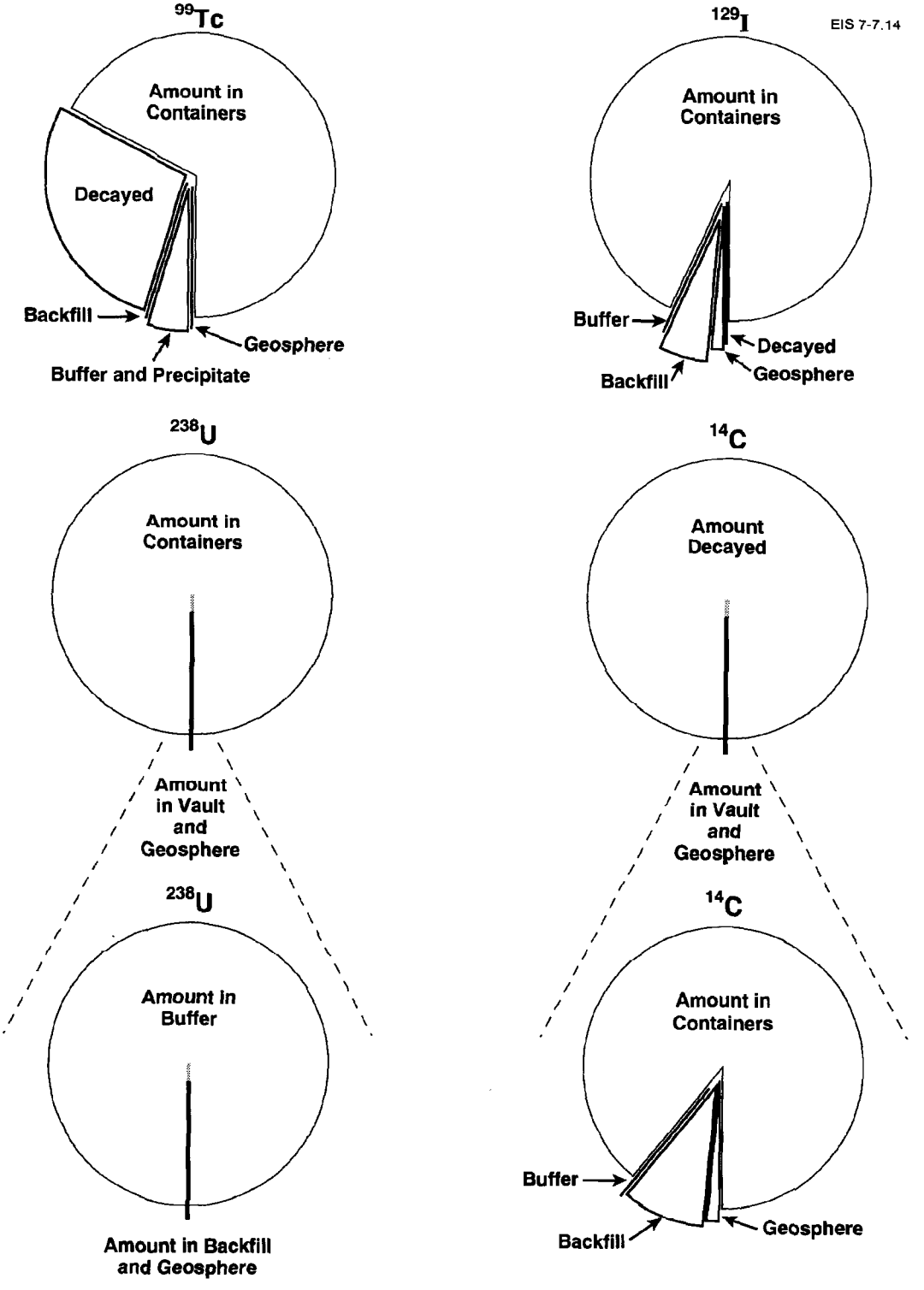

FIGURE 7-14: Distribution of the Amount of ^{129}I, ^{14}C, ^{99}Tc and ^{238}U in the Containers, Buffer, Backfill and Geosphere at 10^5 a, and the Total Amount Decayed by 10^5 a

Technetium-99 precipitates immediately upon release from the used fuel. The low release rate from the precipitate, in conjunction with a large capacity factor in the buffer, means that almost all of the ^{99}Tc released from the used fuel remains in the precipitate and in the buffer at 10^5 a. In summary, almost all of the instant inventory of ^{99}Tc remains precipitated in the buffer at 10^5 a, and virtually all of the congruent inventory is still in the used fuel.

The release rates of the 4n + 2 chain from the used fuel, containers, buffer and backfill were chosen as an example to illustrate the behaviour of an actinide decay chain. The 4n + 2 chain, shortened for modelling purposes, is ^{238}U, ^{234}U, ^{230}Th and ^{226}Ra (Goodwin and Mehta, in preparation). The remaining members are considered to be in secular equilibrium with one of these isotopes: ^{234}Th is in secular equilibrium with ^{238}U, while ^{222}Rn, ^{210}Pb, ^{210}Bi and ^{210}Po are considered to be in secular equilibrium with ^{226}Ra. To carry out dose rate estimations, the release rates of radionuclides in secular equilibrium are calculated from the parent release rates at the exit of the geosphere. There is no instant release from the used fuel for members of the 4n + 2 chain.

The ^{238}U release rates from the used fuel, containers, buffer and backfill for sector 11 are shown in Figure 7-15 for the median-value simulation. The delay in the buffer and the backfill is large because of the large capacity factors for uranium in the buffer and backfill. Consequently, by 10^5 a there is almost no release from the backfill.

The release rates of ^{234}U from the used fuel, containers, buffer and backfill for sector 11 are shown in Figure 7-16. The release rates of ^{234}U and ^{238}U are very similar because diffusion coefficients and capacity factors are identical for isotopes of the same element. The differences result from different inventories and decay rates.

The ^{230}Th release rates for sector 11 are shown in Figure 7-17 The delay in the buffer and backfill is large and equivalent to the delay for ^{238}U and ^{234}U. This is because the diffusion coefficients and capacity factors in the buffer are the same for Th and U in the median-value simulation. The difference between the release rates for ^{230}Th and ^{234}U is mainly caused by the the different rates of ingrowth of these radionuclides from the precursors (Figure 7-18). This causes the release rate of ^{230}Th from the used fuel into the buffer to begin to increase after about ten years.

The ^{226}Ra release rates for sector 11 are shown in Figure 7-19. The delays in the buffer and backfill are small in comparison with U and Th. This is because the buffer and backfill have smaller capacity factors for Ra than for U and Th. Like ^{230}Th, the ingrowth of ^{226}Ra from its precursors is substantial, as shown in Figure 7-18. This causes the release rate from the used fuel to increase after ten years and the release rate from the backfill to increase after 10^4 a. The peaks in the release curves at approximately 3000 a for the containers, buffer and backfill are caused by container failure.

The total inventory of the ^{238}U daughters, ^{234}U, ^{230}Th and ^{226}Ra, as a function of time is given in Figure 7-18. This shows the pattern of

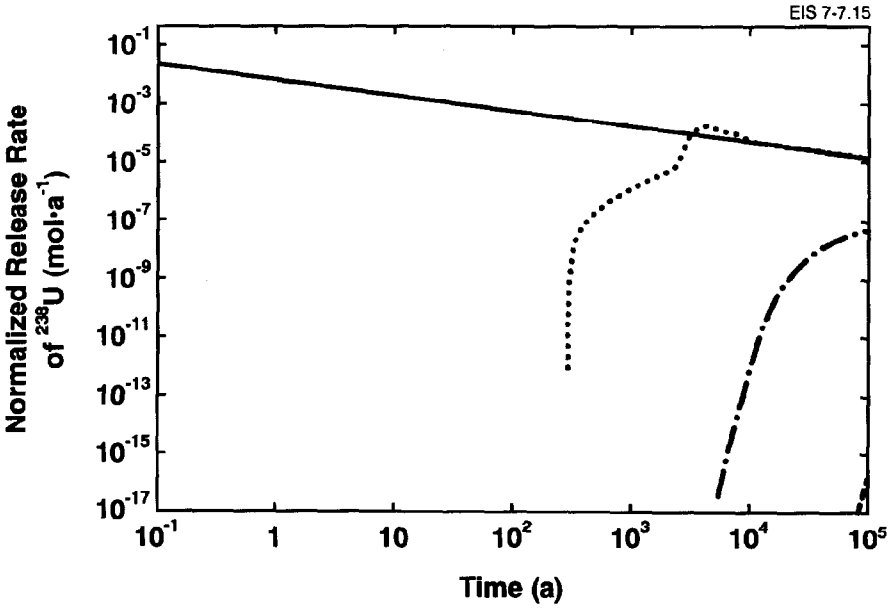

FIGURE 7-15: Release Rates of ^{238}U from the Used Fuel (——), Containers (···), Buffer (-·-·-) and Backfill (– – –) for the Entire Vault. The data are obtained from the median-value simulation, where the sector-dependent mass transfer data and container failure rates for sector 11 are used, because this sector has the highest release rate per unit area.

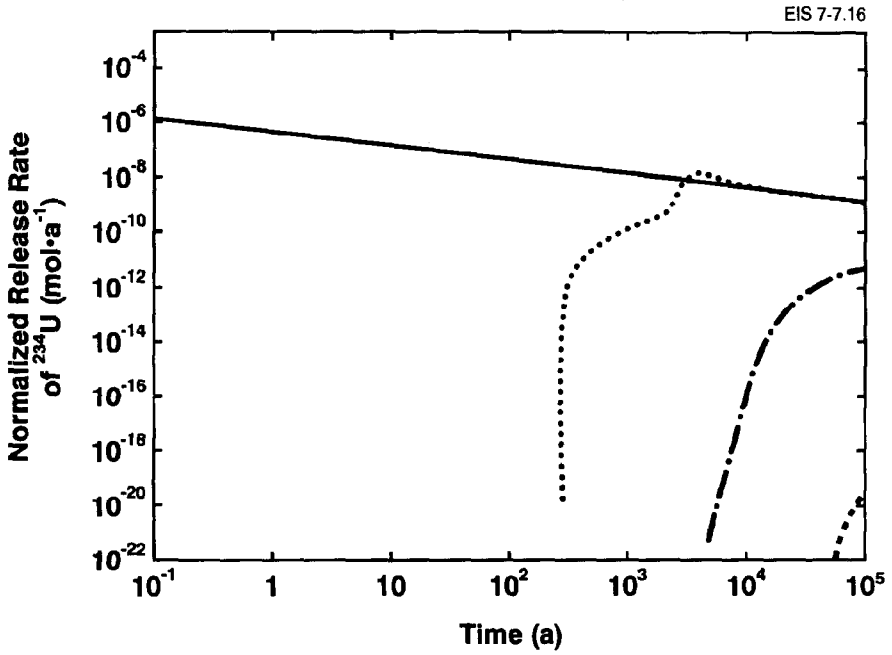

FIGURE 7-16: Release Rates of ^{234}U from the Used Fuel (——), Containers (···), Buffer (-·-·-) and Backfill (– – –) for the Entire Vault. The data are obtained from the median-value simulation, where the sector-dependent mass transfer data and container failure rates for sector 11 are used, because this sector has the highest release rate per unit area.

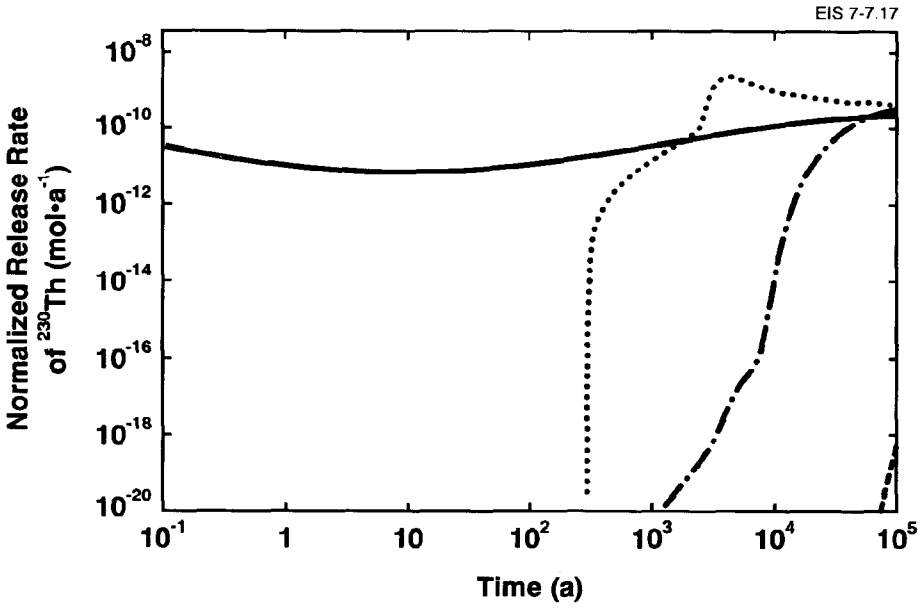

FIGURE 7-17: Release Rates of ^{230}Th from the Used Fuel (——), Containers (···), Buffer (-·-·-) and Backfill (– – –) for the Entire Vault. The data are obtained from the median-value simulation, where the sector-dependent mass transfer data and container failure rates for sector 11 are used, because this sector has the highest release rate per unit area.

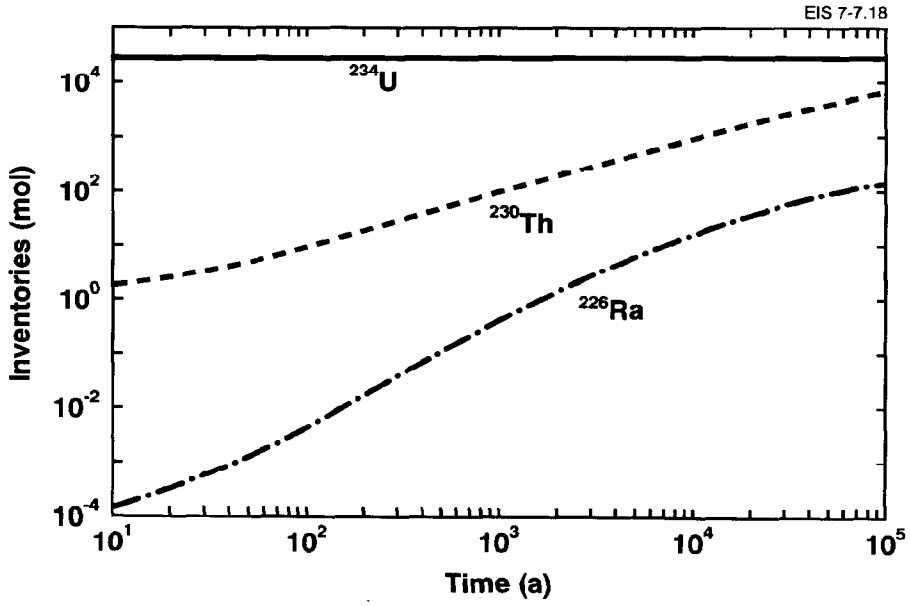

FIGURE 7-18: Inventories of ^{238}U Daughters in the Vault as a Function of Time. The data are from the median-value simulation.

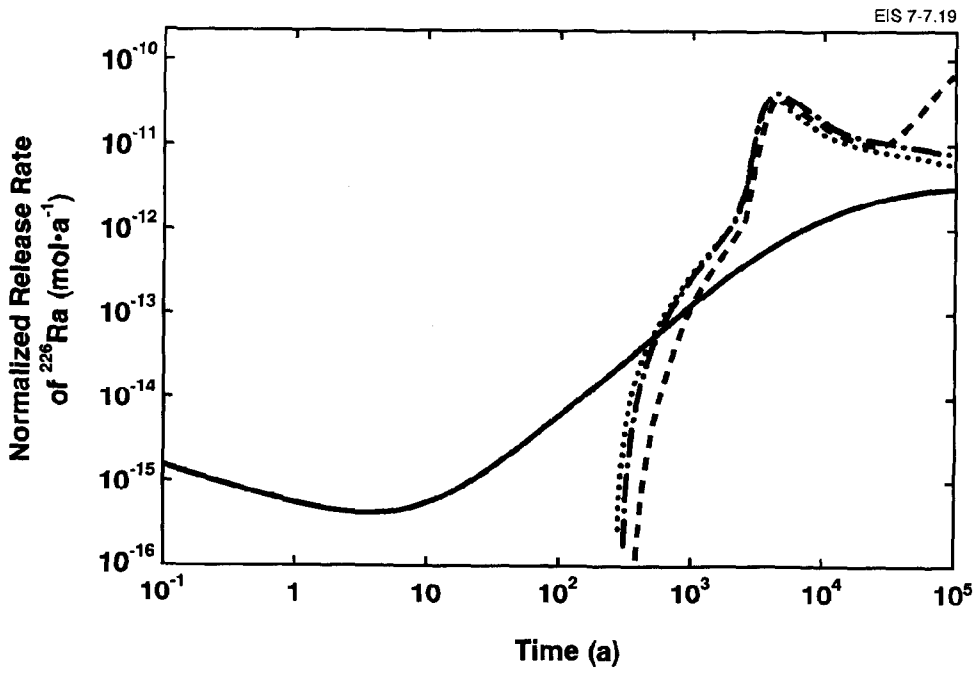

FIGURE 7-19: Release Rates of ^{226}Ra from the Used Fuel (——), Containers (···), Buffer (-·-·-) and Backfill (– – –) for the Entire Vault. The data are obtained from the median-value simulation, where the sector-dependent mass transfer data and container failure rates for sector 11 are used, because this sector has the highest release rate per unit area.

ingrowth from precursors, which contributes to the shape of the release rate curves. The ingrowth of ^{234}U up to 10^5 a is inconsequential, whereas it is quite large and still rising at 10^5 a for ^{230}Th and ^{226}Ra. The inventory of ^{238}U and the time to dissolve all of the used fuel are very large, so the ingrowth of ^{238}U daughters would continue for time scales much larger than one hundred thousand years.

The release rates of ^{238}U and its daughters from the used fuel and the delay times in the buffer and backfill for the median-value simulation can be compared with the estimates furnished by the Equations (7.8) and (7.12). The diffusion coefficients and capacity factors in buffer and backfill for Th are assumed to be the same as for U. The values for the buffer are given in Section 7.2.2.2. The U and Th capacity factor in the backfill is 2.0×10^3; the total intrinsic diffusion coefficient in the backfill is 2.25×10^{-3} m^2·a^{-1}. The values for ^{226}Ra are given in Table 7-8.

The initial inventories of radionuclides in the decay chain in the vault are given in Table 7-9.

The comparison between the estimated release rates from used fuel at one year and the values from the median-value simulation, along with the estimated delay times in the buffer and backfill, are given in Table 7-10.

TABLE 7-8

TOTAL INTRINSIC DIFFUSION COEFFICIENTS AND CAPACITY FACTORS FOR ^{226}Ra

Medium	Total Intrinsic Diffusion Coefficient ($m^2 \cdot a^{-1}$)	Capacity Factor
Buffer	2.55×10^{-3}	4.50
Backfill	3.96×10^{-3}	1.40

TABLE 7-9

INITIAL INVENTORIES OF RADIONUCLIDES IN THE 4n + 2 DECAY CHAIN IN THE VAULT

Radionuclide	Initial Amount (mol)
^{238}U	7.18×10^{8}
^{234}U	3.54×10^{4}
^{230}Th	9.57×10^{-1}
^{226}Ra	4.56×10^{-5}

TABLE 7-10

COMPARISON BETWEEN ESTIMATED AND MEDIAN-VALUE RELEASE RATES FROM USED FUEL AT ONE YEAR AND ESTIMATED DELAY TIMES IN BUFFER AND BACKFILL

Radio-nuclide	Estimated Release Rate ($mol \cdot a^{-1}$)	Median Value Release Rate ($mol \cdot a^{-1}$)	Estimated Buffer Delay time (a)	Estimated Backfill Delay time (a)
^{238}U	7.3×10^{-3}	7.3×10^{-3}	2.9×10^{4}	1.7×10^{5}
^{234}U	3.6×10^{-7}	3.6×10^{-7}	2.9×10^{4}	1.7×10^{5}
^{230}Th	9.7×10^{-12}	1.2×10^{-11}	2.9×10^{4}	1.7×10^{5}
^{226}Ra	4.6×10^{-16}	6.0×10^{-16}	1.1×10^{1}	6.9×10^{1}

The release rates from used fuel for ^{230}Th and ^{226}Ra at one year for the median-value simulation are larger than the estimated rates because both have appreciable ingrowth in their inventory in this time, which is not taken into account in the calculation of the estimated values. The estimated delay times for ^{238}U, ^{234}U and ^{230}Th agree well with those estimated from the rise in the curves in Figures 7-15 to 7-17. For ^{226}Ra, agreement is poor because most of the containers fail at periods longer than the delay time, and this controls the release rates.

7.3 SENSITIVITY ANALYSIS

7.3.1 Determination of the Most Important Parameters in the Vault Model by Sensitivity Analysis

In this section the sensitivity of the simulation releases from the vault to the geosphere and the maximum dose to the critical group up to 10^5 a to the parameters in the vault model are discussed. In the sensitivity analysis, parameters were varied within the ranges specified by their probability distributions only. The parameters that have the most influence on release from the vault were first determined by fractional factorial screening analysis. The sensitivity of the releases from the vault to these important parameters was determined by analyzing the results of simulations in which each of the important parameters was varied in turn while keeping all other parameters fixed at their median value. Subsequently, multiple linear regression analysis was used to analyze the sensitivity of releases from the vault, and of dose, to the important parameters when all parameters were allowed to vary randomly within their specified distributions.

Fractional factorial screening analysis applied to ^{129}I and ^{14}C identified the following parameters as causing the largest change in the time-integrated amount released from the vault to the geosphere up to 10^5 a:

- the initial inventory of ^{14}C per kilogram of uranium,
- the initial inventory of ^{129}I per kilogram of uranium,
- the buffer anion diffusion correlation parameter (DFBANI, Tables 3-2 and 3-3),
- the instant-release fraction of ^{14}C,
- the instant-release fraction of ^{129}I,
- the groundwater velocity scaling factor (Davison et al. 1994b), and
- the tortuosity of the lower rock zone (i.e., the rock horizon in which the vault is situated).

The ratios of the largest to the smallest amounts of ^{129}I and ^{14}C released from the vault when each of the above important parameters is varied throughout its range, with all other parameters fixed at their median values, are given in Tables 7-11 and 7-12 respectively.

The relative effects of each parameter about the median value can be determined from the ratios in the tables. The inventory of ^{129}I per kilogram of uranium has the largest effect on changing the total amount of ^{129}I released from the vault in 10^5 a. Similarly, the inventory of ^{14}C per kilogram of uranium has the largest effect on changing the total amount of ^{14}C released from the vault in 10^5 a.

TABLE 7-11

THE RATIO OF THE LARGEST TO THE SMALLEST INTEGRATED RELEASE OF ^{129}I FROM THE VAULT FOR THE FULL RANGE OF VARIATION OF IMPORTANT PARAMETERS

Parameter Name	Ratio
Initial inventory of ^{129}I in used fuel	31.7
Buffer anion diffusion correlation parameter	18.4
Instant-release fraction of ^{129}I	17.6
Groundwater velocity scaling factor	10.6
Tortuosity of the lower rock zone	2.8

TABLE 7-12

THE RATIO OF THE LARGEST TO THE SMALLEST ^{14}C RELEASE FROM THE VAULT FOR THE FULL RANGE OF VARIATION OF IMPORTANT PARAMETERS

Parameter Name	Ratio
Initial inventory of ^{14}C in used fuel	100.1
Buffer anion diffusion correlation parameter	42.6
Instant-release fraction of ^{14}C	25.0
Groundwater velocity scaling factor	14.6
Tortuosity of the lower rock zone	3.1

The initial inventory per kilogram of uranium determines the initial amount of a radionuclide in the vault. Provided radionuclide solubility limits are not exceeded, the time-integrated release from the vault varies proportionately with the initial inventory. If the initial inventory doubles, the time-integrated release doubles. This relationship is illustrated in Figures 7-20 and 7-21, which show, respectively, the time-integrated release of ^{14}C and ^{129}I from the vault as a function of their inventories, with all other input parameters held at their median values.

The variabilities in the initial inventories of ^{14}C and ^{129}I as specified in the model are illustrated by the histograms of 1000 random simulations shown in Figures 7-22 and 7-23 respectively. The largest possible variation in the time-integrated release of ^{14}C resulting from uncertainty and variability in the initial inventory is two orders of magnitude as determined from truncation bounds of the input distribution. Of all randomly sampled values of the initial inventory of ^{129}I, 99.7% lie between 1.03×10^{-4} and 1.17×10^{-3} mol·kg^{-1} U. Thus, most of the variability is

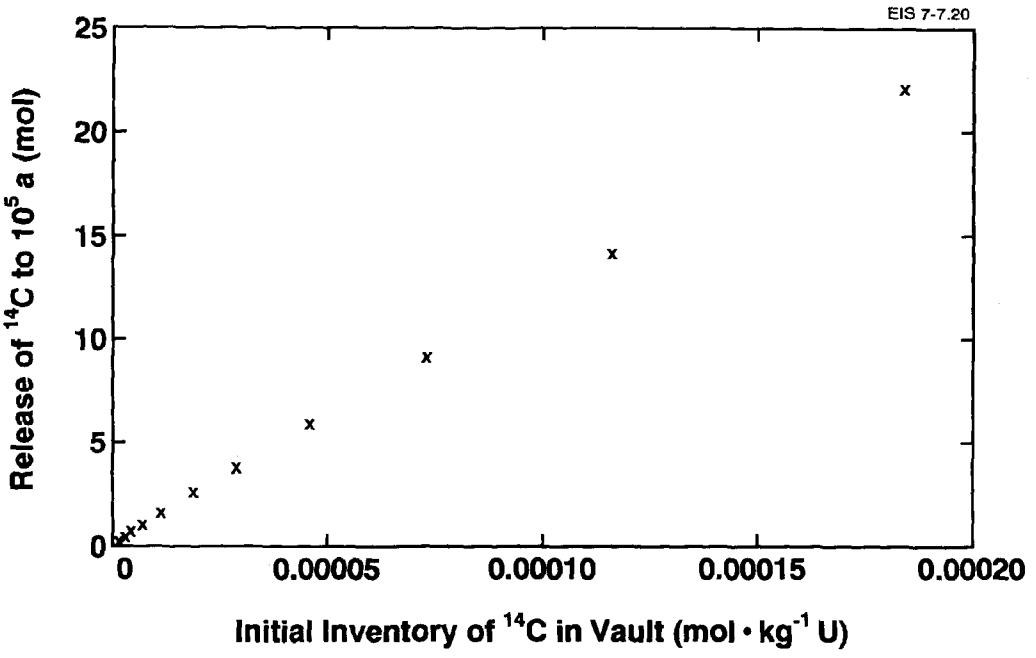

FIGURE 7-20: Time-Integrated Release of ^{14}C up to 10^5 a Versus the Initial Inventory of ^{14}C per Kilogram of Uranium in the Vault. The initial inventory is varied throughout its range. All other parameter values are fixed at their median values.

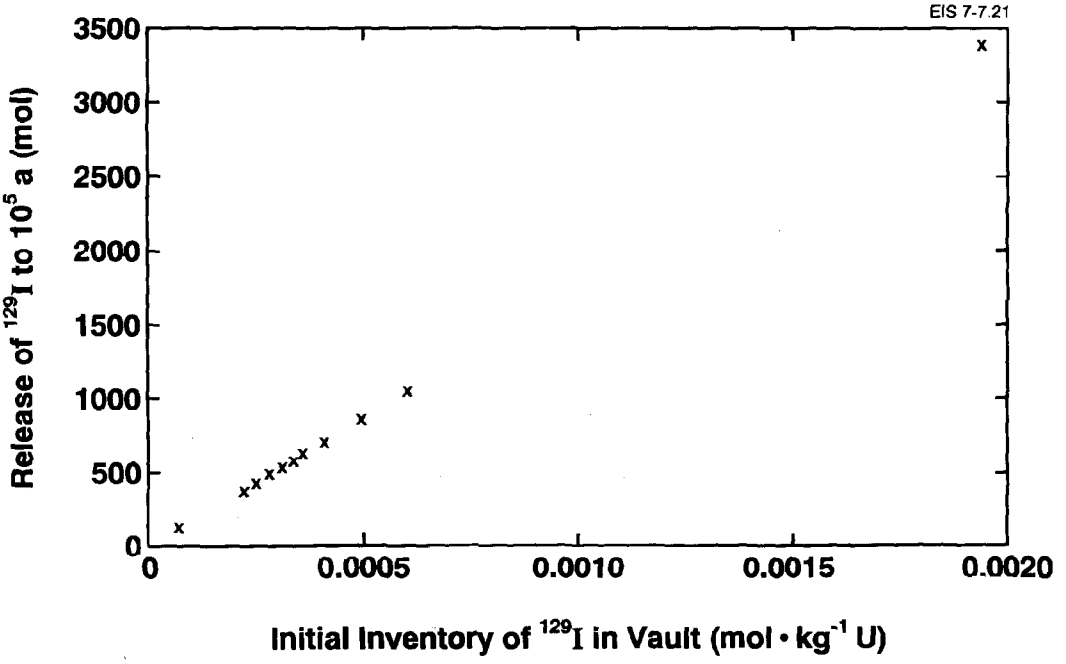

FIGURE 7-21: Time-Integrated Release of ^{129}I up to 10^5 a Versus the Initial Inventory of ^{129}I per Kilogram of Uranium in the Vault. The initial inventory is varied throughout its range. All other parameter values are fixed at their median values.

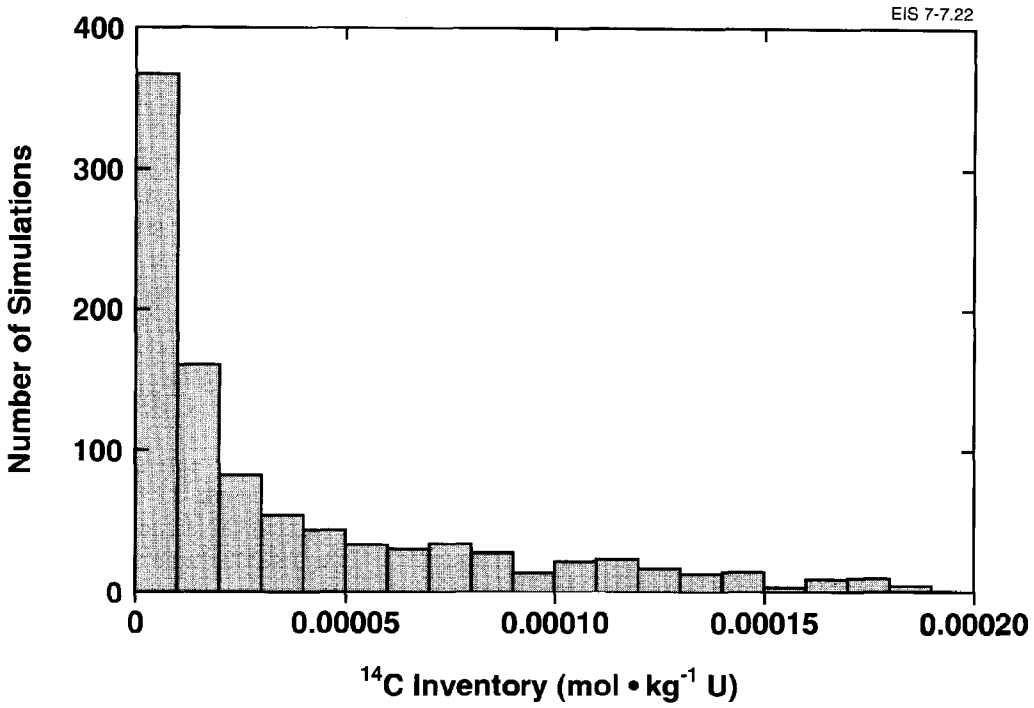

FIGURE 7-22: Histogram of ^{14}C Initial Inventory per Kilogram of Uranium in the Vault

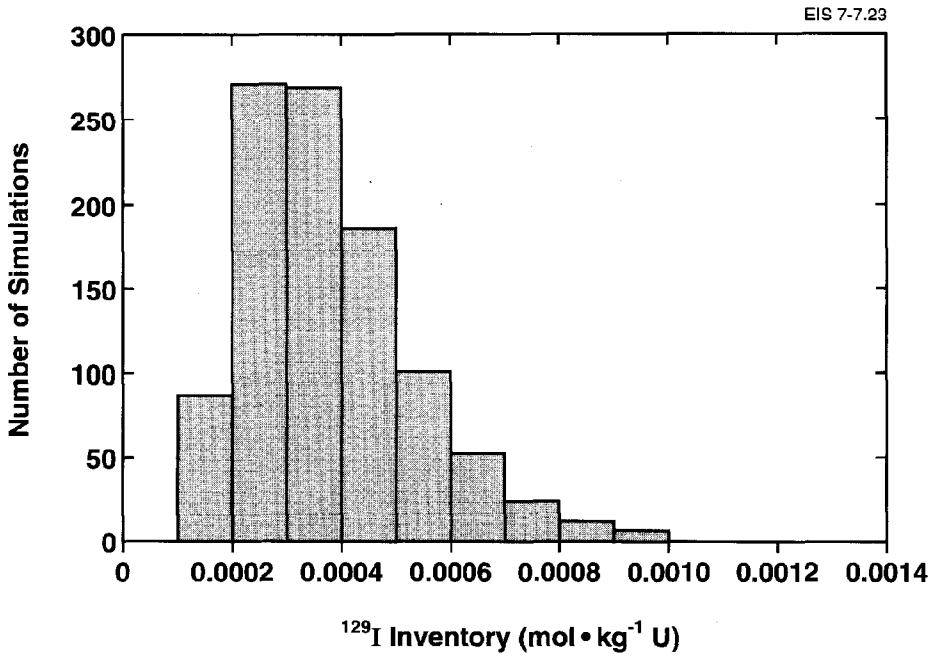

FIGURE 7-23: Histogram of ^{129}I Initial Inventory per Kilogram of Uranium in the Vault

encompassed within one order of magnitude. Consequently, most of the variability in the time-integrated release of ^{129}I from the vault as a result of the variability of the initial inventory of ^{129}I is encompassed within one order of magnitude.

The instant-release fraction determines the amount of a radionuclide released within the container immediately upon failure. Since the release of ^{14}C and ^{129}I from the vault is dominated by instant release, variation in these parameters has the same linear relationship as for variation in their initial inventories, provided the solubility of the instantly released radionuclides is not exceeded. This effect is illustrated in Figures 7-24 and 7-25, which show the time-integrated release of ^{14}C and ^{129}I from the vault as a function of their instant-release fractions, with all other input parameters held at their median values.

The variability in the instant-release fractions of ^{14}C and ^{129}I as specified in the model is illustrated by the histograms of 1000 random simulations shown in Figures 7-26 and 7-27. For ^{14}C, the instant-release fraction varies uniformly between 0.01 and 0.25, or by a factor of twenty-five. The instant-release fraction of ^{129}I varies between 0.012 and 0.25, or by a factor of about twenty. However, the distribution for ^{129}I is more peaked than for ^{14}C, to the extent that the instant-release fraction is unlikely to be beyond the range of 0.051 to 0.11. Thus, the time-integrated release of ^{129}I is unlikely to vary by more than a factor of two because of the uncertainty and variability in the instant-release fraction.

The variation in the time-integrated release from the vault as a result of variation in the buffer anion correlation parameter is more complicated. This parameter is used to correlate the buffer diffusion coefficients and capacity factors of all anionic species in the vault. The correlation is one to one (see Section 3.5.3). In other words, if the buffer diffusion coefficient of any anion, such as I^- or CO_3^{2-}, is given, the buffer diffusion coefficients and capacity factors of all other anions are completely determined. The correlation is positive, so that if the diffusion coefficient increases, the capacity factor also increases. Physically, this positive correlation is explained by the fact that as the porosity of the buffer and the concomitant spacing between buffer particles decrease, as a result of increasing buffer density, for instance, the storage capacity and the diffusion coefficient of anions in the buffer decrease proportionally.

The variation of time-integrated release of ^{129}I from the vault to the geosphere with changes in the buffer anion correlation parameter, with all other parameters at their median values, is shown in Figure 7-28. The buffer anion correlation parameter varies between 9.0×10^{-7} and 3.6×10^{-4}. The graph covers the entire range of variability. The time-integrated release first increases, then decreases as a function of increasing anion correlation parameter. The total variation in the integrated release is more than one order of magnitude, from ~50 mol to ~800 mol.

This non-monotonic behaviour can by explained by the fact that variation in the buffer anion correlation parameter results in competing effects on the release from the container into the buffer and transport through the buffer. As the capacity factor and diffusion coefficient of a radionuclide

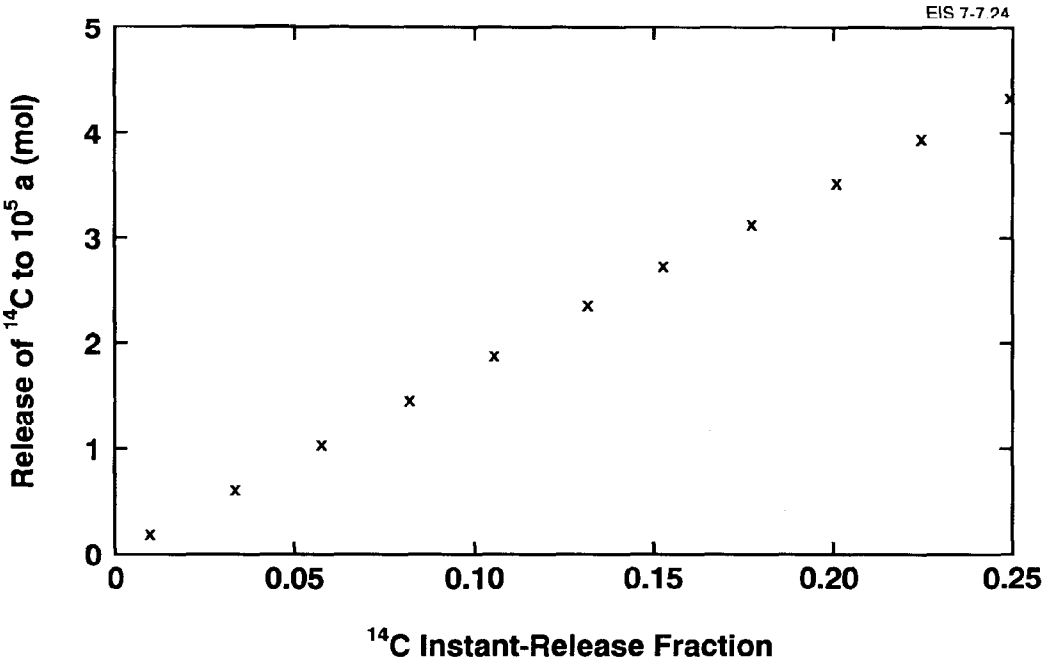

FIGURE 7-24: Time-Integrated Release of ^{14}C from the Vault up to 10^5 a Versus the Instant-Release Fraction of ^{14}C. The instant release is varied throughout its range. All other parameters remain fixed at their median values.

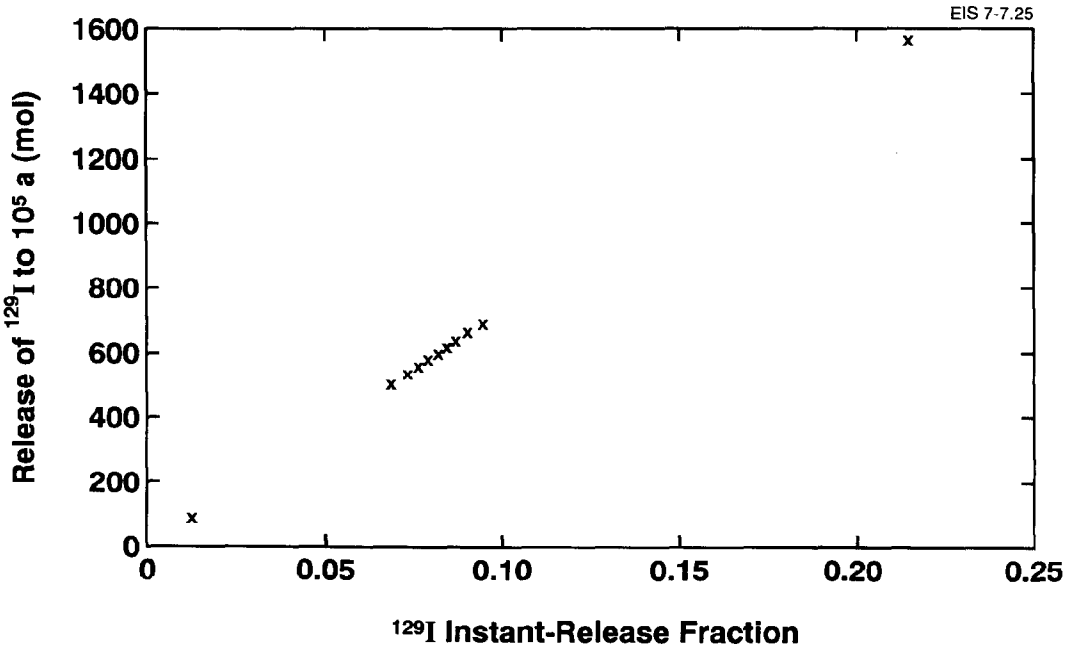

FIGURE 7-25: Time-Integrated Release of ^{129}I from the Vault up to 10^5 a Versus the Instant-Release Fraction of ^{129}I. The instant release is varied throughout its range. All other parameters remain fixed at their median values.

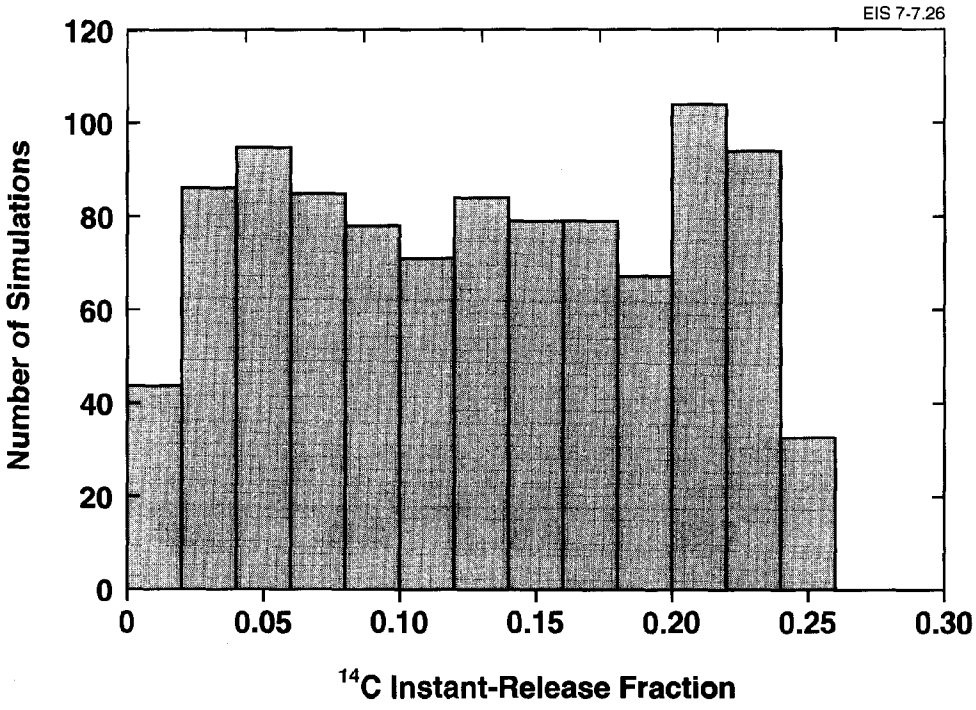

FIGURE 7-26: Histogram of the ^{14}C Instant-Release Fraction

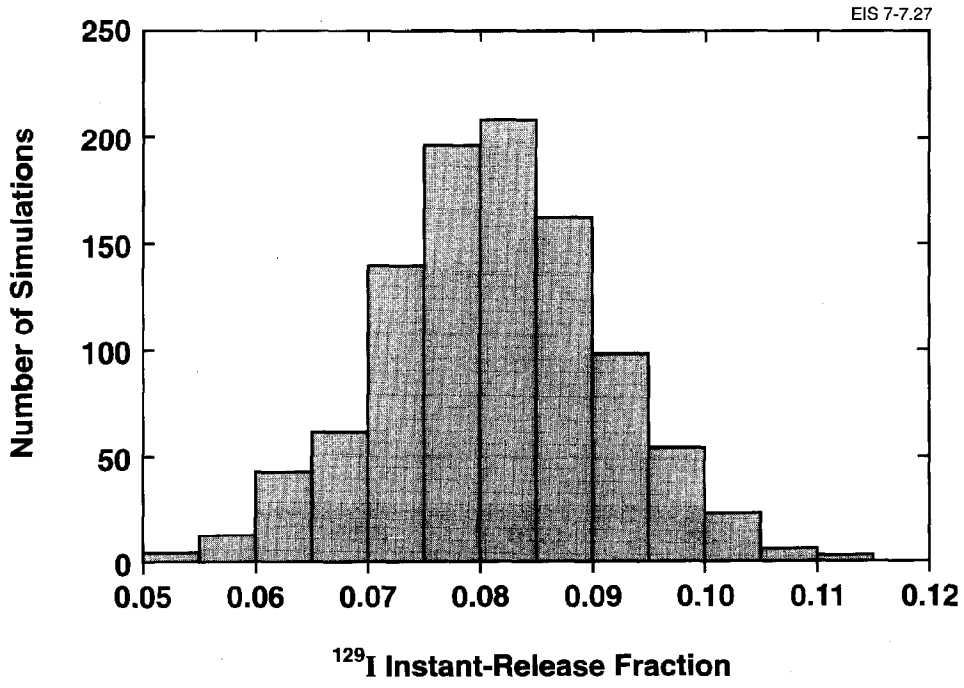

FIGURE 7-27: Histogram of the ^{129}I Instant-Release Fraction

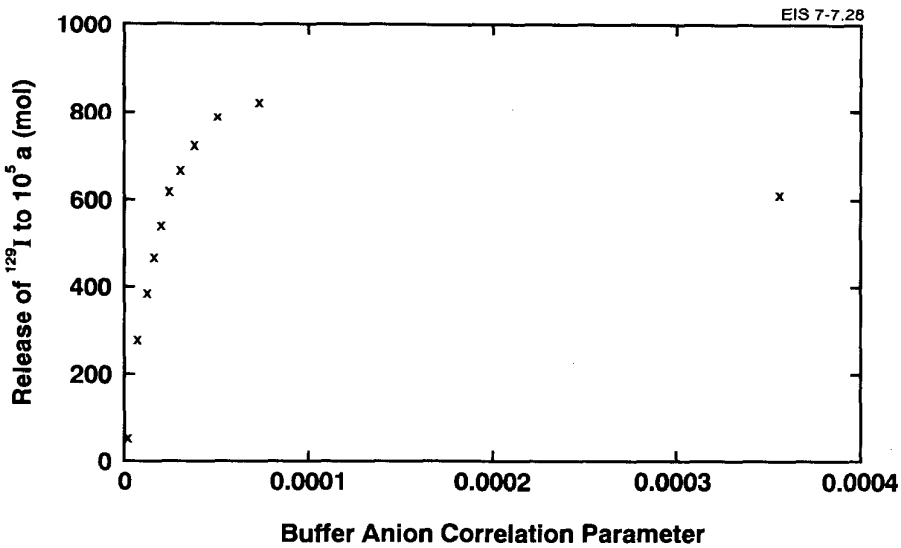

FIGURE 7-28: Time-Integrated Release of ^{129}I up to 10^5 a Versus Buffer Anion Correlation Parameter. The buffer anion correlation parameter is varied throughout its range. All other parameters remain fixed at their median values.

increase concomitantly, as determined by the buffer anion correlation parameter, the radionuclide is drawn into the buffer from the containers at a faster rate. This is illustrated in Figure 7-29, which shows the time-dependency of the release rate of ^{129}I from the used fuel into the buffer as if no containers were present, as a function of increasing buffer anion correlation parameter (i.e., buffer capacity factor and diffusion coefficient). As the capacity factor increases, the release takes longer to progress through the buffer. This effect is illustrated in Figure 7-30, which shows the release rate from the buffer into the backfill in response to the input of a unit impulse of ^{129}I (i.e., the buffer response) as a function of increasing capacity factor and diffusion coefficient. The release rate from the buffer is obtained by a convolution of the release rate from the containers into the buffer with the buffer response. Figure 7-31 shows the release rate of ^{129}I from the buffer to the backfill as a function of increasing buffer capacity factor and diffusion coefficient. This incorporates the release rate to the buffer from the void space of the failed container; the release rate in Figure 7.30 does not. The maximum release rate and the time-integrated release up to 10^5 a increases when the buffer anion correlation parameter changes from its lowest to the median value. This increase is attributable to the increased amount of ^{129}I drawn out of the failed container. As the buffer anion correlation parameter increases further to its highest value, the maximum release rate and time-integrated release decreases. This decrease is attributable to the competing effect of longer delay times in the buffer as a result of increased capacity factor. As discussed previously, the backfill parameters were fixed at their median values. Thus, the non-monotonic effect displayed in the release from the buffer is manifested as well in the release rate from the backfill, as shown in Figure 7-32, which shows the release rate of ^{129}I from the backfill as a function of increasing

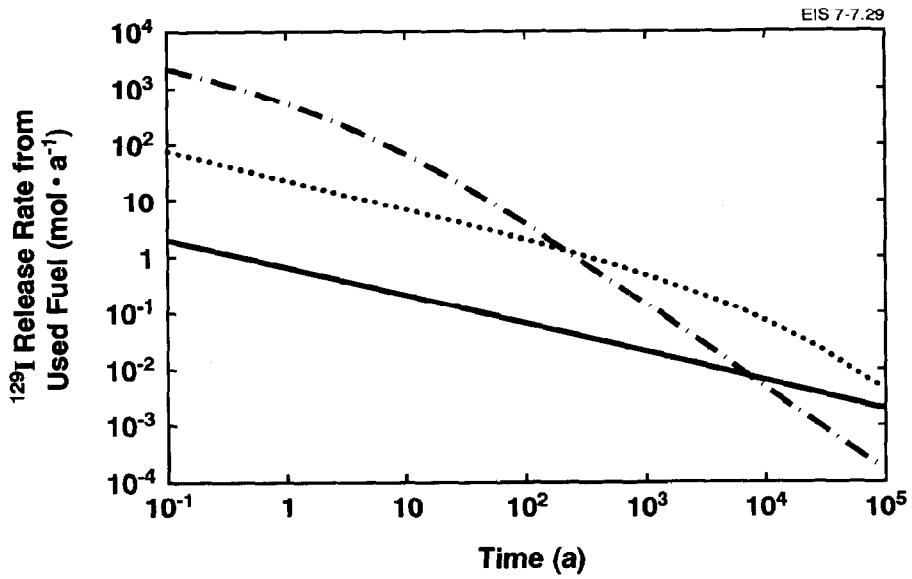

FIGURE 7-29: Total Release Rate of ^{129}I from the Used Fuel into the Buffer as if No Containers Were Present for Lowest, Median and Highest Values of the Buffer Anion Correlation Parameter for the Entire Vault. Sector-dependent mass transfer data for sector 11 are used, because this sector has the highest release rate per unit area.
—— Release rate for buffer anion correlation parameter = 9.0×10^{-7}
··· Release rate for buffer anion correlation parameter = 1.8×10^{-5}
–·– Release rate for buffer anion correlation parameter = 3.6×10^{-4}

buffer anion correlation parameter. (To obtain the release rate from the vault to the geosphere, the release rate from the backfill must be multiplied by the fractional sector area of sector 11.)

Considering the fact that the backfill has a much larger effect than the buffer in delaying the release from the vault, one might wonder why sensitivity analysis did not indicate that the backfill anion correlation parameter was important. The answer to this lies in the comparative range of variability of the parameters in the buffer and the backfill. The ranges of the backfill capacity factors and diffusion coefficients for ^{129}I and ^{14}C are 0.20 to 0.30 and 1.8×10^{-3} m^2·a^{-1} to 2.7×10^{-3} m^2·a^{-1} respectively, whereas for the buffer the ranges are 1.0×10^{-4} to 0.40 and 9.0×10^{-7} m^2·a^{-1} to 3.6×10^{-4} m^2·a^{-1} respectively. In other words, the variability of these parameters in the buffer is over three and two orders of magnitude respectively, while in the backfill, the variability for both is only a factor of 1.5. Subsequent research has shown that the variability in mass transport parameters for the buffer is not this great, as discussed in Section 8.6.

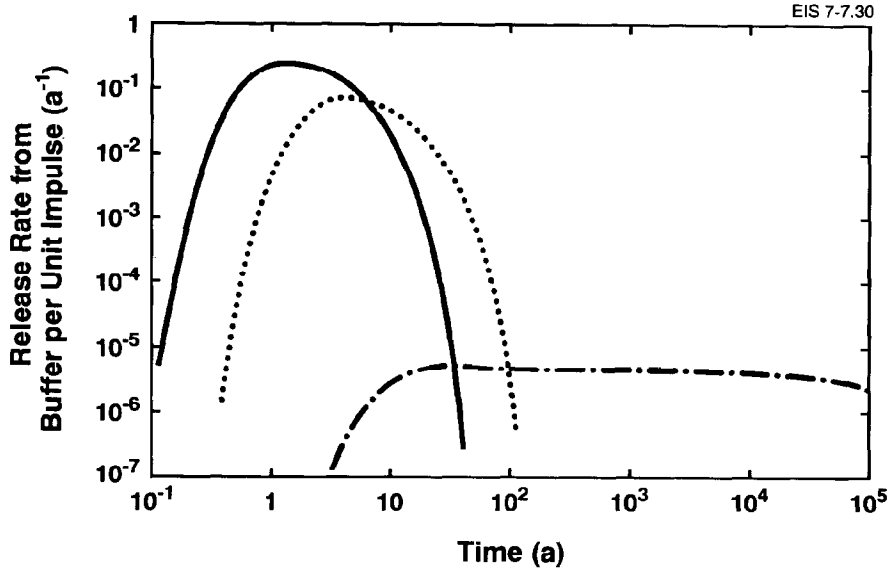

FIGURE 7-30: Release Rate from the Buffer into the Backfill in Response to the Input of a Unit Impulse of ^{129}I for Lowest, Median and Highest Values of the Buffer Anion Correlation Parameter, for the Entire Vault. Sector-dependent mass transfer data for sector 11 are used, because this sector has the highest release rate per unit area.
—— Release rate for buffer anion correlation parameter = 9.0×10^{-7}
··· Release rate for buffer anion correlation parameter = 1.8×10^{-5}
–·– Release rate for buffer anion correlation parameter = 3.6×10^{-4}

The final parameters determined to be important in affecting the time-integrated release from the vault from the fractional factorial screening analysis are the groundwater velocity scaling factor and the tortuosity of the lower rock zone as shown in Figures 7-33 and 7-34 respectively. They influence the release from the vault primarily through the value of the backfill mass transfer coefficient. The groundwater velocity in the geosphere and the backfill changes in proportion to the groundwater velocity scaling factor. The values of the groundwater velocity throughout the entire range in the backfill, as determined by the groundwater velocity scaling factor, are sufficiently small that mass transport by diffusion dominates in the backfill. Increasing the groundwater velocity scaling factor in the geosphere increases the groundwater velocity, which in turn increases the backfill mass transfer coefficient in three ways (see Section 6.8): it increases the minimum value that the backfill mass transfer coefficient can have, which is one half of the Darcy velocity in the backfill; it increases the value of the diffusive backfill mass transfer coefficient (Section 6.8.3) through the value of the total intrinsic

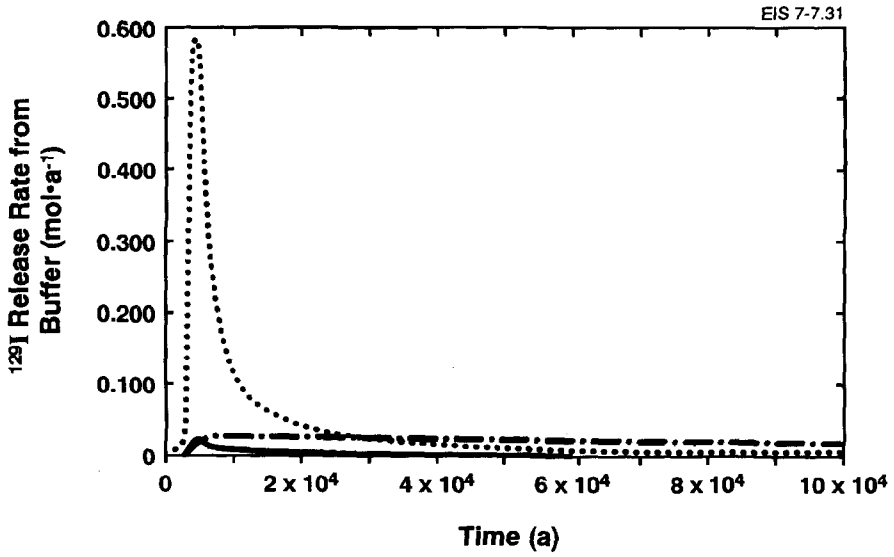

FIGURE 7-31: Release Rate of ^{129}I from Buffer for Lowest, Median and Highest Values of the Buffer Anion Correlation Parameter for the Entire Vault. Sector-dependent mass transfer data for sector 11 are used, because this sector has the highest release rate per unit area.
—— Release rate for buffer anion correlation parameter = 9.0×10^{-7}
··· Release rate for buffer anion correlation parameter = 1.8×10^{-5}
—·— Release rate for buffer anion correlation parameter = 3.6×10^{-4}

dispersion coefficient of the lower rock; or, finally, it increases the value of the convective backfill mass transfer coefficient (Section 6.8.2) through the value of the groundwater velocity in the rock. The maximum of the convective and diffusive backfill mass transfer coefficients is used to determine the final value of the backfill mass transfer coefficient (see Section 6.8.1).

The tortuosity of the lower rock zone in which the vault is situated affects the value of the backfill mass transfer coefficient through the value of the total intrinsic dispersion coefficient in the rock, which varies as the inverse square of the tortuosity (Equation (6.32)). The total intrinsic dispersion coefficient is a function of the porosity of the rock, the free-water diffusion coefficient and the dispersion length, as well as the groundwater velocity and the tortuosity of the rock. The porosity of the rock is a constant; thus, the value of the dispersion length and the free-water diffusion coefficient can affect the variability in the backfill mass transfer coefficient. The sensitivity analysis indicated that the dispersion length and the free water diffusion coefficient were not as important as the tortuosity and the groundwater velocity

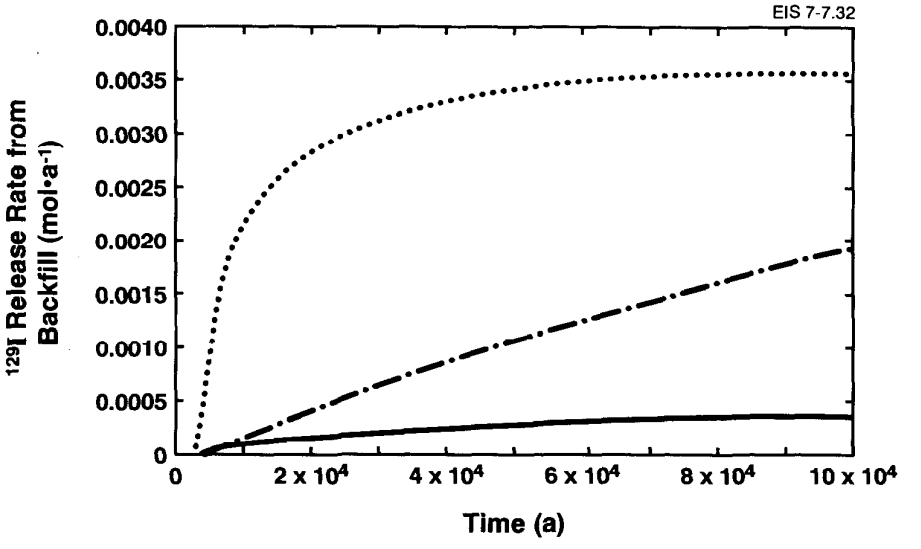

FIGURE 7-32: Release Rate of ^{129}I from Backfill for Lowest, Median and Highest Values of the Buffer Anion Correlation Parameter for the Entire Vault. Sector-dependent mass transfer data for sector 11 are used, because this sector has the highest release rate per unit area.
—— Release rate for buffer anion correlation parameter = 9.0 x 10^{-7}
... Release rate for buffer anion correlation parameter = 1.8 x 10^{-5}
—·— Release rate for buffer anion correlation parameter = 3.6 x 10^{-4}

scaling factor, even though they all affect the backfill mass transfer coefficient. The effect of these four parameters is illustrated in Figures 7-35 and 7-36 for sector 11. The five lines in Figure 7-35 show the variation in the ^{129}I backfill mass transfer coefficient in sector 11 with tortuosity, and with other parameters as follows:

1. all other parameters held at their median values;

2. groundwater velocity in the rock at its maximum and all other parameters at their median values;

3. groundwater velocity in the rock at its minimum with all other parameters at their median values;

4. groundwater velocity in the rock at its maximum, dispersion length and free-water diffusion coefficient at their maxima, and all other parameters at their median values; and

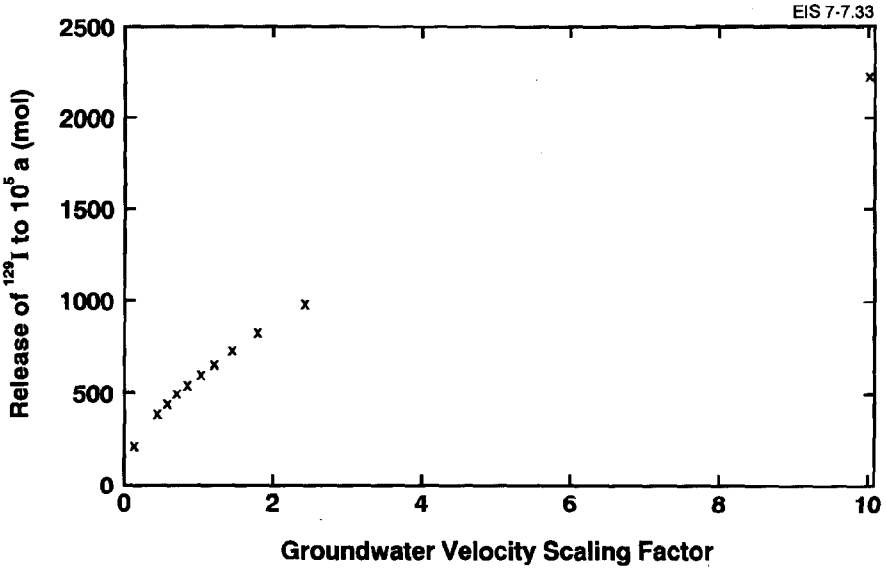

FIGURE 7-33: Time-Integrated Release of ^{129}I from the Vault up to 10^5 a Versus Velocity Scaling Factor. The velocity scaling factor is varied throughout its range. All other parameters remain fixed at their median values.

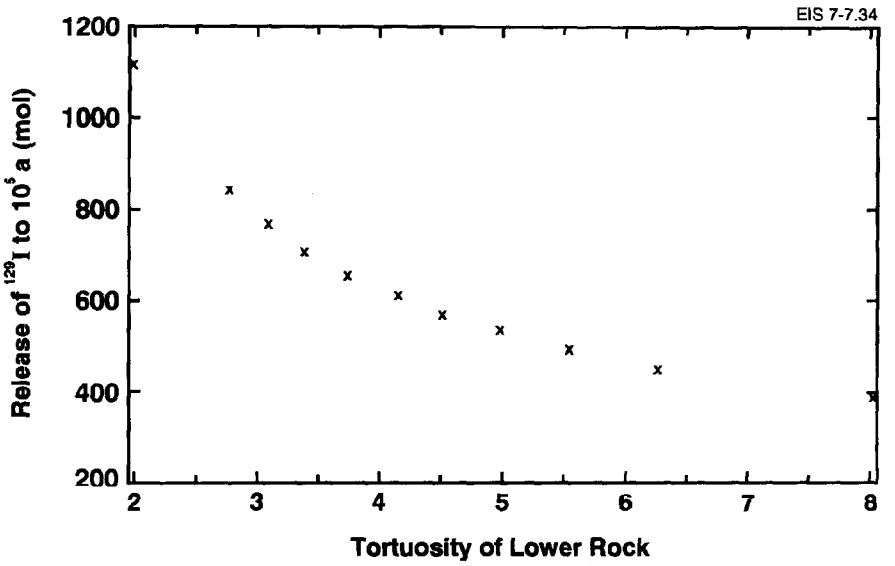

FIGURE 7-34: Time-Integrated Release of ^{129}I from the Vault up to 10^5 a Versus the Tortuosity of the Lower Rock. The tortuosity of the lower rock is varied throughout its range. All other parameters remain fixed at their median values.

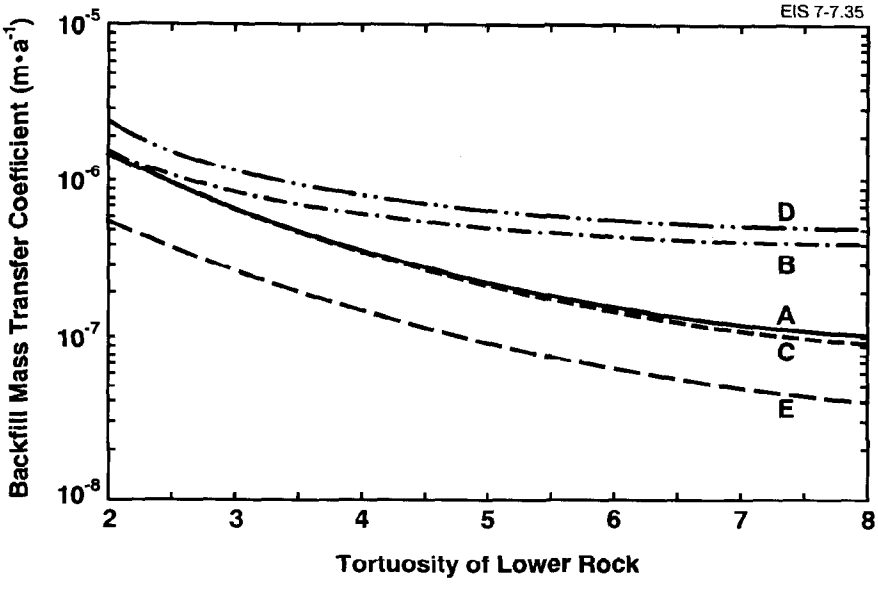

FIGURE 7-35: ^{129}I Backfill Mass Transfer Coefficient for Sector 11 Versus Tortuosity of the Lower Rock
A - all parameters held at median values
B - groundwater velocity scaling factor at maximum
C - groundwater velocity scaling factor at minimum
D - groundwater velocity scaling factor, dispersion length and free-water diffusion coefficient at maxima
E - groundwater velocity scaling factor, dispersion length and free-water diffusion coefficient at minima

5. groundwater velocity in the rock at its minimum, dispersion length and free-water diffusion coefficient at their minima and all other parameters at their median values.

The five lines in Figure 7-36 show the variation in the ^{129}I backfill mass transfer coefficient for sector 11 with groundwater velocity in the adjacent rock segment and with other parameters as follows:

1. all other parameters held at their median values;

2. tortuosity in the rock at its maximum and all other parameters at their median values;

3. tortuosity in the rock at its minimum with all other parameters at their median values;

4. tortuosity in the rock at its minimum, dispersion length and free-water diffusion coefficient at their maxima and all other parameters at their median values; and

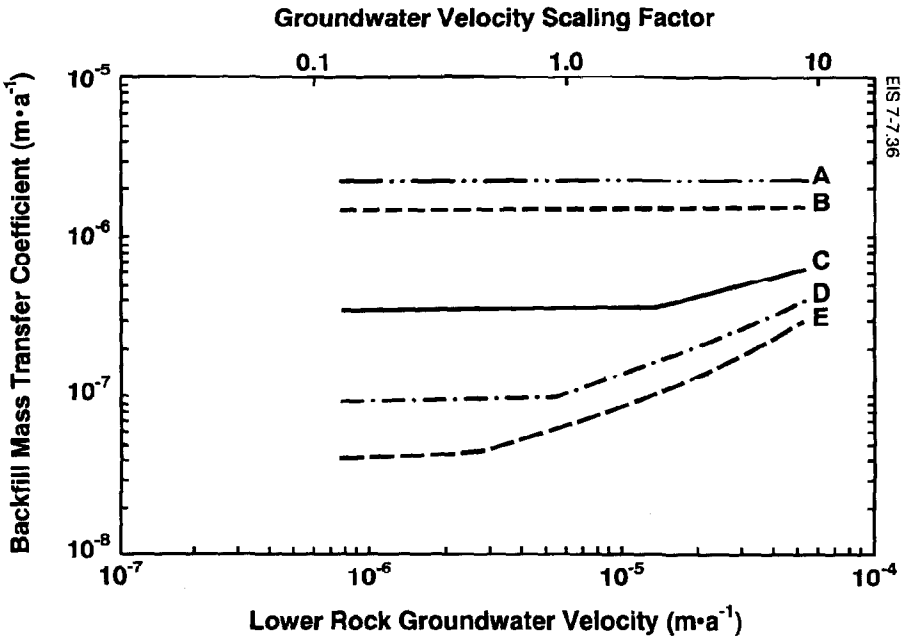

FIGURE 7-36: ^{129}I Backfill Mass Transfer Coefficient for Sector 11 Versus Water Velocity in the Lower Rock Segment Adjoining Sector 11 of the Vault
A - free-water diffusion coefficient and dispersion length at maximum and tortuosity at minimum
B - tortuosity at minimum
C - all parameters held at median values
D - tortuosity at maximum
E free-water diffusion coefficient and dispersion length at minimum and tortuosity at maximum

5. tortuosity in the rock at its maximum, dispersion length and free-water diffusion coefficient at their minima and all other parameters at their median values.

The graphs indicate that there is a total of one order of magnitude variability in the backfill mass transfer coefficient with variation in the rock tortuosity and groundwater velocity scaling factor. An additional approximately one-half order of magnitude variability is attributable to the geosphere parameters, dispersion length and free-water diffusion coefficient. The variation of the backfill mass transfer coefficient as a function of changes in input parameters is quite complex. It is different for every radionuclide and every vault sector. One of the features of this variation for ^{129}I and sector 11, illustrated by the graphs, is that the backfill mass transfer coefficient is increased much more by high groundwater velocities than by low velocities for the bottom three curves in Figure 7-36.

In summary, variation about the median value of each of the most important parameters governing the release of ^{129}I, with all other parameters fixed at their median values, has less than one to two orders of magnitude effect on the time-integrated release from the vault to the geosphere. Further sensitivity analysis of the vault model, including the effect of important vault parameters on dose, is presented in Appendix E. In Appendix E, the constraint of keeping all other parameters fixed has been removed.

7.3.2 Analysis of the Impact of Key Assumptions in the Vault Model

The analysis presented in Section 7.3.1 focused on estimating the effect of variability and uncertainty in the parameters used in the vault model on the time-integrated release from the vault to the geosphere. In such an analysis, parameter variation is restricted to the ranges of values specified in the model. Although this provides valuable information on which parameters have the greatest influence on dose, it does not clarify the extent to which the key assumptions in the various submodels influence the assessment results. Here, we list the key assumptions in the vault model. In particular, the degree of conservatism (i.e., the extent to which doses are overpredicted) arising from various assumptions is discussed. In other cases, where "realistic" models have been developed or, less frequently, where assumptions were not conservative, the potential for underestimating the impacts is outlined. The impact of these assumptions is discussed quantitatively where possible, although in many cases only order-of-magnitude estimates are possible. Each key assumption discussed is cross-referenced to the section of the report in which the justification for the assumption is presented.

7.3.2.1 Assumptions in the Radionuclide Release Model for Used Fuel

Some of the most important assumptions made in developing the radionuclide release model for used fuel (see Chapter 5) are shown in Table 7-13. The assumption that the used-fuel matrix, which contains the great majority of the total radionuclide content, is thermodynamically stable (i.e., its behaviour is described by that of the solids UO_2/U_4O_9 under reducing conditions) has a great impact: it virtually eliminates radiation doses prior to 10^5 a for radionuclides originating in the used-fuel matrix (see Figures 5-9 and 7-1). Alternative models for matrix dissolution have been proposed, based on the assumption that oxidative dissolution occurs. The most conservative approach is described by Werme et al. (1990) and assumes that all the H_2O_2 produced by α-radiolysis of water contacting the fuel contributes to oxidatively dissolving the UO_2 matrix. Such an approach suggests a fractional dissolution rate of approximately 9×10^{-5} a^{-1}, implying complete dissolution of the fuel in ~10^4 a. This result can be compared with the observation that $<10^{-8}$ of the fuel matrix dissolves in the median-value simulation (see Section 7.2.2.2) in 10^5 a. A more realistic oxidative dissolution model has been described by Shoesmith and Sunder (1991). The maximum rate predicted with this model for dissolution driven by α-radiolysis is in the range of 10^{-10} $g \cdot cm^{-2} \cdot d^{-1}$. For a used- fuel surface area of 2 $cm^2 \cdot g^{-1}$ (Johnson 1982), this rate implies that approximately 1% of the matrix could dissolve in 10^5 a. This would have a relatively small incremental dose impact, even at 10^5 a, since instant releases are already assumed to be much greater than this magnitude. Use of the

very conservative model of Werme et al. (1990), based on the assumption of rapid radiolytic oxidation, would lead to a significant increase in doses from ^{129}I (approximately a factor of 10) at times of 10^5 a or more. The impact would be very small for shorter times (~10^4 a) because of the relatively much greater impact of the instantly released radionuclides in contributing to dose (see Figures 5-9 and 7-8). The effect on doses from other radionuclides has not been evaluated, because of the compelling evidence that the radiolytic model of Werme et al. (1990) greatly overestimates dissolution rates (Chapter 5).

The remaining key assumptions in Table 7-13 are conservative and inevitably result in the model overpredicting the dose impact by various degrees. Of particular significance are the instant-release results for ^{14}C obtained by Stroes-Gascoyne et al. (1992) after the model and parameter ranges in Chapter 5 were specified. These data, obtained on fuel samples taken from several different CANDU fuel bundles, show that instant releases of ^{14}C are less than 0.01%. Use of these new data in assessment calculations would decrease ^{14}C doses by at least two orders of magnitude, essentially eliminating this nuclide as a significant dose contributor at any time.

The assumption that the Zircaloy sheath provides no protection is obviously conservative, but the impact of this assumption is difficult to quantify. If crevice corrosion were assumed to occur on all sheaths, the protection provided by the sheath would be very small (i.e., <100 a containment); but if uniform corrosion were the most likely failure mechanism, tens of thousand of years of containment could be envisaged following container failure. Another conservative assumption, that the portion of the sheath remaining after failure provides no mass transport resistance to radionuclide diffusion, is discussed in Section 7.3.2.2

7.3.2.2 Assumptions in the Container Failure Model

The key assumptions used in the container failure model are listed in Table 7-13. The majority of these assumptions (5 out of 6) can be considered conservative and the consequences of relaxing them would be to extend container lifetimes.

The critical assumptions controlling the predicted lifetimes of Grade-2 titanium waste containers are that crevice corrosion would initiate on all containers and that it would propagate indefinitely (Section 4.6.4.4). As a consequence, 97% of all containers are predicted to fail by crevice corrosion. The remaining 3% fail by HIC, since it is assumed that sufficient hydrogen would be absorbed during crevice corrosion to embrittle the container.

All the assumptions in the model that govern when HIC occurs are a direct consequence of this connection between crevice corrosion and HIC. In the absence of a complete understanding of how stresses in the container evolve with time, and of the rate of hydrogen absorption, it is necessary to assume that both the stress intensity and the hydrogen content are sufficient for HIC to fail the container. The assumption that HIC occurs once the temperature falls to ≤30°C is based on observations made on titanium

TABLE 7-13

KEY ASSUMPTIONS IN THE VAULT MODEL AND THEIR SIGNIFICANCE

Model	Assumption and Nature of Assumption, i.e., Realistic (R) Conservative (C), or Model Simplification (S)	Possible Alternative or Supplementary Model	Dose Impact of Alternative or Supplementary Model
Radionuclide Release Model for Used Fuel	"Reducing" model, i.e., fuel matrix is thermodynamically stable (UO_2/U_4O_9) (R) (Sections 5.2 and 5.5.2)	Oxidative model with maximum rate from α-radiolysis or from model of Shoesmith and Sunder (1991)	No significant impact at 10^4 a. Shoesmith and Sunder model predicts 1% dissolution of fuel in 10^5 a.
	Maximum instant-release fraction of ^{14}C = 25% (C) (Section 5.5.1.2)	^{14}C release model based on results of Stroes-Gascoyne et al. (1992)	Dose due to ^{14}C ~100 times smaller
	Grain-boundary inventory for important radionuclides is included in the instant-release fraction (C) (Section 5.5.1)	Kinetic model for leaching of the inventory of radionuclides at grain boundaries	Lower doses for ^{129}I; release in 10^4 a versus instant release
	Solubilities of actinide and technetium oxides controlled by solubilities of amorphous phases (C) (Section 5.5.3.1)	Use crystalline oxide solubilities (10^2 to 10^3 times lower)	Negligible for actinides, probably significant reduction for Tc
	Fuel sheath provides no barrier to radionuclide release (C) (Section 5.4)	Corrosion model for sheath (crevice and/or uniform corrosion)	Relatively small for a lifetime of 50 a (crevice corrosion); very large impact (0 dose at 10^4 a) if sheaths fail by uniform corrosion
	Adoption of (WRA 500-m depth) site-specific parameters to define vault conditions (S) (Sections 5.3 and 8.2)	Evaluate solubilities for broader range of groundwater chemistry	Very small impact on actinide and technetium solubilities

continued...

TABLE 7-13 (continued)

Model	Assumption and Nature of Assumption, i.e., Realistic (R) Conservative (C), or Model Simplification (S)	Possible Alternative or Supplementary Model	Dose Impact of Alternative or Supplementary Model
Container Failure Model	Crevice corrosion (CC) initiates rapidly on all containers (C) (Section 4.6.3.3)	Switch to a material for which crevice corrosion is limited (Grade-12) or does not occur (Ti/Pd alloys)	Orders of magnitude lower doses at 10^5 a
	Sufficient oxygen present for crevice propagation to continue indefinitely (C) (Section 4.6.3.3)	Upgrade present model to include the effect of oxygen exhaustion	Significantly lower doses
	Failure by CC will occur when the general corrosion front exceeds the corrosion allowance (R). (Section 4.6.3.2)	Accept full wall thickness as the corrosion allowance	Small impact because of small effect on container lifetime
	Failure will occur by HIC once $T \leq 30°C$ (C) (Section 4.6.4.1)	On the basis of measurements of hydrogen pickup rates, predict the time required for hydrogen content to exceed $[H]_o$ for HIC	Small effect since 97% of containers fail by crevice corrosion
	The required combination of stress intensity and hydrogen content for HIC will be present when $T \leq 30°C$ (C) (Section 4.6.4.1)	Assume CC does not initiate on cold containers ($T_{max} \leq 70°C$) and predict lifetimes on the basis of general corrosion behaviour	Relatively small impact since only 3% of containers are designated "cold"
	Failed container provides no further protection against fuel leaching (C)	Model the time taken to flood the container and include the mass transfer resistance of container (and sheath) remnants in calculations	Significant impact but difficult to quantify

continued...

TABLE 7-13 (continued)

Model	Assumption and Nature of Assumption, i.e., Realistic (R) Conservative (C) or Model Simplification (S)	Possible Alternative or Supplementary Model	Dose Impact of Alternative or Supplementary Model
Mass Transport Model	One-dimensional plane geometry (S) (Section 6.2.2)	Three-dimensional finite-element model (Garisto and LeNeveu 1989)	Doses likely lower with 3-D model because of dispersion
	Mass transfer coefficient exit boundary condition (S) (Section 6.8)	Two-layer semi-infinite solution using continuity of flux and concentration	Maximum dose up to 10^5 a from the ^{129}I increases by about a factor of two
	Linear sorption isotherm (R) (Section 6.3)	Isotherm with two linear segments from Pigford et al. (1992)	Major contributors to dose are non-sorbing radionuclides; diffusion studies for most other radionuclides indicate linear isotherms (Oscarson et al. 1992)
	No water movement in buffer after saturation (R) (Section 3.5.1)		Unless buffer cracks as a result of degradation, mass transport should be dominated by diffusion
	Coupled irreversible processes are ignored (S) (Chapter 3)	Include complex coupled models in mass transport model	Effect expected to be small (Chapter 3 and Cheung and Gray 1990)
	Precipitation is modelled at the waste form only (C) (Section 5.5.3)	Include precipitation in geosphere model	Precipitation in the geosphere for single radionuclides should impede mass transport and reduce dose. Impact for chains is complex; however, dose from radionuclides in chains negligible

continued...

TABLE 7-13 (concluded)

Model	Assumption and Nature of Assumption, i.e., Realistic (R) Conservative (C) or Model Simplification (S)	Possible Alternative or Supplementary Model	Dose Impact of Alternative or Supplementary Model
Mass Transport Model	Solubility is modelled as isotope-specific rather than element-specific, except for uranium isotopes, which are modelled as element-specific (S)	Apply uranium model to all isotopes	Only Tc, which has just one isotope, is appreciably affected by precipitation; thus, effect is negligible
	Buffer and backfill does not degrade over time (R) (Section 3.3)	Finite-difference model of Garisto and Garisto for cracked buffer (1989)	Study by Garisto and Garisto (1989) indicates cracks in buffer would have little impact
	Mass transport parameter values are independent of time (S)		Time evolution of parameter values too uncertain to model; impact expected to be small
	Buffer and backfill are saturated with water at time of container failure (C) (Section 3.2)		Persistence of unsaturated conditions should reduce mass transport in vault
	There is no gas phase in the vault (S) (Section 3.3.4)	Develop 2-phase transport model	Dose impact at long times uncertain, but no effect is expected for time periods of less than 20 000 a (Section 3.3.4)

alloys known to be much more susceptible to HIC than Grade-2 titanium (Section 4.6.4.1), and the assumption can, therefore, be considered conservative.

Realistically, the period of crevice corrosion would be limited by the combined evolution of temperature and redox conditions as indicated in Figures 4-8a and b and discussed in Section 4.6.3.3. As the vault cooled and oxidants were consumed, crevices would eventually repassivate and further corrosion would occur by general corrosion, a very slow process under vault conditions (Section 4.6.2). The consequences of such a change in corrosion mechanism are major, and lifetimes would be extended considerably. Although not within the scope of the present model, the crevice corrosion period could also be limited by the use of other titanium alloys, such as Grade 12 or Grade 7 (Table 4-1; Section 4.6.3.2).

A likely scenario is that crevice corrosion would initiate on only a small, but undetermined, number of containers, depending on oxygen concentration, temperature and the geometry of the crevice. The latter parameter is unpredictable since crevices would both penetrate into and spread across the container wall (Section 4.6.3.2). If the initiation of crevice corrosion was limited, the majority of containers would be expected to survive much longer than the currently predicted 1200 to 6000 a. In fact, the failure times would be distributed over the range from 1200 a, the approximate time for failure of a hot container subjected to indefinite crevice corrosion, to $>10^6$ a, the estimated failure time for a container subjected only to general corrosion (Section 4.6.2).

Perhaps the least conservative assumption in the container failure model is the assumption that failure occurs when the general corrosion front exceeds the corrosion allowance. If the period of crevice corrosion was limited and eventual failure was by general corrosion, then this definition of failure would be standard engineering practice, and hence conservative. If failure was by crevice corrosion, as predicted by the present model, then the general corrosion front within the crevice would be preceded by a number of localized penetrations and this definition of failure is realistic, as discussed in Section 4.6.3.2. If crevice corrosion were, for some reason, more localized, then it would be appropriate to accept the full container wall thickness as a corrosion allowance (Figure 4-7c). The assumption that containers will not fail as a consequence of structural loading before the time that the corrosion front exceeds the corrosion allowance is discussed in Chapter 3 of Johnson et al. (1994).

The final assumption, that the failed container provides no further protection against fuel leaching, is conservative since it ignores the time taken to flood the container and breach the fuel sheath, as well as the mass transfer resistance resulting from a small failed area through which diffusion might occur. The latter effect is discussed in more detail in Section 8.4.

7.3.2.3 Assumptions in the Mass Transport Model

The key assumptions used for the vault mass transport model are listed in Table 7-13. Of these the major assumption that governs the rate of mass

transport through the buffer and backfill is the use of the diffusion equation with linear sorption for a radioactive decay chain (Equation (3.9)). The diffusion experiments of Oscarson (in press), Cho et al. (1993) and Gillham et al. (1984) with the reference buffer material demonstrate that a diffusion equation with linear sorption can be used successfully to predict mass transport of radionuclides. These studies indicate that the assumption of a linear isotherm is appropriate. Non-linear isotherms, however, cannot be ruled out. In the context of deep geological disposal linear isotherms can be used in a manner that leads to conservative results (Walker and LeNeveu 1987).

To apply the diffusion equation correctly, appropriate boundary conditions and a suitable geometric representation of the system must be used. The use of a one-dimensional diffusion equation for transport across a series of layers, and the use of mass transfer coefficients for exit boundary conditions, are the major assumptions used. The suitability of these assumptions are discussed in detail in Chapters 6 and 8. The use of planar geometry in the vault model is likely to overestimate the dose in comparison with a three-dimensional model, because lateral dispersion is not taken into account when using planar geometry. Comparison of results from the vault model using the mass transfer coefficient exit boundary condition with a two-layer semi-infinite solution using continuity of flux and concentration indicates that the latter approach would increase the maximum calculated doses by a factor of approximately two for periods up to 10^5 a.

Assessment results indicate that precipitation is important only for ^{99}Tc. The assumptions regarding the modelling of precipitation are discussed in detail in Chapter 6.

The remaining assumptions can be regarded as second-order issues. There has been some concern that gas generation could be a significant phenomenon; however, it should be possible to reduce the potential for gas generation in the vault by an appropriate choice of materials. Nevertheless, this is an issue that merits further study. The possible impact of gas production on vault performance is discussed further in Section 7.5.

7.4 VALIDATION AND QUALITY ASSURANCE OF THE VAULT MODEL

7.4.1 Experimental and Model Validation

Validation is the process of demonstrating that a model adequately represents the system that it is meant to describe. In the case of the vault model, validation means showing that our models are appropriate representations of the processes of container corrosion, radionuclide release from used fuel, and mass transport in the conceptual disposal vault.

Validation is normally achieved by showing that model predictions agree with field or experimental observations when all the uncertainties are taken into account. Such a procedure is not possible for some of the models developed for the postclosure assessment. The data are obviously not available for making comparisons with model calculations for thousands of years into the future.

Nonetheless, some processes included in the models have been shown to be appropriately represented. For example, laboratory diffusion experiments have shown that the movement of radionuclides in clay-based buffer and backfill materials can be predicted by the use of diffusion models discussed in Sections 3.5 and 8.6. Similarly, the instant-release model has been shown to be appropriate for used-fuel bundles irradiated under a wide range of conditions (see Section 5.5). Many other processes are modelled on the basis of direct experimental measurements, coupled to conservative assumptions (see Section 7.3.2 for a summary of important assumptions in the models).

Another method of demonstrating that a model is appropriate is through comparison with a relevant natural analogue. A natural analogue is an occurrence in nature in which processes or conditions are either identical or similar to those occurring in man-made situations. The most significant analogues that relate to engineered barrier performance are those related to the used-fuel dissolution model (see Section 5.6 for a discussion of the Oklo natural reactors and the Cigar Lake uranium deposit) and the performance of bentonite barriers (see Sections 3.3.2 and 3.3.6). These analogues provide confidence that the radionuclide release and mass transport processes occurring in a vault are appropriately represented in the vault model.

7.4.2 Quality Assurance

The research on which the vault model is based has been subject to an informal quality assurance (QA) program guided by well-established scientific procedures. These studies were carefully designed and used appropriate equipment and procedures to gather the relevant data. Peer review has helped to ensure that the vault model meets accepted scientific standards. The model and the research program on which it is based have been continually exposed to critical review. They have been discussed at many meetings, both internally with AECL personnel and externally with other national and international experts. Many of the research results have been published in refereed journals. All publications receive a thorough AECL internal peer and management review prior to publication or release to a journal. Finally, since its inception, our program has been reviewed by the Engineered Barriers Subcommittee of the Technical Advisory Committee (TAC), an independent group of distinguished scientists nominated by Canadian professional societies. Members of TAC have complete access to all aspects of the program and have provided direction and critical review (e.g. TAC 1993). Peer review of the vault model was aided by the publication of two interim assessments (Wuschke et al. 1981, 1985a, 1985b), which described the model at intermediate points of the program. The interim assessments provided the opportunity for evaluation and revision of the model.

A formal QA program to guide waste management activities was initiated in 1990 (AECL 1990). This was done in response to stimuli both within AECL and external to it (AECB 1987, TAC 1987), as the value of QA programs to complex projects became more generally recognized. The program provides a framework for the planned and disciplined consideration of all the elements that influence the quality of waste management activities and products. It defines responsibilities and sets out procedures for applying QA principles to planning, executing and documenting all the work activities, including

those associated with data gathering and interpretation, and with model development and application. This will ensure that requirements related to future implementation of the disposal concept are satisfied in a systematic way, and that the results and documentation will be traceable to the source information. The Environmental Impact Statement and its primary references were written to conform to specific QA procedures developed for these documents.

The vault model computer code used for the case study has been verified by a variety of methods. To begin with, a complete set of specifications for the vault model code was produced as part of the code development. The specifications include a code synopsis, a data dictionary, data flow diagrams and module specifications. The module specifications detail all the equations used in the code (LeNeveu, in preparation). The specifications were extensively peer-reviewed to ensure their accuracy and applicability. A configuration control procedure that included analysis, design, coding, review and testing stages was followed for the code development. These procedures are described in more detail in Goodwin et al. (1994). The testing involved inserting each newly developed module into a stand-alone vault model code before installation into a prototype assessment code. One or more tests were done with this stand-alone code to ensure the module was performing as specified before installation into the prototype assessment code. An integration test was then performed on the prototype assessment code with the new module. At intervals the prototype code was frozen. The frozen version called CC305 was used to produce the case study for the assessment.

In addition to the verification procedures required for configuration control, various other quality assurance tests have been applied to the vault model code. A function test of the code used for congruent release, and the response function code used for mass transport across the buffer and backfill layers was performed by Ontario Hydro. The congruent-release code and the response-function code were based on analytical solutions to the convection-diffusion equation with two different sets of boundary conditions. For the Ontario Hydro test, the equations were solved in the Laplace transform domain, and the inversion was done numerically using Talbot's algorithm (Talbot 1979). The agreement between these independent solutions in most cases was of the order of ten significant figures, and in all cases to better than two significant figures, for over 70 000 separate function evaluations determined for all combinations of a three-level factorial sampling design for the time-independent input parameters and for time points covering a span of 10^7 a (Chan and Advani 1991).

A function test was also done for the code used to determine the vault mass transfer coefficients. In this case a separate C code was produced from the vault specifications and compared with the FORTRAN code used for the case study. The agreement, as expected, was of the order of the machine accuracy (16 significant figures) for 256 separate function evaluations determined from a three-level fractional factorial sampling design for the input parameters.

Unit tests on the vault code are being performed by the U.S. Department of Energy (DOE) as part of a co-operative program. In this type of test each

vault module is tested to ensure that every line of code is executed. The expected results are determined prior to the test from the specifications that give the equations upon which the code is based, and the results of the test are compared with the expected results.

A code comparison test has been done with the AREST code used by Pacific Northwest Laboratories. This test showed general agreement on the processes of mass transport and vault release (Engel et al. 1989).

A verification described in Section 7.2 compared the results of the vault model calculations with calculations from simple analytical expressions that would apply over a limited range of values. There was general agreement between the simple expressions and the results from the vault code over the restricted range of the applicability of the comparison.

Other forms of verification are performed during the execution of the code itself. For instance, each time the response functions used for mass transport in the buffer and backfill are evaluated, a check is made to ensure that mass balance is obtained. The response functions are solutions to the convection-diffusion equation for a unit impulse input. The mass balance check is done by ensuring that the time-integrated value of the response function for the release from the buffer or backfill is less than or equal to one. Output files for 10 000 simulations of seven radionuclides were examined for instances of mass balance violation in the vault response functions. In these 10 000 simulations, the response functions were evaluated 1.68×10^6 times with no instances of mass balance violation to within the estimated accuracy of the computation.

These extensive verification procedures confirm the reliability and accuracy of the results produced by the vault model code.

7.5 PERIOD OF VALIDITY OF THE VAULT MODEL AND REASONED ARGUMENTS FOR THE LONG-TERM PERFORMANCE OF THE VAULT

The vault model was developed to describe the performance of engineered barriers in the conceptual vault for a period of at least 10^4 a. Used with caution, and combined with reasoned arguments regarding the long-term performance of the barriers, the vault model can also be used to indicate trends for periods up to 10^5 a. The reasons for limiting the period of extrapolation of the model results are discussed below.

7.5.1 Containers

The vault model calculations indicate that all containers would fail by 10^4 a; thus, there are no time-frame limitations for this part of the model. Because of conservatisms in the container failure model, it is anticipated that containers would actually fail at times much longer than 10^4 a.

7.5.2 Used Fuel

The dissolution model for the used-fuel matrix calculates the dissolution rate based on the uranium concentration gradient existing between the

surface of the fuel and the surrounding buffer material (see Chapter 5). The calculated solubilities depend to a large degree on the oxidation potentials (E_h) assumed for the two locations. E_h values for the fuel surface vary from low values within the UO_2 stability field to much higher values associated with the U_4O_9/U_3O_7 boundary. The latter values are included in the model to reflect the possibility that the high α-activity at the fuel surface may result in higher uranium solubility. Lower E_h values, and therefore lower uranium solubilities, are expected in the buffer where Fe^{2+}/Fe^{3+} equilibria would control the E_h. However, the high α-activity at the fuel surface would decrease to a level comparable to that of a rich uranium ore, such as that at Cigar Lake, within approximately 10^5 a (Johnson et al. 1994). As a result, vault model simulations that involve sampling the high E_h values likely significantly overpredict the dissolution rate of the fuel for periods beyond 10^5 a. For example, 1 in 2000 simulations show ~10% of the fuel matrix dissolving in 10^5 a; such simulations reflect the highest uranium solubilities at the fuel surface and the steepest concentration gradients. Evidence from the Cigar Lake deposit, which has an age of 1.3×10^9 a, shows that such high dissolution rates do not occur for uraninite ores deeply buried in a reducing environment. These results suggest that, although model simulations reflecting such relatively high dissolution rates have been included in the model to ensure conservatism for periods up to 10^5 a, the model should not be applied to time frames longer than 10^5 a. For times longer than 10^5 a, the median-value simulation of the vault model (see Section 7.2.2.4) gives results that are consistent with geological observations, which suggest insignificant dissolution rates of the fuel matrix for times beyond 10^5 a. A more detailed description of natural analogues for the behaviour of used fuel is given in Section 5.6.

7.5.3 Mass Transport in the Vault

The buffer and backfill materials are expected to continue to perform effectively as diffusion barriers for at least 10^5 a. At times greater than this, some degree of illitization may occur, but this is unlikely to significantly alter the transport properties of the buffer material. As discussed in Section 3.3.6, the Avonlea bentonite in its unprocessed state contains fractures that self-seal upon saturation. The buffer material is therefore expected to maintain a sufficiently low hydraulic conductivity such that diffusion will dominate contaminant transport even for periods beyond 10^5 a. Other analogue studies (Pusch and Karnland 1990) have concluded that highly compacted bentonite barriers should perform effectively for millions of years if disposal vault temperatures are kept below 100°C.

The possibility that gases such as hydrogen may eventually accumulate in the vault cannot be discounted. As discussed in Section 3.3.4, conservative estimates suggest that a hydrogen gas phase could form after approximately 20 000 a. However, at the maximum rate at which gas is likely to be produced, the H_2 partial pressure would reach only 10 MPa (twice the hydrostatic pressure at a depth of 500 m) after 40 000 a. The amount of gas accumulated during this time would occupy only ~1% of the total pore space in the buffer and backfill material; thus, the effects on contaminant transport would likely be insignificant. Gas production may, however, introduce greater uncertainties over longer periods of time; thus, the

model calculations may become increasingly uncertain beyond the time frame of ~10^5 a.

7.5.4 Vault-Geosphere Coupling

The rate of mass transfer between the vault and geosphere could vary with time primarily because of changes in groundwater velocity. At vault depth in the presence of low hydraulic conductivity rock and low hydraulic gradients, mass transfer is likely to be dominated by diffusion, with groundwater velocity fluctuations having only a minor effect. However, the onset of glaciation could conceivably perturb the groundwater flow field sufficiently to affect mass transfer rates from the vault to the geosphere. This could place a restriction on the validity of the model to times before the onset of glaciation.

Potential effects of seismicity and glaciation on transport in the geosphere are discussed by Davison et al. (1994b).

8. SUPPLEMENTARY ANALYSES

8.1 INTRODUCTION

A number of additional analyses, related to engineered barriers and required to illustrate the safety of the disposal concept, have been performed. For a variety of reasons, it was recognized that these analyses would be best done outside the SYVAC analysis, which is the focus of Chapters 3 to 7. These analyses are outlined below and discussed in detail in subsequent sections.

1. The general applicability of the vault model results to the siting of a disposal vault at other locations (and depths) on the Canadian Shield was evaluated. In particular, the effects of a broader range of parameter values for groundwater chemistry on used-fuel dissolution and container corrosion are examined.

2. The sensitivity of the vault model results to assumptions made regarding mass transfer from the vault to the geosphere was assessed. A number of different models of radionuclide mass transport in the vault are compared and the implications of the various results are discussed. The reference approach using mass transfer coefficients is compared with results obtained using coupled solution and zero-concentration boundary condition models.

3. A calculation is presented that estimates radionuclide release from prematurely defected containers. Although releases from these containers (1 in 10^3 to 1 in 10^4 of the total number in the vault) are included in the case study, the model for used-fuel matrix dissolution at these early times was the same as the one used for container failures occurring after >1000 a (i.e., "reducing" conditions were assumed). Studies of the dissolution

of UO_2 in high-γ-radiation fields of the magnitude expected in the case of early container failure indicate that more rapid oxidative dissolution of the fuel would occur for such early container failures. An oxidative model is used here to estimate the impact of this mechanism on the dissolution of used fuel in the small number of prematurely failed containers. The results are then compared with those obtained for early failures in the case study.

4. An analysis of the possibility of nuclear criticality is presented; it examines the potential for a scenario involving segregation of ^{239}Pu from the fuel as a result of fuel dissolution, followed by accumulation of a high local concentration of ^{239}Pu within or near a container.

5. Results from recent studies of diffusion of ^{14}C, ^{129}I and ^{99}Tc in buffer material are compared with those presented in Section 3.5.3, and the impact of these new data on dose calculations is shown.

8.2 EFFECTS OF VARIATIONS IN GROUNDWATER CHARACTERISTICS

8.2.1 Groundwater Chemistry in the Canadian Shield

As discussed in Section 3.4, the groundwater chemistry for the case study represents the expected composition range at a depth of 500 m in the WRA. As discussed by Frape et al. (1984), the compositions of deep groundwaters at different locations on the Canadian Shield can vary considerably, and high salinities have been observed at depths of 500 to 1000 m. For example, Cl^- concentrations of 0.3 to 1.5 $mol \cdot L^{-1}$ are reported in Table 1 of Frape et al. (1984) for depths of ~1000 m. However, the maximum Cl^- concentration used in the case study is approximately 0.3 $mol \cdot L^{-1}$. Should a disposal vault ultimately be sited where such high-salinity groundwaters occurred, it is reasonable to ask whether the assessment results would remain valid. To evaluate this, the solubility of uranium and the crevice corrosion rate of titanium in more saline waters were examined. Similarly, the implications of groundwaters being even less saline than WRA groundwater are discussed. The reader is directed to Sections 3.4.1, 4.6.3.2 and 5.5.2.2 for comprehensive discussions on groundwater composition in the vault, crevice corrosion rates of Ti, and U solubilities in the vault groundwater respectively.

8.2.2 Uranium Solubilities

If the groundwater contained large quantities of dissolved salts, the buffer would have a small effect on the composition of the contact water (i.e., the water that would contact the container and used fuel) (Lemire and Garisto 1989). In general, in high-ionic-strength groundwaters, the concentrations of complexing ions, such as carbonate and phosphate, are expected to be lower than in conditioned WRA-500 type groundwaters. The higher calcium concentrations in the high-ionic-strength waters favour formation of calcium-containing solids, such as calcite and hydroxyapatite.

In turn, the lower concentrations of carbonate and phosphate should result in lower total concentrations of dissolved U.

Uranium concentrations were calculated for 40 000 model waters at 100°C having initial $CaCl_2$, NaCl, Na_2SO_4 and total dissolved inorganic carbon concentrations selected from loguniform distributions between the values appropriate for SCSSS (Table 3-1) and SCSB/2 groundwaters. The SCSB/2 (standard Canadian Shield brine) groundwater has an ionic strength of 3.4 $mol \cdot L^{-1}$; its composition is given by Lemire (1988). The initial total inorganic fluoride and phosphate concentrations (not specified for SCSSS and/or SCSB/2) were allowed to vary from $10^{-3.6}$ to $10^{-5.0}$ and from $10^{-5.2}$ to $10^{-8.0}$ respectively. The ionic strength ranged from 1.3 to 3.4 $mol \cdot L^{-1}$. The SCSSS equilibrium constants were used in the calculations and were held constant (i.e., they were not varied with changes in groundwater composition). The ranges of pH and E_z were the same as those used in the solubility calculations discussed in Section 5.5.2.2 (see Figure 5-10). As in the the case of the latter calculations, more than 70% of the calculated U concentrations for the high-ionic-strength waters are lower than 2.5×10^{-10} $mol \cdot L^{-1}$ (see Figure 8-1). However, Figure 8-1 shows that there are markedly fewer cases of calculated U concentrations above 10^{-8} $mol \cdot L^{-1}$ for the more saline solutions.

If necessary, a fourth region of ionic strength, centred about the value for SCSB/2, could be added to the model. Most of the equilibrium constants required to calculate the U solubility in groundwaters similar to SCSB/2 have been documented (Lemire 1988). Reselection of uranium solution species would also be required, although the new sets of species would not be expected to differ greatly from those in the current selected set.

The model could also be extended to predict solubility behaviour in even more saline waters ($I > 4$ $mol \cdot L^{-1}$). However, the required equilibrium constant data are not available. Extensive new experimental work would be required to estimate the values needed to do calculations for very saline groundwaters, such as SCSB ($I \simeq 7.7$ $mol \cdot L^{-1}$), and the results would be specific to the particular groundwater composition.

If the groundwater in the geosphere region outside the vault had a very low concentration of total dissolved solids (especially calcium salts), concentrations of certain anions (such as carbonate or fluoride) in the contact water might be greater than the highest concentrations selected for the distributions described in Table 3-1b. In such cases, the model we have described would still be valid. However, to calculate total concentrations of U, Np, Pu, Th and Tc, it would be necessary to select different subsets of the species listed in Section 3.2 and Appendix B of Lemire and Garisto (1989). The solubility of the UO_2 matrix would probably be increased by less than an order of magnitude except when the value for E_z was above 0.4 V_{SHE}. In the latter case the formation of strong multiligand U(VI) complexes might raise the matrix solubility by as much as 2 to 3 orders of magnitude.

Similarly, if the pH of the contact water was expected to be outside the range of 5 to 10, then a reselection of the species used in the model would also be required. The model, however, does not include formation constants

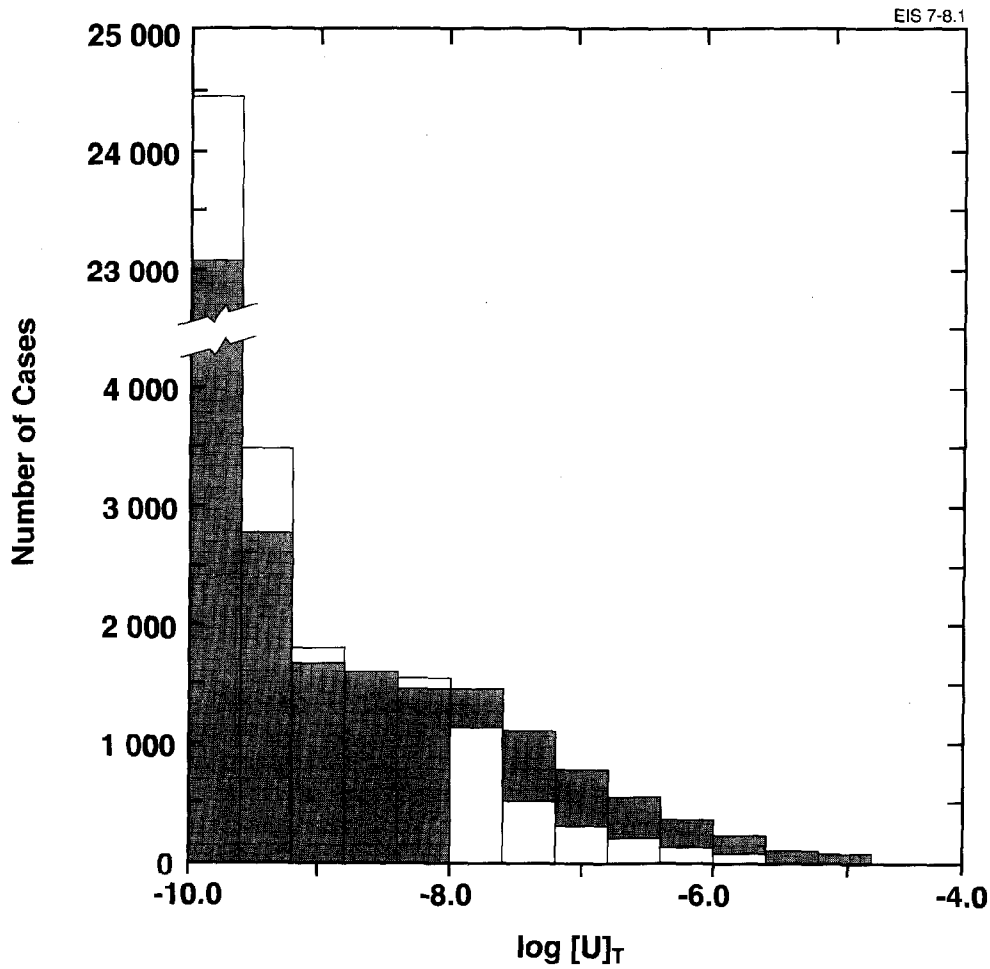

FIGURE 8-1: A Comparison of the Distributions of Uranium Solubility ($mol \cdot L^{-1}$) at 100°C in the Contact Waters (Table 3-1b) (shaded area) and in High-Ionic-Strength Waters (unshaded area). The appropriate equilibrium constants were used for the uranium solubility equilibria in the different media, but were fixed at their most probable values, rather than sampled, for the 40 000 cases.

for HF°, $H_3PO_4^{\circ}$, PO_4^{3-}, HSO_4^- and $CaOH^+$, because they are not important species in solutions with pH values between 5 and 10. If the value of the pH was less than 4.8, changes to the model would have to be made to allow for formation of HF° (also to allow for the formation of HSO_4^- below pH 3.5 and $H_3PO_4^{\circ}$ below pH 3.1). For pH values above 10.0, model changes to allow for formation of $CaOH^+$ (and PO_4^{3-} above pH 11.8) would be required. Furthermore, for pH values greater than 10.0, additional experimental data on the hydrolysis of U(VI) in basic solutions would be needed to properly identify the important U species and to determine their formation constants.

8.2.3 Crevice Corrosion Rate of Titanium

The effects of variations in groundwater chloride concentration and the addition of other species likely to be encountered in groundwaters have been studied for both the titanium alloys, Grade 2 and Grade 12, considered as candidates for the fabrication of waste containers.

The sequence of corrosion events leading to the eventual failure of the containers, outlined in Sections 4.6.3.3 and 4.6.4.4, would remain unchanged with changes in groundwater composition; i.e., a combination of crevice corrosion, hydrogen-induced cracking and general corrosion would still be the most likely sequence of events leading to failure. The duration of the period of crevice corrosion would remain as the most important factor determining container lifetimes.

The principal effect of a change in chloride concentration would be to increase the probability of crevice initiation. Since the current container failure model assumes that crevices initiate rapidly on all containers, this effect becomes irrelevant. Using the galvanic coupling technique described in Section 4.6.3.2 (and in references therein), it was demonstrated that while the rate of activation of crevices (i.e., rate of exposure of active metal) may increase with increasing chloride concentration, the total extent of crevice corrosion is governed by the total amount of available oxidant (Ikeda et al. 1992). Measurements of corrosion penetration depths show, surprisingly, that the depth of crevice penetration is greater for lower than for higher chloride concentrations. This can be attributed to the tendency for the propagation process to become localized in the crevice at the lower chloride concentrations as general crevice activation becomes more difficult. For high chloride concentrations, therefore, localized penetrations should remain <2 mm ahead of the general crevice corrosion front and, hence, should not affect the predictions of the current container failure model for Grade-2 titanium.

Chloride concentration has a marked effect on the crevice corrosion of Grade-12 titanium; but, again, the overall mechanism of the process does not change. The total extent of crevice propagation shows a maximum at a chloride concentration of ~2.0 $mol \cdot L^{-1}$. However, propagation remains suppressed and repassivation occurs under oxidizing conditions over the whole chloride concentration range. Consequently, selection of Grade-12 titanium rather than Grade 2 as the container material would be expected to limit the duration of, and penetration by, crevice corrosion irrespective of the salinity of the groundwater.

The effects of other groundwater constituents on crevice corrosion of Grade-2 titanium were discussed in Section 4.6.3.2. Species likely to be encountered in shallow groundwaters, such as SO_4^{2-} and HCO_3^-/CO_3^{2-}, suppress the rate of crevice propagation and lead to repassivation before all the available oxidant is consumed. However, their presence is unlikely to be a factor in chloride-dominated groundwaters. Of the species to be encountered in extremely saline deep groundwaters, Ca^{2+} and Mg^{2+} are likely to have the greatest effect on crevice propagation (Shoesmith and Ikeda, unpublished data). Substantial concentrations of these cations can change the mode of crevice propagation, leading to deep localized penetrations. In the absence

of a more extensive investigation it is impossible at present to state with certainty how Grade-2 titanium would function in groundwaters containing calcium at concentrations greater than that encountered in SCSSS (Table 3-1a). Consequently, the use of Grade-2 titanium cannot currently be recommended in very saline groundwaters containing >15 000 $mg \cdot L^{-1}$ of Ca^{2+}.

The crevice corrosion of Grade-12 titanium is also accelerated in the presence of large quantities of Mg^{2+} (Westerman 1990). The effect of Ca^{2+} has not been investigated but is likely to be similar to that of Mg^{2+}. Despite this acceleration, crevice propagation is limited on Grade 12, and repassivation is observed prior to total consumption of available oxidant. Although incompletely understood, it is clear that the metallurgical factors that aid the repassivation of Grade 12 under reference groundwater conditions still operate in more aggressive, very saline groundwaters. The Grade-12 alloy would appear appropriate for container fabrication if more saline conditions were expected, although a more detailed experimental program is required to confirm this.

The extent of hydrogen absorption accompanying crevice corrosion is unlikely to change with groundwater composition, although direct evidence is lacking. The amount of hydrogen absorbed would be controlled by the overall extent of crevice corrosion, which, in turn, would be controlled by the total amount of oxidant available in the vault. Since the latter is not likely to change substantially with location on the Canadian Shield, the predictions of the container lifetime model with respect to hydrogen-induced cracking would remain unchanged.

8.3 THE SENSITIVITY OF THE RESULTS FROM A VAULT PERFORMANCE ASSESSMENT TO THE CHOICE OF MASS TRANSFER MODEL FOR THE VAULT/GEOSPHERE INTERFACE

Here, we compare radionuclide release rates from the conceptual vault, calculated using different exit boundary conditions (at the buffer/backfill and backfill/rock interfaces) for solving the mass transport equations (Garisto and LeNeveu 1991). We present the results for radionuclide release rates from vault sectors 1 and 11 (i.e., from a typical sector located far from the assumed fracture zone (sector 1), and another located close to the nearby fracture zone (sector 11)), which could have a strong influence on the release of radionuclides to the surface environment.

The three models that we have studied are (i) a mass transfer coefficient (MTC) model for the buffer/backfill and the backfill/rock interfaces (this is the model used in the case study, see Section 6.8); (ii) a coupled-solution (CS) model (see Garisto et al. 1992); and (iii) a zero-concentration boundary condition model ($C = 0$) at the buffer/backfill and backfill/rock interfaces. The coupled-solution model is based on continuity of flux and concentration conditions at the buffer/backfill and backfill/rock interfaces, and is described in detail in Section 5 of the report by Garisto et al. (1992) on coupled solutions. In a zero-concentration boundary condition, it is assumed that radionuclides are swept away by flowing groundwater as soon as they reach the boundary.

The calculations were carried out for the radionuclide ^{129}I, since it is predicted to be the major contributor to dose (see Chapter 7). The release rates, R(t) ($mol \cdot a^{-1}$), were calculated for up to 10^5 a after vault closure.

Figures 8-2 and 8-3 compare the release rates of ^{129}I to the geosphere from vault sectors 1 and 11 respectively, for the median case (see Chapter 7) calculated using the three models. (In these calculations, all the parameters having frequency distributions were given their median values.) The figures show that the release rates are ordered $R_{C=0}(t) > R_{CS}(t) > R_{MTC}(t)$, as expected (Garisto and LeNeveu 1991, Garisto et al. 1992). The shapes of the release curves in the vicinity of 3000 a are strongly influenced by the shape of the container failure function used in the calculations (see Chapter 4 and Johnson et al. 1992), whereas the long-term decrease in the release rate of ^{129}I for the C = 0 model is caused by the ^{129}I source term that is dominated by an inventory-limited release from the fuel gap and grain boundaries (see Section 5.5.1.3).

The coupled-solution model is considered the most realistic of the three models. The results confirm that the MTC is not a conservative approximation, whereas the zero-concentration boundary condition is an excessively

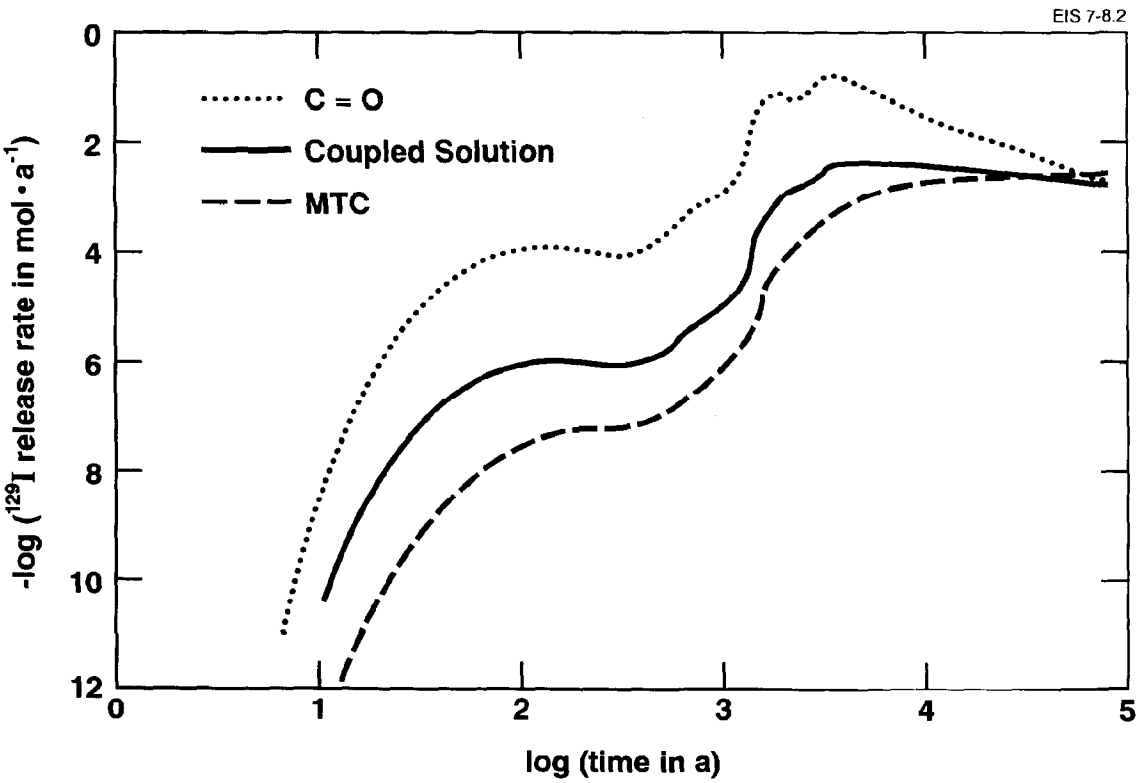

FIGURE 8-2: The Release Rate of ^{129}I from Vault Sector 1 as a Function of Time for Three Different Mass Transport Models for the Median Vault Simulation

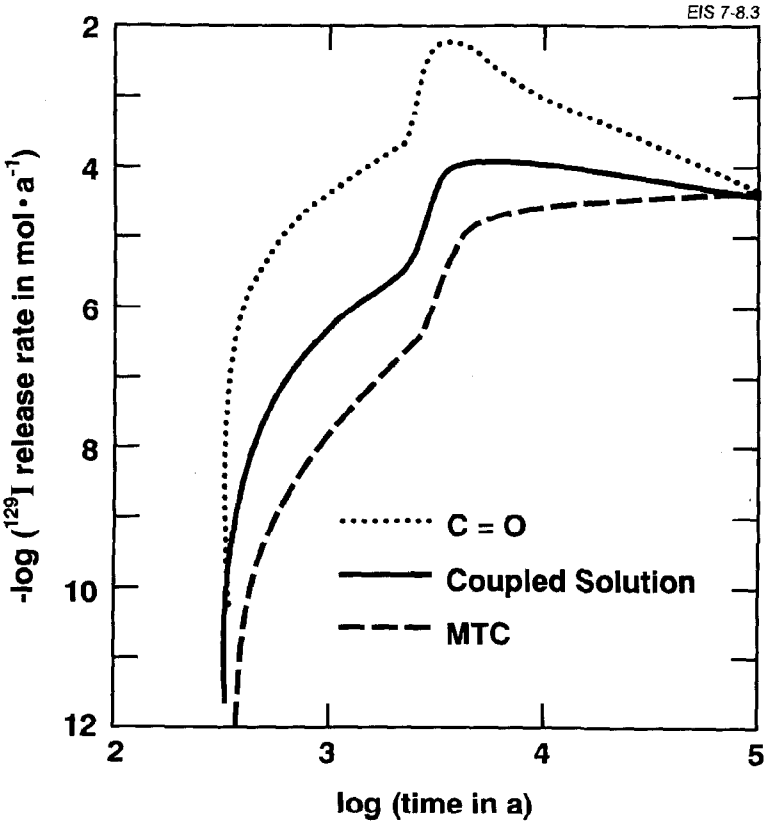

FIGURE 8-3: Release Rate of ^{129}I from Vault Sector 11 as a Function of Time for Three Different Mass Transport Models for the Median Vault Simulation

conservative approximation. Although this latter approximation is often convenient for making quick estimates of release in the absence of suitable hydrogeological data, it can lead to erroneously high dose rates, particularly when applied to cases with non-median parameter values. For the median case that we have studied, the maximum dose rate arising from ^{129}I (over 10^5 a), calculated using the C = 0 approximation, is 1.1×10^{-5} Sv•a^{-1}, which occurs at 10^5 a. This value is lower than the dose limit of 5.0×10^{-5} Sv•a^{-1} implied by the regulatory risk limit (AECB 1987). The corresponding doses calculated using the MTC approximation and the coupled solution are over an order of magnitude lower (4.3×10^{-7} Sv•a^{-1} and 9.5×10^{-7} Sv•a^{-1} respectively also at 10^5 a). As discussed by Garisto et al. (1992), coupled-solution models are expected to give more realistic estimates of release from multilayered media than the MTC and the C = 0 boundary-condition models. However, they have not been used for the case study because they were not sufficiently developed at the time the assessment models were selected. In addition, these models have other limitations. The development of more accurate models for estimating near-field mass transport will necessitate the development of efficient coupled-solution methods and the simplification of non-essential features in near-field models. One such

simplification, i.e., a decrease in the number of sectors used in the vault model, is discussed below.

The major parameters controlling the relative release from the various sectors appear to be the groundwater velocity and the dispersion coefficient (which in turn depends on the groundwater velocity). Table 8-1 lists the values of the linear velocity (v_L, positive in the upward direction and negative in the downward direction), the Darcy velocity (v^R), and the dispersion coefficient for ^{129}I in the rock segments adjacent to the vault sectors (D), as well as the corresponding convective MTC (K^C) at the backfill/rock interface (Garisto and LeNeveu 1991). Also given is the value for the larger of K^C and K^D, the diffusive MTC at the backfill/rock interface. K^C is calculated by assuming that mass transport in the rock occurs by convection, whereas K^D is calculated by assuming that mass transport in the rock occurs by dispersion. Both K^C and K^D are calculated in the vault model and the larger of the two (a conservative assumption) is used to calculate mass transfer (see Chapter 6). The parameter values listed in Table 8-1 indicate that the spatial variability in the host rock from sector to sector (e.g., the mass transport properties of the fracture zone compared with those of intact rock) is hardly felt by the vault, which is in contact only with intact rock with relatively uniform properties. Thus, in the case that we have studied, the groundwater velocities are all similarly small and the dispersion coefficient has a low variability from sector to sector.

The magnitude of the MTC for the various sectors gives an estimate of the relative radionuclide flux across the vault-sector/rock interface. Table 8-1 shows that convective mass transfer is larger (K^C is larger) in sectors 1 to 8 and in sector 12, whereas dispersion is larger (K^D is larger) in sectors 9 to 11. This is not surprising since, in the vault model, K^D decreases as the distance to the fracture zone increases, whereas K^C is independent of the distance to the fracture zone.

The overall variability in the MTCs for the backfill/rock interface in the various sectors is small. The MTCs are all within a factor of 4 of each other in the median-value simulation. We have extended the median-value simulation and performed a stochastic calculation based on 1000 runs, with parameter values chosen from their respective parameter distribution functions. The resulting variability in the MTCs is shown in a histogram in Figure 8-4. The histogram shows that the MTCs for sectors 1 and 11 are within approximately one order of magnitude of each other. These results indicate that a smaller number of sectors should be adequate for a mass transport analysis of the vault in contact with the reference geosphere (see Davison et al. 1994b).

We have presented an analysis of the sensitivity of performance assessment results, calculated using the vault model, to modifications in the models chosen to represent mass transfer at the vault/geosphere interface. Our analysis has shown that simplified, conservative models such as the zero-concentration boundary-condition model for the buffer/backfill and the backfill/rock interfaces are not appropriate for deriving realistic performance assessment results. Although the results of the median case

TABLE 8-1

MEDIAN VALUES OF MASS TRANSPORT PARAMETERS FOR THE VARIOUS VAULT SECTORS

Vault Sector	v_L ($m \cdot a^{-1}$)	$\lvert v^R \rvert$ ($m \cdot a^{-1}$)	D ($m^2 \cdot a^{-1}$)	K^C ($m \cdot a^{-1}$)	$\max(K^C, K^D)$ ($m \cdot a^{-1}$)
1	5.89×10^{-5}	1.76×10^{-7}	1.01×10^{-5}	6.75×10^{-7}	6.75×10^{-7}
2	7.89×10^{-5}	2.37×10^{-7}	1.08×10^{-5}	8.06×10^{-7}	8.06×10^{-7}
3	7.02×10^{-5}	2.11×10^{-7}	1.05×10^{-5}	7.50×10^{-7}	7.50×10^{-7}
4	1.93×10^{-5}	5.78×10^{-8}	8.88×10^{-6}	3.61×10^{-7}	3.61×10^{-7}
5	1.94×10^{-5}	5.83×10^{-8}	8.89×10^{-6}	3.63×10^{-7}	3.63×10^{-7}
6	-3.50×10^{-5}	1.05×10^{-7}	9.38×10^{-6}	5.01×10^{-7}	5.01×10^{-7}
7	5.34×10^{-5}	1.60×10^{-7}	9.96×10^{-6}	6.37×10^{-7}	6.37×10^{-7}
8	4.73×10^{-5}	1.42×10^{-7}	9.76×10^{-6}	5.94×10^{-7}	5.94×10^{-7}
9	-5.92×10^{-6}	1.77×10^{-8}	8.46×10^{-6}	1.96×10^{-7}	2.33×10^{-7}
10	-1.20×10^{-5}	3.60×10^{-8}	8.65×10^{-6}	2.82×10^{-7}	3.59×10^{-7}
11	5.94×10^{-6}	1.78×10^{-8}	8.46×10^{-6}	1.96×10^{-7}	3.51×10^{-7}
12	-8.47×10^{-5}	2.54×10^{-7}	1.09×10^{-5}	8.41×10^{-7}	8.41×10^{-7}

that we have analyzed are all below the dose limit implied by the regulatory risk limit set by the AECB, they (the C = 0 results) are excessively conservative and could therefore lead to unnecessary overdesign of the vault. On the other hand, results based on the MTC approximation represent non-conservative values under certain conditions and care should be exercised in their interpretation (see also Apted et al. 1989a). In the vault model, this non-conservatism is mitigated by overriding conservatisms, such as one-dimensional transport, which tends to overestimate releases. More accurate models such as those using coupled-solution methods are being developed. However, the coupled solutions available at present require significantly larger computer resources than either the C = 0 or the MTC approximation. Their application in the vault model can perhaps be facilitated by simplifying the model geometry, e.g., by using a reduced number of sectors.

8.4 SIMULATION OF DOSE FROM INITIALLY DEFECTED CONTAINERS

As discussed in Chapter 4, it is assumed that a small number of containers fail early because of initial defects. This early failure is modelled as occurring within the first fifty years after vault closure. In the model, reducing conditions are assumed to prevail in the vault during the period when these early container failures occur, as is the case during the period when later failures occur. This may not, however, be the case. When the early container failures occur, oxidizing conditions could still persist in the vicinity of the containers because of oxygen entrapped in the buffer and backfill and because of the γ-radiation emitted by the fuel. This could cause the solubility and sorption characteristics of redox-sensitive radionuclides to be different from those in the model. Of primary concern are the dissolution rate of the UO_2 fuel and the sorption and solubility of

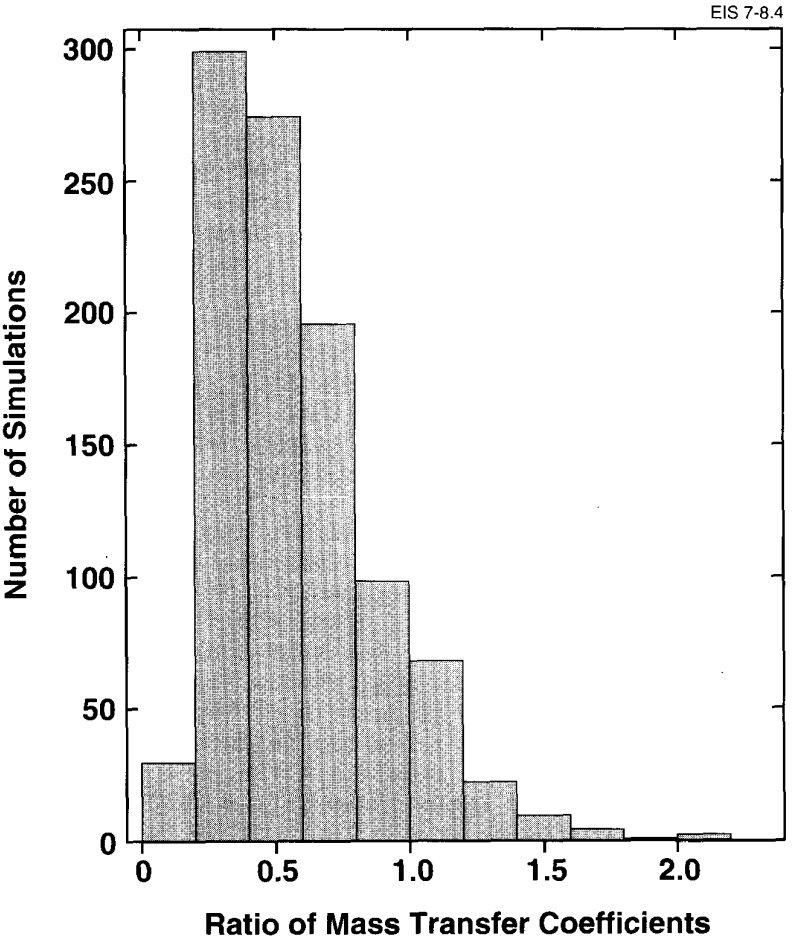

FIGURE 8-4: Ratio of ^{129}I Mass Transfer Coefficients at Backfill/Rock Interface for Sector 11/Sector 1

^{99}Tc under oxidizing conditions. Two cases were simulated to examine the effect on dose resulting from early container failure. The first case modelled the dose resulting from congruent release from the used fuel; the second modelled dose as a result of instant release from the used fuel. Of the instantly released radionuclides, it was assumed that only ^{99}Tc would have different behaviour under oxidizing and reducing conditions.

In the first case a constant dissolution rate model described in Section 8.5.4 was used, in which 6 kg of used fuel in each of the prematurely defected containers was considered to be dissolved in 500 a. Beyond this time conditions were assumed to be reducing, and hence the model outlined in Chapter 5 would be more appropriate. To obtain only the differential dose from congruent release in the defected containers under oxidizing conditions, the instant-release fraction was set to zero and the dissolution rate of UO_2 was set to zero after 500 a. The diffusion coefficient and capacity factor of ^{99}Tc in buffer were modified to 7.3×10^{-4} $m^2 \cdot a^{-1}$ and 0.10 respectively to reflect the oxidizing conditions. The diffusion

coefficient and capacity factor of ^{99}Tc in the backfill were changed to 3.15×10^{-4} $m^2 \cdot a^{-1}$ and 100 respectively to reflect data recently obtained by Oscarson and Hume (1993a) for oxidizing conditions in backfill (see Sections 3.5.4 and 8.6). The new capacity factor of ^{99}Tc in the buffer is significantly lower than the value of 5.3×10^{1} used for reducing conditions in the median-value simulation, and the new diffusion coefficient for ^{99}Tc in the buffer is higher than previously assumed for reducing conditions (1.14×10^{-5} $m^2 \cdot a^{-1}$). The new capacity factor of ^{99}Tc in the backfill is also significantly lower than the value of 2.0×10^{3} used for reducing conditions in the median-value simulation. However, the new diffusion coefficient for ^{99}Tc is about an order of magnitude lower than previously assumed for reducing conditions (2.25×10^{-3} $m^2 \cdot a^{-1}$) (see also Tables 7-3 and 7-6). The net result is that ^{99}Tc should have only slightly more mobility in the backfill under oxidizing conditions than under reducing conditions, but considerably more mobility in the buffer.

Solubilities of all radionuclides were set at 2 $mol \cdot L^{-1}$ so that precipitation did not occur. The number of containers failing early in sectors 10, 11 and 12 was set at 4, 3 and 4 respectively. On a random basis this number of initial failures in these sectors would occur in one per thousand simulations. The combined frequency for this combination of failures in the three sectors is 1 in 10^{9}. In most random simulations no containers would fail in sectors 10, 11 and 12 because of the small number of containers in these sectors. The number of early failures was set abnormally high in sectors 10 through 12 because almost all the dose in the median-value simulation is attributable to these sectors (see Chapter 7). The later failures from crevice corrosion were eliminated so that the dose rate from the early failures alone would be obtained. All the other parameters were assigned their median values. Dose consequence calculations are summarized in Table 8-2.

Release and transport of seven radionuclides were simulated for the congruent release case: ^{14}C, ^{135}Cs, ^{129}I, ^{59}Ni, ^{107}Pd, ^{79}Se and ^{99}Tc. The maximum dose rate obtained in this simulation, 2.6×10^{-29} $Sv \cdot a^{-1}$, was from ^{129}I at 10^{5} a. This is to be contrasted with the dose rate of 4.3×10^{-7} $Sv \cdot a^{-1}$ at 10^{5} a for ^{129}I in the normal median-value simulation. Thus, the differential, or extra, dose arising from the mechanism of congruent dissolution under oxidizing conditions after early failure of a number of containers is negligible.

In the second case, the differential dose resulting from early container failure and instant release from the used fuel was investigated. The diffusion coefficients and capacity factors in buffer and backfill and the number of early failures were the same as in the previous congruent dissolution case. Later container failures were eliminated. The solubilities of all radionuclides were once again set high. Congruent dissolution, however, was suppressed by setting the solubility of UO_2 to a value near zero. The instant-release fractions and all other parameters were set at their median values.

The maximum dose rate for this simulation, 6.8×10^{-10} $Sv \cdot a^{-1}$, was once again from ^{129}I at 10^{5} a. This is considerably higher than the differential dose rate attributable to congruent dissolution, but is still

TABLE 8-2

DOSE CONSEQUENCE FROM INITIALLY DEFECTED CONTAINERS

Case	Number of Early Failures in Sectors 10-12	Redox Conditions	Maximum Dose Rate ^{129}I ($Sv \cdot a^{-1}$)	Maximum Dose Rate ^{99}Tc ($Sv \cdot a^{-1}$)
Normal median-value case	0	Reducing	4.3×10^{-7}	1.9×10^{-28}
Congruent dissolution case for early failure	11	Oxidizing	2.6×10^{-29}	0
Instant-release case for early failure	11	Oxidizing	6.8×10^{-10}	1.1×10^{-15}
Instant-release case with early pinhole failure	11	Oxidizing	3.4×10^{-18}	3.4×10^{-23}

insignificant (3 orders of magnitude lower) in comparison with the total dose rate from the normal failure mode for the median-value simulation under reducing conditions (4.3×10^{-7} $Sv \cdot a^{-1}$ at 10^5 a).

Another factor, which would further mitigate the dose rate resulting from early container failure, should be taken into account. A defective container that escaped detection would likely develop only pinhole through-wall perforation upon failure, whereas the container has been modelled as if it were instantly and completely removed, or degraded, at the time of failure. To estimate the effect of a pinhole defect in reducing release, the volume to surface area ratio of the container was changed from 1.6×10^{-1} m to 7.64×10^{7} m. The latter value is the ratio of the volume of the container to the area of the container that has perforated (i.e., a hole of 0.127 mm in diameter). Tests have shown current methods can detect defects of this size or larger in a container (see Section 4.7.1). Thus, an undetected defect would be smaller than this size. Using a volume to surface area ratio of 7.64×10^{7} m decreased the maximum differential dose rate from instant release of ^{129}I from 6.8×10^{-10} to 3.4×10^{-18} $Sv \cdot a^{-1}$. The reduction in dose rate was by the same factor as the increase in the volume to surface area ratio (a factor of 10^9).

The reduction in dose rate arising from a small hole was obtained using a one-dimensional diffusion equation for transport across a series of layers. This type of model is rather inappropriate for this situation. The diffusion into the buffer from a small hole in the container would be enhanced by

the concentration spreading out into the volume surrounding the hole. This effect is not incorporated in a one-dimensional equation; therefore, the release rate from the hole would be underestimated (Chambré et al. 1987). From a study by Pescatore and Sastre (1988) it can be deduced, for non-interacting holes of radius about 5 mm, that the ratio of the mass release from a hole compared with release from the entire container surface area is about 400 times higher than would be expected on the basis of area reduction alone. Thus, for an area reduction factor of 10^9, the release should be reduced by a factor of about 10^6, still a very substantial amount. A more detailed study would be required to accurately predict this factor for the assumptions and boundary conditions relevant to this assessment.

It should be noted here that the effect of a small failure surface area on radionuclide release from containers was not taken into account in the SYVAC simulations for the case study. This is because of uncertainties regarding the size of corrosion-induced failures. Crevice-corroded areas would be expected to increase in size with time, making it difficult to estimate the surface area of failure.

The dose rate arising from ^{99}Tc warrants special consideration, since it was the only radionuclide of the seven simulated whose diffusion coefficient and capacity factor were considered to be a function of the redox conditions. The maximum dose rate from ^{99}Tc increased from 1.9×10^{-28} $Sv.a^{-1}$ in the normal median-value simulation to 1.1×10^{-15} $Sv.a^{-1}$ in the simulation with early container failure and the instant release from used fuel. This large increase is primarily a result of the increased diffusion coefficients of ^{99}Tc in the buffer and backfill under oxidizing conditions. Although the dose rate from ^{99}Tc increased, it remained small compared with the dose rate from the major contributor, ^{129}I.

The results in Table 8-2 illustrate that, in all cases, the maximum dose rates arising from release from initially defected containers is insignificant compared with dose rates calculated for the median-value simulation. This confirms that it is reasonable to ignore the effect of oxidizing conditions on release from such containers and the subsequent dose contribution in the case study.

8.5 CRITICALITY SAFETY ANALYSIS OF THE DISPOSAL VAULT

8.5.1 Introduction

A used-fuel disposal vault would contain large quantities of ^{239}Pu, uniformly distributed in the fuel at an average concentration of 2.76 g/kg UO_2 (Tait et al. 1989). This raises the question of whether or not there would be any situation where a sustained nuclear chain reaction, i.e., criticality, could occur. Although this is clearly impossible for close-packed intact bundles of used CANDU fuel (see the results of the base-case calculation below), it is necessary to examine the possibility that criticality could occur as a result of segregation of Pu from the fuel, as a result of extensive fuel dissolution, followed by accumulation of a high local concentration of Pu within or near a waste container.

A number of scenarios were examined, and some scoping calculations were performed. In addition, baseline criticality calculations were carried out to determine k_{eff}[17] for a flooded, prematurely defected container. As discussed in Chapter 4, approximately 1 in 5000 containers could be defected at the time of emplacement in the vault. Further analyses were performed to establish critical radii for Pu solutions contained within the buffer, the sand and the backfill (i.e., the minimum radius of a ^{239}Pu solution of a given concentration contained within buffer, sand and backfill that could achieve criticality).

In these calculations, varying concentrations of Pu (from 10^{-3} to 10^{-1} $g \cdot cm^{-3}$) were added to spherical volumes of saturated sand, buffer and backfill. It was conservatively assumed that all Pu present was ^{239}Pu. The radius of the sphere was varied until a critical radius (k_{eff} = 1.000) was obtained. Details of the criticality calculations are reported by McCamis (1992).

8.5.2 Base Case - Criticality Calculation for a Flooded Prematurely Defected Container

In this scenario, a container is assumed to have a through-wall defect sufficiently large to permit inflow of groundwater from the surrounding buffer material. The criticality calculation assumes that all void spaces between the glass beads are filled with water. A maximum k_{eff} value of 0.36 was obtained for 10-a-cooled fuel with a burnup of 684 $GJ \cdot kg^{-1}$ U. This result is expected since CANDU fuel cannot sustain criticality for any configuration with light water as a moderator.

8.5.3 Scenario 1 - Typical Container, with Failure Occurring at 1000 a

For the case of a container failing at any time after approximately 500 a, beyond which time the gamma field would be negligible, the redox conditions are expected to be within the UO_2/U_4O_9 stability field, as discussed in Chapter 5. The range of fractional releases predicted with the model at 10^4 a is shown in Figure 8-5. For the vast majority of cases, the fractional dissolution of the used-fuel matrix is very small, releasing a negligible quantity of Pu. The maximum fractional release at 10^4 a, of 6.8×10^{-3}, corresponds to a maximum dissolution rate of 6.8×10^{-7} a^{-1}. For a constant matrix dissolution rate and a dissolution time significantly greater than the half-life of ^{239}Pu, it can be shown that the inventory of ^{239}Pu released is at a maximum when $t = 1/\lambda$, where λ is the decay constant of ^{239}Pu. This maximum is reached at 35 000 a.

At a constant fuel-matrix dissolution rate of 6.8×10^{-7} a^{-1}, the fraction of the fuel matrix in a container that would be dissolved at 35 000 a is 0.0238 (32 kg), releasing an equivalent fraction of ^{239}Pu (89 g). If we conservatively assume that the entire quantity of released ^{239}Pu is concentrated in one region of the container within the void space surrounding the glass beads, we can compare the results obtained with the critical radii of

---

[17] k_{eff} is the effective neutron multiplication factor: to sustain criticality, a value ≥ 1 must be achieved; for $k < 1$, no self-sustaining chain reaction is possible.

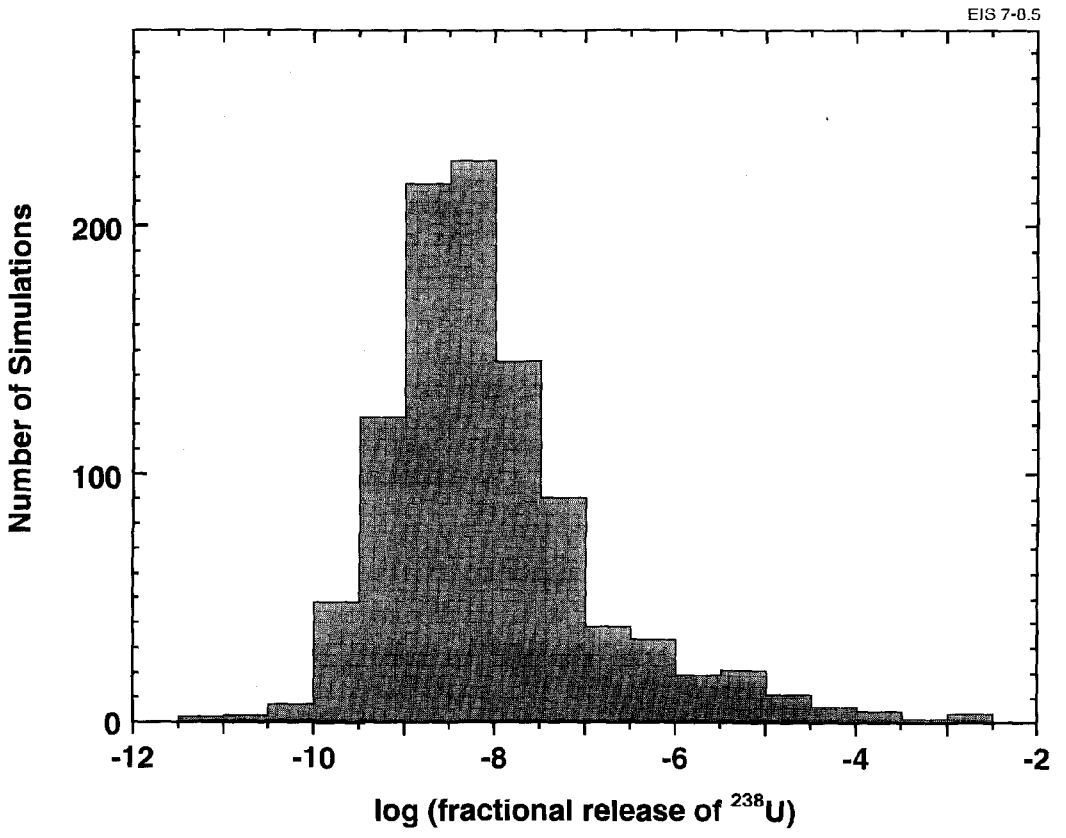

FIGURE 8-5: Distribution of Fractional Release of Uranium from Used Fuel at 10^4 a for 1000 Random Simulations, Based on the Fuel Dissolution Model Described in Chapter 5

Pu solutions in buffer, sand and backfill given in Table 8-3 (McCamis 1992). The values for sand provide a satisfactory approximation for Pu solution in a glass-bead host material. Using the highest concentration of 0.1 $g \cdot cm^{-3}$, it can be shown that a sphere of radius 21.7 cm would have to contain ~4.3 kg of ^{239}Pu to achieve criticality. This far exceeds the total Pu release of 89 g estimated for the case of dissolution of 32 kg of used fuel in one container, and also exceeds the total inventory of ^{239}Pu (3.73 kg for 10-a-cooled fuel) in one container of used fuel. For a lower concentration of 0.01 $g \cdot cm^{-3}$, the critical radius of 33.8 cm gives a ^{239}Pu mass of 1.16 kg, again greatly exceeding the quantity released from one container of used fuel. It is emphasized, in addition, that these calculations are conservative in that no other material except ^{239}Pu and glass beads are assumed to remain. The remnants of fuel sheath, bundle support tubes, fission products and undissolved uranium that would be present would further attenuate neutrons and lead to even higher concentrations of ^{239}Pu being required to achieve criticality.

It is apparent, therefore, that criticality could not occur in this scenario.

TABLE 8-3

CRITICAL RADIUS (in cm) OF SPHERICAL Pu SOLUTION (McCamis 1992)

Host Material	Plutonium Concentration ($g \cdot cm^{-3}$)		
	0.1	0.01	0.001
Buffer	19.048	31.771	(k_{eff}^{∞} = 0.4101 ± 0.0010)
Sand	21.718	33.830	(k_{eff}^{∞} = 0.4960 ± 0.0011)
Backfill	25.367	43.928	(k_{eff}^{∞} = 0.3916 ± 0.0011)

8.5.4 Scenario 2 - Prematurely Defected Container

For this scenario, an analysis was performed to calculate the extent of dissolution of the fuel, on the basis of dissolution rates measured for used fuel, and subsequent release of Pu as a function of time. Experimentally determined dissolution rates of used fuel were used for the period up to 500 a because the high gamma fields in a prematurely defected container would lead to oxidizing conditions; thus, the model presented in Chapter 5 would not be appropriate for such an application. For longer times, the model presented in Chapter 5 was used. The total amount of Pu released during various times was compared with the amount required to form a critical mass in sand, glass beads and buffer material.

During the first 500 a, when the gamma field is sufficiently high to keep the redox conditions above the U_4O_9/U_3O_7 boundary, the dissolution rate would be relatively high. The dissolution rate of the fuel for the first 500 a can be estimated from the results of used-fuel dissolution studies at 100°C and studies of UO_2 dissolution in a γ-radiation field. Johnson et al. (1988) reported a fractional dissolution rate of $<10^{-8}$ d^{-1} for used CANDU fuel in deaerated saline groundwater at 100°C. A similar rate of 10^{-8} $g \cdot cm^{-2} \cdot d^{-1}$ is estimated by Shoesmith and Sunder (1991) for dissolution of UO_2 in deaerated water in a gamma field of ~50 $Gy \cdot h^{-1}$. If one uses an estimated surface area for used fuel of 2 $cm^2 \cdot g^{-1}$ (Johnson 1982), these rates result in dissolution of 2.5 to 6 kg of the used-fuel matrix for one container in 500 a. This would lead to release of a maximum of 17 g of ^{239}Pu. Again, this is an insignificant fraction of the quantity of ^{239}Pu required to achieve criticality. For the subsequent period up to 35 000 a, the release is estimated to be the same as in Scenario 1. The total quantity released is therefore so small that criticality is not possible.

8.5.5 Scenario 3 - Pu Accumulation Resulting from the Failure of Many Containers

The possibility that Pu diffusing from many containers could accumulate in buffer or backfill was examined by considering the amount of ^{239}Pu released in conjunction with Pu diffusion rates through the buffer material. Diffusion coefficients of Pu in buffer material are extremely low. Using the median diffusion coefficient value in the vault model, we estimated the quantity of Pu accumulated in the buffer material in sector 1 (see Figure 8-6). For the 27 468 containers in this vault sector, the amount of ^{239}Pu accumulated in the buffer is ~0.6×10^{-3} mol (1.5 g). The quantity around one container is therefore ~5×10^{-6} g. Even if one assumes an optimum spherical configuration, and accumulations from many containers in one location, the small amount of Pu in the buffer illustrates that criticality is not possible. The combination of low diffusion coefficients and the decay of ^{239}Pu would prevent accumulations in more remote locations of the rock and backfill.

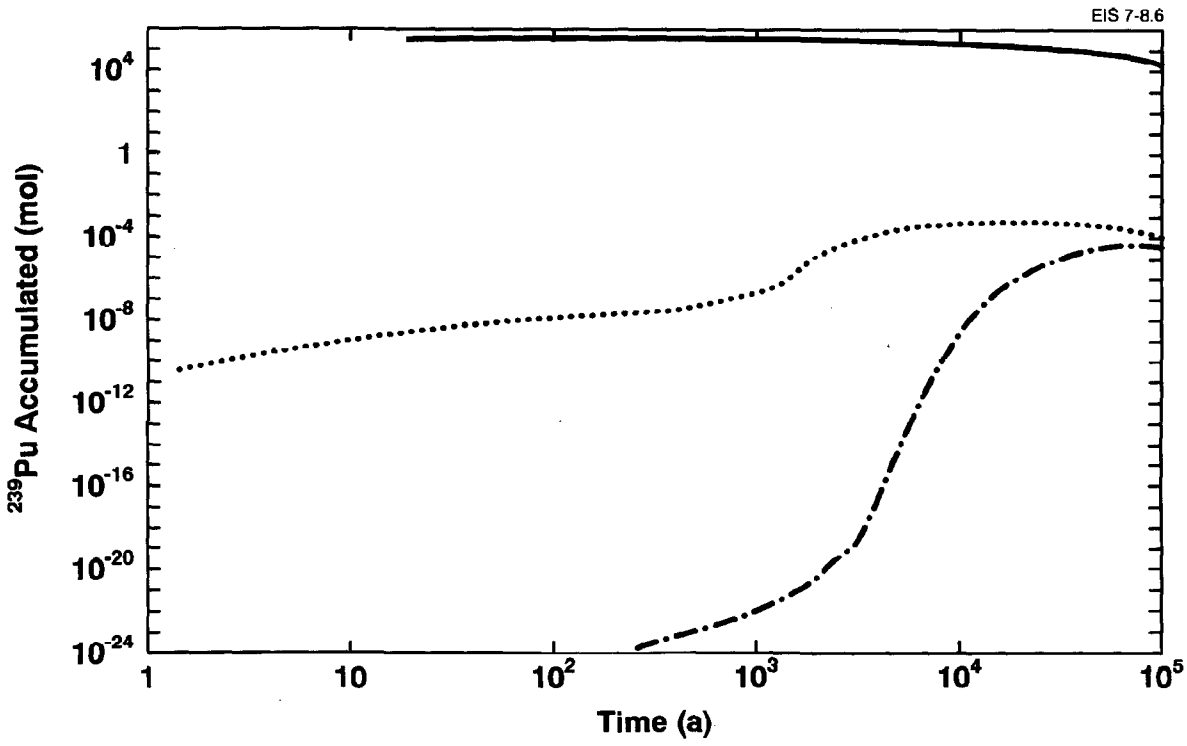

FIGURE 8-6: Pu Accumulated in Buffer and Backfill for Dissolution of Fuel in the 27 468 Containers in Vault Sector 1
Amount of ^{239}Pu in Containers (——)
Amount of ^{239}Pu in Buffer (····)
Amount of ^{239}Pu in Backfill (-·-·-)

8.6 IMPACT OF REVISED DIFFUSION DATA ON DOSE ESTIMATES

Recent experimental evidence indicates that D values are approximately the same for all radionuclides in clay/water systems at a given clay density, temperature and pore-solution composition (Oscarson et al. 1992, Cho et al. 1993, Oscarson and Hume 1993b). For example, at a clay density of 1.2 $Mg \cdot m^{-3}$ (the approximate density of the clay component of both the buffer and backfill materials) and 25°C, D values range from about 3×10^{-4} $m^2 \cdot a^{-1}$ to 2×10^{-3} $m^2 \cdot a^{-1}$. This important finding is consistent with Equation (3.8), which indicates that D values are not radionuclide-dependent. Moreover, as the temperature increases from 25 to 100°C, D increases by about a factor of three to four (Oscarson et al. 1992); this increase is attributed to a decrease in the viscosity of the pore solution with increasing temperature. Also, as the salinity of the pore solution increases, the diffusion coefficient is expected to increase (Muurinen et al. 1989).

Hence, to account for the effects of temperature, pore-water salinity and possible slight variations in clay density, the revised D values for ^{129}I, ^{14}C and ^{99}Tc in both the buffer and backfill were given a range from 1.3×10^{-3} $m^2 \cdot a^{-1}$ to 1.3×10^{-2} $m^2 \cdot a^{-1}$ (Tables 8-5 and 8-7). D_a values for these radionuclides are available from the literature (Oscarson et al. 1992, Oscarson and Hume 1993b, Sawatsky and Oscarson 1991); reasonable ranges of D_a values were chosen to again account for the influence of temperature, pore-water salinity and clay density. The revised range of r values given in Tables 8-9 and 8-11 were obtained from the ratio of D/D_a (Equation (3.10)). The data for diffusion coefficients and capacity factors used in the case study are given in Tables 8-4, 8-6, 8-8 and 8-10 for comparison. One thousand random simulations of the three nuclides determined to have the highest contributions to dose, ^{129}I, ^{14}C and ^{99}Tc, were done with the revised diffusion data. The mean of the maximum doses occurring up to 10^5 a with the revised data was compared with the mean of the maximum doses up to 10^5 a for 1000 random simulations with the diffusion data in the case study. The sampling of all parameters, except those revised, was identical in the two sets of 1000 simulations. Thus, differences in the mean doses are attributable solely to the effect of the revised parameter values. The results of the comparison are shown in Table 8-12.

The increases in the mean-maximum dose rates are small for ^{14}C and ^{129}I (a factor of two for ^{129}I and of four for ^{14}C). The dose rate for ^{99}Tc with the revised data is considerably larger than for the original data, but still insignificant. The increase in the mean-maximum dose for ^{99}Tc can be attributed to the decrease in the geometric mean of the revised capacity factor in the backfill.

In general, the revised diffusion data in the buffer and backfill do not have a large effect on maximum dose estimates.

TABLE 8-4

ORIGINAL DIFFUSION DATA FOR BUFFER

Species	Characteristics of Correlated Lognormal Distribution					
	Geometric Mean ($m^2 \cdot a^{-1}$)	Geometric Standard Deviation	Lower Bound ($m^2 \cdot a^{-1}$)	Upper Bound ($m^2 \cdot a^{-1}$)	Correlated to*	α**
Tc	1.1×10^{-5}	3.2	3.6×10^{-7}	3.6×10^{-4}	DFBACT	1.0
I and C	1.8×10^{-5}	2.7	9.0×10^{-7}	3.6×10^{-4}	DFBANI	1.0

* Dummy correlation parameters used to correlate D values in the same radionuclide group (see Section 3.5.3) and to correlate D and r values
** Correlation coefficient

TABLE 8-5

REVISED DIFFUSION DATA FOR BUFFER

Species	Characteristics of Correlated Lognormal Distribution					
	Geometric Mean ($m^2 \cdot a^{-1}$)	Geometric Standard Deviation	Lower Bound ($m^2 \cdot a^{-1}$)	Upper Bound ($m^2 \cdot a^{-1}$)	Correlated to*	α**
Tc	4.0×10^{-3}	3.2	1.3×10^{-3}	1.3×10^{-2}	DFBACT	0.90
I and C	4.0×10^{-3}	3.2	1.3×10^{-3}	1.3×10^{-2}	DFBANI	0.90

* Dummy correlation parameters used to correlate D values in the same radionuclide group (see Section 3.5.3) and to correlate D and r values
** Correlation coefficient

TABLE 8-6

ORIGINAL DIFFUSION DATA FOR BACKFILL

Species	Characteristics for Correlated Normal Distribution					
	Mean ($m^2 \cdot a^{-1}$)	Standard Deviation ($m^2 \cdot a^{-1}$)	Lower Bound ($m^2 \cdot a^{-1}$)	Upper Bound ($m^2 \cdot a^{-1}$)	Correlated to*	α**
Tc	2.3×10^{-3}	1.5×10^{-4}	1.8×10^{-3}	2.7×10^{-3}	DFKACT	1.0
I and C	2.3×10^{-3}	1.5×10^{-4}	1.8×10^{-3}	2.7×10^{-3}	DFKANI	1.0

* Dummy correlation parameters used to correlate D values in the same radionuclide group (see Section 3.5.3) and to correlate D and r values
** Correlation coefficient

TABLE 8-7

REVISED DIFFUSION DATA FOR BACKFILL

Species	Characteristics of Correlated Lognormal Distribution					
	Geometric Mean ($m^2 \cdot a^{-1}$)	Geometric Standard Deviation	Lower Bound ($m^2 \cdot a^{-1}$)	Upper Bound ($m^2 \cdot a^{-1}$)	Correlated to*	α**
Tc	4.0×10^{-3}	3.2	1.3×10^{-3}	1.3×10^{-2}	DFKACT	0.90
I and C	4.0×10^{-3}	3.2	1.3×10^{-3}	1.3×10^{-2}	DFKANI	0.90

* Dummy correlation parameters used to correlate D values in the same radionuclide group (see Section 3.5.3) and to correlate D and r values
** Correlation coefficient

TABLE 8-8

ORIGINAL CAPACITY FACTORS FOR BUFFER

Species	Characteristics of Correlated Lognormal Distribution					
	Geometric Mean	Geometric Standard Deviation	Lower Bound	Upper Bound	Correlated to*	α^{**}
Tc	53	6.8	4.2×10^{-3}	1.7×10^{4}	DFBACT	1.0
I and C	6.3×10^{-3}	4.0	1.0×10^{-4}	0.40	DFBANI	1.0

* Dummy correlation parameters used to correlate D values in the same radionuclide group (see Section 3.5.3) and to correlate D and r values
** Correlation coefficient

TABLE 8-9

REVISED CAPACITY FACTORS FOR BUFFER

Species	Characteristics of Correlated Lognormal Distribution					
	Geometric Mean	Geometric Standard Deviation	Lower Bound	Upper Bound	Correlated to*	α^{**}
Tc	4.0×10^{2}	1.0×10^{2}	4.0	4.0×10^{4}	-	-
I and C	4.0×10^{-1}	1.0×10^{1}	4.0×10^{-2}	4.0	DFBANI	0.90

* Dummy correlation parameters used to correlate D values in the same radionuclide group (see Section 3.5.3) and to correlate D and r values
** Correlation coefficient

TABLE 8-10

ORIGINAL CAPACITY FACTORS FOR BACKFILL

Species	Characteristics of Normal Distribution					
	Mean	Standard Deviation	Lower Bound	Upper Bound	Correlated to*	α**
I and C	0.25	0.017	0.20	0.30	DFKTRA	1.0
	Characteristics of Correlated Lognormal Distribution					
	Geometric Mean	Geometric Standard Deviation	Lower Bound	Upper Bound	Correlated to*	α**
Tc	2.0×10^3	2.2	31	2.0×10^4	DFKACT	1.0

* Dummy correlation parameters used to correlate D values in the same radionuclide group (see Section 3.5.3) and to correlate D and r values
** Correlation coefficient

TABLE 8-11

REVISED CAPACITY FACTORS FOR BACKFILL

Species	Characteristics of Lognormal Distribution					
	Geometric Mean	Standard Deviation	Lower Bound	Upper Bound	Correlated to*	α**
Tc	4.0×10^2	1.0×10^2	4.0	4.0×10^4	-	-
I and C	4.0×10^{-1}	1.0×10^1	4.0×10^{-2}	4.0	DFKANI	0.90

* Dummy correlation parameters used to correlate D values in the same radionuclide group (see Section 3.5.3) and to correlate D and r values
** Correlation coefficient

TABLE 8-12

COMPARISON OF MEAN OF MAXIMUM DOSES UP TO 10^5 a
WITH ORIGINAL AND REVISED DATA FOR 1000 RANDOM SIMULATIONS

Radionuclide	Mean Dose with Original Data ($Sv \cdot a^{-1}$)	Mean Dose with Revised Data ($Sv \cdot a^{-1}$)
^{14}C	3.5×10^{-9}	1.2×10^{-8}
^{129}I	1.2×10^{-6}	2.8×10^{-6}
^{99}Tc	1.2×10^{-15}	1.6×10^{-11}

9. SUMMARY AND CONCLUSIONS

9.1 INTRODUCTION

This report presents conceptual and mathematical models for engineered barriers for evaluation of the performance of a disposal vault for used CANDU fuel located in plutonic rock of the Canadian Shield. These models are integrated into the vault model, which is coupled to geosphere and biosphere models in the computer code SYVAC, to perform postclosure safety assessment of the conceptual disposal system for periods up to 10^5 a. A probabilistic model is used to permit uncertainty and variability in the various processes to be taken into account.

The reference disposal system for this study is a vault located at a depth of 500 m in rock with the geological characteristics of the Lac du Bonnet batholith, a large plutonic rock body of the Canadian Shield located in southeastern Manitoba. Used-fuel bundles in titanium containers would be emplaced in boreholes drilled in the floor of disposal rooms, with clay-based sealing materials surrounding the containers and filling disposal rooms and shafts. The reference vault would contain a total of 161 730 Mg (U) of used fuel in 118 860 containers.

9.2 THE DEVELOPMENT OF THE VAULT MODEL

The models of the processes of container corrosion, used-fuel dissolution and contaminant transport in the reference vault have been developed over many years as a result of synthesis of research results from the Canadian Nuclear Fuel Waste Management Program and other published studies. The process of selecting an appropriate model and the associated parameter distributions involved a combination of expert judgement and the application of a number of simplifying assumptions. Supplementary analyses have been performed to evaluate the impact of some of these simplifying assumptions. Where information on important processes was limited, conservative

assumptions were incorporated into the models. As a result, the vault model tends to overpredict the consequences of disposal of used fuel, and results should not be considered a realistic prediction of the releases from a disposal vault.

The model that calculates lifetimes of the Grade-2 titanium containers predicts that 0.23% of containers would fail by 10^3 a, with >97% failing in the period between 1200 a and 7000 a. The dominant mode of failure is crevice corrosion, as a consequence of the conservative assumptions that this process initiates on all containers immediately upon emplacement, and that propagation continues at the temperature-dependent rate until failure occurs.

The release of radionuclides from used fuel is expected to be dominated by a small group of radionuclides that are leached from the fuel-sheath gap and fuel grain boundaries. Radionuclide releases arising from dissolution of the used-fuel matrix would be negligible because of the low solubility of uranium, the low rate of matrix dissolution under reducing conditions, and the essentially static groundwater flow conditions expected in the disposal vault.

The mass transport of radionuclides in the vault would occur by diffusion, because of the low hydraulic conductivities of clay-based buffer and backfill materials and the low groundwater velocities in the surrounding rock.

9.3 VAULT MODEL RESULTS

The radiation doses calculated with SYVAC for the reference disposal system are discussed by Goodwin et al. (1994). The results for a single simulation with the system model, where all parameters having frequency distributions are given their median values, show that the maximum dose rate up to 10^5 a of 4.3×10^{-7} Sv·a^{-1}, which occurs at 10^5 a, arises from the radionuclide ^{129}I. This dose rate, as well as the total dose rate for all radionuclides, is one hundred times lower than the AECB regulatory criterion of 5×10^{-5} Sv·a^{-1} established for periods up to 10^4 a.

The assessment results are considered specific to the particular case analyzed, and care should be taken in drawing general conclusions regarding the safety of disposal systems with different engineered barrier designs or geological settings. Nonetheless, some broader inferences can be drawn regarding the performance of this reference design in other settings in the Canadian Shield. If similar mass transport boundary conditions were encountered at the vault/geosphere interface, similar radionuclide releases from used fuel could be expected for significantly more saline groundwaters (up to 2.5 mol·L^{-1} Cl$^-$ or an ionic strength of ~3.4 mol·L^{-1}). Grade-2 titanium would not be recommended under such conditions; the use of Grade-12 titanium would be more appropriate. These conclusions support the view that comparable results for engineered barrier performance would be expected for depths up to 1000 m at many locations in the Canadian Shield.

9.4 CONCLUSIONS

Appropriate models to describe the performance of engineered barriers in a disposal vault for used CANDU fuel have been developed, and a methodology to perform safety analysis of a disposal vault has been demonstrated. The vault model has been peer-reviewed and extensively tested, and the model results give confidence that used fuel can be disposed of safely.

ACKNOWLEDGEMENTS

The authors would like to express their appreciation to the many AECL and Ontario Hydro staff who contributed to this document through their research studies over a period of thirteen years. In addition, we thank M.J. Apted of Intera, P. King, members of the Engineered Barriers Subcommittee of the Technical Advisory Committee, and members of several CANDU Owners Group (COG) Working Parties (J.M. Boag, D. Gratton, J. Freire-Canosa, S. Russell, T. Kempe, T. Klym, and K. Tsui) for their critical review of earlier drafts of this report. Finally, many thanks to E.D. Wright and M.E. McDowall for editorial and secretarial assistance and to Dori Kufflick and Alicia Clarke for assistance with the figures.

The Canadian Nuclear Fuel Waste Management Program is funded jointly by AECL and Ontario Hydro under the auspices of the CANDU Owners Group.

REFERENCES

Abry, D.R.M., R.G.F. Abry, K.V. Ticknor and T.T. Vandergraaf. 1982. Procedure to determine sorption coefficients of radionuclides on rock coupons under static conditions. Atomic Energy of Canada Limited Technical Record, TR-189.*

AECB (Atomic Energy Control Board). 1987. Regulatory policy statement. Regulatory objectives, requirements and guidelines for the disposal of radioactive wastes - long-term aspects. Atomic Energy Control Board Regulatory Document R-104, Ottawa, 1987 June 5.

AECL (Atomic Energy of Canada Limited). 1990. Geological and Environmental Science Division Quality Assurance Manual. Atomic Energy of Canada Limited Quality Assurance Document, 001.001, Revision 0. Unpublished report available from Disposal Technology Division, AECL Research, Whiteshell Laboratories, Pinawa, Manitoba ROE 1LO.

AECL (Atomic Energy of Canada Limited). 1994a. Environmental impact statement on the concept for disposal of Canada's nuclear fuel waste. Atomic Energy of Canada Limited Report, AECL-10711, COG-93-1. Available in French and English.

AECL (Atomic Energy of Canada Limited). 1994b. Summary of the environmental impact statement on the concept for disposal of Canada's nuclear fuel waste. Atomic Energy of Canada Limited Report, AECL-10721, COG-93-11. Available in French and English.

Ahn, J., P.L. Chambré and T.H. Pigford. 1986. Radionuclide dispersion from multiple patch sources into a rock fracture. Lawrence Berkeley Laboratory Report, LBL-23425, UC-70.

Allard, B., U. Olofsson, B. Torstenfelt, H. Kipatsi and K. Andersson. 1982. Sorption of actinides in well-defined oxidation states on geologic media. Materials Research Society Symposium Proceedings 11 (Scientific Basis for Nuclear Waste Management V), 775-782.

Altaner, S.P., J. Hover, G. Whitney and J.L. Aronson. 1984. Model for K-bentonite formation: Evidence from zoned K-bentonites in the disturbed belt, Montana. Geology 12, 412-415.

Anderson, D.M. (compiler). 1983. Smectite alteration. Proceedings of a Colloquium, Buffalo, NY, 1982, Swedish Nuclear Fuel Supply Co. Report, SKBF-KBS-TR-83-03.

Anderson, D.M. (compiler). 1984. Smectite alteration. Proceedings of a Workshop, Washington, DC, 1983, Swedish Nuclear Fuel and Waste Management Co. Report, SKB-KBS-TR-84-11.

Anderson, D.M., J.C. Fountain and C. Waddell. 1982. Chemical stability of clays employed as buffer materials in the storage of nuclear waste materials. In Abstract Volume, Annual Meeting, Circum-Pacific Clay Minerals Society, Hilo, HI, 19, 39.

Andersson, G., A. Rasmuson and I. Neretnieks. 1982. Migration model for the near field. Final report. Swedish Nuclear Fuel Supply Co. Report, SKBF-KBS-TR-82-24.

Andres, T.H. In preparation. SYVAC3 Manual. Atomic Energy of Canada Limited Report, AECL-10982, COG-93-422.

Andrews, R.W., D.W. LaFleur and S.B. Pahwa. 1986. Resaturation of backfilled tunnels in granite. National Cooperative for the Storage of Radioactive Waste (Baden) Report, NAGRA-NTB-86-27.

Apted, M.J., A.M. Liebetrau and D.W. Engel. 1987. Spent fuel as a waste form: Analysis with AREST performance assessment code. In Waste Management '87, Proceedings of the Symposium on Waste Management, Tucson, AZ, 1987, Volume 2, 545-554.

Apted, M.J., D.W. Engel, N.C. Garisto and D.M. LeNeveu. 1989a. Source-term comparison using the AREST and SYVAC vault models: Effects of decay-chain in-growth and precipitation. Materials Research Society Symposium Proceedings 127 (Scientific Basis for Nuclear Waste Management XII), 597-604.

Apted, M.J., A.M. Liebetrau and D.W. Engel. 1989b. The analytical repository source-term (AREST) model: Analysis of spent fuel as a nuclear waste form. Pacific Northwest Laboratory Report, PNL-6347 UC-70.

Aronson, S., R.B. Roof and J. Belle. 1957. Kinetic study of the oxidation of uranium dioxide. Journal of Chemical Physics 27, 137-144.

Atkinson, A., D.J. Goult and J.A. Hearne. 1986. An assessment of the long-term durability of concrete in radioactive waste repositories. Materials Research Society Symposia Proceedings 50 (Scientific Basis for Nuclear Waste Management IX), 239-246.

Baes, C.F. Jr. and R.E. Mesmer. 1976. The Hydrolysis of Cations. Wiley Interscience, New York.

Bailey, M.G., L.H. Johnson and D.W. Shoesmith. 1985. The effects of alpha-radiolysis of water on the corrosion of UO_2. Corrosion Science 25, 233-238. Also Atomic Energy of Canada Limited Reprint, AECL-8430.

Bailey, M.G., B.M. Ikeda, M.J. Quinn and D.W. Shoesmith. In preparation. Crevice corrosion behaviour of Grades-2 and -12 titanium in hot aqueous chloride solutions. Atomic Energy of Canada Limited Report, AECL-10971.

Baumgartner, P., T.V. Tran and R. Burger. In preparation. Sensitivity analyses for the thermal response in a nuclear fuel waste disposal vault. Atomic Energy of Canada Limited Technical Record, TR-621.

Beck, T.R. 1973. Electrochemistry of freshly-generated titanium surfaces - I. Scraped-rotating-disk experiments. Electrochimica Acta 18, 807-814.

Berry, J.A. and K.A. Bond. 1990. Surface diffusion of sorbed radionuclides. U.K. Department of the Environment Report, DOE/HMIP/PR/90/076.

Bird, R.B., W.E. Stewart and E.N. Lightfoot. 1960. Transport Phenomena. John Wiley and Sons, New York.

Blahnik, D.E., U.P. Jenquin and R.J. Guenther. 1988. LWR spent-fuel radiochemical measurements and comparison with ORIGEN2 predictions. Transactions of the American Nuclear Society 57, 44-46.

Blesa, M.A. and E. Matijevic. 1989. Phase transformations of iron oxides, oxohydroxides and hydrous oxides in aqueous media. Advances in Colloid and Interface Science 29, 173-221.

Bohn, H.L., B.L. McNeal and G.A. O'Connor. 1985. Soil Chemistry. 2nd edition, John Wiley & Sons Inc., New York.

Bond, A.M. and G.T. Hefter. 1980. Critical survey of stability constants and related thermodynamic data of fluoride complexes in aqueous solution. Pergamon Press, Oxford.

Bonne, A.A. and R.H. Heremans. 1982. Investigation of the Boom clay, a candidate host rock for final disposal of high-level solid waste. Developments in Sedimentology 35, 799-818.

Boyer, R.R. and W.F. Spurr. 1978. Characteristics of sustained-load cracking and hydrogen effects in Ti-6Al-4V. Metallurgical Transactions 9A, 23-29.

Bradley, D.J., D.G. Coles, F.N. Hodges, G.L. McVay and R.E. Westerman. 1983. Nuclear waste package materials testing report: Basaltic and tuffaceous environments. Pacific Northwest Laboratory Report, PNL-4452.

Braithwaite, J.W. and M.A. Molecke. 1980. Nuclear waste canister corrosion studies pertinent to geologic isolation. Nuclear and Chemical Waste Management 1, 37-50.

Brierley, C.L. 1982. Microbiological mining. Scientific American 247, 44-53.

Brusewitz, A.M. 1986. Chemical and physical properties of paleozoic potassium bentonites from Kinnekulle, Sweden. Clays and Clay Minerals 34, 442-454.

Carslaw, H.S. and J.C. Jaeger. 1959. Conduction of Heat in Solids. 2nd edition, Clarendon Press, Oxford.

Chambré, P.L., W.L. Lee, C.L. Kim and T.H. Pigford. 1987. Transient and steady-state radionuclide transport through penetrations in nuclear waste containers. Materials Research Society Symposium Proceedings 84 (Scientific Basis for Nuclear Waste Management X), 131-140.

Chan, A. and A. Advani. 1991. Verification of vault response function solution. Ontario Hydro Report, 91-26-K, available from Ontario Hydro, 700 University Avenue, Toronto, Ontario, M5G 1X6.

Chan, H.T. and H.S. Radhakrishna. 1986. Hydraulic compression of shaft backfill at the backfill/rock interface. In Canadian Nuclear Society 2nd International Conference on Radioactive Waste Management, Conference Proceedings, Winnipeg, Manitoba, 1986, 228-235.

Chan, T. 1988. An overview of groundwater flow and radionuclide transport modelling in the Canadian Nuclear Fuel Waste Management Program. In Proceedings of the Conference on Geostatistical Sensitivity, and Uncertainty Methods for Ground-Water Flow and Radionuclide Transport Modeling, San Francisco, CA, 1987, 39-61. Also CONF-870971.

Chan, T. and N.W. Scheier. 1987. Finite-element simulation of groundwater flow and heat and radionuclide transport in a plutonic rock mass. In Proceedings of the 6th International Congress on Rock Mechanics, Montreal, Quebec, 1987, 41-46.

Chan, T. and F. Stanchell. 1990. A numerical study of some effects of nuclear fuel waste vault construction and closure on evolution of groundwater flow paths in the geosphere. In High-Level Radioactive Waste Management, Proceedings of the International Topical Meeting, Las Vegas, NV, 1989, Volume 1, 525-536.

Chan, T., N.W. Scheier and J.A. Keith Reid. 1986. Finite-element thermo-hydrogeological modeling for Canadian nuclear fuel waste management. In Canadian Nuclear Society 2nd International Conference on Radioactive Waste Management, Conference Proceedings, Winnipeg, Manitoba, 1986, 653-660.

Chan, T., J.A.K. Reid and V. Guvanasen. 1987. Numerical modelling of coupled fluid, heat and solute transport in deformable fractured rock. In Coupled Processes Associated with Nuclear Waste Repositories, Proceedings of an International Symposium, Berkeley, CA, 1985, 605-625.

Chesnutt, J.C. and N.E. Paton. 1980. Hold time effects on fatigue crack propagation in Ti-6Al and Ti-6Al-4V. In Titanium '80, Science and Technology, Proceedings of the Fourth International Conference on Titanium, Kyoto, Japan, 1980, 1855-1864.

Cheung, S.C.H. 1989. Methods to measure apparent diffusion coefficients in compacted bentonite clays and data interpretation. Canadian Journal of Civil Engineering 16, 434-443.

Cheung, S.C.H. 1990. A new interpretation of measured ionic diffusion coefficients in compacted bentonite-based materials. Engineering Geology 28, 369-378. Also Atomic Energy of Canada Limited Reprint, AECL-10136.

Cheung, S.C.H. and M.N. Gray. 1989. Mechanism of ionic diffusion in dense bentonite. Materials Research Society Symposium Proceedings 127 (Scientific Basis for Nuclear Waste Management XII), 677-681. Also Atomic Energy of Canada Limited Reprint, AECL-9809.

Cheung, S.C.H. and M.N. Gray. 1990. Coupled flow of heat and mass in clay materials and its significance to barrier performance. In Ground Water and Engineering Materials, Proceedings of the Annual Conference and 1st Biennial Environmental Specialty Conference of the Canadian Society of Civil Engineering, Hamilton, Ontario, 1990, Supplementary Volume, 18-27.

Cho, W.J., D.W. Oscarson, M.N. Gray and S.C.H. Cheung. 1993. Influence of diffusant concentration on diffusion coefficients in clay. Radiochimica Acta 60, 159-163.

Christensen, H. and E. Bjergbakke. 1982. Radiolysis of groundwater from HLW stored in copper canisters. Swedish Nuclear Fuel Supply Co. Report, SKBF-KBS-TR-82-02.

Christensen, H. and E. Bjergbakke. 1984. Radiolysis of concrete. Swedish Nuclear Fuel Supply Co. Report, SKBF-KBS-TR-84-02.

Clarke, C.F., D. Hardie and P. McKay. 1986. The cracking of titanium in hot aqueous sodium chloride solutions. Corrosion Science 26, 425-440. Also Atomic Energy of Canada Limited Reprint, AECL-9151.

Clarke, C.F., B.M. Ikeda and D. Hardie. 1989. Effect of crevice corrosion on hydrogen embrittlement of titanium. In Environment-Induced Cracking of Metals, Proceedings of International Corrosion Conference, NACE-10, 419-424.

Clarke, C.F., D. Hardie and B.M. Ikeda. 1992. Assessment of materials for containment of nuclear fuel waste: Environment-sensitive fracture of titanium. Atomic Energy of Canada Limited Report, AECL-10477, COG-92-162.

Cook, A.J. 1988. A desk study of surface diffusion and mass transport in clay. British Geological Survey Technical Report, WE/88/34.

Coons, W.E. (editor). 1987. State-of-the-art report on potentially useful materials for sealing nuclear waste repositories. Swedish Nuclear Fuel and Waste Management Co. Stripa Project Report, STRIPA-TR-87-12.

Cornell, R.M., R. Giovanoli and W. Schneider. 1989. Review of the hydrolysis of iron(III) and the crystallization of amorphous iron(III) hydroxide hydrate. Journal of Chemical Technology and Biotechnology 46, 115-134.

Cotton, F.A. and G. Wilkinson. 1972. Advanced Inorganic Chemistry: A Comprehensive Text. 3rd edition, Interscience, New York.

Couture, R.A. 1985. Steam rapidly reduces the swelling capacity of bentonite. Nature 318, 50-52.

Covington, L.C. 1979. The influence of surface condition and environment on the hydriding of titanium. Corrosion 35, 378-382.

Covington, L.C. and R.W. Schutz. 1981. Effects of iron on the corrosion resistance of titanium. In Industrial Applications of Titanium and Zirconium. E.W. Kleefisch, editor, ASTM Special Technical Publication 728, 613-680.

Cramer, Jan J. 1986. A natural analog for a fuel waste disposal vault. In Canadian Nuclear Society 2nd International Conference on Radioactive Waste Management, Conference Proceedings, Winnipeg, Manitoba, 1986, 697-702.

Cramer, J.J. 1994. Natural analogs in support of the Canadian concept for nuclear fuel waste disposal. Atomic Energy of Canada Limited Report, AECL-10291, COG-92-258.

Cramer, J.J. and H.W. Nesbitt. In preparation. Hydrogeochemistry of the Cigar Lake uranium deposit: Hydrologic and isotopic constraints. For submission to Geochimica et Cosmochimica Acta.

Cramer, J.J. and J.A.T. Smellie. 1993. The AECL/SKB Cigar Lake analog study: Some implications for performance assessment. In Proceedings of the Fifth Meeting of the CEC Natural Analog Working Group, Toledo, Spain, 1993, Commission of the European Communities Report, EUR 15176 EN.

Cramer, J.J., P. Vilks and J.P.A. Larocque. 1987. Near-field analog features from the Cigar Lake uranium deposit. In Natural Analogues in Radioactive Waste Disposal, Proceedings of a Symposium, Brussels, Belgium, 1987, 59-72, EUR 11037 EN.

Cranwell, R.M., J.E. Campbell, J.C. Helton, R.L. Iman, D.E. Longsine, N.R. Oritz, G.E. Runkle and M.J. Shortencarier. 1987. Risk methodology for geologic disposal of radioactive waste: Final report. U.S. Nuclear Regulatory Commission Report, NUREG/CR-2452.

Crosthwaite, J.L. 1992a. Re: SYVAC parameter THIKCT, effective container thickness (FWTB-89-183). In Unpublished Documents Cited in the EIS and Primary References, Atomic Energy of Canada Limited Technical Record, TR-567,* COG-92-27.

Crosthwaite, J.L. 1992b. Re: SYVAC parameter THIKCT, further considerations (FWTB-89-196). In Unpublished Documents Cited in the EIS and Primary References, Atomic Energy of Canada Limited Technical Record, TR-567,* COG-92-27.

Crosthwaite, J.L. In preparation. The performance, assessment and ranking of container design options for the Canadian Nuclear Fuel Waste Management Program. Atomic Energy of Canada Limited Technical Record, TR-500,* COG-93-410.

Curtis, D.B. 1985. The chemical coherence of natural spent fuel at the Oklo natural reactors. Swedish Nuclear Fuel and Waste Management Co. Report, SKB-TR-85-04.

Curtis, D., T. Benjamin, A. Gancarz, R. Loss, K. Rosman, J. DeLaeter, J.E. Delmore and W.J. Maeck. 1989. Fission product retention in the Oklo natural fission reactors. Applied Geochemistry 4, 49-62.

Davis, P.A., R. Zach, M.E. Stephens, B.D. Amiro, G.A. Bird, J.A.K. Reid, M.I. Sheppard, S.C. Sheppard, and M. Stephenson. 1993. The disposal of Canada's nuclear fuel waste: the biosphere model, BIOTRAC, for postclosure assessment. Atomic Energy of Canada Limited Report, AECL-10720, COG-93-10.

Davison, C.C., A. Brown, R.A. Everitt, M. Gascoyne, E.T. Kozak, G.S. Lodha, C.D. Martin, N.M. Soonawala, D.R. Stevenson, G.A. Thorne and S.H. Whitaker. 1994a. The disposal of Canada's nuclear fuel waste: site screening and site evaluation technology. Atomic Energy of Canada Limited Report, AECL-10713, COG-93-3.

Davison, C.C., T. Chan, A. Brown, M. Gascoyne, D.C. Kamineni, G.S. Lodha, T.W. Melnyk, B.W. Nakka, P.A. O'Connor, D.U. Ophori, N.W. Scheier, N.M. Soonawala, F.W. Stanchell, D.R.Stevenson, G.A. Thorne, S.H. Whitaker, T.T. Vandergraaf and P. Vilks. 1994b. The disposal of Canada's nuclear fuel waste: the geosphere model for postclosure assessment. Atomic Energy of Canada Limited Report, AECL-10719, COG-93-9.

Davison, W. and G. Seed. 1983. The kinetics of the oxidation of ferrous iron in synthetic and natural waters. Geochimica et Cosmochimica Acta 47, 67-79.

De Regge, P., P. Henrion, M. Monsecour, M. Put, A. Cremers and A. Maes. 1988. Facts and features of radionuclide migration in Boom clay. Radioactive Waste Management and the Nuclear Fuel Cycle 10, 1-20.

Dixon, D.A., M.N. Gray and A.W. Thomas. 1985. A study of the compaction properties of potential clay-sand buffer mixtures for use in nuclear fuel waste disposal. Engineering Geology 21, 247-255. Also Atomic Energy of Canada Limited Reprint, AECL-8684.

Dixon, D.A., M.N. Gray, P. Baumgartner and G.L. Rigby. 1986. Pressures acting on waste containers in bentonite-based materials. In Canadian Nuclear Society 2nd International Conference on Radioactive Waste Management, Conference Proceedings, Winnipeg, Manitoba, 1986, 221-227.

Donachie, M.J. Jr. (editor). 1982. Titanium and Titanium Alloys. Source Book. Published by ASM International, Metals Park, Ohio, Section 1 p. 5.

Doubt, G.L. 1984. Assessing reliability and useful life of containers for disposal of irradiated fuel waste. Atomic Energy of Canada Limited Report, AECL-8328.

Doubt, G.L. 1985. Container reliability and life prediction. In Corrosion Performance of Nuclear Fuel Waste Containers, Atomic Energy of Canada Limited Technical Record, TR-340,* 73-86.

Dyer, C.K. and J.S.L. Leach. 1978. Reversible reactions within anodic oxide films on titanium electrodes. Electrochimica Acta 23, 1387-1394.

Eary, L.E. and L.M. Cathles. 1983. A kinetic model of uranium dioxide dissolution in acid, hydrogen peroxide solutions that include uranium peroxide hydrate precipitation. Metallurgical Transactions 14B, 325-334.

Engel, D.W., M.J. Apted, N.C. Garisto and D.M. LeNeveu. 1989. Comparison of source-term calculations using the AREST and SYVAC vault models. Radioactive Waste Management and the Nuclear Fuel Cycle 13, 281-296.

Eriksen, T.E. and A. Jacobsson. 1982. Diffusion of hydrogen, hydrogen sulfide, and large molecular weight anions in bentonite. Swedish Nuclear Fuel Supply Co. Report, SKBF-KBS-TR-82-17.

Eriksen, T.E. and A. Jacobsson. 1984. Diffusion in clay - experimental techniques and theoretical models. Swedish Nuclear Fuel Supply Co. Report, SKBF-KBS-TR-84-05.

Fabryka-Martin, J.T. and D.B. Curtis. 1993. Geochemistry of ^{239}Pu, ^{129}I, ^{99}Tc and ^{36}Cl. In Alligator Rivers Analogue Project Final Report, Volume 15, U.K. Department of the Environment Report, DOE/HMIP/RR/92/085.

Federal Environmental Assessment Review Panel. 1992. Final guidelines for the preparation of an environmental impact statement on the nuclear fuel waste management and disposal concept. Federal Environmental Assessment Review Office, 13th floor, Fontaine Building, 200 Sacre-Coeur Blvd., Hull, Quebec.

Finch, R.J. and R.C. Ewing. 1989. Alteration of natural UO_2 under oxidizing conditions from Shinkolobwe, Katanga, Zaire: A natural analogue for the corrosion of spent fuel. Swedish Nuclear Fuel and Waste Management Co. Report, SKB-TR-89-37.

Foroulis, Z.A. 1980. Factors influencing absorption of hydrogen in titanium from aqueous electrolytic solutions. In Titanium '80, Science and Technology, Proceedings of the Fourth International Conference on Titanium, Kyoto, Japan, 1980, 2705-2712.

Forsyth, R.S. and L.O. Werme. 1985. The corrosion of spent UO_2 fuel in synthetic groundwater. Materials Research Society Symposia Proceedings 50 (Scientific Basis for Nuclear Waste Management IX), 327-336.

Frape, S.K., P. Fritz and R.H. McNutt. 1984. Water-rock interaction and chemistry of groundwaters from the Canadian Shield. Geochimica et Cosmochimica Acta 48, 1617-1627.

Fukuzuka, R., K. Shimogori, H. Sato and F. Kamikubo. 1980. Effects of heat treatments on corrosion resistance and hydrogen absorption of commercially pure titanium. In Titanium '80, Science and Technology, Proceedings of the Fourth International Conference on Titanium, Kyoto, Japan, 1980, 2685-2693.

Gacesa, M., V.C. Orpen and I.E. Oldaker. 1983. CANDU fuel design: current concepts. Atomic Energy of Canada Limited Report, AECL-MISC-250-1 (Rev. 1).

Garisto, F. 1986. Solid dissolution: Effect of mass transport-precipitation coupling. Chemical and Engineering Science 41, 3219-3222. Also Atomic Energy of Canada Limited Reprint, AECL-9032.

Garisto, F. 1992. Some notes on H_2 production in the vault. Research Chemistry Branch Memorandum RCB-92-128. In Unpublished Documents Cited in the EIS and Primary References, Atomic Energy of Canada Limited Technical Record, TR-567,* COG-92-27.

Garisto, F. and N.C. Garisto. 1985. A UO_2 solubility function for the assessment of used nuclear fuel disposal. Nuclear Science and Engineering 90, 103-110. Also Atomic Energy of Canada Limited Reprint, AECL-8515.

Garisto, N.C. and F. Garisto. 1984. Reaction path calculations of mineral alteration products: Application to nuclear fuel waste management. Nuclear and Chemical Waste Management 5, 17-25. Also Atomic Energy of Canada Limited Reprint, AECL-8151.

Garisto, N.C. and F. Garisto. 1986. The effect of precipitation on the long-term release of radionuclides from used fuel. Annals of Nuclear Energy 13, 591-596. Also Atomic Energy of Canada Limited Reprint, AECL-9035.

Garisto, N.C. and F. Garisto. 1988a. The effect of model dimensionality on source terms for the assessment of used fuel disposal. Annals of Nuclear Energy 15(9), 471-475. Also Atomic Energy of Canada Limited Reprint, AECL-9589.

Garisto, N.C. and F. Garisto. 1988b. Mass transport-precipitation coupling in finite systems. Atomic Energy of Canada Limited Report, AECL-9562.

Garisto, N.C. and F. Garisto. 1989. Analysis of diffusive mass transport in a cracked buffer. Atomic Energy of Canada Limited Report, AECL-10003.

Garisto, N.C. and F. Garisto. 1990a. The effect of cracks on diffusive mass transport through a clay barrier. Materials Research Society Symposium Proceedings 176 (Scientific Basis for Nuclear Waste Management XIII), 733-739. Also Atomic Energy of Canada Limited Reprint, AECL-10098, COG-90-266.

Garisto, N.C. and F. Garisto. 1990b. Transport of uranium through a cracked clay barrier. Annals of Nuclear Energy 17(4), 183-193. Also Atomic Energy of Canada Limited Reprint, AECL-10119, COG-90-271.

Garisto, N.C. and F. Garisto. 1990c. A preliminary model for carbon-14 transport in a clay buffer. In High Level Radioactive Waste Management, Proceedings of the International Topical Meeting, Las Vegas, NV, 1990, Volume 1, 130-136.

Garisto, N.C. and F. Garisto. In press. The effect of precipitation on the solubility-limited release of radionuclides in a decay chain. Radioactive Waste Management and the Nuclear Fuel Cycle.

Garisto, N.C. and D.M. LeNeveu. 1989. The Vault Model for the disposal of used CANDU fuel: Documentation and analysis of scoping calculations. Atomic Energy of Canada Limited Report, AECL-9578.

Garisto, N.C. and D.M. LeNeveu. 1990. Analysis of mass transport in an engineered barriers system for the disposal of used nuclear fuel. Materials Research Society Symposium Proceedings 176 (Scientific Basis for Nuclear Waste Management XIII), 775-783. Also Atomic Energy of Canada Limited Reprint, AECL-10099, COG-90-267.

Garisto, N.C. and D.M. LeNeveu. 1991. A radionuclide mass-transport model for the performance assessment of engineered barriers in a used nuclear fuel disposal vault. Atomic Energy of Canada Limited Report, AECL-10277.

Garisto, N.C., L.H. Johnson and W.H. Hocking. 1990. An instant release source term for the assessment of used nuclear fuel disposal. In Second International Conference on CANDU Fuel, Conference Proceedings, Pembroke, Ontario, 1989, 352-368.

Garisto, N.C., D.M. LeNeveu and F. Garisto. 1992. The mass transport of radionuclides in a multilayered medium. Atomic Energy of Canada Limited Report, AECL-10384, COG-91-297.

Gascoyne, M. 1988. Reference groundwater composition for a depth of 500 m in the Whiteshell Research Area—Comparison with synthetic groundwater WN-1. Atomic Energy of Canada Limited Technical Record, TR-463.*

Gascoyne, M. 1992. Dissolved gas concentrations in Whiteshell Research Area groundwaters. In Unpublished Documents Cited in the EIS and Primary References, Atomic Energy of Canada Limited Technical Record, TR-567,* COG-92-27.

Gillham, R.W. and J.A. Cherry. 1982. Contaminant migration in saturated unconsolidated geologic deposits. In Recent Trends in Hydrogeology (T.N. Narasimhan, editor). Geological Society of America, Special Paper 189, 31-62.

Gillham, R.W., M.J.L. Robin, D.J. Dytynyshyn and H.M. Johnston. 1984. Diffusion of nonreactive and reactive solutes through fine-grained barrier materials. Canadian Geotechnical Journal 21, 541-550.

Glass, R.S. 1981. Effects of radiation on the chemical environment surrounding waste canisters in proposed repository sites and possible effects on the corrosion process. Sandia National Laboratory Report, SAND-81-1677, Albuquerque, NM.

Glass, R.S. 1983. Effect of intermetallic Ti_2Ni on the electrochemistry of TiCode-12 in hydrochloric acid. Electrochimica Acta 28, 1507-1513.

Goode, J.H. and C.M. Cox. 1970. The distribution of fission product tritium in a Zircaloy-clad UO_2 blanket rod from PWR-1. Oak Ridge National Laboratory Report, ORNL-TM-2994.

Goodwin, B.W. and K.K. Mehta. In preparation. Identification of contaminants of concern for the postclosure assessment of the concept for disposal of Canada's nuclear fuel waste. Atomic Energy of Canada Limited Report, AECL-10901, COG-93-265.

Goodwin, B.W., T.H. Andres, P.A. Davis, D.M. LeNeveu, T.W. Melnyk, G.R. Sherman and D.M. Wuschke. 1987. Post-closure environmental assessment for the Canadian Nuclear Fuel Waste Management Program. Radioactive Waste Management and the Nuclear Fuel Cycle 8, 241-272.

Goodwin, B.W., D.B. McConnell, T.H. Andres, W.C. Hajas, D.M. LeNeveu, T.W. Melnyk, G.R. Sherman, M.E. Stephens, J.G. Szekely, P.C. Bera, C.M. Cosgrove, K.D. Dougan, S.B. Keeling, C.I. Kitson, B.C. Kummen, S.E. Oliver, K. Witzke, L. Wojciechowski and A.G. Wikjord. 1994. The disposal of Canada's nuclear fuel waste: postclosure assessment of a reference system. Atomic Energy of Canada Limited Report, AECL-10717, COG-93-7.

Goodwin, B.W., M.E. Stephens, C.C. Davison, L.H. Johnson and R. Zach. In preparation. Scenario analysis for the postclosure assessment of the concept for disposal of Canada's nuclear fuel wastes. Atomic Energy of Canada Limited Report, AECL-10969.

Goyette, D. 1987. The effect of microorganisms on the transport of iodine and technetium in a biogeochemical simulation of a radioactive waste disposal vault. Master of Science Thesis, Department of Chemical Engineering and Applied Chemistry, University of Toronto.

Grandstaff, D.E. 1976. A kinetic study of the dissolution of uraninite. Economic Geology 71, 1493-1506.

Gray, M.N. 1993. OECD/NEA International Stripa Project 1980-1992, Overview, Volume III, Engineered Barriers. Published by SKB (Swedish Nuclear Fuel and Waste Management Company), Stockholm.

Gray, M.N. and S. Cheung. 1986. Disposal vault sealing. In Proceedings of the Twentieth Information Meeting of the Canadian Nuclear Fuel Waste Management Program (1985 General Meeting), Volume II, 253-263, Atomic Energy of Canada Limited Technical Record, TR-375.*

Gray, M.N., D.A. Dixon, D.W. Oscarson and A.W.L. Wan. 1993. Research on clay-based engineered barrier materials for a nuclear fuel waste repository. Presented at the Workshop on the Thermo-Mechanical Properties of Clays, Bergamo, Italy, 1993.

Gray, W.J. and D.M. Strachan. 1991. UO_2 matrix dissolution rates and grain boundary inventories of Cs, Sr and Tc in spent LWR fuel. Materials Research Society Symposium Proceedings 212 (Scientific Basis for Nuclear Waste Management XIV), 205-212.

Greber, M.A., E.R. Frech and J.A.R. Hillier. 1994. The disposal of Canada's nuclear fuel waste: public involvement and social aspects. Atomic Energy of Canada Limited Report, AECL-10712, COG-93-2.

Grondin, L., W.C. Cheng, C.R. Frost, K. Johansen, T.F. Kempe, J. Lockhart-Grace, M. Paez-Victor, H.E. Reid, S.B. Russell, C.H. Ulster, J.E. Villagran and M. Zeya. 1994. The disposal of Canada's nuclear fuel waste: preclosure assessment of a conceptual system. Ontario Hydro Report. Available from Ontario Hydro, 700 University Avenue, Toronto, Ontario, M5G 1X6.

Hack, J.E. and G.R. Leverant. 1982. The influence of microstructure on the susceptibility of titanium alloys to internal hydrogen embrittlement. Metallurgical Transactions 13A, 1729-1739.

Haire, R.G. and G.W. Beall. 1979. Consequences of radiation from sorbed transplutonium elements on clays selected for waste isolation. In Radioactive Waste in Geologic Storage, ACS Symposium Series No. 100, 291-295.

Hardie, D. 1990. The environment-induced cracking of hexagonal materials: magnesium, titanium and zirconium. In Proceedings of the First International Conference on Environment-Induced Cracking of Metals, Kohler, WI. International Corrosion Conference Series, NACE-10 (R.P. Gangloff and M.B. Ives, editors), 347-361.

Hastings, I.J. 1982. Structures in irradiated UO_2 fuel from Canadian reactors. Atomic Energy of Canada Limited Report, AECL-MISC-249.*

Hastings, I.J., D.H. Rose and J. Baird. 1976. Identification of precipitates associated with intergranular fission gas bubbles in irradiated UO_2 fuel. Journal of Nuclear Materials 61, 229-231.

Heinrich, W.F. and T. Andres. 1985. Response functions of the convection-dispersion equations describing radionuclide migration in a semi-infinite medium. Annals of Nuclear Energy 12(12), 685-691. Also Atomic Energy of Canada Limited Reprint, AECL-8691.

Hiskey, J.B. 1979. Kinetics of uranium dioxide dissolution in ammonium carbonate. Transactions Institute of Mining and Metallurgy C88, C145-152.

Hocking, W.H., A.F. Gerwing, K.M. Wasywich and C.R. Frost. 1990. X-ray photoelectron spectroscopy on used CANDU UO_2 fuel exposed to warm moist-air conditions. In Second International Conference on CANDU Fuel, Conference Proceedings, Pembroke, Ontario, 1989, 322-336.

Ikeda, B.M. and C.F. Clarke. 1986. Titanium corrosion under Canadian nuclear fuel waste disposal conditions. In Canadian Nuclear Society 2nd International Conference on Radioactive Waste Management, Conference Proceedings, Winnipeg, Manitoba, 1986, 605-610.

Ikeda, B.M. and P. McKay. 1985. The corrosion behavior of titanium Grades 2 and 12. In Proceedings of the Nineteenth Information Meeting of the Nuclear Fuel Waste Management Program—Engineered Barriers and Waste Forms, Volume I, 135-157, Atomic Energy of Canada Limited Technical Record, TR-350.*

Ikeda, B.M., M.G. Bailey, C.F. Clarke and D.W. Shoesmith. 1989. Crevice corrosion of titanium under nuclear fuel waste conditions. Atomic Energy of Canada Limited Report, AECL-9568.

Ikeda, B.M., M.G. Bailey, C.F. Clarke and D.W. Shoesmith. 1990a. Crevice corrosion and hydrogen embrittlement of Grade-2 and -12 titanium under Canadian nuclear waste vault conditions. In Corrosion of Nuclear Fuel Waste Containers, Proceedings of a Workshop, Winnipeg, MB, 1988, 45-66, Atomic Energy of Canada Limited Report, AECL-10121, COG-90-273.

Ikeda, B.M., M.G. Bailey, M.J. Quinn and D.W. Shoesmith. 1990b. The effect of temperature on crevice corrosion of titanium. In Innovation and Technology Transfer for Corrosion Control, Proceedings of the 11th International Corrosion Congress, Florence, Italy, 1990, Volume 5, 5.371-5.378.

Ikeda, B.M., M.G. Bailey, D.C. Cann and D.W. Shoesmith. 1990c. Effect of iron content and microstructure on the crevice corrosion of Grade-2 titanium under nuclear waste vault conditions. In Advances in Localized Corrosion, Proceedings of the Second International Conference on Localized Corrosion, Orlando, FL, 1987, 439-444. Also Atomic Energy of Canada Limited Reprint, AECL-10394.

Ikeda, B.M., M.G. Bailey, M.J. Quinn and D.W. Shoesmith. 1991. Localization in the crevice corrosion of titanium. In Mechanical Behaviour of Materials-VI, Proceedings of the Sixth International Conference, Kyoto, Japan, 1991, 619-625. Also Atomic Energy of Canada Limited Reprint, AECL-10360.

Ikeda, B.M., M.G. Bailey, M.J. Quinn and D.W. Shoesmith. 1992. The effect of chloride concentration on the crevice corrosion of Grade-2 titanium. In Critical Factors in Localized Corrosion (G. Frankel and R.C. Newman, editors), Electrochemical Society Symposium Proceedings, Phoenix, AZ, 1991, Volume 92-9, 431-447.

Ikeda, B.M., M.G. Bailey, M.J. Quinn and D.W. Shoesmith. In press. The development of an experimental database for the lifetime predictions of titanium nuclear waste containers. In Application of Accelerated Corrosion Tests to Service Life Prediction of Materials (G. Cragnolino and N. Sridhar, editors), American Society for Testing and Materials.

Ito, K. and T. Kanno. 1988. Sorption behavior of carrier-free technetium-95 m on minerals, rocks and backfill materials under both oxidizing and reducing conditions. Journal of Nuclear Science and Technology 25, 534-539.

Jeffery, B.M. 1967. Microanalysis of inclusions in irradiated UO_2. Journal of Nuclear Materials 22, 33-40.

Johnson, L.H. 1982. The dissolution of irradiated UO_2 fuel in groundwater. Atomic Energy of Canada Limited Report, AECL-6837.

Johnson, L.H. and H.H. Joling. 1984. Fission product leaching from used CANDU fuel: An estimate of fuel-sheath gap and grain boundary inventories and probable releases after disposal. Atomic Energy of Canada Limited Technical Record, TR-280.*

Johnson, L.H. and D.W. Shoesmith. 1988. Spent fuel. In Radioactive Waste Forms for the Future (W. Lutze and R.C. Ewing, editors), Elsevier Science Publishers B.V., 635-698. Also Atomic Energy of Canada Limited Reprint, AECL-9583.

Johnson, L.H., K.I. Burns, H.H. Joling and C.J. Moore. 1983. Leaching of ^{137}Cs, ^{134}Cs and ^{129}I from irradiated UO_2 fuel. Nuclear Technology 63, 470-475. Also Atomic Energy of Canada Limited Reprint, AECL-8031.

Johnson, L.H., D.W. Shoesmith and S. Stroes-Gascoyne. 1988. Spent fuel: Characterization studies and dissolution behaviour under disposal conditions. Materials Research Society Symposium Proceedings 112 (Scientific Basis for Nuclear Waste Management XI), 99-113. Also Atomic Energy of Canada Limited Reprint, AECL-9651.

Johnson, L.H., D.W. Shoesmith, B.M. Ikeda and F. King. 1992. Lifetimes of titanium and copper containers for the disposal of used nuclear fuel. Materials Research Society Symposium Proceedings 257 (Scientific Basis for Nuclear Waste Management XV), 439-446.

Johnson, L.H., J.C. Tait, D.W. Shoesmith, J.L. Crosthwaite and M.N. Gray. 1994. The disposal of Canada's nuclear fuel waste: engineered barriers alternatives. Atomic Energy of Canada Limited Report, AECL-10718, COG-93-8.

Johnston, R.M. and H.G. Miller. 1984. The effect of pH on the stability of smectite. Atomic Energy of Canada Limited Report, AECL-8366.

Johnston, R.M. and H.G. Miller. 1985. Hydrothermal stability of bentonite-based buffer materials. Atomic Energy of Canada Limited Report, AECL-8376.

Joint Statement. 1978. Joint statement by the Minister of Energy, Mines and Resources Canada and the Ontario Energy Minister, 1978 June 5. Printing and Publishing, Supply and Services Canada, Ottawa, Ontario.

Joint Statement. 1981. Joint statement by the Minister of Energy, Mines and Resources Canada and the Ontario Energy Minister, 1981 August 4. Printing and Publishing, Supply and Services Canada, Ottawa, Ontario.

Kamineni, D.C., J.J.B. Dugal and R.B. Ejeckam. 1984. Geochemical investigations of granitic core samples from boreholes at the Underground Research Laboratory site near Lac du Bonnet, Manitoba. Atomic Energy of Canada Limited Technical Record, TR-221.*

Kempe, T.F. 1992. Record of discussion with A. Ohuchi, Japan. Memorandum File 906-N-37450P, In Unpublished Documents Cited in the EIS and Primary References, Atomic Energy of Canada Limited Technical Record, TR-567,* COG-92-27.

Kim, Y.J. and R.A. Oriani. 1987a. Corrosion properties of the oxide film formed on Grade-12 titanium in brine under gamma radiation. Corrosion 43, 85-91.

Kim, Y.J. and R.A. Oriani. 1987b. Brine radiolysis and its effect on the corrosion of Grade-12 titanium. Corrosion 43, 92-97.

Kimberley, M.M. (editor). 1978. Uranium Deposits, Their Mineralogy and Origin; Mineralogical Association of Canada Short Course Handbook, Volume 3. University of Toronto Press, Toronto, Ontario.

Kjartanson, B.H., M.N. Gray and B.C.M. Pulles. 1991. Developments for in situ tests on compacted bentonite-based buffer material. Materials Research Society Symposia Proceedings 212 (Scientific Basis for Nuclear Waste Management XIV), 467-474. Also Atomic Energy of Canada Limited Reprint, AECL-10472.

Kleykamp, H. 1979. The chemical state of LWR high-power rods under irradiation. Journal of Nuclear Materials 84, 109-117.

Kobayashi, M., Y. Araya, S. Fujiyama, Y. Sunayama and H. Uno. 1980. Study on crevice corrosion of titanium. In Titanium '80, Science and Technology, Proceedings of the Fourth International Conference on Titanium, Kyoto, Japan, 1980, Volume 4, 2613-2622.

Kozak, E.T. and C.C. Davison. 1992. Hydrogeology of the rock mass encountered at the 240 Level of Canada's Underground Research Laboratory. Atomic Energy of Canada Limited Report, AECL-10346, COG-92-293.

Kruger, J. and K. Rhyne. 1982. Current understanding of pitting and crevice corrosion and its application to test methods for determining the corrosion susceptibility of nuclear waste metallic containers. Nuclear and Chemical Waste Management 3, 205-227.

Langmuir, D. 1969. The Gibbs free energies of substances in the system $Fe-O_2-H_2O-CO_2$ at 25°C. U.S. Geological Survey Prof. Paper 650-B, B180-B184.

Langmuir, D. 1971. Particle size effect on the reaction goethite → hematite + water. American Journal of Science 271, 147-156 and Correction 272, 972.

Langmuir, D. 1978. Uranium solution-mineral equilibria at low temperatures with applications to sedimentary ore deposits. Geochimica et Cosmochimica Acta 42, 547-569.

Lasaga, A.C. 1981. Transition state theory. In Kinetics of Geochemical Processes (A.C. Lasaga and R.J. Kirkpatrick, editors), Reviews in Mineralogy, Volume 8, 135-169, Mineralogical Society of America.

Law, K.R., H.W. Nesbitt and F.J. Longstaffe. 1991. Weathering of granitic tills and the genesis of a podzol. American Journal of Science 291, 940-976.

Lederich, R.J., S.M.L. Sastry and P.S. Pao. 1982. Temperature dependence of sustained-load subcritical crack growth in Ti-6Al-6V-2Sn. Metallurgical Transactions 13A, 497-500.

Lee, C.F., D.W. Oscarson and S.C.H. Cheung. 1986. The preservation of a cadaver by a clay sealant: Implications for the disposal of nuclear fuel waste. Nuclear and Chemical Waste Management 6, 65-69. Also Atomic Energy of Canada Limited Reprint, AECL-8689.

Lee, J.-I., P. Chung and C.-H. Tsai. 1986. A study of hydriding of titanium in sea water under cathodic polarization. Presented at Corrosion '86 Conference, Houston, TX, 1986. National Association of Corrosion Engineers, Paper No. 259.

Lemire, R.J. 1988. Effects of high ionic strength groundwaters on calculated equilibrium concentrations in the uranium-water system. Atomic Energy of Canada Limited Report, AECL-9549.

Lemire, R.J. and F. Garisto. 1989. The solubility of U, Np, Pu, Th and Tc in a geological disposal vault for used nuclear fuel. Atomic Energy of Canada Limited Report, AECL-10009.

Lemire, R.J. and F. Garisto. 1992. The effect of ionic strength, groundwater composition and temperature on calculated radionuclide solubilities. Radiochimica Acta 58/59, 37-44.

LeNeveu, D.M. 1986. Vault submodel for the second interim assessment of the Canadian concept for nuclear fuel waste disposal: Post-closure phase. Atomic Energy of Canada Limited Report, AECL-8383.

LeNeveu, D.M. 1987. Response function of the convection-dispersion equations describing radionuclide migration in a finite medium. Annals of Nuclear Energy 14(2), 77-82. Also Atomic Energy of Canada Limited Reprint, AECL-9166.

LeNeveu, D.M. In preparation. Analysis specifications for the CC3 vault model. Atomic Energy of Canada Limited Report, AECL-10970.

LeNeveu, D.M. and N.C. Garisto. 1988. Sensitivity surfaces for the assessment of waste package performance. Materials Research Society Symposium Proceedings 112 (Scientific Basis for Nuclear Waste Management XI), 323-329. Also Atomic Energy of Canada Limited Reprint, AECL-9584.

LeNeveu, D.M. and L.H. Johnson. 1986. Reducing radiation doses from ^{129}I disposal by isotopic dilution. In Canadian Nuclear Society 2nd International Conference on Radioactive Waste Management, Conference Proceedings, Winnipeg, MB, 1986, 661-666.

Lever, D.A. 1986. Some notes on experiments measuring diffusion of sorbed nuclides through porous media. U.K. Atomic Energy Research Establishment Report, AERE-R-12321.

Liening, E.L. 1983. Unusual corrosion failures of titanium chemical processing equipment. Materials Performance 22(11), 37-44.

Little, B., P. Wagner and F. Mansfeld. 1991. Microbiologically influenced corrosion of metals and alloys. International Materials Reviews 36, 253-272.

Lindsay, W.L. 1988. Solubility and redox equilibria of iron compounds in soils. In Iron in Soils and Clay Minerals (edited by J.W. Stucki, B.A. Goodman and U. Schwertmann). NATO Advanced Study Institute Series, Volume 217, Chapter 3. D. Reidel Publishing Co., Dordrecht, Holland.

Lustman, B. 1961. Irradiation effects in uranium dioxide. In Uranium Dioxide: Properties and Nuclear Applications (J. Belle, editor), Chapter 9, United States Atomic Energy Commission, Washington.

Maak, P.Y.Y. and M.D.C. Moles. 1986. Welding and inspection of nuclear fuel waste disposal container. In Canadian Nuclear Society International Conference on Radioactive Waste Management, Conference Proceedings, Winnipeg, Manitoba, 1986, 570-575.

Mansfeld, F. and B. Little. 1991. A technical review of electrochemical techniques applied to microbiologically influenced corrosion. Corrosion Science 32(3), 247-272.

Manzel, R., F. Sontheimer and R. Wurtz. 1984. The radial distribution of fission gases and other fission products in irradiated PWR fuel. Journal of Nuclear Materials 126, 132-143.

Martin, C.D. 1989. Shaft excavation response in a highly stressed rock mass. In Excavation Response in Geological Repositories for Radioactive Waste, Proceedings of an NEA Workshop, Winnipeg, Manitoba, 1988, 331-340.

Martin, C.D., E.T. Kozak and N.A. Chandler. 1992. Hydraulic properties of the excavation-disturbed zone around underground openings. In Proceedings of 45th Canadian Geotechnical Society Conference, Toronto, Ontario, 1992, 89-1 to 89-10.

Mathers, W.G. 1985. HOTROC, a program for calculating the transient temperature field from an underground nuclear waste disposal vault. Atomic Energy of Canada Limited Technical Record, TR-336.*

Mattsson, E. (Chairman). 1978. Corrosion resistance of copper canisters for final disposal of spent nuclear fuel. Appendix A:5. Swedish Nuclear Fuel Supply Co. Report, KBS-TR-90.

Mattsson, E. 1979. Corrosion resistance of canisters for final disposal of spent nuclear fuel. In Scientific Basis for Nuclear Waste Management 1, (G.J. McCarthy, editor), Plenum Press, New York, 271-281.

Mattsson, H. and I. Olefjord. 1984. General corrosion of Ti in hot water and water saturated bentonite clay. Swedish Nuclear Fuel and Waste Management Company Report, SKB-KBS-TR-84-19.

Mattsson, H. and I. Olefjord. 1990. Analysis of oxide formed on titanium during exposure in bentonite clay. I. The oxide growth. Werkstoffe und Korrosion 41, 383-390.

Mattsson, H., C. Li and I. Olefjord. 1990. Analysis of oxide formed on titanium during exposure in bentonite clay. II. The structure of the oxide. Werkstoffe und Korrosion 41, 578-584.

McCamis, R.H. 1992. Criticality safety calculations in support of the used-fuel disposal vault. Atomic Energy of Canada Limited Technical Record, TR-537,* COG 92-342.

McKay, P. 1984a. Crevice corrosion of Ti-0.8% Ni-0.3% Mo alloy (ASTM Grade-12) in chloride environments at elevated temperature. In Proceedings of the Ninth International Congress on Metallic Corrosion, Toronto, Ontario, 1984, Volume 3, 288-297.

McKay, P. 1984b. Crevice corrosion kinetics on titanium and a Ti-Ni-Mo alloy in chloride solutions at elevated temperature. In Corrosion Chemistry Within Pits, Crevices and Cracks, Proceedings of a Conference, Teddington, Middlesex, 1984, 107-128.

McKay, P. and D.B. Mitton. 1985. An electrochemical investigation of localized corrosion on titanium in chloride environments. Corrosion 41, 52-62. Also Atomic Energy of Canada Limited Reprint, AECL-8622.

Meier, H., E. Zimmerhackl, G. Zeitler, P. Menge and W. Hecker. 1987. Influence of liquid/solid ratios in radionuclide migration studies. Journal of Radioanalytical and Nuclear Chemistry 109, 139-151.

Minister of the Environment, Canada. 1989. Terms of reference for the nuclear fuel waste management and disposal concept environmental assessment panel. Printing and Publishing, Supply and Services Canada, Ottawa, Ontario.

Mitchell, J.K. 1976. Fundamentals of Soil Behaviour. Wiley and Sons, New York.

Mitchell, J.K. 1991. Conduction phenomena: from theory to geotechnical practice. Géotechnique 41(3), 299-340.

Molecke, M.A., J.A. Ruppen and R.B. Diegle. 1982. Materials for high-level waste canister/overpacks in salt formations. Sandia National Laboratory Report, SAND-82-0429, Albuquerque, NM.

Moody, N.R. and W.W. Gerberich. 1980. Hydrogen-induced slow crack growth in Ti-6Al-6V-2Sn. Metallurgical Transactions 11A, 973-981.

Moody, N.R. and W.W. Gerberich. 1982. The effect of stress state on internal hydrogen-induced crack growth in Ti-6Al-4V-2Sn. Metallurgical Transactions 13A, 1055-1061.

Muurinen, A., P. Penttila-Hiltunen and K. Uusheimo. 1989. Diffusion of chloride and uranium in compacted sodium bentonite. Materials Research Society Symposium Proceedings 127 (Scientific Basis for Nuclear Waste Management XII), 743-748.

Murai, T., M. Ishikawa and C. Miura. 1977. Absorption of hydrogen into titanium under cathodic polarization. Boshoku Gijutsu 26, 177-183.

Neal, W.L., S.A. Rawson and W.M. Murphy. 1988. Radionuclide release behavior of light water reactor spent fuel under hydrothermal conditions. Materials Research Society Symposium Proceedings 112 (Scientific Basis for Nuclear Waste Management XI), 505-515.

Nelson, H.G., D.P. Williams and J.E. Stein. 1972. Environmental hydrogen embrittlement of an α-β titanium alloy: Effect of microstructure. Metallurgical Transactions 3, 469-475.

Neretnieks, I. 1977. Retardation of escaping nuclides from a final depository. Swedish Nuclear Fuel Supply Co. Report, KBS-TR-30.

Neretnieks, I. 1978. Transport of oxidants and radionuclides through a clay barrier. Swedish Nuclear Fuel Supply Co. Report, KBS-TR-79.

Neretnieks, I. 1982. The movement of a redox front downstream from a repository for nuclear waste. Swedish Nuclear Fuel Supply Co. Report, SKBF-KBS-TR-82-16.

Neretnieks, I. and C. Skagius. 1978. Diffusivity measurements of Na-lignosulphonate, Sr^{2+} and Cs^{+} in wet clay. AECL Translation of KBS TR-87, AECL-TR-MISC 469.*

Nesbitt, H.W. and G.M. Young. 1984. Prediction of some weathering trends of plutonic and volcanic rocks based on thermodynamic and kinetic considerations. Geochimica et Cosmochimica Acta 48, 1523-1534.

Neuman, S.P. 1987. Waste isolation experiments from the hydrologist's point of view. In Coupled Processes Associated with Nuclear Waste Repositories, Proceedings of an International Symposium, Berkeley, CA, 1985, 765-769.

Nilsson, L., L. Moreno, I. Neretnieks and L. Romero. 1991. A resistance network model for radionuclide transport into the near field surrounding a repository for nuclear waste. Swedish Nuclear Fuel and Waste Management Co. Report, SKB-TR-91-30.

Nordstrom, D.K. 1986. Redox chemistry of deep groundwaters in Sweden. Swedish Nuclear Fuel and Waste Management Co. Report, SKB-TR-86-03.

Notley, M.J.F. 1979. ELESIM: A computer code for predicting the performance of nuclear fuel elements. Nuclear Technology 44, 445-450.

Nuttall, K. 1983. Some aspects of the prediction of long-term performance of fuel disposal containers. Canadian Metallurgical Quarterly 22, 403-409. Also Atomic Energy of Canada Limited Reprint, AECL-7851.

Nuttall, K. and V.F. Urbanic. 1981. An assessment of materials for nuclear fuel immobilization containers. Atomic Energy of Canada Limited Report, AECL-6440.

Ohtsuka, T., M. Masuda and N. Sato. 1987. Cathodic reduction of anodic oxide films formed on titanium. Journal of the Electrochemical Society 134, 2406-2410.

Ohuchi, A. and H. Sakurai. 1988. Studies on fission products behavior in BWR fuel rods. In Proceedings of the International Topical Meeting on LWR Fuel Performance, Williamsburg, VA, 1988, 180-188.

Oldfield, J.W. 1987. Test techniques for pitting and crevice corrosion resistance of stainless steels and nickel-based alloys in chloride-containing environments. International Materials Reviews 32, 153-170.

Oldfield, J.W. and W.H. Sutton. 1978a. Crevice corrosion of stainless steels. I. A mathematical model. British Corrosion Journal 13, 13-22.

Oldfield, J.W. and W.H. Sutton. 1978b. Crevice corrosion of stainless steel, II. Experimental studies. British Corrosion Journal 13, 104-111.

Oldfield, J.W. and W.H. Sutton. 1980. New technique for predicting the performance of stainless steels in sea water and other chloride-containing environments. British Corrosion Journal 15, 31-34.

Oscarson, D.W. In press. Comparison of measured and calculated diffusion coefficients for iodide in compacted clays. Clay Minerals.

Oscarson, D.W. and S.C.H. Cheung. 1983. Evaluation of phyllosilicates as a buffer component in the disposal of nuclear fuel waste. Atomic Energy of Canada Limited Report, AECL-7812.

Oscarson, D.W. and D.A. Dixon. 1989a. Elemental, mineralogical, and pore-solution compositions of selected Canadian clays. Atomic Energy of Canada Limited Report, AECL-9891.

Oscarson, D.W. and D.A. Dixon. 1989b. The effect of steam on montmorillonite. Applied Clay Science 4, 279-292. Also Atomic Energy of Canada Limited Reprint, AECL-10026.

Oscarson, D.W. and D.A. Dixon. 1990. Effect of heating unsaturated bentonite on the swelling and hydraulic properties of subsequently saturated clay. In Proceedings of the Annual Conference and 1st Biennial Environmental Speciality Conference of the Canadian Society of Civil Engineering, Hamilton, Ontario, Volume II-1, 312-323.

Oscarson, D.W. and R.B. Heimann. 1988. The effect of an Fe(II)-silicate on selected properties of a montmorillonitic clay. Clay Minerals 23, 81-90. Also Atomic Energy of Canada Limited Reprint, AECL-9593.

Oscarson, D.W. and H.B. Hume. 1993a. Contaminant diffusion through engineered earthen barriers: effect of barrier composition. In Agronomy Abstracts, 1993 Annual Meeting American Society of Agronomy, Crop Science Society of America and Soil Science Society of America, Cincinnati, OH, 43.

Oscarson, D.W. and H.B. Hume. 1993b. Diffusion of ^{14}C in dense saturated bentonite under steady-state conditions. Transport in Porous Media 13 (in press).

Oscarson, D.W., R.L. Watson and D.M. LeNeveu. 1984. A compilation of distribution coefficients for radioactive and other toxic contaminants with bentonite for use in SYVAC. Atomic Energy of Canada Limited Technical Record, TR-288.*

Oscarson, D.W., S. Stroes-Gascoyne and S.C.H. Cheung. 1986. The effect of organic matter in clay sealing materials on the performance of a nuclear fuel waste disposal vault. Atomic Energy of Canada Limited Report, AECL-9078.

Oscarson, D.W., D.A. Dixon and M.N. Gray. 1990. Swelling capacity and permeability of an unprocessed and a processed bentonitic clay. Engineering Geology 28, 281-289.

Oscarson, D.W., H.B. Hume, N.G. Sawatsky and S.C.H. Cheung. 1992. Diffusion of iodide in compacted bentonite. Soil Science Society of American Journal 56, 1400-1406.

Oversby, V.M. 1987. Spent fuel as a waste form - data needs to allow long-term performance assessment under repository disposal conditions. Materials Research Society Symposium Proceedings 84 (Scientific Basis for Nuclear Waste Management X), 87-101.

Paquette J. and R.J. Lemire. 1981. A description of the chemistry of aqueous solutions of uranium and plutonium to 200°C using potential-pH diagrams. Nuclear Science and Engineering 79, 26-48. Also Atomic Energy of Canada Limited Reprint, AECL-7037.

Paquette, J., J.A.K. Reid and E.L.J. Rosinger. 1980. Review of technetium behaviour in relation to nuclear waste disposal. Atomic Energy of Canada Limited Technical Record, TR-25.*

Pardee, W.J. and N.E. Paton. 1980. Model of sustained load cracking by hydride growth in Ti alloys. Metallurgical Transactions 11A, 1391-1400.

Paton, N.E. 1984. Low temperature hydrogen embrittlement of titanium alloys. In Titanium. Science and Technology, Proceedings Fifth International Conference on Titanium, Volume 4, 2519-2526.

Paton, N.E., B.S. Hickman and D.H. Leslie. 1971. Behavior of hydrogen in α-phase Ti-Al alloys. Metallurgical Transactions 2, 2791-2796.

Peacor, D.R., E.J. Essene and J.H. Lee. 1986. Investigation of the stability of clay/basalt packing materials. U.S. Nuclear Regulatory Commission Report, NUREG/CR-4585.

Pedersen, K., S. Ekendahl and J. Arlinger. 1991. Microbes in crystalline bedrock. Assimilation of CO_2 and introduced organic compounds by bacterial populations in groundwater from deep crystalline bedrock at Laxemar and Stripa. Swedish Nuclear Fuel and Waste Management Co. Report, SKB-TR-91-56.

Pescatore, C. and C. Sastre. 1988. Mass transfer from penetrations in waste containers. Materials Research Society Symposium Proceedings 112 (Scientific Basis for Nuclear Waste Management XI), 773-782.

Philip, J.R. and D.A. DeVries. 1957. Moisture movement in porous materials under temperature gradients. Transactions American Geophysical Union 38, 171-187.

Phillips, I.I., P. Poole and L.L. Shreir. 1972. Hydride formation during cathodic polarization of Ti. I. Effect of current density on kinetics of growth and composition of hydride. Corrosion Science 12, 855-866.

Pigford, T.H., P.L. Chambré and W.W.L. Lee. 1992. A review of near-field mass transfer in geologic disposal systems. Radioactive Waste Management and the Nuclear Fuel Cycle 16(3,4), 205-210.

Pope, D.H., D. Duquette, P.C. Wayner, Jr. and A.H. Johannes. 1989. Microbially Influenced Corrosion: A State-of-the-Art Review. Second edition, Materials Technology Institute, St. Louis, MO.

Pourbaix, M.J.N. 1966. Atlas of Electrochemical Equilibria in Aqueous Solutions. Pergamon Press, Oxford.

Prussin, S.G., D.R. Olander, W.K. Lau and L. Hansson. 1988. Release of fission products (Xe, I, Te, Cs, Mo and Tc) from polycrystalline UO_2. Journal of Nuclear Materials 154, 25-37.

Pusch, R. 1978. Self-injection of highly compacted bentonite into rock joints. Swedish Nuclear Fuel Supply Co. Report, KBS-TR-73.

Pusch, R. 1982. Chemical interaction of clay buffer materials and concrete. Swedish Nuclear Fuel Supply Co. Report, SKBF/KBS-SFR-82-01.

Pusch, R. 1988. Rock sealing - Large scale field test and accessory investigations. Swedish Nuclear Fuel and Waste Management Co. Stripa Project Report, TR-88-04.

Pusch, R. 1992. Executive summary and general conclusions of the rock sealing project. Swedish Nuclear Fuel and Waste Management Co. Stripa Project Report, TR-92-27.

Pusch, R. and M.N. Gray. 1989. Sealing of radioactive waste repositories in crystalline rock. In Sealing of Radioactive Waste Repositories, Proceedings OECD Workshop, 1989, 214-228.

Pusch, R. and O. Karnland. 1990. Preliminary report on longevity of montmorillonite clay under repository-related conditions. Swedish Nuclear Fuel and Waste Management Co. Report, SKB-TR-90-44.

Pusch, R., L. Borgesson and G. Ramqvist. 1985a. Final report of the buffer mass test - Vol. 2: Test results. Swedish Nuclear Fuel and Waste Management Co. Stripa Project Report, TR-85-12.

Pusch, R., L. Ranhagen and K. Nilsson. 1985b. Gas migration through MX-80 bentonite. National Cooperative for the Storage of Radioactive Waste (Baden) Report, NAGRA-NTB-85-36.

Pusch, R., L. Borgesson and M. Erlstrom. 1987a. Alteration of isolating properties of dense smectite clay in repository environment as exemplified by seven pre-quarternary clays. Swedish Nuclear Fuel and Waste Management Co. Report, SKB-TR-87-29.

Pusch, R., H. Hökmark and L. Börgesson. 1987b. Outline of models of water and gas flow through smectite clay buffers. Swedish Nuclear Fuel and Waste Management Co. Report, SKB-TR-87-10.

Pusch, R., O. Karnland, A. Lajudie and A. Decarreau. 1992. MX-80 clay exposed to high temperatures and gamma radiation. Swedish Nuclear Fuel and Waste Management Co. Technical Report, SKB-TR-93-03.

Quigley, R.M. 1984. Quantitative mineralogy and preliminary pore-water chemistry of candidate buffer and backfill materials for a nuclear fuel waste disposal vault. Atomic Energy of Canada Limited Report, AECL-7827.

Quinn, M.J., M.G. Bailey, B.M. Ikeda and D.W. Shoesmith. 1993. Image-analysis techniques for investigating localized corrosion processes. Atomic Energy of Canada Limited Report, AECL-10966, COG-93-405.

Radhakrishna, H.S. 1982. Evaluation of the thermal properties of buffer materials for a deep underground nuclear waste disposal vault. Atomic Energy of Canada Limited Technical Record, TR-183.*

Radhakrishna, H.S., H.T. Chan, A.M. Crawford and K.C. Lau. 1989. Thermal and physical properties of candidate buffer-backfill materials for a nuclear fuel waste disposal vault. Canadian Geotechnical Journal 26(4), 629-639.

Radhakrishna, H.S., K.C. Lau and A.W. Crawford. 1990. Experimental modelling of the near-field thermal regime in a nuclear fuel waste disposal vault. Engineering Geology 28, 337-351.

Rai, D. 1984. Solubility product of Pu(IV) hydrous oxide and equilibrium constants of Pu(IV)/Pu(V), Pu(IV)/Pu(VI) and Pu(V)/Pu(VI) couples. Radiochimica Acta 35, 97-106.

Rai, D., J.L. Swanson and J.L. Ryan. 1987. Solubility of $NpO_2 \cdot xH_2O$(am) in the presence of Cu(I)/Cu(II) redox buffer. Radiochimica Acta 42, 35-41.

Rawson, S.A., W.L. Neal and J.R. Burnell. 1988. The effect of waste package components on radionuclides released from spent fuel under hydrothermal conditions. Materials Research Society Symposium Proceedings 112 (Scientific Basis for Nuclear Waste Management XI), 453-463.

Riskin, I.V., V.B. Torshin, Ya.B. Skuratnik and M.A. Dembrovsky. 1984. Corrosion of titanium by cathodic currents in chloride solutions. Corrosion 40, 266-271.

Roberson, H.E. and R.W. Lahann. 1981. Smectite to illite conversion rates: Effects of solution chemistry. Clays and Clay Minerals 29, 129-135.

Robin, M.J.L., R.W. Gillham and D.W. Oscarson. 1987. Diffusion of strontium and chloride in compacted clay-based materials. Soil Science Society of America Journal 51, 1102-1108.

Rothman, A.J. 1984. Potential corrosion and degradation mechanisms of Zircaloy cladding on spent nuclear fuel in a tuff repository. Lawrence Livermore National Laboratory Report, UCID-20172.

Ryan, S.R., C.F. Clarke, B.M. Ikeda, F. King, C.D. Litke, P. McKay and D.B. Mitton. 1994. An investigation of the long-term corrosion behaviour of selected nuclear fuel waste candidate container materials under possible disposal vault conditions. Atomic Energy of Canada Limited Technical Record, TR-489.*

Saadat, F., J. Graham and M.N. Gray. 1989. High pressure behavior of sand-bentonite buffer for nuclear fuel waste containment. In 42nd Canadian Geotechnical Conference, Materials: From Theory to Practice, Winnipeg, MB, 1989, 280-288.

Sawatsky, N.G. and D.W. Oscarson. 1991. Diffusion of technetium in dense bentonite under oxidizing and reducing conditions. Soil Science Society of America Journal 55, 1261-1267.

Schulz, R.K., R.W. Ridky and E. O'Donnell. 1989. Control of water infiltration into near surface LLW disposal units. U.S. Nuclear Regulatory Commission Report, NUREG/CR-4918, Volume 3.

Schutz, R.W. 1986. Titanium. In Titanium in Process Industry Corrosion - The Theory and Practice (B.J. Moniz and W.I. Pollock, editors), National Association of Corrosion Engineers, Houston, TX, 503-527.

Schutz, R.W. 1988. Titanium alloy crevice corrosion: Influencing factors and methods of prevention. In Proceedings of the Sixth International Conference on Titanium, Cannes, France, 1988, 1917-1922.

Schutz, R.W. 1991. A case for titanium's resistance to microbiologically influenced corrosion. Materials Performance 30, 58-61.

Schutz, R.W. and L.C. Covington. 1981. Effect of oxide films on the corrosion resistance of titanium. Corrosion 37, 585-591.

Schutz, R.W. and J.A. Hall. 1984. Optimization of mechanical/corrosion properties of TiCode-12 plate and sheet, Part 1: Compositional effects. Sandia National Laboratory Report, SAND-83-7438, Albuquerque, NM.

Schutz, R.W. and D.E. Thomas. 1987. Corrosion of titanium and titanium alloys. In Metals Handbook, ninth edition, Volume 13, Corrosion. ASM International, Metals Park, OH, p. 669.

Selvadurai, A.P.S. 1990. Heat-induced moisture movement within a clay-based sealing material. Engineering Geology 28, 325-335.

Sharland, S.M. and P.W. Tasker. 1988. A mathematical model of crevice and pitting corrosion - I. The physical model. Corrosion Science 28, 603-620.

Sharland, S.M., C.P. Jackson and A.J. Diver. 1989. A finite-element model of the propagation of corrosion crevices and pits. Corrosion Science 29, 1149-1166.

Sharma, H.D. and D.W. Oscarson. 1989. Diffusion of plutonium(IV) in dense bentonite-based materials. Materials Research Society Symposium Proceedings 127 (Scientific Basis for Nuclear Waste Management XII), 735-741.

Shimogori, K., H. Sato, F. Kamikubo and T. Fukuzuka. 1977. Corrosion resistance of titanium in a MSF desalination plant. Desalination 22, 403-413.

Shoesmith, D.W. and S. Sunder. 1991. An electrochemistry-based model for the dissolution of UO_2. Atomic Energy of Canada Limited Report, AECL-10488.

Shoesmith, D.W. and S. Sunder. 1992. The prediction of nuclear fuel (UO_2) dissolution rates under waste disposal conditions. Journal of Nuclear Materials 190, 20-35. Also Atomic Energy of Canada Limited Reprint, AECL-10677.

Shoesmith, D.W., S. Sunder, M.G. Bailey, G.J. Wallace and F.W. Stanchell. 1984. Anodic oxidation of UO_2. IV. X-ray photoelectron spectroscopic and electrochemical studies of film growth in carbonate-containing solutions. Applications of Surface Science 20, 39-57. Also Atomic Energy of Canada Limited Reprint, AECL-8174.

Shoesmith, D.W., S. Sunder, B.M. Ikeda and F. King. 1989. The development of a mechanistic basis for modelling fuel dissolution and container failures under waste vault conditions. Materials Research Society Symposium Proceedings 127 (Scientific Basis for Nuclear Waste Management XII), 279-291. Also Atomic Energy of Canada Limited Reprint, AECL-9827.

Shoesmith, D.W., B.M. Ikeda, D. Hardie, M.G. Bailey and C.F. Clarke. 1992. Impact of various parameters on the corrosion of titanium nuclear fuel waste containers under disposal conditions. In Proceedings of the Topical Meeting on Nuclear Waste Packaging, Focus '91, Las Vegas, NV, 1991, 193-200.

Shoesmith, D.W., F. King and B.M. Ikeda. In preparation (a). An assessment of the feasibility of indefinite containment for the Canadian Nuclear Fuel Waste Management Program. Atomic Energy of Canada Limited Report, AECL-10972.

Shoesmith, D.W., B.M. Ikeda and D.M. LeNeveu. In preparation (b). A model for predicting the lifetimes of Grade-2 titanium nuclear waste containers. Atomic Energy of Canada Limited Report, AECL-10973.

Sillen, L.G. and A.E. Martell. 1964, 1971. Stability constants of metal ion complexes. Special Publication 17, The Chemical Society, London (1964) and Supplement No. 1, Special Publication 25. (1971).

Simmons, G.R. and P. Baumgartner. 1994. The disposal of Canada's nuclear fuel waste: engineering for a disposal facility. Atomic Energy of Canada Limited Report, AECL-10715, COG-93-5.

Simpson, C.J. and C.E. Ells. 1974. Delayed hydrogen embrittlement in Zr-2.5 wt% Nb. Journal of Nuclear Materials 52, 289-295.

Simpson, J.P. and R. Schenk. 1989. Corrosion induced hydrogen evolution on high level waste overpack material in synthetic groundwaters and chloride solutions. Materials Research Society Symposium Proceedings 127 (Scientific Basis for Nuclear Waste Management XII), 389-396.

Skagius, K. and I. Neretnieks. 1985. Diffusion measurements of cesium and strontium in biotite gneiss. Swedish Nuclear Fuel and Waste Management Co. Report, SKB-TR-85-15.

Sommer, A.W. and D. Eylon. 1983. On fatigue crack propagation of titanium alloys under dwell time conditions. Metallurgical Transactions 14A, 2178-2181.

Sorensen, N.R. 1990. Laboratory studies of the corrosion and mechanical properties of titanium Grade-12 under WIPP repository conditions. In Corrosion of Nuclear Fuel Waste Containers, Proceedings of a Workshop, Winnipeg, MB, 1988, 29-44, Atomic Energy of Canada Limited Report, AECL-10121.

Sorensen, N.R. and J.A. Ruppen. 1985. The environmental cracking of TiCode-12 in aqueous chloride environments. Corrosion 41, 560-569.

Spinks, J.W.T. and R.J. Woods. 1964. An Introduction to Radiation Chemistry. John Wiley and Sons, New York, 2nd edition.

Stobbs, J.J. and A.J. Swallow. 1962. Effects of radiation on metallic corrosion. Metallurgical Reviews 7, 95-131.

Stroes-Gascoyne, S. 1989. The potential for microbial life in a Canadian high-level nuclear fuel waste disposal vault: a nutrient and energy source analysis. Atomic Energy of Canada Limited Report, AECL-9574.

Stroes-Gascoyne, S. 1992. Trends in the short-term release of fission products and actinides to aqueous solution from used CANDU fuels at elevated temperature. Journal of Nuclear Materials 190, 87-100. Also Atomic Energy of Canada Limited Reprint, AECL-10664.

Stroes-Gascoyne, S. and D.M. Sellinger. 1986. The effect of fuel power on the leaching of cesium and iodine from used CANDU fuel. In International Conference on CANDU Fuel, Conference Proceedings, Chalk River, Ontario, 1986, 383-400.

Stroes-Gascoyne, S., L.H. Johnson, P.A. Beeley and D.M. Sellinger. 1986. Dissolution of used CANDU fuel at various temperatures and redox conditions. Materials Research Society Symposia Proceedings 50 (Scientific Basis for Nuclear Waste Management IX), 318-326. Also Atomic Energy of Canada Limited Reprint, AECL-8889.

Stroes-Gascoyne, Simcha, Lawrence H. Johnson and Dennis M. Sellinger. 1987. The relationship between gap inventories of stable xenon, ^{137}Cs, and ^{129}I in used CANDU fuel. Nuclear Technology 77, 320-330.

Stroes-Gascoyne, S., L.H. Johnson, J.C. Tait and D.M. Sellinger. 1989. Leaching of whole, defected used CANDU™ fuel elements in saline solutions under argon pressure. Materials Research Society Symposium Proceedings 127 (Scientific Basis for Nuclear Waste Management XII), 301-308. Also Atomic Energy of Canada Limited Reprint, AECL-9591.

Stroes-Gascoyne, S., J.C. Tait, N.C. Garisto, R.J. Porth, J.P.M. Ross, G.A. Glowa and T.R. Barnsdale. 1992. Instant release of ^{14}C, ^{99}Tc, ^{90}Sr and ^{137}Cs from used CANDU fuel at 25°C in distilled deionized water. Materials Research Society Symposium Proceedings 257 (Scientific Basis for Nuclear Waste Management XV), 373-380. Also Atomic Energy of Canada Limited Reprint, AECL-10526.

Stroes-Gascoyne, S., J.C. Tait, R.J. Porth, J.L. McConnell, T.R. Barnsdale and S. Watson. 1993. Measurements of grain-boundary inventories of ^{137}Cs, ^{90}Sr and ^{99}Tc in used CANDU fuel. Materials Research Society Symposium Proceedings 294 (Scientific Basis for Nuclear Waste Management XVI), 41-46.

Sunder, S. and D.W. Shoesmith. 1991. Chemistry of UO_2 fuel dissolution in relation to the disposal of used nuclear fuel. Atomic Energy of Canada Limited Report, AECL-10395.

Sunder, S. and D.W. Shoesmith. 1992. Oxidative dissolution of used fuel due to the alpha radiolysis of water (FWTB-93-202). In Unpublished Documents Cited in the EIS and Primary References, Atomic Energy of Canada Limited Technical Record, TR-567,* COG-92-27.

Sunder, S., P. Taylor and J.J. Cramer. 1988. XPS and XRD studies of uranium rich minerals from Cigar Lake, Saskatchewan. Materials Research Society Symposium Proceedings 112 (Scientific Basis for Nuclear Waste Management XI), 465-472. Also Atomic Energy of Canada Limited Reprint, AECL-9469.

Sunder, S., G.D. Boyer and N.H. Miller. 1990. XPS studies of UO_2 oxidation by alpha radiolysis of water at 100°C. Journal of Nuclear Materials 175, 163-169. Also Atomic Energy of Canada Limited Reprint, AECL-10303.

Sunder, S., J.J. Cramer and N.H. Miller. 1992. X-ray photoelectron spectroscopic study of Cigar Lake uranium ore: a natural analog for used fuel. Materials Research Society Symposium Proceedings 257 (Scientific Basis for Nuclear Waste Management XV), 449-457. Also Atomic Energy of Canada Limited Reprint, AECL-10531.

TAC (Technical Advisory Committee on the Nuclear Fuel Waste Management Program (L.W. Shemilt, Chairman)). 1987. Eighth annual report. Technical Advisory Committee Report, TAC-8. (Available from Prof. L.W. Shemilt, McMaster University, Hamilton, ON L8S 4K1).

TAC (Technical Advisory Committee on the Nuclear Fuel Waste Management Program (L.W. Shemilt, Chairman)). 1993. Thirteenth annual report. Technical Advisory Committee Report, TAC-13. (Available from Prof. L.W. Shemilt, McMaster University, Hamilton, ON L8S 4K1).

Tait, J.C., D.L. Wilkin and R.F. Hamon. 1986. Gamma-radiolysis effects on leaching of nuclear fuel waste forms: Influence of groundwaters and granite on gaseous radiolysis products. Atomic Energy of Canada Limited Report, AECL-8731.

Tait, J.C., I.C. Gauld and G.B. Wilkin. 1989. Derivation of initial radionuclide inventories for the safety assessment of the disposal of used CANDU fuel. Atomic Energy of Canada Limited Report, AECL-9881.

Tait, J.C., S. Stroes-Gascoyne, W.H. Hocking, A.M. Duclos, R.J. Porth and D.L. Wilkin. 1991. Dissolution behaviour of used CANDU fuel under disposal conditions. Materials Research Society Symposium Proceedings 212 (Scientific Basis for Nuclear Waste Management XIV), 189-196. Also Atomic Energy of Canada Limited Reprint, AECL-10344.

Talbot, A. 1979. The accurate numerical inversion of Laplace transforms. Journal of the Institute of Mathematics and Its Applications 23, 97-120.

Tammemagi, H.Y., P.S. Kerford. J.C. Requeima and C.A. Temple. 1980. A geological reconnaissance study of the Lac du Bonnet batholith. Atomic Energy of Canada Limited Report, AECL-6439.

Teper, B. 1988. Test program of the prototype of the TWPP container. Part 3 - Detailed stress analysis and comparison with test results. Ontario Hydro Research Division Report, 87-296-K, available from Ontario Hydro, 800 Kipling Avenue, Toronto, Ontario, M8Z 5S4.

Teper, B. 1992. Residual shell thickness for SYVAC analyses. In Unpublished Documents Cited in the EIS and Primary References, Atomic Energy of Canada Limited Technical Record, TR-567/COG-92-27.*

Torresi, R.M., O.R. Camara and C.P. DePauli. 1987a. Hydrogen evolution reaction on anodic titanium oxide films. Electrochimica Acta 32, 1291-1301.

Torresi, R.M., O.R. Camara and C.P. DePauli. 1987b. Influence of the hydrogen evolution reaction on the anodic titanium oxide film properties. Electrochimica Acta 32, 1357-1363.

Torstenfelt, B. and B. Allard. 1986. Migration of fission products and actinides in compacted bentonite. Swedish Nuclear Fuel and Waste Management Co. Report, SKB-TR-86-14.

Tsai, A. 1993. Three dimensional thermal and thermo-mechanical analyses for the near-field of a disposal vault with the borehole emplacement option. Ontario Hydro Report, GHED-DR-8821, unrestricted report available from Ontario Hydro, 700 University Avenue, Toronto, Ontario, M5G 1X6.

Van Konynenburg, R.A., C.F. Smith, H.W. Culham and C.H. Otto. 1985. Behavior of carbon-14 in waste packages for spent fuel in a repository in tuff. Materials Research Society Symposium Proceedings 44 (Scientific Basis for Nuclear Waste Management VIII), 405-412.

Van Konynenburg, R.A., C.F. Smith, H.W. Culham and H.D. Smith. 1987. Carbon-14 in waste packages for spent fuel in a tuff repository. In Materials Research Society Symposium Proceedings 84 (Scientific Basis for Nuclear Waste Management X)), 185-196.

Velbel, M.A. 1985. Geochemical mass balances and weathering rates in forested watersheds of the southern Blue Ridge. American Journal of Science 285, 904-930.

Wackett, L.P., W.H. Orme-Johnson and C.T. Walsh. 1989. Transition metal enzymes in bacterial metabolism. In Metal Ions and Bacteria (T.S. Beveridge and R.J. Doyle, editors), John Wiley and Sons, New York, 165-206.

Wagman, D.D., W.H. Evans, V.B. Parker, R.H. Schumm, I. Halow, S.M. Bailey, K.L. Churney and R.L. Nuttall. 1982. The NBS tables of chemical thermodynamic properties. Journal of Physical Chemical Reference Data 11 Suppl. No. 2.

Walker, J.R. and D.M. LeNeveu. 1987. Nonlinear chemical sorption isotherms in the assessment of nuclear fuel waste disposal. Atomic Energy of Canada Limited Report, AECL-8394.

Wanner, H. 1987. Modeling interaction of deep groundwaters with bentonite and radionuclide speciation. Nuclear Technology 79, 338-347.

Wasywich, K.M. 1993. Characteristics of used CANDU fuel relevant to the Canadian Nuclear Fuel Waste Management Program. Atomic Energy of Canada Limited Report, AECL-10463, COG-91-340.

Wasywich, K.M., W.H. Hocking, D.W. Shoesmith and P. Taylor. 1993. Differences in oxidation behaviour of used CANDU fuel during prolonged storage in moisture-saturated air and dry air at 150°C. Nuclear Technology 104, 309-329.

Weaver, C.E. 1979. Geothermal alteration of clay minerals and shales: Diagenesis. Battelle Office of Nuclear Waste Isolation, Technical Report, ONWI-21.

Weber, M.F., L.C. Schumacher and M.J. Dignam. 1982. Effect of hydrogen on the dielectric and photoelectrochemical properties of sputtered TiO_2 films. Journal of the Electrochemical Society 129, 2022-2028.

Werme, L.O. and R.S. Forsyth. 1988. Spent UO_2 fuel corrosion in water; release mechanisms. Materials Research Society Symposium Proceedings 112 (Scientific Basis for Nuclear Waste Management XI), 443-452.

Werme, L.O., P. Sellin and R. Forsyth. 1990. Radiolytically induced oxidative dissolution of spent nuclear fuel. Swedish Nuclear Fuel and Waste Management Co. Report, SKB-TR-90-08.

Westerman, R.E. 1990. Hydrogen absorption and crevice corrosion behaviour of titanium Grade-12 during exposure to irradiated brine at 150°C. In Corrosion of Nuclear Fuel Waste Containers, Proceedings of a Workshop, Winnipeg, Manitoba, 1988, 67-84, Atomic Energy of Canada Limited Report, AECL-10121.

Westerman, R.E., S.G. Pitman and J.L. Nelson. 1982. General corrosion, irradiated corrosion and environmental-mechanical evaluation of nuclear waste package structural barrier materials. Pacific Northwest Laboratory Report, PNL-4364 (UC-70).

Wikberg, P. 1986. The assessment of reducing conditions at depth in granitic rock. Materials Research Society Symposia Proceedings 50 (Scientific Basis for Nuclear Waste Management IX), 137-144.

Wikberg, P. 1988. The natural chemical background conditions in crystalline rocks. Materials Research Society Symposium Proceedings 112 (Scientific Basis for Nuclear Waste Management XI), 373-382.

Wilkin, G.B. 1992. Source strength and shielding calculations for nuclear fuel waste disposal containers (NTB-85-289). In Unpublished Documents Cited in EIS and Primary References, Atomic Energy of Canada Limited Technical Record, TR-567,* COG-92-27.

Williams, D.N. 1962. The hydrogen embrittlement of titanium alloys. Journal of the Institute of Metals 91, 147-152.

Williams, D.N. 1974. Subcritical crack growth under sustained load. Metallurgical Transactions 5, 2351-2358.

Williams, D.N. 1975. Effect of specimen thickness on subcritical crack growth under sustained load. Materials Science and Engineering 18, 149-155.

Wilson, C.N. 1988. Summary of results from the Series 2 and Series 3 NNWSI bare fuel dissolution tests. 1988. Materials Research Society Symposium Proceedings 112 (Scientific Basis for Nuclear Waste Management XI), 473-483.

Wilson, C.N. and H.F. Shaw. 1987. Experimental study of the dissolution of spent fuel at 85°C in natural groundwater. Materials Research Society Symposium Proceedings 84 (Scientific Basis for Nuclear Waste Management X), 123-130.

Wisbey, S.J. 1986. Preliminary studies on the effect of radiolytic oxidation on radionuclide solubility. United Kingdom Atomic Energy Authority (Harwell Laboratory) Report, AERE-R-11992.

Wuschke, D.M., K.K. Mehta, K.W. Dormuth, T. Andres, G.R. Sherman, E.L.J. Rosinger, B.W. Goodwin, J.A.K. Reid and R.B. Lyon. 1981. Environmental and safety assessment studies for nuclear fuel waste management. Volume 3: Post-closure assessment. Atomic Energy of Canada Limited Technical Record, TR-127-3.*

Wuschke, D.M., P.A. Gillespie and D.E. Main. 1985a. Second interim assessment of the Canadian concept for nuclear fuel waste disposal. Volume 1: Summary. Atomic Energy of Canada Limited Report, AECL-8373-1.

Wuschke, D.M., P.A. Gillespie, K.K. Mehta, W.F. Heinrich, D.M. LeNeveu, V.M. Guvanasen, G.R. Sherman, D.C. Donahue, B.W. Goodwin, T.H. Andres and R.B. Lyon. 1985b. Second interim assessment of the Canadian concept for nuclear fuel waste disposal. Volume 4: Post-closure assessment. Atomic Energy of Canada Limited Report, AECL-8373-4.

Yao, L-A., F-X. Gan, Y-X. Zhao, C-L. Yao and J.L. Bear. 1991. Microelectrode monitoring the crevice corrosion of titanium. Corrosion 47, 420-423.

Yong, R.N. and B.P. Warkentin. 1975. Soil Properties and Behaviour. Elsevier, Amsterdam.

Yong, R.N., P. Boonsinsuk and G. Wong. 1986. Formulation of backfill material for a nuclear fuel waste disposal vault. Canadian Geotechnical Journal 23, 216-228.

Yong, R.N., A.M.O. Mohamed and S.C.H. Cheung. 1990. Thermal behaviour of backfill material for a nuclear fuel waste disposal vault. Materials Research Society Symposium Proceedings 176 (Scientific Basis for Nuclear Waste Management XIII), 649-656.

Yong, R.N., D.M. Xu, A.M.O. Mohamed and S.C.H. Cheung. 1992. An analytical technique for evaluation of coupled heat and mass flow coefficients in unsaturated soil. International Journal for Numerical and Analytical Methods in Geomechanics 16, 233-246.

Yourdon, E. 1989. Modern Structured Analysis. Yourdon Press, Englewood Cliffs, NJ.

---

* Internal report, available from SDDO, AECL Research, Chalk River Laboratories, Chalk River, Ontario K0J 1J0

LIST OF ACRONYMS

AECB	Atomic Energy Control Board
ASTM	American Society for Testing and Materials
BMT	buffer mass test
CANDU	CANada Deuterium Uranium (registered trademark of AECL)
CNFWMP	Canadian Nuclear Fuel Waste Management Program
CS	coupled solution
DOE	Department of Energy (U.S.)
EDZ	excavation-disturbed zone
EIS	Environmental Impact Statement
FCG	fast crack growth
GM	geometric mean
GSD	geometric standard deviation
HCB	highly compacted bentonite
HIC	hydrogen-induced cracking
IRF	instant-release fraction
KBS	Kärnbränslesäkerhet (Swedish Nuclear Fuel Safety Project)
LWR	light-water reactor
MIC	microbially induced corrosion
MT	mass transport
MTC	mass transfer coefficient
MW	molecular weight
OECD/NEA	Organization for Economic Cooperation/Nuclear Energy Agency
PTFE	polytetrafluoroethylene
QA	quality assurance
RBM	reference buffer material

SCC	stress-corrosion cracking
SCG	slow crack growth
SCSB	standard Canadian Shield brine
SCSSS	standard Canadian Shield saline solution
SEM	scanning electron microscopy
SHE	standard hydrogen electrode
SKB	Swedish Nuclear Fuel and Waste Management Company
SLC	sustained load cracking
TAC	Technical Advisory Committee
TDS	total dissolved solids
URL	Underground Research Laboratory
WIPP	Waste Isolation Pilot Plant (New Mexico)
WRA	Whiteshell Research Area
XPS	X-ray photoelectron spectroscopy
XRD	X-ray diffraction

LIST OF SYMBOLS

α^R	dispersion length in the rock
α^u	dissolution rate constant for UO_2
γ_c	clay density—the ratio of the dry mass of clay to the combined volume of clay and voids
γ_d	dry bulk density of the clay
$\delta(t)$	Dirac delta function
ϵ	porosity of a porous medium
ϵ^R	rock porosity
λ_i	decay constant of radionuclide i
μ	mean valve
μ^A	mean crevice corrosion rate associated with temperature t_1^A
μ^E	mean crevice corrosion rate associated with temperature t_1^E
μ_{r1}	mean value of the crevice corrosion rate for the period when the surface temperature of containers designated as hot is assumed to be at its first constant value
μ_{r2}	mean value of the crevice corrosion rate for the period when the surface temperature of containers designated as hot is assumed to be at its second constant value
σ	standard deviation
σ_{r1}	standard deviation of the crevice corrosion rate for the period when the surface temperature of containers designated as hot is assumed to be at its first constant value
σ_{r2}	standard deviation of the crevice corrosion rate for the period when the surface temperature of containers designated as hot is assumed to be at its second constant value
τ	pore geometry factor of a porous medium
τ^R	rock tortuosity
ψ_p	hydraulic pressure
ψ_z	elevation potentials
ψ_π	osmotic potential

∇h	hydraulic gradient
a^B	effectiveness thickness of the buffer
a^I	initial value of the distance into the buffer where a uranium precipitate forms
a_n	thickness of layer n
a^u	distance into the buffer where a uranium precipitate forms
A	plan area of the vault
A_k^A	fraction of containers designated as cool in sector k of vault
A^C	surface area of the container
A^D	fraction of containers that fail as a result of crevice corrosion during the period when container surface temperature is assumed to be at its second constant value
A_k^E	fraction of containers designated as cold in sector k of the vault
A^F	vault surface area
$A_i(t)$	amount of precipitate formed as a function of time for radionuclide i
A^N	fraction of containers that fail as a result of crevice corrosion during the period when container surface temperature is assumed to be at its first constant value
A_k^R	fraction of containers designated as hot in sector k of vault
C	concentration of a species in the pore water of a porous medium
C_b	bulk concentration on surface of sphere and plane
C_i	concentration of radionuclide i in pore water
$C_{ij}(a^B,t)$	contribution to the pore-water concentration at the exit from the buffer of radionuclide i, from the unit impulse input of precursor, j, as a function of time, t
$C_j(x,t)$	concentration of a radionuclide in a decay chain in the pore water of the medium (buffer or backfill) as a function of space and time, $1 \leq j \leq i$, where j is a precursor to radionuclide i in the decay chain
C_n	pore-water concentration in layer n

C^s	solubility of UO_2 in pore water (also Cu)
C_u	solubility of UO_2 in pore water (also C^s)
D	total intrinsic diffusion coefficient
D_a	apparent diffusion coefficient
D_i^B	total intrinsic diffusion coefficient of radionuclide i in the buffer
D_u^B	total intrinsic diffusion coefficient in the buffer for uranium species
D_i	total intrinsic diffusion coefficient in the medium for radionuclide i
D_n	total intrinsic diffusion coefficient in layer n
D_0	diffusivity of solute in bulk water - also called free-water diffusion coefficient
D_p	diffusion coefficient of a species in the pore water of a porous medium
D_u	total intrinsic diffusion coefficient of uranium species
E_h	oxidation potential in groundwater
E^P	redox potential in the buffer
E_X^P	maximum buffer redox potential
E_z	sampled potential used for calculating oxidation potential
E_I^z	redox potential at the used-fuel surface
E_M^z	minimum redox potential (= 0)
f_H^c	container failure rate due to hydrogen-induced cracking
$f_k^c(t)$	total container failure rate for sector k of the vault. It is the sum of the failure rates resulting from initial defects, crevice corrosion, and hydrogen-induced cracking.
f_m^c	maximum container failure rate for sector 11
f_{ij}^c	container failure rate response function for radionuclide i and precursor j
$f^c(t)$	container failure rate

$f_I^C(t)$ early failure rate of titanium containers due to initial defects

$f_M^C(t)$ container failure rate for the period when the surface temperture of containers is assumed to be at its first constant value

$f_P^C(t)$ container failure rate for the period when the container surface temperature is assumed to be at its second constant value

f_i^I fraction of the amount of radionuclide i in used fuel that is assumed to be released to the interior of the container immediately upon container failure; also called instant-release fraction of radionuclide i

f_u fraction of uranium released into a semi-infinite medium based on a constant source concentration of uranium and mass transport by diffusion

F_i^A release rate of radionuclide i to the buffer

$F_i(t)$ congruent release rate of radionuclide i from the used fuel

$F_i^T(t)$ release rate from the waste form of radionuclide i as modified by the container failure rate

$F^U(t)$ dissolution rate of the used-fuel matrix

F_i^W sum of instant- and congruent-release rate of radionuclide i from used fuel

F_j^W sum of instant- and congruent-release rate of precursor j from used fuel

$F_i^P(t)$ radionuclide release rate as determined by solubility and as modified by container failure rate

$F_i^S(t)$ radionuclide release rate from used fuel as determined by solubility and unmodified by container failure rate

$F_i^Y(x,t)$ release rate of radionuclide i

G^B thickness of buffer

$G_i^I(t)$ release rate of radionuclides in the fuel-sheath gaps and grain boundaries (instant radionuclides) from the interior of the container to the buffer; also called instant-release rate

$G_i^S(t)$ estimate of the initial instant-release rate from the waste for the entire vault

I^F fraction of containers that fail early as a result of initial defects

I_i	initial amount of radionuclide i in the vault
$I_i(t)$	amount of radionuclide i at time t
I°	a unit inventory
I_u	total amount of UO_2 in the vault
I_j^u	unit amount of radionuclide j
J	diffusive flux of a species in a medium
k	hydraulic conductivity
K_d	solid/liquid distribution coefficient in a porous medium
K^s	source mass transfer coefficient
K_i^B	mass transfer coefficient in the buffer for radionuclide i
K^C	convective mass transfer coefficient
K_n^D	steady-state diffusive mass transfer coefficient
K_i^F	radionuclide mass transfer coefficient in the backfill
K_i^P	perception mass transfer coefficient
K_{iT}	equilibrium constant at temperature T governing groundwater composition in contact with used fuel
m_i	fitting parameter for describing temperature dependence of k_{iT}
$M_p(t)$	total flux per unit surface area from a plane source into a semi-infinite one-dimensional medium integrated up to time t
$M_s(t)$	total flux per unit area from a spherical waste form into an infinite medium integrated up to time t
N^C	total number of containers in the vault
p^C	capacity factor of the container
p(w)	distribution in thickness of container corrosion allowance following crevice corrosion during the period when the container surface temperature is assumed to be at its first constant value
$P_{i-1}(t)$	contribution to $F_i^A(t)$ from the decay of a precipitated parent
P_1	normalization factor for crevice corrosion rate pertaining to the period when the container surface temperature is assumed to be at its first constant value

P_3 fraction of containers failing when the container surface temperature is assumed to be at its second constant value for an infinite duration of this value

q amount of a species associated with the solid phase of a porous medium

r capacity factor

r_i^B capacity factor of the radionuclide i in the buffer

r_n capacity factor in layer n

r_1^N crevice corrosion rate for the period when the surface temperature of containers designated as hot is assumed to be at its first constant value

r_2^N crevice corrosion rate for the period when the surface temperature of containers designated as hot is assumed to be at its second constant value

r^R capacity factor in the rock

r_u capacity factor of uranium species

R retardation factor

R^B random factor chosen such that E^P will be a uniform distribution between E_M^Z and E_M^P

$R_{ij}^B(t)$ release rate of radionuclide i from the buffer for a unit impulse input of precursor j into the buffer

R_i^P compartment model response for precipitation given by $\exp(-\lambda_i t)$

R_{ij} response of radionuclide i to the unit impulse input of precursor j

S_E Nernstian slope for temperature, T, at the container surface used for calculating oxidation potential

S_j input rate of precursor j

t time

t_H^A duration of failure from hydrogen-induced cracking for containers designated as cool

t_p^A time period of crevice corrosion for containers designated as cool

t_1^A time period over which the surface temperature of containers designated as cool is assumed to be at a single constant value

t_I^B	delay time in the buffer
t_H^E	duration of failure from hydrogen-induced cracking for containers designated as cold
t_p^E	time period of crevice corrosion for containers designated as cold
t_I^E	time period over which the surface temperature of containers designated as cold is assumed to be at a single constant value
t^F	period over which the failures in containers occur as a result of intial defects
t_p^R	estimated time of failure of the container on the basis of crevice corrosion
t_1^R	the time period over which the surface temperature of containers designated as hot is assumed to be at its first constant value
t_2^R	the time period over which the surface temperature of containers designated as hot is assumed to be at its second constant value
v	velocity of flow or Darcy velocity
v^B	Darcy velocity in the buffer
v^F	Darcy velocity in the backfill
v^R	Darcy velocity in the rock
V	volume of the container
V^A	ratio of volume to surface area of the container
w	length of the mass transfer zone
w^x	thickness of container corrosion allowance
x	distance variable
x_{ij}^j	Bateman coefficients
Y^m	complexing ligand for uranium solution species

APPENDIX A

RADIONUCLIDE INVENTORIES

CONTENTS

A.1 RADIONUCLIDE INVENTORIES

The sources for radiotoxic elements in a used-fuel bundle are the activation and fission products from the UO_2, from the activation of the Zircaloy sheath, and from the activation of impurities in both the fuel and the Zircaloy fuel sheath. The inventories for these elements in moles per kilogram initial uranium (not the total inventory in a vault) were calculated for a Bruce A reactor fuel, cooled for ten years, with a reference burnup of 685 $GJ \cdot kg^{-1}$ U using the ORIGEN-S radionuclide generation/depletion code (Tait et al. 1989). The inventories used in the vault model are summarized in Table A-1, which also gives the distribution functions chosen to allow for variability in radionuclide inventories. The half-lives of these nuclides are given in Table A-2. The radionuclides in Table A-1 were selected on the basis of a screening study by Goodwin and Mehta (in preparation).

The ORIGEN-S code (Hermann and Westfall 1984, Ryman 1984) was developed by Oak Ridge National Laboratories with the objective of producing reactor-specific, burnup-dependent cross-section libraries to provide bulk-property data on used nuclear fuels. A multicode comparison of selected source-term codes (ORIGEN2, ORIGEN-S, CINDER-2) has been performed to assess their abilities to predict inventories of light-water reactor (LWR) fuels (Hermann et al. 1989). These codes all agreed to within 30% in predicting fission-product inventories, while most predictions of actinides agreed to within 5%; several isotopes were identified where disagreement was greater than 30%.

A similar comparison was done between the ORIGEN-S code and the CANIGEN and WIMS codes for CANDU fuel (Tait et al. 1989). Predictions for the majority of fission products agreed to within 5%, although disagreement for a few nuclides was greater than 20%. For the actinides, agreement was generally better than 20%; however, for a few isotopes, disagreement was greater than 50%. A more complete discussion of the reasons for the discrepancies between these predictive codes can be found in Tait et al. (1989).

A comparison was made between inventory predictions from the ORIGEN2 code and analytical data for 33 radioisotopes in an LWR fuel (Roddy and Mailen 1987). Data for about half of the isotopes agreed with predictions to within 10%, 13 agreed to within 50%, and for 3 agreement was greater than 50%. Most of the important actinides and fission products fell in the first group.

Only a limited comparison of analytical isotopic data and code predictions has been made for CANDU fuel (Smith et al. 1987). However, a detailed comparison of the inventories predicted by the ORIGEN-S code with measured inventories for used Pickering CANDU fuel is in progress and results will be reported at a later date.

To allow for variability between code predictions and actual inventories, distribution functions were chosen for the ORIGEN-S radionuclide inventory data used in the vault model. For radionuclides that could be characterized by analysis, a lognormal distribution function was chosen, using the ORIGEN-S value as the geometric mean value. A geometric standard deviation

(GSD) was chosen for each mean inventory value. The GSDs ranged from 1.003 to 2.0, with the higher value representing 95% of the data falling within a factor of 4 of the mean value. The choice of the GSD was based on the type of accuracy observed from available characterization data on an LWR fuel using the ORIGEN2 code (Roddy and Mailen 1987). The LWR comparison was chosen to reasonably represent the type of agreement that might be expected between code predictions and analytical data. For radionuclides that were poorly characterized (either no experimental verification or poor agreement between a code and experimental results) a loguniform distribution was chosen with an upper and lower limit a factor of 10 from the ORIGEN-S inventory value. The inventory of ^{238}U, which is assumed to be accurate to within 0.03%, isotopes of ^{239}Pu, ^{237}Np, and ^{135}Cs, which are likely to be within 10% of a predicted value, and isotopes of ^{129}I, ^{3}H and ^{99}Tc, which were assumed to be within 50% of the predicted value, are examples of lognormal distributions. Poorly characterized isotopes, such as ^{125}Sb, or isotopes of low inventory, such as Ra, Po and Pb, were given loguniform distributions, where there is an equal probability that the inventory value lies anywhere within a range of a factor of 10 on either side of the predicted value.

For all fuel impurities and Zircaloy impurities, a loguniform distribution function was chosen with upper and lower limits a factor of 10 from the ORIGEN-S value. This includes the inventory of ^{14}C in the fuel, which is dependent on knowledge of the concentration of ^{14}N impurity in the fuel (since neutron activation of ^{14}N is the primary production path for ^{14}C). This impurity level is not known for each fuel, and thus the maximum permissible ^{14}N concentration allowed by fuel fabrication specifications was used to calculate the mean ^{14}C inventory.

For all lognormal distributions, a quantile upper and lower bound value was chosen. A complete description of the lognormal and loguniform probability distribution functions, the geometric mean and standard deviation and quantile bounds can be found in Stephens et al. (1989).

A.2 RADIOACTIVE DECAY AND BUILDUP IN THE VAULT MODEL

During transport, radionuclides will, of course, continue to undergo nuclear decay. The quantity of radionuclides in the system will therefore change with time as both buildup from precursor radionuclides and decay to daughter products occur. Radionuclides with short half-lives will decay completely during transport through the buffer.

The vault model was designed to deal with decay chains with any number of members; however, the chains used in the assessment calculations have been approximated by one- to four-member chains (Goodwin et al. 1994). This approximation saves computer resources and is not expected to have a significant effect on the results of the calculations. Thus, because of this approximation, some parent isotope inventories have been added to their daughter inventories. The inventories for ^{237}Np, ^{234}U and ^{232}U in Table A-1 are thus higher than those in Tait et al. (1989), and a lognormal distribution function was chosen.

REFERENCES

Goodwin, B.W. and K.K. Mehta. In preparation. Identification of contaminants of concern for the postclosure assessment of the concept for disposal of Canada's nuclear fuel waste. Atomic Energy of Canada Limited Report, AECL-10901, COG-93-265.

Goodwin, B.W., D.B. McConnell, T.H. Andres, W.C. Hajas, D.M. LeNeveu, T.W. Melnyk, G.R. Sherman, M.E. Stephens, J.G. Szekely, P.C. Bera, C.M. Cosgrove, K.D. Dougan, S.B. Keeling, C.I. Kitson, B.C. Kummen, S.E. Oliver, K. Witzke, L. Wojciechowski, and A.G. Wikjord. 1994. The disposal of Canada's nuclear fuel waste: postclosure assessment of a reference system. Atomic Energy of Canada Limited Report, AECL-10717, COG-93-7.

Hermann, O.W., R.M. Westfall. 1984. ORIGEN-S: SCALE system module to calculate fuel depletion, actinide transmutation, fission product buildup and decay, and associated radiation source terms. U.S. Nuclear Regulatory Commission Report, NUREG/CR-0200, Revision 2, Volume 2, Section F7.

Hermann, O.W., C.V. Parks, J.P. Renier, J.W. Roddy, R.C. Ashline, W.B. Wilson and R.J. LaBauve. 1989. Multicode comparison of selected source-term computer codes. Oak Ridge National Laboratory Report, ORNL/CSD/TM-251.

Roddy, J.W. and J.C. Mailen. 1987. Radiological characteristics of light-water reactor spent fuel: A literature survey of experimental data. Oak Ridge National Laboratory Report, ORNL/TM-10105.

Ryman, J.C. 1984. ORIGEN-S Data Libraries. Nuclear Regulatory Commission Report, NUREG/CR-0200, Revision 2, Volume 3, Section M6.

Smith, H.J., J.C. Tait and R.E. Von Massow. 1987. Radioactive decay properties of BRUCE 'A' CANDU™ UO_2 fuel and fuel recycle waste. Atomic Energy of Canada Limited Report, AECL-9072.

Stephens, M.E., B.W. Goodwin and T.H. Andres. 1989. Guidelines for defining probability density functions for SYVAC3-CC3 parameters. Atomic Energy of Canada Limited Technical Record, TR-479.*

Tait, J.C., I.C. Gauld, and G.B. Wilkin. 1989. Derivation of initial radionuclide inventories for the safety assessment of the disposal of used CANDU fuel. Atomic Energy of Canada Limited Report, AECL-9881.

---

* Internal report available from SDDO, AECL Research, Chalk River Laboratories, Chalk River, Ontario K0J 1J0

TABLE A-1

RADIONUCLIDE INVENTORIES (SOURCE TERMS) IN THE USED-FUEL VAULT MODEL USED IN SYVAC

Nuclide	Probability Distribution Function	Inventory (lower limit) ($mol \cdot kg^{-1}$ U)	Inventory (upper limit) ($mol \cdot kg^{-1}$ U)	Inventory Geometric Mean ($mol \cdot kg^{-1}$ U)	Geometric Standard Deviation	Lower Bound Quantile	Upper Bound Quantile
Actinide Products							
^{241}Am	lognormal			3.62×10^{-4}	1.5	0.00001	0.99999
^{242}Pu	lognormal			2.50×10^{-4}	1.1	0.00001	0.99999
^{241}Pu	lognormal			5.94×10^{-4}	1.1	0.00001	0.99999
^{240}Pu	lognormal			4.29×10^{-3}	1.1	0.00001	0.99999
^{239}Pu	lognormal			1.15×10^{-2}	1.1	0.00001	0.99999
^{238}Pu	lognormal			2.02×10^{-5}	1.1	0.00001	0.99999
^{237}Np	lognormal			1.12×10^{-3}	1.1	0.00001	0.99999
$^{238}U^{*}$	lognormal			4.14×10^{0}	1.003	0.001	0.999
^{236}U	lognormal			3.25×10^{-3}	1.1	0.00001	0.99999
$^{235}U^{*}$	lognormal			8.58×10^{-3}	1.1	0.00001	0.99999
$^{234}U^{*}$	lognormal			2.04×10^{-4}	1.1	0.00001	0.99999
^{233}U	lognormal			9.26×10^{-10}	2.0	0.00001	0.99999
^{232}U	loguniform	1.80×10^{-11}	1.80×10^{-9}				
^{233}Pa	loguniform	5.65×10^{-13}	5.65×10^{-11}				
^{231}Pa	loguniform	1.33×10^{-11}	1.33×10^{-9}				

* Original components of fuel

continued...

TABLE A-1 (continued)

Nuclide	Probability Distribution Function	Inventory (lower limit) ($mol \cdot kg^{-1}$ U)	Inventory (upper limit) ($mol \cdot kg^{-1}$ U)	Inventory Geometric Mean ($mol \cdot kg^{-1}$ U)	Geometric Standard Deviation	Lower Bound Quantile	Upper Bound Quantile
Actinide Products							
^{234}Th	lognormal			6.11×10^{-11}	2.0	0.00001	0.99999
^{232}Th	lognormal			9.99×10^{-10}	2.0	0.00001	0.99999
^{231}Th	lognormal			3.55×10^{-14}	2.0	0.00001	0.99999
^{230}Th	lognormal			5.52×10^{-9}	2.0	0.00001	0.99999
^{229}Th	lognormal			3.22×10^{-14}	2.0	0.00001	0.99999
^{228}Th	lognormal			3.91×10^{-12}	2.0	0.00001	0.99999
^{227}Th	lognormal			3.96×10^{-17}	2.0	0.00001	0.99999
^{227}Ac	loguniform	1.71×10^{-15}	1.71×10^{-13}				
^{225}Ac	loguniform	1.20×10^{-20}	1.20×10^{-18}				
^{228}Ra	loguniform	1.75×10^{-20}	1.75×10^{-18}				
^{226}Ra	loguniform	2.63×10^{-14}	2.63×10^{-12}				
^{225}Ra	loguniform	1.78×10^{-20}	1.78×10^{-18}				
^{224}Ra	loguniform	2.05×10^{-15}	2.05×10^{-13}				
^{223}Ra	loguniform	2.45×10^{-18}	2.45×10^{-16}				
^{222}Rn	loguniform	1.72×10^{-19}	1.72×10^{-17}				
^{210}Po	loguniform	6.31×10^{-19}	6.31×10^{-17}				
^{210}Bi	loguniform	2.28×10^{-20}	2.28×10^{-18}				
^{210}Pb	loguniform	3.71×10^{-17}	3.71×10^{-15}				

continued...

TABLE A-1 (continued)

Nuclide	Probability Distribution Function	Inventory (lower limit) ($mol \cdot kg^{-1}$ U)	Inventory (upper limit) ($mol \cdot kg^{-1}$ U)	Inventory Geometric Mean ($mol \cdot kg^{-1}$ U)	Geometric Standard Deviation	Lower Bound Quantile	Upper Bound Quantile
Fission Products							
^{3}H	lognormal			2.76×10^{-6}	1.5	0.00001	0.99999
^{79}Se	lognormal			1.64×10^{-5}	2.0	0.00001	0.99999
^{81}Kr	lognormal			6.73×10^{-11}	1.5	0.00001	0.99999
^{85}Kr	lognormal			3.69×10^{-5}	1.5	0.00001	0.99999
^{87}Rb	loguniform	6.31×10^{-5}	6.31×10^{-3}				
^{90}Sr	lognormal			1.13×10^{-3}	1.5	0.00001	0.99999
^{93}Zr	lognormal			1.81×10^{-3}	2.0	0.00001	0.99999
^{99}Tc	lognormal			2.07×10^{-3}	1.5	0.00001	0.99999
^{107}Pd	loguniform	5.08×10^{-5}	5.08×10^{-3}				
^{113m}Cd	loguniform	1.74×10^{-8}	1.74×10^{-6}				
^{125}Sb	loguniform	1.87×10^{-7}	1.87×10^{-5}				
^{126}Sn	lognormal			3.92×10^{-5}	2.0	0.00001	0.99999
^{129}I	lognormal			3.47×10^{-4}	1.5	0.00001	0.99999
^{135}Cs	lognormal			1.76×10^{-4}	1.5	0.00001	0.99999

continued...

TABLE A-1 (continued)

Nuclide	Probability Distribution Function	Inventory (lower limit) (mol·kg^{-1} U)	Inventory (upper limit) (mol·kg^{-1} U)	Inventory Geometric Mean (mol·kg^{-1} U)	Geometric Standard Deviation	Lower Bound Quantile	Upper Bound Quantile
Fuel Impurities							
^{3}H	loguniform	1.50×10^{-11}	1.50×10^{-9}				
^{10}Be	loguniform	8.54×10^{-11}	8.54×10^{-9}				
^{14}C	loguniform	1.84×10^{-6}	1.84×10^{-4}				
^{32}Si	loguniform	1.52×10^{-15}	1.52×10^{-13}				
^{39}Ar	loguniform	2.03×10^{-11}	2.03×10^{-9}				
^{40}K	loguniform	2.21×10^{-8}	2.21×10^{-6}				
^{41}Ca	loguniform	1.31×10^{-7}	1.31×10^{-5}				
^{59}Ni	loguniform	3.55×10^{-7}	3.55×10^{-5}				
^{63}Ni	loguniform	5.98×10^{-8}	5.98×10^{-6}				
^{93}Mo	loguniform	1.62×10^{-10}	1.62×10^{-8}				
^{99}Tc	loguniform	1.69×10^{-9}	1.69×10^{-7}				

continued...

TABLE A-1 (continued)

Nuclide	Probability Distribution Function	Inventory (lower limit) (mol·kg^{-1} U)	Inventory (upper limit) (mol·kg^{-1} U)	Inventory Geometric Mean (mol·kg^{-1} U)	Geometric Standard Deviation	Lower Bound Quantile	Upper Bound Quantile
Zircaloy Impurities							
^{3}H	loguniform	3.20×10^{-12}	3.20×10^{-10}				
^{10}Be	loguniform	1.67×10^{-11}	1.67×10^{-9}				
^{14}C	loguniform	3.27×10^{-7}	3.27×10^{-5}				
^{32}Si	loguniform	3.88×10^{-16}	3.88×10^{-14}				
^{59}Ni	loguniform	1.02×10^{-7}	1.02×10^{-5}				
^{63}Ni	loguniform	1.73×10^{-8}	1.73×10^{-6}				
^{93}Mo	loguniform	2.51×10^{-10}	2.51×10^{-8}				
^{93}Zr	lognormal			1.95×10^{-4}	2.0	0.00001	0.99999
^{94}Nb	loguniform	6.40×10^{-8}	6.40×10^{-6}				
^{99}Tc	loguniform	2.63×10^{-9}	2.63×10^{-7}				
^{125}Sb	loguniform	1.12×10^{-8}	1.12×10^{-6}				
^{182}Hf	loguniform	2.20×10^{-9}	2.20×10^{-7}				
^{187}Re	loguniform	2.69×10^{-7}	2.69×10^{-5}				
^{205}Pb	loguniform	2.29×10^{-10}	2.29×10^{-8}				
^{208}Bi	loguniform	9.66×10^{-15}	9.66×10^{-13}				
^{210m}Bi	loguniform	1.44×10^{-13}	1.44×10^{-11}				

continued...

TABLE A-1 (concluded)

Nuclide	Probability Distribution Function	Inventory (lower limit) ($mol \cdot kg^{-1}$ U)	Inventory (upper limit) ($mol \cdot kg^{-1}$ U)	Inventory Geometric Mean ($mol \cdot kg^{-1}$ U)	Geometric Standard Deviation	Lower Bound Quantile	Upper Bound Quantile
Chemical Toxics							
Br	loguniform	6.56×10^{-6}	6.56×10^{-4}				
Cd	loguniform	1.18×10^{-5}	1.18×10^{-3}				
Cr	loguniform	1.56×10^{-3}	2.99×10^{-3}				
Cs	lognormal			4.20×10^{-3}	1.1	0.00001	0.99999
Mo	lognormal			8.23×10^{-3}	2.0	0.00001	0.99999
Sb	loguniform	1.99×10^{-6}	1.99×10^{-4}				
Sm	lognormal			1.46×10^{-3}	2.0	0.00001	0.99999
Tc	lognormal			2.07×10^{-3}	1.5	0.00001	0.99999

TABLE A-2

RADIONUCLIDE HALF-LIVES USED IN SYVAC

Actinides		Fission Products		Fuel/Zircaloy Impurities	
Nuclide	Half-Life (a)	Nuclide	Half-Life (a)	Nuclide	Half-Life (a)
^{210}Pb	2.23×10^{1}	^{3}H	1.24×10^{1}	^{3}H	1.24×10^{1}
^{210}Bi	1.37×10^{-2}	^{79}Se	6.50×10^{4}	^{10}Be	1.60×10^{6}
^{210}Po	3.79×10^{-1}	^{81}Kr	2.10×10^{5}	^{14}C	5.73×10^{3}
^{222}Rn	1.05×10^{-2}	^{85}Kr	1.07×10^{1}	^{32}Si	4.50×10^{2}
^{223}Ra	3.13×10^{-2}	^{87}Rb	4.70×10^{10}	^{39}Ar	2.69×10^{2}
^{224}Ra	1.00×10^{-2}	^{90}Y	7.30×10^{-3}	^{40}K	1.28×10^{9}
^{225}Ra	4.05×10^{-2}	^{90}Sr	2.91×10^{1}	^{41}Ca	1.40×10^{5}
^{226}Ra	1.60×10^{3}	^{93}Zr	1.53×10^{6}	^{59}Ni	7.50×10^{4}
^{228}Ra	5.75	^{99}Tc	2.13×10^{5}	^{63}Ni	9.60×10^{1}
^{225}Ac	2.74×10^{-2}	^{107}Pd	6.50×10^{6}	^{93}Zr	1.53×10^{6}
^{227}Ac	2.18×10^{1}	^{113m}Cd	1.36×10^{1}	^{93}Mo	3.50×10^{3}
^{227}Th	5.12×10^{-2}	^{125}Sb	2.77	^{94}Nb	2.03×10^{4}
^{228}Th	1.91	^{126}Sn	1.00×10^{5}	^{99}Tc	2.13×10^{5}
^{229}Th	7.34×10^{3}	^{129}I	1.57×10^{7}	^{125}Sb	2.77
^{230}Th	7.70×10^{4}	^{135}Cs	2.30×10^{6}	^{182}Hf	9.00×10^{6}
^{231}Th	2.91×10^{-3}			^{187}Re	5.00×10^{10}
^{232}Th	1.40×10^{10}			^{205}Pb	1.43×10^{7}
^{234}Th	6.60×10^{-2}			^{208}Bi	3.68×10^{5}
^{231}Pa	3.28×10^{4}			^{210m}Bi	3.00×10^{6}
^{233}Pa	7.39×10^{-2}				
^{232}U	7.20×10^{1}				
^{233}U	1.58×10^{5}				
^{234}U	2.44×10^{5}				
^{235}U	7.04×10^{8}				
^{236}U	2.34×10^{7}				
^{238}U	4.47×10^{9}				
^{237}Np	2.14×10^{6}				
^{238}Pu	8.77×10^{1}				
^{239}Pu	2.41×10^{4}				
^{240}Pu	6.54×10^{3}				
^{241}Pu	1.44×10^{1}				
^{242}Pu	3.76×10^{5}				
^{241}Am	4.32×10^{2}				

APPENDIX B

DATA AND CALCULATIONS DESCRIBING GAS SOLUBILITIES AND TRANSPORT IN VAULT GROUNDWATER

CONTENTS

B.1 INITIAL CONDITIONS AND BACKGROUND GAS CONCENTRATIONS IN GROUNDWATER

The void volume per container can be summarized as follows:

(i) particulate in container 192 L (0% saturation at emplacement)

(ii) sand layer surrounding container 342 L (0% saturation at emplacement)

(iii) buffer material 400 L (80% saturation at emplacement)

(iv) overlying backfill 8000 L (80% saturation at emplacement)

The gas volume per container = 0.2 [(iii) + (iv)] + (i) + (ii)
= 2200 L (at 0.1 MPa).

The total dissolved N_2 in the ~9000-L void space per container is the sum of the following three quantities:

(i) the amount in the gas phase within the container, buffer and backfill, i.e.,

$$= 0.8\ [\text{gas vol. per container (2200 L)}]\left[\frac{1\ \text{mol}}{24.5\ \text{L}}\right] = 71.8\ \text{mol}$$

(ii) the amount dissolved in the pore water present in the buffer and backfill materials at emplacement, i.e.,

$$6800\ \text{L}[\text{solubility of } N_2 \text{ at 0.1 MPa } (7 \times 10^{-4}\ \text{mol/L})] = 4.8\ \text{mol}$$

(iii) the amount dissolved in groundwater (40 mL N_2/L H_2O (Gascoyne 1992)) that flows from the surrounding rock into the buffer and backfill, i.e.,

$$\left[\text{average } N_2 \text{ conc. in groundwater } \left[\frac{40\ \text{mL } N_2}{\text{L } H_2O}\right]\right]\left[2200\ \text{L}\right]\left[\frac{0.001\ \text{mol}}{24.5\ \text{mL}}\right] = 3.6\ \text{mol}$$

Therefore, the concentration of N_2 in the pore water in the vault after complete saturation would be

$$\frac{80\ \text{mol}}{9000\ \text{L}} \simeq 9 \times 10^{-3}\ \frac{\text{mol}}{\text{L}}\ .$$

This is well below the solubility at 5 MPa (2.3×10^{-2} mol·L^{-1} at 80°C (Himmelblau 1960)). As a result, although N_2 degassing to form a gas phase may occur temporarily prior to restoration of the water table, the N_2 should redissolve under the increasing hydrostatic pressure.

Other relevant gas solubility data are summarized below.

- Concentrations of H_2 and CH_4 are close to the detection limit (0.00 to 0.5 mL/L H_2O) in WRA groundwater at a depth of 500 m (Gascoyne 1992).

- The solubility of H_2 in pure water at 5 MPa (60°C) = 3.7×10^{-2} mol·L^{-1} (Himmelblau 1960).

- The solubility of CH_4 in pure water at 5 MPa (60°C) = 4.6×10^{-2} mol·L^{-1} (Himmelblau 1960).

(Note: The suppression of gas solubilities due to "salting out" is ignored in these calculations.)

B.2 MAXIMUM TRANSPORT RATE OF GAS THROUGH OVERLYING ROCK

At steady state, the maximum diffusive flux of dissolved gas through a plane layer of porosity ϵ and thickness h, with gas at saturation on one side and maintained at zero concentration in water at the other side of the layer, is given by

$$Q_D = \frac{D_g C_g A \epsilon}{h}$$

where D_g is the diffusion coefficient for the dissolved gas in water (10^{-3} $m^2 \cdot a^{-1}$ for H_2),

C_g is the solubility of the gas at vault depth,

A is the planar area of the overlying rock per container (21 m^2),

ϵ is the porosity of the rock (10^{-3}), and

h is the thickness of the rock layer (500 m).

For H_2, $Q_D \simeq 1 \times 10^{-6}$ mol·a^{-1}.

B.3 RATES OF HYDROGEN PRODUCTION PER CONTAINER AS A RESULT OF UNIFORM CORROSION OF ZIRCALOY AND TITANIUM

The rates of hydrogen production as a result of uniform corrosion of Zircaloy and Ti can be summarized as follows:

- the corrosion rate of Ti (Mattsson and Olefjord 1984) = 2×10^{-3} $\mu m \cdot a^{-1}$,

- the surface area of Ti per container = 4.7 m^2,

- the rate of H_2 production from Ti corrosion = 1.8×10^{-3} mol·a^{-1}, assuming

  $Ti + 2H_2O = TiO_2 + 2H_2$,

- the corrosion rate of Zircaloy (by analogy with Ti) = 2×10^{-3} μm·a^{-1},

- the surface area of fuel sheath per container = 55.7 m^2, and

- the rate of H_2 production from Zircaloy corrosion = 1.6×10^{-2} mol·a^{-1}.

B.4 PRODUCTION RATES OF HYDROGEN RESULTING FROM GAMMA AND ALPHA RADIOLYSIS OF WATER

B.4.1 GAMMA RADIOLYSIS

The estimated hydrogen production rate at emplacement for a surface dose rate of 9.7 Gy·h^{-1} = 8×10^{-3} mol·a^{-1} (Christensen and Bjergbakke 1982). Note that this would decrease by a factor of 10^4 in 500 a.

B.4.2 ALPHA RADIOLYSIS

Data relevant to the production of H_2 by alpha radiolysis of water can be summarized as follows:

- the primary yield of H_2 ($G(H_2)$) = 1.3,

- the H_2 production rate (no recombination) = 3.5×10^{-15} mol·cm^{-2}·s^{-1},

- the production rate per container (no recombination) = 0.48 mol·a^{-1}, and

- the H_2 production rate (including effect of the Fe^{2+}/Fe^{3+} couple acting as a recombiner) = 9×10^{-3} mol·a^{-1} (Christensen and Bjergbakke 1982, Garisto 1992).

B.5 TIME TO SATURATION OF NEAR FIELD WITH H_2

Because the production rate greatly exceeds the rate at which dissolved H_2 can diffuse away, the time (t) to saturation can be estimated using the following equation, assuming a mean container lifetime of 1500 a:

$$\frac{r_1(t - t_0) + r_2(t - t_0) + r_3 t}{V} = b$$

where $r_1 = 9 \times 10^{-3}$ mol·a^{-1} of H_2
$r_2 = 1.6 \times 10^{-2}$ mol·a^{-1} of H_2
$r_3 = 1.8 \times 10^{-3}$ mol·a^{-1} of H_2
$t \simeq 18\ 000$ a
$t_0 = 1500$ a
$V = 9000$ L (void space per container), and
$b = 3.7 \times 10^{-2}$ mol·L^{-1} of H_2.

REFERENCES

Christensen, H. and Bjergbakke, E. 1982. Radiolysis of ground water from spent fuel. Swedish Nuclear Fuel Supply Co. Report, SKBF-KBS-TR-82-18.

Garisto, F. 1992. Some notes on H_2 production in the vault. Research Chemistry Branch Memorandum RCB-92-128. In Unpublished Documents Cited in the EIS and Primary References, Atomic Energy of Canada Limited Technical Record, TR-567*, COG-92-27.

Gascoyne, M. 1992. Fuel Waste Technology Branch Memorandum. In Unpublished Documents Cited in the EIS and Primary References, Atomic Energy of Canada Limited Technical Record, TR-567,* COG-92-27.

Himmelblau, D.M. 1960. Solubilities of inert gases in water. Journal of Chemical and Engineering Data 5, 10-15.

Mattsson, H. and Olefjord, I. 1984. General corrosion of Ti in hot water and water-saturated bentonite clay. Swedish Nuclear Fuel and Waste Management Co. Report, SKB-KBS-TR-84-19.

* Internal report, available from SDDO, AECL Research, Chalk River Laboratories, Chalk River, Ontario K0J 1J0

APPENDIX C

ANALYSIS OF CONTAINER TEMPERATURE PROFILES

C.1 ANALYSIS OF CONTAINER TEMPERATURE PROFILES

Each container within the conceptual vault would possess a different temperature profile (Section 4.5). However, the similarity in the shapes of these profiles (Figure 4-2) means that the change in temperature for all containers can be represented by a small number of similar cooling functions. This categorization according to cooling behaviour has been achieved by dividing the containers into three groups, based on the calculated distribution in container temperatures after 500 a of cooling (Figure C-1). A time of 500 a was chosen because it is in the slow cooling period when container temperatures remain relatively constant and within which containers spend the large majority of their time for temperatures above ambient (see Figure 4-2). The shape of this distribution at 500 a suggests three groupings of containers:

- containers, designated hot, whose temperature remains above 54°C at 500 a,
- containers, designated cold, which have cooled to below 38.5°C by 500 a, and
- containers, designated cool, with temperatures between 38.5°C and 54°C at 500 a.

The separation of containers into these three groups is evident in Figure C-1, but the selection of 54°C and 38.5°C as the boundaries between groups is somewhat arbitrary and some containers could be more appropriately categorized. However, attempts to identify and move such containers between categories has only a minor effect on the averaging procedure described below.

For containers designated hot, the cooling profile is approximated by a two-level step function, the first level corresponding to the early hot period and the second level to the slow cooling period (Figure 4-13a).

To determine the temperature that defines the first level, the container temperatures at 27 a, a time around which most containers are close to their maximum temperature (Section 3.2.1), are averaged. This average temperature, and its associated $\pm 1\sigma$ value (assuming a normal distribution), $T_1 \pm \sigma_{T1}$, is then attributed to all containers in this category. A similar temperature mean ($T_2 \pm \sigma_{T2}$), calculated at 500 a, is attributed to all containers to define the second level. The mean of these two average temperatures is taken as a transition temperature between the first and second levels of the step function. The mean time of this transition ($t_{r1} \pm \sigma_{t1}$) is then determined by taking the average of the times at which the containers cool to this transition temperature. The same procedure is used to determine the final transition, marking the change from crevice corrosion to hydrogen-induced cracking (HIC) as the predominant failure mode. In this case, the transition temperature is taken as 30°C and the average time at which the containers cool to 30°C ($t_{r2} \pm \sigma_{t2}$) is the transition time. The reasons for selecting 30°C as the temperature for defining this final transition time are given in Section 4.6.4.1.

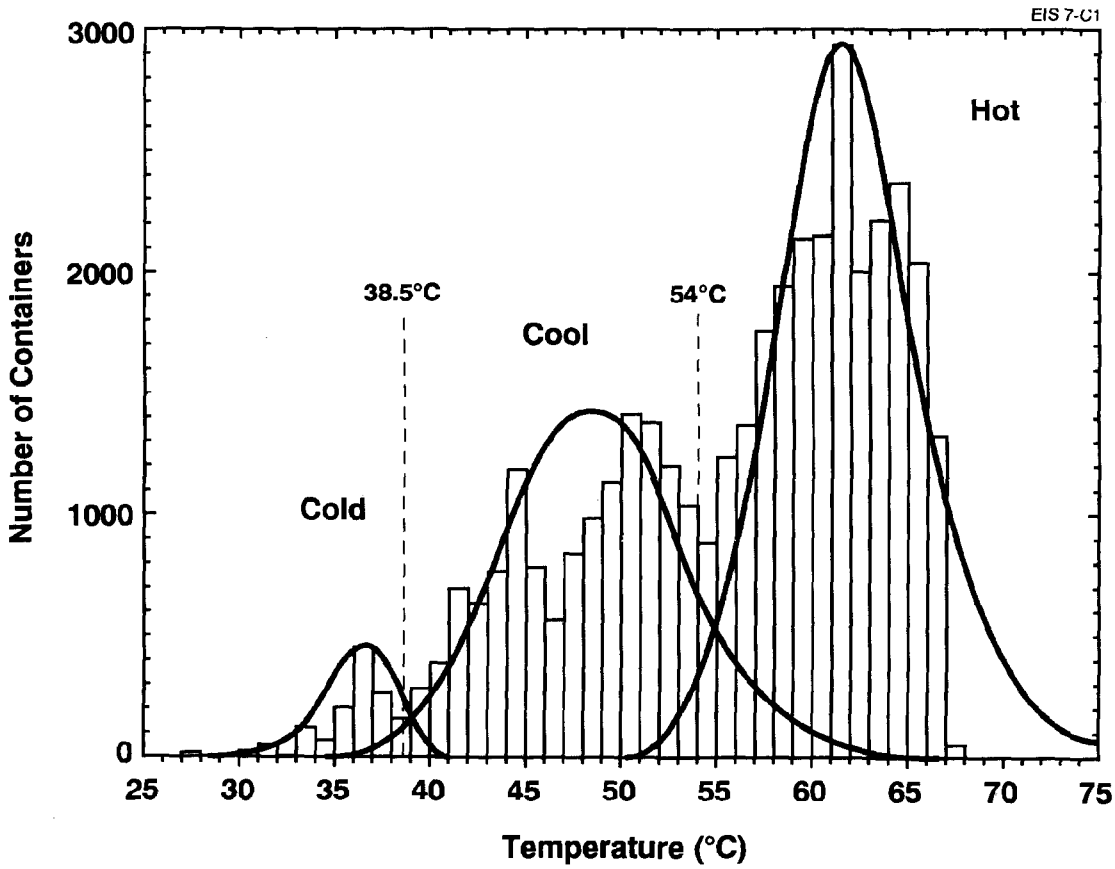

FIGURE C-1: Calculated Distribution of Container Temperatures 500 a After Emplacement. This distribution is approximated by the three normal distributions shown. Hot containers are defined as those whose temperature remains above 54°C at 500 a; cold containers are defined as those that have cooled to <38.5°C at 500 a; cool containers are defined as those with temperatures in the range 54°C to 38.5°C at 500 a.

Figure C-2 summarizes the parameters defining the shape of the two-level step function used to determine the effect of temperature on the crevice corrosion of those containers designated as hot. A calculated temperature profile for one of the hottest containers in the vault is shown to illustrate the conservatism entrenched in this averaging procedure.

Since cooling is more rapid for cool and cold containers than for hot containers, the early hot period is ignored and the temperature profiles approximated by single-step functions. The average temperature, calculated at 500 a, defines the step function for cool containers. Since cold containers cool rapidly, the average temperature to define the step function is calculated for 100 a. As a consequence of this averaging at shorter times, the cold containers appear to be hotter than the cool containers. The final transition time, marking the change from crevice corrosion

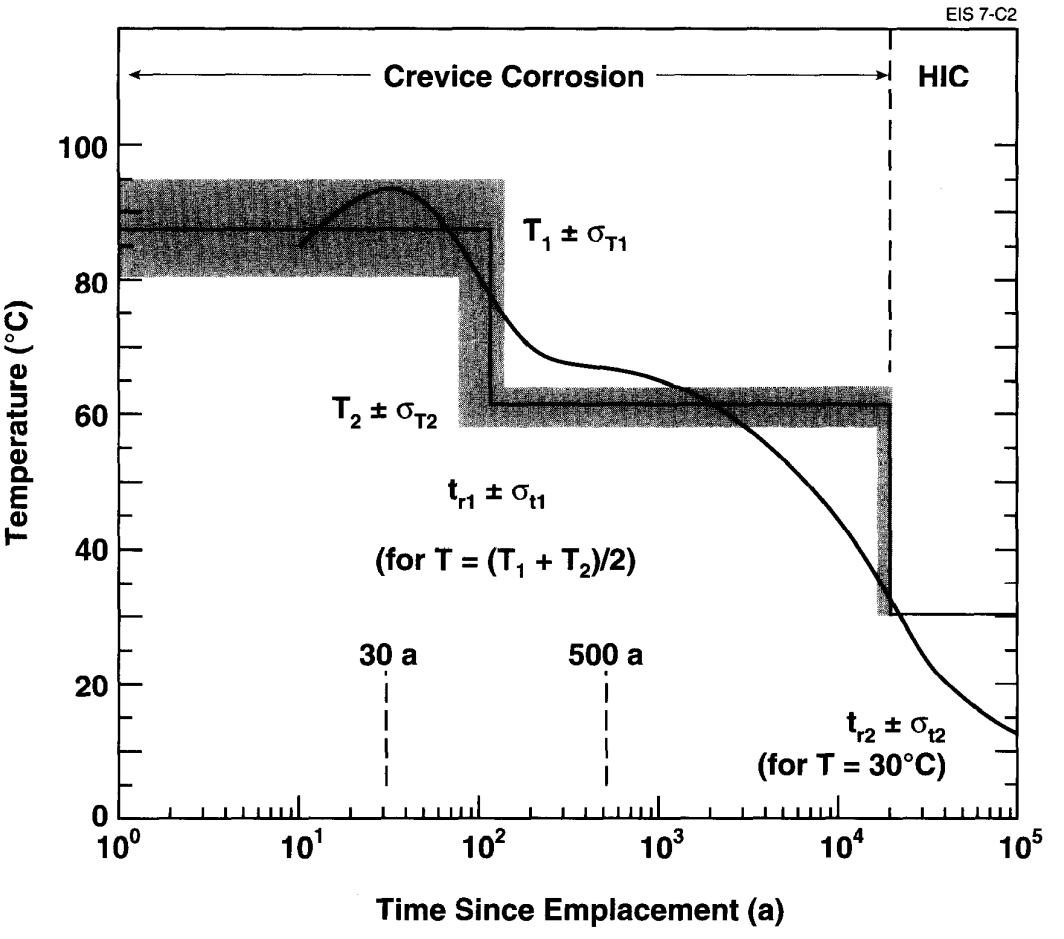

FIGURE C-2: Schematic Summarizing the Temperature and Time Parameters Used to Define the Shape of the Two-Level Temperature Step Function Used for Hot Containers. A calculated temperature profile for one of the hottest containers is also shown.

to HIC as the predominant failure mode, is obtained for both cool and cold containers by determining the average time at which the containers cool to 30°C. For cold containers, this average time is used as the apex of the triangular distribution used to describe HIC failure times.

The temperatures and transition times calculated for the step functions defining all three categories of container are given in Table 4-3. These values are plotted in Figures 4-13a, 4-13b and 4-13c and compared with a number of real profiles that define the range of profiles used in the averaging procedure for each category of container. For containers designated cool and cold; the lack of conservatism that arises from ignoring the initial hot period is compensated for by the overestimate of the temperature during the slow cooling period (Figures 4-13b and 4-13c).

APPENDIX D

THE EFFECT OF ORGANIC COMPLEXATION ON URANIUM CONCENTRATIONS IN THE VAULT

CONTENTS

D.1 INTRODUCTION

The vault model code has been written to permit inclusion of data on complexation of uranium by two unspecified organic complexes. A lack of data on the nature of, and equilibrium constants for, organic ligands that may be present in the contact water, however, precludes the use of this option. Nonetheless, some information on uranium complexation exists that permits simplified calculations to be performed to evaluate whether or not the exclusion of organic complexation of uranium from the vault model is a significant omission.

D.2 COMPLEXING CAPACITIES OF ORGANICS IN GROUNDWATERS

The concentration of dissolved organic matter in groundwaters has been measured in a variety of subsurface environments. For granitic groundwaters in Sweden, values of 1 to 8 $mg \cdot L^{-1}$ have been reported (Swedish Nuclear Fuel Supply Co. 1983). The complexing capacity of such groundwaters has been estimated to be 10^{-5} to 10^{-6} $eq \cdot L^{-1}$. For saline groundwaters in the Canadian Shield, values of 1 to 4 $mg \cdot L^{-1}$ have been reported, with complexing capacities ranging from 2×10^{-7} to 6×10^{-5} $eq \cdot L^{-1}$ (Tessman and Barker 1985). For shallower groundwaters from the Shield, including values from overlying sediments, values up to 28 $mg \cdot L^{-1}$ have been reported. It is emphasized, however, that there is no apparent correlation between complexing capacity and dissolved organic carbon concentrations (Tessman and Barker 1985). The organic matter concentration in the pore water of Avonlea bentonite buffer material has not been measured; however, it is unlikely to differ significantly from the values noted above. For the calculation of complexation of uranium by organic matter, we have assumed a complexing capacity of 7×10^{-6} $eq \cdot L^{-1}$, a typical value from the range suggested by Choppin (1988) for carboxylate ligands in humates and fulvates.

Although, as is shown in the calculations, there are some combinations of conditions that could lead to organic complexes of uranium reaching concentrations that are of the same order of magnitude as inorganic uranium complexes, it is emphasized that there are other factors that would have a significant influence on whether or not this would occur. In particular, the mobility of humates in compacted clays is expected to be very low. For example, studies of the diffusion of large organic molecules through highly compacted clays indicate that diffusion coefficients are several orders of magnitude lower than those of uranium and mono- and divalent cations (see Section 3.4.3). As a result, even if some complexation were to occur, the rate of supply of humates to the fuel as well as the rate of migration of complexed uranium (or other radionuclides) away from the fuel would be severely limited by the slow diffusion of these species in buffer material.

D.3 ESTIMATION OF REALISTIC EQUILIBRIUM CONSTANTS

Because of the nature of humic materials, it is not possible to define unique thermodynamic parameters for the interaction of "humic acid" with uranium in solution. The apparent protonation constants of the large molecular weight polyelectrolytes that are referred to as humic acid vary with pH, as do the binding constants, β_i, of the humates with a particular cation, the number of acid groups per gram of sample and the pH value at which the degree of ionization, α, equals 0.5. Data for fulvic acids are not as extensive, and, since the complexation of humates and fulvates is generally similar, only humate complexes are considered here.

There have been a number of experimental studies of the association of UO_2^{2+} with humates (Choppin 1988, Shanbhag and Choppin 1981). The reported values for $\log_{10}\beta_1$ range from 5.0 at pH 4 to 6.7 at pH 6. (The value 4.11 quoted by Choppin (1988) appears to be a misquotation of the 5.11 value (α = 0.47, pH = 4) reported by Shanbhag and Choppin (1981)). The smaller values are for values of $\alpha \ll 1.0$ and are actually reasonable upper limits for $\log_{10}\beta_1$ at pH 4 (where $\alpha \leq 0.5$). Similarly, an upper limit for $\log_{10}\beta_2$ at this pH can be set at 9.0. For pH values $\geq$7, it is reasonable to assume that $\alpha \simeq 1$. As shown by Nash and Choppin (1980), on the basis of electrostatic considerations, the values of $\log_{10}\beta_1$ and $\log_{10}\beta_2$ would be expected to increase by 4 as α varies from 0.0 to 1.0. In fact, for other humates, the increase is slightly less than this theoretical value, and an increase of 3.5 is not unreasonable. Thus, for pH values from 7 to 10, $\log_{10}\beta_1$ = 8 and $\log_{10}\beta_2$ = 12 are satisfactory values, similar to $\log_{10}\beta_1$ = 7.6 and $\log_{10}\beta_2$ = 11.5 estimated by Shanbhag and Choppin (1981) for pH 8, and larger than those reported for pH 6 by Li et al. (1980), although it is not clear if hydrolysis effects were treated adequately in the latter study. The source of the much higher values shown in Figure 5 of Choppin (1988) (which are not consistent with the values in Table 3 of the same reference) is not clear.

Thorium(IV) provides a satisfactory model for U(IV) with respect to the formation of humate complexes. The values for $\log_{10}\beta_i$ for pH 3.95, α = 0.25 (Li et al. 1980) are accepted for pH 4, as is the slope of log β_i versus α, which is used to obtain $\log_{10}\beta_1$ = 16.2 and $\log_{10}\beta_2$ = 21.2 for pH $\geq$ 7 (α = 1.0). Reasonable values for $\log_{10}\beta_1$ and $\log_{10}\beta_2$ for pH values between 4 and 7 are estimated by assuming a linear relationship. The estimated $\log_{10}\beta$ values used in the calculations described below are summarized in Table D-1. The effective pK_a of the humic acid is also assumed to change linearly with pH from a value of 4.0 at pH 4 to 5.0 at pH $\geq$ 7. These values are consistent with those reported for various humic acids (Shanbhag and Choppin 1981, Nash and Choppin 1980, Li et al. 1980).

The values calculated here, while generally based on conservative assumptions, rely on the rather crude complexation constants available for humate complexation. If these values are in error, the concentrations of uranium generated by humate complexation will correspondingly be in error.

TABLE D-1

ESTIMATED β_1 AND β_2 VALUES FOR HUMATE COMPLEXES OF U(VI) AND U(IV)

	U(VI)		U(IV)	
pH	$\log_{10}\beta_1$	$\log_{10}\beta_2$	$\log_{10}\beta_1$	$\log_{10}\beta_2$
4.0	5.0	9.0	11.1	16.2
4.5	5.5	9.5	12.0	17.0
5.0	6.0	10.0	12.8	17.8
5.5	6.5	10.5	13.7	18.7
6.0	7.0	11.0	14.5	19.5
6.5	7.5	11.5	15.3	20.4
7.0-10.0	8.0	12.0	16.2	21.2

D.4 CALCULATIONS

Regardless of formation of complexes with inorganic groundwater ions, it is clear that, if the concentrations of the humic acid complexes are less than or comparable to those of the simple uranium ions and their hydrolysis species, the effects on equilibrium dissolution of UO_2 would be small. Two sets of calculations were done for pH values from 5 to 10, i.e., the pH range for the vault model. One set, with E_z = 0.1 V, is for a typical reducing environment. The second, E_z = 0.516 V, is for the most strongly oxidizing conditions (at each pH value) considered in the solubility model. The results are shown in Table D-2.

It is apparent that humate complexes of U(IV) would make essentially no contribution to uranium solubility at any value of pH within the selected range. For the more highly oxidizing conditions, the U(VI) humate complexes are unimportant with respect to $UO_2(OH)_2(aq)$, $UO_2(OH)_4^{2-}$ and $U(OH)_4(aq)$ for pH values $\geq$ 9. Between pH values of 5 and 9 for oxidizing conditions, the concentrations of the humate complexes are somewhat greater than the sum of $[UO_2^{2+}]$ plus the concentrations of hydrolyzed U species, but by no more than a factor of 25. Thus, omission of humate complexes should not result in significant underestimates of the total uranium solubility under any conditions.

One way of putting the possible contributions to uranium solubility of humate complexation into perspective is to compare these with the contributions calculated for the inorganic ligands in the contact water. If the ligand concentrations are set at the mean values in the contact waters as determined in vault model calculations (Lemire and Garisto 1989), the contribution from humate complexation is less than 40% of the contribution from inorganic complexes for solutions having a pH value of 7 (Table D-3).

TABLE D-2

CALCULATED URANIUM CONCENTRATIONS IN WATER AT E_z = 0.1 V AND E_z = 0.516 V IN THE PRESENCE AND ABSENCE OF HUMATES

pH	E_z = 0.100 V		E_z = 0.516 V	
	log[U-humates]	log[U aq + hyd.]	log[U-humates]	log[U aq + hyd.]
5.0	-15.0	-9.95	-5.64	-6.33
5.5	-16.0	-9.95	-6.09	-7.18
6.0	-17.1	-9.95	-6.57	-7.88
6.5	-18.5	-9.95	-7.05	-8.40
7.0	-19.4	-9.95	-7.56	-8.78
7.5	<-20.	-9.95	-8.55	-8.96
8.0	<-20.	-9.95	-9.55	-9.04
8.5	<-20.	-9.95	-10.5	-9.07
9.0	<-20.	-9.95	-11.5	-9.07
9.5	<-20.	-9.95	-12.5	-9.03
10.0	<-20.	-9.95	-13.5	-8.72

Above pH 7, the U(VI)-carbonate complexes are sufficiently strong that, on average, the contributions of the humate complexes to the uranium solubility would be minor.

The maximum fluoride concentration in the contact waters is 1.58×10^{-3} mol·L^{-1}. The maximum free carbonate concentration (40 000 model contact waters at 25°C (Lemire and Garisto 1989)) is 3.8×10^{-3} mol·L^{-1}. Therefore, the maximum total carbonate concentration is equal to or greater than this value. Calculations were done using 1.58×10^{-3} mol·L^{-1} for the fluoride concentration and 3.8×10^{-3} mol·L^{-1} for the total carbonate concentration, and the results are shown in Table D-3. In all cases, the uranium solubilities resulting from fluoride and/or carbonate complexation exceed those from humate complexation.

If humates were found in the contact water during the first 10 000 a after closure of the vault, some enhancement of uranium solubility might result, particularly for relatively oxidizing conditions at pH < 9. However, because the concentrations of the humate complexes are expected to be well below those resulting from the maximum concentrations of inorganic complexants in the groundwaters, the effect on the overall distribution of uranium solubilities would be small, except perhaps for the most oxidizing solutions having pH values near 6. In no case does the calculated concentration of humate complexes exceed 20% of the maximum solubility that might result from complexation with anions in the contact water.

TABLE D-3

COMPARISON OF CONCENTRATIONS OF ORGANIC AND INORGANIC COMPLEXES OF URANIUM IN CONTACT WATERS FOR MEAN AND MAXIMUM LIGAND CONCENTRATIONS

	E_z = 0.516 V		
pH	log[U-humates]	log[U] mean lig. conc.	log[U] $\log[F^-] = -2.8/\log[CO_3^{2-}] = -2.42$
5.0	-5.64	-5.83	-3.97
5.5	-6.09	-6.99	-4.96
6.0	-6.57	-7.21	-5.77
6.5	-7.05	-7.28	-5.64
7.0	-7.56	-7.11	-5.07
7.5	-8.55	-6.81	-4.53
8.0	-9.55	-6.41	-4.02
8.5	-10.5	-5.98	-3.55

REFERENCES

Choppin, G.R. 1988. Humics and radionuclide migration. Radiochimica Acta 44/45, 23-28.

Lemire, R.J. and F. Garisto. 1989. The solubility of U, Np, Pu, Th and Tc in a geological disposal vault for used nuclear fuel. Atomic Energy of Canada Limited Report, AECL-10009.

Li, W.C., D.M. Victor and C.L. Chakrabarti. 1980. Effect of pH and uranium concentration on ineraction of uranium(VI) and uranium(IV) with organic liquids in aqueous solutions. Analytical Chemistry 52, 520-523.

Nash, K.L. and G.R. Choppin. 1980. Interaction of humic and fulic acids with Th(IV). Journal of Inorganic and Nuclear Chemistry 42, 1045-1050.

Shanbhag, P.M. and G.R. Choppin. 1981. Binding of uranyl by humic acid. Journal of Inorganic and Nuclear Chemistry 43, 3369-3372.

Swedish Nuclear Fuel Supply Company. 1983. Final storage of spent nuclear fuel, KBS-3, Volume III, Barriers. Swedish Nuclear Fuel and Waste Management Company Report, KBS-3.

Tessman, J.S and J.F. Barker. 1985. Apparent complexing capacity of aqueous solutions - Evaluation of analytical techniques and measurements in selected groundwaters. Atomic Energy of Canada Limited Technical Record, TR-326.*

* Internal report available from SDDO, AECL Research, Chalk River Laboratories, Chalk River, Ontario K0J 1J0

APPENDIX E

PROBABILISTIC SENSITIVITY ANALYSIS

CONTENTS

E.1 PROBABILISTIC SENSITIVITY ANALYSIS

Linear regression analysis was performed by the method of least squares to determine the parameters that, when varied within their defined distributions, have the largest effect on the release from the vault for 1000 random simulations. A complete list of all the parameters in the vault model is given in Table E-1. These are referred to here as important parameters. In this analysis, it was assumed that the output variable, Y, was linearly related to the input variables, X_i, in the form

$$Y = b_o + b_1X_1 + b_2X_2 + \ldots + b_nX_n \ . \qquad (E.1)$$

In this case the output variable, Y, was chosen to be the time-integrated release of ^{129}I and ^{14}C up to 10^5 a (TABSAV(03) and TABSAV(01) respectively). The unknown coefficients, b_i, are identified by minimizing the square of the deviations of the observed values from the expected as determined by Equation (E.1). A coefficient of multiple determination, R^2, can be evaluated that estimates the portion of the variability in the output parameter, Y, arising from the variability of the input parameters, X_i. R^2 ranges from 0 to 1.0. A value of zero means none of the variability is a result of the variability of the input parameters, while a value of one means all the variability is a result of the variability of the input parameters.

Linear regression analysis is commonly done in the biological and social sciences when the relationships between input and output parameters are not known. We have the advantage that the model equations are known and have, in fact, been explicitly formulated by us to obtain the results. We can use the information from the model equations to aid us in our analysis. For instance, we know that precipitation in the buffer does not occur for the radionuclides that contribute most to the dose, ^{14}C and ^{129}I. Thus we can eliminate all parameters used to calculate the solubility of these radionuclides in buffer from consideration in our sensitivity analysis. We can also eliminate all constant parameters and parameters pertaining to radionuclides other than ^{14}C and ^{129}I from our analysis. Once we perform this elimination, we are left with a fairly small number of parameters relating to ^{14}C and ^{129}I to investigate, as listed below:

INVPKG(01)	- initial inventory of ^{14}C per kilogram of uranium
INVPKG(03)	- initial inventory of ^{129}I per kilogram of uranium
IRFRAV(01)	- instant-release fraction of ^{14}C
IRFRAV(03)	- instant-release fraction of ^{129}I
DFBANI	- buffer anion correlation parameter
VSCALE	- groundwater scaling factor
SGTORA(01)	- tortuosity of lower rock
DFKANI	- backfill anion correlation parameter
DIFFN(01)	- free-water diffusion coefficient of ^{14}C in lower rock
DIFFN(03)	- free-water diffusion coefficient of ^{129}I in lower rock
SGDSVY(1-21)	- dispersivity of lower rock
MUA	- mean corrosion rate of cool containers

MUE	- mean corrosion rate of cold containers
MUR1	- mean corrosion rate of containers at initial hot temperature
MUR2	- mean corrosion rate of containers at secondary hot temperature

The first six of these parameters have been identified by fractional factorial screening analysis as being the most important. Tortuosity of the lower rock was identified as one of the most important parameters for the release of ^{129}I from the vault, but not for ^{14}C. In the fractional factorial screening analysis all the vault parameters were used.

Multiple linear regression of the effect of the important parameters pertaining to ^{129}I on TABSAV(03) gave an R^2 value of 0.70. However, the same analysis on the logarithm of the parameter values gave an R^2 of 0.89. Clearly, much more of the variability is explained by regressing on the logarithm of the parameter values. This is not unexpected. We know from the constitutive equations that most of the parameters appear either as multiplicative factors or in terms that are multiplicative. When we take the logarithm of a multiplicative relationship, a linear relationship is obtained. For example, log(ab) = log(a) + log(b), and thus we expect the regression on the logarithm of the parameter values to give a higher R^2.

If we regress on the logarithm of all the parameters listed above, rather than just those deemed important, the R^2 value rises only from 0.89 to 0.94. Conversely, if we remove one of the important parameters, such as INVPKG(03), R^2 decreases a larger amount, from 0.94 to 0.66. Similar results are obtained by removing the other important parameters.

The instant-release fraction of ^{129}I was not identified as an important parameter in the probabilistic sensitivity analysis, whereas it was shown to be important when all other parameters were fixed at their median values (see Section 7.3.1). This is mainly because the standard deviation of the probability distribution for this parameter was very small with respect to the upper and lower truncation bounds.

Multiple linear regression on the logarithm of the important parameters pertaining to ^{14}C and the logarithm of TABSAV(01) gave an R^2 value of 0.95, whereas regression on the logarithm of all the parameters listed above increased the R^2 for ^{14}C to only 0.98. Removing the important parameter INVPKG(01) causes the R^2 value to decrease from 0.98 to 0.41. Similar large decreases are obtained by removing other important parameters.

We conclude that the linear regression on the logarithm of the parameters agrees with fractional factorial screening analysis as to what are the most important vault parameters.

The sensitivity analysis of the probabilistic results has been demonstrated through the use of scatter plots of the important parameters as identified from fractional factorial screening. Figures E-1 to E-10 are the scatter plots showing the effect of the important parameters on the integrated release from the vault up to 10^5 a. The lines generated by varying a single parameter while keeping the other parameters fixed at their median

value are also displayed on the graphs. The lines generated by least squares fitting of the logarithms of the parameter values are shown on the graphs. In this case the regression was done on each parameter separately rather than on all the parameters at once as in multiple regression. The degree of spread around the line is a reflection of how the variability in the other parameters affects the relationship expressed when a single parameter is varied.

The degree of spread in each of the lines can be quantified through the correlation coefficients based on the logarithm of the parameter values. Correlation coefficients vary between -1 and 1. A coefficient of 1.0 means that the parameters are completely linearly correlated in a positive manner; i.e., when the parameter increases, so does the result. A correlation coefficient of 0 means they are uncorrelated and a coefficient of -1 means that they are completely negatively correlated; i.e., when the parameter increases, the result decreases. The smaller the spread around the line, the higher the absolute value of the coefficient. Thus, for a coefficient of 1 we would have a line with a positive slope with no scatter about the line. The correlation coefficients can also be used to rank the parameters. The larger the absolute value of the coefficient, the more important the parameter.

Numerous methods (Saltelli and Marivoet 1990) exist for ranking parameters according to their importance, including correlation coefficients, Spearman's coefficients and fractional factorial coefficients. Spearman's correlation coefficient is obtained by the same method as the normal correlation coefficient except that the rank of the parameter is used instead of the value (Saltelli and Marivoet 1990). The rank of a parameter is simply a number ordering the parameter in terms of its value from smallest to largest. Thus a rank of one corresponds to the smallest parameter value.

The relative importance, described in Appendix E (Section E.3) of Goodwin et al. (1994) is used to rank the parameter by fractional factorial methods. Unlike the other correlation coefficients, its values are not restricted to lie between -1 and 1.

The correlation coefficients based on the logarithm of parameter values, the Spearman's correlation coefficient and the relative importance are listed for TABSAV(03), TABSAV(01), MXLDT(03) and MXLDT(01) in Tables E-2 to E-5 respectively. Included with the correlation coefficients are the 95% confidence bounds. The correlation coefficient for the logarithm of the parameter values was determined by a "z" transformation (Sokal and Rohlf 1969). The 95% confidence intervals for the Spearman's coefficient are identical and equal to $1.96/\sqrt{(n-1)}$ where n is the number of parameter values (1000) (Walker 1987). Absolute values of relative importance smaller than 1.0 were not considered to be significant and were not calculated.

The correlation coefficients and associated 95% confidence bounds are illustrated in Figures E-11 to E-14. The importance rankings by all methods generally agree. Most discrepancies occur between parameters where the confidence intervals overlap, with the exception of the effect of VSCALE on MXLTDT(01). The relative importance rates the effect of VSCALE

on MXLDT(01) significantly higher than the other methods. The methods clearly identify INVPKG(01) as the dominant parameter influencing the release of ^{14}C from the vault, whereas DFBANI, INVPKG(03) and VSCALE have the largest effect on the release of ^{129}I from the vault. As the correlation coefficients decrease, the overlap in the confidence intervals increases and it becomes more difficult to discriminate between the effects of the parameters. Parameters with absolute values of correlation coefficients below about 0.2, or relative importance below about 10, should not be considered as having much effect on the release from the vault, although the choice of a cutoff value is somewhat arbitrary.

In general, the correlation coefficients of the parameters important to maximum dose are smaller than the correlation coefficients of the parameters important to release from the vault. The added variability introduced by the geosphere and biosphere parameters accounts for the lower values. SGTORA(01) and VSCALE are exceptions. The correlation of SGTORA(01) to dose is greater than to release from the vault for both ^{14}C and ^{129}I, whereas the correlation of VSCALE to dose is higher than to release from the vault for ^{14}C only. The explanation of this effect is that both VSCALE and SGTORA(01) affect the release from the geosphere as well as the vault. The selective effect of VSCALE on ^{14}C and the effect of SGTORA(01) on ^{14}C and ^{129}I on the release from the geosphere is explained in Section 3.3.6.3 of Goodwin et al. (1994).

The behaviour of the important vault parameters when a single parameter was varied and the remaining were held fixed at their median values was discussed previously. Scatter plots together with the lines generated by least squares fitting to the logarithm of parameter values can be used to further investigate the effect of these parameters, particularly with respect to the effect of varying all parameters. The effect of the important parameters on the release from the vault are shown in the scatter plots of Figures E-1 to E-10.

In general, the lines generated by linear regression on the logarithm of the parameter values for the scatter plots agree well with the lines generated when all other parameters are fixed at their median values. The only point of departure between the lines on the graphs is for the behaviour of release from the vault with DFBANI. The assumed linear behaviour on the logarithm of parameter values used for the regression line is not capable of following the non-monotonic behaviour of vault release with DFBANI. Nevertheless the trend of the behaviour of DFBANI is captured by the regression line. This indicates that the relationships explained in Section 3.3.6.2 of Goodwin et al. (1994) pertaining to the lines generated by varying a single parameter and keeping all other parameters fixed at their median values carry through to the case where all parameters are allowed to vary.

Scatter plots showing the effect of the important vault parameters on dose are illustrated in Figures E-15 to E-24. Generally the trends of the two lines on the plots agree, although the agreement is not always as strong as in the case of release from the vault. This is a result of the added variability introduced by the geosphere and biosphere parameters and is consistent with the generally smaller correlation coefficients.

This analysis has quantified the effect of the important parameters on the release from the vault and has shown the influence of the variability in the remaining parameters on this effect. A single parameter, INVPKG(01) was found to have the most influence on release of ^{14}C from the vault. Three parameters, DFBANI, INVPKG(03) and VSCALE had the most influence on the release of ^{129}I from the vault.

The analysis has also demonstrated that the effect of the important vault parameters on dose is reduced from their effect on release from the vault, because of the added variability of geosphere and biosphere parameters. The exceptions are SGTORA(01) and VSCALE. The analysis has demonstrated that only SGTORA(01) carries through its effect on the release of ^{129}I from the vault to dose from ^{129}I. Both SGTORA(01) and VSCALE carry through their effect on release of ^{14}C from the vault to dose from ^{14}C.

REFERENCES

Goodwin, B.W., D.B. McConnell, T.H. Andres, W.C. Hajas, D.M. LeNeveu, T.W. Melnyk, G.R. Sherman, M.E. Stephens, J.G. Szekely, P.C. Bera, C.M. Cosgrove, K.D. Dougan, S.B. Keeling, C.I. Kitson, B.C. Kummen, S.E. Oliver, K. Witzke, L. Wojciechowski, and A.G. Wikjord. 1994. The disposal of Canada's nuclear fuel waste: postclosure assessment of a reference system. Atomic Energy of Canada Limited Report AECL-10717, COG-93-7.

Saltelli, A. and J. Marivoet. 1990. Non-parametric statistics in sensitivity analysis for model output: a comparison of selected techniques. Reliability Engineering and System Safety 28, 229-253.

Sokal, R.R. and J.F. Rohlf. 1969. Biometry, The Principles and Practices of Statistics in Biological Research. W.H. Freeman and Company, San Fransisco.

Walker, J.R. 1987. Sensitivity analysis in multi-parameter probabilistic systems: An example using the MCROC rock microcracking model. Atomic Energy of Canada Limited Report, AECL-9091.

TABLE E-1

PARAMETER VALUES FOR THE VAULT MODEL

Sampled Values

Code Name	Definition	Median Value	Units	Probability Density Attributes	Location in Text
AFRACA(11)	The fraction of containers that cool at an intermediate rate within sector 11 of the vault	8.66860×10^{-1}		constant	Chapter 4
AFRACE(11)	The fraction of containers subjected to rapid cooling within sector 11 of the vault	1.33140×10^{-1}		constant	Chapter 4
AFRACR(11)	The fraction of containers subjected to slow cooling within sector 11 of the vault	0.00000		constant	Chapter 4
AREACV	The total area of the vault with rooms above the fracture zone LD1. It is used for estimating the release rate when contaminants are assumed not to penetrate the backfill (BAKSWT<0). In the case study the rooms above LD1 were removed and the sum of the fractional sector areas (FRSECA) was less than 1.0. This effectively reduces the total vault area to 3.16×10^6 m^2.	3.38720×10^6	m^2	constant	Table 2-1 Section 2.1
AREADN	The total area of the vault with rooms above the fracture zone LD1. It is used for estimating the release rate when contaminants are assumed to penetrate the backfill (BAKSWT>0). In the case study the rooms above LD1 were removed and the sum of the fractional sector areas (FRSECA) was less than 1.0. This effectively reduces the total vault area to 3.16×10^6 m^2.	3.38720×10^6	m^2	constant	Table 2-1 Section 2.1

continued...

TABLE E-1 (continued)

Sampled Values

Code Name	Definition	Median Value	Units	Probability Density Attributes	Location in Text
BAKSWT(11)	A switch that controls whether or not a contaminant released from the containers will enter the backfill. If BAKSWT is greater than zero, the contaminant will enter the backfill. If BAKSWT is less than or equal to zero the contaminant will not enter the backfill. Only the value for sector 11 of the vault is given here.	1.00000		constant	Section 6.2.2
DELHDA	The length of time the containers designated cool fail as a result of hydrogen-induced cracking	2.94000×10^{3}	a	constant	Table 4-6
DELHDE	The length of time the containers designated as cold fail as a result of hydrogen-induced cracking	7.40000×10^{3}	a	constant	Table 4-6
DELHDR	The length of time the containers designated as hot fail prematurely as a result of hydrogen-induced cracking	2.86000×10^{3}	a	constant	Table 4-6
DELTIF	The time period when the containers will fail prematurely as a result of initial defects	5.00000×10^{1}	a	constant	Table 4-6
DFBACT	Dummy correlation parameter for total intrinsic diffusion coefficient for actinide in buffer	1.13800×10^{-5}		lognormal geometric mean = 1.138×10^{-5} geometric standard deviation = 3.163 lower truncation value = 3.6×10^{-7} upper truncation value = 3.6×10^{-4}	Table 3-2
DFBANI	Dummy correlation parameter for total intrinsic diffusion coefficient for anions in buffer	1.80000×10^{-5}		lognormal geometric mean = 1.8×10^{-5} geometric standard deviation = 2.714 lower truncation value = 9.0×10^{-7} upper truncation value = 3.6×10^{-4}	Table 3-2

continued...

TABLE E-1 (continued)

Sampled Values

Code Name	Definition	Median Value	Units	Probability Density Attributes	Location in Text
DFBCAT	Dummy correlation parameter for total intrinsic diffusion coefficient for cations in buffer	2.54600×10^{-3}		lognormal geometric mean = 2.54×10^{-3} geometric standard deviation = 1.414 lower truncation value = 9.0×10^{-4} upper truncation value = 7.20×10^{-3}	Table 3-3
DFBTRA	Dummy correlation parameter for total intrinsic diffusion coefficient for tracers in buffer	2.40000×10^{-3}		normal mean = 2.4×10^{-3} standard deviation = 1.00×10^{-4} lower truncation value = 2.10×10^{-3} upper truncation value = 2.70×10^{-3}	Table 3-3
DFKACT	Dummy correlation parameter for total intrinsic diffusion coefficient for actinides in backfill	2.25000×10^{-3}		normal mean = 2.25×10^{-3} standard deviation = 1.50×10^{-4} lower truncation value = 1.80×10^{-3} upper truncation value = 2.70×10^{-3}	Table 3-5
DFKANI	Dummy correlation parameter for total intrinsic diffusion coefficient for anions in backfill	2.25000×10^{-3}		normal mean = 2.25×10^{-3} standard deviation = $.50 \times 10^{-4}$ lower truncation value = 1.80×10^{-3} upper truncation value = 2.70×10^{-3}	Table 3-4
DFKCAT	Dummy correlation parameter for total intrinsic diffusion coefficient for cations in backfill	3.96000×10^{-3}		normal mean = 3.96×10^{-3} standard deviation = 1.80×10^{-4} lower truncation value = 3.42×10^{-3} upper truncation value = 4.50×10^{-3}	Table 3-5
DFKTRA	Dummy correlation parameter for total intrinsic diffusion coefficient for tracers in backfill	2.25000×10^{-2}		normal mean = 2.5×10^{-2} standard deviation = 1.50×10^{-3} lower truncation value = 1.80×10^{-2} upper truncation value = 2.70×10^{-2}	Table 3-5
EFTHKB	The thickness of the slab used to represent the buffer in the vault model	2.50000×10^{-1}	m	constant	Section 6.2.2 Figure 1-4
EZI	The initial reference potential for the system (at pH = 0) interpolated to the reference vault temperature	2.58000×10^{-1}	V	uniform, lower value = 0.0 upper value = 0.516	

continued...

TABLE E-1 (continued)

Sampled Values

Code Name	Definition	Median Value	Units	Probability Density Attributes	Location in Text
FRSECA(11)	The effective area for nuclide release for sector 11 divided by the total effective area of the vault for nuclide release. The sum of FRSECA for all sectors pertaining to the disposal vault with rooms above the fracture zone LD1 is 1.0. For smaller vaults such as the one discussed in detail in the postclosure assessment case study, with no rooms above the fracture zone LD1 and a 50-m exclusion zone from the fracture, the sum of FRSECA for all sectors will be less than one. Thus to model vaults of different sizes, the approach is to leave the total amount of fuel and the total number of containers in the vault unchanged and to modify FRSECA.	1.48500×10^{-1}		constant	Section 6.2.3 Figure 6-4
IFAILQ(11)	The probability variate for a cumulative binomial distribution. Its values are uniformly distributed between 0 and 1. It is used to determine the number of containers failing in sector 11 of the vault.	5.00000×10^{-1}		uniform, lower value = 0.0 upper value = 1.0	Section 4.7.1
IFRACT	The estimated fraction of containers that will have one or more initial defects leading to premature failure of the container following emplacement	2.04487×10^{-4}		lognormal geometric mean = 2.0×10^{-4} geometric standard deviation = 1.5 lower truncation value = 1.0×10^{-4} upper truncation value = 1.0×10^{-3}	Section 4.7.1

continued...

TABLE E-1 (continued)

Sampled Values

Code Name	Definition	Median Value	Units	Probability Density Attributes	Location in Text
MATPRI(01)	The distance from the waste form that the used-fuel matrix precipitates. To flag the case where the matrices do not precipitate, MATPRI should be given a negative value in the input file, and to flag the case where a user-supplied dissolution rate is used, MATPRI should be given a value larger than the effective thickness of the buffer. The value is adjusted to take into account the finite dissolution rate of the waste form determined by reaction kinetic constraints.	1.25000×10^{-1}	m	uniform, lower value = 0.0 upper value = 0.25	Section 5.5.3.2
MUA	The mean corrosion rate of containers designated cool during the initial thermal transient	1.08427×10^{-6}	$m \cdot a^{-1}$	normal mean = 1.16×10^{-6} standard deviation = 5.8×10^{-7} lower truncation value = 1.0×10^{-8} upper truncation value = 1.82×10^{-6}	Table 4-6
MUE	The mean corrosion rate of containers designated as cold during the initial thermal transient	1.15485×10^{-6}	$m \cdot a^{-1}$	normal mean = 1.24×10^{-6} standard deviation = 6.2×10^{-7} lower truncation value = 1.0×10^{-8} upper truncation value = 1.93×10^{-6}	Table 4-6
MUR1	The mean corrosion rate of containers designated as hot during the first thermal transient	6.60465×10^{-6}	$m \cdot a^{-1}$	normal mean = 6.71×10^{-6} standard deviation = 3.36×10^{-6} lower truncation value = 1.0×10^{-8} upper truncation value = 1.23×10^{-5}	Table 4-6
MUR2	Mean corrosion rate of containers designated as hot during the second thermal transient	1.90440×10^{-6}	$m \cdot a^{-1}$	normal mean = 2.14×10^{-6} standard deviation = 1.07×10^{-6} lower truncation value = 1.0×10^{-8} upper truncation value = 3.05×10^{-6}	Table 4-6
PH	Negative logarithm of the hydrogen ion concentration (note: not the negative logarithm of the hydrogen ion activity)	7.73861×10^{0}		triangular, lower value = 5.0 middle value = 8.0 upper value = 10.0	Section 5.5.2.2

continue

TABLE E-1 (continued)

Sampled Values

Code Name	Definition	Median Value	Units	Probability Density Attributes	Location in Text
PORCON	The capacity factor of the container infilling material and sand annulus. For the case of no sorption this is equivalent to the void fraction.	2.48700×10^{-1}		constant	Section 5.5.1.3
POTBFM	The maximum potential in the buffer. Oxidizing species produced by radiolysis in and near the fuel may cause a redox gradient to occur in the buffer. The maximum buffer potential is the maximum potential that would exist in the buffer without the effect of radiolysis, assuming radiolysis effects have a limited range in the buffer.	4.70000×10^{-1}	V	constant	Section 5.5.3.2
RANPTF	A factor used to calculate the buffer potential from the fuel potential	9.53313×10^{-1}		beta, lower bound = 0.0 upper bound = 1.0, shape parameter 1 = 5.0 shape parameter 2 = 0.5	Section 5.5.3.2
SIGMAA	The standard deviation of the corrosion rate of the containers designated as cool during the initial thermal transient	2.200×10^{-7}	$m \cdot a^{-1}$	constant	Table 4-7
SIGMAE	The standard deviation of the corrosion rate of the containers designated as cold during the initial thermal transient	2.300×10^{-7}	$m \cdot a^{-1}$	constant	Table 4-7
SIGMR1	The standard deviation of the corrosion rate of containers designated as hot during the first thermal transient	1.850×10^{-6}	$m \cdot a^{-1}$	constant	Table 4-7
SIGMR2	The standard deviation of the corrosion rate of the containers designated as hot during the second thermal transient	3.000×10^{-7}	$m \cdot a^{-1}$	constant	Table 4-7

continued...

TABLE E-1 (continued)

Sampled Values

Code Name	Definition	Median Value	Units	Probability Density Attributes	Location in Text
T1EDGE	The average time when the temperature for the cold containers drops below 30°C	3.00000×10^{2}	a	constant	Table 4-7
T1ISLE	The average time when the temperature for the containers designated as hot drops below 30°C	1.26380×10^{4}	a	constant	Table 4-7
T1ROOM	The average time when the temperature for the containers designated as hot drops below 72°C	1.05500×10^{2}	a	constant	Table 4-7
T2ROOM	The average time when the temperature for the containers designated as hot drops below 30°C	1.84100×10^{4}	a	constant	Table 4-7
TEMPSC	The average temperature of the second peak in the predicted container skin temperature versus time curve at the centre of a panel in the vault	3.37500×10^{2}	K	normal mean = 337.5 standard deviation = 3.1 lower truncation value = 284.0 upper truncation value = 423.0	Figure 5-4 Section 5-3
TFUEL	Mass of the used fuel in the reference disposal vault expressed as the corresponding mass of elemental uranium fed into the reactor. This value refers to the vault with rooms above the fracture zone LD1. In the postclosure assessment case study, rooms above LD1 were removed and the sum of the fractional sector areas (FRESCA) was less than 1.0. This effectively reduced TFUEL from 1.73374×10^{8} to 1.617×10^{8} kg.	1.73374×10^{8}	kg		Table 2-1 Section 2.1

continued...

TABLE E-1 (continued)

Sampled Values

Code Name	Definition	Median Value	Units	Probability Density Attributes	Location in Text
THIKTE	The amount of the original thickness of the container shell that is available for corrosion before the container will fail as a result of structural loading	4.20000×10^{-3}	m	constant	Sections 4.6.3 & 4.7.5.2
THKBAK	The thickness of the slab used to represent the backfill in the vault model	1.40000×10^{0}	m	constant	Section 6.2.2
TNCONV	The total number of waste containers in the disposal vault. In the case study, rooms were removed from LD1 and the sum of fractional sector areas was less than 1.0. This means that the actual number of containers for the postclosure assessment case study was 1.1868×10^{5}.	1.27224×10^{5}		constant	Table 2-1 Section 2.1
TRANFB	The length of the mass transfer zone along the borehole	2.25000×10^{0}	m	constant	Section 6.8.2
TRANFF	The length of the mass transfer zone along the vertical side of a backfilled room	5.00000×10^{0}	m	constant	Section 6.8.2
UO2RAT	The first-order constant that determines the maximum rate at which UO_2 can dissolve when all dissolution products are removed from the surface as fast as they are formed	4.72500×10^{0}	$m \cdot a^{-1}$	uniform, lower value = 3.15 upper value = 6.30	Section 5.5.3.2
VOLARE	The ratio of the volume to the surface area of the space contained within the inner boundary of the buffer for a unit of emplaced waste. For the reference disposal vault this includes the volume of one container and the volume of sand that separates the container from the buffer material.	1.60000×10^{-1}	m	constant	Section 5.5.1.3

continued...

TABLE E-1 (continued)

Sampled Values

Code Name	Definition	Median Value	Units	Probability Density Attributes	Location in Text
CAPBFE(01)	The capacity factor of carbon in the buffer	6.33000×10^{-3}		correlated lognormal geometric mean = 6.33×10^{-3} geometric standard deviation = 3.984 lower truncation value = 1.0×10^{-4} upper truncation value = 0.40 correlated to DFBANI correlation coefficient = 1.0	Table 3-3
CAPBKE(01)	The capacity factor of carbon in the backfill	2.50000×10^{-1}		correlated normal, mean = 0.250 standard deviation = 1.667×10^{-2} lower truncation value = 0.20 upper truncation value = 0.30 correlated to DFKANI correlation coefficient = 1.0	Table 3-5
DIFBAK(01)	The total intrinsic diffusion coefficient of carbon in the backfill	2.250×10^{-3}	$m^2 \cdot a^{-1}$	correlated normal, mean = 2.25×10^{-3} standard deviation = 1.5×10^{-4} lower truncation value = 1.8×10^{-3} upper truncation value = 2.7×10^{-3} correlated to DFKANI correlation coefficient = 1.0	Table 3-4
DIFBUF(01)	The total intrinsic diffusion coefficient of carbon in the buffer	1.800×10^{-5}	$m^2 \cdot a^{-1}$	correlated lognormal geometric mean = 1.8×10^{-5} geometric standard deviation = 2.714 lower truncation value = $9. \times 10^{-7}$ upper truncation value = 3.6×10^{-4} correlated to DFBANI correlation coefficient = 1.0	Table 3-2
CAPBFE(02)	The capacity factor of cesium in the buffer	1.75000×10^{1}		correlated normal, mean = 17.5 standard deviation = 5.167 lower truncation value = 2.0 upper truncation value = 33.0 correlated to DFBCAT correlation coefficient = 1.0	Table 3-3
CAPBKE(02)	The capacity factor of cesium in the backfill	6.00000×10^{0}		correlated normal, mean = 6.0 standard deviation = 0.6667 lower truncation value = 4.0 upper truncation value = 8.0 correlated to DFKCAT correlation coefficient = 1.0	Table 3-5

continued...

TABLE E-1 (continued)

Sampled Values

Code Name	Definition	Median Value	Units	Probability Density Attributes	Location in Text
DIFBAK(02)	The total intrinsic diffusion in the backfill	8.100×10^{-3}	$m^2 \cdot a^{-1}$	correlated normal, mean = 8.1×10^{-3} standard deviation = 6.0×10^{-4} lower truncation value = 6.3×10^{-3} upper truncation value = 9.9×10^{-3} correlated to DFKCAT correlation coefficient = 1.0	Table 3-4
DIFBUF(02)	The total intrinsic diffusion in the buffer	7.312×10^{-3}	$m^2 \cdot a^{-1}$	correlated lognormal geometric mean = 7.312×10^{-3} geometric standard deviation = 1.596 lower truncation value = 1.80×10^{-3} upper truncation value = 2.97×10^{-2} correlated to DFBCAT correlation coefficient = 1.0	Table 3-2
CAPBFE(03)	The capacity factor of iodine in the buffer	6.330×10^{-3}		correlated lognormal geometric mean = 6.33×10^{-3} geometric standard deviation = 3.984 lower truncation value = $1. \times 10^{-4}$ upper truncation value = 0.40 correlated to DFBANI correlation coefficient = 1.0	Table 3-3
CAPBKE(03)	The capacity factor of iodine in the backfill	2.500×10^{-1}		correlated normal, mean = 0.250 standard deviation = 1.667×10^{-2} lower truncation value = 0.20 upper truncation value = 0.30 correlated to DFKANI correlation coefficient = 1.0	Table 3-5
DIFBAK(03)	The total intrinsic diffusion coefficient of iodine in the backfill	2.250×10^{-3}	$m^2 \cdot a^{-1}$	correlated normal, mean = 2.25×10^{-3} standard deviation = 1.5×10^{-4} lower truncation value = 1.8×10^{-3} upper truncation value = 2.7×10^{-3} correlated to DFKANI correlation coefficient = 1.0	Table 3-4
DIFBUF(03)	The total intrinsic diffusion coefficient of iodine in the buffer	1.80×10^{-5}	$m^2 \cdot a^{-1}$	correlated lognormal geometric mean = 1.8×10^{-5} geometric standard deviation = 2.714 lower truncation value = $9. \times 10^{-7}$ upper truncation value = 3.6×10^{-4} correlated to DFBANI correlation coefficient = 1.0	Table 3-2

continued...

TABLE E-1 (continued)

Sampled Values

Code Name	Definition	Median Value	Units	Probability Density Attributes	Location in Text
CAPBFE(04)	The capacity factor of nickel in the buffer	4.500×10^{0}		correlated normal, mean = 4.5 standard deviation = 1.167 lower truncation value = 1.0 upper truncation value = 8.0 correlated to DFBCAT correlation coefficient = 1.0	Table 3-3
CAPBKE(04)	The capacity factor of nickel in the backfill	1.40000×10^{0}		correlated normal, mean = 1.4 standard deviation = 0.20 lower truncation value = 0.8 upper truncation value = 2.0 correlated to DFKCAT correlation coefficient = 1.0	Table 3-5
DIFBAK(04)	The total intrinsic diffusion coefficient of nickel in the backfill	3.960×10^{-3}	$m^2 \cdot a^{-1}$	correlated normal, mean = 3.96×10^{-3} standard deviation = 1.8×10^{-4} lower truncation value = 3.42×10^{-3} upper truncation value = 4.50×10^{-3} correlated to DFKCAT correlation coefficient = 1.0	Table 3-4
DIFBUF(04)	The total intrinsic diffusion of nickel in the buffer	2.546×10^{-3}	$m^2 \cdot a^{-1}$	correlated lognormal geometric mean = 2.546×10^{-3} geometric standard deviation = 1.414 lower truncation value = 9.0×10^{-4} upper truncation value = 7.20×10^{-3} correlated to DFBCAT correlation coefficient = 1.0	Table 3-2
CAPBFE(05)	The capacity factor of palladium in the buffer	4.49999×10^{0}		correlated normal, mean = 4.5 standard deviation = 1.167 lower truncation value = 1.0 upper truncation value = 8.0 correlated to DFBCAT correlation coefficient = 1.0	Table 3-3
CAPBKE(05)	The capacity factor of palladium in the backfill	1.40000×10^{0}		correlated normal, mean = 1.4 standard deviation = 0.20 lower truncation value = 0.8 upper truncation value = 2.0 correlated to DFKCAT correlation coefficient = 1.0	Table 3-5

continued...

TABLE E-1 (continued)

Sampled Values

Code Name	Definition	Median Value	Units	Probability Density Attributes	Location in Text
DIFBAK(05)	The total intrinsic diffusion coefficient of palladium in the backfill	3.960×10^{-3}	$m^2 \cdot a^{-1}$	correlated normal, mean = 3.96×10^{-3} standard deviation = 1.8×10^{-4} lower truncation value = 3.42×10^{-3} upper truncation value = 4.50×10^{-3} correlated to DFKCAT correlation coefficient = 1.0	Table 3-4
DIFBUF(05)	The total intrinsic diffusion coefficient of palladium in the buffer	2.546×10^{-3}	$m^2 \cdot a^{-1}$	correlated lognormal geometric mean = 2.546×10^{-3} geometric standard deviation = 1.414 lower truncation value = 9.0×10^{-4} upper truncation value = 7.20×10^{-3} correlated to DFBCAT correlation coefficient = 1.0	Table 3-2
CAPBFE(06)	The capacity factor of selenium in the buffer	6.330×10^{-3}		correlated lognormal geometric mean = 6.33×10^{-3} geometric standard deviation = 3.984 lower truncation value = 1.0×10^{-4} upper truncation value = 0.40 correlated to DFBANI correlation coefficient = 1.0	Table 3-3
CAPBKE(06)	The capacity factor of selenium in the backfill	2.500×10^{-1}		correlated normal, mean = 0.250 standard deviation = 1.667×10^{-2} lower truncation value = 0.20 upper truncation value = 0.30 correlated to DFKANI correlation coefficient = 1.0	Table 3-5
DIFBAK(06)	The total intrinsic diffusion of selenium in the backfill	2.250×10^{-3}	$m^2 \cdot a^{-1}$	correlated normal, mean = 2.25×10^{-3} standard deviation = 1.5×10^{-4} lower truncation value = 1.8×10^{-3} upper truncation value = 2.7×10^{-3} correlated to DFKANI correlation coefficient = 1.0	Table 3-4
DIFBUF(06)	The total intrinsic diffusion coefficient of selenium in the buffer	1.80×10^{-5}	$m^2 \cdot a^{-1}$	correlated lognormal geometric mean = 1.8×10^{-5} geometric standard deviation = 2.714 lower truncation value = $9. \times 10^{-7}$ upper truncation value = 3.6×10^{-4} correlated to DFBANI correlation coefficient = 1.0	Table 3-2

continued...

TABLE E-1 (continued)

Sampled Values

Code Name	Definition	Median Value	Units	Probability Density Attributes	Location in Text
CAPBFE(07)	The capacity factor of technetium in the buffer	5.28104×10^{1}		correlated lognormal geometric mean = 5.281×10^{1} geometric standard deviation = 6.813 lower truncation value = 4.175×10^{-3} upper truncation value = 1.67×10^{4} correlated to DFBACT correlation coefficient = 1.0	Table 3-3
CAPBKE(07)	The capacity factor of technetium in the backfill	2.00×10^{3}		correlated lognormal geometric mean = 2.0×10^{3} geometric standard deviation = 2.154 lower truncation value = 3.077×10^{1} upper truncation value = 2.0×10^{4} correlated to DFKACT correlation coefficient = 1.0	Table 3-5
DIFBAK(07)	The total intrinsic diffusion coefficient of technetium in the backfill	2.250×10^{-3}	$m^2 \cdot a^{-1}$	correlated normal, mean = 2.25×10^{-3} standard deviation = 1.5×10^{-4} lower truncation value = 1.80×10^{-3} upper truncation value = 2.70×10^{-3} correlated to DFKACT correlation coefficient = 1.0	Table 3-4
DIFBUF(07)	The total intrinsic diffusion coefficient of technetium in the buffer	1.138×10^{-5}	$m^2 \cdot a^{-1}$	correlated lognormal geometric mean = 1.138×10^{-5} geometric standard deviation = 3.163 lower truncation value = 3.6×10^{-7} upper truncation value = 3.6×10^{-4} correlated to DFBACT correlation coefficient = 1.0	Table 3-2
CAPBFE(08)	The capacity factor of uranium in the buffer	5.281×10^{1}		correlated lognormal geometric mean = 5.281×10^{1} geometric standard deviation = 6.813 lower truncation value = 1.67×10^{-1} upper truncation value = 1.67×10^{4} correlated to DFBACT correlation coefficient = 1.0	Table 3-3

continued...

TABLE E-1 (continued)

Sampled Values

Code Name	Definition	Median Value	Units	Probability Density Attributes	Location in Text
CAPBKE(08)	The capacity factor of uranium in the backfill	2.00000×10^{3}		correlated lognormal geometric mean = 2.0×10^{3} geometric standard deviation = 2.154 lower truncation value = 2.0×10^{2} upper truncation value = 2.0×10^{4} correlated to DFKACT correlation coefficient = 1.0	Table 3-5
DIFBAK(08)	The total intrinsic diffusion coefficients of uranium in the backfill	2.250×10^{-3}	$m^2 \cdot a^{-1}$	correlated normal, mean = 2.25×10^{-3} standard deviation = 1.5×10^{-4} lower truncation value = 1.80×10^{-3} upper truncation value = 2.70×10^{-3} correlated to DFKACT correlation coefficient = 1.0	Table 3-4
DIFBUF(08)	The total intrinsic diffusion coefficient of uranium in the buffer	1.138×10^{-5}	$m^2 \cdot a^{-1}$	correlated lognormal geometric mean = 1.138×10^{-5} geometric standard deviation = 3.163 lower truncation value = 3.6×10^{-7} upper truncation value = 3.6×10^{-4} correlated to DFBACT correlation coefficient = 1.0	Table 3-2
HLIFE(01)	Half-life of ^{14}C	5.73000×10^{3}	a	constant	Table A-2
INVPKG(01)	The initial amount of ^{14}C in the used-fuel matrix in the vault expressed in moles per kilogram total initial ^{238}U	1.84×10^{-5}	$mol \cdot kg^{-1}$	loguniform, lower value = 1.84×10^{-6} upper value = 1.84×10^{-4}	Table A-1
IRFRAV(01)	The instantly released fraction of ^{14}C inventory in used fuel	1.300×10^{-1}		uniform, lower value = 1.0×10^{-2} upper value = 0.25	Section 5.5.1.2
HLIFE(02)	Half-life of ^{135}Cs	2.300×10^{6}	a	constant	
INVPKG(02)	The initial amount of ^{135}Cs in the used-fuel matrix in the vault expressed in moles per kilogram total initial ^{238}U	1.76×10^{-4}	$mol \cdot kg^{-1}$	lognormal geometric mean = 1.76×10^{-4} geometric standard deviation = 1.5 lower truncation quantile = 1.0×10^{-5} upper truncation quantile = 0.99999	Table A-1
IRFRAV(02)	The instantly released fraction of ^{135}Cs inventory in used fuel	8.100×10^{-2}		normal, mean = 8.1×10^{-2} standard deviation = 1.0×10^{-2} lower truncation value = 1.2×10^{-2} upper truncation value = 0.25	Section 5.5.1.2

continued...

TABLE E-1 (continued)

Sampled Values

Code Name	Definition	Median Value	Units	Probability Density Attributes	Location in Text
HLIFE(03)	Half-life of ^{129}I	1.570×10^{7}	a	constant	Table A-2
INVPKG(03)	The initial amount of ^{129}I in the used-fuel matrix in the vault expressed in moles per kilogram total initial ^{238}U	3.47×10^{-4}	$mol \cdot kg^{-1}$	lognormal geometric mean = 3.47×10^{-4} geometric standard deviation = 1.5 lower truncation quantile = 1.0×10^{-5} upper truncation quantile = 0.99999	Table A-1
IRFRAV(03)	The instantly released fraction of ^{129}I inventory in used fuel	8.100×10^{-2}		normal, mean = 8.1×10^{-2} standard deviation = 1.0×10^{-2} lower truncation value = 1.2×10^{-2} upper truncation value = 0.25	Section 5.5.1.2
HLIFE(04)	Half-life of ^{59}Ni	7.500×10^{4}	a	constant	Table A-2
INVPKG(04)	The initial amount of ^{59}Ni in the used-fuel matrix in the vault expressed in moles per kilogram total initial ^{238}U	$3.55 \times 10^{-}$	$mol \cdot kg^{-1}$	loguniform, lower value = 3.55×10^{-7} upper value = 3.55×10^{-5}	Table A-1
IRFRAV(04)	The instantly released fraction of ^{59}Ni inventory in used fuel	0.00000		constant	Section 5.5.1.2
HLIFE(05)	Half-life of ^{107}Pd	6.50×10^{6}	a	constant	Table A-2
INVPKG(05)	The initial amount of ^{107}Pd in the used-fuel matrix of the vault expressed in moles per kilogram total initial ^{238}U	5.08×10^{-4}	$mol \cdot kg^{-1}$	loguniform, lower value = 5.08×10^{-5} upper value = 5.08×10^{-3}	Table A-1
IRFRAV(05)	The instantly released fraction of ^{107}Pd inventory in used fuel	0.00000		constant	Section 5.5.1.2
HLIFE(06)	Half-life of ^{79}Se	6.50×10^{4}	a	constant	Table A-2
INVPKG(06)	The initial amount of ^{79}Se in the used-fuel matrix in the vault expressed in moles per kilogram total initial ^{238}U	1.64×10^{-5}	$mol \cdot kg^{-1}$	lognormal geometric mean = 1.64×10^{-5} geometric standard deviation = 2.0 lower truncation quantile = 1×10^{-5} upper truncation quantile = 0.99999	Table A-1
IRFRAV(06)	The instantly released fraction of ^{79}Se inventory in used fuel	8.10×10^{-2}		normal, mean = 8.1×10^{-2} standard deviation = 1.0×10^{-2} lower truncation value = 1.2×10^{-2} upper truncation value = 0.25	Section 5.5.1.2

continued...

TABLE E-1 (continued)

Sampled Values

Code Name	Definition	Median Value	Units	Probability Density Attributes	Location in Text
HLIFE(07)	Half-life of ^{99}Tc	2.13×10^{5}	a	constant	Table A-2
INVPKG(07)	The initial amount of ^{99}Tc in the used-fuel matrix in the vault expressed in moles per kilogram total initial ^{238}U	2.07×10^{-3}	$mol \cdot kg^{-1}$	lognormal geometric mean = 2.07×10^{-3} geometric standard deviation = 1.5 lower truncation quantile = 1×10^{-5} upper truncation quantile = 0.99999	Table A-1
IRFRAV(07)	The instantly released fractions of ^{99}Tc inventory in used fuel	6.0×10^{-2}		normal, mean = 6.0×10^{-2} standard deviation = 1.0×10^{-2} lower truncation value = 1.2×10^{-2} upper truncation value = 0.25	Section 5.5.1.2
HLIFE(08)	Half-life of ^{238}U	4.46800×10^{9}	a	constant	Table A-2
INVPKG(08)	The initial amount of ^{238}U in the used-fuel matrix in the vault expressed in moles per kilogram total initial ^{238}U	4.14×10^{0}	$mol \cdot kg^{-1}$	lognormal geometric mean = 4.14 geometric standard deviation = 1.003 lower truncation quantile = 1×10^{-3} upper truncation quantile = 0.999	Table A-1
IRFRAV(08)	The instantly released fractions of ^{238}U inventory in used fuel	0.00000		constant	Section 5.5.1.2

continued...

TABLE E-1 (continued)

Calculated Values

Code Name	Definition	Median Value	Units	Location in Text
DARBV(11)	Darcy velocity in sector 11 of buffer	0.000000+00	$m \cdot a^{-1}$	Section 6.8.1
DARKV(11)	Darcy velocity in sector 11 of backfill	6.60069×10^{-8}	$m \cdot a^{-1}$	Table 6-4 Section 6.8.4 & 6.8.2
IFRACV(11)	The defect fraction for sector 11 leading to premature failure of the containers	0.00000		Section 4.7.5.1
MATPRV(01)	The distance from the waste form that the matrices precipitate. To flag the case where the matrices do not precipitate, MATPRV is given a negative value, and to flag the case where a user-supplied dissolution rate is used, MATPRV is given a value larger than the effective thickness of the buffer. The value has been truncated at a lower bound determined by kinetic constraints on how fast the waste form can dissolve.	-1.00000×10^{0}	m	Section 5.5.3.2
POTBUF	Buffer potential	2.45955×10^{-1}	V	Section 5.5.3.2
SMTCBV(11,01)	Source mass transfer coefficient for sector 11 for used fuel	6.16432×10^{-7}	$m \cdot a^{-1}$	Section 6.8.2
SMTCFV(11,01)	Backfill mass transfer coefficient for sector 11 for used fuel	2.15542×10^{-7}	$m \cdot a^{-1}$	Section 6.8.2
SOLMAT(01)	The solubility of UO_2 in the buffer groundwater	1.55040×10^{-7}	$mol \cdot m^{-3}$	Section 5.5.2.2

continued...

TABLE E-1 (continued)

Calculated Values

Code Name	Definition	Median Value	Units	Location in Text
*INVTRY(01)	The initial amount of ^{14}C in the vault with rooms above the fracture zone LD1	3.19008×10^{3}	mol	Appendix A
*INVTRY(02)	The initial amount of ^{135}Cs in the vault with rooms above the fracture zone LD1	3.05138×10^{4}	mol	Appendix A
*INVTRY(03)	The initial amount of ^{129}I in the vault with rooms above the fracture zone LD1	6.01608×10^{4}	mol	Appendix A
*INVTRY(04)	The initial amount of ^{59}Ni in the vault with rooms above the fracture zone LD1	6.15478×10^{2}	mol	Appendix A
*INVTRY(05)	The initial amount of ^{107}Pd in the vault with rooms above the fracture zone LD1	8.80740×10^{4}	mol	Appendix A
*INVTRY(06)	The initial amount of ^{79}Se in the vault with rooms above the fracture zone LD1	2.84333×10^{3}	mol	Appendix A
*INVTRY(07)	The initial amount of ^{99}Tc in the vault with rooms above the fracture zone LD1	3.58884×10^{5}	mol	Appendix A
*INVTRY(08)	The initial amount of ^{238}U in the vault with rooms above the fracture zone LD1	7.17768×10^{8}	mol	Appendix A

*Note: In the postclosure assessment case study, rooms were removed from LD1 so that the sum of the fractional sector areas was 0.93284 instead of 1.0. This means that the actual inventories used are the product of 0.93284 and the inventories given in the table.

continued...

TABLE E-1 (continued)

Calculated Values

Code Name	Definition	Median Value	Units	Location in Text
PMSTCV(11,01)	Precipitation mass transfer coefficient for sector 11 ^{14}C	4.36762×10^{-5}	$m \cdot a^{-1}$	Section 6.8.2
PMSTCV(11,02)	Precipitation mass transfer coefficient for sector 11 ^{135}Cs	6.76829×10^{-6}	$m \cdot a^{-1}$	Section 6.8.2
PMSTCV(11,03)	Precipitation mass transfer coefficient for sector 11 ^{129}I	2.90405×10^{-7}	$m \cdot a^{-1}$	Section 6.8.2
PMSTCV(11,04)	Precipitation mass transfer coefficient for sector 11 ^{59}Ni	2.33600×10^{-5}	$m \cdot a^{-1}$	Section 6.8.2
PMSTCV(11,05)	Precipitation mass transfer coefficient for sector 11 ^{107}Pd	5.00751×10^{-7}	$m \cdot a^{-1}$	Section 6.8.2
PMSTCV(11,06)	Precipitation mass transfer coefficient for sector 11 ^{79}Se	9.25217×10^{-6}	$m \cdot a^{-1}$	Section 6.8.2
PMSTCV(11,07)	Precipitation mass transfer coefficient for sector 11 ^{99}Tc	2.27601×10^{-3}	$m \cdot a^{-1}$	Section 6.8.2
SOLUNN(07)	The solubility of ^{99}Tc inside the container calculated from element-specific solubilities	1.50595×10^{-5}	$mol \cdot m^{-3}$	Section 5.5.3.2
SOLUNN(08)	The solubility of ^{238}U inside the container calculated from element-specific solubilities	1.55044×10^{-7}	$mol \cdot m^{-3}$	Section 5.5.3.2
SOLUNX(07)	The minimum of the solubility of ^{99}Tc in the container and the solubility of ^{99}Tc in the buffer	2.87232×10^{-6}	$mol \cdot m^{-3}$	Section 5.5.3.2
SOLUNX(08)	The minimum of the solubility of ^{238}U in the container and the solubility of ^{238}U in the buffer	1.55040×10^{-7}	$mol \cdot m^{-3}$	Section 5.5.3.2

continued...

TABLE E-1 (continued)

Calculated Values

Code Name	Definition	Median Value	Units	Location in Text
SOLUPP(07)	The solubilities of ^{99}Tc inside the buffer calculated from element-specific solubilities	2.87232×10^{-6}	$mol \cdot m^{-3}$	Section 5.5.3.2
SOLUPP(08)	The solubilities of radionuclides inside the buffer calculated from element-specific solubilities	1.55040×10^{-7}	$mol \cdot m^{-3}$	Section 5.5.3.2
VMSTBV(11,01)	Buffer mass transfer coefficient sector 11 ^{14}C	3.60000×10^{-3}	$m \cdot a^{-1}$	Section 6.8.2
VMSTBV(11,02)	Buffer mass transfer coefficient sector 11 ^{135}Cs	1.46240×10^{0}	$m \cdot a^{-1}$	Section 6.8.2
VMSTBV(11,03)	Buffer mass transfer coefficient sector 11 ^{129}I	3.60000×10^{-3}	$m \cdot a^{-1}$	Section 6.8.2
VMSTBV(11,04)	Buffer mass transfer coefficient sector 11 ^{59}Ni	5.09199×10^{-1}	$m \cdot a^{-1}$	Section 6.8.2
VMSTBV(11,05)	Buffer mass transfer coefficient sector 11 ^{107}Pd	1.41781×10^{-6}	$m \cdot a^{-1}$	Section 6.8.2
VMSTBV(11,06)	Buffer mass transfer coefficient sector 11 ^{79}Se	3.60000×10^{-3}	$m \cdot a^{-1}$	Section 6.8.2
VMSTBV(11,07)	Buffer mass transfer coefficient sector 11 ^{99}Tc	2.92026×10^{-7}	$m \cdot a^{-1}$	Section 6.8.2
VMSTFV(11,01)	Backfill mass transfer coefficient sector 11 ^{14}C	3.51285×10^{-7}	$m \cdot a^{-1}$	Section 6.8.2
VMSTFV(11,02)	Backfill mass transfer coefficient sector 11 ^{135}Cs	2.89286×10^{-1}	$m \cdot a^{-1}$	Section 6.8.2

continued ...

TABLE E-1 (concluded)

Calculated Values

Code Name	Definition	Median Value	Units	Location in Text
VMSTFV(11,03)	Backfill mass transfer coefficient sector 11 ^{129}I	3.51285×10^{-7}	$m \cdot a^{-1}$	Section 6.8.2
VMSTFV(11,04)	Backfill mass transfer coefficient sector 11 ^{59}Ni	1.41429×10^{-1}	$m \cdot a^{-1}$	Section 6.8.2
VMSTFV(11,05)	Backfill mass transfer coefficient sector 11 ^{107}Pd	6.80920×10^{-7}	$m \cdot a^{-1}$	Section 6.8.2
VMSTFV(11,06)	Backfill mass transfer coefficient sector 11 ^{79}Se	8.03571×10^{-2}	$m \cdot a^{-1}$	Section 6.8.2
VMSTFV(11,07)	Backfill mass transfer coefficient sector 11 ^{99}Tc	2.02386×10^{-7}	$m \cdot a^{-1}$	Section 6.8.2
TABSAV(01)	Total amount of ^{14}C released from the vault up to 10^5 a	1.85007×10^{0}	mol	Appendix E
TABSAV(02)	Total amount of ^{135}Cs released from the vault up to 10^5 a	2.34324×10^{3}	mol	Appendix E
TABSAV(03)	Total amount of ^{129}I released from the vault up to 10^5 a	5.19347×10^{2}	mol	Appendix E
TABSAV(04)	Total amount of ^{59}Ni released from the vault up to 10^5 a	2.68638×10^{-6}	mol	Appendix E
TABSAV(05)	Total amount of ^{107}Pd released from the vault up to 10^5 a	3.67917×10^{-4}	mol	Appendix E
TABSAV(06)	Total amount of ^{79}Se released from the vault up to 10^5 a	1.47775×10^{2}	mol	Appendix E
TABSAV(07)	Total amount of ^{99}Tc released from the vault up to 10^5 a	1.72363×10^{-10}	mol	Appendix E

TABLE E-2

IMPORTANCE RANKING OF VAULT PARAMETERS FOR INTEGRATED RELEASE OF ^{129}I UP TO 10^5 a (TABSAV(03))

Parameter Name	Correlation Coefficient of log(value)	Upper 95% Confidence Limit	Lower 95% Confidence Limit	Spearman's Coefficient	Fractional Factorial Relative Importance
DFBANI	0.56	0.60	0.52	0.54 ± .06	8.6
INVPKG(03)	0.53	0.57	0.48	0.52 ± .06	9.9
VSCALE	0.46	0.50	0.41	0.44 ± .06	9.7
SGTORA(01)	-0.28	-0.22	-0.34	-0.29 ± .06	-2.2
DFKANI	-0.15	-0.09	-0.21	-0.16 ± .06	-1.7
IRFRAV(03)	0.14	0.20	0.08	0.13 ± .06	1.6

TABLE E-3

IMPORTANCE RANKING OF VAULT PARAMETERS FOR INTEGRATED RELEASE OF ^{14}C UP TO 10^5 a (TABSAV(01))

Parameter Name	Correlation Coefficient of log(value)	Upper 95% Confidence Limit	Lower 95% Confidence Limit	Spearman's Coefficient	Fractional Factorial Relative Importance
INVPKG(01)	0.74	0.77	0.71	0.75 ± .06	1.0×10^2
IRFRAV(01)	0.42	0.46	0.36	0.38 ± .06	1.9×10^1
DFBANI	0.36	0.41	0.30	0.33 ± .06	1.6×10^1
VSCALE	0.25	0.31	0.19	0.24 ± .06	1.3×10^1
SGTORA(01)	-0.12	-0.06	-0.18	-0.11 ± .06	-1.7
DIFFN(01)	0.11	0.17	0.10	0.11 ± .06	2.1
MUA	0.09	0.15	0.03	0.06 ± .06	1.8
DFKANI	-0.09	-0.02	-0.15	-0.08 ± .06	-1.3

TABLE E-4

IMPORTANCE RANKING OF VAULT PARAMETERS FOR MAXIMUM DOSE OF ^{129}I UP TO 10^5 a (MXLDT03)

Parameter Name	Correlation Coefficient of log(value)	Upper 95% Confidence Limit	Lower 95% Confidence Limit	Spearman's Coefficient	Fractional Factorial Relative Importance
SGTORA(01)	-0.55	-0.51	-0.60	-0.56 ± .06	-1.9×10^3
DFBANI	0.18	0.24	0.12	0.18 ± .06	5.6
INVPKG(03)	0.13	0.19	0.06	0.11 ± .06	8.4
VSCALE	0.12	0.18	0.06	0.09 ± .06	3.8×10^1
IRFRAV(03)	0.08	0.14	0.02	0.08 ± .06	1.8
DFKANI	-0.07	-0.01	-0.13	-0.07 ± .06	-2.2

TABLE E-5

IMPORTANCE RANKING OF VAULT PARAMETERS FOR MAXIMUM DOSE OF ^{14}C UP TO 10^5 a (MXLDT01)

Parameter Name	Correlation Coefficient of log(value)	Upper 95% Confidence Limit	Lower 95% Confidence Limit	Spearman's Coefficient	Fractional Factorial Relative Importance
SGTORA(01)	-0.45	-0.40	-0.50	-0.48 ± .06	-2.0×10^4
VSCALE	0.36	0.41	0.30	0.30 ± .06	6.1×10^6
INVPKG(01)	0.18	0.24	0.12	0.20 ± .06	3.1×10^2
DIFFN(01)	0.14	0.20	0.08	0.12 ± .06	9.6×10^1
IRFRAV(01)	0.12	0.18	0.05	0.10 ± .06	3.5×10^1
DFBANI	0.10	0.16	0.03	0.12 ± .06	1.9×10^1
MUA	0.08	0.14	0.02	0.09 ± .06	6.2
DFKANI	-0.06	0.00	-0.13	-0.07 ± .06	-1.1×10^1

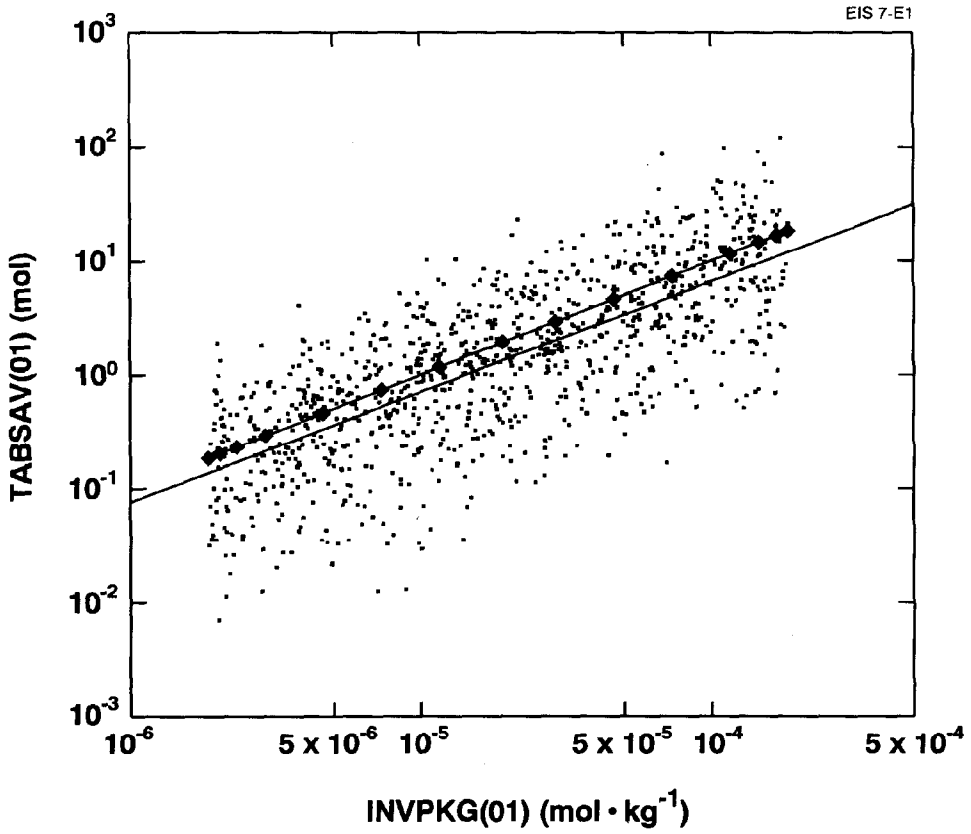

FIGURE E-1: Time-Integrated Vault Release of ^{14}C up to 10^5 a in Moles (TABSAV(01)) Versus Initial Inventory of ^{14}C in Moles per Kilogram of Uranium (INVPKG(01)). A scatter plot is shown with both axes on a logarithmic scale as well as the line generated by varying INVPKG(01) through its allowed range while holding all other parameters fixed at their median values (◆-◆). The line generated by linear least squares regression on the logarithm of the parameter values is also shown (—).

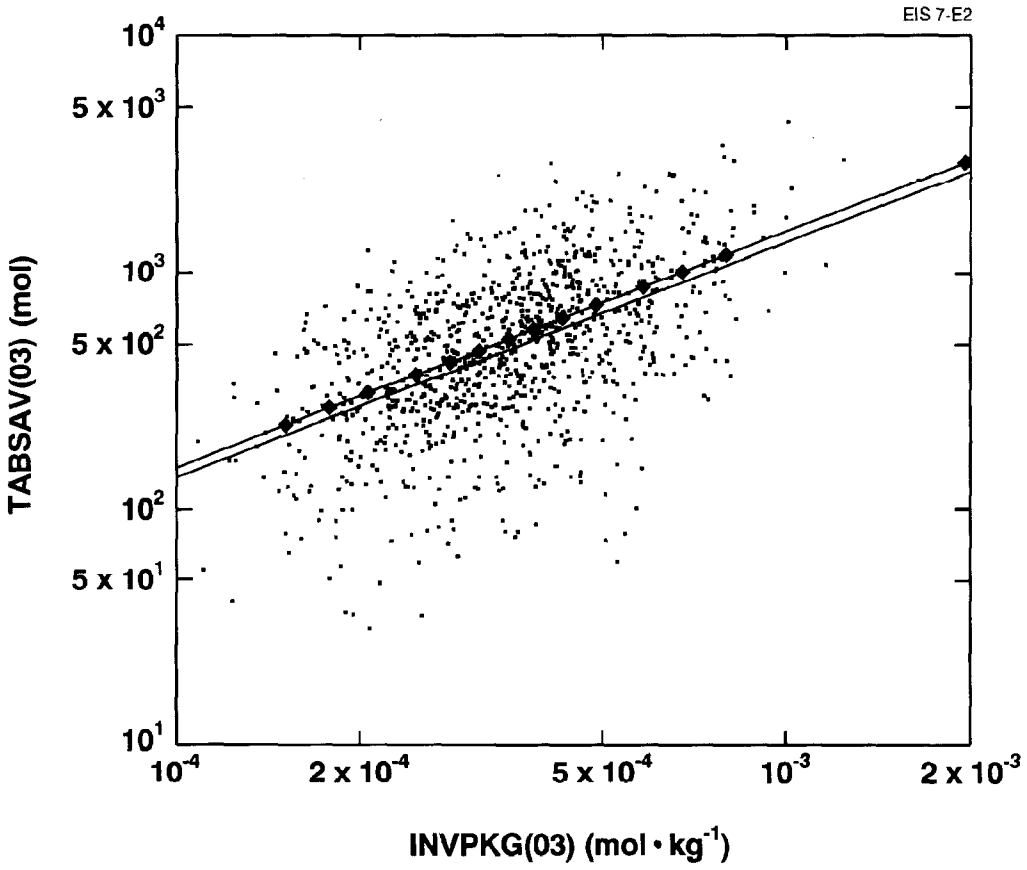

FIGURE E-2: Time-Integrated Vault Release of ^{129}I up to 10^5 a in Moles (TABSAV(03)) Versus Initial Inventory of ^{129}I in Moles Per Kilogram of Uranium (INVPKG(03)). A scatter plot is shown with both axes on a logarithmic scale as well as the line generated by varying INVPKG(03) through its allowed range while holding all other parameters fixed at their median values (◆-◆). The line generated by linear least squares regression on the logarithm of the parameter values is also shown (—).

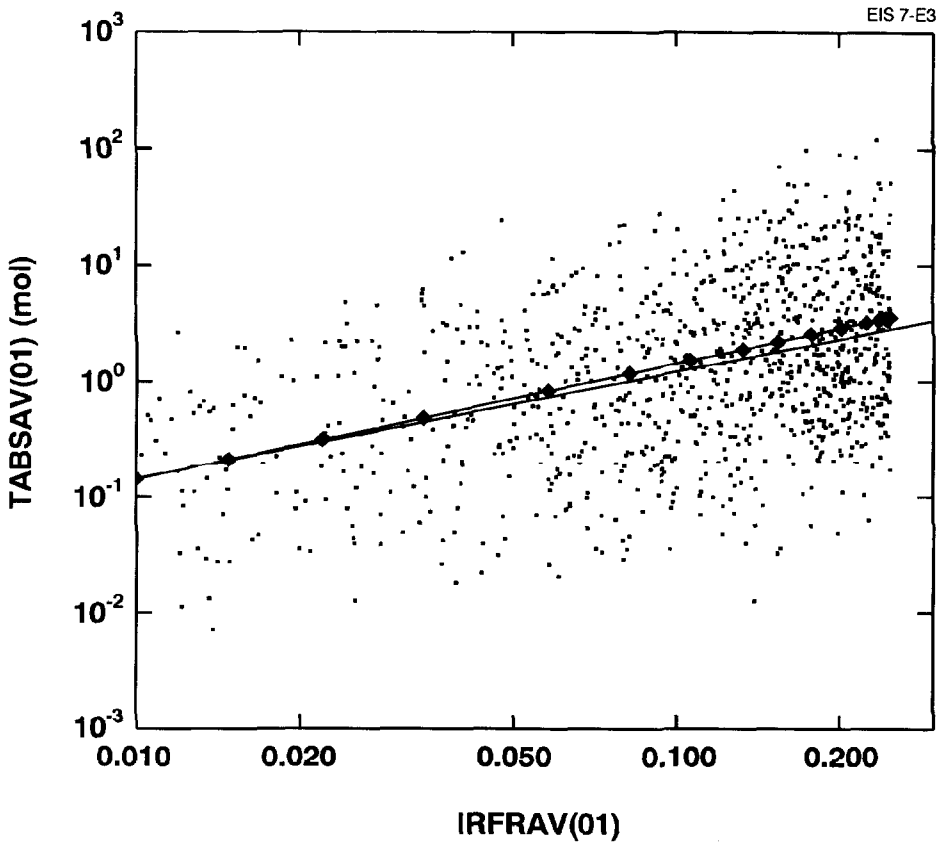

FIGURE E-3: Time-Integrated Vault Release of ^{14}C up to 10^5 a in Moles (TABSAV(01)) Versus Instant Release Fraction of ^{14}C (IRFRAV(01)). A scatter plot is shown with both axes on a logarithmic scale as well as the line generated by varying IRFRAV(01) through its allowed range while holding all other parameters fixed at their median values (◆-◆). The line generated by linear least squares regression on the logarithm of the parameter values is also shown (—).

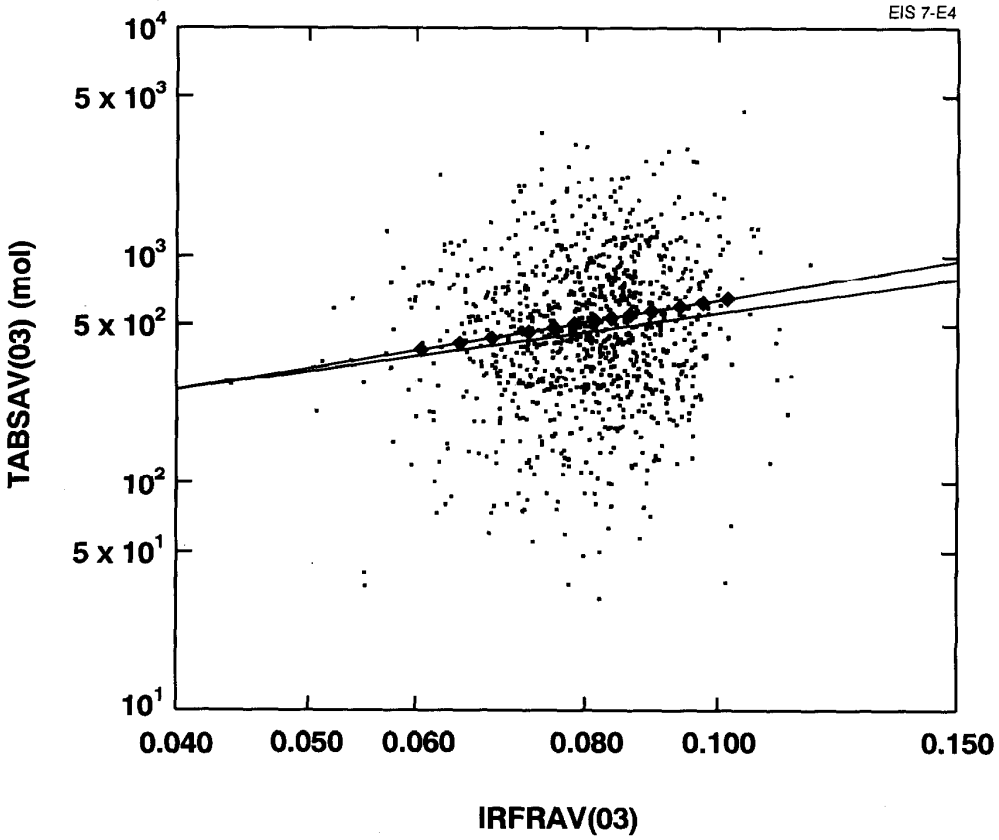

FIGURE E-4: Time-Integrated Vault Release of ^{129}I up to 10^5 a in Moles (TABSAV(03)) Versus Instant Release Fraction of ^{129}I (IRFRAV(03)). A scatter plot is shown with both axes on a logarithmic scale as well as the line generated by varying IRFRAV(03) through its allowed range while holding all other parameters fixed at their median values (◆-◆). The line generated by linear least squares regression on the logarithm of the parameter values is also shown (—).

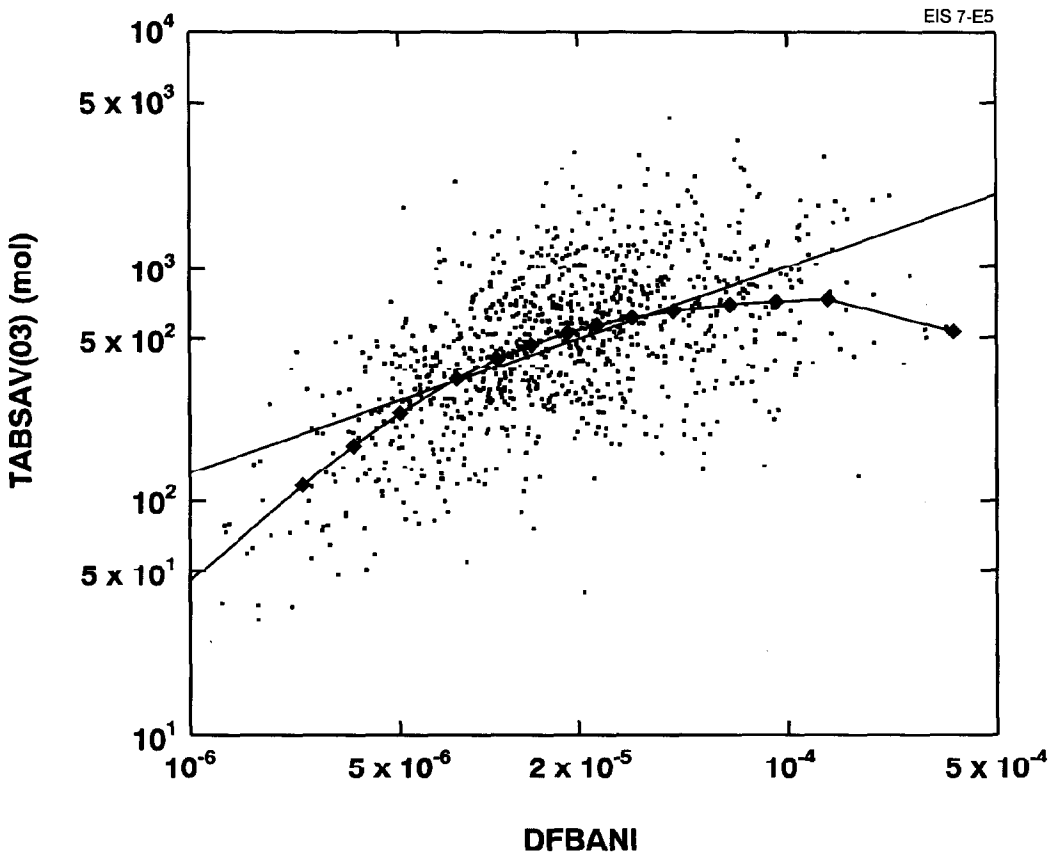

FIGURE E-5: Time-Integrated Vault Release of ^{129}I up to 10^5 a in Moles (TABSAV(03)) Versus Anion Correlation Parameter (DFBANI). A scatter plot is shown with both axes on a logarithmic scale as well as the line generated by varying DFBANI through its allowed range while holding all other parameters fixed at their median values (◆-◆). The line generated by linear least squares regression on the logarithm of the parameter values is also shown (—).

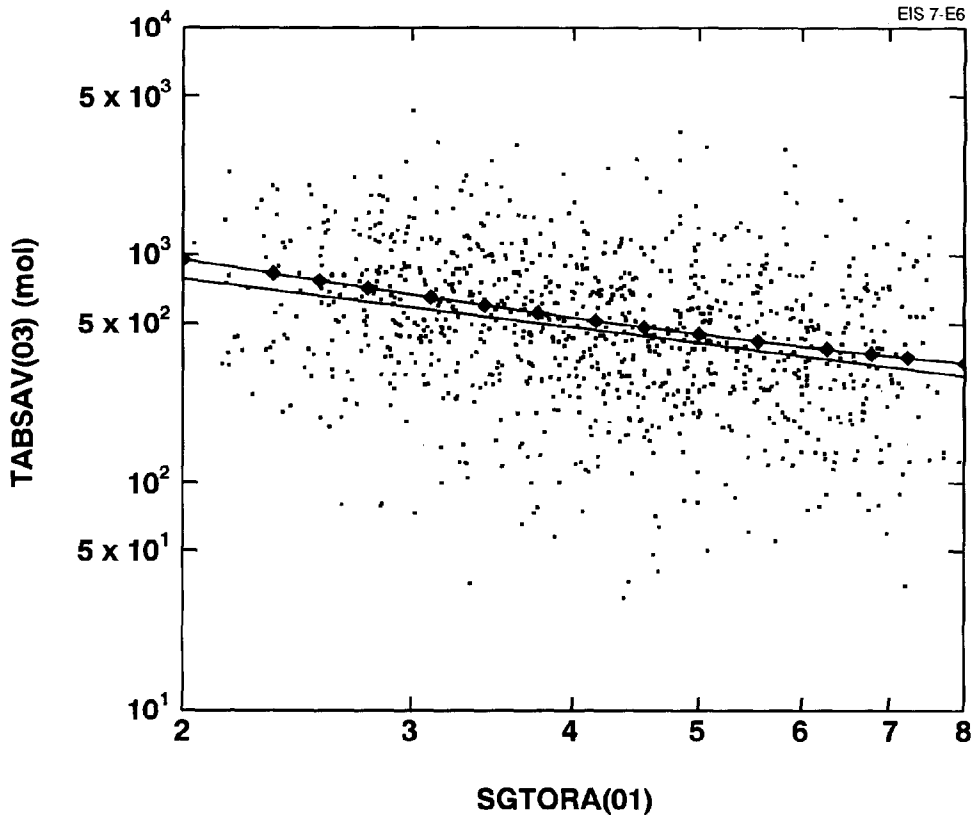

FIGURE E-6: Time-Integrated Vault Release of ^{129}I up to 10^5 a in Moles (TABSAV(03)) Versus Tortuosity of Lower Rock (SGTORA(01)). A scatter plot is shown with both axes on a logarithmic scale as well as the line generated by varying SGTORA(01) through its allowed range while holding all other parameters fixed at their median values (◆-◆). The line generated by linear least squares regression on the logarithm of the parameter values is also shown (—).

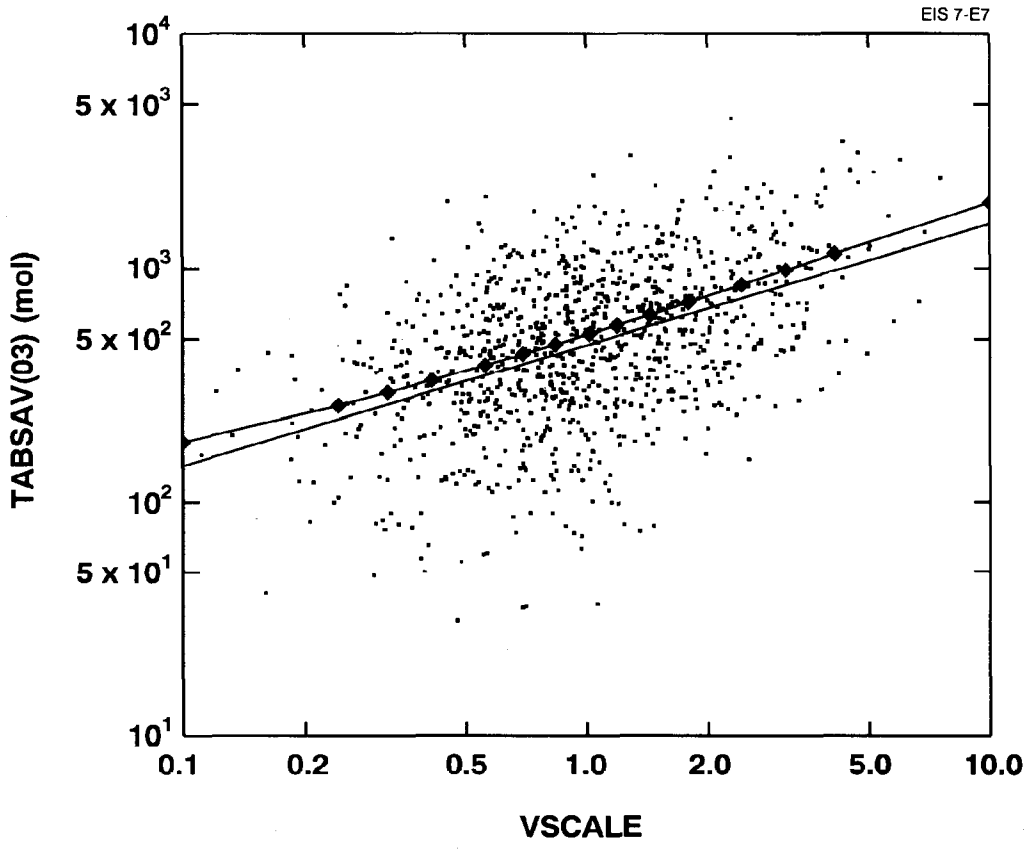

FIGURE E-7: Time-Integrated Vault Release of ^{129}I up to 10^5 a in Moles (TABSAV(03)) Versus Velocity Scaling Factor (VSCALE). A scatter plot is shown with both axes on a logarithmic scale as well as the line generated by varying VSCALE through its allowed range while holding all other parameters fixed at their median values (◆-◆) and the line generated by linear least squares regression on the logarithm of the parameter values (—).

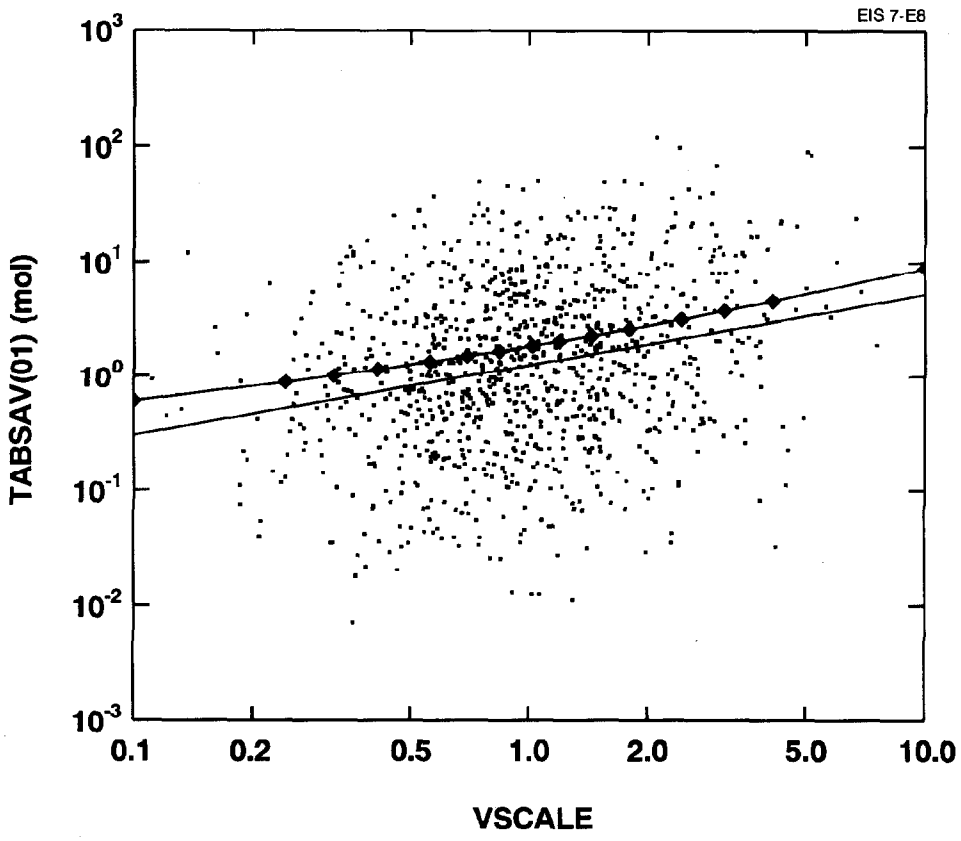

FIGURE E-8: Time-Integrated Vault Release of ^{14}C up to 10^5 a in Moles (TABSAV(01)) Versus Velocity Scaling Factor (VSCALE). A scatter plot is shown with both axes on a logarithmic scale as well as the line generated by varying VSCALE through its allowed range while holding all other parameters fixed at their median values (◆-◆) and the line generated by linear least squares regression on the logarithm of the parameter values (—).

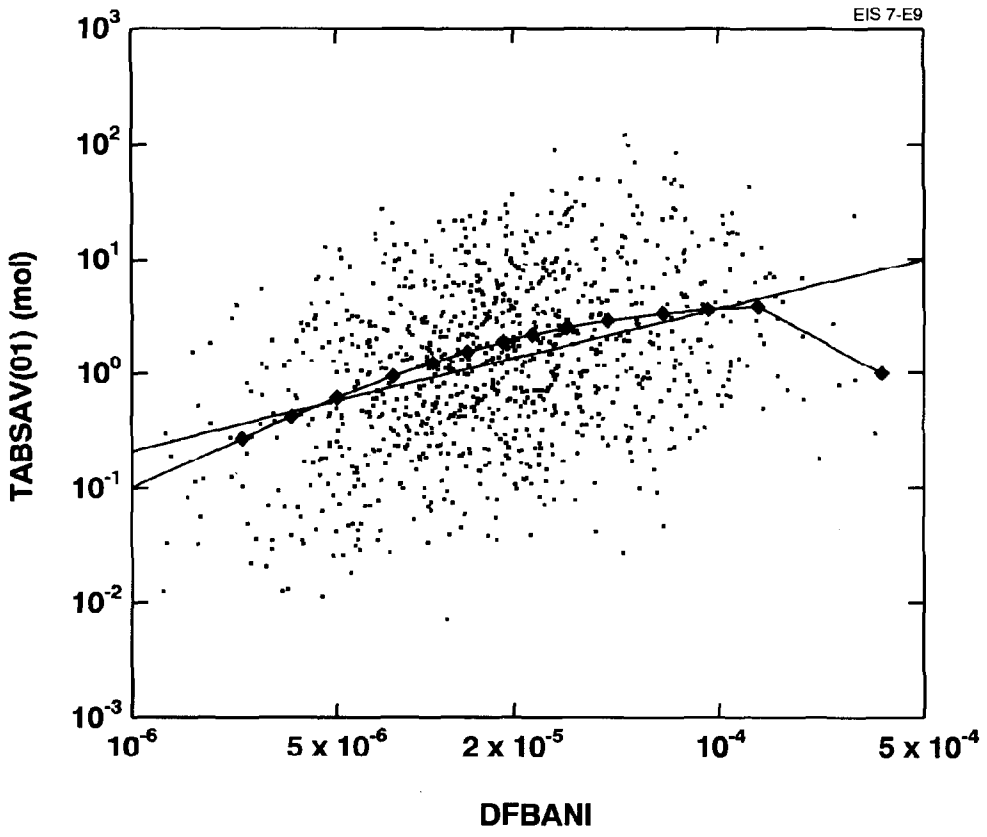

FIGURE E-9: Time-Integrated Vault Release of ^{14}C up to 10^5 a in Moles (TABSAV(01)) Versus Anion Correlation Parameter (DFBANI). A scatter plot is shown with both axes on a logarithmic scale as well as the line generated by varying DFBANI through its allowed range while holding all other parameters fixed at their median values (◆-◆) and the line generated by linear least squares regression on the logarithm of the parameter values (—).

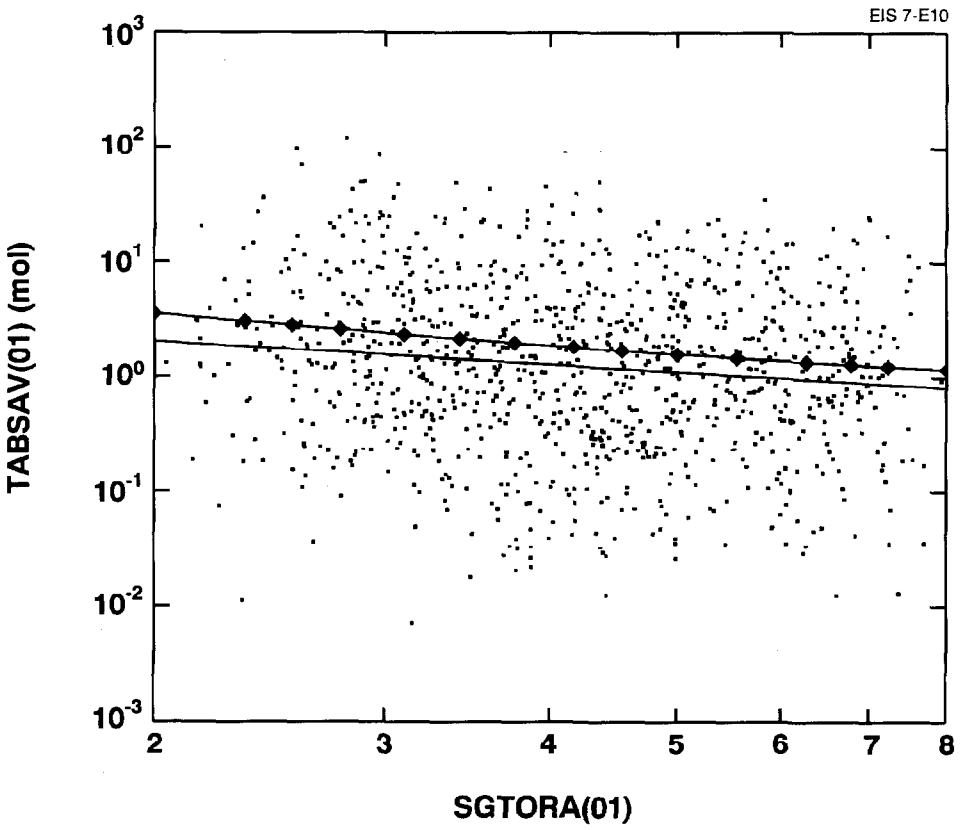

FIGURE E-10: Time-Integrated Vault Release of ^{14}C up to 10^5 a in Moles (TABSAV(01)) Versus Tortuosity of the Lower Rock (SGTORA(01)). A scatter plot is shown with both axes on a logarithmic scale as well as the line generated by varying SGTORA(01) through its allowed range while holding all other parameters fixed at their median values (◆-◆) and the line generated by linear least squares regression on the logarithm of the parameter values (—).

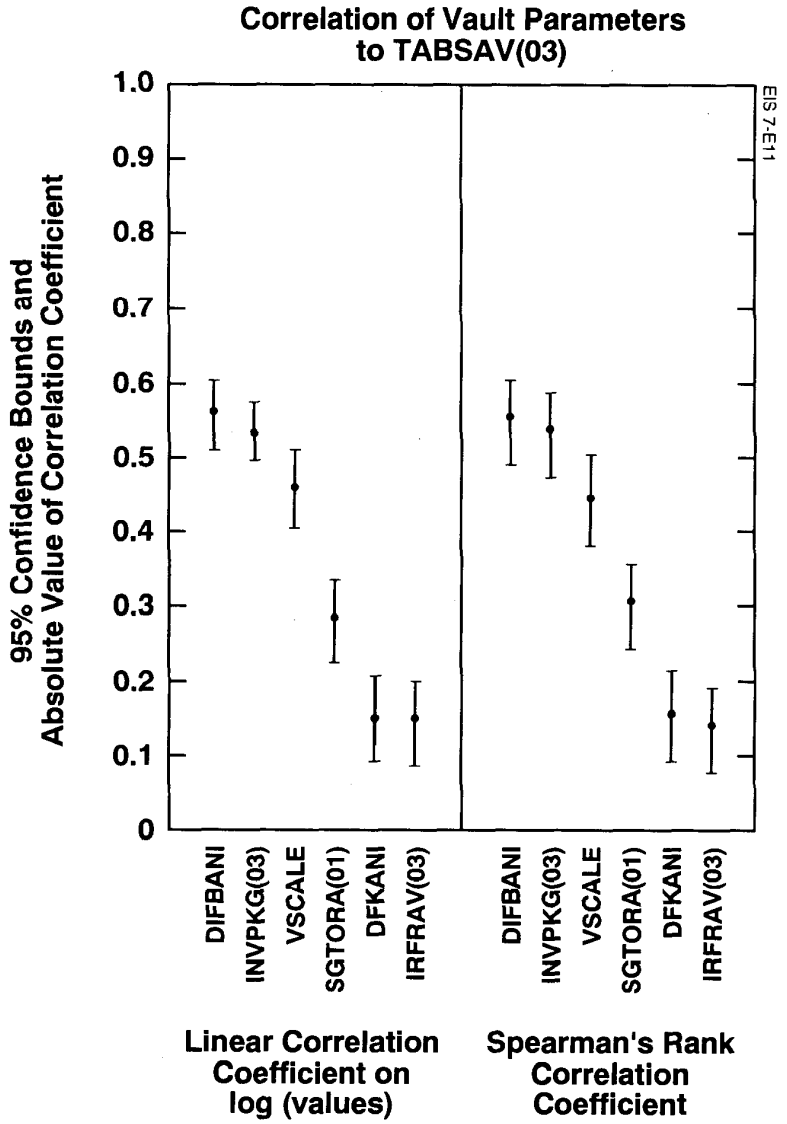

FIGURE E-11: Correlation of Important Vault Parameters to Release of ^{129}I from the Vault Integrated to 10^5 a (TABSAV(03)). The linear correlation coefficient based on the logarithm of parameter values and the Spearman's rank correlation coefficients are given together with the 95% confidence bounds.

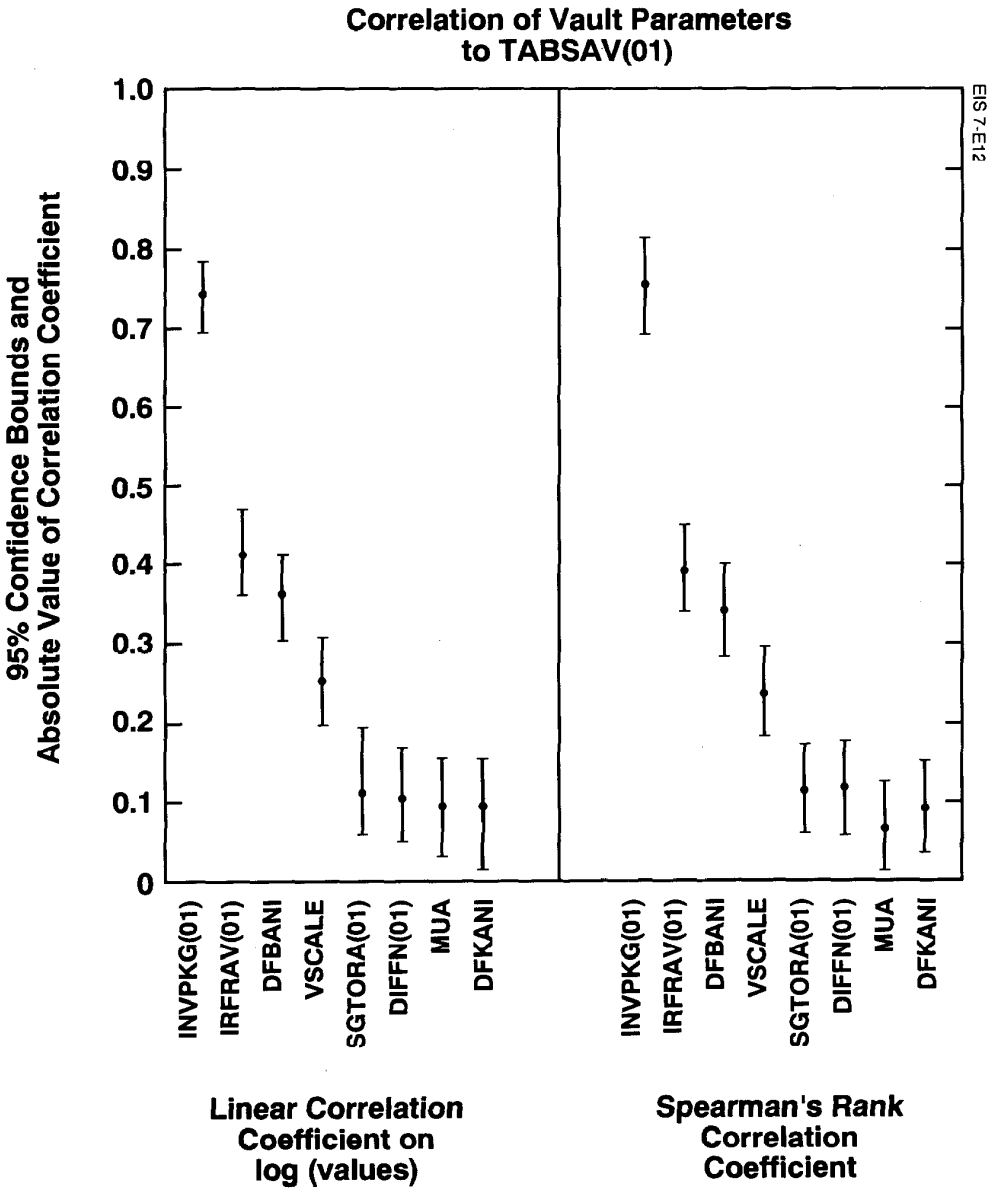

FIGURE E-12: Correlation of Important Vault Parameters to Release of ^{14}C from the Vault Integrated to 10^5 a (TABSAV(01)). The linear correlation coefficient based on the logarithm of parameter values and the Spearman's rank correlation coefficients are given together with the 95% confidence bounds.

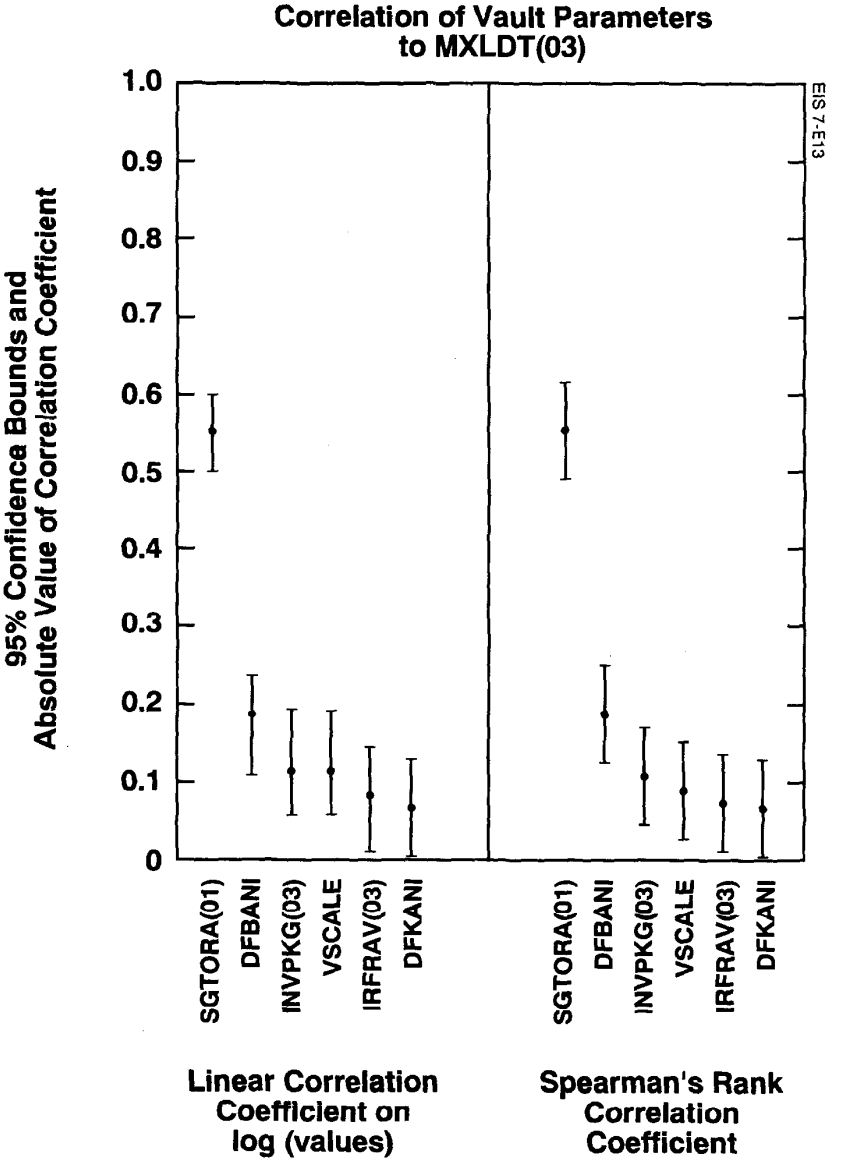

FIGURE E-13: Correlation of Important Vault Parameters to the Maximum Dose of ^{129}I up to 10^5 a (MXLDT(03)). The linear correlation coefficient based on the logarithm of parameter values and the Spearman's rank correlation coefficients are given together with the 95% confidence bounds.

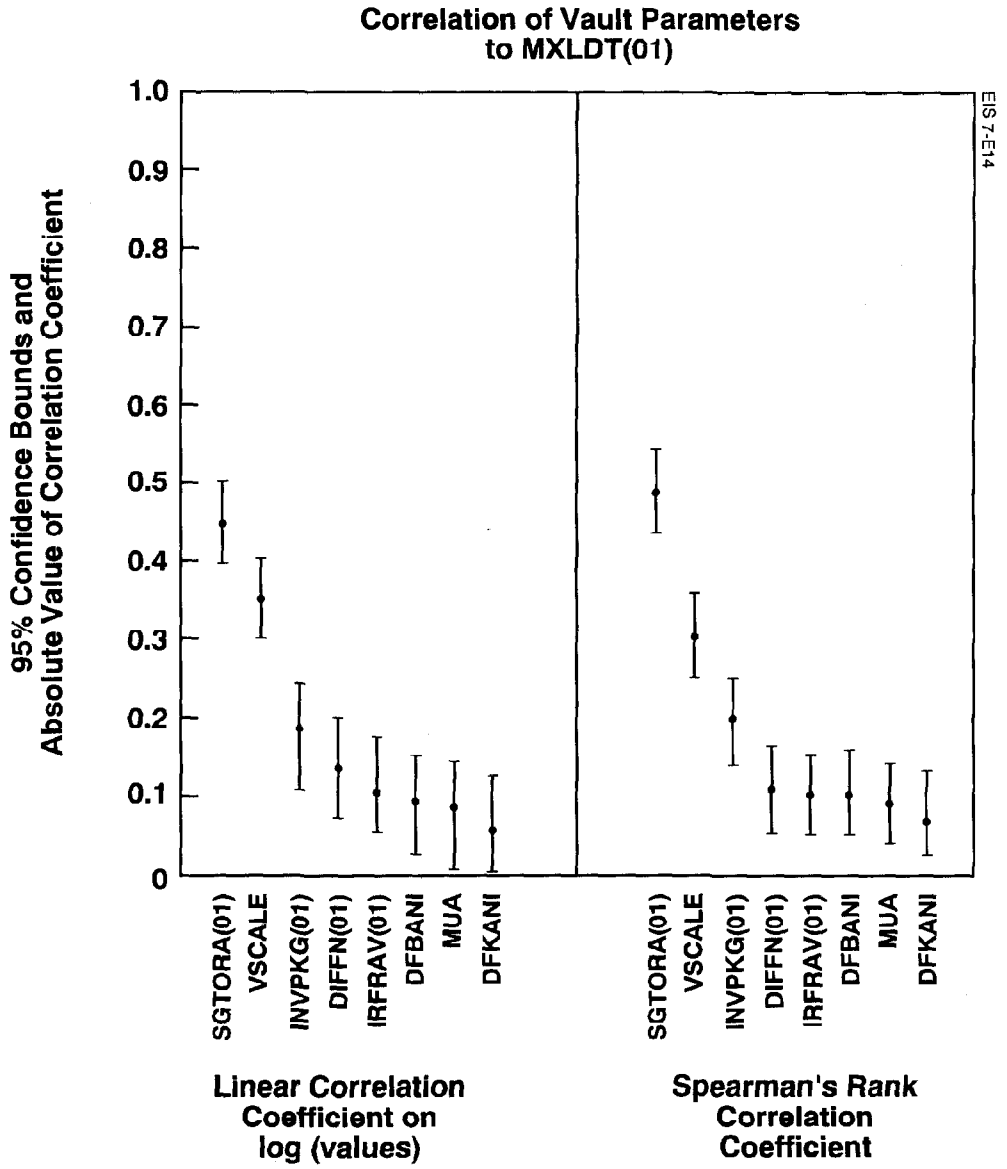

FIGURE E-14: Correlation of Important Vault Parameters to the Maximum Dose of ^{14}C up to 10^5 a (MXLDT(01)). The linear correlation coefficient based on the logarithm of parameter values and the Spearman's rank correlation coefficients are given together with the 95% confidence bounds.

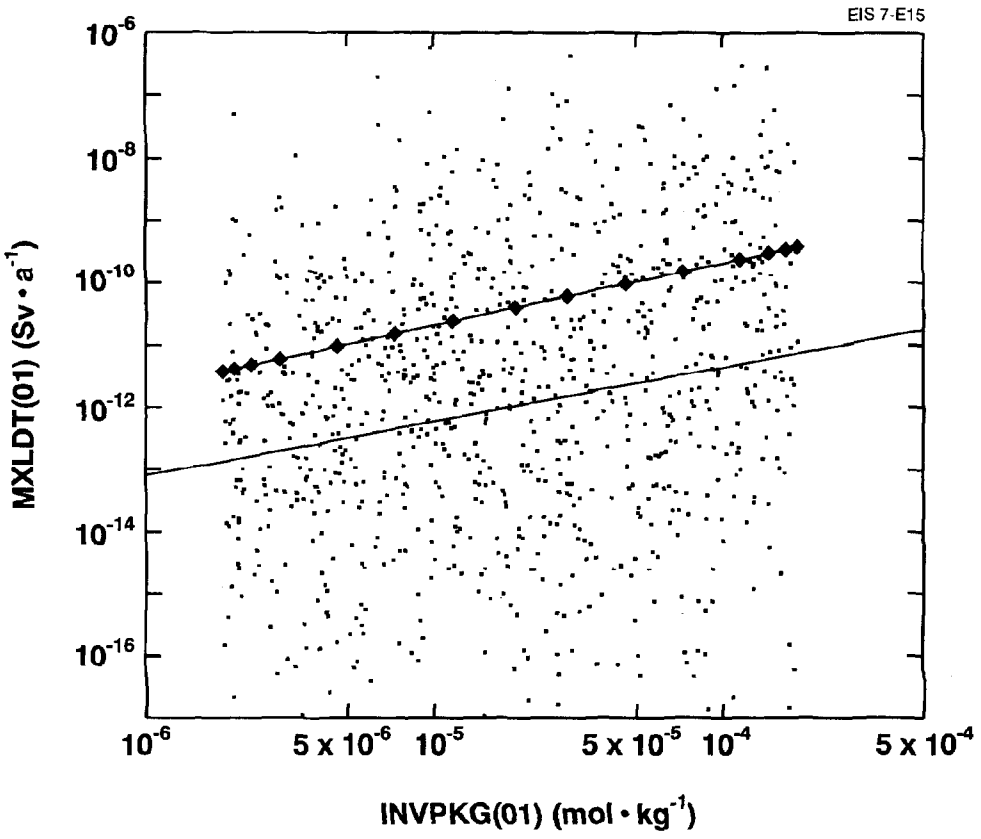

FIGURE E-15: Maximum Dose of ^{14}C up to 10^5 a in $Sv \cdot a^{-1}$ (MXLDT(01)) Versus Initial Inventory of ^{14}C in Moles per Kilogram of Uranium (INVPKG(01)). A scatter plot is shown with both axes on a logarithmic scale as well as the line generated by varying INVPKG(01) through its allowed range while holding all other parameters fixed at their median values (◆-◆) and the line generated by linear least squares regression on the logarithm of the parameter values (—).

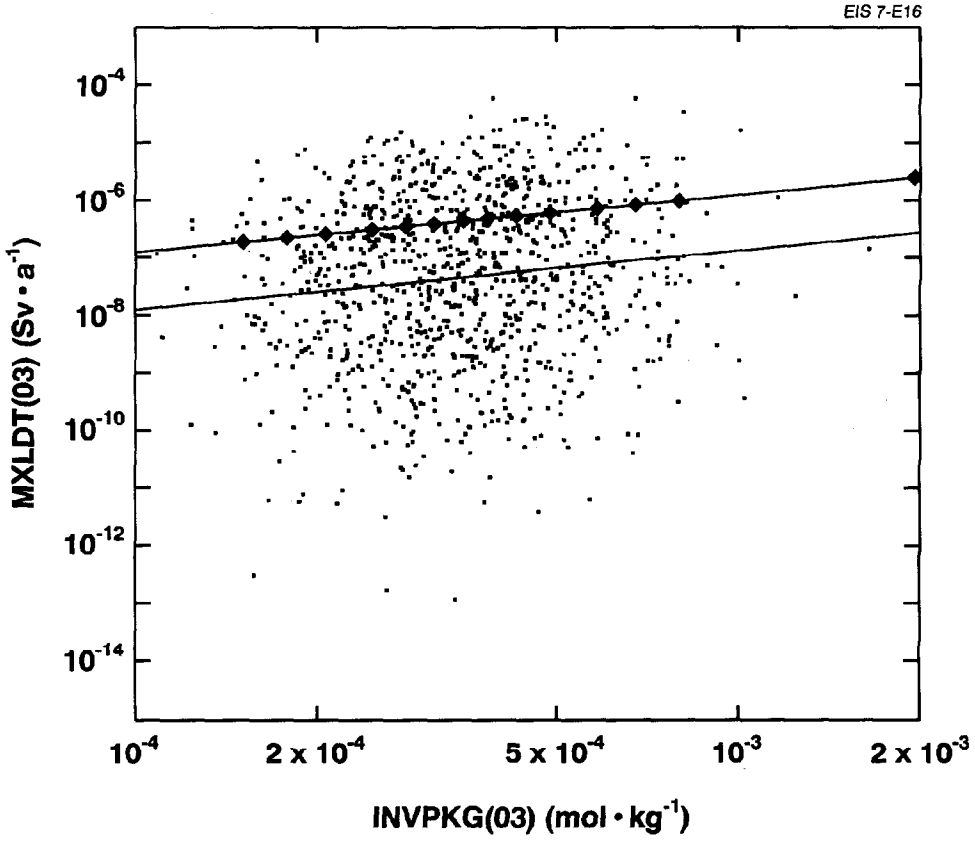

FIGURE E-16: Maximum Dose of ^{129}I up to 10^5 a in $Sv \cdot a^{-1}$ (MXLDT(03)) Versus Initial Inventory of ^{129}I in Moles per Kilogram of Uranium (INVPKG(03)). A scatter plot is shown with both axes on a logarithmic scale as well as the line generated by varying INVPKG(03) through its allowed range while holding all other parameters fixed at their median values (◆-◆) and the line generated by linear least squares regression on the logarithm of the parameter values (—).

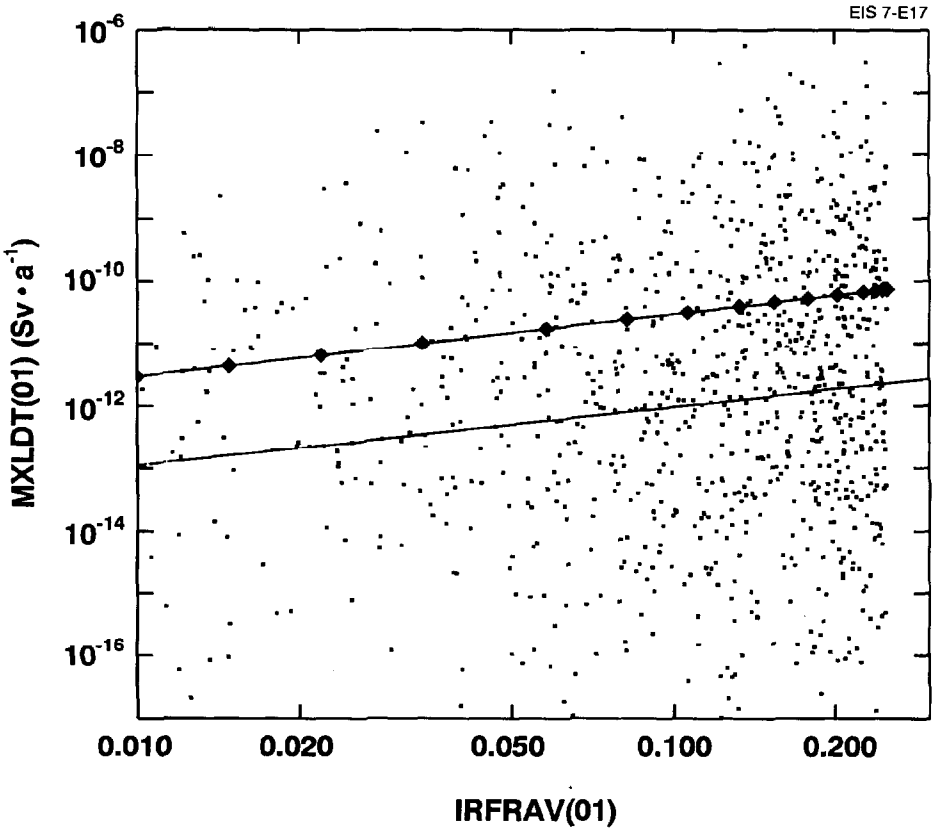

FIGURE E-17: Maximum Dose of ^{14}C up to 10^5 a in $Sv \cdot a^{-1}$ (MXLDT(01)) Versus Instant-Release Fraction of ^{14}C (IRFRAV(01)). A scatter plot is shown with both axes on a logarithmic scale as well as the line generated by varying IRFRAV(01) through its allowed range while holding all other parameters fixed at their median values (◆-◆) and the line generated by linear least squares regression on the logarithm of the parameter values (—).

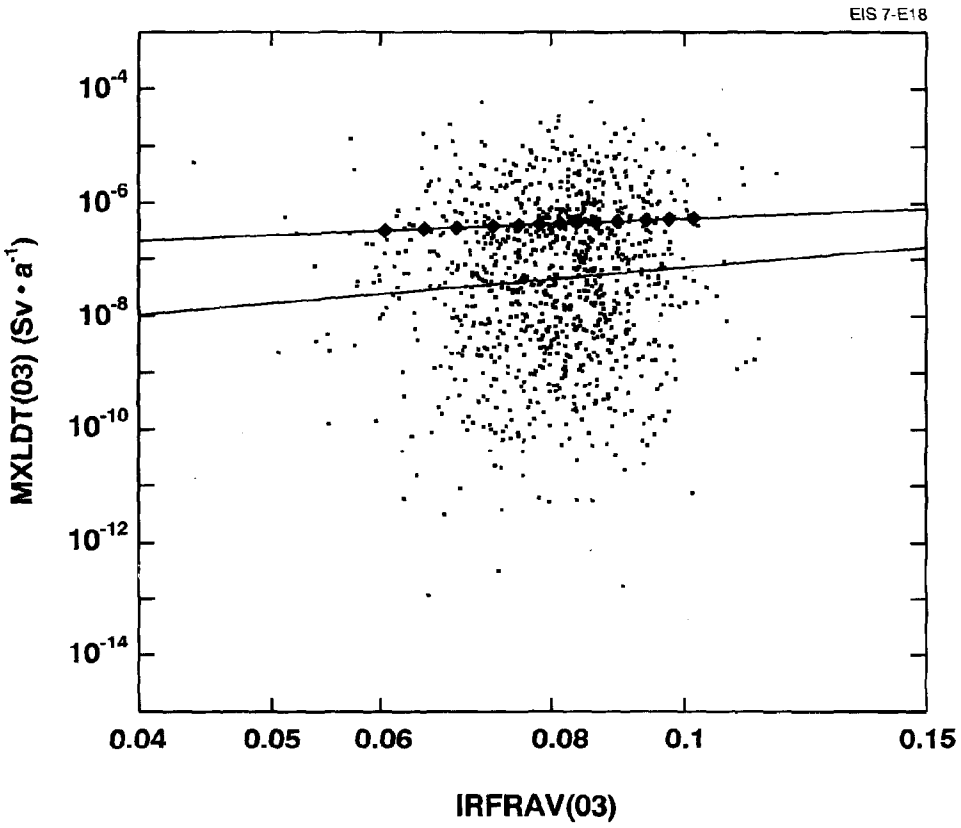

FIGURE E-18: Maximum Dose of ^{129}I up to 10^5 a in $Sv \cdot a^{-1}$ (MXLDT(03)) versus Instant-Release Fraction of ^{129}I (IRFRAV(03)). A scatter plot is shown with both axes on a logarithmic scale as well as the line generated by varying IRFRAV(03) through its allowed range while holding all other parameters fixed at their median values (◆-◆) and the line generated by linear least squares regression on the logarithm of the parameter values (—).

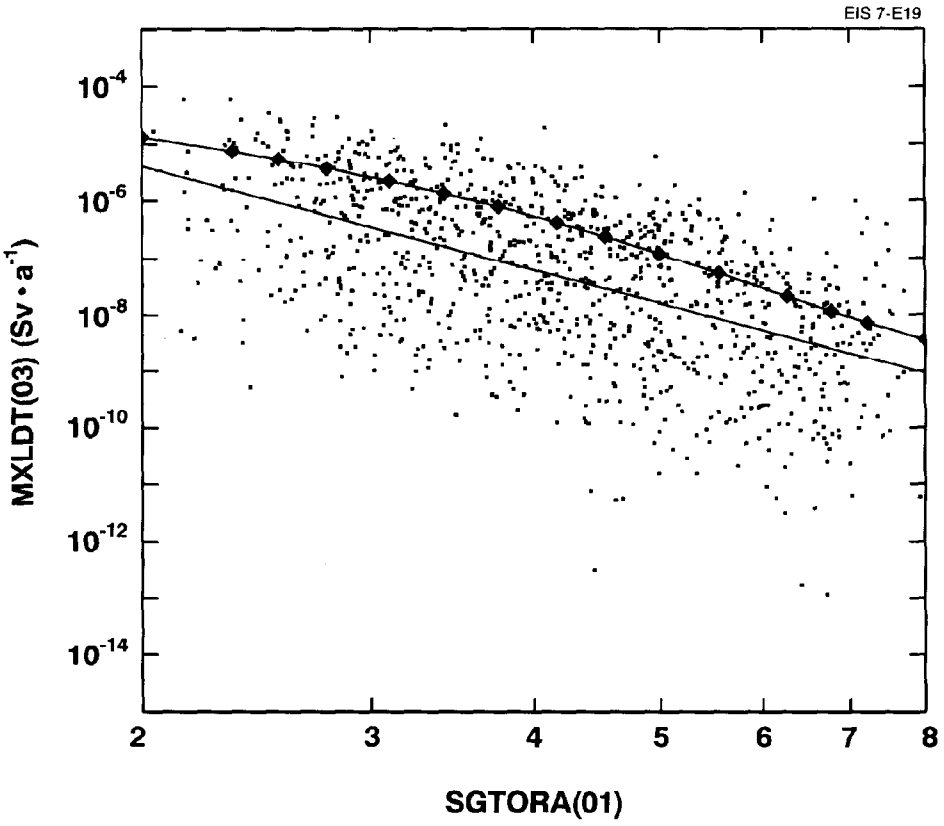

FIGURE E-19: Maximum Dose of ^{129}I up to 10^5 years in $Sv \cdot a^{-1}$ (MXLDT(03)) Versus Tortuosity of Lower Rock (SGTORA(01)). A scatter plot is shown with both axes on a logarithmic scale as well as the line generated by varying SGTORA(01) through its allowed range while holding all other parameters fixed at their median values (◆-◆) and the line generated by linear least squares regression on the logarithm of the parameter values (—).

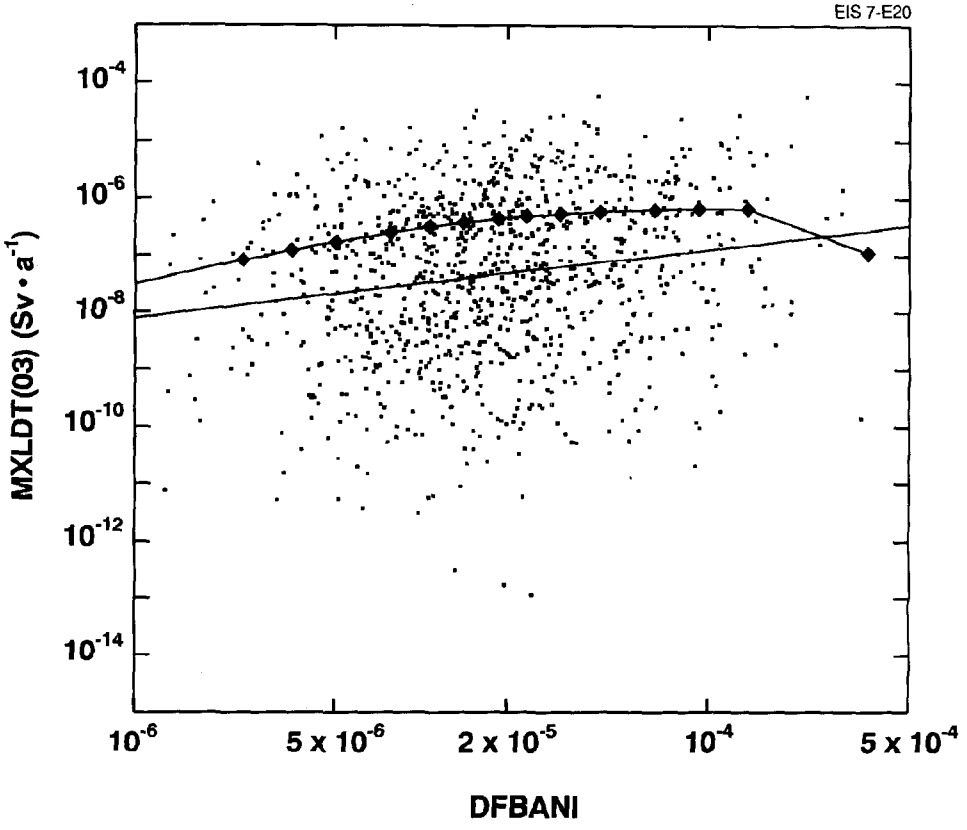

FIGURE E-20: Maximum Dose of ^{129}I up to 10^5 a in $Sv \cdot a^{-1}$ (MXLDT(03)) Versus Anion Correlation Parameter (DFBANI). A scatter plot is shown with both axes on a logarithmic scale as well as the line generated by varying DFBANI through its allowed range while holding all other parameters fixed at their median values (◆-◆) and the line generated by linear least squares regression on the logarithm of the parameter values (—).

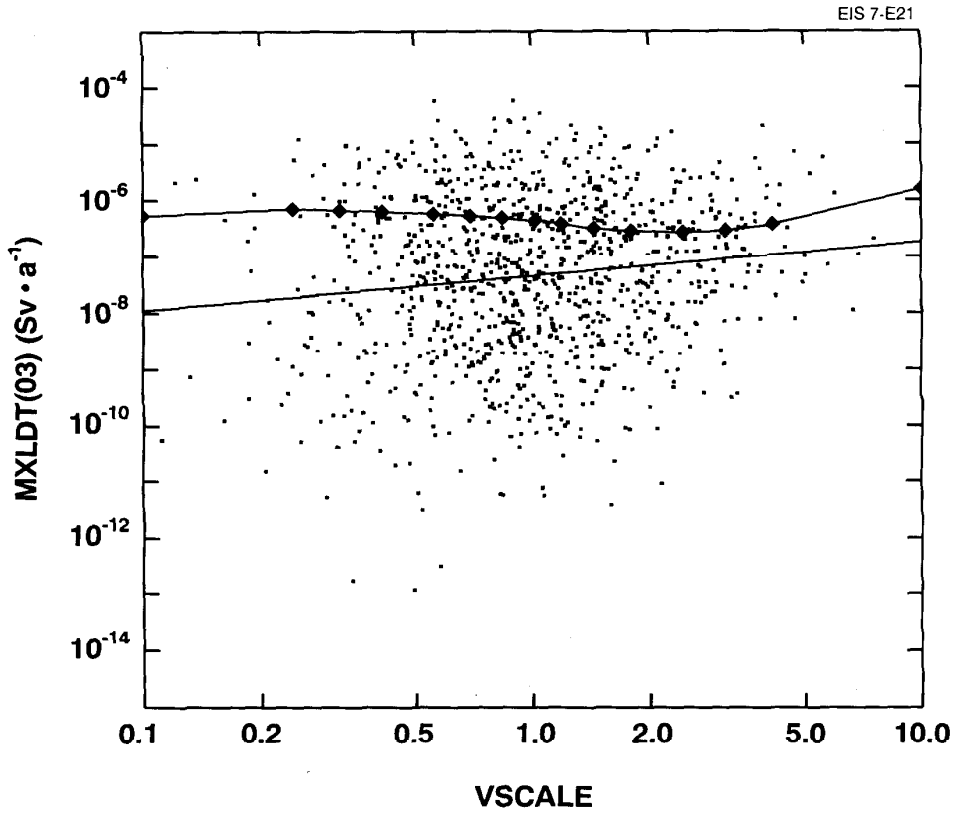

FIGURE E-21: Maximum Dose of ^{129}I up to 10^5 a in $Sv \cdot a^{-1}$ (MXLDT(03)) Versus Velocity Scaling Factor (VSCALE). A scatter plot is shown with both axes on a logarithmic scale as well as the line generated by varying VSCALE through its allowed range while holding all other parameters fixed at their median values (◆-◆) and the line generated by linear least squares regression on the logarithm of the parameter values (—).

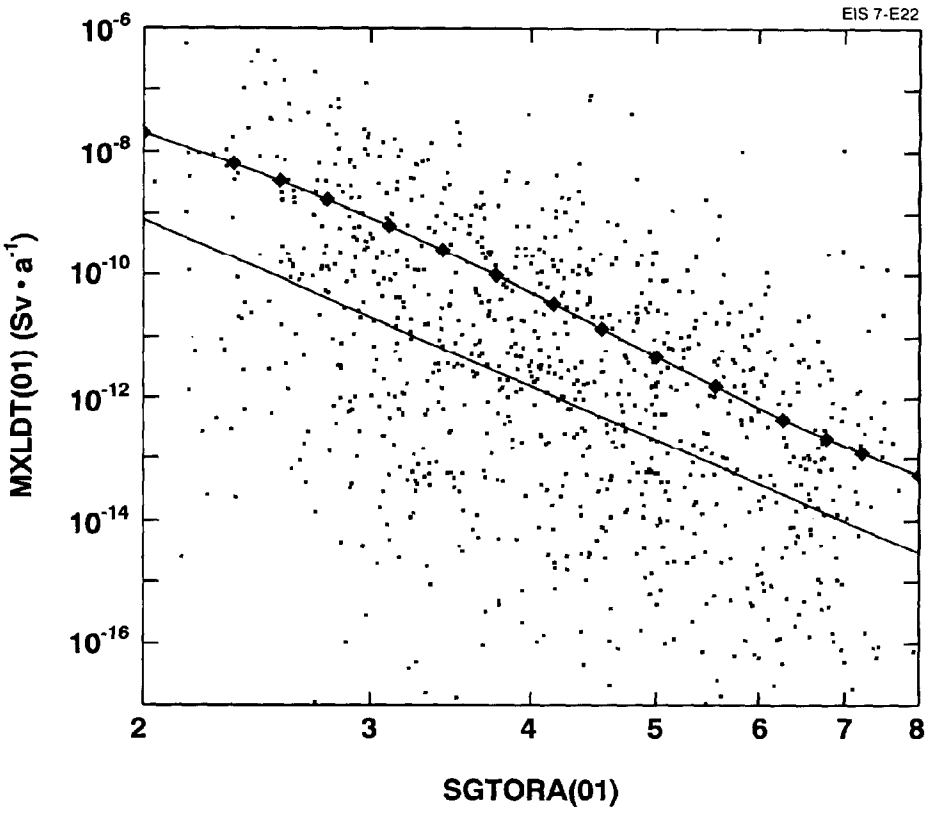

FIGURE E-22: Maximum Dose of ^{14}C up to 10^5 a in Sv-a^{-1} (MXLDT(01)) Versus Tortuosity of Lower Rock (SGTORA(01)). A scatter plot is shown with both axes on a logarithmic scale as well as the line generated by varying SGTORA(01) through its allowed range while holding all other parameters fixed at their median values (◆-◆) and the line generated by linear least squares regression on the logarithm of the parameter values (—).

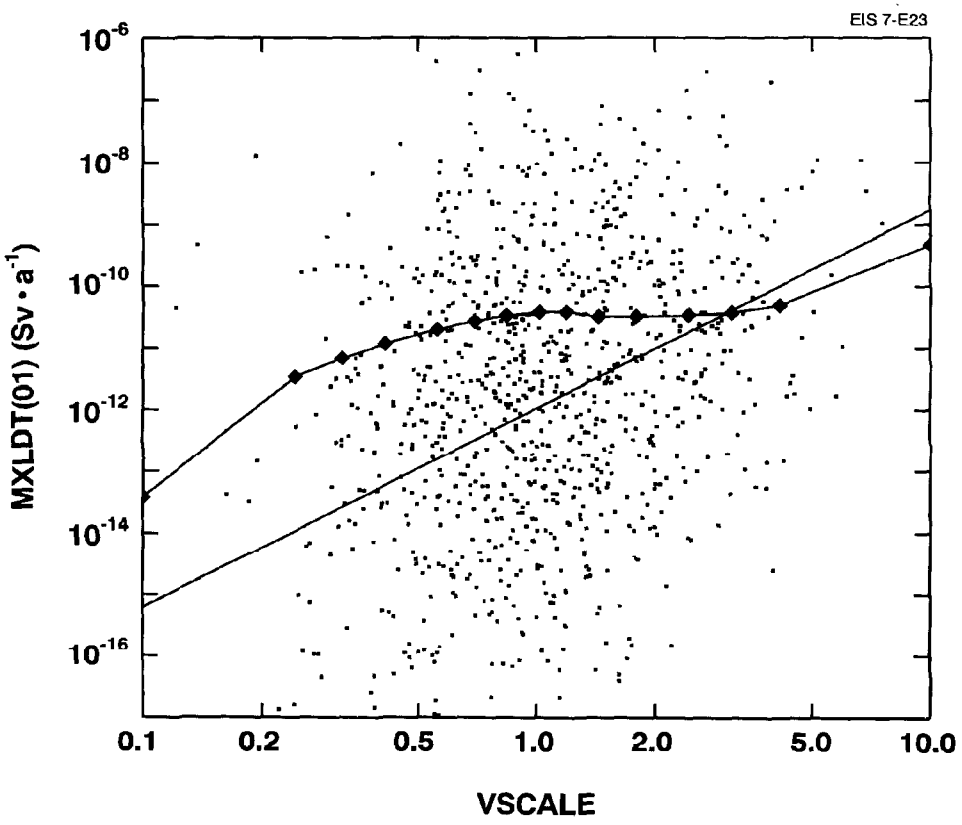

FIGURE E-23: Maximum Dose of ^{14}C up to 10^5 years in $Sv \cdot a^{-1}$ (MXLDT(01)) Versus Velocity Scaling Factor (VSCALE). A scatter plot is shown with both axes on a logarithmic scale as well as the line generated by varying VSCALE through its allowed range while holding all other parameters fixed at their median values (◆-◆) and the line generated by linear least squares regression on the logarithm of the parameter values (—).

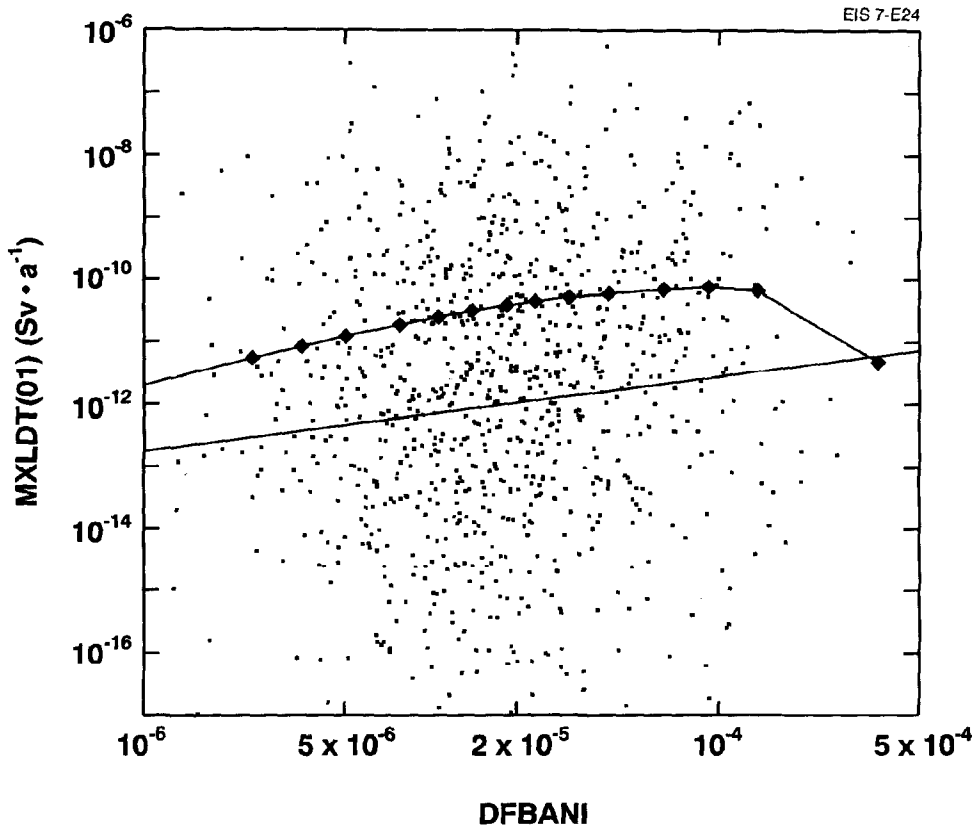

FIGURE E-24: Maximum Dose of ^{14}C up to 10^5 a in $Sv \cdot a^{-1}$ (MXLDT(01)) Versus Anion Correlation Parameter (DFBANI). A scatter plot is shown with both axes on a logarithmic scale as well as the line generated by varying DFBANI through its allowed range while holding all other parameters fixed at their median values (◆-◆) and the line generated by linear least squares regression on the logarithm of the parameter values (—).